Draft version October 21, 2026
Typeset using LaTeX **default** style in AASTeX7.0.1

Fundamental Noise Processes in Pulsar Timing

James M. Cordes [1], Stella Koch Ocker [2,3], Shami Chatterjee [1], Timothy Dolch [4,5], Ross J. Jennings [6], Michael T. Lam [7,8,9] and Jacob E. Turner [10]

[1] *Cornell Center for Astrophysics and Planetary Science, and Department of Astronomy, Cornell University, Ithaca, NY 14853, USA*
[2] *Cahill Center for Astronomy and Astrophysics, California Institute of Technology, Pasadena, CA 91125, USA*
[3] *Carnegie Science Observatories, Pasadena, CA 91101, USA*
[4] *Department of Physics, Hillsdale College, 33 E. College Street, Hillsdale, MI 49242, USA*
[5] *Eureka Scientific, 2452 Delmer Street, Suite 100, Oakland, CA 94602-3017, USA*
[6] *NANOGrav Physics Frontiers Center Postdoctoral Fellow*
[7] *SETI Institute, 339 N Bernardo Ave Suite 200, Mountain View, CA 94043, USA*
[8] *School of Physics and Astronomy, Rochester Institute of Technology, Rochester, NY 14623, USA*
[9] *Laboratory for Multiwavelength Astrophysics, Rochester Institute of Technology, Rochester, NY 14623, USA*
[10] *Green Bank Observatory, P.O. Box 2, Green Bank, WV 24944, USA*

ABSTRACT

The stability of spin rates and emission regions of radio-emitting neutron stars (pulsars) has enabled remarkable advances, including the detection of exoplanets, testing theories of gravity, and stimulating the vigorous exploration of a new window in gravitational wave astronomy an nanohertz frequencies.

An ideal astrophysical clock would emit identical pulses at a constant rate, propagating along single geodesics through a perfect vacuum. In reality, the timing precision achievable with pulsars is limited by spin noise, variability in the beam produced in a complex magnetosphere, and multipath propagation through a turbulent interstellar medium, with additional limitations from uncertainties in the changing pulsar – observatory vector and instrumental effects.

Here we present the fundamentals of pulsar timing, its current limitations, and prospects for improvements in timing precision. We develop metrics to assess the timing quality of a pulsar and use them to evaluate sources currently included in pulsar timing arrays (PTAs) as a means for characterizing the quality of future pulsar discoveries. With increases in telescope sensitivity, pulsar timing precision will increasingly be limited by propagation effects in the interstellar medium. We identify sources of non-Gaussianity in timing residuals and separate out effects that are chromatic or achromatic, as well as effects that vary on short (seconds to minutes) and longer (days to months) timescales.

Modern wide-bandwidth receivers provide simultaneous arrival times across a range of frequencies, enabling the robust mitigation of chromatic interstellar effects and the identification of non-Gaussian events superimposed on random fluctuations. We recommend changes to timing procedures that leverage instrumentation advances to improve timing precision.

Keywords: Neutron stars, pulsar timing array, interstellar medium, interstellar turbulence, interstellar scattering.

Email: jmc33@cornell.edu, corresponding author

Contents

1. Introduction 6

2. Nomenclature 9

3. The gist of pulsar timing and its limitations 9
3.1. What limits arrival time precision and timing predictions? 12

4. Pulsar spin stability and orbital noise 16
4.1. Types of spin noise 17
4.2. Structure function slopes and spectral indices 17
4.2.1. Constraints from phase structure functions 19
4.2.2. Constraints from scaling of variance with T 19
4.3. Allan variance for red noise 20
4.4. Scaling laws for the variance and spectrum of red spin noise 22
4.5. Comparison with the nanohertz GW stochastic background 23
4.6. Orbital noise 25

5. Elements of pulsar signals and their propagation 27
5.1. From fields to baseband voltages 28
5.2. Stokes parameters from baseband fields 29
5.3. Pulsar emission is modulated polarized shot noise 30
5.4. Pulse shapes and average profiles 31
5.5. Plasma propagation effects at radio wavelengths 33
5.6. Interstellar impulse response functions 38
5.7. Intensity statistics for scintillated amplitude modulated shot noise 40
5.8. Gravitational lensing 40

6. TOA estimation using template matching 41
6.1. Evaluation using pulsar and telescope parameters 42
6.2. Full Stokes template fitting 44
6.3. Chromatic changes in profile shape 46
6.4. Shape shifters: pulsars with epoch-dependent profile shapes 46

7. TOA variations from single-pulse stochasticity 49
7.1. Pulsar self noise 49
7.2. Timing jitter from stochastic pulse envelope modulations 49
7.2.1. Single component pulses 49
7.2.2. Multiple component pulses 50
7.3. Jitter vs. noise dominated TOA errors 51
7.4. Estimation of jitter properties 53

8. Instrumental effects 55
8.1. Instrumental polarization and calibration 55
8.2. Digitization and interference 57
8.3. Time transfer to the Solar System barycenter 58
8.4. Astrometric errors, proper motion, and parallax 60

9. ISM structure and propagation scaling laws 60
9.1. Interstellar electron density wavenumber spectrum 62
9.2. Propagation through plasma fluctuations with a power-law wavenumber spectrum 63
9.3. Scaling laws for propagation effects from a power-law density spectrum 64
9.4. Scintillation and scattering regimes 67
9.5. Example calculations using Table 4 69

10. Interstellar analytics 70
10.1. Dispersion measures 70

10.2. Angular deviations and broadening 72
10.3. Scintillations: dynamic spectrum and secondary spectrum 73
10.4. Pulse broadening 75
10.5. Cyclic spectrum (field correlation function) 79

11. A gallery of pulse broadening functions 81
11.1. Thin-screen geometry 81
11.2. PBFs from thin and thick media with power-law ('Kolmogorov like') wavenumber spectra 84
11.3. Anisotropic scattering and refraction 84
11.4. Inhomogenous and truncated screens 89
11.5. Bandwidth averaging and phase wrapping 91

12. Timing variations from chromatic plasma effects 92
12.1. Temporal DM variations [DM(t)] 93
12.1.1. Pulse frequency variations 93
12.1.2. ToA error from asynchronous frequency sampling of DM delays 94
12.2. Chromatic DM variations [DM(ν)] 95
12.2.1. Two-frequency DM difference 95
12.2.2. Wideband timing errors from chromatic DM variations 96
12.3. Angle-of-arrival variations 98
12.4. PBF stochasticity from nanoseconds to years 99
12.5. Rapid stochasticity of PBFs and ToA noise 100
12.5.1. Scintillation induced changes in effective center frequency 101
12.5.2. Rapid changes in PBF shape (the "finite scintle error" (FSE)) 102
12.6. Slow stochasticity of PBF envelopes and ToA bias 103
12.6.1. Inapplicability of the 'mean-shift' scattering regime 104
12.6.2. Time delays from heavy tailed PBF envelopes 107
12.6.3. ToA shifts from scattering islands 108
12.6.4. Implications for the frequency scaling of timing offsets from scattering 110
12.7. Systematic timing errors from mismatched templates and PBFs 111

13. Chromatic leakage into achromatic arrival times and residuals 112

14. Gaussian and non-Gaussian timing fluctuations 114

15. Fluctuation spectra of timing delays and residuals 119
15.1. White noise processes 119
15.2. Achromatic red noise with power-law spectral components 120
15.3. Chromatic red noise with low-pass cutoffs 120
15.4. Chromatic bandpass noise 122
15.5. Intrinsic pulse shape variations 123
15.6. Instrumental discontinuities 124
15.7. Aliasing of fluctuation spectra 124
15.8. Example spectra for four MSPs 126

16. Red noise assessment of MSPs in PTAs 128

17. Profile modeling summary and arrival time models 131
17.1. Profile modeling 131
17.2. Template modeling **and matching** 132
17.3. PBF models 135
17.4. Arrival time equations 136
17.4.1. No ISM terms 136
17.4.2. Inclusion of an epoch independent dispersion term 137
17.4.3. Full expression for ToAs at the SSBC 137

18. ToA error corrections 139
18.1. Mitigation of intrinsic (emitted) pulse shape variations (jitter etc.) 139

18.2. Removing DM variations 140
18.3. Conditions where ToA scattering bias is negligible 140
18.4. Mitigation of rapid PBF variations related to scintillation fluctuations 142
18.5. Mitigation of slow epoch-to-epoch scattering time (τ) variations 142
18.5.1. Intensity (incoherent) deconvolution of pulse broadening 144
18.5.2. Forward modeling of pulse shapes 145
18.5.3. Correction of ToAs using extant or contemporaneous estimates of the pulse broadening time τ. 146
18.5.4. Scattering corrections using template fitting + dynamic spectrum analysis 146
18.5.5. Phase retrieval with the Hilbert Transform (HT) 148
18.6. Assessment of MSPs for scattering mitigation 149

19. Spin noise triage 152

20. Evaluating timing quality of individual pulsars 152
20.1. Quality measures for fast ToA fluctuations 154
20.1.1. Template fitting 155
20.1.2. Pulse jitter 155
20.1.3. Diffractive ISS PBF variations ('finite scintle effect') 155
20.2. Quality measures for slow timing variations 156
20.2.1. Spin fluctuations 156
20.2.2. Long term variations of the pulse broadening time 156
20.2.3. Temporal DM variations and asynchronous multifrequency observations 157
20.2.4. Frequency-dependent DMs 157
20.3. Meta-analysis of quality measures 159
20.3.1. Initial MSP comparisons 159
20.3.2. Forward looking MSP comparison 160

21. Summary and Recommendations 161
21.1. Building a Pulsar Timing Array 161
21.2. Customized scattering mitigation for individual MSPs 165

Appendix A. Nomenclature 167

Appendix B. Spectral representations 171

Appendix C. Structure functions 173

Appendix D. Modulated complex noise 174

Appendix E. ToA variations from frequency-dependent dispersion deasures 175
E.1. Errors in ToA and DM Estimates 176
E.2. Variances 176
E.3. Derivation of the cross correlation $\Gamma_{\Delta\overline{\mathrm{DM}}}(\nu_1, \nu_2, \nu_3)$ 178

Appendix F. Simulation of propagation through thin plasma screens 182
F.1. Diffraction and lensing from a thin screen 182
F.2. Refractive distortions of scattered Images and PBFs 182

Appendix G. Inventory of timing effects from dispersion, scattering, and refraction 184
G.1. With epoch-dependent dispersion and multipath propagation 187

Appendix H. Temporal spectra for screen phase and refraction angle 188

Appendix I. Derivation of TOA errors from rapid changes in pulse broadening functions 190
I.1. Pulse Broadening Function 190
I.2. Mean Delay 191
I.3. Delay Variance 191
I.3.1. Narrow-scintle Regime 192

I.3.2. Integration Times Longer than the Scintillation Time 193

Appendix J. Dynamic spectra computation and estimation errors 195
J.1. Phase-resolved spectroscopy (PRS) 195
J.1.1. Degrees of freedom in the DS 196
J.1.2. Error budget of DS 196
J.1.3. Errors in estimating $\Delta\nu_{\rm d}$ from the spectral ACF 197
J.2. Cyclic spectroscopy (CS) 198
J.2.1. CS estimation errors 199
J.2.2. Role of Pulse Jitter 202
J.2.3. Constraints on CS parameters 202
J.3. ACF Statistics 203

Appendix K. Hilbert transform solutions for non-minimum delay functions 205

Appendix L. Quality Measure Evaluation Code 206

References 207

1. INTRODUCTION

The methodology of pulsar timing exploits the narrow pulses and stable spins of neutron stars (NSs) for their use as astrophysical clocks. It is now applied across the entire electromagnetic spectrum, primarily at radio, X-ray, and γ-ray frequencies, for a host of unique applications. The existence of gravitational waves was demonstrated by timing studies of binary pulsars (Taylor and Weisberg 1982; Taylor 1994; Weisberg et al. 2010), which also provided fundamental tests of General Relativity and other theories of gravity (Kramer et al. 2021), along with precise determinations of the orbits and masses of neutron stars (Özel and Freire 2016) with specific cases reported by Demorest et al. (2010); Antoniadis et al. (2013); Cromartie et al. (2020). Neutron star masses provide key constraints on the equation of state of supra-nuclear matter, especially in concert with X-ray observations that constrain NS radii (e.g. Lattimer 2021; Miller et al. 2021; Rutherford et al. 2024). Recently, precision timing of millisecond pulsars has provided evidence for the presence of a stochastic background of long-wavelength gravitational waves. Propagation delays through intervening plasmas and spacetime are necessarily accounted for in pulsar timing and they provide unique information about plasma densities, magnetic fields, and (upper bounds on) dark matter. Finally, long timing programs on some pulsars now extend to nearly a half century, yielding some of the best upper bounds on variations in the gravitational constant G and other fundamental constants (Kaplan et al. 2022).

Steady improvement in the precision of time-of-arrival (TOA) measurements has underpinned testing theories of gravity with higher-order relativistic terms (Kramer et al. 2021) and searching for timing perturbations from low-frequency (nanohertz) gravitational waves (GWs). The effects of GWs on pulsar timing were first discussed by Sazhin (1978); Detweiler (1979) and initial upper limits were made by Hellings and Downs (1983); Romani and Taylor (1983) using data on slowly rotating pulsars (periods $P \sim 1\,\mathrm{s}$) from the JPL timing program (Downs and Reichley 1983). We refer readers to Taylor (2021); Sesana and Figueroa (2025); Mingarelli et al. (2026) for recent reviews of the state-of-the-art in GW astrophysics with pulsar timing.

Usage of millisecond pulsars (MSPs) for GW detection began with the discovery of the MSP B1937+21 (J1939+2134) (Backer et al. 1982), whose narrow pulse and short 1.56 ms period suggested that greater sensitivity to cosmological GW backgrounds could be achieved (Bertotti et al. 1983). Initial observations verified this possibility (Cordes and Stinebring 1984; Davis et al. 1985). Comprehensive discussions of pulsar timing by Blandford et al. (1984) and Backer and Hellings (1986) laid further groundwork for gravity science using pulsars, leading to the notion of a 'pulsar timing array' (PTA) by Foster and Backer (1990) for GW detection.

The first MSP-based limits reported by Davis et al. (e.g. 1985) were based on RMS timing residuals $\sim 0.9\,\mathrm{ms}$ over a 2-yr period and expressed as an upper bound on the GW energy density relative to closure density of the universe, $\Omega_{\rm gw} \lesssim 10^4$, corresponding to a dimensionless strain $h_{\rm c} \lesssim 3 \times 10^{-14}$, more than an order of magnitude larger than the sensitivity of current PTAs. Subsequent studies (Stinebring et al. 1990; Kaspi et al. 1994) gave more stringent limits but also identified extra correlated noise in B1937+21 that in current data sets makes this pulsar unsuitable for GW detection compared to other MSPs.

Discovery of new MSPs combined with improved timing methods increased the plausibility of detection of nanohertz GWs (Lommen and Backer 2001; Kramer et al. 2004; Cordes et al. 2004b; Jenet et al. 2005, 2006; Hobbs et al. 2009; Demorest et al. 2009; Hobbs et al. 2010) and led to the formation of several research groups in pursuit of PTA science. In a series of papers published in 2023, evidence for detection of a stochastic GW background was reported (Agazie et al. 2023b; EPTA Collaboration and InPTA Collaboration et al. 2023; Reardon et al. 2023b; Xu et al. 2023) that was corroborated by a more recent analysis using data from the MeerKAT telescope (Miles et al. 2025).

The most demanding timing application is GW detection of ∼nanohertz GWs, which not only relies on ToAs with small measurement errors but it also requires that *all* contributions to the net timing residuals be of order $\sim \mu$s or better. This requires adequate signal-to-noise ratios of measured pulse profiles but it also requires corrections for chromaticity to be accurate to the same order or better. Chromatic effects are primarily interstellar in origin but are also caused by processes intrinsic to the pulsar emission. Evidence for the stochastic GW background emerged from measurements with μs *ToA* precision but further characterization of its spectrum and detection of continuous wave (CW) signals from (e.g.) supermassive black hole binaries (SMBHBs) requires significant improvements in ToA measurements. Achieving this precision brings into play all effects that influence arrival times, from processes interior

to the neutron star and its magnetosphere, to plasma effects along the entire propagation path, and to the digitized data streams that are analyzed. Improving timing sensitivity to GWs and for other purposes (e.g. more stringent contraints on theories of gravity) similarly requires attention to all of these end-to-end effects.

MSPs provide the timing precision for GW detection that 'canonical pulsars' (CPs) cannot. CPs, with surface magnetic fields $\sim 10^{12\pm1}$ G and periods $P \gtrsim 10$ ms), show much larger spin noise (e.g. Hobbs et al. 2010) (and pulse shape variations (Lyne et al. 2010)) that translate into pulse phase variations up to 10^6 times greater than for MSPs (Shannon and Cordes 2010; Lam et al. 2017; Parthasarathy et al. 2019). Nonetheless, CPs are useful for probing the ISM and may present unique opportunities for probing high-value targets, such as a black-hole pulsar binary (including pulsars orbiting Sgr A*).

Pulsar timing methodology is summarized in *The Handbook for Pulsar Astronomy* **(Lorimer and Kramer 2005, Chapter 8). Essential features of pulsar timing are given in § 3 for the purposes of** this paper, which inventories processes that limit timing efficacy and explores methods for its improvement. It is therefore both a review and a forward-looking analysis aimed at reducing systematic and random timing errors for individual pulsars, selecting pulsars that yield the lowest astrophysical contributions to timing errors, and striving for optimization of timing programs, including those for PTAs. We present scaling laws for forecasting the measurement precisions of astrophysical parameters. These provide the means for testing the completeness of our understanding of timing delays as well as for identifying areas of improvements, including the benefits of new telescopes and instrumentation. The paper builds on a number of works that have characterized arrival time variance on an empirical basis. References are given in individual sections of the paper that compare magnetars with CPs and MSPs. Pulsar timing array collaborations have presented the most detailed studies of MSPs. Though our presentation makes extensive use of data from the NANOGrav collaboration[11], we also use or refer to other data sources and the results are intended to be independent of any particular PTA group.

Optimization of pulsar timing requires assessment of each pulsar's quality as an astrophysical clock, including the intrinsic properties of the neutron star and its magnetosphere, any binary motion, its immediate environment, and the plasmas encountered along the line of sight (LoS). Also relevant is our ability to measure pulse times of arrival (TOAs) precisely and refer them to the solar system barycenter accurately.

By its focus on timing limitations and optimization, the paper does not delve into the optimization of model fitting to long arrival-time sequences nor to optimized inference using frequentist or Bayesian methods. Instead the paper is meant to inform how to construct covariance matrices employed for parameter inference and to minimize the values of covariance matrix elements.

Table 1. Overview of timing delays and ToA estimation

Contribution	Effect[a]	Mitigation[b,c]		Amplitude[d]	RF	Fluctuation	Paper
		Type	Instr		Chromaticity[e]	Signature[f]	Section
Source & Source Environment							
Spin noise	δt	triage	$\cdots$	$\sim 100\,\mathrm{ns}$ – s	a	R/PL (f^{-4}–f^{-6})	4, 19
Pulse shape	δt	triage	$\cdots$	μs – ms	c ($\nu^{-0.3}$)	Err	5.4, 6.2
Pulse jitter	$\widehat{t}$	NM	T	$\lesssim \mu$s – ms	a (c)	W	7.2
Orbital noise	δt	triage	$\cdots$	$\lesssim$ ms	a	R/PL ($\sim f^{-3}$)	4.6
Interstellar Medium							
Dispersion	δt	C	B	$\lesssim$ ms	C (ν^{-2})	R/PL,LP $r^{-8/3}$	12.1, 10.1
Multipath [DM(ν)	$\widehat{t}, \delta t$	PC, NM	ν, B	$\lesssim 100\,\mathrm{ns}$	C ($\nu^{-23/6}$)	R/LP	12.2

Table 1 *continued on next page*

[11] https://nanograv.org

Table 1 *(continued)*

Contribution	Effect[a]	Mitigation[b,c] Type	Mitigation[b,c] Instr	Amplitude[d]	RF Chromaticity[e]	Fluctuation Signature[f]	Paper Section
Faraday rotation	δt	C	Pol cal	$\lesssim$ ns	C (ν^{-3})	Lin	5.5
Pulse broadening	$\widehat{t}, dt$	PC, NM, triage	ν	ns – s	C ($\sim \nu^{-4}$)	R/PL,LP	11
Interstellar intensity scintillation (S/N variations)							
Diffractive	$\widehat{t}$	NM	B, T	$\lesssim \mu$s – ms	C	R/LP	6.1, 9.3
Refractive	$\widehat{t}$	NM	ν	$\lesssim \mu$s	C	R/LP	6.1, 9.3
Angle of Arrival	δt	PC	ν	$\lesssim \mu$s	C (ν^{-2} & ν^{-4})	R/PL,LP	10.2, 12.3
Instrumentation & Analysis							
Astrometric & clock errors	δt	C		$\lesssim$ 10 ns	a	Err	8.4
SSBC uncertainties	δt	PC, NM	Ephem	<100 ns	a	Osc	8.3
Polarization	δt	C	Pol cal	$\ll \mu$s	C	Err	8.1
Radiometer noise[g]	$\widehat{t}$	NM	B, T	$< \mu$s – ms	c ($\nu^0 \rightarrow \nu^{-2.7}$)	W	6
Gravitational Waves	δt	None		$\lesssim$ 100 ns	a	R/PL, Osc	1

NOTE—
[a] Effect: $\widehat{t}$ signifies an influence on ToA estimation while δt implies contribution of a systematic ToA offset that is epoch dependent;
[b] Mitigation type: triage = PSR choice; C = correctable; PC = partially correctable; NM = include in noise model;
[c] Instrumental mitigation: ν = radio frequency; B = bandwidth; T = integration time per epoch;
Pol cal = polarization calibration; Ephem = solar system ephemeris
[d] Amplitude of arrival time delay or timing residual either before or after mitigation (as relevant);
[e] Dependence on radio frequency ($= \nu$):
a = achromatic; c = weakly chromatic, C = strongly chromatic with approximate scaling (if simple);
[f] Signature of fluctuation spectrum in long time series (yr):
W = white; R/PL = red with power-law spectrum; R/LP = red with ∼flat low-pass spectrum;
Lin = typically a linear spectrum, Osc = oscillatory, Err = erratic or episodic
[g] The ToA error from radiometer noise depends on the flux density spectrum of the pulsar, which typically scales as ν^{-y}, with $y \sim 0$ to 4.

Table 1 gives a broad overview of salient contributions to arrival times and timing residuals — from neutron star to digital processing. These are grouped into effects that take place in and near the source, those involving propagation through the ISM and other plasmas, and local (solar system) and instrumental delays. Some of these contribute systematic biases or random errors (or both) that are achromatic (or nearly so) while others, especially plasma effects, are highly frequency-dependent. A wide range of temporal variability is also seen, ranging from uncorrelated perturbations between epochs (white noise) to red noise processes with steep power law spectra $\propto f^{-1}$ to f^{-6}. Timing residuals include both Gaussian and non-Gaussian astrophysical processes, the latter from processes internal to the neutron star, magnetospheric effects, and the ISM. The table indicates whether an effect contributes to a random error in a ToA estimate $\widehat{t}$ or instead introduces a systematic arrival time offset (or bias) δt. The table also indicates how a contribution can be mitigated, where 'triage' simply means that only some pulsars warrant inclusion in a timing program. Representative amplitudes of timing errors or offsets are given along with their dependence, if any, on radio frequency ν. The signature in the power spectrum of timing residuals is given in the penultimate column. Relevant paper sections are indicated in the last column, which serves as a rough roadmap for some aspects of the review.

The text is organized into seven major parts followed by twelve appendices that contain definitions and derivations:

Part I. *Preliminaries* (§§1 – 2). This includes the Introduction and a short discussion of nomenclature.

Part II. *Basics of pulsar timing* (§§3 – 8). The foundations of pulsar includes descriptions of pulsar signals and their propagation through the interstellar medium (ISM) along with a presentation of template matching for ToA estimation.

Part III. *Interstellar effects*: (§§9 – 12). A summary of what we know about the interstellar plasma is presented following detailed analysis of its effects on individual arrival times.

Part IV. *Chromatic leakage, gaussianity, fluctuation spectra, and red noise* (§§13 – 16). The phenomenology of aggregated, multiepoch arrivaltimes is discussed in the time domain, the radio frequency domain, and the fluctuation-frequency domain.

Part V. *Timing equations and mitigations* §§(17 – 18). Model timing equations and the mitigation of ToA errors are discussed.

Part VI. *Prioritizing MSPs for optimization of pulsar timing arrays* (§§19 – 20. Previous material is employed for selecting the best MSPs for PTA applications.

Part VII. *Summary and Recommendations* (§21). The salient elements of our analysis are summarized by considering how a pulsar timing array might be assembled *ab initio* but taking into account timing phenomenology and methodology covered in the review.

2. NOMENCLATURE

Discussions of pulsar timing necessarily involve an abundance of symbols and acronyms.

We use standard nomenclature for electromagnetic frequency ν and its relationship with vacuum wavelength $\lambda = c\nu^{-1}$ where c is the speed of light.

We use f to designate "fluctuation frequencies" of various quantities, including gravitational waves. Fluctuation frequencies are the independent variables for power spectra of time series; for our applications time series extend over multiple years and we refer to their power spectra as 'fluctuation spectra' with frequencies expressed in Hz or $\text{cycles}\,\text{yr}^{-1}$.

We use f_s for the pulse rates of pulsars, which are closely related to the spin frequencies of the associated neutron stars (modulo the usually unknown Doppler shift).

We refer to pulsars using standard notation, usually in terms of the J2000 epoch (e.g. J1713+0747) and, for a few well-known objects, the B1950 epoch (e.g. B1937+21). Where needed we use the PSR, MSP, or CP prefixes (pulsar, millisecond pulsar, and 'canonical' pulsar) where CP refers to pulsars that have not undergone accretion-driven spinup ("recycling").

Many more definitions are needed for modeling the pulsar signal and for its propagation through the ISM. A comprehensive list is given in Appendix A.

3. THE GIST OF PULSAR TIMING AND ITS LIMITATIONS

This section summarizes the foundations of pulsar timing methodology and the range of factors that contribute to its limitations. The main intent here is to classify those factors and set the stage for the detailed analysis that follows.

Pulsar timing amounts to counting pulses over time spans ranging from minutes to decades, taking into account that they are only quasi-periodic and pulse frequencies are nonstationary due to spindown of NSs. Also, pulses arrive early or late depending on Earth's location in its orbit and similarly, depending on orbital phase for objects in binary systems. Most pulsars are isolated but about 2/3 of MSPs are in binary systems with white dwarf companions (ATNF pulsar catalog, Manchester et al. 2005).

These deterministic effects are captured in a model for pulse phase, $\Phi(t)$ that parameterizes the NS spin, orbital elements, and astrometric terms. A perfect model yields integers at measured arrival times but unmodeled effects can appear as random and systematic errors in measured ToAs and/or to phase residuals, yielding $\Phi(t) = \text{integer} + \delta\phi(t)$.

Timing methodology relies on an empirical foundation that has unfolded over the last half century:

1. Rotational stability of MSPs is sufficient to allow individual turns of a NS to be predicted with high precision so that only infrequent monitoring is needed to track pulse phase and to look for departures caused by astrophysical effects of interest, including plasma and gravitational perturbations from both static fields and GWs;
2. Emitted pulses are cross-sectional slices through a beam of radiation whose orientation is locked to the spinning NS crust (in the mean);
3. Relative to a fiducial phase locked to the NS, the phases (and amplitudes) of single pulses vary stochastically with stationary statistics; as a result, the average pulse profile obtained from a large number of single pulses averaged synchronously with the rotation converges to a stable form that *largely* does not change with time;
4. Average profiles change smoothly as a function of radio frequency; however, these chromatic shapes change very little from epoch to epoch. **However, notable exceptions occur, as discussed in § 6.4 and § 6.3.**

As examples, pulse profiles for 112 MSPs from multiple PTA programs that contribute to the International Pulsar Timing Array program **(e.g. Perera et al. 2019)** are shown in Fig. 1. Each is the average of more than a million single pulses and represents the shape to which all averages from a given pulsar are assumed to converge for template fitting. **While actual profiles closely conform to this assumption, deviations occur from both intrinsic (to the pulsar) and extrinsic processes.**

Fig. 2 shows the simulated properties of single pulses and how they are averaged into profiles for calculating arrival times. Emitted pulses are inherently stochastic. As discussed in Sect. 5, they comprise narrow shot pulses of coherent radio emission. Shots are grouped incoherently to form single pulses, which can be viewed statistically as an envelope that modulates shots to give the instantaneous pulse shape. Pulses incident on the ISM are broadened by multipath propagation from scattering, which operates as a linear filter. The convolution of the broadening function is with the electromagnetic field components of the pulsar signal and pulse intensities (after squaring field components) are averaged synchronously with the pulse period following removal of systematic dispersion delays. The convolution operation does not apply to single pulse intensities but it does apply to the (hypothetical) ensemble average pulse. Template fitting is essentially the outcome of cross correlation between a template and a measured profile, as indicated, although it is usually effected in the frequency domain after Fourier transformation (Taylor 1992, and Sect. 6).

The ToA of a pulse is the net effect of many processes that occur between emission in a pulsar's magnetosphere and reception at an observatory, with subsequent referencing of the ToA to the solar-system barycenter (SSBC) using a solar-system ephemeris. GW perturbations contribute to the overall noise budget as well as to the signal that is the target of PTA observations.

Once ToAs are obtained, referencing them to the SSBC requires knowledge of astrometric parameters of the pulsar (sky location, proper motion, and parallax), determinable by fitting to a multiyear sequence of ToAs or through very-long-baseline interferometry (VLBI). An issue with using sky positions from VLBI is that the International Celestial Reference Frame (ICRF) based on equatorial coordinates differs from the dynamical reference frame based on Solar System ephemerides. A discussion of reference frame alignment can be found in Sosa Fiscella et al. (2026).

To elucidate the complexity of ToAs, we relate the emission time t_e from a location $\mathbf{x}_e$ in a pulsar's magnetosphere to the topocentric arrival time t_A at an observatory location $\mathbf{x}_o$ ((with measurement errors or other perturbations implicit),

$$t_A[\mathbf{x}_o(t_A), \nu)] = t_e[\mathbf{x}_e(t_e, \nu)] + t_{\rm prop}(\text{ISM}, \phi_{\rm grav}, \nu) + t_{\rm gw}(t_A), \tag{3.1}$$

where $t_{\rm prop}(\text{ISM}, \phi_{\rm grav}, \nu)$ lumps together the plasma and (non-GW) gravitational delays associated with propagation to the observatory; $t_{\rm gw}$ is the gravitational perturbation. Chromatic contributions to t_A are signified by the dependence on radio frequency ν. Referral to the SSBC involves compensation for the Römer and relativistic clock delays by adding a term $\Delta t_{\rm E,SSBC}$ to t_A, yielding $t_{\rm SSBC} = t_A + \Delta t_{\rm E,SSBC}$.

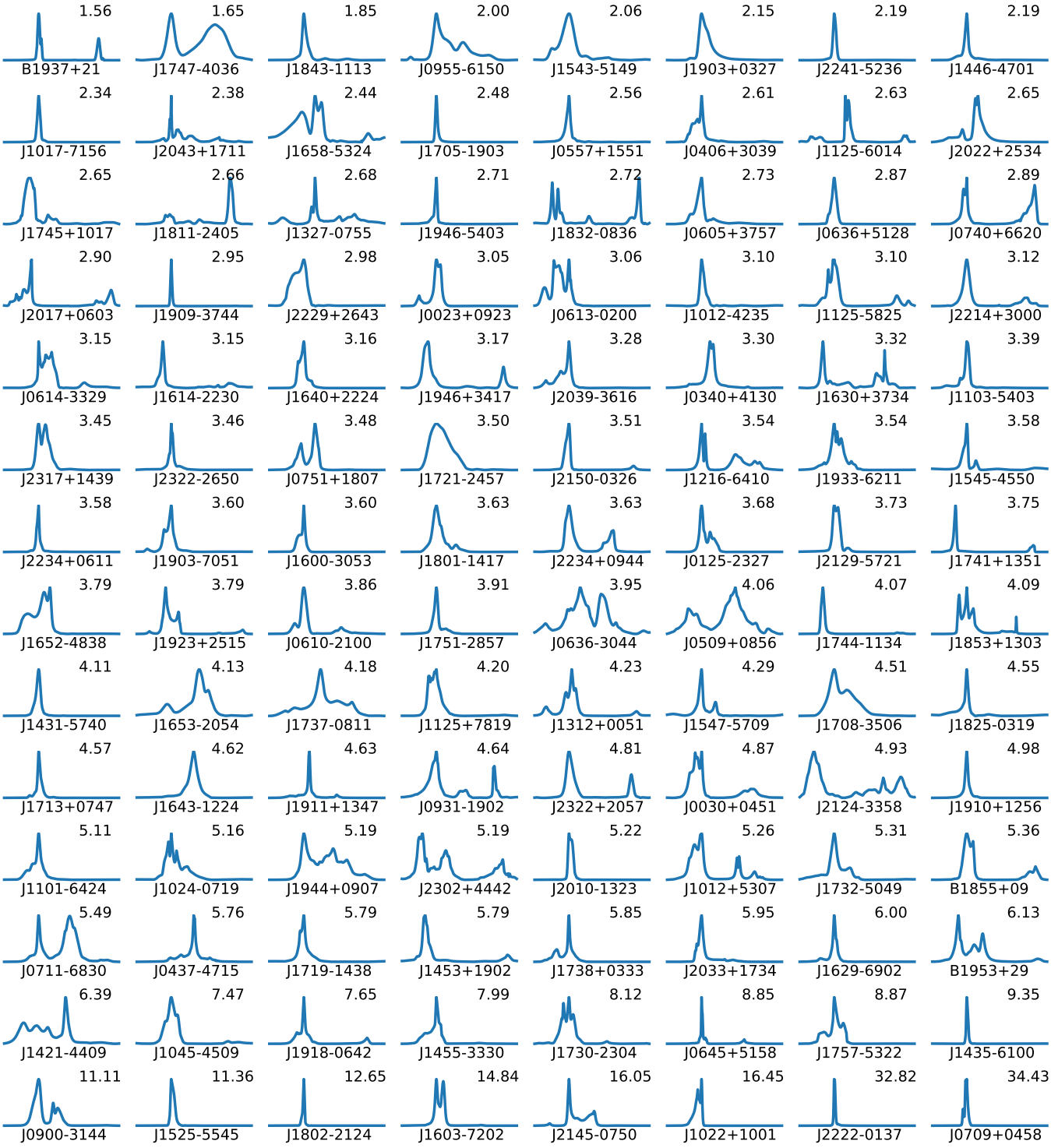


Figure 1. Pulse profiles (total Stokes intensities) at L-band for 112 pulsars timed by the IPTA. Profiles are shown for a full phase cycle and are ordered by increasing pulse period from left to right. The pulse period is shown in milliseconds at the top right of each profile.

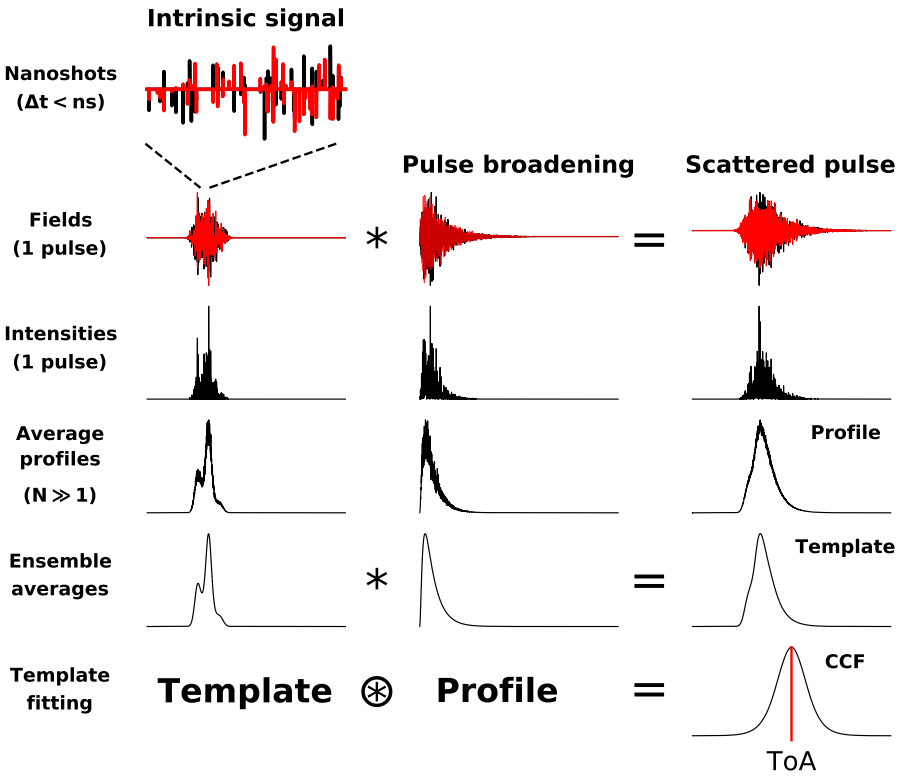


Figure 2. Graphical display of the averaging of single pulses to form pulse profiles from which ToAs are obtained using template fitting. The asterisk and circled asterisk denote convolution and cross-correlation operations, respectively.
Columns: (1) the intrinsic (emitted) signal; (2) interstellar broadening functions; and (3) the net scattered pulses.
Rows: (1) nanoshots, the fundamental units of coherent emission; (2) field or 'voltage' quantities for a single pulse; (3) intensity quantities equal to the squared magnitudes of row (2); (4) average intensities for a large number of pulses; (5) ensemble averages; and (6) calculation of ToAs by fitting a template to an individual profile.
Nanoshots and field quantities are complex if quadrature mixers are used to obtain baseband voltages; real and imaginary parts are shown in black and red, respectively. In practice, average profiles combine two independent polarizations to form the intensity Stokes parameter. Template fitting is typically implemented by least squares fitting in the Fourier domain. Formally, this is identical to using the maximum of the cross correlation function (CCF) to determine the ToA but it has significant practical advantages.

3.1. *What limits arrival time precision and timing predictions?*

ToAs are obtained by template matching to measured average profiles under the assumptions of matched filtering (see Sect. 5.4). Average profiles deviate from the template *at minimum* due to radiometer noise that adds to the pulsar signal. If ToA precision were determined solely by the limitations from radiometer noise, it would be feasible to achieve sub-ns precision for the brightest pulsars[12]. However, the real world intrudes on predictions based on idealized matched filtering.

Precision commonly refers to the repeatability of measurements in contrast to *accuracy*, which refers to the fidelity of measurements to the true values of some quantity. Arrival times are affected by a slew of systematic and random errors but their true values are unknown. We must rely on the self consistency of measurements with underlying physics. Binary pulsars are the only examples in the pulse timing context where the relativistic descriptions of their orbits can

[12] A notable example is the bright MSP J1939+2134 (B1937+21), with $P = 1.56\,\mathrm{ms}$, $S_{0.4\,\mathrm{GHz}} = 240\,\mathrm{mJy}$, and $W = 38\,\mu s$ (Manchester et al. 2005). Expressions and quantities detailed in later sections (e.g. Eq. (6.8)) are evaluated with an integration time of $10^3\,\mathrm{s}$ and bandwidth of $0.1\,\mathrm{GHz}$ on a large highly optimized telescope with $S_{\mathrm{sys}} = 1$ Jy. For example $S_{\mathrm{sys}} \sim 1.24\,\mathrm{Jy}$ at $1.4\,\mathrm{GHz}$ for the FAST telescope (Xi et al. 2022), though it does not operate currently at 0.4 GHz), the RMS timing error would be $\sigma_{t_{\mathrm{S/N}}} \simeq 0.04\,\mathrm{ns}$. At 1 to 2 GHz, the lower flux density $S_{1.4\,\mathrm{GHz}} = 14\,\mathrm{mJy}$ still yields $\sigma_{t_{\mathrm{S/N}}} \simeq 0.2\,\mathrm{ns}$ that is much smaller than actual ToA precisions.

provide multiple constraints on measurement (and model) fidelity. Essentially all other timing contributions lack any ground truth at the sub-100 ns level.

In our analysis, we distinguish between phenomena that affect the time-tagging of pulses — TOA estimation — and the astrophysics of the pulsar clock. This distinction is exemplified by considering a delta-function pulse with infinite S/N emitted at a random time by a pulsar with a stochastic spin rate and propagated through the stochastic ISM. The ToA of the impulse at an observatory with a perfect clock would have no uncertainty. However, the timing residuals from a model fitted to a sequence of such ToAs would be affected by the stochastic elements and would have substantial variance.

ToA estimation errors are often dominated by radiometer noise but in other cases by sometimes larger effects, namely *pulse jitter* intrinsic to pulsars that distorts pulse profiles from the template shape and *diffractive scattering*, which causes intensity scintillation and also causes changes in pulse shape (Sect. 12).

Groupings of terms are shown schematically in Eq. (3.2), including gravitational wave perturbations comprising two terms associated with the dimensionless strain at the Earth and at the pulsar.

$$t_{\rm SSBC} = \begin{array}{c}\textbf{Deterministic terms}\\ \text{spindown polynomial}\\ \text{astrometric terms}\\ \text{pulsar orbit}\\ \text{pulse shape vs . } \nu\end{array} + \begin{array}{c}\textbf{Stochastic terms}\\ \text{white noise}\\ \text{(receiver, jitter \& ISM)}\\ \text{red noise}\\ \text{(spin, ISM}\end{array} + \begin{array}{c}\textbf{Systematic Errors}\\ \text{planetary emphemeris}\\ \text{time transfer (GPS)}\\ \text{observatory clocks}\\ \text{polarization calibration}\end{array}$$

$$+ \begin{array}{c}\textbf{Gravitational Wave Perturbations}\\ \text{Earth term + Pulsar term}\end{array} \qquad (3.2)$$

Several broad questions arise when assessing the utility of an MSP for precision timing:

1. How stable is the spin rate of a NS?
2. How well are emission regions and directions locked to the spin phase of the NS?
3. How are pulses modified and delayed by the ISM? and
4. How well can pulses be time tagged at an observatory and referred to the barycenter of the solar system?

The first two issues relate to the quality of a NS as a clock while the last two involve determination of when pulses arrive as measured against an observatory clock. Related to these questions is the distinction between pulse phase jitter and red spin noise. Phase jitter is a zero mean process with respect to a fiducial point in the pulsar magnetosphere and is physically associated with variations in location and relativistic beaming. Spin noise, however, represents actual departures in the rotational phase from that of a smoothly spinning down object.

Table 2. Salient Equations for arrival time errors and fluctuations [a]

Term (1)	Symbol (2)	Nominal Value (3)	Scaling (4)	Equations (5)
Rapid TOA Variations ($\lesssim$ hours)				
Radiometer noise	$\sigma_{t_{\rm S/N}}$	15	$\frac{S_{\rm sys}({\rm Jy})}{S_{\rm psr}({\rm mJy})}\frac{W_{100}^{3/2}}{\sqrt{(n_{\rm pol}/2)B_{\rm GHz}T_{{\rm int},3}P_{\rm ms}}}$	(6.6), (6.8), (6.10
Pulse jitter	$\sigma_{t_{\rm J}}$	33	$W_{100}\left(\frac{F_{\rm J}}{1/3}\right)\left(\frac{P_{\rm ms}}{T_{{\rm int},3}}\right)^{1/2}$	(7.3)
Diffractive scintillation	$\sigma_{t_{\rm DISS}} \simeq \frac{\tau}{\sqrt{N_{\rm scint}}}$	10	$\left(\frac{100\,{\rm MHz}}{\Delta\nu_{\rm d}}\right)\left(\frac{\Delta t_{\rm d}}{T}\frac{\Delta\nu_{\rm d}}{B}\right)^{1/2}$	(12.38)
Slow TOA Variations ($\gtrsim$ days)				
Spin / torque noise	$\sigma_{t_{\rm spin}}$	400	$P_{\rm ms}^{-0.8}\dot{P}_{-20}^{1.1}(T/10\,{\rm yr})^2$	(4.10)
Scattering variability vs. epoch	$\sigma_{\tau(t)}$	33	$({\rm DM}/30\,{\rm pc\ cm^{-3}})^{1.5}\nu_{\rm GHz}^{-4.4}$	
DM(t) mis-estimation	$\sigma_{t_{\rm DM(t)}}$	2.2	$\nu_{\rm GHz}^{-1}\left(\frac{3R^2/4}{R^2-1}\right)\left[\frac{\Delta T({\rm d})}{\Delta t_{\rm d}({\rm hr})}\right]^{5/6}$	(12.9)
DM(ν) mis-estimation	$\sigma_{t_{\rm DM(\nu)}}$	various	$\propto \nu_{\rm GHz}^{-23/6}d^{5/6}I_{t_\infty}(R)^{1/2}{\rm SM}$ $\sim \frac{2.5\,{\rm ns}}{\nu_{\rm GHz}^{1/6}}\left(\frac{\Delta\nu_{\rm d}}{100\,{\rm MHz}}\right)^{-5/6}$	(12.16)

[a] Definitions:

1. *Telescope and observation parameters (default values):*
   $S_{\rm sys}$ = system equivalent flux density (SEFD) (1 Jy)
   $n_{\rm pol}$ = number of polarization channels (2)
   ν = center frequency (1 GHz)
   B = bandwidth (1 GHz)
   $R > 1$ = frequency ratio of two frequencies used to estimate DM (2)
   $T_{\rm int} = 10^3\,{\rm s} \times T_{{\rm int},3}$ integration time to obtain a TOA at a single epoch
2. *Pulsar and line of sight parameters:*
   $S_{\rm psr}$= period averaged flux density (1 mJy)
   P = spin period (1 ms)
   $\dot{P}_{-20}$ = period derivative in units of $10^{-20}\,{\rm s\,s^{-1}}$
   W_{100} = pulse width (FWHM) in units of 100 μs
   DM = dispersion measure in units pc cm^{-3}
   SM = scattering measure in units kpc m$^{-20/3}$
   $I_{t_\infty}(R)$ = dimensionless factor for calculating frequency-dependent DM
   v_{100} = effective transverse velocity ($v_\perp/(100\,{\rm km\,s^{-1}})$)
   $\Delta\nu_{\rm d}$ = scintillation bandwidth (100 MHz)
   $\Delta t_{\rm d}$ = scintillation time (1 hr)
   $N_{\rm scint}$ is the number of independent scintillation fluctuations ('scintles') included in an observation
3. *Data sets:*
   $T_{\rm data}$ = length of data set (years)
   ΔT = difference in epochs for two frequency measurements used to estimate DM (days)

The relative contributions of three effects relevant to measuring arrival times can be found in Table 2 along with a prominent subset of the many distinct effects comprising the overall timing error budget, namely spin noise and ISM propagation effects. Nominal values are given by the coefficients in column (3) and are based on typical values of observing parameters (see table footnotes) *except* for the telescope sensitivity (the system equivalent flux density (SEFD), $S_{\rm sys} = 1\,$Jy), which is an order of magnitude better (i.e. smaller) than for a 100-m class telescope and about half the value for the Chinese Five Hundred Meter Aperture Spherical Telescope (FAST). The first three entries in the table correspond to rapidly changing errors and are listed in order of (current) importance: radiometer noise (finite signal to noise ratio), phase jitter (intrinsic to pulsars), and diffractive scintillations from turbulence in the ISM. The remaining, slowly changing processes alter arrival times due to emission and propagation delays but do not alter the precision of individual ToAs. They are not errors, as such, but rather are fluctuations that affect the net timing residuals.

For MSPs used in PTAs, short-term timing errors are typically dominated by radiometer noise but a bright MSP like J1939+2134 is significantly affected by jitter and scintillation. In §7.3 we discuss the crossover between noise and jitter-dominated ToAs and the important consequence that improvements in telescope sensitivity do not benefit ToA precision once it is jitter or scintillation dominated.

Another conclusion is that the slowly changing processes listed in the table can also exceed, by a large multiple, the ToA precision obtained in decades-long data sets. J1939+2134 is again illustrative in this regard because strong red noise from spin or orbital noise completely dominates the overall timing error budget.

The inventory and properties of timing effects in Tables 1, 2 and Eq. (3.2) suggest a schematic model for arrival times at the SSBC[13],

$$t_\nu = t_\infty + \left[\Delta t_{\rm S/N} + \Delta t_{\rm J} + \Delta t_{\rm DISS}\right]_{\rm fast} + \left[\Delta t_{\rm spin} + \Delta t_{\rm PBF} + \Delta t_{{\rm DM}(t)} + \Delta t_{{\rm DM}(\nu)}\right]_{\rm slow} + \Delta t_{\rm SS} + \Delta t_{\rm astr} + \Delta t_{\rm Instr} + \Delta t_{\rm ISM,other}, \tag{3.3}$$

where t_∞ is the arrival time extrapolated to infinite frequency that would be measured if there were no contributions from intervening plasmas and if all deterministic terms (e.g. regular spin phase, orbital delays, dispersion terms, astrometric terms, etc.) were modeled perfectly. We consider t_∞ to be the arrival time that contains the signal of likely astrophysical interest (e.g. GWs in the case of PTAs). For this reason we include spin noise as one of the slow TOA fluctuations. Included in t_∞ is the perturbation from GWs and any other gravitational effects, such as lensing from intervening objects. GW perturbations can be stochastic, oscillatory, or burst like. GWs passing through the solar system generate correlated perturbations while those passing near pulsars are uncorrelated between pulsars. The delays that perturb t_∞ are a mixture of achromatic, mildly chromatic, and strongly chromatic terms, as presented in the paper. The next seven terms adding to t_∞ in the first line of Eq. (3.3) correspond to the items in Table 2 and are grouped into 'fast' and 'slow' variations with characteristic times of seconds to hours and days to years, respectively. Time offsets between the topocentric arrival time and the SSBC arrival time are contained in $\Delta t_{\rm SS}$, which includes the Römer, Einstein, and Shapiro delays, and astrometric terms are contained in $\Delta t_{\rm astr}$. Instrumental terms are included in $\Delta t_{\rm Instr}$ (observatory clock offsets, variable electronic pathlengths, polarization calibration errors) and $\Delta t_{\rm ISM,other}$, which can include angle of arrival effects due to refraction in the ISM, which couples to errors associated with reference of arrival times to the SSBC. Detailed timing models for binary pulsars can be found in Blandford and Teukolsky (1976); Backer and Hellings (1986); Damour and Deruelle (1986) and discussions of time transfer to the solar system barycenter are given by (e.g.) Doroshenko and Kopeikin (1990); Stairs (2002); Edwards et al. (2006).

While the tremendous successes of pulsar timing applications pertain to t_∞, the focus of this review is on the stochastic terms in Eq. (3.3) with the goal of allowing quantitative evaluation timing accuracy on a term by term basis. As well as being pulsar and telescope dependent, the net results are also a strong function of the procedures used in a timing program. For an individual pulsar, timing precision is ultimately limited by the S/N and shape of the measured pulse profile (the widths of the narrowest components in particular; see Sect. 6), on the spin stability of the NS, and

[13] The form given here is a streamlined version of a detailed expression in Eq. (17.17) that encompasses the span of processes analyzed in the paper.

on stochastic variations from the ISM. In PTA work, overall precision can be maximized by pulsar triage, avoiding pulsars that are dim and show excessive spin or interstellar noise. Even then, white and red noise from finite pulse S/N, low-level spin variations, and ISM effects will contend with GWs from the stochastic background and from individual sources. In order to cover all possible situations involving radio timing, we discuss a comprehensive set of perturbations that originate everywhere along the line of sight, from inside the NS to the output of a receiver system.

Our treatment does not cover 'noise modeling' in the sense that it is used in analyses of collections of arrival times. That term typically refers to the covariance matrix used in frequentist or Bayesian statistical inference of model parameters. Instead, our aim is to characterize noise contributions and to differentiate between those effects that can or cannot be corrected for or otherwise mitigated. Given the slate of options for possible mitigations, it is clear that noise modeling is necessarily methodology dependent. Of course any effect that cannot be mitigated should be included in the noise covariance matrix.

4. PULSAR SPIN STABILITY AND ORBITAL NOISE

The spindown rate $\dot{f}_{\rm s} \equiv df_{\rm s}/dt$ of nonaccreting NS is typically modeled with a power law $\dot{f}_{\rm s} \propto {f_{\rm s}}^n$, where n is the braking index. Magnetic dipole radiation corresponds to $n = 3$ while $n < 3$ for the few values estimated from timing measurements, presumably due to departures from dipole fields and induced currents in the magnetosphere (Melatos 1997; Vargas and Melatos 2024, and references therein). This yields a spindown phase written in terms of the phase, spin rate, and its derivative at fiducial epoch t_0,

$$\phi_{\rm spin}(t) = \phi_0 + f_{\rm s0}\tau_0\left(\frac{n-1}{n-2}\right)\left\{\left[1+\frac{t-t_0}{\tau_0}\right]^{\frac{n-2}{n-1}} - 1\right\} \simeq \phi_0 + f_{\rm s0}(t-t_0) + \frac{1}{2}\dot{f}_{\rm s0}(t-t_0)^2 + \frac{1}{6}\ddot{f}_{\rm s0}(t-t_0)^3\cdots, \quad (4.1)$$

where the "spindown time" is $\tau_0 = f_{\rm s0}/(n-1)\dot{f}_{\rm s0}$ at the start time t_0 of a set of measurements and the approximate equality holds for $t - t_0 \ll \tau_0$. This is a good approximation since τ_0 is typically millions of years for CPs and >Gyr for many MSPs. **Note, however, that it is well known that the spindown time is not a good approximation to the chronological age of a pulsar. The spindown time depends on the spin period at its birth and on any evolution of the magnetic field since birth. Pulsar kinematics revealed this discrepancy empirically early on (Lyne et al. 1975, 1985) for canonical pulsars. More recent work on the spinup process for MSPs and a comparison ages of MSPs with their companion white-dwarfs yields a consistent conclusion (Tauris 2012).** Pulse phase models necessarily include a quadratic or, for canonical pulsars, a cubic polynomial to account for spindown, causing fits to arrival times to remove low frequency power from other contributions, as discussed later.

Deviations from the smooth spindown phase result from processes occurring both inside the neutron star and in the magnetosphere. These comprise distinct events (glitches and microjumps) and spin noise, a sustained process distinct from glitches and more relevant to PTA programs.

Glitches comprise rapid spinups $\Delta f_{\rm s}/f_{\rm s} \sim 10^{-9}$ to 10^{-6}, often combined with jumps in frequency derivative $\Delta\dot{f}_{\rm s}$. Glitch signatures are largely $\Delta f_{\rm s} > 0$ and $\Delta\dot{f}_{\rm s} < 0$ (or +,−) in form, with some exceptions. Glitches are more common in young pulsars with large spindown rates ($\dot{f}_{\rm s}$) and amplitudes of $\Delta\dot{f}_{\rm s}$ are correlated with those of $\Delta f_{\rm s}$; the latter has a bimodal distribution with peaks near $\Delta f_{\rm s} \sim 10^{-8}\,{\rm Hz}^{-1}$ and $10^{-5}\,{\rm Hz}^{-1}$ (Basu et al. 2022). Glitch recovery corresponds to relaxation of the spin rate $f_s(t)$ to its pre-glitch trajectory. In some cases this recovery is incomplete before the next glitch occurs while in others the recovery is slow or indiscernible. Evidently, glitches are primarily due to transfer of angular momentum from vortices in the neutron superfluid to the NS's crust (Anderson and Itoh 1975; Eya et al. 2017).

Despite the propensity for glitch activity in young pulsars, small, rare glitch-like events have been identified in three MSPs: PSR B1821−24 in the globular cluster M28 (Cognard and Backer 2004), J0613−0200, an MSP included in PTAs (McKee et al. 2016), and J0900−3144 (Bhat et al. 2026b). These are much smaller in amplitude than those from canonical pulsars, with $\Delta f_{\rm s}/f_{\rm s} \lesssim 10^{-11}$ and $|\Delta\dot{f}_{\rm s}/\dot{f}_{\rm s}| \lesssim 10^{-4}$. The J0613−0200 event follows the (+,−) signature of large glitches, in contrast to the (+,+) signature for B1821−24. Only the positive $\Delta f_{\rm s}/f_{\rm s}$ has been measured for the third case (J0900−3144). It is unclear if these events have the same physical origin as large glitches. Fortunately, MSP

events are rare, having occurred only three times in over a thousand pulsar-years in MSP timing programs (Bhat et al. 2026b). Nonetheless, this rate implies that small glitches in long-duration MSP timing programs are to be expected.

Spin noise, as used here, refers to sustained stochastic variations in phase distinct from those caused by glitches (Bhat et al. 2026b, and references therein). Some of these may arise from internal torque variations from crust-superfluid interactions or crustquakes. The interplay of spin noise and glitches while estimating parameters of a two-component crust-superfluid model is recently discussed by O'Neill et al. (2024), who employ Kalman filters as part of the modeling. Other variations are clearly caused by changes in the magnetic torque responsible for spindown (e.g. Kramer et al. 2006). An early overview of possible effects was given by Cordes and Greenstein (1981).

4.1. *Types of spin noise*

Empirically, spin noise is manifested as several types of variations in spindown rate $\dot{f}_s$ (Fig. 3) or in time-correlated timing residuals (Fig. 4):

1. Slow, smooth variations with no evidence for individual features and a red spectrum with a steep power law component, $S_{\mathcal{R}}(f) \propto f^{-x_{\rm spin}}$ with a spectral index $x_{\rm spin} \sim 4$ to 6 (D'Alessandro et al. 1997).
2. Bandlimited spin noise, similar to the first case, but with a quasi-periodic appearing time sequence in $\dot{f}_s$, signifying a narrower range of frequencies than for a power law spectrum.
3. Individual events (microjumps) in spin frequency or its derivative that individually have either sign, unlike glitches which largely have $\Delta\nu > 0$ and $\Delta\dot{\nu} < 0$ (CD85; D'Alessandro et al. 1995) For the Vela pulsar, microjump amplitudes in both ν and $\dot{\nu}$ are about 100 times smaller than glitch amplitudes (Cordes et al. 1988). Data spans encompassing many events show consistency with a power law spectrum with slope dependent on whether the spin phase is dominated by microjumps in ν or in $\dot{\nu}$.
4. Switching between discrete values of spindown rate $\dot{f}_s$ that persist for weeks to years (e.g. Kramer et al. 2006; Lyne et al. 2010). In some pulsars, state switching is quasi-periodic (e.g. Keith and Niţu 2023) and is consistent with stochastic resonance in the CP B1931+24. Fig. 3 shows quasiperiodicity in $\dot{f}_s$ for four canonical pulsars over time spans of up to 32 yr. Recent work (Keith et al. 2025) has shown that correlations between profile changes and spindown rate are quite common on time scales of tens to hundreds of days. State switching on shorter time scales (seconds to hours), manifested as nulling, profile mode changes, or quantized rates of subpluse drift, appears consistent with Markov processes (Cordes 2013). State switching so far appears to be a phenomenon occurring primarily in CPs (Wang et al. 2007). Nulling, for example, is either absent in most MSPs (e.g. Rajwade et al. 2014; Sheikh and MacDonald 2021) or occurs on too fast a time scale (e.g. MSP B1957+20; Mahajan et al. 2018) to manifest stochastically in timing data. However, mode changes in the MSP J1909−3744 have been reported by Miles et al. (2022).

Red noise in pulsar residuals has been interpreted in terms of random walk processes (e.g. Boynton et al. 1972; Cordes and Helfand 1980; Kopeikin 1997) and analyzed with a variety of time-domain (e.g. CD85, D'Alessandro et al. 1997) and frequency domain methods (e.g. Groth 1975; Deeter and Boynton 1982; Coles et al. 2011; Shannon et al. 2013). The first two types of spin noise listed above are amenable to spectral methods. Alternatives to Fourier based methods are necessary because the underlying spectra are steeper than f^{-2}, causing spectral leakage and mis-estimation of the spectral index. Principal component analysis, autoregressive (AR) model fitting (identical to maximum entropy methods), Cholesky decomposition, or Bayesian model fitting avoid leakage effects. Structure functions are useful because the spectral index is related to the structure function exponent. The third and fourth types of spin noise are best analyzed with time-domain methods if characterization of discrete events is the primary goal. Structure functions, for example, can be employed for testing the reality of apparent events in residual time series (CD85).

4.2. *Structure function slopes and spectral indices*

Definitions for the variety of spectral representations used in pulsar timing are given in Appendix B. We make use of structure functions (SFs; defined and related to power spectra in Appendix C) as tools for inferring the properties of red noise in pulse phase.

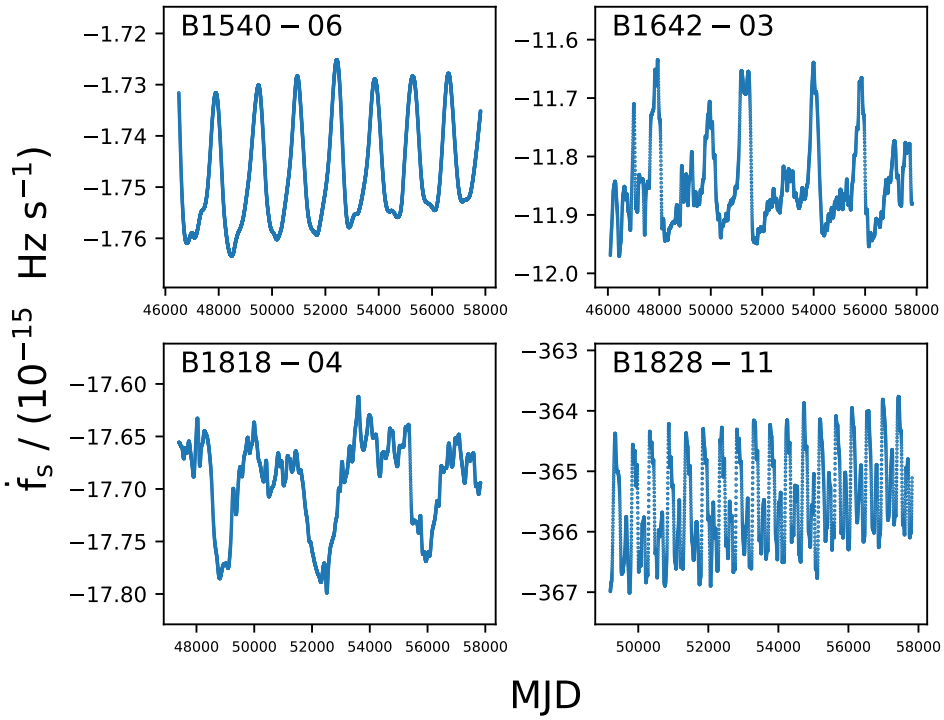


Figure 3. Time series of $\dot{f}_s$ for four pulsars from Keith and Niţu (2023) (data downloaded from zenodo.7664166).

We define the spectrum of phase fluctuations between low and high frequencies f_l, f_h as

$$S_\phi(f) = S_0 f^{-x_{\rm red}}, \quad f_l \le f \le f_h, \tag{4.2}$$

where the low-frequency cutoff is assumed to be much smaller than the lowest frequency $\sim 1/T$ sampled in a data span of length T. The phase variance for the data is then the integral of the spectrum over a frequency range $[\sim 1/T, f_h]$ and phase structure functions $D_\phi^{(m)}(\tau)$ of different orders m are similarly related to the spectrum (Sect. 4.2).

The best use of SFs requires consideration of the spectral index $x_{\rm red}$ in choosing the order m. The appropriate order to apply to the phase (or residual) is $m > (x_{\rm red} - 1)/2$, which follows from the integral relation between the spectrum and structure functions defined in Eq. (C.3) in Appendix C and consideration of the interplay between spectral slope $x_{\rm red}$ and the SF order. This specification yields an SF that is independent of T and has a scaling $\tau^{x_{\rm red}-1}$ vs. lag τ. Otherwise the scaling is $\tau^{2m} T^{x_{\rm red}-1-2m}$, whose τ dependence is uninformative about the spectral shape.

Random walk processes are useful models for spin noise because it is physically plausible that discrete jumps in spin phase, spin frequency, or spin-frequency derivative (i.e. jumps in torque) can occur. Referring to these as $k^{\rm th}$ order random walks with $k = 1, 2, 3$ respectively, they correspond to power-law spectra $\propto f^{-2k}$ (Boynton et al. 1972, CD85, Table 3).

For most pulsar data, the appropriate order of structure function to use for spectral constraints is $m = 3$, for two reasons: (a) it is uninfluenced by removal of the quadratic spin phase, $\phi_{\rm sd}(t) = \phi_0 + f_s t + \dot{f}_s t^2/2$; and (b) red noise processes are evidently as steep as $x_{\rm red} = 6$ (CD85, D'Alessandro et al. 1997; Parthasarathy et al. 2019; Yuan et al. 2024; Agazie et al. 2023c) requiring $m > 2.5$. We note, however, some pulsars show shallower spectra that allow lower-order SFs to be informative.

4.2.1. *Constraints from phase structure functions*

Measured phases include white noise $\phi_{\rm wn}$ with variance $\sigma^2_{\rm wn}$ so structure functions of the phase, $\phi(t) = \phi_{\rm red} + \phi_{\rm wn}(t)$, where the two terms are uncorrelated, have the form for $\tau > 0$,

$$D^{(m)}_{\phi}(\tau) = a_m \sigma^2_{\rm wn} + D^{(m)}_{\phi,{\rm red}}(\tau), \tag{4.3}$$

where $a_1 = 2$, $a_2 = 6$, and $a_3 = 20$ (CD85, Table 3). If red noise dominates the white noise at large lags, the scaling index of the SF $\propto \tau^{x_{\rm red}-1}$ yields a determination of $x_{\rm red}$ by fitting the SF in log-log space. The phase variance of the red noise

$$\sigma^2_{\rm red}(T) = \frac{S_0 T^{x_{\rm red}-1}}{x_{\rm red}-1}, \tag{4.4}$$

can be inverted to an estimate for the spectral coefficient,

$$S_0 = (x_{\rm red}-1) T^{-(x_{\rm red}-1)} \sigma^2_{\rm red}(T), \tag{4.5}$$

where it is assumed that $f_{\rm Ny} T \gg 1$ and $x_{\rm red} > 1$.

Timing residuals and structure functions are shown in Fig. 4 for three MSPs, two CPs, and one magnetar (J1622-4950). The MSPs shown in the top three panels have varying degrees of red noise, with B1937+21 having the largest, J1909−3744 having smaller, and J1643−1224 with minimal red noise but with distinctly non-white variations. Accordingly, the structure functions in the right-hand column go from steepest to flattest. The Vela pulsar (J0835−4510) displays strong red noise with a steep SF. Red noise for the other CP, B1929+10, comprises discrete events (see CD85, Figure 10q) that collectively yield a steep SF. Finally, magnetar J1622−4950 in the bottom row has the strongest, steep spectrum red noise, consistent with spin noise being highly correlated with spin frequency derivative and, thus, surface magnetic field strength of the NS.

4.2.2. *Constraints from scaling of variance with T*

The total phase variance is the quadratic sum of the white and red noise variances, $\sigma^2_{\phi}(T) = \sigma^2_{\rm wn} + \sigma^2_{\rm red}(T)$. Estimation of $\sigma^2_{\rm red}(T)$ can use the quadratic difference $\sigma^2_{\rm red}(T) = \sigma^2_{\phi}(T) - \sigma^2_{\rm wn}$ for cases where the red noise is strongly dominant and the white noise variance is obtained using the structure function in Eq. (4.3) for small lags where the second term is negligible (as in CD85, Eq. 12). Alternatively, the red noise variance can be obtained from the Bayesian posterior PDF for the model in Eq. (4.3).

The dependence of the red noise variance on data span length T can also be used to determine S_0 and $x_{\rm red}$. This requires that the red and white noise variances are separable for a wide range of sub-spans, which is possible for pulsars with large enough red noise and numerous samples across the total span (e.g. CD85, § V).

Red spin noise of some pulsars has been demonstrated to be a mixed process, comprising a superposition of events in both P and $\dot{P}$. Individually, each type of event would produce spectral indices $x_{\rm red} = 4$ and 6 and SF scalings $D^{(3)}_{\phi} \propto \tau^3$ and τ^5, respectively. The resulting SFs generally comprise at least two red-noise terms, with more than two if events in P and $\dot{P}$ occur together. For several CPs, the asymptotic scalings of $\sigma^2_{\rm red}(T)$ for large T and of $D^{(3)}_{\phi}(\tau)$ for large τ are dominated by events in $\dot{P}$ (CD85; Cordes et al. 1988; D'Alessandro et al. 1995), corresponding to a strong low frequency component to the spectrum with $x_{\rm red} \simeq 6$.

Fig. 5 shows spectral index estimates $x_{\rm red} = x_{\rm SF} + 1$ derived from SF slopes $x_{\rm SF}$ evaluated from timing data in the JPL and UTMOST timing programs. The estimates formally range between $x_{\rm red} = 2$ and $x_{\rm red} = 8$ but maximize at $x_{\rm red} \sim 4.5$, which is intermediate between the slope expected for spin noise comprising step functions in $f_{\rm s}$ and $\dot{f}_{\rm s}$. Individual sequences of these two types of step functions yield fluctuation spectra $\propto f^{-4}$ and f^{-6}, respectively. Physical contexts likely involve mixtures of both types of step functions, yielding a composite spectrum that can have an intermediate slope index between −4 and −6 or one or the other extremes, depending on the length of a data set. The Vela pulsar, for example displays both kinds of events (Cordes et al. 1988).

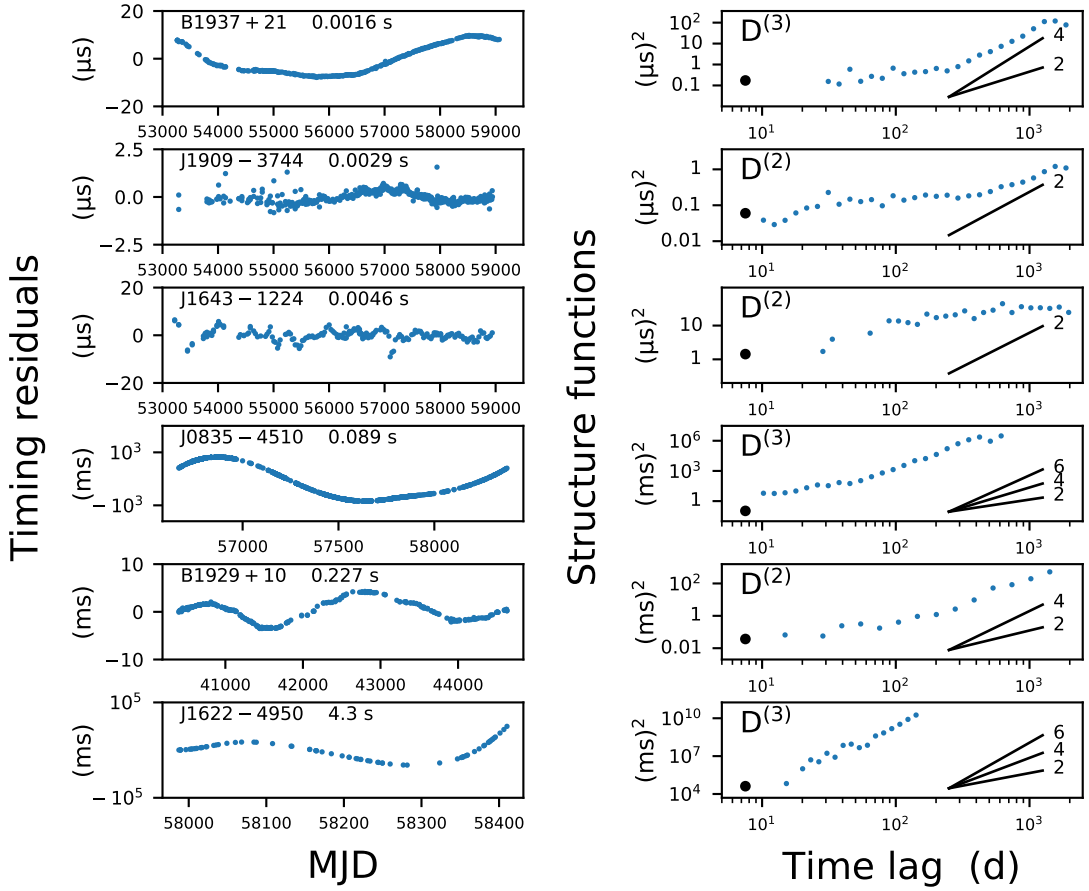


Figure 4. Timing residuals (left) and structure functions (SFs, right) for a sample of pulsars. Top three rows: millisecond pulsar data from NANOGrav's 15 yr data relase (Agazie et al. 2023a). Bottom three rows: residuals for three long period, high magnetic field pulsars. Data for pulsars J0835-1224 (the Vela pulsar) and J1622-4950 are from the UTMOST timing program (Lower et al. 2020) and data for B1929+10 are from the JPL timing program (CD85; Downs and Reichley 1983). In each SF panel in the right column, the type of SF is designated as $D^{(m)}$ with $m = 2$ or 3, blue dotted points are estimates of the binned structure function and the black circle represents the SF value due to white noise only. Slanted lines show scaling laws $D^{(m)}(\tau) \propto \tau^{x_{\rm SF}}$ for $x_{\rm SF} = 2, 4, 6$.

4.3. *Allan variance for red noise*

Frequency standards and clocks are often characterized using structure functions (Rutman 1978; Rutman and Walls 1991) , including the Allan variance (Allan 1966) and the same tools have been applied to pulsar timing data (CD85; Backer and Hellings 1986; Matsakis et al. 1997; Hartnett and Luiten 2011). Though MSPs once rivaled terrestrial frequency standards in frequency stability, new technologies have surpassed the stability of the most stable pulsars (Fig. 6). Nonetheless, pulsars are unique tools for applications in fundamental astrophysics and it is useful to characterize and compare their stabilities using standard methods.

Let $f_{\rm s}(t)$ be the time-dependent frequency of a clock or synthesizer and define the normalized frequency, $y(t) = f_{\rm s}(t)/\langle f_{\rm s}\rangle$, and its running average over an interval τ,

$$\overline{y}(t) = \frac{1}{\tau}\int_t^{t+\tau} dt'\, y(t'). \tag{4.6}$$

The Allan variance is the mean-square of the first increment of $\overline{y}(t)$, $\Delta^{(1)}_{\overline{y}}(t,\tau) \equiv \overline{y}(t+\tau) - \overline{y}(t)$,

$$\sigma^2_y(t,\tau) = \frac{1}{2}\left\langle [\overline{y}(t+\tau) - \overline{y}(t)]^2 \right\rangle = \frac{1}{2}\left\langle \left[\Delta^{(1)}_{\overline{y}}(t,\tau)\right]^2 \right\rangle. \tag{4.7}$$

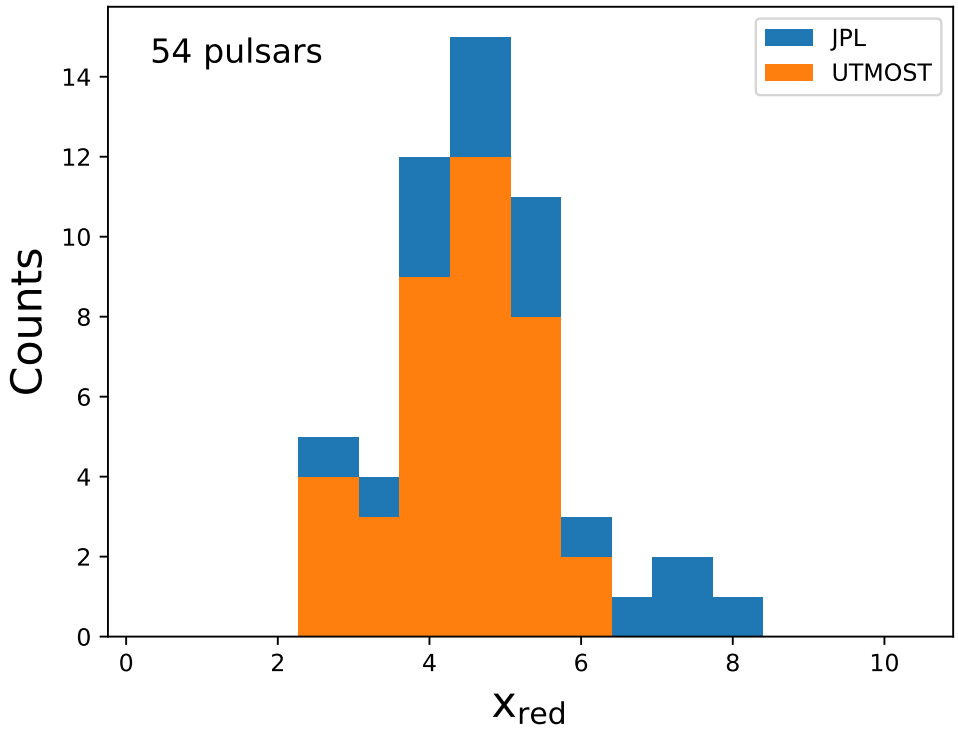


Figure 5. Histogram of inferred spectral indices for red noise assuming it has a power-law spectrum. Spectral indices are estimated from the asymptotic slope of the third order structure function using the relation $x_{\rm red} = x_{\rm SF} + 1$.

The Allan variance is therefore proportional to the first order structure function of y, which is written in terms of the second order phase SF,

$$\sigma_y^2(t,\tau) = \frac{1}{2} D_y^{(1)}(t,\tau) \equiv \frac{D_\phi^{(2)}(t,\tau)}{2(\langle f_{\rm s}\rangle \tau)^2}. \tag{4.8}$$

The SF for timing residuals $\mathcal{R}(t) = f_{\rm s}\delta\phi(t)$ is $\sigma_y^2(t,\tau) = D_{\mathcal{R}}^{(2)}(t,\tau)/2\tau^2$.

Extension: For some processes the Allan variance is independent of t and therefore not dependent on the data set length and the explicit t dependence is usually dropped from $\sigma_y^2(t,\tau)$. For other processes with higher-order nonstationarity, the t dependence remains. For example, a random walk in $\dot{\nu}$ (i.e. in the second derivative of the phase) requires a third-order SF to eliminate any t dependence. This can be used to define an analogous Allan-variance-like quantity (CD85)

$$\Sigma_y^2(t,\tau) = \frac{1}{9} D_y^{(2)}(t,\tau) = \frac{1}{9}\left\langle \left[\Delta_{\overline{y}}^{(2)}(t,\tau)\right]^2 \right\rangle = \frac{D_\phi^{(3)}(t,\tau)}{(3\langle f_{\rm s}\rangle\tau)^2} \tag{4.9}$$

Figure 6 compares the Allan deviation (AD) $\sigma_{\overline{y}}$ of four long period, high magnetic field CPs and four MSPs with a laser-cooled cesium fountain frequency standard (Heavner et al. 2005). For small lags τ the AD for pulsars follows that expected for white noise in pulse phase, $\sigma_{\overline{y}} \propto \tau^{-1}$ while the cesium frequency standard shows white noise in frequency, corresponding to $\sigma_{\overline{y}} \propto \tau^{-1/2}$. For $\tau \gtrsim 30$ to 200 d, the CPs show upturns in the AD due to achromatic spin noise. The MSPs show much smaller ADs. For the two best MSPs in PTA timing samples, J1713+0747 and J1909-3744, the ADs decline monotonically, with only a slight deviation from a white-noise scaling for J1909-3744, consistent with the NG15 noise modeling (Agazie et al. 2023c) using alternative methods. The MSP J1939+2134 (B1937+21) has the lowest AD at small lags (from white noise) but is the worst MSP in terms of correlated red noise, as seen for the

large upturn in AD at $\tau \sim 100\,\mathrm{d}$. This red noise is similar, statistically, to that seen from spin noise in CPs but an alternative explanation in terms of a circumpulsar asteriod belt has also been explored (Shannon et al. 2013). The large-DM MSP J1903+0327 shows a shallow upturn from a white-noise only AD that is apparently interstellar in origin (Geiger et al. 2025). In particular, this pulsar manifests the effects of incomplete correction for the combined effects of dispersion and scattering (pulse broadening). For comparison we show an AD curve for length of day variations of the Earth, which shows worse stability than most pulsars but is far more stable than the magnetar J1622−4950 also shown (data from Lower et al. 2020).

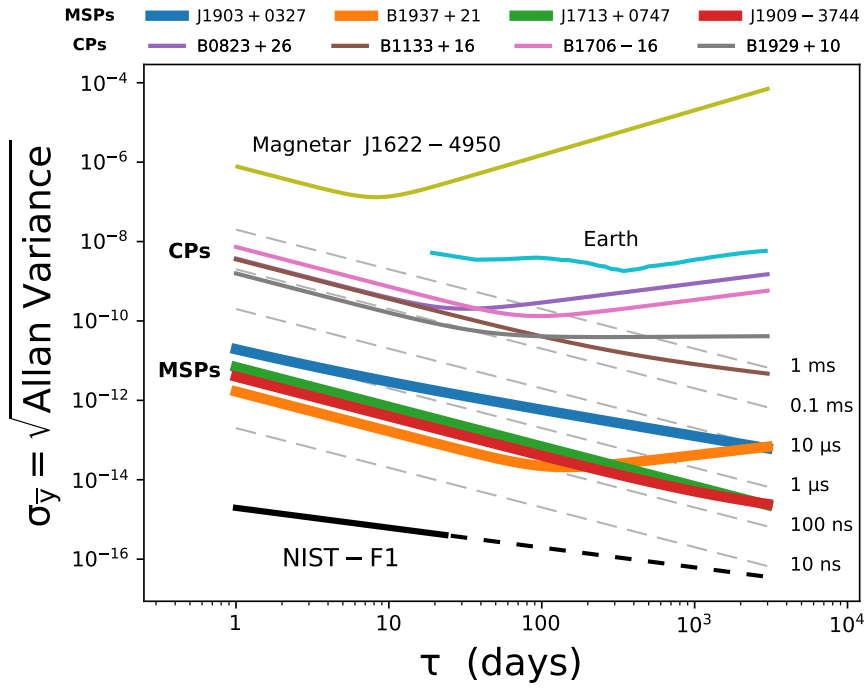


Figure 6. Allan deviation $\sigma_{\overline{y}}$ for pulsars compared to a cesium clock (NIST-F1) (Heavner et al. 2005). Curves are shown for four MSPs from the NANOGrav 15-yr data set (thick lines labeled 'MSPs') and four long-period canonical pulsars from the JPL timing program (thin lines labeleld 'CPs') (Downs and Reichley 1983; CD85) Also shown are curves for the magnetar J1622−4950 (Lower et al. 2020) and for length of day variations of the Earth (https://www.iers.org/IERS/EN/DataProducts/data.html). Faint dashed lines correspond to white noise with the labeled RMS values while the heavy dashed line for the NIST-F1 has been arbitrarily extrapolated to longer times for visual purposes (we do not have access to measurements for such an extrapolation).

4.4. *Scaling laws for the variance and spectrum of red spin noise*

Spin noise is well established for canonical pulsars (CPs), those with spin periods longer than $\gtrsim 10$ ms and with surface magnetic fields $\gtrsim 10^{11}$ G. However, the underlying physics of torque variations and superfluid dynamics are not well understood. Spin noise has a very red power spectrum that causes the variance in timing residuals to have non-stationary statistics dependent on the length of the data span, T. While there is a correlation of the spin-noise variance with a combination of spin frequency and its time derivative (Cordes et al. 1988; D'Alessandro et al. 1995; Shannon and Cordes 2010; Parthasarathy et al. 2019), it is not known how well it extends to MSPs given the significantly lower variance manifested in MSPs.

Past analyses (e.g. those just cited) have used a scaling law for the RMS spin noise after removal of a quadratic fit,

$$\sigma_{\mathrm{red},2}(T) = C_2\, {f_{\mathrm{s}}}^{\alpha_{\mathrm{r}}}\, |\dot{f}_{\mathrm{s}}|^{\beta_{\mathrm{r}}}\, T^{\gamma_{\mathrm{r}}}, \tag{4.10}$$

with parameters $C_2, \alpha_{\mathrm{r}}, \beta_{\mathrm{r}}$ and γ_{r}. The large scatter about this relationship for different objects is characterized using a log-normal distribution with standard deviation $\sigma_{\ln \sigma_{\mathrm{red},2}(T)}$.

Shannon and Cordes (2010) used a large body of measurements on canonical pulsars and a limited amount on MSPs to estimate parameters of the scaling law. At the time, only two MSPs showed red-noise similar to that of CPs [J1939+2134 (B1937+21) and J1824−2452A], while only upper limits were available on other MSPs. The maximum likelihood estimates of the spin-noise parameters for the 'CP+MSP' fit in their Table 1 are

$$\mathrm{C}_2 = 5^{+2.4}_{-1.6}\,\mu\mathrm{s}, \qquad \alpha_\mathrm{r} = -1.4 \pm 0.1, \qquad \beta_\mathrm{r} = 1.1 \pm 0.1, \qquad \gamma_\mathrm{r} = 2 \pm 0.2, \tag{4.11}$$

for f_s in Hz, $|\dot{f}_\mathrm{s}|$ in 10^{-15} Hz s^{-1}, and T in yr. The empirical spread about the scaling law is $\sigma_{\ln\sigma_{\mathrm{red},2}} = 1.6 \pm 0.1$. Errors on parameters are $\pm 2\sigma$.

Similar scaling laws have been estimated by others. Lam et al. (2017) included more MSPs than SC10 in their analysis and obtained for the 'CP+MSP$_{10,\mathrm{PPTA}}$ +NANO' fit in their Table 4, $C_2 = 6^{+1.3}_{-1.6}\,\mu s, \alpha_\mathrm{r} = -1.32 \pm 0.04, \beta_\mathrm{r} = 1.08 \pm 0.03, \gamma_\mathrm{r} = 1.96 \pm 0.08$ and $\sigma_{\ln\sigma_{\mathrm{red},2}} = 1.56 \pm 0.05$. Lower et al. (2020) analyzed non-recycled pulsars (aka CPs) to obtain $\alpha_\mathrm{r} = -0.84^{+0.47}_{-0.49}$ and $\beta_\mathrm{r} = 0.97^{+0.16}_{-0.19}$ and demonstrated consistency with SC10 and other previous results Hobbs et al. (2010); Parthasarathy et al. (2019).

Figure 7 shows the spin noise scaling law projected onto the period-period derivative (P–$\dot{P}$) plane with various pulsar types identified. The gray bands indicate the ranges of spin-parameter values that yield the same RMS ToA for data spans of 15 to 30 yr.

Fluctuation spectrum: The T dependence of $\sigma_{\mathrm{red},2}(T) \propto T^{2\pm0.2}$ corresponds to a power-law spectrum $\propto f^{-x_\mathrm{red}}$ with $x_\mathrm{red} = 1 + 2\gamma_\mathrm{r} = 5 \pm 0.4$. The spectrum is calculated from $\sigma_{\mathrm{red},2}(T)$ by expressing the coefficient S_0 (Eq. (4.5)) of the phase spectrum (Eq.(4.2)) in terms of the phase variance and assuming a lower-frequency cutoff η/T with $\eta \simeq 1$,

$$S_\mathcal{R}(f) = (x_\mathrm{red} - 1)\eta^{(x_\mathrm{red}-1)}\sigma^2_{\mathrm{red},2}(T)T^{1-x_\mathrm{red}} f^{-x_\mathrm{red}}. \tag{4.12}$$

Substituting for $\sigma_{\mathrm{red},2}$ from Eq. (4.10) yields

$$S_\mathcal{R}(f) = 2\gamma(C_2 {f_\mathrm{s}}^{\alpha_\mathrm{r}} |\dot{f}_\mathrm{s}|^{\beta_\mathrm{r}})^2 f^{-x_\mathrm{red}}. \tag{4.13}$$

Note there is no net dependence on the length of the time series T.

Utility and complications: The expressions for spin-noise variance (Eq. (4.10)) and the corresponding red-noise spectrum (Eq. (4.13)) are statistical descriptions of the pulsar population in the simplest terms. They are useful for making an initial assessment of the timing quality of a newly discovered pulsar. Also, as a new pulsar is timed over an initial year or two, any strong departures from the scaling law may suggest that other processes are in play, such as latent orbital motion.

Any specific pulsar can depart from this description in both the amplitude of spin variations and in the scaling law indices, $\alpha_\mathrm{r}, \beta_\mathrm{r}$, and γ_r. Moreover, an actual spectrum that has a piecewise power-law form but us analyzed as a single power law will yield an index γ_r and hence frequency scaling index $x_\mathrm{red} = 1 + 2\gamma_\mathrm{r}$ that will show dependence on the data span T. This arises from the underlying physics of the spin noise, which appears to comprise individual events in the spin torque having the idealized forms of narrow pulses or step functions or combinations of the two. These give fluctuation spectra $\propto f^{-4}$ and $\propto f^{-6}$, respectively. The population average $\gamma_\mathrm{r} \approx 5$ among canonical pulsars suggests that both kinds of events are seen across the population. The situation is less clear for MSPs but longer timing data sets on more MSPs should provide future clarity.

Another possible departure from the picture presented here is that achromatic timing noise may have a different cause than spin fluctuations and the stochastic GW background. For example, orbital noise from an asteroid belt can produce a power-law residuals spectrum; asteroids may plausibly grow out of debris from the accretion driven spinup proccess in some cases (e.g. Shannon et al. 2013; Jennings et al. 2020). This is discussed further in Sect. 4.6.

4.5. *Comparison with the nanohertz GW stochastic background*

It is useful to express the red-noise spectrum in terms that can be compared with those used for the long-wavelength GW spectrum. The characteristic dimensionless strain is represented with a dimensionless amplitude A_gw and a

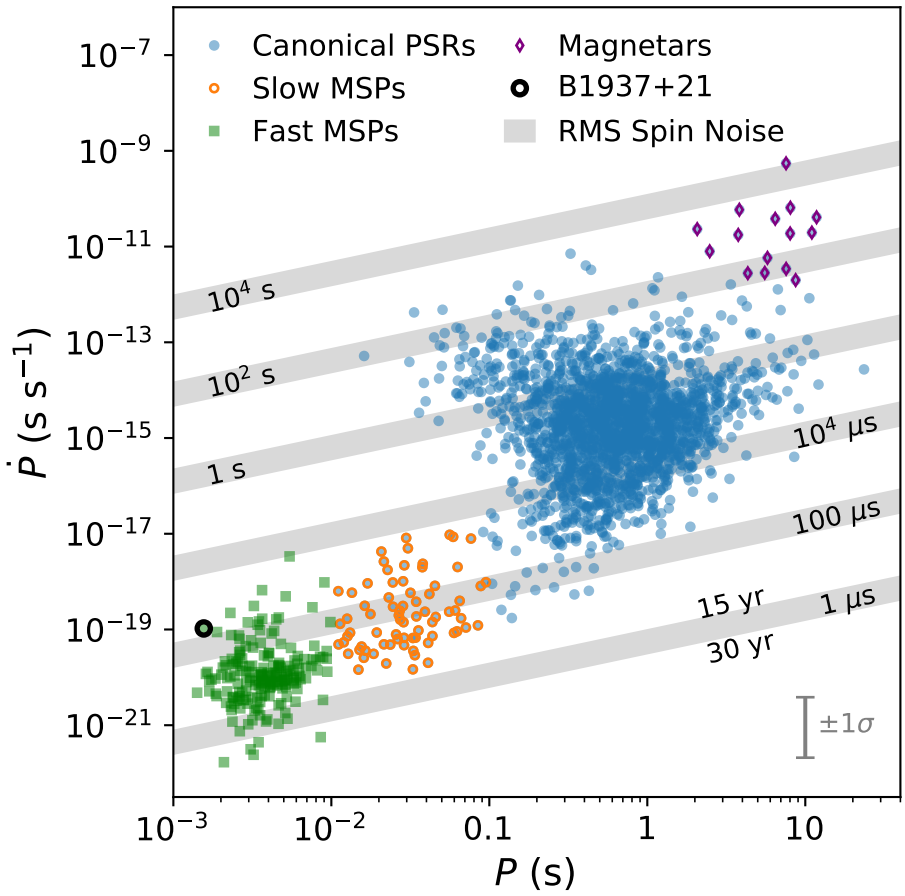


Figure 7. Spin period derivative $\dot{P}$ vs. period P in seconds for all pulsars in the ATNF catalog. $\dot{P}$ has been corrected for the Shklovskii effect where possible. (The Shklovskii effect is the contribution to $\dot{P}$ from translational motion of a pulsar. It is insignificant for CPs but can be important for MSPs with small intrinsic $\dot{P}$.) Grey bands indicate the range of RMS timing variations due to spin noise for data timespans between 15 and 30 years. The estimated spin noise is based on the scaling relation fit in Lam et al. (2017) across canonical pulsar, MSP, and magnetar populations (Equation (4.10)).

power-law frequency dependence,

$$h_{\rm c}(f) = A_{\rm gw}\left(\frac{f}{f_{\rm ref}}\right)^{-x_{\rm h}} \tag{4.14}$$

and the corresponding spectrum for arrival-time residuals is (Appendix B)

$$S_{\mathcal{R}}^{(\rm gw)}(f) = \frac{A_{\rm gw}^2}{12\pi^2 f^3}\left(\frac{f}{f_{\rm ref}}\right)^{-2x_{\rm h}} = \frac{A_{\rm gw}^2}{12\pi^2 f_{\rm ref}^3}\left(\frac{f}{f_{\rm ref}}\right)^{-(3+2x_{\rm h})} . \tag{4.15}$$

Using $f_{\rm ref} = 1\,{\rm cy\,yr^{-1}}$ with $A_{\rm gw} = 10^{-15}A_{\rm gw,-15}$ and expressing the spectrum in units of $\mu{\rm s}^2\,{\rm yr}$, the spectrum becomes

$$S_{\mathcal{R}}^{(\rm gw)}(f) = K_{S_r}A_{\rm gw,-15}^2\left(\frac{f}{f_{\rm ref}}\right)^{-x_{\rm red}} \tag{4.16}$$

with $x_{\rm red} = 3 + 2x_{\rm h}$ and the leading coefficient is

$$K_{S_r} = \frac{10^{-30}}{12\pi^2}(\mu{\rm s\,per\,yr})^2 = 8.41\times10^{-6}\,\mu{\rm s}^2\,{\rm yr}. \tag{4.17}$$

For reference, the simplest form for $h_c(f)$ results from a population of supermassive black hole binaries with orbital decay solely from GW emission, giving $x_h = 2/3$ and $x_{red} = 13/3$ (Rajagopal and Romani 1995; Phinney 2001; Jaffe and Backer 2003) This reference spectrum is currently used by all PTA groups as a comparison with empirical spectra. Actual spectra from merging black hole binaries are affected by the finite number of such systems that contribute significantly to PTA measurements and to other contributions to the spiral-in rate from gas dynamics and stellar interactions (Sesana and Figueroa 2025).

Using the same spectral form, we solve for the dimensionless amplitude $A_{\mathrm{rsn},-15}$ in terms of the residuals spectrum (Eq. (4.16)) and evaluate it using Eq. (4.13),

$$A_{\mathrm{rsn},-15} = \left(\frac{2\gamma_r}{K_{S_r}}\right)^{1/2} C_2(\mu s) f_s{}^{\alpha_r} |\dot{f}_s|^{\beta_r} \approx 3.45 \times 10^3 \, f_s{}^{-1.4} |\dot{f}_{s,-15}|^{1.1}, \tag{4.18}$$

with f_s in Hz and $\dot{f}_s$ in units of $10^{-15}\,\mathrm{Hz\,s^{-1}}$ and where the approximation uses only the nominal value for C_2.

As an example, the highly stable MSP J1909-3744 with $\nu = 339\,\mathrm{Hz}$ and $\dot{\nu} = -1.62 \times 10^{-15}\,\mathrm{Hz\,s^{-1}}$ gives $A_{\mathrm{rsn},-15} \simeq 1.7$ (comparable to constraints reported for this pulsar by, e.g., Shamohammadi et al. 2024; Chalumeau et al. 2022), and slightly below the gravitational wave amplitudes $A_{\mathrm{gw},-15} \simeq 2.0 - 2.5$ reported by Agazie et al. (2023b); EPTA Collaboration and InPTA Collaboration et al. (2023); Reardon et al. (2023b).

For the pulsar population at large, we compare *predictions* for the dimensionless amplitude $A_{\mathrm{rsn},-15}$ for red spin noise (using Eq. (4.18)) with $A_{\mathrm{gw},-15}$ for the GW stochastic background using histograms of their ratio $A_{\mathrm{rsn},-15}/A_{\mathrm{gw},-15}$ (Fig. 8). The histograms demonstrate that some (but not all) MSPs, which have small spindown rates, have spin stabilities yielding $A_{\mathrm{rsn}} \lesssim A_{\mathrm{gw}}$, making them potentially useful for GW detection with PTAs. We emphasize that additional considerations (e.g. red noise from interstellar propagation and ToA precision vs. S/N) also determine inclusion of any given MSP in a PTA program, as discussed in §20.

For fixed spin period, pulsars with smaller $\dot{P}$ values have greater predicted spin stability. Solving for the value of $\dot{P}$ that satisfies the condition $A_{\mathrm{rsn}} \leq A_{\mathrm{gw}}$ and using Eq. (4.18), we find values that make a pulsar potentially useful for GW detection,

$$\dot{P} \leq \dot{P}_{\mathrm{max}} = 10^{-15}\,\mathrm{s\,s^{-1}} \left(\frac{K_{S_r}}{2\gamma_r}\right)^{1/2\beta_r} \left[\frac{A_{\mathrm{gw},-15}}{C_2(\mu s)}\right]^{1/\beta_r} P^{2+\alpha_r/\beta_r} \simeq 6.08 \times 10^{-19}\,\mathrm{s\,s^{-1}} P^{0.73} A_{\mathrm{gw},-15}^{0.91}. \tag{4.19}$$

where P is in s. Fig. 9 shows this condition for $A_{\mathrm{gw},-15} = 2.4$ plotted as a black line on the P-$\dot{P}$ diagram along with points color coded for pulsars on above or below the line. Three MSPs are highlighted, two that easily satisfy the condition (J1713+0747, J1909-3744) and another, J1939+2134 (B1937+21) that is well known to show significant red noise. Equation 4.19 and Fig. 9 suggest that for most MSPs with typical periods $P < 0.01$ s, sources with $\dot{P}_{\mathrm{max}} \lesssim 10^{-20}$ s s^{-1} will satisfy the spin stability criterion for expected GW amplitudes.

4.6. *Orbital noise*

Orbital noise may derive from interactions of a pulsar with its companion, as in 'spider' pulsars or from a population of asteroids orbiting a pulsar (and its stellar companion, if any). Spider pulsars have low-mass companions that are ablated by pulsar emission and generally show stochastic variations in their orbits that, although of intrinsic interest, make most of them unsuitable for precision timing. Chalumeau et al. (2022) discuss timing stability of spider pulsars and identify a few cases where orbital noise is not seen.

We focus the remainder of this section on asteroids, which may form in the aftermath of the accretion-driven spinup process which may leave residual gas near the neutron star that solidifies into small objects. The first detected exoplanets around the MSP B1257+12 (Wolszczan and Frail 1992) exemplify the presence of small bodies around recycled pulsars. A detailed study of the orbital dynamics of the planets indicate that there are stable orbits in the system (Goździewski et al. 2005), allowing the presence of dust or larger objects. Neutron stars with white dwarf companions also have stability regions outside the semi-major axis of the binary (Jennings et al. 2020).

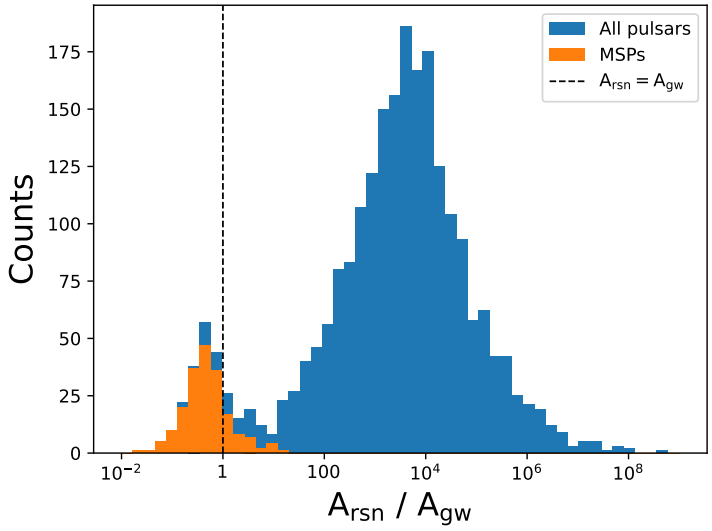


Figure 8. Histogram of the ratio of predicted dimensionless spectral amplitude $A_{\rm rsn}$ for red spin noise (using cataloged values for spin frequencies and their derivatives) to $A_{\rm gw}$ for the nanohertz GW background using the NANOGrav value. The blue histogram for all pulsars in the ATNF pulsar catalog shows bimodality that reflects the much larger spin noise for non-recycled pulsars. The orange applies to catalog MSPs, defined as $P \leq 20\,$ms and $\dot{P} < 10^{-17}$s s^{-1}. The vertical line indicating $A_{\rm rsn} = A_{\rm gw}$ demonstrates that the nominal red noise for some recycled pulsars is a larger signal than the GW background.

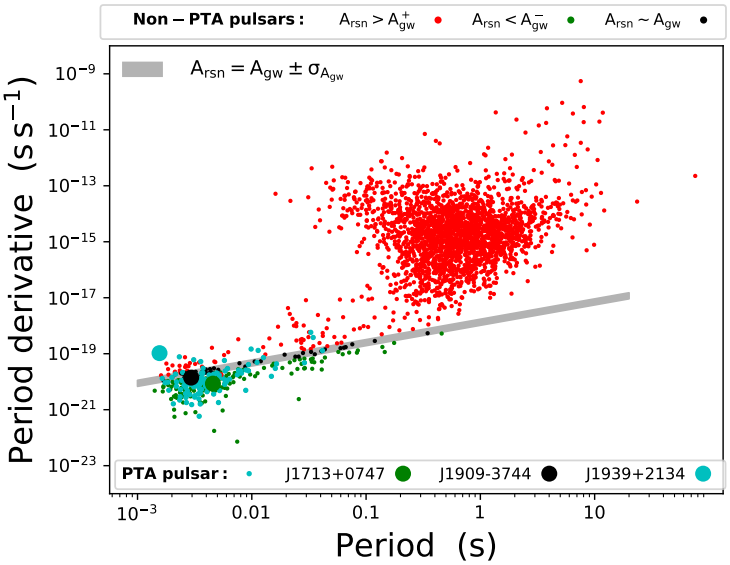


Figure 9. Period-Period derivative diagram showing pulsars with red-noise spectral amplitudes $A_{\rm rsn}$ above (red points), below (green points), or inside (small black points) the gray band where they are approximately equal to the GW background's spectral amplitude $A_{\rm gw}$. The 125 pulsars included in PTA programs by the NANOGrav, EPTA, PPTA, InPTA, CPTA, and MPTA groups are indicated in cyan. Indicated by large symbols are two MSPs J1713+0747 and J1909-3744 used in PTA programs because of their high spin stability along with another, J1939+2134 (B1937+21, large black circle), that has poor spin stability. MSPs in globular clusters have been excluded because their $\dot{P}$ values are perturbed by cluster gravitational potentials.

This leads to the possible explanation of red noise seen in timing of the isolated MSP B1937+21 as orbital rather than spin noise (Shannon et al. 2013). To match the large measured red noise (§4.2) a total mass $M_{\rm belt} \lesssim 0.05 M_{\oplus}$

extending to at least 15 au yields orbital periods longer than the analyzed data span. This case illustrates that a small debris mass can, in principle, produce large timing effects. Most well studied MSPs show substantially less red noise than B1937+21, indicating that any debris disks have very small total masses. Nonetheless, as timing data sets grow longer, the red noise from an asteroid belt will grow along with other red-noise processes, including spin noise and GWs, although with a different dependence on data span.

An orbital companion produces a cyclical TOA variation due to recoil motion of the NS. An ensemble of asteroids contributes a noise process to ToAs with variance that grows with longer data spans if the maximum orbital period is longer than the data span length (Shannon et al. 2013). Recent work considering asteroid belts around MSPs with white dwarf companions (Jennings et al. 2020) derives asteroid noise spectra for individual MSPs. Asteroids are assumed to be distributed in mass as $f_m(m) \propto m^{\alpha_a - 1}$ and in orbital radius as $f_a(a) \propto a^{\beta_a - 1}$. For N asteroids with total mass $M_{\rm belt}$ and NS mass M, the spectrum for ToA perturbations is a power law,

$$S_{\rm ast}(f) = \left[\frac{G}{(2\pi M)^2}\right]^{2/3} \left(\frac{M_{\rm belt}\sin i}{2c\sqrt{N}}\right)^2 \frac{\langle m^2\rangle}{\langle m\rangle^2} \left[\frac{2\beta_{\rm a} f^{-(2\beta_{\rm a}+7)/3}}{3(f_-^{-2\beta_{\rm a}/3} - f_+^{-2\beta_{\rm a}/3})}\right], \quad f_- \le f \le f_+, \tag{4.20}$$

where the frequency cutoffs are related to the extent of the asteroid belt, $f_\pm = \sqrt{M} a_{\rm min,max}^{-3/2} \simeq \sqrt{1.4} a_{\rm min,max}^{-3/2}$ for M in solar masses, frequencies in cy yr^{-1}, and orbital radii in au. The spectrum is expressed in terms of the index $\beta_{\rm a}$ for the distribution of orbital radii a, which is related to the index $\beta_f = -2\beta_{\rm a}/3$ used by Jennings et al. (2020) for the corresponding distribution in orbital frequencies. The ratio of moments $\langle m^2\rangle/\langle m\rangle^2$ is determined solely by the mass ratio $r = m_2/m_1$ of the largest and smallest asteroid masses,

$$\frac{\langle m^2\rangle}{\langle m\rangle^2} = \frac{(\alpha_{\rm a}+1)^2}{\alpha_{\rm a}(\alpha_{\rm a}+2)} \left[\frac{(r_{\rm a}^{\alpha}-1)(r^{\alpha_{\rm a}+2}-1)}{(r^{\alpha_{\rm a}+1}-1)^2}\right]. \tag{4.21}$$

These expressions follow from (Jennings et al. 2020) except for the use of a distribution in semimajor axis a rather than frequency f.

Evaluating for $\alpha_{\rm a} = -5/6$ (the steady-state value for self-similar populations of colliding bodies, as determined by Dohnanyi (1969)), $\beta_{\rm a} = 1$ (corresponding to a uniform distribution in orbital radius), $M_{\rm belt} = 10^{-3} M_\oplus$ with $N = 10^4$ asteroids, a mass ratio $r = 10^{-4}$, and a NS mass $M = 1.4\ M_\odot$,

$$S_{\rm ast}(f) = 135\,{\rm ns}^2\ {\rm yr} \left[\frac{(M_{\rm belt}\sin i/10^{-3}\,M_\oplus)^2}{N/10^4}\right] \left[\frac{\langle m^2\rangle/\langle m\rangle^2}{100}\right] \left(\frac{f}{1\ {\rm cy\ yr}^{-1}}\right)^{-3}. \tag{4.22}$$

Defining the spectral form $S_{\rm ast}(f) = A_{\rm ast}^2 f^{-\gamma_{\rm a}}$, again for frequencies in cycles yr^{-1}, the dimensionless amplitude is

$$A_{\rm ast} = 11.6\ {\rm ns\ yr}^{1/2} \left[\frac{(M_{\rm belt}\sin i/10^{-3}\,M_\oplus)}{\sqrt{N/10^4}}\right] \left[\frac{\langle m^2\rangle/\langle m\rangle^2}{100}\right]^{1/2} \tag{4.23}$$

$$\gamma_{\rm a} = (2\beta_{\rm a}+7)/3 = 3. \tag{4.24}$$

Later we compare the spectrum of this achromatic process with other processes.

5. ELEMENTS OF PULSAR SIGNALS AND THEIR PROPAGATION

Itemizing the timing error budget requires consideration of emitted wavefields and how they are affected by propagation through intervening plasmas (along with effects from instrumentation). Before introducing the timing model, we must first lay out the key elements of pulsar signals, including their basic emission properties and the plasma propagation effects incurred in the observed signal. Together these elements form a pulsar signal model (e.g. Fig. 2), which is distinct from and a prerequisite for the timing models discussed later.

Radio pulsars emit radiation from their magnetospheres with brightness temperatures as high as 10^{42} K that entail coherent emission from highly relativistic particles. Emission radii $r_{\rm em} = |\mathbf{x}_{\rm e}|$ are intermediate between the NS radius $R_* \sim 10$ km and the light cylinder radius $r_{\rm LC} = c/\Omega_{\rm s} = cP_{\rm s}/2\pi \simeq 5\times10^4 P\,{\rm km} \gg R_*$ for P in s.

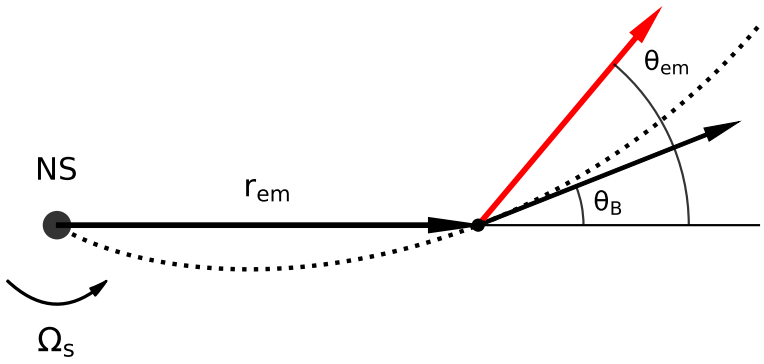


Figure 10. Schematic of emission at radius $r_{\rm em}$ into a direction angle $\theta_{\rm em}$. The tangent to the magnetic field line (dotted) is at an angle $\theta_{\rm B}$ from the radial vector. The difference between $\theta_{\rm em}$ and $\theta_{\rm B}$ is from rotational aberration and gravitational bending of the ray path. A change in emission radius alters $\theta_{\rm em}$, yielding emission directed toward an observer at an offset spin phase, altering the observed pulse phase. Similarly, a change along a different magnetic field line also changes the observed pulse phase.

Beaming is tangential to the magnetic field (Fig. 10) and aberrated by the NS spin into a net emission angle $\theta_{\rm em}$ relative to the radius vector $\mathbf{x}_{\rm e}$ measured from the NS center (Cordes 1978; Krzeszowski et al. 2009; Hassall et al. 2012). The field direction and aberration angle both depend on the emission location $\mathbf{x}_{\rm e}$. Emission is seen when the beam closely approaches the observer's direction. Because field lines and thus ray paths are non-radial, gravitational bending must also occur, as analyzed for the Crab pulsar (Medvedev 2026). Additionally, polarization-dependent refraction may be significant in some pulsar magnetospheres (Middleton et al. 2025).

Collective radiation from large particle numbers is in the form of 'nanoshots' i.e. $\lesssim$ ns-duration impulses that extend to $\gtrsim$GHz frequencies (Cordes 1976, see also Sect. 5.3). Individual pulses seen once per spin period have widths $\gtrsim 30\,\mu$s and up to hundreds of ms for CPs (Manchester et al. 2005). The MSP observed in multiple PTA programs, J1909−3744, in fact has the narrowest average pulse width. Thus they generally comprise incoherent ensembles of many nanoshots[14] with different shapes from one period to the next owing to variations in both emission radius and coherence strength from the dynamic particle flow. This variability underlies temporal jitter with respect to strictly periodic emission times.

Evidently particle flows and emission are controlled, in the mean, by the strong magnetic field of the NS, as evidenced by the convergence of average pulse profiles to distinct shapes, whose stability has been demonstrated over the decades since pulsars were discovered. (We note that magnetars, by contrast, have dynamic magnetic fields that cause their average profiles to vary significantly.)

5.1. *From fields to baseband voltages*

Pulsar processing typically involves manipulation of digitized voltages that are proportional to electric field components selected by the antenna polarization. The scalar field in a specific polarization $\widehat{\mathbf{p}}$ is $E(t) = \mathbf{E}(t)\cdot\widehat{\mathbf{p}}$ and the field is typically modified by a transfer function with impulse response $H_{\rm ext}(t)$, which may be polarization specific. The receiver selects a frequency band according to an impulse response $R(t)$. The net narrowband field $E_\Delta(t)$ is then the convolution of three real quantities,

$$E_\Delta(t) = E_i(t) * H_{\rm ext}(t) * R(t), \tag{5.1}$$

where $E_i(t)$ is the initial, emitted field. A baseband mixer translates the field to a complex baseband field through the operation,

$$\varepsilon(t) = \left[e^{2\pi i\nu_0 t}E_\Delta(t)\right] * B_{\rm lp}(t), \tag{5.2}$$

[14] A special case is the young Crab pulsar from which individual nanoshots have been measured (Hankins et al. 2003)

where $B_{\rm lp}$ is a low pass filter that enforces limitation of ε limited to frequencies $\nu \in [-B/2, B/2]$ with bandwidth B. We simplify ε by expanding each of $E_i, H_{\rm ext}$, and R into negative and positive frequency components as (e.g.) $E_i(t) = E_{i,-}(t) + E_{i,+}(t)$. Hermiticity of the Fourier transform $\widetilde{E}_i(\nu)$ requires $E^*_{i,-}(t) = E_{i,+}(t)$. Defining baseband quantities, $\varepsilon_i(t) = e^{2\pi\nu_0 t}E_{i,+}(t), h_{\rm ext}(t) = e^{2\pi\nu_0 t}H_{\rm ext\,+}(t)$ and $r(t) = e^{2\pi\nu_0 t}R_+(t)$, the baseband field is $\varepsilon(t) = \varepsilon_i(t) * h_{\rm ext}(t) * r(t) * B_{\rm lp}(t)$. By lumping together the last three quantities in the convolution into an effective impulse response, $h(t) = h_{\rm ext}(t) * r(t) * B_{\rm lp}(t)$, the baseband field is written succinctly as

$$\varepsilon(t) = \varepsilon_i(t) * h(t), \tag{5.3}$$

where $h(t)$ is understood to include both astrophysical (wave propagation) and receiver contributions.

Generally the impulse response $h(t)$ in Eq. (5.3) could be polarization dependent because it can include birefringent propagation, as discussed below, along with scattering. In practice dispersion and Faraday rotation are removed separately, so $h(t)$ then represents only the effects of scattering along with receiver contributions.

5.2. *Stokes parameters from baseband fields*

.

Pulsar emission is generally polarized, requiring separate baseband signals for two polarization channels $p = x, y$ for measurements with linearly polarized antennas or $p = r, l$ for circular polarization. The four Stokes parameters (I, Q, U, V) involve auto-and-cross products of ε_p. Pulsar timing typically makes use of only the total Stokes intensity $I = \sum_p |\varepsilon_p|^2$ though some studies (see Sect. 6.2) have explored the use of sharper features in the linearly polarized intensity $L = \sqrt{Q^2 + U^2}$ or in the circular polarization V (see §6.2).

Adopting either a circular or linear polarization basis, the Stokes vector is expressed in terms of two baseband fields, $\varepsilon_{\rm r}, \varepsilon_\ell$ or $\varepsilon_{\rm x}, \varepsilon_{\rm y}$,

$$\mathbf{S} = \begin{pmatrix} I \\ Q \\ U \\ V \end{pmatrix} = \begin{pmatrix} I_{\rm r} + I_\ell \\ 2\mathcal{R}\{\varepsilon_{\rm r}\varepsilon^*_\ell\} \\ 2\mathcal{I}\{\varepsilon_{\rm r}\varepsilon^*_\ell\} \\ I_{\rm r} - I_\ell \end{pmatrix} = \begin{pmatrix} I_{\rm x} + I_{\rm y} \\ I_{\rm x} - I_{\rm y} \\ 2\mathcal{R}\{\varepsilon_{\rm x}\varepsilon^*_{\rm y}\} \\ 2\mathcal{I}\{\varepsilon_{\rm x}\varepsilon^*_{\rm y}\} \end{pmatrix}. \tag{5.4}$$

These are defined without any time averaging, contrary to the usual case, because we wish to consider both the mean and variance of each Stokes parameter, requiring moments $\langle \mathbf{S} \rangle$ and $\langle \mathbf{S} \circ \mathbf{S} \rangle$, the latter being the mean of the Hadamard (i.e. element-wise) product. In the following we also make use of the complex quantity $L = Q + iU$.

The variance of the total intensity I is polarization dependent and it also depends on scintillation modulations (Cordes et al. 2004a). Instrumental polarization is represented as a transformation of the true Stokes vector using a 4×4 Mueller matrix $\boldsymbol{M}$ to give the nominal measured Stokes parameters, $\mathbf{S}_{\rm meas} = \boldsymbol{M}\mathbf{S}$. Without inversion, instrumental polarization yields additional arrival time errors, as discussed later (see Sect. 8.1).

The degrees of polarization are defined in terms of ensemble average Stokes parameters[15],

$$d_L = \frac{\sqrt{\langle Q \rangle^2 + \langle U \rangle^2}}{\langle I \rangle} \equiv \frac{|\langle L \rangle|}{\langle I \rangle}, \qquad d_V = \frac{\langle V \rangle}{\langle I \rangle} \qquad d_{\rm p} = (d_L^2 + d_V^2)^{1/2} \leq 1. \tag{5.5}$$

As defined, the variances of the unaveraged Stokes parameters satisfy

$$\langle |L|^2 \rangle + \langle V^2 \rangle = \langle I \rangle. \tag{5.6}$$

This equality follows from the fact that the instantaneous polarization in Nyquist sampled data is effectively 100%. However, a partially polarized signal varies with time so that

$$\langle Q \rangle^2 + \langle U \rangle^2 + \langle V \rangle^2 \leq \langle I \rangle^2 \tag{5.7}$$

[15] For pulsar signals it is useful to think of an ensemble average as an average at fixed pulse phase over an ensemble of pulses for which stationary statistics can apply. Pulsars are thus said to be cyclostationary, at least in the mean. However, all quantities are strong functions of pulse phase and thus are non-stationary vs. phase.

Later we need to refer to Stokes parameters of a noiselike polarized signal that is added to unpolarized noise and we utilize the signal to noise ratio of pulses in each of the Stokes parameters.

The intensity modulation index,

$$m_I = \frac{\sigma_I}{\langle I\rangle} = \left(\frac{1+d_{\rm p}^2}{2}\right)^{1/2}, \tag{5.8}$$

depends on the total degree of polarization $d_{\rm p}$ and, by inspection, is smallest for an unpolarized signal ($d_{\rm p}=0$). This follows because Stokes I for an unpolarized signal has four degrees of freedom while a completely polarized signal has only two.

We need RMS values for the Stokes parameters for calculations of the signal to noise ratios of Stokes-parameter pulse profiles. Expressed as the ratios of RMS values of L, Q, U, and V to the RMS I, we have

$$\frac{\sigma_L}{\sigma_I} = \left[\frac{2(1-d_V^2)}{1+d_{\rm p}^2}\right]^{1/2}, \tag{5.9}$$

$$\frac{\sigma_Q}{\sigma_I} = \left[\frac{1-d^2+2d_L^2\sin^2 2\chi}{1+d_{\rm p}^2}\right]^{1/2}, \tag{5.10}$$

$$\frac{\sigma_U}{\sigma_I} = \left[\frac{1-d_{\rm p}^2+2d_L^2\cos^2 2\chi}{1+d_{\rm p}^2}\right]^{1/2}, \tag{5.11}$$

$$\frac{\sigma_V}{\sigma_I} = \left[\frac{1+d_V^2-d_L^2}{1+d_{\rm p}^2}\right]^{1/2}. \tag{5.12}$$

These ratios reflect the number of degrees of freedom in each Stokes parameter and depend on polarization-dependent correlations such as $\langle I_{\rm r} I_\ell\rangle = (1/4)(1+d_L^2-d_V^2)\langle I\rangle^2$. A completely polarized signal ($d_{\rm p}=1$) has perfectly correlated $I_{\rm r}$ and I_ℓ and thus fewer degrees of freedom, so the Stokes-I modulation index, $m_I=1$, is larger than for an unpolarized signal with $m_I = 1/\sqrt{2}$.

The RMS ratios for a completely polarized signal depend on the type of polarization, $\sigma_L/\sigma_I = \sqrt{1-d_V^2}$, $\sigma_Q/\sigma_I = d_L|\sin 2\chi|$, $\sigma_U/\sigma_I = d_L|\cos 2\chi|$, and $\sigma_V/\sigma_I = \sqrt{1-d_L^2}$.

For the unpolarized case with $d_{\rm p}=d_L=d_V=0$, the ratios are $\sigma_L/\sigma_I=\sqrt{2}$, and $\sigma_Q/\sigma_I=\sigma_U/\sigma_I=\sigma_V/\sigma_I=1$, which are all equal to or larger than the fully polarized case.

5.3. *Pulsar emission is modulated polarized shot noise*

Here we investigate the statistical properties of pulsar signals as polarized shot noise that includes a modulation function that shapes either the shot amplitudes or their rates. Cordes and Wasserman (2016, Appendix A) show that when shot noise is 'dense' (comparable widths and separations of shots), amplitude-modulated shots and rate-modulated shots are indistinguishable statistically. In Sect. 5.7 we discuss additional, extrinsic modulations from interstellar scintillation that yields an extended description of the pulsar signal as (Cordes et al. 2004a) 'scintillated amplitude-modulated polarized shot noise' or SAMPSN[16].

Regardless of the radiation physics underlying coherence (e.g. plasma maser vs. charge bunching), the fundamental radiation unit is a shot pulse having temporal structure narrower than the reciprocal, ν^{-1}, of the observation frequency, e.g. sub-nanosecond, as follows from Fourier analysis. Large numbers of shots then comprise observed pulses with durations and internal structure from microseconds to many milliseconds.

Let $\Delta(t-t_j)$ be the form of a single shot emitted at time t_j with an impulsive form determined by the emission process and modified by the temporal response of a receiver. Though narrowband shots in the form of oscillatory wave packets

[16] A similar portrayal has been made by Osłowski et al. (2011) in what they term 'stochastic wide-band impulse modulated self-noise' or SWIMS. We note that our usage of the terms 'self-noise' and 'jitter' (see below) differ from that in Osłowski et al. (2011)

are conceivable, there is no empirical evidence in support of their presence. Moreover, the occurrence of broadband shots (i.e. bandwidths $\gtrsim 20\%$ of the center frequency) has been established for the Crab pulsar (Hankins and Eilek 2007) and for the MSP J0437−4715 (Osłowski et al. 2011). Our assumption of its generality suffices, statistically, for our analysis of pulsar timing.

Pulsar signals are often treated as complex baseband voltages obtained by mixing the signal selected in a narrowband receiver channel in a single hand of polarization with a complex local oscillator signal, $e^{-2\pi i\nu_0 t}$, and low-pass filtering. The baseband signal of Eq. (5.3) for shot noise is then

$$\varepsilon(t) = \sum_j a_j \Delta(t - t_j). \tag{5.13}$$

where the coefficients a_j are complex amplitudes. A rectangular receiver bandpass yields $\Delta(t) = \mathrm{sinc} B_\mathrm{r} t \equiv (\sin \pi B_\mathrm{r} t)/\pi B_\mathrm{r} t$. The amplitude a_j is related to the peak shot flux density as $|a_j| = (2\pi S_{\nu_0,\mathrm{max},j}/cB_\mathrm{r})^{1/2}$. A general statistical model would include a joint distribution $f_\mathrm{shots}(a_j, t_j)$; however, empirical and practical considerations imply that it is sufficient to consider shot amplitudes and delays to be decoupled[17].

Pulses and their substructures are orders of magnitude wider than shots (e.g. μs and ms vs. ns for shots) , requiring variable shot amplitudes a_j or a variable shot emission rate. This is motivated by the amplitude modulated polarized shot-noise (AMPSN) model (Rickett 1975; Cordes 1976) with applications to the Crab pulsar that include interstellar scintillation (Cordes et al. 2004a), and extended to FRB contexts by Cordes and Wasserman (2016); Nimmo et al. (2022). For a single polarization channel the baseband voltage is written as the product,

$$\varepsilon(t) = a(t)m(t), \tag{5.14}$$

where a is a real modulation and m is complex noise. In the rest of the paper, we specify the statistical moments of m as

$$\begin{array}{ll} \langle m \rangle = 0 & \text{zero mean} \\ \langle m(t_1) m(t_2) \rangle = 0 & \text{zero correlation} \\ \langle m(t_1) m^*(t_2) \rangle = \sigma_m^2 \Delta(t_1 - t_2) & \text{variance } \sigma_m^2 \text{ and auto correlation function } \Delta. \end{array} \tag{5.15}$$

The corresponding single-polarization intensity is

$$I(t) = a^2(t)|m(t)|^2 \equiv A(t)M(t) \tag{5.16}$$

where $M(t)$ has moments $\langle M \rangle = 1$ and $\langle M^2 \rangle = 1 + m_M^2$ written in terms of the modulation index, $m_M \equiv \sigma_M/\langle M \rangle$. For dense shot noise with separations comparable or less than shot widths, $m_M = 1$ whereas sparse shots $m_M > 1$. Most pulsar investigations yield $m_M = 1$ for a few CPs and the MSP B1937+21 (e.g. Cordes and Hankins 1979; Jenet et al. 2001) except for high time resolution studies of the Crab pulsar that have revealed individual shots (Hankins et al. 2003; Hankins and Eilek 2007).

5.4. *Pulse shapes and average profiles*

Pulsar timing methodology is usually based on averages of a large number of single pulses, each formed by time averaging over $\Delta t \sim 1\,\mu$s intervals for MSPs and up to ~ 1 ms for long period objects. Average profiles are usually formed with 1024 to 4096 time bins per period. This intrapulse averaging reduces the shot noise modulation index by a factor $(\Delta t B)^{-1/2}$, where the time-bandwidth product $\Delta t \times B$ is typically $\gg 1$. The remaining variance from this 'self noise' makes a very small contribution to the overall error in ToA estimates compared to those from additive radiometer noise and pulse jitter, as discussed later.

Amplitude modulations of the self noise involve multiple pulse components with varying amplitudes and pulse phases in individual pulses that average into the stable forms shown in Fig. 1. Pulse components physically correspond

[17] Examples shown in Hankins and Eilek (2007); Hankins et al. (2003)] show no strong relation between amplitude and delay.

to sub-beam structure in the 'lighthouse' beam that rotates through the LoS. This physical view is consistent with observations showing that jitter is largely independent between components, as can be seen in Fig. 11, which shows a typical example for PSR J0738−4042. This picture is substantiated by statistical and Fourier studies of single pulses going back to the early days of pulsar science (e.g. Backer 1973). The number of components and their separations are significant factors in the overall timing variance for a given pulsar. Here we present a suitable model for average profiles that includes components and their fluctuations.

The envelope of the $j^{\rm th}$ pulse is a sum over n_c pulse components,

$$A_j(t) = \sum_{i=1}^{n_c} c_{ij} A_{ij}^{(\rm c)}(t - t_{ij}), \tag{5.17}$$

where subpulse amplitudes c_{ij} and delays $t_{\rm ij}$ vary statistically about mean values from processes intrinsic to the pulsar (e.g. jitter) but also from propagation through intervening plasmas (next section). For pulsars, these quantities generally have well defined mean values that determine the shape of the template profile average at a specific center radio frequency. For simplicity we have suppressed the radio frequency dependence of A_j because it is relatively gentle. A few pulsars deviate from this simple characterization, including the Crab pulsar (J0534+2200) that has shown a secular change in component separations (Lyne et al. 2013) and MSP J1713+0747 that has shown a sustained transient evolution of its average pulse shape (Jennings et al. 2024b, and references therein)[18].

The average profile is the sum over N pulses,

$$I_N(t) = N^{-1} \sum_{j=1}^{N} \sum_{i=1}^{n_c} c_{ij} A_i(t - t_{\rm ij}). \tag{5.18}$$

A good approximation is that c_{ij} and $t_{\rm ij}$ are statistically independent of each other and between different pulses (different j) as seen in Fig. 11. Pulse sequences from some objects do show correlations in the form of 'drifting subpulses' and other effects (Backer et al. 1975), but these do not alter our analysis significantly. Also, for MSPs, these correlations seem to be largely absent.

An illustration of this empirical model is shown in Fig. 11. The average profile in the top panel displays several components. Single pulses comprise subpulses that occur preferentially in these profile components, as demonstrated in the histogram of the pulse phases in which single-pulse maxima occur. The main panel shows that subpulse amplitudes and phases occur independently in different components and with different frequencies of occurrence. The average profile is determined by both the amplitudes of subpulses and their frequency of occurrence in pulse phase.

The template shape is idealized as the ensemble average (corresponding to $N \to \infty$),

$$U(t) = \langle I_N(t) \rangle = \sum_i \langle c_{ij} \rangle A_i(t - \langle t_{\rm ij} \rangle). \tag{5.19}$$

In practice, templates are based on finite N averages and application of a denoising procedure to minimize the influence of off-pulse noise on ToA estimates.

ToAs are calculated through cross correlation or, equivalently, least-squares fitting of the template to a measured profile. The ToA is given by the maximum cross correlation obtained as the solution of $C'_{I_N U}(\tau) = 0$ where $C_{I_N U}$ is the cross correlation function between the template and a finite-sum profile. Differences between U and I_N yield ToA errors that add in quadrature to those from additive noise and template fitting. We refer to these differences as 'pulse jitter' in the ToA error budget.

Implicit in Eq. (5.18)-(5.19) is that the time t extends over only one period (and thus corresponds to pulse phase $\phi = t/P$ for a period P). This requires alignment of pulses according to a previously generated timing ephemeris. It is also assumed that plasma dispersion delays have been removed with small enough error that pulse shapes are undistorted.

[18] The shapes of fast radio bursts (FRBs) can be described similarly but with two significant differences. First, they are not periodic in the same way as pulsars and, second, the components have different center frequencies and relatively narrow bandwidths.

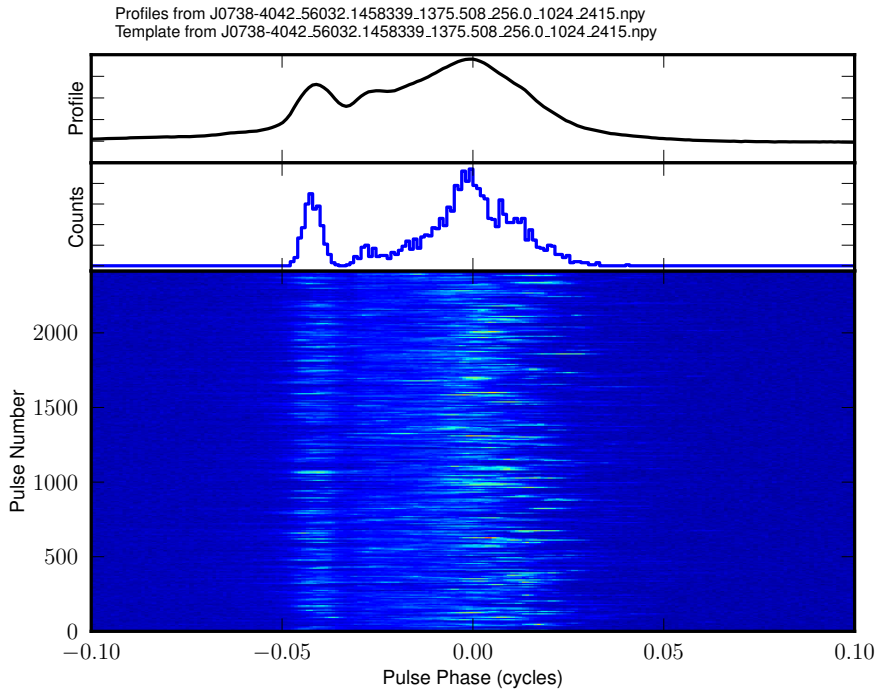


Figure 11. Main panel: a sequence of pulses from PSR J0738-4042 ($P = 0.37\,\mathrm{s}$, DM $= 161\,\mathrm{pc\ cm^{-3}}$) obtained at 1.38 GHz with the Parkes telescope (R. Shannon, private communication). Top panel: average profile from the 2500 pulses shown. Middle panel: counts of pulse maxima vs. pulse phase.

Identifying and modeling profile components is another method for constructing templates using Gaussian functions. The motivation is to better understand how the number of components and their separations contribute to the ToA error budget. An objective approach to component identification identifies inflection points in the profile $U(\phi)$ using the first derivative, $U'(\phi)$ (where we now use pulse phase ϕ rather than time). Fig. 12 shows profiles, derivatives, and autocorrelation functions for two MSPs. We have plotted $U'(\phi)$ vs. $U(\phi)$ in the middle panels to highlight inflection points in the profile that occur at low as well as high amplitude locations of $U(\phi)$. The red points in the top two panels indicate zero crossings of U' where U exceeds a threshold U_{min}, yielding $n_c = 1$ for J1909-3744 and $n_c = 5$ components for J1853+1303. The relative contributions to ToA errors scale as the squares of the component amplitudes because ToAs are determined through template fitting that involves multiplication of a template with a measured average profile.

Examples of polarization profiles (Fig. 13) show how Stokes L and V profiles differ from Stokes I and that the degree of linear polarization can be large. We refer to these profiles in Sect. 6.2 where ToA estimation using all Stokes parameters is discussed.

5.5. *Plasma propagation effects at radio wavelengths*

Atomic and molecular gas have essentially no influence on pulse propagation except in narrow emission lines that increase the system noise and absorption lines that diminish the pulsar signal (de Jager et al. 1968; Dickey et al. 1981; Frail et al. 1991). In extraordinary circumstances the pulsar signal can be enhanced by maser amplification, as seen in the OH line (Weisberg et al. 2005).

Variations in gravitational potential also affect pulse propagation times and in very rare circumstances may produce multiple images. Effects from binary companions produce the well known Shapiro delay that has famously been used for precision determinations of NS masses (e.g. Cromartie et al. 2020, and references therein). That subject is beyond the purview of this paper. However, Shapiro delays can be measured from intervening stars, planets, and dark matter clumps (e.g. Desai and Kahya 2018; Hosokawa et al. 1999). By and large, these instances in the weak field regime are

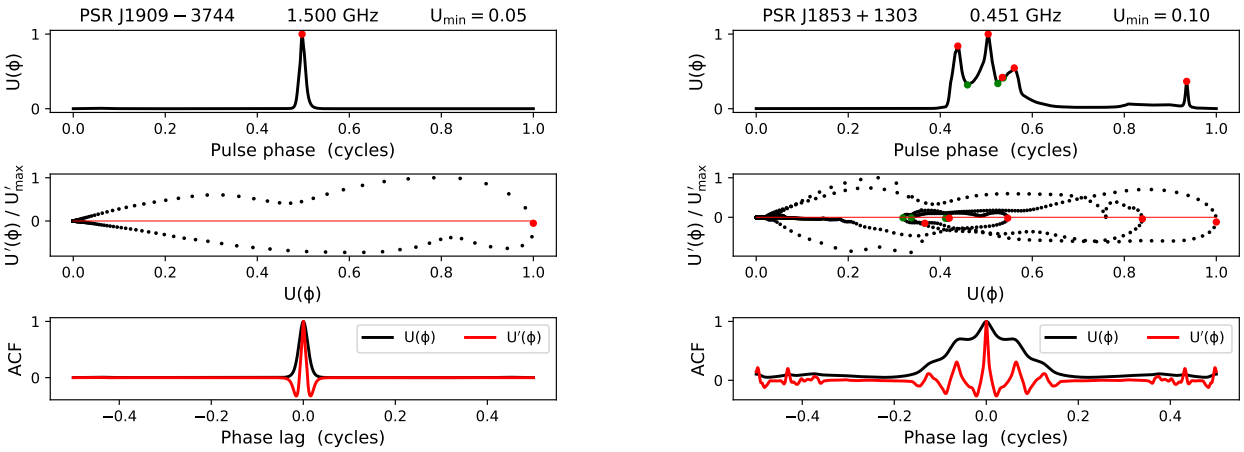


Figure 12. Profile component analysis for J1909-3744 (left) and J1853+1303 (right). The top panels show the template $U(\phi)$, the middle panels $U'(\phi)$vs. $U(\phi)$, and the bottom panels the autocorrelation functions of U and U'. Data are from NANOGrav's 15-yr data release.

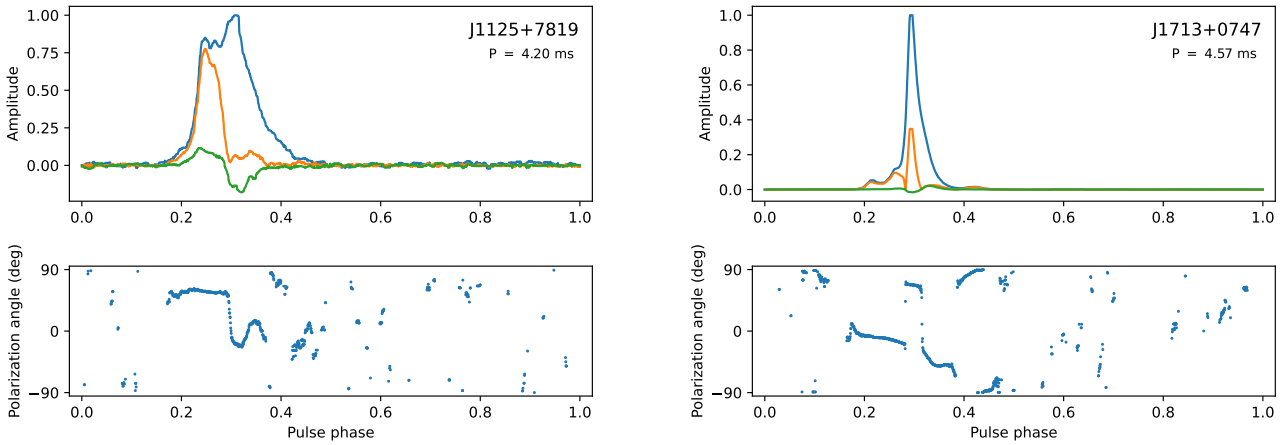


Figure 13. Stokes profiles for two millisecond pulsars in NANOGrav's timing program. Profiles are from the analysis of NANOGrav's 12.5 yr data set (Wahl et al. 2022) and were downloaded from https://nanograv.org/science/data/polarization-calibration-data (Version 2.1). For each case the top panel shows Stokes I (blue), L (orange), and V (green) and the bottom shows the polarization angle for values of L larger than $3\sigma_L$. Left: J1125+7819, an example of high linear polarization that is narrower than Stokes I. Right: J1713+0747, an example complex, narrower structure in L than in I but with less than 40% linear polarization

addressed by expressing the gravitational potential Φ as an equivalent index of refraction, $n_{\rm r} \simeq 1 - 2\Phi/c^2$ (Misner et al. 1973, § 24.5).

By far the most prominent effects are dispersion and scattering caused by plasmas encountered along the LoS, including the Earth's ionosphere and the solar wind, but the dominant effects are from partially ionized gas in multiscale ISM structures and turbulence extending from ~ 100 km to kpc scales. These media are compared in Table 3 and dispersion and scattering are discussed below in this section and in more detail in Part III 'Interstellar Effects.'

All relevant effects on pulsar signals can be analyzed in terms of the index of refraction $n_{\rm r}$ of a cold, tenuous, and magnetized plasma with electron plasma frequency $\nu_{\rm p} = \omega_{\rm pe}/2\pi = (n_{\rm e}e^2/\pi m_{\rm e})^{1/2}$ and cyclotron frequency $\nu_{\rm c} = \omega_{\rm c}/2\pi = eB/2\pi m_{\rm e}c$, where e and $m_{\rm e}$ are the electron charge and mass, $n_{\rm e}$ is the electron number density, and B is the

Table 3. Plasma parameters for the Ionosphere, interplanetary medium (IPM), and interstellar medium (ISM)

Quantity	Units	Symbol	Ionosphere[b]	IPM@1 au[c]	ISM[d]
Electron density	cm $^{-3}$	n_e	10^6 [max]	5	0.03
Magnetic field	μG	B	$3{\times}10^5$	100	3
Plasma frequency	kHz	ν_p	9000	20	2
Electron cyclotron frequency	Hz	$\nu_{c,e}$	10^6	300	10
δ(refractive index) @ 1 GHz	—	$\delta n_r = 1 - n_r$	10^{-5}	10^{-10}	10^{-12}
Integrated measures[a]					
Dispersion measure	pc cm^{-3}	DM	10^{-6} - 10^{-5}	$\gtrsim 3 \times 10^{-5}$	3 to 1700
Rotation measure	rad m^{-2}	|RM|	0.5 - 2	$\gtrsim 4 \times 10^{-4}$	few to $> 10^3$
Emission measure	pc cm^{-6}	EM	~ 3	$\gtrsim 10^{-4}$	< 1 to $> 10^5$

[a] Integrated measures are given for lines of sight away from the Sun. Much larger DM and RM values have been measured for LoS making close approaches (e.g. Spangler 2005; Jensen et al. 2018; Kooi et al. 2022).

[b] n_e: Bilitza et al. (2022, IRI model), Malins et al. (2018); Magnetic field: Thébault et al. (2015, IGRF-12 model); RM: Porayko et al. (2019)

[c] n_e: Ratcliffe (1972); B: Russell (2001); Borovsky (2020); RM: Kooi et al. (2022)

[d] Draine (2011)

magnetic field. Table 3 gives typical values of these quantities and integrated measures for the ISM, which dominates pulsar measurements, along with those for the IPM near the solar system and the ionosphere.

For $\nu_c \ll \nu_p \ll \nu$ along with quasi-longitudinal propagation at an angle θ from the magnetic field direction, and neglecting very small contributions from ions (predominantly protons),

$$ {n_r}^2 = \left(\frac{kc}{2\pi\nu}\right)^2 \approx 1 - \left(\frac{\nu_p}{\nu}\right)^2 \left(\frac{1}{1 \mp \nu_{c_\parallel}/\nu}\right). \tag{5.20} $$

where $\nu_{c_\parallel} \equiv \nu_c \cos\theta$ and the upper and lower signs apply to right-hand and left-hand polarizations, respectively (IEEE and IAU conventions).

Chromatic effects are time dependent owing to geometrical changes in the propagation path, predominantly caused by translational motions of the pulsars, which have much higher velocities than main-sequence stars. In some cases, Earth's motion around the Sun and orbital motion of binary pulsars also contributes significantly to characteristic time scales, especially for MSPs.

Physical effects that need to be accounted for in pulsar timing, either through mitigation or inclusion in the measurement error budget, are as follows:

We make use of standard propagation measures expressed in their standard units (with distances in pc or kpc, n_e in cm^{-3}, and $B_\parallel$ in μG) and integrations from 0 at the source to a distance z along the propagation path,

$$ \begin{aligned} &\text{Dispersion measure:} && \mathrm{DM} = \textstyle\int ds\, n_e && \text{pc cm}^{-3}, \\ &\text{Faraday rotation measure:} && \mathrm{RM} = \frac{e^3}{2\pi m_e^2 c^4} \textstyle\int ds\, n_e B_\parallel = 0.81 \int ds\, n_e B_\parallel && \text{rad m}^{-2}, \\ &\text{Emission measure:} && \mathrm{EM} = \textstyle\int ds\, {n_e}^2 && \text{pc cm}^{-6} \\ &\text{Scattering measure:} && \mathrm{SM} = \textstyle\int ds\, \mathrm{C}_n^2 && \text{kpc m}^{-20/3}. \end{aligned} \tag{5.21} $$

Definitions for these measures can be found in (Lorimer and Kramer 2005) with more details in (Draine 2011). The first three measures are discussed immediately below while the scattering measure is deferred to Sect. 9.2.

Phase perturbations: Propagation imposes an extra phase equal to the integral of $k(n_{\rm r}-1)$ along the propagation path. Paraxial optics applies because deflections from vacuum geodesics are typically less than one arcsecond so the integral can often be taken along an undeflected path. The phase at a transverse position $\mathbf{x}$ at position z along the path is

$$\begin{aligned}\phi(\mathbf{x},z) &\simeq -\left[\lambda r_{\rm e}{\rm DM}(\mathbf{x},z) \pm \lambda^2 {\rm RM}(\mathbf{x},z) + \left(\frac{\lambda^3 r_{\rm e}^2}{4\pi}\right){\rm EM}(\mathbf{x},z)\right]. \\ &\simeq -\left[2.61\times10^7\left(\frac{\rm DM}{\nu}\right) \pm 0.0899\left(\frac{\rm RM}{\nu^2}\right) + 5.25\times10^{-4}\left(\frac{\rm EM}{\nu^3}\right)\right]\ {\rm rad} \end{aligned} \tag{5.22}$$

where $r_{\rm e}$ is the classical electron radius and the frequency ν is in GHz.

Dispersion: The group delay adding to the vacuum propagation delay d/c is $t_{\rm d} = (1/2\pi)d\phi/d\nu$ or, equivalently, the integral involving the group velocity $v_{\rm g} = \partial\omega/\partial k = c(n_{\rm r} + \nu dn_{\rm r}/d\nu)^{-1}$ over the pulsar-solar system distance[19] d, $t_{\rm d} = \int_0^d ds\,(v_{\rm g}^{-1} - c^{-1})$. Evaluating to first order in $\nu_{\rm c\|}/\nu$ and fourth order in $\nu_{\rm p}/\nu$ (Suresh and Cordes e.g. 2019; see also Phillips and Wolszczan 1991; Hassall et al. 2012),

$$t_{\rm d} = t_{\rm DM} \pm t_{\rm RM} + t_{\rm EM} \simeq K_{\rm DM}\left(\frac{\rm DM}{\nu^2}\right) \pm K_{\rm RM}\left(\frac{\rm RM}{\nu^3}\right) + K_{\rm EM}\left(\frac{\rm EM}{\nu^4}\right) \tag{5.23}$$

where the coefficients are

$$K_{\rm DM} = \frac{e^2}{2\pi m_{\rm e} c} = \frac{c r_{\rm e}}{2\pi} = 4.15\ {\rm ms}, \quad K_{\rm RM} = \frac{c^2}{\pi} = 28.6\ {\rm ps}, \quad K_{\rm EM} = \frac{3e^4}{8\pi^2 m_{\rm e}^2 c} = 0.251\ {\rm ps}, \tag{5.24}$$

for standard units of pc cm^{-3} for DM, rad m^{-2} for RM, and pc cm^{-6} for EM. DM fluctuations occur on a wide range of time scales associated with transport of the LoS across multiscale density structures by various motions. Because DM delays are large, these fluctuations must be tracked vs. epoch, as discussed in the next section.

Values of plasma quantities in Table 3 indicate that dispersive time delays are dominated by the ISM. Nonetheless, contributions from the ionosphere and IPM make noticeable contributions to the most precise arrival times and their

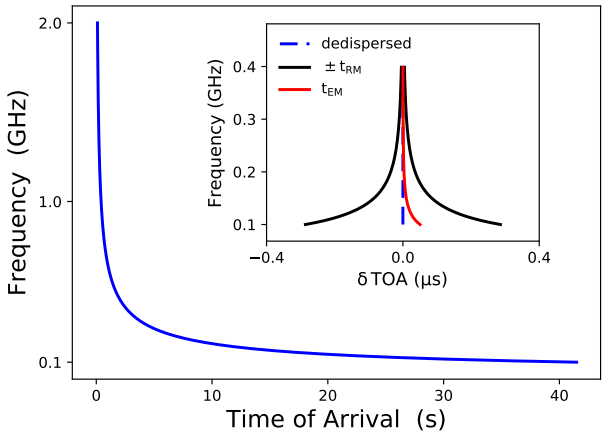


Figure 14. Excess time of arrival vs. frequency for DM = 100 pc cm^{-3}, RM = 10 rad m^{-2} and EM = 20 pc cm^{-6}, values chosen to illustrate the effects not to model any particular line of sight. Inset: Excess arrival time after dedispersion of only the DM term.

[19] Note that pulsar timing analyses are referenced to the solar system barycenter, which implies that the Doppler shift from the Earth's motion needs to be included.

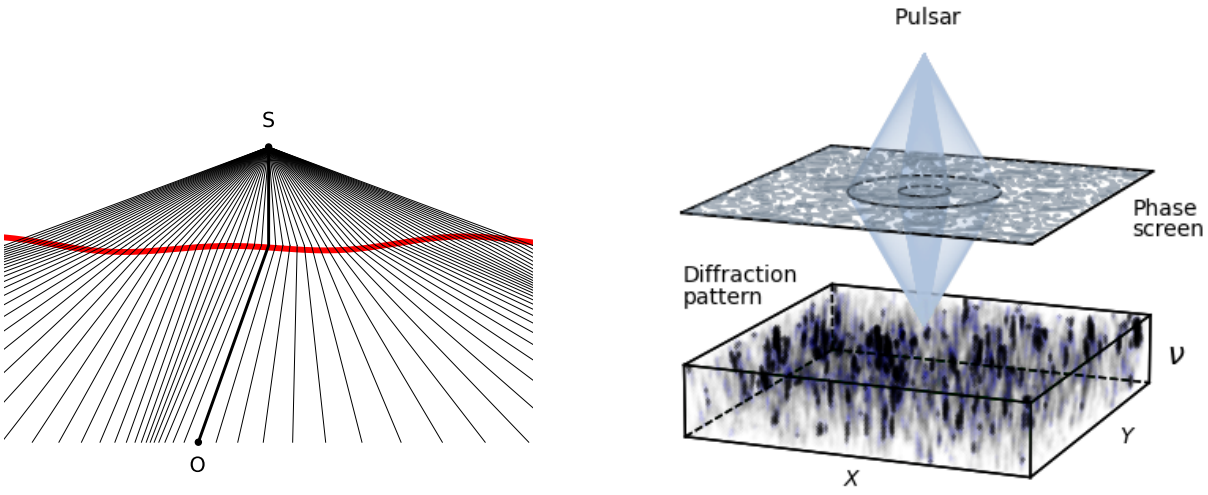


Figure 15. Left: Schematic thin refracting screen that changes the wavefront (red) and thus the angle of arrival seen by an observer O and the intensity, represented by the variable density of rays in geometrical optics. Refraction in the local ISM is sometimes dominated by a single screen-like structure while for distant objects it is a cumulative effect from multiple structures. Right: Illustration of scattering from a thin screen with phase fluctuations produced by Kolmogorov fluctuations in refractive index. The cones with apexes at a pulsar and at an observer's position in the observation plane represent ray path bundles of scattered radiation. The narrow and wide cones correspond to a high and a low frequency, respectively. The diffraction pattern is shown as a function of X, Y in the observation plane and as a function of radio frequency ν.

variability on short time scales (hours, days) implies a contribution to the timing error budget if they are not mitigated using multifrequency observations. As an example, a 10 ns delay at 1 GHz corresponds to $\delta\mathrm{DM} \sim 2.4 \times 10^{-6}$ pc cm^{-3}, a value that is reached for all three media characterized in the table.

Birefringence and Faraday rotation: The birefringent RM terms imply that a narrow pulse splits into its differentially arriving circularly-polarized components (Suresh and Cordes 2019). The DM term in Eq. (5.23) is by far dominant and it is only in very dense, highly magnetized clouds that the RM and EM terms will matter in low-frequency observations, as demonstrated in Fig. 14. The inset shows that the RM and EM terms reach μs levels only at frequencies $\ll 1$ GHz. They may be important for burst emitters in dense regions with large magnetic fields (e.g. fast radio burst sources) but for precision timing of Galactic millisecond pulsars, the EM term is negligible and the RM term is typically less than a few ns.

Birefringence is typically measured as rotation of the E vector vs. wavelength by the angle $\psi = (\phi_+ - \phi_-)/2 = \lambda^2\mathrm{RM}$. Ideally it would have no effect on arrival times but instrumental polarization and miscalibration of polarization channels can render it important. Under those conditions, imperfect removal of Faraday rotation across the data band will yield a systematic error that can be epoch dependent.

Refraction:. Large scale density variations on $\gtrsim$ au scales alter the angle of arrival (AoA) and cause slow flux density variations (refractive interstellar scintillations, RISS; Rickett et al. 1984). Fig. 15 (left panel) shows these effects schematically for a thin screen geometry. In this case the deflection angle produced by the screen is $\theta_\mathrm{r} = k^{-1}\nabla_{\mathbf{x}}\phi(\mathbf{x}, z)$ and intensity variations are related to the second derivative. Refractive scintillations alter the signal-to-noise ratio and thus cause episodic changes in achievable RMS ToA errors from matched filtering. Variations in AoA introduce further arrival time delays to the dispersive delays. If deflection angles are large enough, bright intensity caustics and ray crossing can cause pulse echoes that perturb estimated ToAs. Collectively the empirical manifestations of these effects are referred to as 'extreme scattering events' (ESEs) even though they are refractive in origin. Instances of ESEs in pulsar timing appear to be rare (Cognard et al. 1993; Kerr et al. 2018).

Diffraction (scattering):. Diffraction arises if the wavelike property of incident radiation plays a role in changing the direction of propagation, in contrast to geometrical optics. Fig. 16 shows the geometry for a thin screen at distances $d_{\rm sl}$ and $d_{\rm so} - d_{\rm sl}$ from the source and an observer, respectively. A representative diffraction angle $\theta_{\rm d}$ corresponds to an initially emitted angle $\theta_{\rm i}$ and an observed angle $\theta_{\rm o}$. Density variations on small scales ($\ll$ au) cause forward scattering and multipath propagation that produce important effects for pulsar timing: diffractive intensity scintillations (DISS) vs. time and frequency and pulse distortion from differential propagation times. These effects are illustrated in Fig. 15 (right hand panel).

The pulse broadening function (PBF) is typically defined using only geometrical path length differences and represents the scattered pulse shape produced for an emitted delta-function. In the frequency domain, multipath is manifest as constructive and destructive interference that strongly modulates the spectrum. A spectrum and PBF are illustrated in Fig. 17. The constructive and destructive interference underlying scintillations is distinct from caustics that occur in geometrical optics, where deflections are related to phase gradients that occur even in the limit of infinitesimal wavelengths.

Reflection: A plasma structure can reflect radiation if the plasma frequency is comparable to the electromagnetic frequency or if there is grazing incidence on an interface between two plasma densities. Reflections will alter the flux density and polarization. While currently it is unclear whether reflections have influenced any pulsar observations to date, they may be manifested in rare occasions as multiple images and pulse echoes in long timing programs.

5.6. *Interstellar impulse response functions*

The net impulse response of the ISM is a combination of scalar dispersion (i.e. not dependent on the wave polarization), Faraday rotation, and multipath propagation (where we ignore the very small EM term). The phase given in Eq. (5.22) for the two hands of circular polarization indicate that the impulse response due to DM and RM is simply a phase change of Fourier components by a complex factor $\widetilde{h}_{\rm DM,RM}(\nu) = \exp[i\phi(\mathbf{x}, z)]$ for the observer's location, which is factorable into separate DM and RM components, $\widetilde{h}_{\rm DM}$ and $\widetilde{h}_{\rm RM}$. Coherent dedispersion comprises multiplication of measured Fourier components by the complex conjugate of this factor. In practice, this operation is applied to baseband data with bandwidth B and, to date, only the DM contribution to the phase is considered in the vast majority of applications. Multipath, primarily from diffraction accompanied by refraction is not so simple to mitigate. Pulse broadening, as already described, involves a 'field' PBF denoted as $h_{\rm d}(t)$. The total interstellar impulse response is the time-domain convolution of the three factors (and a receiver bandwidth factor that we keep implicit),

$$h_{\rm ism}(t) = h_{\rm DM}(t) * h_{\rm RM}(t) * h_{\rm d}(t). \tag{5.25}$$

Dedispersion of the $h_{\rm DM}$ term and derotation of the $h_{\rm RM}$ term are both exercises in matched filtering and can be done exactly if the true DM and RM values are known.

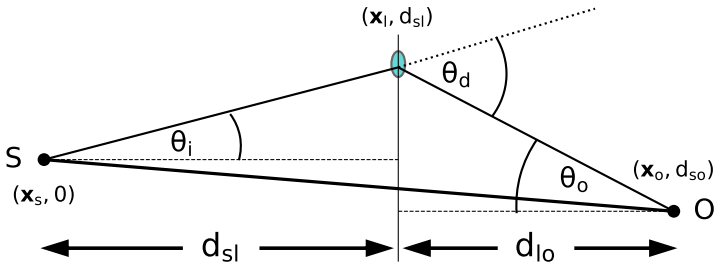


Figure 16. Thin screen geometry for diffraction and ray tracing and for the application of the Fresnel-Kirchhoff diffraction integral. Small angles $\ll 1$ rad are assumed for diffraction into an angle $\theta_{\rm d}$ in the screen at distance $d_{\rm so}$ from the source S. Transverse coordinates $\mathbf{x}_{\rm s}, \mathbf{x}_{\rm l}$ and $\mathbf{x}_{\rm o}$ define locations in the source, screen layer, and observation planes.

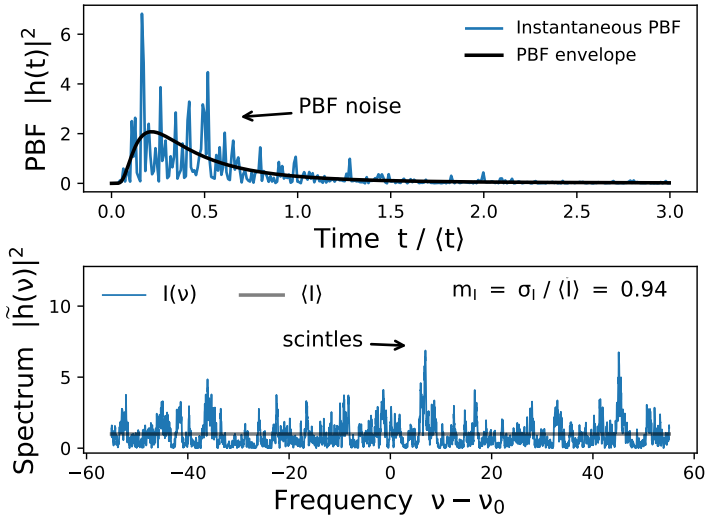


Figure 17. Top: Pulse broadening function for for a pervasive medium with a Kolmogorov electron density spectrum and negligible inner scale. The single realization shown displays the noise-like process that is modulated by an envelope function. The noise process remains constant over a DISS time scale while the envelope is sustained for much longer time spans. Bottom: Spectrum corresponding to the field PBF normalized to the spectral mean (black line) and plotted against the radio frequency ν minus a center frequency ν_0. Spectral amplitudes are exponentially distributed so the ensemble average modulation of the spectral intensity is unity. The single realization shown here slightly departs (statistically) from a modulation index of unity.

Dedispersion: The dispersion delay in Eq. (5.23) varies significantly across frequency bands used in pulsar studies and thus must be removed before summing pulse intensities over frequency to improve the signal to noise ratio and to maximize the net time resolution and timing precision.

An approximate method is 'post-detection' or *incoherent dedispersion* used for intensities obtained with a multi-channel receiver. Pulses from each channel are aligned by shifting each intensity by $t_{\rm d}(\nu_{\rm ref}) - t_{\rm d}(\nu)$, where $\nu_{\rm ref}$ is a reference frequency. This method cannot remove the differential delay across a frequency channel and thus distorts the pulse from its emitted form. The minimum smearing time of the pulse results when the dispersion delay across a channel $(dt_{\rm d}/d\nu)$ equals the natural channel response time $\Delta\nu^{-1}_{\rm channel}$, so narrower channels can minimize but not remove this effect.

The more advanced (and exact) approach is *coherent dedispersion* that properly corrects the Fourier phase of the sampled electric field contained in the baseband voltage (Hankins 1971; Hankins and Rickett 1975). The gist of the method is easily seen by considering the measured electric field $E(t,z) = \int d\nu\, \widetilde{E}(\nu,0)\exp\{i(k(\nu)z - 2\pi\nu t)\}$ in terms of the Fourier transform of the emitted field $\widetilde{E}(\nu,0)$ for a medium with constant refractive index $n_{\rm r}$ given by Eq. (5.20). The wavenumber is $k(\nu) = n_{\rm r}(\nu)k_0$ where k_0 is the vacuum wavenumber. The dedispersed signal is obtained by multiplying the Fourier transform of the measured field $\widetilde{E}(\nu,z)$ by $\exp\{-ik(\nu)\}$. Inspection of Eq. (5.22) shows that the dominant phase term involves the DM term. In principle, large values of |RM| (or low frequency observations) may require inclusion of the ν^{-3} (e.g. Bondonneau et al. 2021) term but to date there has not been routine implementation of coherent Faraday derotation in pulsar timing programs.

For most cases, DM is the sole parameter needed for coherent dedispersion and the required precision on DM to avoid pulse distortion depends on radio frequency and on the widths of pulse features (Hankins and Rickett 1975; Cordes and McLaughlin 2003). We discuss the details of DM determination in a later section.

Implementation of coherent dedispersion with baseband data is discussed in the original papers by Hankins (1971) and Hankins and Rickett (1975), with applications to full Stokes parameters (Cordes and Hankins 1977; Stairs 2002),

and execution of graphics processing units for high data rate applications to pulsars and FRBs (e.g. Reddy et al. 2017; Bondonneau et al. 2018; Zhang et al. 2024).

In most of the paper, we assume that dedispersion is perfect across relevant observing bands, requiring that epoch-to-epoch variations in DM are included; the primary element of the net impulse response is then the diffraction term.

5.7. *Intensity statistics for scintillated amplitude modulated shot noise*

Emitted signals from pulsars, as discussed previously, are well described as modulated shot noise. Later, in Sect. 7, we discuss contributions to ToA errors from elements of this signal model. Here we discuss, using a simple approach, how interstellar scintillation affects the statistics of the pulsar intensity. A salient point is that in the limit of dense shot noise and strong scintillations, both the emitted signal and the scintillation modulation conform to Gaussian statistics. The multiplicative aspect of scintillation enhances the net variance of the measured pulsar intensity, which in turn is relevant to the ToA error budget.

Diffraction causes multipath propagation at radio frequencies where phase fluctuations exceed about 1 rad (RMS) over a transverse separation smaller than a Fresnel scale (discussed in detail in §10.3). Multiple paths replicate individual shots in the shot noise signal of Eq. (5.13). Representing the the impulse response for propagation as a weighted sum of delta functions, $g(t) \sim \sum_k g_k \delta(t - t_k)$ the scintillated signal (with 's' subscript) becomes (e.g. Cordes et al. 2004a)

$$\varepsilon_{\rm s}(t) = \sum_j a_j \sum_k g_k \Delta(t - t_j - t_{{\rm s}_k}). \tag{5.26}$$

Intensity statistics in the frequency domain are useful for assessing timing errors. The voltage Fourier transform,

$$\widetilde{\varepsilon}_{\rm s}(\nu) = \widetilde{\Delta}(\nu) \sum_j a_j e^{-2\pi i \nu t_j} \sum_k g_k e^{-2\pi i \nu t_{{\rm s}_k}}, \tag{5.27}$$

is the product of two independent, complex Gaussian noise processes when the number of terms in each sum is large[20]. The squared magnitude of $\widetilde{\varepsilon}_{\rm s}(\nu)$ is the spectrum having an overall extent determined by $|\widetilde{\Delta}(\nu)|^2$,

$$S_{\rm s}(\nu) = |\widetilde{\Delta}(\nu)|^2 A(\nu) G(\nu), \quad A(\nu) = \left| \sum_j a_j e^{-2\pi i \nu t_j} \right|^2, \quad G(\nu) = \left| \sum_k g_k e^{-2\pi i \nu t_{{\rm s}_k}} \right|^2. \tag{5.28}$$

The random processes $A(\nu)$ and $G(\nu)$ are positive semi-definite with RMS values equal to their mean values in the limit of a large number of terms in their respective sums, which have complex Gaussian statistics. The PDFs for A and G are thus one-sided exponentials because they are χ^2_2 random variables with two degrees of freedom. Each quantity has a characteristic frequency scale determined by the time dependence of the amplitudes a_j and g_k. The shot amplitudes have pulse-like envelopes with duration $W_{\rm A}$ leading to a characteristic frequency scale $W_{\rm A}^{-1}$. The multipath amplitudes g_k follow an impulse response with width equal to the scattering time τ; its reciprocal is the characteristic scintillation bandwidth. The net modulation index (RMS/mean) m_S of $S_{\rm s}(\nu)$ is given by

$$1 + m_S^2(\nu) = [1 + m_I^2(\nu)][1 + m_G^2(\nu)]. \tag{5.29}$$

For χ^2_2 statistics, $m_I = m_G = 1$ and $m_S = \sqrt{3}$.

5.8. *Gravitational lensing*

Pulses encounter weak changes in the interstellar gravitational potential which act as a variable, achromatic refractive index that adds to small refractive index variations from magnetized plasmas in the ISM, IPM, and ionosphere. The

[20] The amplitude modulated noise (AMN) sum $A(\nu)$ has many terms if the shot noise is dense. The propagation term has many terms under the conditions of 'strong scintillation,' as defined later.

LoS integrated gravitational potential from individual stars with masses m_i and locations $\mathbf{x}_i$ yields a geodesic noise component to ToA variations of the simplified form (Golat and Contaldi 2021),

$$\delta t_{gn}(\mathbf{x}_\mathrm{o}, t_\mathrm{A}) \simeq -\frac{2G}{c^3}\sum_i m_i \ln\left[\frac{|\mathbf{x}_i| - \widehat{\mathbf{k}}\cdot\mathbf{x}_i}{|\mathbf{x}_\mathrm{o}-\mathbf{x}_i| - \widehat{\mathbf{k}}\cdot(\mathbf{x}_\mathrm{o}-\mathbf{x}_i)}\right] \tag{5.30}$$

based on a thorough treatment by Kopeikin and Schäfer (1999) and where $\widehat{\mathbf{k}}$ is the unit vector along the (unperturbed) propagation direction; velocities are assumed small enough to not matter and retarded times for evaluation of stellar positions are implicit. The RMS value is $\sigma_\mathrm{gn} \sim 10\,\mathrm{ns}$ (Golat and Contaldi 2021), a non-negligible value compared to some of the best ToA precisions. The characteristic time scale for variations in δt_gn along any LoS are very long, decades to centuries (Desai and Kahya 2016), and any close encounters of the LoS with an individual star have low probability, of order the 'optical depth' $\sim 10^{-6}$ for gravitational lensing. Over the current ∼three decades of extant timing data, such variations are removed by fitting for the pulsar spin parameters. The situation differs for pulsars in globular clusters where the gravitational potential can affect estimates for the spindown rate $\dot{f}_\mathrm{s}$.

Pulsar timing data can be used to place upper limits on dark matter clumps that contribute to δt_gn (Seto and Cooray 2007; Ramani et al. 2020; Chakrabarti et al. 2026). Gravitational lensing from small objects, though extremely rare, could produce oscillations in intensity vs. time and frequency due to interference between two or more images produced by the lensing.

6. TOA ESTIMATION USING TEMPLATE MATCHING

The quality of pulsars as astrophysical clocks is best introduced with a description of how well TOAs are estimated by matched filtering (MF) of pulse profiles with a template function. The fundamental assumption of MF is that the measured pulse is an exact copy of a template scaled in amplitude and shifted in time with noise added. These conditions are largely satisfied but the highest timing precision requires attention to the frequency dependence of pulse shapes and departures in shape that arise from emission jitter, from propagation through the ISM, and from instrumental distortions.

Arrival times are most often computed for the pulse profile in Stokes I, which we discuss first. We discuss the potential benefits of full-Stokes template fitting later. Here, we consider the simplest 1D case of arrival time estimation from a narrow-band profile in order to illustrate some basic points and in later sections consider 2D estimation that addresses profile chromaticity. The minimum ToA error is achieved when profile and template are exact matches to within additive noise. All other effects increase the error. We discuss template starting with the presentation in (Taylor 1992). Let U_t be the template profile sampled at N_ϕ discrete times, $t \in [0, N_\phi - 1]$ corresponding to one cycle of pulse phase. The data profile $D_t = P_t + N_t$ thus comprises a scaled and shifted version of the template $P_t = b\,U_{t-t_0}$ added to noise N having variance σ_N^2. Here and below, P_t is normalized to have unity maximum. Data are fitted with a numerical model, $D_t = a + b\,U_{t-t_0}$, by minimizing the χ^2 cost function to estimate the ToA t_0 along with the baseline a and scale factor b, while the rms noise σ_N is estimated separately. Least squares fitting is equivalent to finding the ToA from the time lag where the cross correlation function of the template and profile maximizes. With sampled data, the optimization is far easier in the frequency domain to avoid interpolation issues that arise in the time domain[21] (Taylor 1992). Using tildes to denote discrete Fourier transforms (DFTs) of the data and template, $\widetilde{D}_f$ and $\widetilde{U}_f$, with discrete frequency indices $f \in [0, N_\phi - 1]$, the TOA estimate is the solution of

$$\sum_{f=1}^{N_\phi/2} \mathrm{Im}\{f\widetilde{D}_f\widetilde{U}_f^* e^{2\pi i f t_0/\Delta t N_\phi}\} = 0. \tag{6.1}$$

The sum excludes the $f = 0$ elements, which determine the estimate of the baseline a but are not needed for the TOA; the sum extends only to $N_\phi/2$ by Hermiticity of the DFTs. If the template and parameters yield a good fit, the

[21] Interpolation in the time domain requires use of the appropriate interpolation function, which is $\mathrm{sinc}(Bt) = (\sin\pi Bt)/\pi Bt$ where B = bandwidth, which has slowly decaying oscillations. This interpolation function is discussed in standard derivations of the sampling theorem for uniformly sampled data.

minimum TOA error is (see also van Straten 2006)

$$\sigma_{t_{\rm S/N}} = \frac{P}{2\pi(S/N)} \left(\frac{N_\phi}{2}\right)^{1/2} \left[\sum_{f=1}^{N_\phi/2} f^2 |\widetilde{U}_f|^2\right]^{-1/2} . \tag{6.2}$$

The f^2 factor in the sum causes higher frequency components in the template to be emphasized. Narrower pulses or those with sharper features yield a larger sum, thus reducing the TOA error. The signal to noise ratio is defined as (pulse peak) / (rms noise), or $\mathrm{S/N} \equiv \mathrm{b}/\sigma_{\rm N}$. Eq. (6.2) applies for $\mathrm{S/N} \gg 1$ because it is based on the quadratic expansion of a cost function that assumes small errors.

The TOA error is also written in a form that separates pulsar properties from telescope and analysis parameters,

$$\sigma_{t_{\rm S/N}} = \frac{W_{\rm eff}}{N_\phi^{1/2}(S/N)}, \tag{6.3}$$

where the effective pulse width involves both the spin period and the pulse shape and is expressed in either the frequency or time domain,

$$W_{\rm eff} = \left(\frac{N_\phi P}{2\pi\sqrt{2}}\right) \left[\sum_{f=1}^{N_\phi/2} f^2 |\widetilde{U}_f|^2\right]^{-1/2} = P\left[N_\phi \sum_t \left(U_{t+1} - U_t\right)^2\right]^{-1/2} \xrightarrow{\Delta t \to 0} \frac{P^{1/2}}{\left\{\int_0^P dt\, \left[U'(t)\right]^2\right\}^{1/2}}. \tag{6.4}$$

This expression for $W_{\rm eff}$ is consistent with the expression given by Downs and Reichley (1983) for the ToA error. By inspection of Eq. (6.4), narrow pulses or those with sharp features have larger denominators than wide pulses. This is also evident in the continuum limit that involves the derivative of the template, $U' \equiv dU/dt$: larger derivatives correspond to smaller TOA errors. The continuum limit shows that the effective width involves both the spin period P and the actual pulse shape. However, it does not depend on the number of samples across the pulse, N_ϕ, as long as all relevant features in the pulse profile are resolved.

Fig. 18 shows $W_{\rm eff}$ vs. period for pulsars in the 15-yr NANOGrav PTA along with the ACF width of each profile and the widths of single profile components calculated from the ACF of the profile's first derivative (c.f. Fig. 12). All three widths show an upward trend with period but with the smallest scatter for $W_{\rm eff}$ and the largest for individual components.

6.1. *Evaluation using pulsar and telescope parameters*

The rms noise in a pulse profile with N_ϕ bins is $\sigma_N = S_{\rm sys}/\sqrt{n_{\rm pol} B T_{\rm int}/N_\phi}$, where $S_{\rm sys} = T_{\rm sys}/G$ is the system temperature, $T_{\rm sys}$, expressed in Jy units using the telescope gain $G = A_{\rm e}/2k_{\rm B}$ in K Jy^{-1} (with $A_{\rm e}$ = effective telescope area and $k_{\rm B}$ = Boltzmann constant). Dominant contributions to $T_{\rm sys}$ include receiver noise, ground 'spillover' noise, and the sky background that includes free-free and synchrotron emission from the Galaxy, and the cosmic microwave background. Other parameters include the number of polarization channels used with $n_{\rm pol} = 2$ for Stokes I profiles; B is the bandwidth; and $T_{\rm int}$ is the total integration time (typically $\sim$ minutes to an hour). The integration time per profile sample is $T_{\rm int}/N_\phi$.

This gives a signal-to-noise

$$\mathrm{S/N} = \frac{\mathrm{S_{pk}}}{\sigma_{\rm N}} = \frac{\mathrm{P}\langle \mathrm{S}_\nu\rangle_\phi}{\mathrm{W}} = \frac{\langle \mathrm{S}_\nu\rangle_\phi}{\mathrm{S_{sys}}} \frac{\mathrm{P}}{\mathrm{W}} \left(\frac{\mathrm{n_{pol} B T_{int}}}{\mathrm{N}_\phi}\right)^{1/2} \simeq 3437 \times \frac{\langle \mathrm{S}_\nu\rangle_\phi (\mathrm{mJy})}{\mathrm{S_{sys}(Jy)}} \frac{\mathrm{P_{ms}}}{\mathrm{W_{100}}} \left[\frac{(\mathrm{n_{pol}}/2)\mathrm{B_{GHz}T_{int,3}}}{\mathrm{N}_\phi/2048}\right]^{1/2} \tag{6.5}$$

where the peak flux density is expressed in terms of the catalogued flux density averaged over pulse phase, $S_{\rm pk} \simeq P\langle S_\nu\rangle_\phi/W$, and the pulse duty cycle, W/P. [22]

[22] For individual pulses or fast radio bursts we would use the peak flux density directly to calculate S/N and the ToA error.

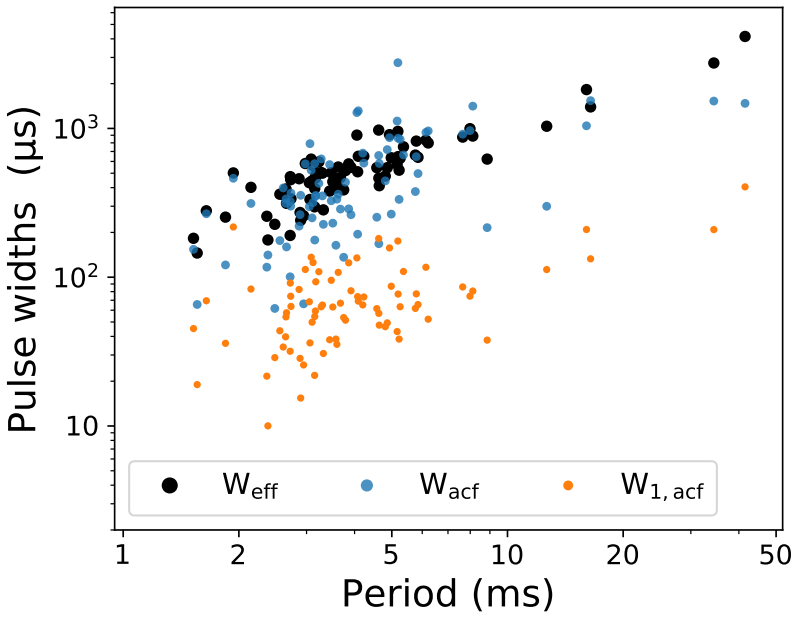


Figure 18. Pulse widths vs. period. The effective width $W_{\rm eff}$, ACF width $W_{\rm acf}$, and single component width $W_{1,\rm acf}$ were calculated from template profiles for pulsars in NANOGrav's 15-yr PTA.

The pulsar's flux density typically scales as a power-law $\langle S_\nu \rangle_\phi \propto \nu^{-\alpha_S}$ with spectral indices $0 \lesssim \alpha_S \lesssim 3$ (e.g. Xu et al. 2024). In some cases the spectrum turns over at low frequencies $\lesssim 0.3$ GHz and in others the spectrum steepens at high frequencies. At frequencies $\lesssim 1$ GHz, the scaling of the synchrotron background, $T_{\rm sync} \propto \nu^{-2.7}$, is nearly cancelled by that of the flux density for pulsars with larger spectral indices, yielding S/N that is less dependent on frequency than the individual factors. The ToA error is

$$\sigma_{t_{\rm S/N}} = \frac{W_{\rm eff} W S_{\rm sys}}{P \langle S_\nu \rangle_\phi \sqrt{n_{\rm pol} B T_{\rm int}}} \tag{6.6}$$

Example of a single-component Gaussian pulse of width W (FWHM): The effective width is

$$W_{\rm eff} = \left(\frac{WP}{\sqrt{2\pi \ln 2}} \right)^{1/2} \simeq 219\ \mu{\rm s} \sqrt{W_{100\,\mu{\rm s}} P_{\rm ms}}, \tag{6.7}$$

for a nominal 1 ms period and 100 μs width. The corresponding TOA error is

$$\sigma_{t_{\rm S/N}} = \frac{1}{(2\pi \ln 2)^{1/4}} \frac{S_{\rm sys}}{\langle S_\nu \rangle_\phi} \frac{W^{3/2}}{(n_{\rm pol} B T_{\rm int} P)^{1/2}} \simeq 15\,{\rm ns} \times \frac{S_{\rm sys}({\rm Jy})}{S_{\rm psr}({\rm mJy})} \frac{W_{100}^{3/2}}{\sqrt{(n_{\rm pol}/2) B_{\rm GHz} T_{{\rm int},3} P_{\rm ms}}} \tag{6.8}$$

where we have used an integration time $T_{\rm int} = T_{{\rm int},3} \times 10^3$ s, a bandwidth in GHz, $S_{\rm sys}$ (SEFD) in Jy, and the pulsar period averaged flux density $S_{\rm psr}$ in mJy. Pulsars show a variety of periods, widths, and strengths, yielding TOA errors ranging from sub-μs to several ms or more for long period pulsars and magnetars.

For later use, we express the signal to noise ratio of the average profile ${\rm S/N} = ({\rm S/N})_1/\sqrt{\rm N}$ in terms of the single pulse value, $(S/N)_1$, assuming that amplitudes are statistically independent between $N = T_{\rm int}/P$ pulses [23] , yielding

$$\sigma_{t_{\rm S/N}} \simeq \frac{4.8\ {\rm ns} P_{\rm ms}}{(S/N)_1} \left(\frac{W_{100}}{T_{{\rm int},3} N_\phi / 2048} \right)^{1/2}. \tag{6.9}$$

[23] Some pulsars show amplitude correlations between neighboring pulses but, for steady pulsars that show no changes in profile state, statistical independence is a reasonable assumption. State changes are discussed later in Sect. 6.4.

Multiple component profiles: While some pulsars display single-component pulse profiles, many show two or more components with different amplitudes and different degrees of component overlap in pulse phase. To account for these in a simple way, we let all n_c components have the same width $W_{\rm c}$. Assuming no phase overlap, the effective width is a factor $n_c^{-1/2}$ smaller (cf. Eq. (6.4)) and the peak flux density for a component $S_{\rm pk_c} = \langle S_\nu \rangle_\phi P/n_c W_{\rm c}$ is smaller by a factor n_c^{-1}. The net effect is that the TOA error is larger by a factor $n_c^{1/2}$.

For profiles comprising n_c components with the same characteristic width $W_{\rm c}$ but different amplitudes a_j, the weighted number is $n_{\rm c_2} = \sum_j (a_j/a_{\rm max})^2 \leq n_c$, yielding $W_{\rm eff} = (W_{\rm c} P/n_{\rm c_2}\sqrt{2\pi \ln 2})^{1/2}$. The period-averaged flux density in Eq. (6.6) becomes $S_\phi \rightarrow S_\phi/n_{\rm c_1}$ and the net ToA error is

$$\sigma_{t_{\rm S/N}} = \frac{K_U}{\sqrt{n_{\rm pol} B T_{\rm int}}} \frac{S_{\rm sys}}{S_\phi} \left(\frac{n_{\rm c_1}}{\sqrt{n_{\rm c_2}}}\right) \left(\frac{W_{\rm c}^3}{P}\right)^{1/2}, \tag{6.10}$$

where $K_U \sim 1$ is a pulse-shape dependent factor. For Gaussian shaped components, $K_U = [\pi/32(\ln 2)^3]^{1/4} = 0.74$.

Identifying the role of the number of profile components in ToA uncertainties helps enable an assessment of the timing quality of, say, a newly discovered pulsar and whether it can contribute significantly to the sensitivity of a PTA program.

Equations (6.4)–(6.10) provide the means for identifying key factors and improvements that can be made to minimize the TOA error:

1. The error decreases inversely as S/N, as usual for matched filtering, and thus also for bright pulsars;
2. Interstellar scintillation modulations of the emitted flux density can be large (up to $\sim 100\%$ variations for DISS and ~ 10 to 30% for RISS), making the S/N and thus the RMS TOA error epoch dependent and stochastic;
3. Pulsars with smaller effective widths $W_{\rm eff}$ yield smaller errors, illustrating how smaller periods P and narrower pulses (or narrow pulse structure) are beneficial;
4. Effective widths increased by instrumental or astrophysical broadening degrade timing precision;
5. Larger telescopes and lower $T_{\rm sys}$ yield better precision in proportion to smaller $S_{\rm sys} = T_{\rm sys}/G = 2kT_{\rm sys}/A_{\rm e}$; and
6. Larger bandwidths and longer integration times reduce $\sigma_{t_{\rm S/N}}$[24].

These features underly our later discussion in Sect. 20 of quality measures for precision timing of MSPs.

6.2. *Full Stokes template fitting*

Template fitting using the full Stokes vector **S** (Eq. (5.4)) has been assessed in recent work (e.g. Rogers et al. 2024a; Dey et al. 2024; Guillemot et al. 2025) that builds upon the formalism developed in van Straten (2002, 2006, 2013). Here we outline the conditions under which improvements over scalar Stokes I template fitting can be expected. We refer to profiles in $Q, U, L = Q + iU$ and V as polarization profiles distinct from the total intensity profile I. Our treatment here ignores instrumental polarization, a discussion of which is deferred to Sect. 8.1.

Polarization profiles typically show sharper pulse features than in Stokes I, as they must given that pulsars generally show systematic changes in polarization state across pulse phase (Fig. 13). The potential for these sharper features to yield more precise ToAs must be weighed against their lower S/N if the degree of polarization, $d_{\rm p} \equiv \sqrt{d_L^2 + d_V^2}$, is not large.

To assess this we take into account the properties of polarized signals and unpolarized noise (Sect. 5.2) and refer to Eqs. (6.3) - (6.10). The ToA error from matched filtering is $\sigma_{t_{\rm S/N}} \propto W_{\rm eff}/{\rm S/N}$. Using a single component profile as an example, the effective width $W_{\rm eff} \propto \sqrt{WP}$, where W is the actual component width and P is the spin period. For an individual pulsar, we can ignore the period dependence for now. Defining the component width as W_s and the

[24] However, as discussed in Sect. 12.2, large bandwidths introduce significant complications from scattering that can counteract the improvement of the ToA error from a greater S/N in the matched filtering operation.

peak amplitude $|s|_{\rm pk}$ for each Stokes parameter ($s =$ I, Q, U, V) and taking into account that Q, U and V are signed quantities, the MF error for each Stokes parameter is $\sigma_{t_s} = \sigma_{t,I}\sqrt{W_s}/s_{\rm pk}$. Note that the implied signal to noise ratios underlying the ToA error are based on additive noise having the same RMS value in the Stokes parameters (Sect. 5.2). Further, recognizing that peaks do not align in pulse phase, we define $I_{{\rm pk},s}$ as the Stokes-I value at the phase where the Stokes-s extremum occurs. This allows us to express ToA errors in terms of the polarization state using peak values of d_L and d_V and in terms of the error in Stokes-I,

$$\sigma_{t,I} \propto \frac{W_I^{1/2}}{I_{\rm pk}}, \tag{6.11}$$

$$\sigma_{t,Q} \simeq \frac{\sigma_{t,I}}{|d_L \cos 2\chi|_{\rm pk}} \left(\frac{W_Q}{W_I}\right)^{1/2} \frac{I_{\rm pk}}{I_{{\rm pk},Q}} \tag{6.12}$$

$$\sigma_{t,U} \simeq \frac{\sigma_{t,I}}{|d_L \sin 2\chi|_{\rm pk}} \left(\frac{W_U}{W_I}\right)^{1/2} \frac{I_{\rm pk}}{I_{{\rm pk},U}} \tag{6.13}$$

$$\sigma_{t,V} \simeq \frac{\sigma_{t,I}}{|d_V|_{\rm pk}} \left(\frac{W_V}{W_I}\right)^{1/2} \frac{I_{\rm pk}}{I_{{\rm pk},V}} \tag{6.14}$$

Another expression results by using $L = Q + iU$,

$$\sigma_{t,L} \simeq \frac{\sqrt{2}\sigma_{t,I}}{d_{L\,{\rm pk}}} \left(\frac{W_L}{W_I}\right)^{1/2} \frac{I_{\rm pk}}{I_{{\rm pk},L}}, \tag{6.15}$$

where the $\sqrt{2}$ factor represents the larger RMS noise in L compared to the individual Stokes parameters. Improved ToAs result if sharper Stokes parameters outweigh the potentially lower S/N . This holds if the degrees of polarization are large enough, e.g.

$$d_{L\,{\rm pk}} > \sqrt{2}\left(\frac{W_L}{W_I}\right)^{1/2} \frac{I_{\rm pk}}{I_{{\rm pk},L}} \qquad \text{and} \qquad d_{V\,{\rm pk}} > \left(\frac{W_V}{W_I}\right)^{1/2} \frac{I_{\rm pk}}{I_{{\rm pk},V}}, \tag{6.16}$$

along with similar expressions for Q and U individually. The intensity ratios $I_{\rm pk}/I_{{\rm pk},L}$ and $I_{\rm pk}/I_{{\rm pk},V}$ are ≥ 1 while the width ratios ≤ 1, demonstrating the tradeoff between these quantities.

Joint fitting of all four Stokes parameters is optimal because additive noise is statistically independent between Stokes parameters. We illustrate with a highly simplified approach that estimates ToAs by minimizing a cost function,

$$C(a, \hat{t}_0) = \sum_t \sum_s^{I,Q,U,V} \frac{\left[aU_s(t - \hat{t}) - s(t)\right]^2}{{\rm Var}(s_{\rm off})}, \tag{6.17}$$

which sums over Stokes parameters s and time t across pulse phase and where U_s is a known template shape for Stokes-s, a is a scale factor, and $\widehat{t}$ is the estimated ToA. Each term is weighted by the off-pulse variance ${\rm Var}(s_{\rm off})$. This example assumes that the Stokes profiles U_s are known and the polarization state is epoch independent (after Faraday rotation correction) so that only a single scale factor is needed.

From Eqs. (6.11)–(6.17) we estimate the maximum improvement factor for using full Stokes ToA estimates compared to Stokes-I only. Using a representative set of Stokes profiles on 23 MSPs at 1.5 GHz from the NANOGrav program[25], we forecast maximum improvements in ToA errors from 5% to about 70%. Actual results reported by Rogers et al. (2024a) are based on a combination of enhanced polarization calibration as well as use of full-Stokes template matching for 25 MSPs. They find median improvements in ToA errors of 33% with no improvement in the worst case and the best (85%) improvement for bright MSP J0437−4715. Using similar analyses, Dey et al. (2024) find improvements of 14% to 33% for the three MSPs they studied in detail. More recently Guillemot et al. (2025) found improvements for observations using the Nançay telescope similar to those achieved by Rogers et al. (2024a).

[25] https://nanograv.org/science/data/polarization-calibration-data

While full-Stokes fitting is more complicated than illustrated here (e.g. van Straten 2013, and see also Sect. 8.1), the key points are evident, namely that the form of the cost function is based on the statistical independence of off-pulse noise and that the net results depend on polarization states and pulse widths that are unique to each pulsar. PTA measurements with more sensitive telescopes can enable implementation of this benefit, with each pulsar assessed individually to fully optimize this aspect of ToA estimation as in the work of Rogers et al. (2024a).

6.3. *Chromatic changes in profile shape*

A notable departure from idealized template matching is the nearly ubiquitous chromaticity of pulse shapes associated with the emission process. Most pulsars show significant variations of average pulse shape vs. frequency, usually as changes in relative amplitudes and spacings of profile features that can be identified across wide frequency ranges. All of the MSP profiles shown in Fig. 1 for ~ 1.5 GHz evolve with frequency. An example of profile variations over a 10:1 frequency range is shown in Fig. 19 for the MSP J0437-4715. Others can be found for CPs (e.g. Hankins and Rickett 1986; Hankins and Rankin 2009; Hassall et al. 2012) and MSPs (e.g. Kondratiev et al. 2016) that show similar but also a diversity of properties. The general trend is for profiles to broaden at lower frequencies with counterexamples for some CPs by the growing prominence of narrow 'core' components relative to broader 'conal' components (e.g. Rankin 1983), making the net pulse shape effectively narrower at lower frequencies for these cases. Much of the frequency dependence is captured in multicomponent profile models like those described in Sect. 5.4 with frequency dependent amplitudes, widths, and phases. In practice, timing errors induced by chromatic profile evolution are typically modeled by PTAs using a frequency-dependent (FD) model that parameterizes the additional timing errors as a power-law in log-frequency ($\propto C_{\rm FD}(\log\nu)^{-p}$, where $C_{\rm FD}$ and p are the fitted constant and spectral index, respectively) (NANOGrav Collaboration et al. 2015). This procedure often requires many free parameters to accommodate the chromaticity of different pulse components, as well as to account for differences in data reduction and pulse templates between different observing systems.

6.4. *Shape shifters: pulsars with epoch-dependent profile shapes*

The above considerations are based on the assumption that pulse variability is ergodic, i.e. that pulses are drawn from a homogeneous 'population' of pulses so that average profiles are convergent to a time-invariant (though chromatic) ensemble average. However, even after averaging out single-pulse stochasticity, there are several classes of non-convergent profiles manifested in pulsars. All of these have significant effects on ToA estimation.

As mentioned briefly in Sect. 5, the shape of an average profile is ultimately linked to the magnetic field topology where radio emission is produced in the magnetosphere of the NS. This field is a combination of the frozen-in field of the NS and the field produced by magnetospheric currents. The orientation of the NS's spin vector and its rate then map the emission beam into the observed shape. The net pulse shape also depends on any variation in emission altitude, which increases the scatter in single-pulse arrival times due to aberration and retardation. The emission strength also depends on the relativistic particle flows along the field lines and the degree of coherence. Empirically, the stability of profiles implies that all of these ingredients are also stable, on average, in most cases.

Secular and stochastic profile variations: The Crab pulsar has been observed for almost 60 yr since its discovery in 1968, representing about 6% of the time since its apparent birth in 1054. A secular change in the separation of the primary main-pulse and interpulse components suggests that the magnetic field is evolving on the spindown time scale (Lyne et al. 2013). For the Crab pulsar, this evolution is likely due to migration of the magnetic axis relative to the spin axis. It is slow enough that it does not limit timing precision; however, substantial glitch activity and spin noise make the Crab pulsar, like most young pulsars, an imprecise pulsar clock.

More striking examples can be found among magnetars, which show large profile changes on time scales of months that are accompanied by changes in the spindown torque e.g. Swift J1818.0−1607 (Fisher et al. 2024) and PSR J1745-2900 (Pearlman et al. 2018; Yan et al. 2018; Wharton et al. 2019; Suresh et al. 2021). For these objects, stochastic magnetic evolution drives shape changes as well as spin variability and X-ray emission.

Discrete, recurrent states: Some objects, primarily CPs, show two or more discrete profile shapes that sustain for multiple spin periods with switching between multistable states occuring rapidly, $\lesssim 1$ spin period ('mode' changes

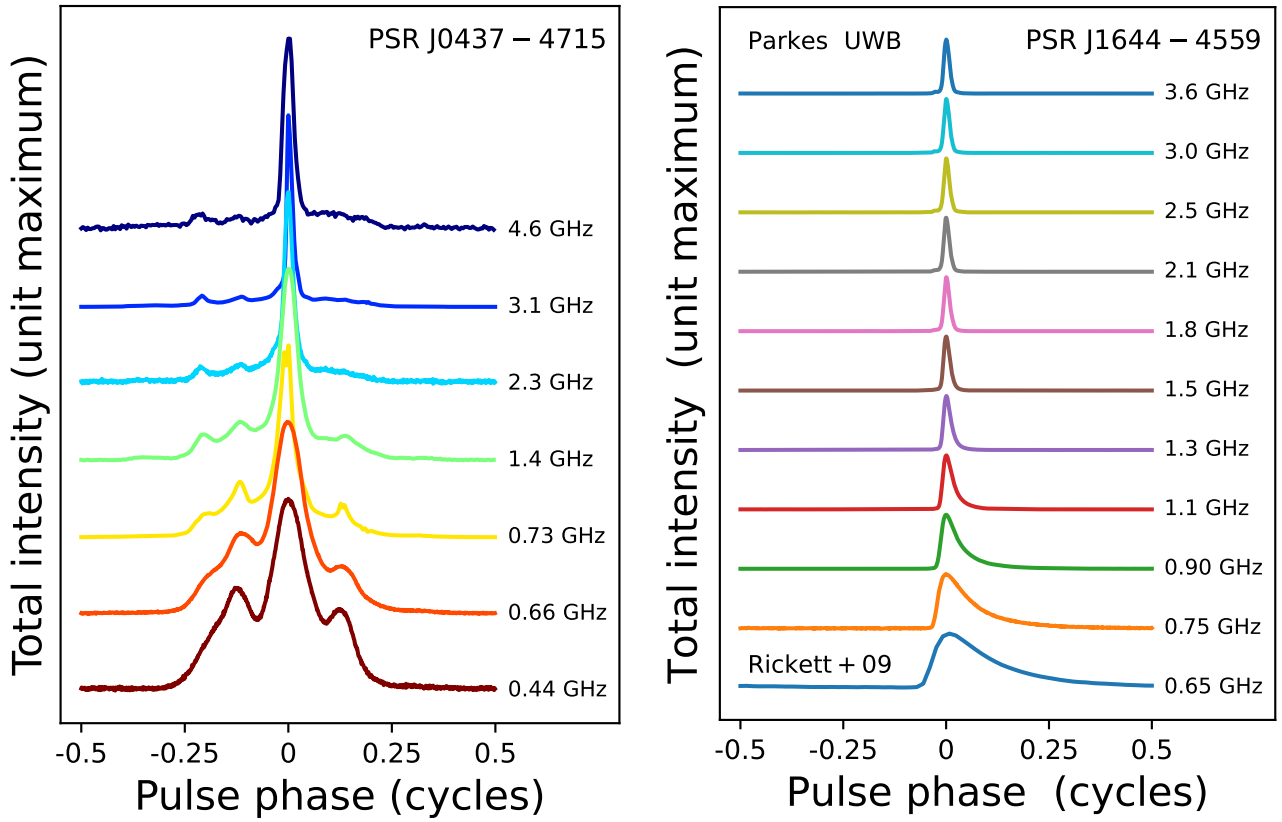


Figure 19. Left: Average profiles for the MSP J0437-4715 showing the change in shape over more than a decade in radio frequency. The profiles have been aligned using the strong central component that appears in all the profiles. Profiles are from the EPN database (Manchester and Johnston 1995; Bell et al. 1997; Dai et al. 2015). Right: Profiles for the heavily scattered pulsar J1644-4559 at multiple frequencies obtained simultaneously using the Parkes Ultra Wideband Feed (Sobey et al. 2021, https://doi.org/10.25919/gptm-d012) along with a profile at 0.65 GHz from Rickett et al. (2009). Profiles are aligned by their maxima. Proper alignment requires fitting for a contemporaneous value of DM estimated by taking into account actual pulse broadening shapes at each frequency.

Backer 1970; Lyne 1971; Bartel et al. 1982; Rankin 1986). Switching appears to be consistent with a Markov process, which gives exponential distributions for the durations of states (Cordes 2013). Arrival time offsets are substantial between the different modes but can be accounted for in a timing analysis if individual templates are used for each mode.

Another type of recurrence is 'nulling,' where the states are defined by highly disparate pulse intensities, where they either vanish during a null or become much smaller for durations of a few to a large number of pulse periods (Biggs 1992; Ng et al. 2020). Some pulsars display systematic drifts of pulse centroids over a few to a few dozen pulse periods (Basu et al. 2019, and references therein) and some objects show multiple, repeatable drift rates that are harmonically related, indicating another class of discrete states (Cordes 2013, and references therein).

The underlying physics of metastable states and switching between them is not well understood but appears to involve recurrent states in the particle flows generated by acceleration in pulsar magnetospheres. One object, the CP B1931+24, has residence times of weeks in high and low states, where radio emission during low states has only recently been detected (Rusul et al. 2025). State durations are long enough to establish that the spindown torque is larger in the high state by $\sim 50\%$ (Kramer et al. 2006). Torque jumps of this amplitude require changes in current on the scale of the entire magnetosphere, signifying that radio emission by itself, though a small part of the energy budget of a NS, traces large-scale magnetospheric activity. Much shorter nulls (tens to hundreds of spin periods) in other pulsars may also involve changes in torque, but their durations are too small to allow changes in $\dot{f}_{\rm s}$ to be measured.

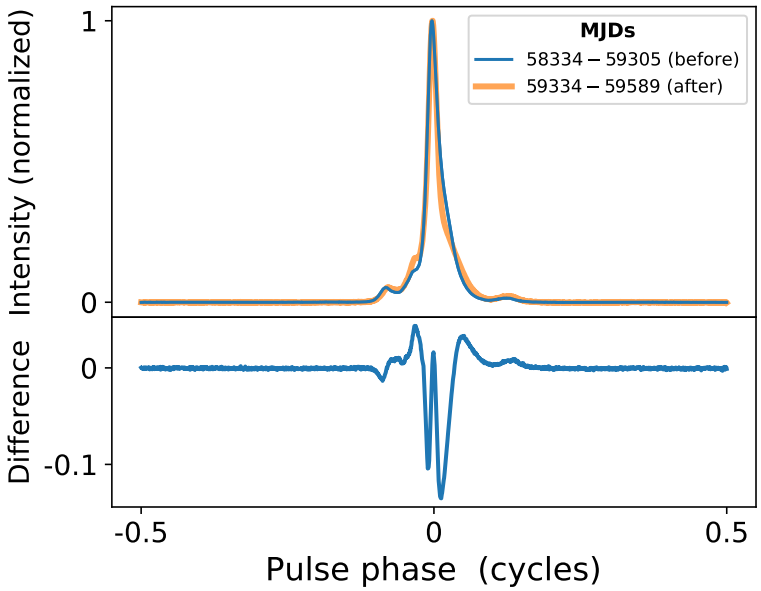


Figure 20. Average profiles for the MSP J1713+0747 before and after a sudden change in shape at MJD $\sim$ 53920 (top panel). The profiles were aligned by using the 'before' profile as a template for the 'after' profile in order that the differences between the two profiles (bottom panel) reflect the actual change in shape and not include the effects of a time offset.

Profile mode changes and nulling appear less common in MSPs and have not yet had a significant impact on timing precision for those MSPs used in PTAs.

Discrete events: The MSP J1713+0747 has shown a transitory, highly chromatic change in pulse shape (Xu et al. 2021; Singha et al. 2021) that recovered to its original form after about two years (Jennings et al. 2024b, and references therein). Fig. 20 shows profiles averaged over a data span of about 10^3 days prior to the event and 250 days after. The $\gtrsim 14\%$ change is in contrast to $\ll 1\%$ changes between high S/N profiles prior to the event. Confinement of the event to a specific range of epochs is fortunate because this pulsar otherwise shows some of the smallest timing residuals in PTA analysis. This pulsar has shown two similar previous events (Lam et al. 2018a; Lam 2021) with smaller arrival time shifts than the event in 2020-2021. Along with sparse time sampling the weakness of these events has not allowed a detailed study of the pulse shape changes during these two events. It is possible, but as yet unknown, if similar transitory events occur regularly for J1713+0747. Similar events have been seen in the MSPs J1643−1224 (Shannon et al. 2016) and J0437−4715 (Shamohammadi et al. 2024). The events from all three MSPs correspond to chromatic changes in pulse shape that are not plausibly related to interstellar propagation, although initial reports (see references in above-quoted papers) identified them to changes in DM or to scattering effects.

There is ongoing debate as to whether the J1713+0747 events are intrinsic to the pulsar or a propagation effect (e.g. Lin et al. 2021) but most indications suggest an intrinsic origin. Fortunately, reversion to the original shape suggests that its effects are confined to a small range of epochs that can be avoided in PTA analyses. Without correction, they would contribute distinctly non-Gaussian fluctuations into timing residuals.

Jacobson-Bell et al. (2026) recently developed a semi-automated method for identifying similar events in ToA data. In a preliminary analysis it reproduced events found in J1713+0747 and J1643−1224 (data on J0437−4715 were not available) but did not identify events in seven other pulsars (application to a larger sample is ongoing).

7. TOA VARIATIONS FROM SINGLE-PULSE STOCHASTICITY

The signal model of Sect. 5 implies that ToA errors will exceed those expected from idealized template fitting discussed in Sect. 6. Any departure of an average profile's shape from the template causes an offset in the ToA. Here we discuss profile shape changes caused by statistical variations in the N individual pulses used to calculate an average profile. Departures of profiles from the template shape diminish as $N^{-1/2}$ and thus do not fully vanish. Even for $N \gtrsim 10^5$ typical for the timing of MSPs, the $\lesssim 0.3\%$ shape variations can cause significant timing offsets.

In the following we discuss pulsar self noise as a process distinct from pulse jitter. Self noise was discussed in Sect. 5.3 as the stochastic emission by a pulsar that is modulated by a pulse shape envelope. ToA variations will arise from this AMN process even if the envelope is identical from one realization to the next. We define jitter as the change in the pulse envelope that does occur between realizations; it includes amplitude fluctuations along with departures in pulse phase from a strictly periodic sequence of pulses. We discuss these two contributions to timing errors separately in what follows.

7.1. *Pulsar self noise*

The AMPSN model discussed in Sect. 5.3 for the emitted pulsar signal represents 'self' noise $Z(t)$ that produces an arrival time error (using $A(t)$ as a template). For a single pulse, this error scales as the pulse width $W_{\rm A}$ divided by the square root of the number of independent samples, $n \sim W_{\rm A} B_{\rm r}$ where $B_{\rm r}$ is the receiver bandwidth. For a single pulse with 100 μs width and receiver bandwidth in GHz, $\sigma_{t_{\rm Z}} = m_Z \sqrt{W_{\rm A}/B_{\rm r}} \simeq 316\,{\rm ns} \times m_Z \sqrt{W_{\rm A,100}/B_{\rm GHz}}$ where the self-noise modulation index $m_z \simeq 1$ for dense shot noise that is applicable to most pulsar observations but exceeds unity for sparse noise.

For a sum of $N = T_{\rm int}/P = 10^6 T_{\rm int,3}/P_{\rm ms}^{-1}$ pulses, the error is

$$\sigma_{t_{\rm Z}} \simeq 0.32\ {\rm ns} \times m_Z \left(\frac{W_{\rm A,100} P_{\rm ms}}{B_{\rm GHz} T_{\rm int,3}} \right)^{1/2} . \tag{7.1}$$

Radio pulsar timing almost always involves the total intensity (i.e. Stokes I) equal to the sum of intensities of two polarization channels. If unpolarized, $Z_p(t)$ (with $p = 1, 2$) is uncorrelated between the two polarizations and the self noise error is reduced by $2^{-1/2}$. For 100% polarization, however, there is no reduction because $Z_1 \equiv Z_2$.

This contribution to the ToA error nominally contributes very little to the timing budget. However, it is larger than the error expected under the very idealized conditions of template fitting (Sect. 3.1 , serving as a proof of principle that self-noise alone causes excess ToA errors. Also, by inspection of Eq. (7.1), narrower bandwidths, shorter integration times, wider pulses, and longer periods can yield much larger self-noise timing errors.

7.2. *Timing jitter from stochastic pulse envelope modulations*

Fluctuations in pulsar emission cause pulse envelopes to vary in both amplitude and pulse phase as demonstrated in Fig. 11. These produce ToA errors that far exceed those caused by self-noise and can be larger than template fitting errors and those caused by interstellar scintillation discussed in the next section.

We model jitter effects by assuming the single-pulse shapes are the same but their amplitudes and phases vary. Actual pulses change shape dramatically, partly due to self noise but also from bona fide envelope shape variability. However, envelopes have characteristic widths for a given pulsar and for the purposes of our analysis the extra parameters needed to describe shape variability can be absorbed into a minimal set of parameters.

7.2.1. *Single component pulses*

We first consider cases there there is only one pulse component in the sense of Eq. (5.17). The template is equated to an ensemble average ($N_{\rm p} \to \infty$ assuming no time evolution of the pulse statistics), $U(t) = \langle I_N(t) \rangle$. This allows

expression of the template as an integral over a joint distribution for a_j and τ_j,

$$U(t) = \iint da\, d\tau\, f_{a,\tau}(a,\tau) a A(t-\tau) \longrightarrow \langle a \rangle \int d\tau\, f_\tau(\tau) A(t-\tau), \tag{7.2}$$

where the second expression applies when the joint PDF $f_{a,\tau}$ for a and τ is separable. The width $W_{\rm J}$ of the jitter distribution f_τ contributes to the net width of the template $W_{\rm U} = \sqrt{W_{\rm A}^2 + W_{\rm J}^2}$. For a toy model that gives approximate values and a useful scaling relation, we assume the width $W_{\rm A}$ is the same for all single pulses and that both f_τ and $A(t)$ have Gaussian shapes.

Given these assumptions, the RMS arrival time from template fitting can be shown to be

$$\sigma_{t_{\rm J}} = \frac{\sigma_{\rm J}(1+m^2)^{1/2}}{N_{\rm p}^{1/2}} \equiv \frac{F_{\rm J} W_{\rm U}}{N_{\rm p}^{1/2}}, \tag{7.3}$$

where $\sigma_{\rm J}$ is the rms time jitter (the rms of τ_j) and the modulation index is $m = \sigma_a/\langle a \rangle$. The second equality defines the rms TOA in terms of a 'jitter parameter' defined as

$$F_{\rm J} \equiv \frac{(1+m^2)^{1/2}}{2\sqrt{2\ln 2}} \frac{W_{\rm J}}{W_{\rm U}}. \tag{7.4}$$

For this case (only), amplitude variations alone ($\sigma_{\rm J} = 0$) do not cause arrival time variations but they enhance the TOA error by the factor $(1+m^2)^{1/2}$ when $\sigma_{\rm J} > 0$. A typical value for the jitter parameter is $F_{\rm J} \simeq 0.3$ although there is substantial variation between pulsars. Lam et al. (2016a) report a median value for an alternative jitter fraction defined relative to the spin period, $k_{\rm J} = \sigma_{\rm J}/P \simeq 0.010^{+0.023}_{-0.006}$ that corresponds to $F_{\rm J} = k_J P (1+m^2)^{1/2}/W_{\rm U} \simeq 0.3^{+0.6}_{-0.1}$ for assumed values $m = 1$ and a typical pulse duty cycle $W_{\rm U}/P \sim 0.05$.

Using $N = T_{\rm int}/P$ and nominal values for other parameters, the jitter TOA variation is

$$\sigma_{t_{\rm J}} \simeq 33 \text{ ns} \times W_{100} \left(\frac{F_{\rm J}}{1/3}\right) \left(\frac{P_{\rm ms}}{T_{\rm int,3}}\right)^{1/2}. \tag{7.5}$$

Fig. 21 shows the combined RMS ToA from template fitting and pulse jitter vs. signal to noise ratio. For $F_{\rm J} = 0$, the RMS error scales as $({\rm S/N})^{-1}$, as expected for matched filtering. The curves bottom out, however, for non-zero jitter.

7.2.2. *Multiple component pulses*

Timing variance changes significantly for pulsars with two or more profile components, especially if they overlap, as is the case for many pulsars, including those shown in Fig. 1. In addition to the number of components and their separations, TOA fluctuations depend on the widths and relative amplitudes of components:

1. *Multiple components with no overlap:* Components with separations larger than their widths yield rms TOAs smaller by a factor $\propto n_c^{-1/2}$ compared to a single component, with a proportionality constant determined by the amplitude ratios of the components. For the signal-to-noise dependent TOA error, $W_{\rm eff}$ is smaller with $n_c > 1$ components because there are more terms in the sum with large template derivative values. For the jitter contribution, if $F_{\rm J} W_{\rm U}$ is taken to represent the value for a single component, independence of jitter between components also implies a reduction by $n_c^{-1/2}$. As with the single component case, there is no TOA variance if there is no phase jitter in any of the components ($F_{\rm J} = 0$).
2. *Overlapping components:* With overlap, amplitude variations in the absence of phase jitter can induce TOA variance. This is a consequence of amplitude variations in different components affecting the entire profile shape even if some components were to not have amplitude variations (which is not typically the case for radio pulsars). The two-component case demonstrates these trends. When two Gaussian components have identical $1/e$ widths W, identical mean and RMS amplitudes of single pulses (quantified by a modulation index m_c), the the RMS ToA variation as a function of mean component separation Δ_{12} is

$$\langle \hat{\tau}^2 \rangle^{1/2} = \left(\frac{m_c}{W\sqrt{N}}\right) \frac{1}{\sqrt{2}} \frac{(\Delta_{12}/W)\, e^{-(\Delta_{12}/2W)^2}}{[1 + (1-(\Delta_{12}/W)^2] e^{-\Delta_{12}/2W)^2]}}. \tag{7.6}$$

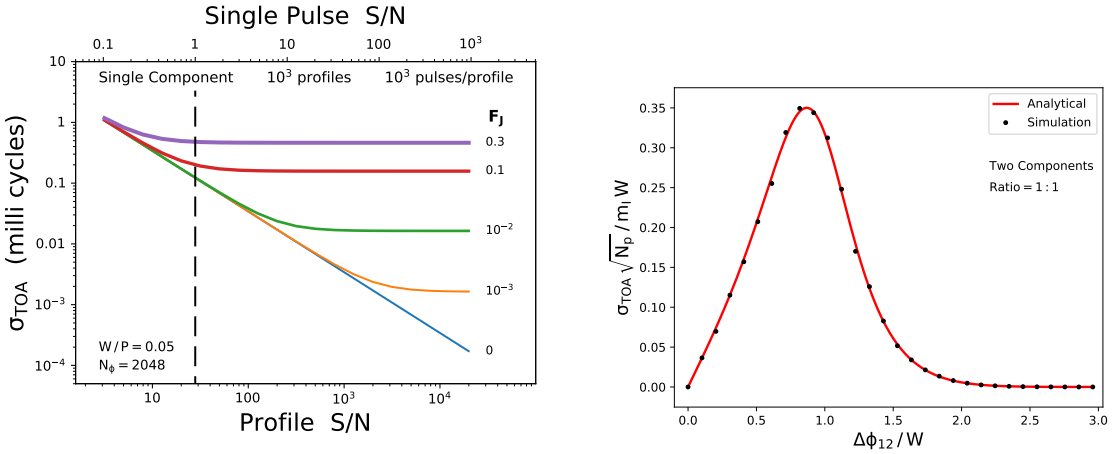


Figure 21. Results of simulations of single pulses with jitter and a range of signal-to-noise ratios. Left: RMS arrival time vs signal to noise ratio S/N for simulated data comprising pulses with duty cycles $W/P = 0.05$, phase jitter parametrized by $F_{\rm J}$ (as labeled), and additive noise. TOAs were calculated from averages of 10^3 pulses in $N_\phi = 2048$ phase bins to yield a profile S/N ~ 30 times larger than the single-pulse S/N. Plots are based on 10^3 realizations for each pair of values for $F_{\rm J}$ and S/N. Right: RMS TOA vs. component separation for two identical Gaussian components with single pulses in each having amplitude variations but no phase jitter. The amplitude variations are uncorrelated between components. The points show the RMS TOA vs. component separation, where both axes are normalized by the component width W (FWHM) to make them dimensionless. The plotted line is the analytical expression in Eq. (7.6).

Figure 21 (right panel) shows the RMS TOA error vs. component offset for the equal amplitude case when there are only amplitude variations of single pulses. Plotted points are based on 1000 realizations of simulated profiles and the solid line is an analytical calculation of the TOA error for the assumed Gaussian pulse components with independent single-pulse amplitudes. For non-overlapping components, the amplitude fluctuations do not affect the location of the components nor is there any component crosstalk. For vanishing separation, the two superposed components act as a single component and again the amplitude variations produce no TOA variations. Jennings et al. (2024a) give further discussion about ToA errors for multicomponent profiles.

7.3. *Jitter vs. noise dominated TOA errors*

A criterion is needed for assessing whether, on average, a pulsar has S/N or jitter dominated timing errors. Improved S/N can be achieved using a larger telescope with more bandwidth but if ToAs are jitter dominated, the primary means for improvement is with longer integration times. Jitter is correlated over broad frequency ranges (~ 1 GHz, e.g. Shannon et al. 2014) so jitter is not reduced by frequency averaging over bandwidths smaller than this correlation bandwidth. Conceivably, high frequency timing with the ngVLA may incorporate very wide bandwidths that would reduce some of the jitter error in a few cases. However, this improvement will most likely be negated by other timing errors.

Fig. 21 (left panel) shows the combined ToA error $\sigma_t = (\sigma_{t_{\rm S/N}}^2 + \sigma_{t_{\rm J}}^2)^{1/2}$ plotted vs. S/N for simulated Gaussian pulses for several values of the jitter parameter $F_{\rm J}$ along with additive noise. For small S/N the variation is noise dominated and decreases as S/N^{-1}, as expected from Eq. (6.3), while the variations are jitter dominated at large S/N.

The transition occurs for a single-pulse signal to noise ratio S/N$_1$ = N$^{-1/2}$S/N obtained by equating Eq. (6.3) with Eq. (7.3) and using Eq. (6.7) for the effective width of a Gaussian pulse shape to obtain

$$\mathrm{S/N}_{1,\rm trans} = \frac{1}{(2\pi \ln 2)^{1/4}\mathrm{F_J}} \left(\frac{\mathrm{P}}{\mathrm{N}_\phi \mathrm{W}}\right)^{1/2} \simeq 0.145 \times \frac{\mathrm{P_{ms}}}{(\mathrm{N}_\phi \mathrm{W}_{100}/2048)^{1/2}} \left(\frac{1/3}{\mathrm{F_J}}\right). \tag{7.7}$$

For many pulsars $P_{\rm ms}/W_{100} \sim 10$, so a useful rule of thumb is that when single pulses have S/N$_1 \gtrsim 1$, the ToA errors are jitter dominated, regardless of the total integration time.

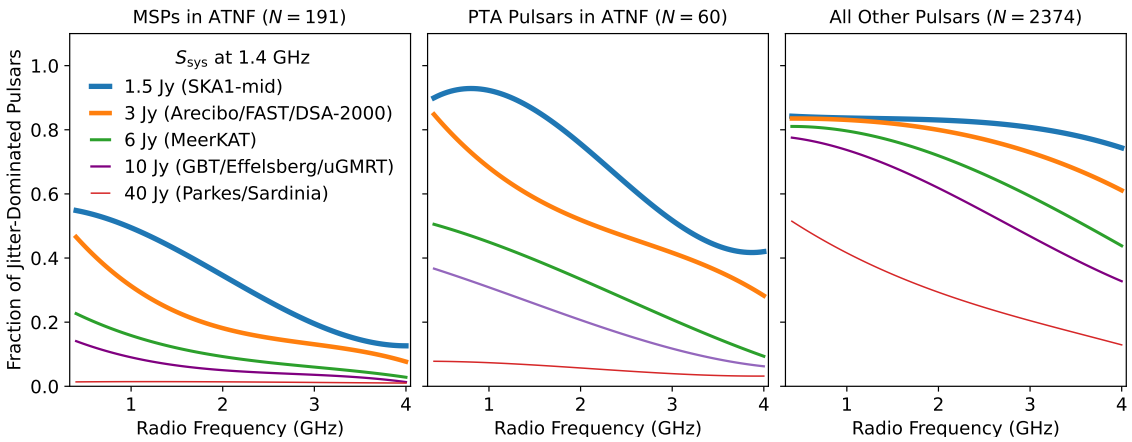


Figure 22. Fraction of pulsars that are jitter-dominated as a function of radio frequency, for MSPs (left; 191 LOS), PTA MSPs (middle; 60 LOS), and other pulsars (right; 2374 LOS) in the ATNF catalog. Fractions are calculated for five values of the system equivalent flux density $S_{\rm sys}$ at 1.4 GHz. The curves shown are cubic polynomials fit to the jitter-dominated fraction calculated at $\nu = 0.4$, 0.8, 1.4, 2, 3, and 4 GHz, for 10% radio bandwidths B below 1 GHz and $B = 0.4$, 0.8, 1, and 1 GHz at $\nu = 1.4$, 2, 3, and 4 GHz. For simplicity, pulse shapes are assumed to be single-component Gaussians, and only pulsars with cataloged widths are used. For $S_{\rm sys} = 1.5$, the synchrotron radio background contributes enough to cause a non-monotonic dependence on radio frequency.

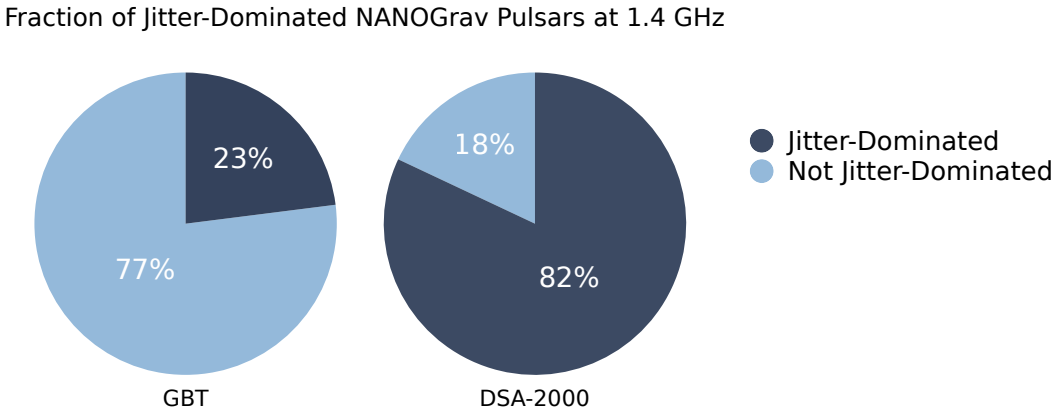


Figure 23. Fraction of NANOGrav pulsars that are jitter-dominated at 1.4 GHz for the GBT and DSA-2000, based on their respective sensitivities and bandwidths. The GBT fraction assumed a bandwidth of 0.5 GHz; increasing the bandwidth to that of the ultrawideband receiver under commissioning would increase the jitter-dominated fraction to about 50%.

We now assess how many pulsars are expected to have jitter-dominated ToA errors. Fig. 22 shows the fraction of pulsars with jitter-dominated TOA variations as a function of radio frequency, calculated by counting the number of pulsars in the ATNF PSRCAT catalog[26] (Manchester et al. 2005) for which $\sigma_{t_{\rm J}} > \sigma_{t_{\rm S/N}}$ (or equivalently, $\rm S/N_1 > 1$). The TOA error due to radiometer noise was calculated assuming a sky background dominated by synchrotron radiation, $T_{\rm sky} \propto \nu^{-2.7}$, and a pulsar spectrum $\propto \nu^{\alpha_p}$. The pulsar spectral index α_p was inferred from flux densities cataloged at 400 and 1400 MHz where possible, otherwise $\alpha_p = -2$ was adopted. Fig. 22 demonstrates how the fraction of jitter-dominated pulsars increases with telescope sensitivity. Arrival times of pulsars with $\rm S/N_1 \gtrsim 1$ are not improved by any increases in telescope sensitivity insofar as radiometer noise and jitter are concerned. Larger bandwidths reduce the arrival time variance due to radiometer noise by a factor $B^{-1/2}$. Larger bandwidths can also reduce arrival time variance due to interstellar scintillation (Sect. 12.5.2), which can dominate over radiometer noise and jitter for pulsars with high DMs or observations at low frequencies.

[26] http://www.atnf.csiro.au/research/pulsar/psrcat

The fractions shown in Fig. 22 correspond to three subsets of pulsars in PSRCAT: all MSPs, MSPs currently timed by PTAs, and all non-MSPs. A significantly larger fraction of PTA pulsars are jitter-dominated because they are chosen to be bright: the mean flux density at 1400 MHz $\langle S_{1400} \rangle = 4$ mJy for PTA pulsars in PSRCAT, whereas $\langle S_{1400} \rangle = 1.6$ mJy for the total MSP population in PSRCAT. TOA variations due to radiometer noise are linearly dependent on flux density, resulting in a factor of ~ 2 difference between the jitter-dominated fractions calculated for all MSPs vs. PTA pulsars. The fraction of jitter-dominated pulsars timed by NANOGrav is shown in Fig. 23 for the GBT and DSA-2000, demonstrating the dramatic increase in jitter-dominated pulsars that may be expected for the NANOGrav program on DSA-2000. Regardless of increases in telescope bandwidth and sensitivity, PTAs will always contend with jitter.

While jitter becomes increasingly dominant at high sensitivities and low radio frequencies for the observed pulsar population, it likely will not be a limiting factor for timing Galactic Center pulsars. Rescaling the flux densities of the entire pulsar population in PSRCAT to their equivalent values at the distance of the Galactic Center yields 50% of pulsars dominated by jitter at 8 GHz for $S_{\rm sys} = 0.3$ Jy and 20% at 8 GHz for $S_{\rm sys} = 3$ Jy. Optimistically, roughly 50% of Galactic Center pulsars will have jitter-dominated TOA variations for the ngVLA, if observed at high enough radio frequencies. These estimates do not explicitly account for scattering, which is significant near the Galactic Center and further reduces pulsar flux densities.

For simplicity, we have assumed single-component Gaussian profiles to estimate the fraction of jitter-dominated pulsars shown in Fig. 22. However, the presence of multiple pulse components alters the TOA errors due to radiometer noise and jitter, by an amount that depends on the number of components and their phase overlap (see previous section). This effect is compounded by the frequency-dependence of pulse components, making it difficult to quantify across the pulsar population. The jitter fractions calculated here nonetheless provide useful benchmarks for understanding the relative roles of jitter and radiometer noise for pulsar timing with current and future telescopes.

7.4. *Estimation of jitter properties*

The above subsections demonstrate how amplitude and phase jitter of single pulses increase ToA errors. The variety of template shapes seen among pulsars with different numbers and mean amplitudes of components and different component stochasticity implies that the net effect on ToAs is pulsar specific. For most pulsars it is difficult to make a multicomponent predictive jitter model unless all parameters for each profile component can be estimated. This is easiest if single pulses can be analyzed but in principle they could be estimated using N-pulse averages with variable N. However, forward modeling of this kind is not necessary in order to assess the overall timing budget of a pulsar.

Several empirical methods can be used for identifying and quantifying jitter, some applicable to cases where single pulses are strong and others when only average profiles can be analyzed:

1. *Analysis of variance of ToAs*: Modeling allows separation of a S/N dependent term (from template fitting) from S/N-independent contributions, which are often dominated by jitter and sometimes accompanied significantly by interstellar scintillation noise. Lam et al. (2016a) used this approach to characterize the jitter contribution at 1.4 GHz in ∼60% of the MSPs reported in NANOGrav's 9-yr data set (NANOGrav Collaboration et al. 2015); the ToAs of the remaining 40% were dominated by template-fitting errors that prevented jitter from being quantified. Typically, the RMS jitter is about 1% of the pulse period. Similar results were found in an analysis of MSPs observed at Parkes (Shannon et al. 2014).
2. *Cross correlation analysis of timing residuals between different frequency bands:* Jitter is highly correlated across frequency separations $\lesssim 1$ GHz (Shannon et al. 2014) while additive radiometer noise is uncorrelated and scintillation-caused TOA variations are correlated over separations $\lesssim$ scintillation bandwidth. The cross correlation therefore can determine the contribution from jitter in relation to the other contributions. For single pulses with S/N > 1 and frequency separations much wider than the scintillation bandwidth, the correlation coefficient is close to unity.
3. *Autocorrelation function analysis of template and single pulses:* Pulse jitter always makes the template broader than single pulses. So too is the ACF of the template vs. time (or phase) lag. For Gaussian pulse components and a Gaussian phase jitter PDF, the net width of the template is the quadratic sum of a typical component width and the RMS jitter multiplied by a factor accounting for multiple components. Let the widths of the two ACFs

be $W_{\rm U,acf}$ and $W_{\rm 1,acf}$, then the width of an *effective* phase jitter distribution is $W_{\rm J,eff} \equiv (W^2_{\rm U,acf} - W^2_{\rm 1,acf})^{1/2}/\sqrt{2}$, where the $\sqrt{2}$ accounts for the ACF width being larger than the widths of pulses by this factor. This method was used by Edwards and Stappers (2003, Fig. 9) to show that single pulses are significantly (40%) narrower than the template for the CP J1518+4904. A similar analysis of the MSP J1939+2134 (B1937+21) showed only a small difference in ACF widths (FWHM) for the ACF of template and the ACF of single pulses, $W_{\rm U,acf} - W_{\rm 1,acf} \sim 2\,\mu s$ with $W_{\rm U,acf} \sim W_{\rm 1,acf} \simeq 50\,\mu s$, which was incorrectly interpreted as indicating the absence of jitter (Jenet et al. 2001, Fig. 4). Using the quadrature difference in ACF widths and converting from ACF width to width of jitter distribution yields $W_{\rm J} \simeq 7\,\mu s$ or $\sigma_{\rm J} \simeq 3\,\mu s$.

4. *Crosscorrelation analysis of template and profiles vs. number of pulses averaged*: The correlation coefficient between the template and an average profile formed from Gaussian shaped single pulses with amplitude modulation index m_c can be shown to be

$$\rho(N) = \left[\frac{1 + (1+m_c^2)/(N-1)}{1 + (1+m_c^2)S_U/(N-1)}\right]^{1/2} \simeq 1 - \frac{(1+m_c^2)(S_U - 1)}{2(N-1)}, \tag{7.8}$$

where the approximate equality applies for $N \gg 1$ and $S_U = W_{\rm U}/W_a = \sqrt{1 + (W_{\rm J}/W_a)^2}$ is the ratio of the template width to the single-pulse width W_a. The absence of jitter corresponds to $S_U = 1$ and perfect correlation, $\rho(N) = 1$. Rearranging yields $S_U \simeq 1 + [2(N-1)(1-\rho_N)/(1+m_c^2)]$ which can be used to evaluate the width of the jitter distribution as $W_{\rm J} = W_a\sqrt{S_U^2 - 1}$.

Helfand et al. (1975) first used this method to demonstrate how average profiles converge to template shapes as N increases. Application to other CPS showed break points in $1 - \rho(N)$ vs. N for some objects, indicating that pulse to pulse correlations persisted for a few to $\lesssim 100$ pulses Rathnasree and Rankin (1995). Application to millisecond pulsars by Liu et al. (2012) showed that jitter properties of MSPs are very similar to those of CPs.

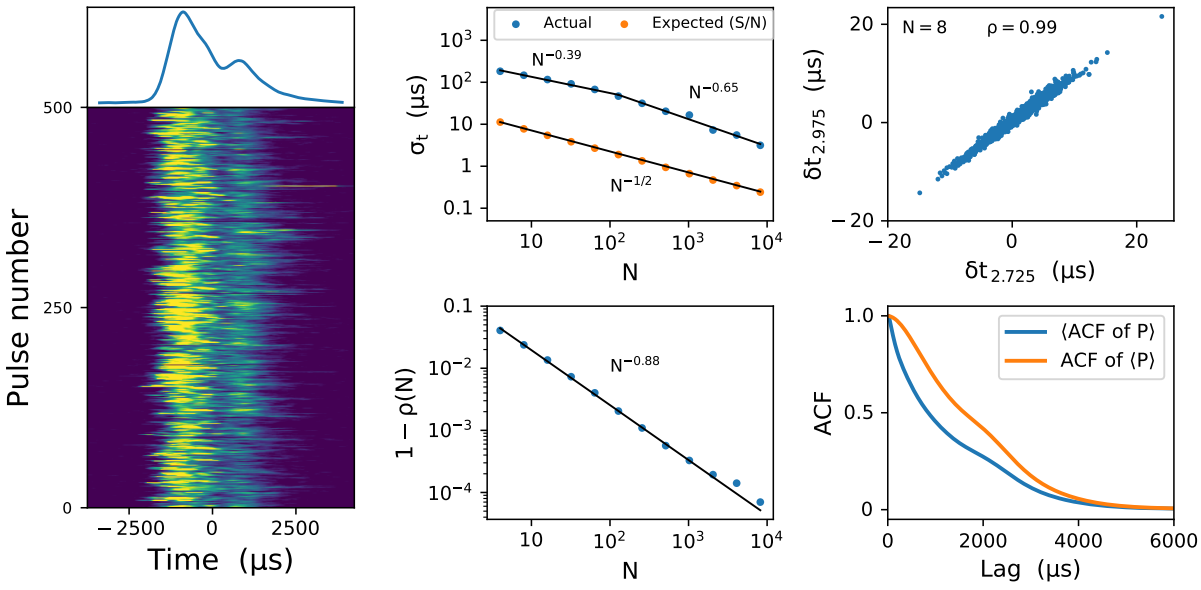


Figure 24. Left panel: sequence of 500 pulses and average profile from the Vela pulsar J0835-4510 ($P = 89$ ms) at 2.7 to 3 GHz. Right panels: Analysis of pulse jitter. Top left: RMS arrival time error vs N = number of pulses averaged (blue) and the predicted matched-filtering errors (red). The scaling with N is shown for two segments of the actual RMS error and for the expected $N^{-1/2}$ dependence if pulses are statistically independent. Top right: ToA deviations for two frequency bands (2.725 and 2.975 GHz) that show the large correlation. Bottom left: Correlation coefficient $\rho(n)$ between profiles calculated from N pulses and the template shape, plotted as $1 - \rho(N)$ vs. N. Bottom right: Autocorrelation functions of single pulses ($\langle$ACF of $P\rangle$) and of the template (ACF of $\langle P\rangle$).

We demonstrate these methods using pulses from the Vela pulsar obtained with the Parkes telescope at 2 to 3 GHz (Matthew Kerr, private communication; Ross Jennings, private communication). The strong single pulses, with average single-pulse S/N ~ 12, yield ToA errors dominated by jitter with minimal contributions from either radiometer noise or DISS. A sequence of 500 pulses is shown in the left panel of Fig. 24.

The right panel of Fig. 24 shows diagnostics of jitter in four frames similar to results obtained by (Jennings et al. 2024a). The top left shows the actual and predicted (based on matched filtering) RMS ToA vs. the number of pulses N used to compute average profiles. The actual RMS exceeds the predicted RMS by more than a factor of ten. The ToA errors are highly correlated between non-overlapping frequency channels separated by 50 MHz (top right frame). The excess ToA variations are from pulse jitter and not DISS because the latter would be uncorrelated between frequency channels. Using the values for the smallest $N = 4$ value shown, the RMS jitter for single pulses is $\sigma_{t_J}(N = 1) \simeq 370\,\mu s$.

Another estimate for RMS jitter results from the template-profile correlation analysis. The bottom left frame shows $1 - \rho(N)$ vs. N that declines with increasing N as expected for profiles shapes that converge to the template shape. However, the scaling $1 - \rho(N) \propto N^{-0.88}$ is slightly shallower than the N^{-1} dependence expected for pulse jitter that is uncorrelated between pulses. Using Eq. (7.8) and $1 - \rho(4) \sim 0.041$ we obtain $\sigma_J(1) \simeq 310$ to 390 μs for single-pulse modulation indices of 1 to 1.5, consistent with the jitter value from ToAs.

Finally, the ACFs in the bottom right frame yield effective Gaussian widths (FWHM) of $W_{\rm U} = 2.3$ and $W_a = 1.23$ ms for the template and single pulses, respectively. These yield a value, $\sigma_{t_J}(1) \simeq 830\mu s$, more than twice the values obtained from the other methods; this is due to the fact that pulses comprise two primary components that cause the template profile width to exceed that expected from single-pulse widths if there were only one component. Jitter occurs independently in each of the two components and is thus about half the nominal value, or 415 μs, consistent with the other estimates.

It is useful to define a dimensionless *jitter parameter* $f_{\rm J}$ to allow comparison of pulsars. Expressing jitter as an RMS quantity σ_{t_J}, we define $f_{\rm J} = 2\sqrt{2\ln 2}/{\rm FWHM}$. Using the first two methods applied above to the Vela pulsar yields $f_{\rm J} \simeq (370\,\mu{\rm s}/2300\,\mu{\rm s})2\sqrt{2\ln 2} \simeq 0.37$. This value is similar to those obtained for other pulsars, including MSPs.

The chromaticity of average profiles (Sect. 6.3) follows that of single pulses. We therefore expect pulse jitter, though highly correlated between nearby frequencies, to show only partial correlation for frequency ratios $\gtrsim 2:1$. Profile component spacing changes slowly with frequency, thus so too will the centroid phases of single pulses. However, the amplitudes of single pulses also appear to have limited bandwidths, albeit broad.

In practice, PTAs typically account for jitter using the so-called "ECORR" parameter, which assumes white noise that is temporally uncorrelated and completely correlated across radio frequency, and adds in quadrature to the template-fitting errors of ToAs. This procedure is known to overestimate the expected jitter noise (Lam et al. 2016a) and does not account for decorrelation of jitter when observations are performed over very large frequency bandwidths (Kulkarni et al. 2024), therefore motivating the need for the alternative methods summarized in this section.

8. INSTRUMENTAL EFFECTS

While this paper's primary focus is on astrophysical noise processes in pulsar timing, understanding and forecasting of timing precision requires consideration of ancillary effects. Included here are brief summaries of several prominent contributions, including polarization calibration, radio frequency and instrumental interference, digitization issues, time transfer, and the accuracy of solar system ephemerides.

8.1. *Instrumental polarization and calibration*

Radio pulsar timing involves template fitting to Stokes I (total intensity) profiles. Any alteration of the Stokes I profile from its true shape (or, more specifically, from the template shape) produces a ToA error. The polarized nature of pulsar signals implies that improper calibration will contribute to such errors. The primary effects to consider are (a) cross coupling between the antenna responses to the two desired polarization modes and (b) errors in the relative gain

calibration of the the two channels. The general issues of polarization calibration are well discussed in the literature (Heiles 2002), but primarily for continuum and spectral line applications. Careful calibration of pulsar data is done routinely and there is ongoing assessment of its imperfections on arrival times (Rogers et al. 2024a; Dey et al. 2024).

For specificity, we consider two nominal circularly polarized channels. Generally, these will have responses with some ellipticity and they need not be exactly orthogonal. The Jones matrix $\boldsymbol{J}$ encompasses these effects as a 2×2 matrix whose complex elements determine the real elements of the 4×4 Mueller matrix $\boldsymbol{M}$, which relates the measured Stokes vector $\mathbf{S}'$ to the true $\mathbf{S}$ (defined in Sect. 5.2).

The Jones matrix for the feed antennas (e.g. Conway and Kronberg (1969, Appendix II); Stinebring et al. (1984, Appendix); Heiles (2002)),

$$\boldsymbol{J}_{\rm A}(\boldsymbol{\theta}_{J_{\rm A}}) = \begin{bmatrix} \dfrac{1}{(1+\epsilon_1^2)^{1/2}} & \dfrac{\epsilon_1 e^{i\psi_1}}{(1+\epsilon_1^2)^{1/2}} \\ \dfrac{\epsilon_2 e^{i\psi_2}}{(1+\epsilon_2^2)^{1/2}} & \dfrac{1}{(1+\epsilon_2^2)^{1/2}} \end{bmatrix}, \tag{8.1}$$

is characterized with the parameter vector, $\boldsymbol{\theta}_{J_{\rm A}} = {\rm col}(\epsilon_1, \epsilon_2, \psi_1, \psi_2)$ and is augmented by a gain matrix. A full expression for the corresponding Mueller matrix $\boldsymbol{M}_{\rm GA}$ that includes ellipticity and non-orthogonality is given by Stinebring et al. (1984, Appendix), which builds upon earlier work by Conway and Kronberg (1969), and various factorizations of $\boldsymbol{M}$ are discussed in Han et al. (1997); Heiles et al. (2001); van Straten (2002, 2006, 2013); Gentile et al. (2018), including treatment of the Stokes vector as a Minkowskian four vector (Britton 2000).

Gain variations have a strong influence on the accuracy of Stokes parameters. Another matrix $\boldsymbol{J}_{\rm g}(\boldsymbol{\theta}_{J_{\rm g}} = {\rm diag}(g_{\rm R}, g_{\rm L})$ accounts for departures of the channel gains from unity. Together the product $\boldsymbol{J}_{\rm g}\boldsymbol{J}_{\rm A}$ transforms the true electric fields into the measured voltages. The corresponding Mueller matrix is $\boldsymbol{M}_G$. The combined Mueller matrix has a total of 6 parameters, $\boldsymbol{\theta}_M = {\rm col}(\epsilon_1, \epsilon_2, \psi_1, \psi_2, G_{\rm R}, G_{\rm L})$ where $G_{\rm L,R} = |g_{\rm L,R}|^2$. An additional parameter can account for an overall phase but can be absorbed into other quantities.

The simplest form for $\boldsymbol{M}_{GA}$ is for orthogonal responses (found to be applicable in some cases) with $\psi_2 = \psi_1 + \pi$ and small coupling and gain elements, $\epsilon = \epsilon_1 = \epsilon_2 \ll 1$. and $\Delta G = G_{\rm R} - G_{\rm L} \ll 1$, with $G_{\rm R}G_{\rm L} = 1$,

$$\boldsymbol{M}_{\rm GA} \simeq \begin{bmatrix} 1 & 0 & 0 & (\Delta G)/2 \\ 0 & 1 & 0 & -2\epsilon\cos\psi_1 \\ 0 & 0 & 1 & -2\epsilon\sin\psi_1 \\ (\Delta G)/2 & 2\epsilon\cos\psi_1 & 2\epsilon\sin\psi_1 & 1 \end{bmatrix}, \tag{8.2}$$

This shows that Stokes-I is altered by Stokes-V and vice versa but the latter is also influenced by the linear polarization, which itself is unaffected by Stokes-I.

To illustrate the effects on ToAs we use the simplest case of orthogonal polarization responses combined with differential gains for the two hands of polarization, giving intensities $I'_{\rm R} = G_{\rm R}I_{\rm R}$ and $I'_{\rm L} = G_{\rm L}I_{\rm L}$. Alteration of the Stokes I profile depends on the first row of the Mueller matrix, which gives

$$I' = \overline{G}I + \epsilon\Delta G(\cos\psi_1 Q + \sin\psi_1 U) + (\Delta G/2)V, \tag{8.3}$$

where the average and differential gain are $\overline{G} = (G_{\rm R} + G_{\rm L})/2$ and $\Delta G = (G_{\rm R} - G_{\rm L})$ and $\epsilon \ll 1$ is a measure of the cross coupling. If all four Stokes parameters have the same temporal shape, only the amplitude of Stokes I is altered with no change in ToA. However, polarization profiles of pulsars invariably differ from the Stokes I profile, so pulse distortion and the resulting ToA error are inevitable.

We use the degrees of linear and circular polarization, d_L and d_V, to estimate the fractional error in Stokes I

$$\frac{\delta I}{I} = (\Delta G/2)\left[d_V + 2\epsilon d_L\cos(2\chi - \psi_1)\right], \tag{8.4}$$

where χ is the polarization angle of the incident field, and ψ_1 is the phase of the cross coupling. We have set the average gain $\overline{G} = (G_{\rm R} + G_{\rm L})/2 = 1$ and $\Delta G = (G_{\rm R} - G_{\rm L})$. For wideband systems now used routinely in pulsar timing, the

frequency dependence of relevant quantities (i.e. $\Delta G, d_V, d_L, \epsilon$ and the argument $2\chi - \psi_1$) implies frequency-dependent calibration. The error in Eq. (8.4) should then be considered for each subband in a wideband system, as implemented in some pulsar analysis code packages.

Generally, pulse shapes in the polarized components differ from the Stokes I profile, so $\delta I/I$ is a measure of the distortion of the Stokes I profile. ToA errors scale as $\delta\text{ToA} \sim (\delta I/I)W$, where W is the profile width. In principle, the measured profile can be corrected for cross coupling and the gain calibration difference ΔG thus made arbitrarily small. In practice, however, neither of these is the case and a ToA error is inevitable. We expect both ΔG and ϵ to be small and often $d_V \ll d_L$ but the two terms inside the square brackets in Eq. (8.4) will typically be comparable unless ϵ is very small. Using fiducial values, the ToA error (without the variable cos factor) is

$$\delta\text{ToA} \simeq 50\,\text{ns} \left(\frac{\Delta G}{0.01}\right) \left(\frac{W}{100\,\mu s}\right) \left(\frac{d_V + \epsilon d_L}{0.1}\right). \tag{8.5}$$

This expression applies to each subband or to the aggregate effect in a wideband system, where relevant quantities are band averages.

Ongoing work has demonstrated the correctability of instrumental polarization and gain errors (Rogers et al. 2024a; Dey et al. 2024). This requires use of template Stokes pulse profiles for a pulsar combined with average profiles obtained at different parallactic angles, measurements of unpolarized continuum sources, and noise calibration signals to solve for cross coupling and gain parameters along with arrival times and average flux densities at each epoch (Stinebring et al. 1984); see also (Heiles 2002).

For our purposes here, we include the inference of arrival times along with Mueller matrix parameters. Writing the model Stokes vector as $\mathbf{S}_\text{m} = \text{col}(s), s = (I, Q, U, V)$,

$$\mathbf{S}_\text{m}(t, \bar{t}|t_0, \psi_r, \boldsymbol{\theta}_M) = \boldsymbol{M}_\text{GA}(\boldsymbol{\theta}_M(\bar{t}))\boldsymbol{M}_\text{r}(\psi_r)\mathbf{S}(t - t_0), \tag{8.6}$$

where a rotation matrix $\boldsymbol{M}_\text{r}$ is included that could account for Faraday rotation of the wavefield before incidence on antennas; t and $\bar{t}$ represent pulse phase and epoch, respectively. The cost function for template fitting (Eq. (6.17)) becomes

$$C(t_0, \psi_r, \boldsymbol{\theta}_M) = \sum_t \sum_s^{I,Q,U,V} \left|\mathbf{S}_\text{m}(t, \bar{t}|t_0, \psi_r, \boldsymbol{\theta}_M, t_0, \psi_r) - \mathbf{S}(t, \bar{t})\right|^2 / \text{Var}(s_\text{off}). \tag{8.7}$$

With seven total parameters in the most general form for $\boldsymbol{M}_\text{GA}(\boldsymbol{\theta}_M(\bar{t}))\boldsymbol{M}_\text{r}(\psi_r)$ or four parameters for the orthogonal, small coupling case, there are sufficient degrees of freedom in pulsar profiles and ancillary data to estimate parameters and allow inversion of the total Mueller matrix to calculate a corrected Stokes vector.

The question is, how well can instrumental polarization be removed to benefit ToA estimation, either from only Stokes-I or from full-Stokes estimation? The recent studies cited above (see also Osłowski et al. 2013; Gentile et al. 2018; Wahl et al. 2022) indicate that improvements of order a factor of two or more are obtainable for some but not all cases. It is beyond the scope of this paper to assess individual pulsars but it is clear that the demand for higher precision ToAs will require close attention to instrumental polarization on a pulsar-by-pulsar basis as well as on a telescope-by-telescope basis.

8.2. *Digitization and interference*

Further ToA errors arise from aliasing and radio frequency interference . We describe both of these in general terms by considering terms that add to true profile shapes. Unbalanced, interleaved analog-to-digital conversion (ADC) yields an aliased copy of pulses that appear with, effectively, a negative dispersion measure. NANOGrav data analysis routinely removes this deterministic effect, as described in (Alam et al. 2020). It requires determination of the ADC imperfection (time skew with unequal separation of time samples or gain mismatch) and values for relevant parameters. Alam et al. (2020) report correction of the dominant time skew to $\sim 10\%$ of ToA errors that would otherwise range from a few tens of nanoseconds to $\sim 1\,\mu s$, depending on the pulsar's DM and period.

Radio frequency interference (RFI) has diverse time-frequency signatures, including impulsive and oscillatory forms. Additional instrumental inteference can originate from leakage of power-line oscillations into the signal path. In many instances, the resulting pulse shape distortions are dramatic and the data are excised. In less severe cases, more subtle oscillations may occur across the entire profile as oscillations or ripple in the profile baseline. Even low-level ripple can skew ToAs but it is potentiallly correctable.

A derivation of the effect of baseline ripple on arrival times (Jones et al. 2021, Appendices A and B) is summarized and used here. Let the intensity profile include a sinusoidal ripple term with amplitude r and frequency $f_{\rm r}$,

$$I(t) = A\,U(t-t_0) + r\cos[2\pi f_{\rm r}(t-t_0)+\phi]. \tag{8.8}$$

For a small ripple-to-signal ratio, $r/A \ll 1$, the template fitting error is written in terms of the Fourier transform $\widetilde{U}$,

$$\delta t_{\rm r} = -\left(\frac{r f_{\rm r}}{2\pi A}\right)\frac{{\rm Im}\{e^{-i\phi}\widetilde{U}(f_{\rm r})\}}{\int df'\, f'^2|\widetilde{U}(f')|^2}, \tag{8.9}$$

where Im denotes imaginary part. For small ripple amplitudes, multiple ripple terms that add linearly to the net TOA error can be easily dealt with, including an arbitrarily shaped baseline perturbation represented as a Fourier sum.

For a Gaussian pulse of width W and sinusoidal ripple, the ToA error is

$$\frac{\delta t_{\rm r}}{W} = K\sin\phi\left(\frac{r}{A}\right)\left(\frac{W}{P_r}\right)e^{-\pi K(W/P_r)^2}, \tag{8.10}$$

with $K = \pi/(4\ln 2)$. The error vanishes for $\sin\phi = 0$ because the cosine maximum aligns with the peak of the Gaussian. It also vanishes as $W/P_r \to \infty$ because the increasing number of integrated ripple cycles integrated in template matching leads to cancellation and also when $W/P_r \ll 1$ because the perturbation is essentially constant over the pulse. In terms of $x = W/P_r$, the scaled TOA error follows a universal curve $\delta t_{\rm r} A/rW\sin\phi = Kx\exp\left(-\pi K x^2\right)$ shown in Fig. 25, which maximizes at $x_{\rm max} = 1/\sqrt{2\pi K} = 0.375$, corresponding to a ripple period $P_{\rm r_{max}} \simeq 2.67W$ and ToA error $\delta t_{\rm r,max} \simeq 0.258W(r\sin\phi/A)$.

For persistent ripple in a multi-epoch data set, we expect ϕ to be uniformly distributed in $[0, 2\pi]$ yielding $\sigma_{\sin\phi} = 1/\sqrt{2}$. Assuming constant r/A at the 1% level (only for illustration since ripple is episodic) and other fiducial values, the RMS error is

$$\delta t_{\rm r} = 0.80\,\mu s\,\times\left(\frac{r/A}{0.01}\right)\left(\frac{W}{100\,\mu s}\right)\left(\frac{W}{P_{\rm r}}\right)e^{-3.56(W/P_{\rm r})^2}. \tag{8.11}$$

This error is nominally quite large compared to the best timing precision of MSPs < 100 ns. In most data, the various factors in Eq. (8.11) evidently are much less than unity. However, there are data sets with substantial ripple that limit timing precision (e.g. Jones et al. 2021).

8.3. *Time transfer to the Solar System barycenter*

Topocentric arrival times are assigned according to an observatory clock synchronized to a hydrogen maser that, in turn, is synchronized to the time standard provided by the Global Positioning System (GPS) or other global navigation satellite system. The maser provides short term stability of the observatory clock while global time standards provide long-term stability. Commercially-available hydrogen masers drift by $\lesssim 0.1$ ns per day, and have achieved accuracies of better than 1 part in 10^{16} (i.e., ∼few ns) over ∼year timescales. PTAs generally rely on post-corrected timescales from the Bureau International des Poids et Mesures (e.g., TT(BIPM)) for long-term stability.

Barycentric arrival times: Arrival time analyses are easiest in the quasi-inertial barycentric frame. Topocentric ToAs are referenced to the Solar System barycenter (SSBC) by removing the light-travel time from the observatory to the SBC, correcting for relativistic time offsets, and correcting for Doppler shifts. Given a topocentric ToA $t(\nu)$, the barycentric ToA $t_b(\nu')$ at the Doppler shifted frequency ν' is

$$t_b(\nu') = t(\nu) + \frac{\mathbf{r}\cdot\hat{\mathbf{n}}}{c} + \frac{(\mathbf{r}\cdot\hat{\mathbf{n}})^2 - |\mathbf{r}|^2}{2cd} - \frac{K_{\rm DM}{\rm DM}}{\nu'^2} + \Delta_{E\odot} + \Delta_{S\odot} + \Delta_{A\odot}, \tag{8.12}$$

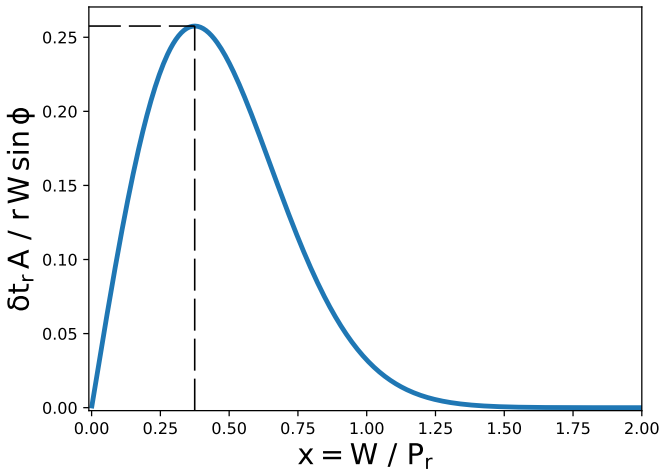


Figure 25. The normalized ToA perturbation from baseline ripple. The dashed lines designate $x_{\max} = 0.38$ and the maximum of $\delta\tau A/rW \sin\phi = 0.26$.

where $\mathbf{r}$ is the observatory-SSBC vector[27], $\hat{\mathbf{n}}$ is the unit vector from the SSBC towards the observed pulsar (see Fig. 26), $K_{\rm DM}{\rm DM}/\nu'^2$ is the frequency-dependent dispersion delay (introduced in Sect. 5.5 and discussed in detail later sections), and the Δ terms are, respectively, the Einstein delay due to gravitational redshift and time dilation, the Shapiro delay due to the curvature of spacetime around the Sun, and the aberration delay due to the Earth's rotation. Further explanation can be found in Backer and Hellings (1986); Stairs (2003) and Taylor (2021, Ch. 3) and implementation in Edwards et al. (2006).

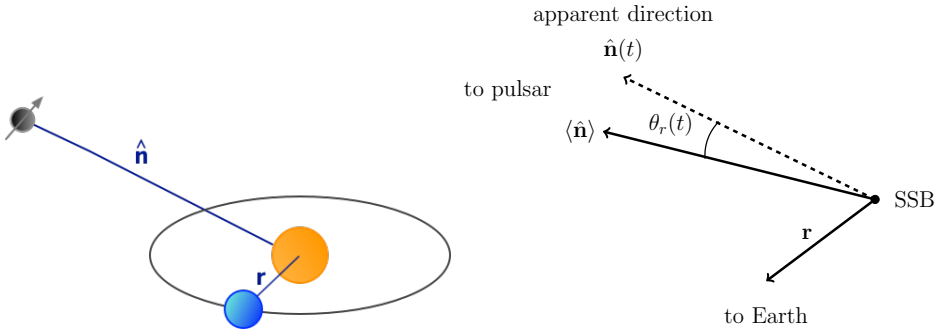


Figure 26. Left: The geometry of the observatory-SSBC-pulsar system where $\hat{\mathbf{n}}$ is the unit vector from the SSBC to the pulsar and $\mathbf{r}$ is the vector from the SSBC to the observatory. Both vectors are functions of epoch due to, respectively, the pulsar's proper motion and the Earth's spin and orbital motions. Right: In addition, the pulsar direction is slightly different in the observatory frame from parallax and refraction in the ISM by an epoch dependent angle $\boldsymbol{\theta}_{\rm r}$ also can cause the apparent pulsar direction to differ.

Translation of ToAs to the SSBC requires a maximum error in $\mathbf{r}$ tolerated by the astrophysical goals of the timing program. The most demanding timing application, GW detection, therefore requires better than 50 light-ns precision. Along with an observatory position on the surface of the Earth (updated, e.g., for continental drift for VLBI applications and less critically for pulsar timing), an accurate model for the Earth's rotation and orbit around the SSB is required[28]. Solar system ephemerides have been devised primarily for interplanetary spacecraft navigation (e.g. Park et al. 2021)

[27] The observatory location is strictly the focal point of the telescope.

[28] We note that the location of the SSB changes with respect to the Sun due to the orbits of the planets (primarily Jupiter and to a lesser extent Saturn) and can be located outside the Sun at certain epochs.

and also rely on spacecraft missions for measurements of the mass and moment of inertia of the giant planets. Errors in estimating the location of the SSB impose approximately a yearly sinusoidal variation in pulsar ToAs that have been translated to the SSBC. Such a variation would be *correlated* for all pulsars analyzed using the same ephemeris with a dipolar angular signature. For instance, the loss of the main antenna on the *Galileo* spacecraft mission led to reduced tracking accuracy and hence a lower accuracy measurement of Jupiter's orbital elements, introducing correlated timing residuals in the NANOGrav 11-year dataset. We refer the reader to Tiburzi et al. (2016); Vallisneri et al. (2020) for detailed discussion.

As an aside, we note that very long baseline interferometry (VLBI) also involves telescope positions changing by large distances compared to the observation wavelengths during the course of an observation due to the Earth's rotation. VLBI observations are typically referenced to the geocenter as a fixed point, and the reference frame created by VLBI observations of distant quasars (which defines the International celestial Reference Frame; Charlot et al. (2020) differs from the timing reference frame defined by solar system ephemerides at the 0.1–1 mas level (Madison et al. 2013; Deller et al. 2019). As a result, the positions measured for pulsars via pulse timing (as discussed below) and VLBI imaging can differ at the mas level, and can in turn be used to refine the frame tie between the two systems.

8.4. *Astrometric errors, proper motion, and parallax*

Referencing ToAs to the SSBC also requires a precise sky position $\hat{\mathbf{n}}$ to calculate the delays in the second and third terms of Eq. (8.12). An angle error of $\delta\theta = 1\,\mathrm{mas}$ yields an error in the SSBC ToA $\delta t \simeq \delta\theta \times 1\,\mathrm{au}/c \simeq 2.42\,\mu s$. Errors in sky positions from VLBI are of this order while inclusion of the corresponding terms in the timing analysis allows sky positions with smaller errors by up to two orders of magnitude.

Pulsars are moving targets owing to their proper motions, which can be as large as $1\,\mathrm{arc\,sec\,yr}^{-1}$, yielding a yearly cyclical variation with growing amplitude if a fixed sky position is used for SSBC referencing. Instead, an appropriate term is usually included in the timing analysis to solve for the proper motion and remove its contribution to the ToA.

Nearby pulsars can also show a sizable parallax (third) term in Eq. (8.12), $\Delta t_\varpi = (\mathbf{r}\cdot\hat{\mathbf{n}})^2 - |\mathbf{r}|^2/2cd$, with a 6-month period and maximum amplitude $\Delta t_\varpi \simeq 1.21\,\mu s\,d^{-1}$ for a pulsar in the ecliptic plane at distance d in kpc. This effect can be measured and removed in the timing analysis of some pulsars and the corresponding angular parallax, $\varpi = (1\,\mathrm{au}/1\,\mathrm{kpc}) \times d^{-1} = 1\,\mathrm{mas} \times d^{-1}$, can be measured with VLBI for some objects. Recent results on timing proper motions and parallaxes are reported by Shamohammadi et al. (2024).

Either way, parallax measurements are difficult: timing parallax can be masked by spin noise and interstellar fluctuations while VLBI is subject to errors from plasma fluctuations in the ionosphere. Another issue is that, while VLBI observations can provide independent measurements of the astrometric parameters for pulsars, incorporating them into timing solutions requires addressing the reference frame ties between the two different systems. In practice, incorporating VLBI measurements can help expedite the refinement of other timing parameters for a newly-timed pulsar (e.g. Madison et al. 2013; Sosa Fiscella et al. 2026), but the self-consistency of astrometric parameters measured directly from the timing observations has been prioritized in PTA observations so far.

9. ISM STRUCTURE AND PROPAGATION SCALING LAWS

The ISM is greatly heterogeneous in its density-temperature phase structure and with respect to mixtures of ionized, atomic, and molecular gas. Radio propagation effects are strongest where the free electron density and magnetic fields are largest. This then implies that the warm ionized medium (WIM) is the dominant phase contributing to pulse propagation, with a minor contribution from the hot ionized medium (HIM) and minimally by atomic and molecular clouds, where low level ionization occurs primarily from cosmic rays. Some contributions may involve interfaces between discrete clouds and the WIM or HIM, which are subject to ionizing radiation or ionizing shocks.

For this paper, we are concerned with ISM effects on timing, so our focus is on descriptions of the medium insofar as they are needed to quantify timing effects. Also, since timing is affected only minimally by magnetic fields (c.f. Eq. (5.23)-(5.24)), most of our presentation concerns the electron density and its fluctuations.

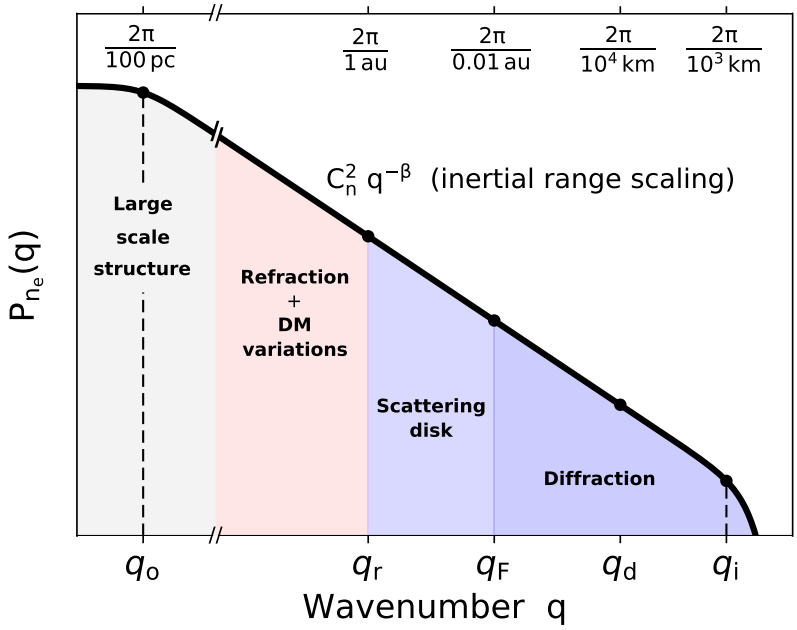


Figure 27. Schematic wavenumber spectrum for electron density. The colored regions indicate wavenumber ranges characterized by different features or phenomena: 'Large scale structure' (pc to kpc) refers to (e.g.) spiral arms and interstellar clouds; 'Refraction + DM variations' are effects caused by scales ($\gg$ au) much larger than those associated with scattering; 'Scattering disk' refers to the scale $\sim$ au spanned by the scattering cone due to multipath scattering (as in the cone diameter in the phase screen of Fig. 15); and 'diffraction' refers to scales $\ll$ au the cause diffractive effects (angular and pulse broadening). Though density fluctuations span more than 14 orders of magnitude in wavenumber, it has not been demonstrated that a turbulent cascade is responsible nor that any single process underlies all scales. Additionally, strong evidence exists for the presence of discrete structures on some scales (e.g. 'extreme scattering events' (ESEs); see text) that enhance fluctuations that do appear to follow a power-law form.

Dispersion and scattering both appear to result from the same regions along a line of sight where the electron density is largest (e.g. Cordes et al. 1991). This need not be the case, of course, because though all ionized regions contribute to DM, density fluctuations on scales smaller than the Fresnel scale $r_{\rm F} \lesssim 10^{11}$ cm (10^6 km) are needed to produce multipath propagation. This requires the occurrence of processes that create and sustain density fluctuations, such as shocks from supernovae and cloud-cloud collisions, and bow shocks from super-Alfvénic stellar motions. These are local processes whose occurrence is much higher in the inner Galaxy than at the solar circle and beyond because star formation is more prevalent in the Galactic interior, producing a higher supernova rate.[29]

Dispersion, scattering, and Faraday rotation are used to probe and model ISM structure. Galactic electron density models (e.g. NE2001, Cordes and Lazio 2002; Yao et al. 2017, hereafter YMW16) are used primarily for estimating pulsar distances from their DMs and for estimating foreground contributions to the DMs of FRBs [30]. These models include parameterized large scale structures (thin and thick disks and spiral arms) that are constrained by pulsar DMs. NE2001 also models density fluctuations on large and small scales using a power-law wavenumber spectrum along with parameters for the strength of the fluctuations in different Galactic locations. Electron density models are also integral to modeling the Galactic magnetic field (e.g. Unger and Farrar 2024) using large samples of RMs from pulsars and extragalactic sources (AGNs, and FRBs) (e.g. for FRBs Pandhi et al. 2022).

[29] The topic of Galactic stellar populations is vast. Recent modeling of the Galactic supernova population (Kachelrieß and Mikalsen 2025) incorporates astronomical tracers of high-mass star formation.

[30] NE2001 has recently been updated to include improvements based on new data obtained over the last quarter century (Ocker and Cordes 2026).

9.1. *Interstellar electron density wavenumber spectrum*

A power-law wavenumber spectrum is the most frequently assumed form because fluctuations in electron density are known to exist in the ISM on a large range of scales, **as may be seen in theoretical analyses (e.g. Lee and Jokipii 1976), observational constraints on the ionized ISM (e.g. Lee and Jokipii 1976; Cordes et al. 1985; Armstrong et al. 1995; Chepurnov and Lazarian 2010), and the very local ISM probed by the Voyager spacecraft (e.g. Lee and Lee 2019; Ocker et al. 2021b).** In this respect, the ISM parallels the interplanetary medium (IPM), which is much better characterized with *in situ* satellite measurements along with ground-based remote sensing. The IPM displays density and magnetic-field fluctuations with power-law spectra that include an inertial subrange, with a Kolmogorov slope during some of that range, (e.g. Schekochihin et al. 2009) and dissipation on small scales. IPM turbulence is anisotropic and combines with other structures generated by solar activity (Smith and Vasquez 2021). As with the IPM, there is evidence for anisotropies in the ISM along some lines of sight, implying that turbulent eddies have preferred orientations due to magnetic fields in specific regions in the ISM (Stinebring et al. 2001; Rickett 2018-08). A general form for the spectrum $P_{\delta n_e}(\mathbf{q})$ with a vector wavenumber $\mathbf{q}$ includes this anisotropy as an argument $(Aq_x^2 + A^{-1}q_y^2)^{1/2}$, where A is the axial ratio. However, to focus on integrated effects along a LoS, which likely average over anisotropies, we adopt an isotropic form for the spectrum,

$$P_{\delta n_e}(q) = \mathrm{C}_\mathrm{n}^2 q^{-\beta} e^{-(q/q_\mathrm{i})^2}, \tag{9.1}$$

where C_n^2 is the spectral coefficient and the wavenumber cutoffs or rolloffs $q_\mathrm{i}, q_\mathrm{o}$ correspond to the *inner* and *outer scales* of the fluctuations, $q_\mathrm{o} = 2\pi/l_\mathrm{o}$ and $q_\mathrm{i} = 2\pi/l_\mathrm{i}$. The integral over all wavenumbers gives the density variance, $\sigma_{n_\mathrm{e}}^2 = \int d\mathbf{q}\, P_{\delta n_e}(q)$ with $d\mathbf{q} = 4\pi q^2 dq$. Examples of this and similar spectral forms can be found in Lee and Jokipii (1976); Cordes et al. (1985); Coles et al. (1987); Armstrong et al. (1995) and Goodman (1985) and references therein. A Kolmogorov spectrum corresponds to a spectral index $\beta = 11/3$.

The spectrum, shown schematically in Fig. 27, has an amplitude C_n^2 that varies by several orders of magnitude across the Galaxy (Ocker et al. 2021a), as incorporated in the Galactic electron density models NE2001 and NE2025. Length scales described by the spectrum span more than ten orders of magnitude with $l_\mathrm{i} \lesssim 10^3$ km and $l_\mathrm{o} \sim 100$ pc in the thick disk component of the Galaxy. The very large outer scale is essentially irrelevant to timing measurements made over tens or even hundreds of years, so the specific form is not critical.

Support for the general form of the spectrum includes radio astronomical measurements of pulsars and other objects (e.g. Armstrong et al. 1995); small scales are sampled by scattering measurements while the largest scales for these objects are probed in decades-long time series of dispersion measures (Sect. 10.1). Familiar Galactic structures (atomic and molecular clouds, HII regions, filaments, etc.), some of which are known to include turbulent motions, comprise the largest scales.

Additional evidence for a broad power-law spectrum comes from studies of the cosmic ray proton energy spectrum, which extends from ~ 1 to 10^8 GeV in a smooth power law (with a change in slope at higher energies). Protons scatter off of magnetic irregularities on scales comparable to their gyro radii, $r_\mathrm{g} \simeq 0.074$ au $\times E(\mathrm{GeV})(B/3\ \mu\mathrm{G})$. The smoothness of the proton spectrum implies a spectrum of magnetic irregularities spanning a range at least as large as $\lesssim 0.1$ au to 40 pc. In theories of compressible turbulence, these magnetic fluctuations are accompanied by density fluctuations on the same scales (e.g. Jokipii 1988; Goldreich and Sridhar 1995).

There are strong variations in the spectral coefficient C_n^2, the inner, and the outer scale across the Galaxy. The outer scale appears to be smaller in denser regions toward the inner Galaxy and larger in the thick disk component of the electron density distribution. The notion that a continuous broad spectrum of scales is produced by a single physical process has not been demonstrated in the ionized ISM.

Though a turbulent cascade plausibly accounts for some of the wavenumber range, the diversity of density-temperature regimes in the ISM (Draine 2011) suggests that multiple processes are at work. There appear to be small, discrete structures in the ISM that superpose with power-law fluctuations that distort the wavenumber spectrum from a pure power-law with fixed spectral index. Their presence is manifested in ESEs ('extreme scattering events') manifested in AGN light curves (Fiedler et al. 1987; Vedantham et al. 2017; Bannister et al. 2016), AGN imaging (Koryukova et al. 2023), pulsar light curves and timing (Cognard et al. 1993; Lestrade et al. 1998; Maitia et al. 2003; Kerr et al. 2018),

refractive scintillations from pulsars (Roberts and Ables 1982; Hewish et al. 1985; Cordes and Wolszczan 1986) The statistics of such structures are not easily modeled because they are both sparse and diverse in nature but they suggest the presence of structures on $\sim$ au scales that cause plasma lensing (e.g. Romani et al. 1987; Clegg et al. 1998). Their existence in the ISM is subject to a variety of interpretations (e.g. Walker 2007).

The importance of the au structures responsible for ESE-type events is that they induce arrival time variations in a variety of ways, as we elucidate throughout much of the rest of the article.

Fig. 27 also designates regions defined by characteristic propagation scales that are indicated with approximate values along the top horizontal axis. From smallest to largest, these are the diffraction scale, the Fresnel scale, the refraction scale corresponding to the size of the scattering disk (c.f. Fig. 15), and still larger scales that are manifested as variations in DM and refractive scintillations. These scales are discussed in more detail in Sect. 9.3.

9.2. *Propagation through plasma fluctuations with a power-law wavenumber spectrum*

A thin screen suffices for identifying and analyzing propagation effects relevant to pulsar timing, which we summarize here. Thick screens or otherwise extended media yield the same phenomena but with different amplitudes and scaling laws that need consideration for analyzing individual LoS. These are described more selectively in what follows.

The *phase structure function* appears frequently in analyses of wave propagation because many observables are related to phase differences rather than to the absolute phase. Specifying $\phi(\mathbf{x})$ as the electromagnetic phase perturbation induced by a screen and $\delta\mathbf{x}$ as a transverse spatial separation across the screen, the phase SF is

$$D_\phi(\delta\mathbf{x}) \equiv \left\langle [\phi(\mathbf{x}+\delta\mathbf{x}) - \phi(\mathbf{x})]^2 \right\rangle . \tag{9.2}$$

where $\mathbf{x}$ and $\delta\mathbf{x}$ are vectors in the screen plane transverse to the propagation direction. In terms of the wavenumber spectrum $P_{\delta n_e}(\mathbf{q}; z)$,

$$D_\phi(\delta\mathbf{x}) = 4\pi(\lambda r_\mathrm{e})^2 \int dz \int d\mathbf{q}_\perp \, [1 - e^{i\mathbf{q}_\perp\cdot\delta\mathbf{x}}] P_{\delta n_e}(\mathbf{q}_\perp, q_z = 0; z). \tag{9.3}$$

Application to specific cases must take into account that a source embedded in or near the medium emits diverging, spherical waves, which requires the replacement $\delta\mathbf{x} \to (z/d_\mathrm{so})\delta\mathbf{x}$ in the complex exponential, where d_so is the source-observer distance.

For isotropic density fluctuations, the spectrum depends only on $|\mathbf{q}_\perp|$ and integration over azimuthal angle in the $\mathbf{q}_\perp$ plane yields an SF dependent only on the scalar offset δx,

$$D_\phi(\delta x) = 8\pi^2(\lambda r_\mathrm{e})^2 \int dz \int dq_\perp [1 - J_0(q_\perp \delta x)] P_{\delta n_e}(q_\perp, q_z = 0; z), \tag{9.4}$$

where J_0 is the zeroth-order Bessel function of the first kind.

For the spectrum in Eq. (9.1) with isotropic irregularities and plane-wave incidence on a screen, the phase structure function is (e.g. Coles et al. 1987)

$$D_\phi(\delta x) = \frac{8\pi^2(\lambda r_\mathrm{e})^2 \Gamma(2-\beta/2)}{(\beta-2) q_\mathrm{i}^{\beta-2}} \int_0^d ds \, \mathrm{C}_\mathrm{n}^2(s) \left[{}_1F_1\left(1 - \beta/2, 1, -(s q_\mathrm{i} \delta x/2d)^2\right) - 1 \right] \tag{9.5}$$

where ${}_1F_1$ is the confluent hypergeometric function of the first kind. If C_n^2 is constant along the line of sight, the phase SF is proportional to the product $\lambda^2\mathrm{SM}$, a measure of the scattering strength where SM is the LoS integral of C_n^2 and three regimes can be identified,

$$D_\phi(\delta x) = (\lambda r_\mathrm{e})^2 \mathrm{SM} \times \begin{cases} \pi^2 \Gamma(2-\beta/2)\, q_\mathrm{i}^{4-\beta}\, \delta x^2, & q_\mathrm{i}\delta x \ll 1 \quad \text{I.} \quad \text{Square-law regime,} \\ f_\beta\, \delta x^{\beta-2}, & q_\mathrm{i}^{-1} \ll \delta x \ll q_\mathrm{o}^{-1} \quad \text{II.} \quad \text{Inertial subrange regime,} \\ \left(\dfrac{8\pi^2}{\beta-2}\right) q_\mathrm{o}^{2-\beta}, & q_\mathrm{o}\delta x \gg 1. \quad \text{III.} \quad \text{Asymptotic regime,} \end{cases} \tag{9.6}$$

where

$$f_\beta = \frac{8\pi^2 \Gamma\left(2-\beta/2\right)}{(\beta-2)2^{\beta-2}\Gamma(\beta/2)} \overset{\beta=11/3}{\simeq} 88.3. \tag{9.7}$$

The three scaling regimes are, respectively, for: (I) lags δx smaller than the inner scale, where $D_\phi \propto \delta x^2 l_{\rm i}^{\beta-4}$ is a function of the inner scale ($\lesssim 10^3$ km for the ISM); (II) intermediate lags between the inner and outer scale (the inertial subrange), where the dependence is shallower, $D_\phi \propto \delta x^{\beta-2}$ and independent of either scale; and (III) lags much larger than the outer scale, $\delta x \gg q_{\rm o}^{-1}$, where the SF asymptotes to a constant $\propto l_{\rm o}^{\beta-2}$ that can be very large (many square radians) if the outer scale is large.

The form of the phase SF $D_\phi(b)$ is given in Eq. (9.6) for an isotropic medium where only the magnitude $b = |\boldsymbol{b}|$ matters.

The scattered image of a point source is the 2D Fourier transform of the visibility (the van Cittert-Zernike theorem); these are given by

$$\Gamma(\boldsymbol{b}) = e^{-D_\phi(\boldsymbol{b})/2}, \qquad I(\boldsymbol{\theta}) = \int d\boldsymbol{b}\, e^{ik\boldsymbol{b}\cdot\boldsymbol{\theta}} \Gamma(\boldsymbol{b}), \tag{9.8}$$

where $\boldsymbol{b}$ is a vector between two positions in the observation plane. The phase SF in the observation plane is identical to that in the screen plane (with $\delta\mathbf{x}$ replaced by $\boldsymbol{b}$ for scattering through a thin screen).

For isotropic density irregularties, the expressions depend only on the magnitudes of $\boldsymbol{b}$ and $\boldsymbol{\theta}$. Many observations of scattered images are in the square-law regime (I) in order for scattering diameters to be resolved with terrestrial baselines. Observations of Cyg X-3 (Molnar et al. 1995) spanned the transition between the square-law and inertial subrange regimes and thus provided an estimate of the inner scale ~ 300 km (50% error). A study of angular scattering along eight lines of sight by Spangler and Gwinn (1990) indicates values $l_{\rm i} \simeq 50$ to 200 km.

Radio pulsar timing measurements at ~ 0.5 to 1 GHz are largely in regime II except for distant pulsars observed at low frequencies where the square-law regime applies. The differences between regimes I and II are relevant to methods for correcting ToAs for scattering delays. The asymptotic regime III corresponds to (twice) the total phase variance along a line of sight and is dominated by large scale Galactic structure.

9.3. *Scaling laws for propagation effects from a power-law density spectrum*

Here we define useful quantities for describing dispersion, scattering, and scintillation that we present as scaling laws in Table 4 along with evaluations for a Kolmogorov spectrum ($\beta = 11/3$). Where unspecified, the units used are distances in kpc, radio frequencies (ν) in GHz, fluctuation frequencies (f) in cycles yr^{-1}, velocities in 100 km s^{-1}, and time lags (δt) in yr. Scattering measures are SM $= 10^{-3.5}\,\mathrm{SM}_{-3.5}$ kpc m$^{-20/3}$.

DM variations: The amplitude of the phase structure function can be related to the variance of spatial variations of pulsar DMs. The asymptotic $b \to \infty$ ensemble average phase structure function implies a total RMS dispersion measure $\sigma_{\rm DM} = (\lambda r_{\rm e})^{-1}\left[D_\phi(\infty)\right]^{1/2}$ that is also dominated by the largest scales in the spectrum for $\beta < 4$. Using $q_{\rm o} = 2\pi/l_{\rm o}$ in Eq. (9.6), we obtain the first entry in Table 4.

DM structure function: The DM SF is closely related to the phase SF, $D_{\rm DM}(\delta\mathbf{x}) = (\lambda r_{\rm e})^{-2} D_\phi(\delta\mathbf{x})$, and it is useful for ISM diagnostics (c.f. Sect. 10) to express the spatial offset as a time offset multiplied by an effective velocity. An expression that applies to thin screens and extended media alike is obtained by letting $b = v_{\mathrm{eff}_\perp}\delta t$,

$$D_{\rm DM}(\delta t) = f_\beta \int_0^{d_{\rm so}} ds\, \mathrm{C}_{\rm n}^2(s)\, |v_{\mathrm{eff}_\perp}(s)\delta t|^{\beta-2}\,, \tag{9.9}$$

where $\mathbf{v}_{\mathrm{eff}_\perp} = (s/d_{\rm so})\mathbf{v}_{\mathrm{p}_\perp} + (1-s/d_{\rm so})\mathbf{v}_{\mathrm{obs}\perp}$ and the effective scattering measure $\mathrm{SM}_{\rm eff} \le \mathrm{SM}$ is the weighted integral,

$$\mathrm{SM}_{\rm eff} = \int_0^d d\bar{s}\, \mathrm{C}_{\rm n}^2(\bar{s})\, (1-\bar{s}/d)^{\beta-2}\,. \tag{9.10}$$

Table 4. Dispersion, Scattering, and Scintillation Scaling Laws for Power-law Media

Item No.	Quantity	Expression[a]	Evaluation for $\beta = 11/3$[b] Coefficient	Scaling
1	SM	$\frac{(2\pi)^{\beta-2}}{f_\beta r_e^2 c^{(\beta+2)/2}} \left[\frac{\tau}{d'}\right]^{(\beta-2)/2} \nu^\beta$	$10^{-3.26}$ kpc m$^{-20/3}$	$\left(\tau_1/d'\right)^{5/6}$
2	$\sigma_{\rm DM}$	$\frac{(2\pi)^{(4-\beta)/2}}{(\beta-2)^{1/2}} l_o^{(\beta-2)/2} {\rm SM}^{1/2}$	0.097 pc cm^{-3}	$l_o^{5/6}$(pc) $(\tau_1/{\rm d}')^{5/12}$
3	$D_{\rm DM}(\delta t)$	$\frac{D_\phi({\rm v_{eff}}\delta t)}{(\lambda r_e)^2} = \frac{(\delta t/\Delta t_{\rm d})^{\beta-2}}{(\lambda r_e)^2}$	$\left(2.15\times10^{-4}\,{\rm pc\ cm^{-3}}\right)^2$	$(\delta t_{\rm yr}/\Delta t_{\rm d100})^{5/3}$
4	$S_{\rm DM}(f)$	$a_\beta {\rm SM} {\rm v_{eff}}^{\beta-2} f^{-(\beta-1)}$	$\frac{(7.70\times10^{-5}\,{\rm pc\ cm^{-3}})^2}{\rm cy\ yr^{-1}}$	$v_{100}^{5/3}\,(\tau_1/d')^{5/6}\,f^{-8/3}$
5	$r_{\rm F}$	$\left(\lambda d'/2\pi\right)^{1/2}$	8.1×10^{-3} au	$(d'/\nu)^{1/2}$
6	$l_{{\rm d}_I} = \frac{l_{{\rm d}_\theta}}{2^{1/(\beta-2)}}$	$\frac{1}{2^{(4-\beta)/2(\beta-2)}} \frac{1}{2\pi\nu} \left(\frac{cd'}{\tau}\right)^{1/2}$	1.43×10^4 km	$\nu^{6/5}\left(d'/\tau_1\right)^{1/2}$
7	$l_{\rm r}$	${r_{\rm F}}^2/l_{{\rm d}_I}$	0.69 au	$\nu^{-11/5}\ \left(d'\tau_1\right)^{1/2}$
8	$\theta_{\rm d}$ (FWHM)	$\frac{2\sqrt{\ln 2}}{\pi}\frac{\lambda}{l_{{\rm d}_\theta}}$	1.51 mas	$\nu^{-11/5}\ \left(\tau_1/d'\right)^{1/2}$
9	$\theta_{\rm r}$ (RMS)	$(c/2\pi\nu)[D_\phi(l_{\rm r})]^{1/2}/l_{\rm r}$	0.157 mas	$\nu^{-49/30}\,{d'}^{-1/2}\tau_1^{1/3}$
10	$\nu_{\rm trans}$	$\nu(2\pi\tau\nu/C_1)^{(\beta-2)/(\beta+2)}$	13.1 GHz	$(\tau_1/C_1)^{5/17}$
11	τ	$\frac{d'{\theta_{\rm d}}^2}{8\ln 2\, c}$	0.44 μs	$\nu^{-22/5} d'\theta_1^2$(mas)
12	$\Delta\nu_{\rm d}$	$C_1(2\pi\tau)^{-1}$	0.16 MHz	$\nu^{22/5}(C_1/\tau_1)$
13	$\Delta t_{\rm d}$	$\frac{l_{{\rm d}_I}}{\rm v_{eff}}$	143 s	$\nu^{6/5}\,v_{100}^{-1}\ \left(d'/\tau_1\right)^{1/2}$
14	$\Delta t_{\rm r}$	$\frac{l_{\rm r}}{\rm v_{eff}}$ or $\frac{1}{\Delta t_{\rm d}}\left(\frac{r_{\rm F}}{\rm v_{eff}}\right)^2$	11.9 d	$\nu^{-11/5}\,v_{100}^{-1}\ \left(d'\tau_1\right)^{1/2}$
15	$\Delta\nu_{\rm sb}$	$(2\pi\Delta t_{\rm d})^{-1}$	0.97 mHz	$\nu^{-6/5}\,v_{100}\ \left(\tau_1/d'\right)^{1/2}$
16	$N_{\rm scint}$	$\eta_{\rm t}\eta_\nu(B/\Delta\nu_{\rm d})(T/\Delta t_{\rm d})$	3960	$\nu^{-28/5}\,B_{\rm GHz}T_{1000}v_{100}\ \left(\tau_1^3/d'\right)^{1/2}$

[a] Expressions are for the strong scintillation regime and a thin screen with phase structure function $D_\phi(b) \propto b^{\beta-2}$.

[b] Numerical results for $\beta = 11/3$ use scattering time $\tau_1 \equiv \tau(1\,{\rm GHz}) = 1\,\mu$s, angular scattering diameter $\theta_1 \equiv \theta_{\rm d}(1\,{\rm GHz}) = 1$ mas, effective distance $d' = 1$ kpc. The center frequency ν is in GHz.

Definitions and units:

All distances are in kpc: ($d_{\rm so}, d_{\rm sl}, d_{\rm lo}, d'$ = effective distance $\equiv d_{\rm sl}d_{\rm lo}/d_{\rm so}$)
f = fluctuation frequency (cycles yr^{-1})
SM = scattering measure $= \int_0^{d_{\rm so}} ds\, {\rm C_n^2}(s) = 10^{-3.5}\,{\rm SM_{-3.5}}$ kpc m$^{-20/3}$, ${\rm SM_{eff}} = \int_0^{d_{\rm so}} ds\, {\rm C_n^2}(s)(1-s/d)^{\beta-2}$
$a_\beta = \left[\frac{\pi^{1/2}}{(2\pi)^{\beta-3}}\frac{\Gamma((\beta-1)/2)}{\Gamma(\beta/2)}\right] \overset{\beta=11/3}{\rightarrow} 0.494, \quad f_\beta = \frac{8\pi^2\Gamma(2-\beta/2)}{(\beta-2)2^{\beta-2}\Gamma(\beta/2)} \overset{\beta=11/3}{\rightarrow} 88.3$
$l_{\rm o}$ = outer scale in pc, v_{100} = effective transverse velocity = $\rm v_\perp/(100\,km\,s^{-1})$
$\Delta\nu_{\rm d}$ and $\Delta t_{\rm d}$ = scintillation bandwidth and scintillation time for DISS, $\Delta t_{\rm r}$ = scintillation time for RISS
$C_1 \simeq 1$ to 2 (dependent on β and line of sight distribution of electron density fluctuations)
$\eta_{\rm t} \sim \eta_\nu = 0.3$ (filling factors); B = bandwidth in GHz; T = observation time in 1000 s.

For a thin screen at distance $d_{\rm sl}$ from the source, $\mathrm{SM_{eff}} = \mathrm{SM}(1 - d_{\rm sl}/d_{\rm so})^{\beta-2}$. If the pulsar velocity dominates the time dependence, the expression simplifies to the form given in the second line of the table. Additional contributions to DM(t) from discrete ISM structures and from the solar wind augment the SF, as discussed in Sect. 10.

DM power spectrum: The power spectrum is the Fourier transform of the ACF, $R_{\rm DM}(\tau) = R_{\rm DM}(0) - D_{\rm DM}(\tau)/2$. The result is given in the fourth line of Table 4.

RM fluctuations: Though RM variations are not of great concern for precision timing of low-DM and low-RM pulsars, for completeness, we point out that for a constant magnetic field along the LoS, $\mathrm{RM} = (e^3/2\pi m_{\rm e}^2 c^4) B_\parallel \mathrm{DM} = 0.81 B_\parallel \mathrm{DM}$ (c.f. Eq. (5.21)), where the numerical value holds for standard units of rad m^{-2} for RM, pc cm^{-3} for DM, and fields in μG. DM structure functions etc. are then easily transformable to RM structure functions. However, we note that Minter and Spangler (1996) have shown that electron density fluctuations are accompanied by magnetic field fluctuations, also consistent with a Kolmogorov spectrum, which increase the RM SF over that from density fluctuations alone.

Fresnel scale ($r_{\rm F}$): The rough division between diffraction and refraction is defined by the Fresnel scale. For a thin screen at $d_{\rm sl}$ from the source, we define the Fresnel scale as $r_{\rm F} = 2\pi/q_{\rm F} = \sqrt{\lambda d'/2\pi} \sim 0.01$ au $\sim 10^6$ km, where the effective distance is $d' \equiv d_{\rm sl} d_{\rm lo}/d_{\rm so}$ with $d_{\rm lo} = d_{\rm so} - d_{\rm sl}$. Alternative definitions for $r_{\rm F}$ are found in the literature with 2π replaced by π or unity. In our case, the Fresnel scale corresponds to a phase difference between a deflected and a direct ray path of 1/2 radian.

Diffraction scale ($l_{\rm d}$) and visibility function ($\Gamma(\delta\mathbf{x})$): Diffraction is caused by scales $l_{\rm d}$ smaller than the Fresnel scale. Most pulsar measurements correspond to very small diffraction scales $l_{\rm d} = 2\pi/q_{\rm d} \sim 10^2$ to 10^4 km. These appear to straddle the inner scale $l_{\rm i}$, ~ 100 to 10^3 km (e.g. Rickett et al. 2009).

The diffraction scale is related to the size of the scattered image, the pulse broadening time τ, and the DISS bandwidth $\Delta\nu_{\rm d}$. It is convenient to use two definitions, one for which the visibility function $= 1/e$ given by $D_\phi(l_{\mathrm{d}_\theta}) = 2$ rad^2, and another from $D_\phi(l_{\mathrm{d}_I}) = 1$ rad^2, which yields the $1/e$ scale of the intensity rather than the field, as in item 6 of Table 4.

Scattering diameter ($\theta_{\rm d}$): A scattered image represents the distribution of angles into which incident radiation from a point source is scattered. Scattered images are generally non-Gaussian but a convenient scattering diameter is obtained by matching a Gaussian function to the non-Gaussian image at the half-amplitude value. This yields a scattering diameter (FWHM) $\theta_{\rm d} = 2\sqrt{\ln 2}\lambda/\pi l_{\rm d}$. An observer sees a scattering diameter $\theta_{\rm obs} = (d_{\rm sl} d_{\rm lo}/d_{\rm so})\theta_{\rm d} \equiv d'\theta_{\rm d} \lesssim \theta_{\rm d}$ that is larger for screens close to the observer. The scattering disk is the patch size of the cone of rays contributing to the scattered radiation measured by an observer (Fig. 15). The patch or cone size is $\ell_{\rm cone} = d_{\rm lo}\theta_{\rm obs}$ for an observed scattering disk size $\theta_{\rm obs}$ from a screen at distance $d_{\rm lo}$ from the observer.

Refraction scale ($l_{\rm r}$): Refractive scintillations result from scales that focus or defocus incident waves according to geometrical optics. For a Kolmogorov-like spectrum, refraction is dominated by scales $l_{\rm r} \sim \ell_{\rm cone}$. A convenient relation between the refraction and diffraction scales is $l_{\rm d} l_{\rm r} \equiv {r_{\rm F}}^2$. DM variations on time scales up to ~ 50 yr correspond to lengths up to $\sim 10^3 l_{\rm r} \sim 10^3$ au.

The cone of scattered ray paths has a projected diameter $\ell_{\rm cone} = d_{\rm lo}\theta_{\rm obs}$ at the screen-observer distance $d_{\rm lo}$. Motion of the source, screen, or observer causes the scattering cone to move along the screen, acting as a smoothing function of the screen phase. This manifests as a variation in intensity due to refractive focusing and defocusing, which defines a refraction scale For screens with 'shallow' ($\beta < 4$) wavenumber spectra, intensity variations from refractive focusing and defocusing are dominated by the scale of this smoothing function. The refraction scale is accordingly defined as $l_{\rm r} \equiv \ell_{\rm cone}$.

Pulse broadening function $p_{\rm d}(t)$ and its $1/e$ time scale τ: An emitted impulse arrives differentially along multiple scattered ray paths. For a screen, ToAs are directly related to the square of AoAs. The distribution of arrival times is the pulse broadening function (PBF), usually characterized with a $1/e$ width. The PBF and τ typically are measures of only geometrical path length delays and exclude any differential dispersion between individual ray paths. This and other complications, such as the relation between the mean scattering time and analysis methods are discussed in other sections.

Diffractive interstellar scintillation (DISS) bandwidth $\Delta\nu_{\rm d}$: Diffraction yields a spatial intensity pattern from constructive and destructive interference with a characteristic scale $l_{\rm d}$ in the observation plane (transverse to the line of sight). The diffraction pattern also has a characteristic diffraction bandwidth $\Delta\nu_{\rm d}$ (also known as the scintillation or decorrelation bandwidth). Like the pulse broadening time, it is determined by path length differences and the two are related by an 'uncertainty' relation (Sutton 1971),

$$2\pi\Delta\nu_{\rm d}\tau = C_1, \tag{9.11}$$

where $C_1 \simeq 1$ to 2 is a constant dependent on the the index β of the wavenumber spectrum. This relation applies to all cases (not just thin screens) with C_1 also depending on the thickness and location of the scattering region (Cordes and Rickett 1998; Lambert and Rickett 1999). At frequencies $\nu \lesssim 1\,$GHz, the DISS bandwidth is small, $\Delta\nu_{\rm d} \ll \nu$.

DISS time scale $\Delta t_{\rm d}$: Sweep of the diffraction pattern across the LoS by an effective velocity $v_{\rm eff}$ yields the scintillation time scale (or decorrelation time) $\Delta t_{\rm d} = l_{\rm d}/v_{\rm eff}$. In most cases, the effective velocity is dominated by either the pulsar or the observer's motion; bulk or turbulent motions of the screen appear to be small enough so that the diffraction pattern may be considered frozen.

Refractive interstellar scintillation (RISS) time scale $\Delta t_{\rm r}$ *and bandwidth* $\Delta\nu_{\rm r}$: Similarly, the refraction time scale is $\Delta t_{\rm r} = l_{\rm r}/v_{\rm eff}$. Because RISS does not involve constructive/destructive interference, it is correlated over wide frequency ranges, $\Delta\nu_{\rm r} \sim \nu$.

Diffractive spectral broadening $\Delta\nu_{\rm sb}$*:* While not relevant to broadband pulsar signals, we include spectral broadening for completeness and because it is simply the reciprocal of the DISS time scale. It may apply to situations of very strong scattering, such as low-frequency measurements of recombination lines, and may influence narrowband features found in FRBs. A narrowband signal is broadened by phase fluctuations that ensue from transport of the diffraction pattern across the LoS, yielding changes in frequency $\delta\nu \sim (d\phi/dt)\delta t$. One can also view this as the frequency broadening of a pure sine wave modulated by DISS. The broadening bandwidth $\Delta\nu_{\rm sb}$ is related to the scintillation time by another uncertainty relation (Cordes and Lazio 1991), $2\pi\Delta\nu_{\rm sb}\Delta t_{\rm d} \simeq 1$.

Together, the DISS bandwidth and time scale determine the number of scintles contributing to an observation over a total bandwidth B and time span T.

Fig. 28 shows the scintillation time and number of scintles vs. frequency for five DM values. These scale with frequency as $\Delta t_{\rm d} \propto \nu^{-6/5}$ and $N_{\rm scint} \propto \nu^{-28/5}$ for a Kolmogorov spectrum when the scintillations are strong and the inertial subrange of wavenumbers is applicable. These quantities are calculated from the scattering time τ_1 evaluated using Eq. (10.16) and assuming a thin screen midway to the pulsar. They also assume an effective transverse speed of $50\,{\rm km\ s^{-1}}$ (corresponding to a pulsar velocity of $100\,{\rm km\ s^{-1}}$ and a screen midway between pulsar and observer ($s = 1/2$) and assuming negligible contribution from Earth's velocity or from the ISM).

Fig. 29 shows scintillation times vs. DM for different frequencies (left) and different effective velocities (right) at 1 GHz. The right-hand panel also shows measured scintillation times scaled to 1 GHz for 136 pulsars. The red points designate MSPs ($P \le 10\,$ms) and the yellow points indicate large scintillation times that occur yearly for three MSPs. The velocity labels are the assumed pulsar velocities for the three black lines, which apply only for a midway scattering screen.

9.4. *Scintillation and scattering regimes*

Except for observations at frequencies above ~ 5 GHz for the nearest pulsars, the phase variance across one Fresnel scale in the screen is many square radians. In this so-called *strong scintillation* regime, the various length scales defined above satisfy the inequalities when the diffraction scale is larger than the inner scale ($l_{\rm d} > l_{\rm i}$),

$$l_{\rm i} \ll l_{\rm d} \ll r_{\rm F} \ll l_{\rm r} \lll l_{\rm o}, \quad \text{Strong scintillation.} \tag{9.12}$$

In the *hyperstrong scintillation regime*, the order of $l_{\rm i}$ and $l_{\rm d}$ is interchanged when the product $\lambda^2{\rm SM}$ is large:

$$l_{\rm d} \ll l_{\rm i} \ll r_{\rm F} \ll l_{\rm r} \lll l_{\rm o}, \quad \text{Hyperstrong scintillation.} \tag{9.13}$$

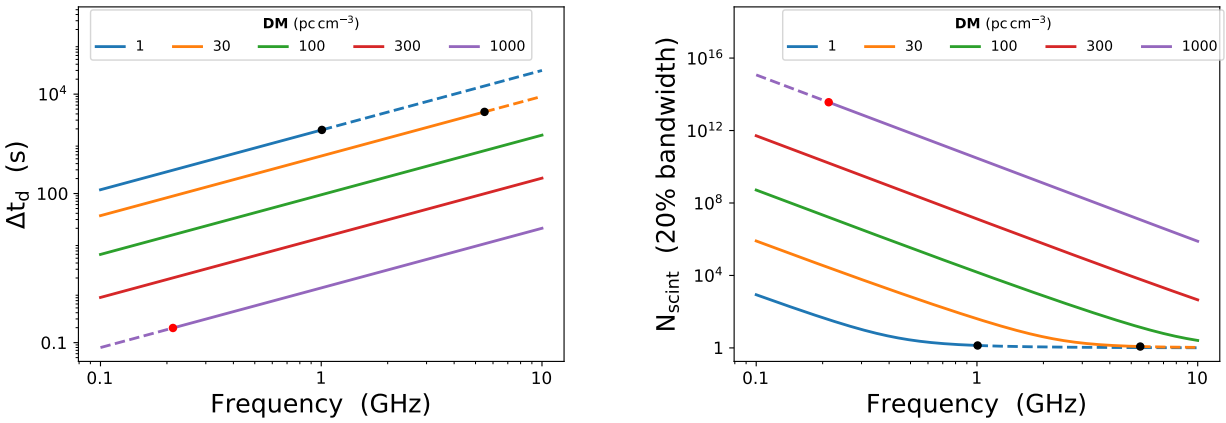


Figure 28. Computed values for the scintillation time (left) and number of scintles (right) for a thin screen with Kolmogorov fluctuations. The number of scintles is calculated for a 20% bandwidth. Solid lines indicate where the scintillations are strong with $\Delta\nu_{\rm d} \leq \nu$ and where the scintillation time scale exceeds the scattering time. The black dots show the transition to weak scattering with dashed lines indicating the scaling that otherwise would have occurred. The red dot marks the transition where the scattering time equals the scintillation time scale. The curves are calculated for a pulsar speed of 100 km s^{-1} and a screen midway to the pulsar, giving $v_{\rm eff} = 50\,{\rm km\,s^{-1}}$. A larger effective speed shifts the scintillation time downward $\propto 1/v_{\rm eff}$ and the number of scintiles $\propto v_{\rm eff}$.

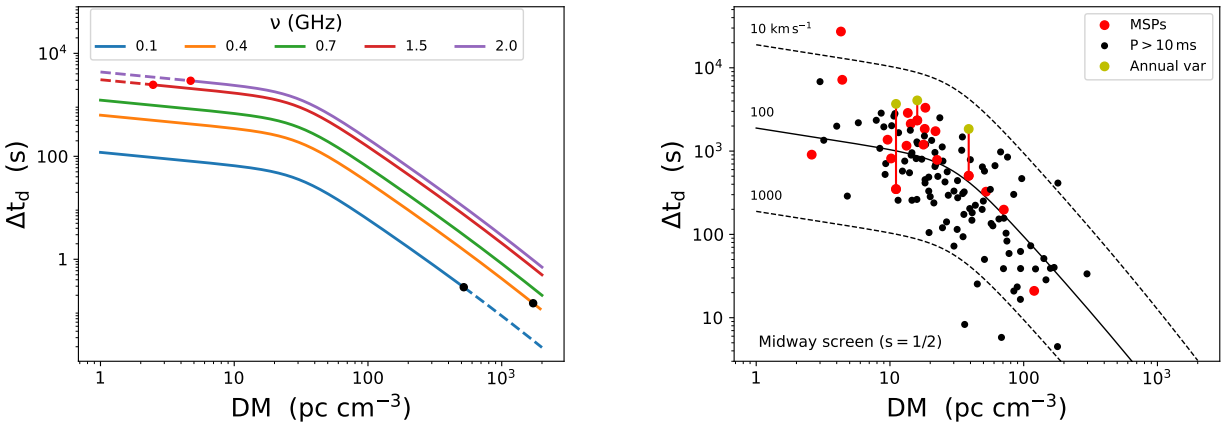


Figure 29. Left: Computed values for the scintillation time vs. DM for different frequencies and a pulsar velocity = 100 km s^{-1}. As with Fig. 28, calculations are for a thin, midway screen ($s = 1/2$) with Kolomogorov fluctuations. Right: Measured values of $\Delta t_{\rm d}$ are shown for millisecond pulsars (red) and pulsars with $P > 10$ ms (black). The yellow points for three pulsars show maximum values for $\Delta t_{\rm d}$ that ensue from annual variations. The dashed lines show expected values for three different effective, transverse velocities, which bracket the wide velocity distribution of pulsars. Data are from Cordes (1986); Wang et al. (2018); Johnston and Lower (2021); Liu et al. (2022).

If the RMS phase variation on the Fresnel scale is small, i.e. $D_\phi(r_{\rm F}) \ll 1$ rad^2, the diffraction and refraction scales merge and the only characteristic scale manifested in scintillations is the Fresnel scale:

$$l_{\rm i} \ll l_{\rm d} \sim l_{\rm r} \sim r_{\rm F} \lll l_{\rm o}, \quad \text{Weak scintillation.} \tag{9.14}$$

The transition from weak to strong scintillation occurs at a frequency that is LoS dependent and can be calculated in two ways. First by finding the frequency where the phase structure function $D_\phi(r_{\rm F}) = 1$ rad^2 and second by requiring $\nu = \Delta\nu_{\rm d}$. Either approach gives $\nu_{\rm trans} \simeq \nu[2\pi\tau(\nu)\nu]^{(\beta-2/(\beta+2)} = \nu[2\pi\tau(\nu)\nu]^{5/17}$ for a scattering time $\tau(\nu)$ measured

at frequency ν. Using Eq. (9.6) and solving for ν yields the expression for $\nu_{\rm trans}$ in Table 4 in terms of the scattering time τ.

The boundary between weak and strong scintillation is shown in Fig. 30 for DMs from 1 to 1000 pc cm^{-3}, based on the empirical τ(DM) ("hockey-stick") relation (see Sect. 10.4). Strong scintillation corresponds to diffractive scintles being narrower than the radio frequency, $\Delta\nu_{\rm d} \ll \nu$. This becomes $\tau \gg C_1/2\pi\nu > 0.16\,{\rm ns}\,C_1\nu^{-1}$ (ν in GHz, as usual) from the uncertainty relation in Eq. (9.11).

Most pulsar observations in the strong-scintillation regime are below the $\nu_{\rm trans}$ line where DISS is 100% modulated (if there is no bandwidth smoothing). In particular, most MSPs observed in PTA programs are in the strong scintillation regime apart from a few low-DM objects observed near the transition line, including J0437−4715 (DM = 2.6 pc cm^{-3}). Near the transition region $2\pi\tau\nu \sim 1$ there is no bandwidth attenuation of the $\sim 100\%$ intensity fluctuations, so arrival time precision will vary markedly from the highly variable S/N. Conversely, large scattering times, e.g. those with $\tau \gtrsim 0.1\,\mu$s, correspond to intensities that are far less modulated by a factor $\propto (2\pi\tau B)^{-1}$ for bandwidths $B \gg 1$ MHz like those used in current receivers.

9.5. *Example calculations using Table 4*

We illustrate usage of Table 4 by considering observations at 1.5 GHz of a pulsar with dispersion measure DM = 10 pc cm^{-3}, corresponding to a distance[31] $d_{\rm so} \simeq 0.33$ kpc. Using the hockey-stick relation (Eq. (10.16)), we obtain a scattering time $\tau_1 = 6.2$ ns at 1 GHz that scales to 1.0 ns at 1.5 GHz. This implies that the strong scintillation regime applies up to $\nu_{\rm trans} \simeq 2.9$ GHz.

Adopting a thin screen halfway between the pulsar and Earth, the effective distance, $d' = d_{\rm so}/4 = 0.083$ kpc, yields a Fresnel scale $r_{\rm F} \simeq 1.9 \times 10^{-3}$au. Electron density fluctuations on scales smaller than $r_{\rm F}$ yield multipath scattering of the pulsar signal while larger scales cause refraction. For the assumed Kolmogorov spectrum, refractive bending of ray

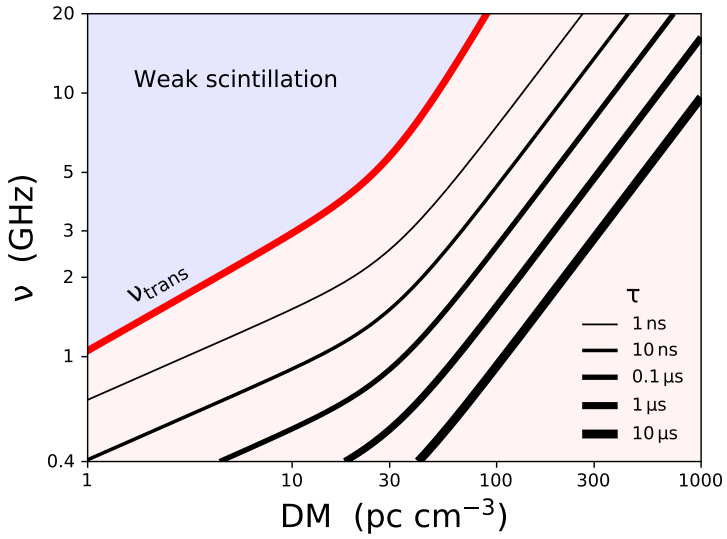


Figure 30. Weak and strong regimes for diffractive interstellar scintillation (DISS). The transition frequency $\nu_{\rm trans}$(DM) (red line) was calculated by approximating $\nu_{\rm trans} \sim \Delta\nu_{\rm d}$ and using the τ(DM) 'hockey stick' relation in Eq. (10.16) (see Sect. 10.4) with the uncertainty relation Eq. (9.11) to calculate $\Delta\nu_{\rm d}$(DM). The $\nu_{\rm trans}$ line is fuzzy given that there is empirical spread around the nominal τ(DM) relation. Lines of constant scattering time $\tau = (2\pi\Delta\nu_{\rm d})^{-1}$ are also based on this relation.

[31] We could also specify Galactic coordinates to obtain a distance using the NE2025 model but it is adequate for our example to use an approximate relation given by $d_{\rm so} = ({\rm DM}/n_{\rm e0})/(1 + {\rm DM}/1000)/1000$ with DM in standard units(pc cm^{-3}) and an electron density $n_{\rm e0} = 0.03\,{\rm cm}^{-3}$.

paths by angles $\theta_{\rm r} \simeq 0.052\,$mas is typically smaller than the multipath caused by diffraction, which yields a scattering disk of size $\theta_{\rm d} \simeq 0.26\,$mas.

Intensity scintillations from refraction and diffraction have estimated characteristic time scales, $\Delta t_{\rm r} \simeq 0.11\,$d and $\Delta t_{\rm d} \simeq 846\,$s, where we have adopted an effective transverse velocity $\mathrm{v_{eff}} = 100\,\mathrm{km\ s^{-1}}$ (see Sect. 10.1 for discussion). The characteristic scintillation bandwidth is $\Delta\nu_{\rm d} \simeq 152\,$MHz which, combined with $\Delta t_{\rm r}$ and assuming a 0.3 GHz total bandwidth and time span $T \simeq 1800\,$s for the observations, implies that only a few scintles, $N_{\rm scint} \simeq 3$, contribute to the measurements.

For a pulsar with DM $= 100\,\mathrm{pc\ cm^{-3}}$ corresponding to a more distant pulsar $d_{\rm so} \simeq 3.0\,$kpc and $d' \simeq 0.76\,$kpc, the larger scattering time $\tau \simeq 1.16\,\mu s$ is given by the scattering disk, $\theta_{\rm d} \simeq 2.8\,$mas which refractively wanders by $\theta_{\rm r} \simeq 0.18\,$mas. The refractive scintillation time is now larger, $\Delta t_{\rm r} \simeq 11\,$d while the diffraction time scale is smaller, $\Delta t_{\rm d} \simeq 77\,$s. With a scintillation bandwidth $\Delta\nu_{\rm d} \simeq 0.14\,$MHz, the number of scintles is much larger, $N_{\rm scint} \simeq 5000$.

10. INTERSTELLAR ANALYTICS

Interstellar propagation effects are significant limiting factors in timing precision at radio wavelengths with current practices. To understand these limits and develop methods for improving arrival times, it is important to characterize and understand the ISM as much as possible. The phenomena and scaling laws summarized in §9 and Table 4 are diagnosed and tested using various tools applied to observational data for pulsars and other objects. Our emphasis is on pulse broadening and intensity scintillations, which are more directly intertwined with estimates of timing precision.

10.1. *Dispersion measures*

A primary tool for characterizing DM fluctuations is the DM structure function defined earlier and evaluated in Eq. (9.9) for the power-law electron density spectrum (Eq. (9.1)). Here we include further contributions to DM(t) that are manifested in some pulsar timing data sets.

DM varies because motions of the Earth, ISM, and pulsar change the Earth-pulsar distance and direction of the LoS. For velocities $v \sim 100$ km s^{-1}, distances ~ 1 kpc, and time scales $t \lesssim$ decades, the fractional change in distance $vt/d \lesssim 10^{-6}$ and it is dominated by velocity components parallel to the line of sight whereas the direction of propagation is due to transverse components. Using $v_{e_\parallel}$ and $v_{p_\parallel}$ for the parallel velocities of the Earth and pulsar and using an approach similar to that in Lam et al. (2016b), the time dependence of DM is

$$\mathrm{DM}(t) = \mathrm{DM}(0) + \left\{v_{e_\parallel}\overline{n}_{\rm e}[\mathbf{x}_{\rm e}(t)] - v_{p_\parallel}\overline{n}_{\rm e}[\mathbf{x}_p(t)]\right\} t + \int_0^{d_{\rm so}0} ds\,\Delta n_{\rm e}(s,t), \tag{10.1}$$

where the second term is linear in time and involves electron densities $\overline{n}_{\rm e}[\mathbf{x}_{\rm e}(t)]$ and $\overline{n}_{\rm e}[\mathbf{x}_p(t)]$ that are averaged at the observer's and pulsar's locations over LoS segments of length $v_{e_\parallel}t$ and $v_{p_\parallel}t$, respectively. The integrand in the stochastic third term,

$$\Delta n_{\rm e}(s,t) = n_{\rm e}[\mathbf{x}_{\rm p_0} + \widehat{\mathbf{n}}_0 s + \mathbf{v}_{\mathrm{eff}_\perp}(s)t] - n_{\rm e}[\mathbf{x}_{\rm p_0} + \widehat{\mathbf{n}}_0 s], \tag{10.2}$$

involves the transverse components of the effective velocity,

$$\mathbf{v}_{\mathrm{eff}_\perp}(s) = \mathbf{v}_{\rm eff}(s)(\mathbf{I} - \widehat{\mathbf{n}}_0\widehat{\mathbf{n}}_0) = (1 - s/d_{\rm so})\mathbf{v}_{p_\perp} + (s/d_{\rm so})\mathbf{v}_{e_\perp}, \tag{10.3}$$

using the 2×2 unit matrix $\mathbf{I}$. Eq. (10.2) is general but we now consider only interstellar contributions. The DM structure function then combines the contribution from the power-law density variations presented in Eq. (9.9) with terms involving the electron density in local interstellar environments of the pulsar and the solar system. Breaking these into 'linear' and 'power-law' terms,

$$\begin{aligned} D_{\rm DM}(\delta t) &= D_{\rm DM}^{\rm (lin)}(\delta t) + D_{\rm DM}^{\rm (pl)}(\delta t) \\ &\simeq \left[v_{e_\parallel}\overline{n}_{\rm e}(\mathbf{x}_{\rm e}) - v_{p_\parallel}\overline{n}_{\rm e}(\mathbf{x}_p)\right]^2 (\delta t)^2 + f_\beta \int_0^{d_{\rm so}0} ds\,\mathrm{C}_{\rm n}^2(s)\left[v_{\mathrm{eff}_\perp}(s)\delta t\right]^{\beta-2}. \end{aligned} \tag{10.4}$$

If the pulsar velocity dominates the time dependence, then

$$D_{\rm DM}(\delta t) \simeq \overline{n}_{\rm e}{}^2(\mathbf{x}_p)\,(v_{p_\parallel}\,\delta t)^2 + f_\beta\,{\rm SM}_{\rm eff}\,(v_{p_\perp}\delta t)^{\beta-2}. \tag{10.5}$$

For nominal values of electron density, scattering measure, and transverse pulsar velocity, the DM structure function terms are

$$\begin{aligned} D_{\rm DM}^{\rm (lin)}(\delta t) &\simeq \left[3.1\times10^{-6}\ {\rm pc\ cm^{-3}} \times \left(\frac{\overline{n}_{\rm e}}{0.03\ {\rm cm^{-3}}}\right)\left(\frac{v_{p_\parallel}}{100\ {\rm km\ s^{-1}}}\right)\right]^2 \times (\delta t_{\rm yr})^2, \\ D_{\rm DM}^{\rm (pl)}(\delta t) &\simeq \left[7.8\times10^{-4}\ {\rm pc\ cm^{-3}} \times \left(\frac{{\rm SM}_{\rm eff}}{10^{-3.5}\ {\rm kpc\ m^{-20/3}}}\right)^{1/2}\left(\frac{\mathbf{v}_{p_\perp}}{100\ {\rm km\ s^{-1}}}\right)^{5/6}\right]^2 \times (\delta t_{\rm yr})^{5/3}. \end{aligned} \tag{10.6}$$

By definition the DISS time scale $\Delta t_{\rm d} = l_{\rm d}/v_{{\rm eff}_\perp}$ corresponds to a phase structure function value $D_\phi(l_{\rm d}) = 1\,{\rm rad}^2$. Using $D_{\rm DM} = (\lambda r_{\rm e})^{-2} D_\phi$, this yields an empirical scaling law for the power-law component (second term in Eq. (10.4)) with ν in GHz,

$$D_{\rm DM}^{\rm (pl)}(\delta t) = \left(\frac{1}{\lambda r_{\rm e}}\right)^2\left(\frac{\delta t}{\Delta t_{\rm d}}\right)^{\beta-2} = (3.84\times10^{-8}\,{\rm pc\ cm^{-3}})^2 \times \nu^2 \left(\frac{\delta t}{\Delta t_{\rm d}}\right)^{\beta-2}. \tag{10.7}$$

Measurement errors contribute a constant floor to the structure function that is twice the noise variance, $2\sigma^2_{\rm DM,\,noise}$ for all $\delta t > 0$.

For some pulsars, published structure functions show features with both the quadratic τ^2 term and the shallower Kolmogorov-like term $\propto \tau^{\beta-2} \to \tau^{5/3}$ (Rickett 1990; Cordes et al. 1990; Kaspi et al. 1994; Keith et al. 2012; Lam et al. 2016b). The results are consistent with the overall picture that the ISM includes density structure on a wide range of scales extending from $\lesssim 10^3$ km to $\gtrsim v_{\rm p} T \sim 600$ au for 100 km s^{-1} and data spans of $T \gtrsim 30$ yr.

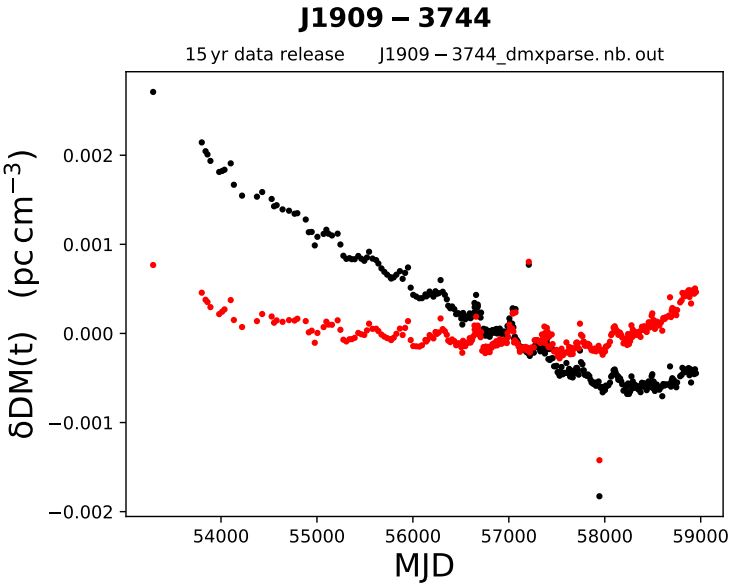


Figure 31. Time series of $\delta{\rm DM}(t)$ for J1909-3744 from the NANOGrav 15-yr data set (Agazie et al. 2023a). Black points show departure of DM from a constant value; red points show departure from a linear fit to the black points.

The DM time series for MSP J1909-3744 (Fig. 31) shows two additional features not seen for B1937+21: an annual variation and a linear trend over most of the 15-yr data set. The annual variation is due to the close approach of the LoS to the solar corona and the linear downward trend that appears to bottom out and reverse suggests that motion of the pulsar through a local region of variable electron density is in action. In a study of 37 MSPs in the NANOGrav

timing program, Jones et al. (2017) found that 19 objects show periodic, yearly variations consistent with contributions from the solar corona and 28 show linear-like trends. Similar studies by You et al. (2007); Keith et al. (2012); Donner et al. (2020); Kumar et al. (2025) (among others) suggest that many pulsars have DM variations well explained by turbulent ISM density fluctuations, with pulsars at low ecliptic latitudes exhibiting periodic DM variations from the solar wind (Madison et al. 2019; Tiburzi et al. 2021), and a general correlation between the magnitude of the DM gradients and the total DM (e.g. Hobbs et al. 2004).

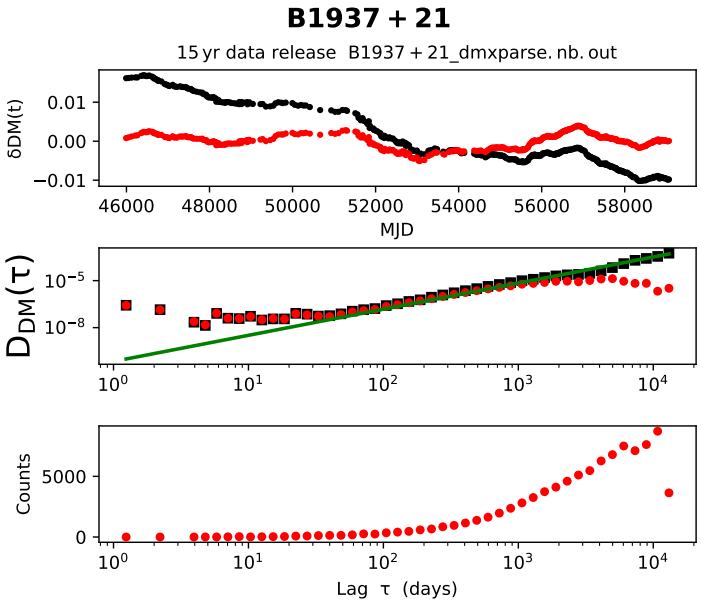


Figure 32. DM Time series and structure function for the MSP J1939+2134 (B1937+21) from the 15-yr NANOGrav data release (Agazie et al. 2023a). Top: DM(t) before (black) and after (red) removing a straight line. Middle: Structure function before (black) and after (red) removing a straight line. The solid green line is the Kolmogorov inertial subrange scaling $D_{\rm DM} \propto \tau^{5/3}$. Bottom: The number of counts in each lag bin from the irregularly sampled DM.

Fig. 32 shows a DM time series for PSR B1937+21 over a 15 yr span in the NANOGrav data set (Agazie et al. 2023a). It is possibly the superposition of a downward secular trend and a stochastic component with a red power spectrum, but, unlike the case of J1909-3744 discussed below, it is actually consistent with fluctuations expected from only a power-law process. The DM structure function shown in the middle panel has a slope consistent with the $\tau^{5/3}$ scaling expected for a Kolmogorov process. This result is corroborated by the SF calculated from a longer time series obtained by combining earlier measurements of DM(t) Vivekanand (2020, and references therein) with the NANOGrav 15-yr data. Fig. 33 shows the resulting SF along with curves indicating the 5/3 scaling law for Kolmogorov fluctuations and a curve for a square-law scaling. The noise floor dominates the SF at lags $\lesssim 30$ days and for larger lags the SF appears consistent with the Kolmogorov scaling. The expected scaling using the measured scintillation time $\Delta t_{\rm d} \simeq 3$ to 5 min at 1.5 GHz is consistent with the asymptotic part of the SF. This implies that length scales in the ISM along this LoS span a range of at least 20 yr/4 min = 6.4 orders of magnitude ($\sim 10^4$ km to 200 au using an effective velocity of 50 km s^{-1}).

10.2. *Angular deviations and broadening*

Radio interferometric imaging has provided scattering diameter $\theta_{\rm d}$ measurements useful for establishing the index β, the inner scale $l_{\rm i}$, and anisotropies of the wavenumber spectrum (Spangler and Cordes 1988; Moran et al. 1990; Molnar et al. 1995; Lazio 2004) and the outer scale (e.g. Minter and Spangler 1996). These interferometric measurements of the visibility function in the $D_\phi \propto b^{\beta-2}$ regime have yielded constraints on β for (relatively) weakly scattered objects while heavily scattered objects that also sample the $D_\phi \propto b^2$ regime(c.f. Eq. (9.6)) have yielded estimates of the inner scale (e.g. Spangler and Gwinn 1990). Image ellipticities also seen in the examples reported in these references and

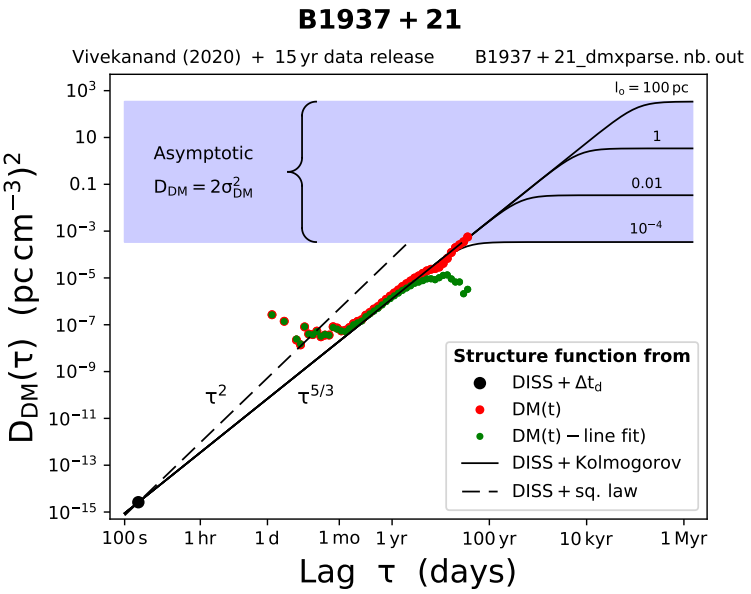


Figure 33. Structure function of DM for the MSP J1939+2134 (B1937+21) for a 37 yr data set obtained by combining the 15-yr NANOGrav DM time series (Agazie et al. 2023a) with the 31-yr **DM** time series from Vivekanand (2020, and references therein). Where there was overlap, the NANOGrav time series was used. The DM SF is shown before (red points) and after (green points) removing a straight line fit to DM(t). Points at lags $\lesssim 1$ month are dominated by additive measurement errors in DM that produce a flat component to the SF. Black solid lines show the SF expected from a Kolmogorov medium with different outer scales l_o, as indicated. These lines scale as $\delta t^{5/3}$ for intermediate lags between $\sim 1/3$ to 20 yr and saturate at lags $\gtrsim l_o/v_{eff}$. The black circle at $\tau \sim 300$ s indicates the characteristic DISS timescale (Turner et al. 2024) and the implied DM SF calculated from Eq. (10.7). The dashed line shows the square-law scaling that is clearly inconsistent with the measured values.

toward heavily scattered sources in the Galactic center (e.g. Bower et al. 2025) are a direct consequence of anisotropic scattering.

Referring to Table 4, for scattering angles $\simeq 1$ mas and path lengths ~ 1 kpc at 1 GHz, the corresponding diffraction scale $l_d \simeq 10^4$ km and refraction scale $l_r \simeq 1$ au, compared to inner scales estimated as ~ 50 to 1000 km.

10.3. *Scintillations: dynamic spectrum and secondary spectrum*

Diffractive scintillations are manifested in the *dynamic spectrum* (DS), the radio spectrum measured at multiple times t,

$$I(\nu, t) = \langle |\widetilde{\varepsilon}(\nu, \bar{t})|^2 \rangle_T, \tag{10.8}$$

where $\widetilde{\varepsilon}(\nu, \bar{t})$ is the Fourier transform of the baseband voltage with bandwidth B for a data block of duration $T = N\delta t$ centered on $\bar{t}$, where N is the FFT length and $\delta t = B^{-1}$ is the sample interval[32]. For total intensity data (i.e. Stokes I), the DS would be the sum of the individual DS for each of two polarization channels. **The time average indicated in Eq. (10.8) typically includes averaging over a narrow window in pulse phase as well as averaging over multiple pulses.**

With *phase resolved spectroscopy* (PRS), the DS is formed by averaging (after dedispersion), as in Eq. (10.8), over an on-pulse window (i.e. wide enough to span the duration of the pulse) and over multiple pulses corresponding to elapsed times T of order seconds but shorter than the scintillation time Δt_d. **This approach has been commonly used to produce pulsar dynamic spectra and has the limitation that spectral resolution is determined by the reciprocal of the pulsar width.** A corresponding off-pulse average $\langle I_{off}(\nu) \rangle$ is used to remove the receiver

[32] We use the Nyquist criterion for complex baseband data as opposed to the criterion $\delta t = (2B)^{-1}$ for real data.

bandpass shape by subtracting and dividing it from the on-pulse spectrum. This approach maximizes the S/N of the scintillation signal before further analysis of the DS. An alternative approach for computing the DS, *cyclic spectroscopy*, is discussed below.

The two-dimensional ACF of the DS is frequently used to determine scintillation parameters,

$$\Gamma_I(\delta\nu, \delta t) = \langle I(\nu, t) I(\nu + \delta\nu, t + \delta t)\rangle = \langle |\widetilde{\varepsilon}(\nu, t)|^2 |\widetilde{\varepsilon}(\nu + \delta\nu, t + \delta t)|^2\rangle = \langle I\rangle^2 + |\Gamma_{\widetilde{\varepsilon}}(\delta\nu, \delta t)|^2, \tag{10.9}$$

where the last equality follows for any stochastic process $\widetilde{\varepsilon}$ having complex Gaussian statistics, including the scintillation modulated pulsar signal in the strong scintillation regime (e.g. Rickett 1990). Such statistics are expected because scintillations typically result from the superposition of a large number of propagation paths (Central Limit Theorem). Codona et al. (1986) have pointed out that departures from Gaussian statistics can be caused by strong refraction from large scales in the medium along a single or a small number of paths. The autocovariance is the ACF of the fluctuating intensity, $\Gamma_{\delta I}(\delta\nu, \delta t) = |\Gamma_\varepsilon(\delta\nu, \delta t)|^2$. The scintillation feature in the 2D ACF often is slanted in the $\delta\nu$ - δt lag domain, an effect caused by refraction and characterized as a drift rate $d\nu/dt$.

Assuming $\Gamma_{\delta I}(\delta\nu, \delta t)$ is normalized to unit maximum, the scintillation bandwidth $\Delta\nu_{\rm d}$ is the HWHM of the 1D slice $\Gamma_{\delta I}(\Delta\nu_{\rm d}, 0) = 1/2$ and the scintillation time $\Delta t_{\rm d}$ is the HWe of $\Gamma_{\delta I}(0, \Delta t_{\rm d}) = e^{-1}$. Usage of these particular measures is motivated by a thin screen with a square-law phase structure function, which yields $\Gamma_{\delta I}(\Delta\nu_{\rm d}, 0) = [1 + \delta\nu/\Delta\nu_{\rm d})^2]^{-1}$ for the slice along the $\delta\nu$ axis and $\Gamma_{\delta I}(0, \Delta t_{\rm d}) = \exp(-\delta t/\Delta t_{\rm d})$ along the time-lag axis. Though a square-law SF is not a viable form for many instances of radio scattering in the ISM, it is analytically tractable and provides functional forms that are useful for quantifying measurements. A square-law structure function could correpond to a $\beta = 4$ wavenumber spectrum, which corresponds to a medium comprising step functions (Lambert and Rickett 2000) that has mathematically divergent variance. However, inspection of Eq. (9.6) indicates the SF is square-law in form for spatial lags $\ll$ inner scale, a regime that dominates the measurements of heavily scattered sources.

The Fourier transform of the 2D ACF (equivalent to the squared magnitude of the 2D Fourier transform of the DS by the Wiener-Khinchin theorem), though containing the same information, has proven to be enormously useful for ISM studies. Using $\mathcal{F}_{2D}$ to denote 2D transform, this *secondary spectrum* (SS) is

$$S_2(f_\nu, f_{t_s}) = |\mathcal{F}_{2D}\{I(f_\nu, f_t)\}|^2 = |\mathcal{F}_{2D}\{|\widetilde{\varepsilon}(\nu, t)|^2\}|^2, \tag{10.10}$$

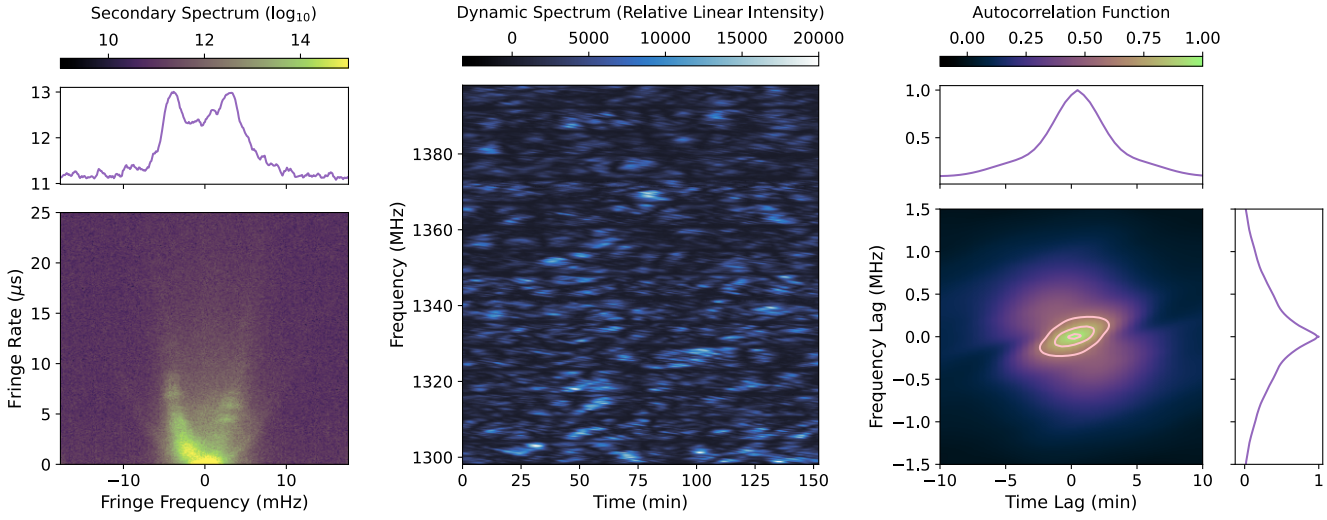


Figure 34. Scintillation diagnostics for B1937+21 from Arecibo observations conducted in 2012 and processed using cyclic spectroscopy. The dynamic spectrum (relative linear intensity as a function of frequency and time) is shown in the middle panel at a time resolution of 28 s and a frequency resolution of 0.61 MHz. The left panel shows the secondary spectrum (2D FFT of the dynamic spectrum), including a 1D average over fringe rates > 10 μs. The right panel shows the 2D autocorrelation function (ACF) with three evenly spaced contours between 0.2 and 1, along with 1D slices through the ACF at zero lag along the frequency and time axes. The ACF yields a decorrelation bandwidth and timescale of about 0.4 MHz and 3 minutes, respectively, at 1360 MHz. Data courtesy of Tim Dolch and Jacob Turner (see Turner et al. 2023).

with variables f_ν and f_t that are conjugate to ν and t with units of time and frequency, respectively. The second equality in Eq. (10.10) shows by inspection that the SS is a fourth moment of the wavefield ε. Often f_ν is referred to as a "delay," a term we avoid because it may be misinterpreted as the delay of a pulse imposed by ISS rather than as (effectively) the lag of a correlation function.

The SS often displays remarkable *scintillation arcs* (Stinebring et al. 2001), parabolic features corresponding to discrete scattering screens along the LoS of interest for ISM studies. It is also used for assessing delays from multipath propagation that contribute to ToA stochasticity (e.g. Hemberger and Stinebring 2008). The SS as defined excludes phase information contained in the Fourier transform $\mathcal{F}_{2D}\{I(f_\nu, f_t)\}$; other authors have exploited phase information for ISM studies (Brisken et al. 2010; Simard et al. 2019; Baker et al. 2023; Zhu et al. 2023).

Fig. 34 shows examples of these tools for the MSP J1939+2134 (B1937+21), including the DS (center), the 2D ACF and 1D slices through it (right-hand panel), and the SS in the left panel. The central feature of the 2D ACF is slightly slanted due to refraction from scales larger than those that scatter the radiation.

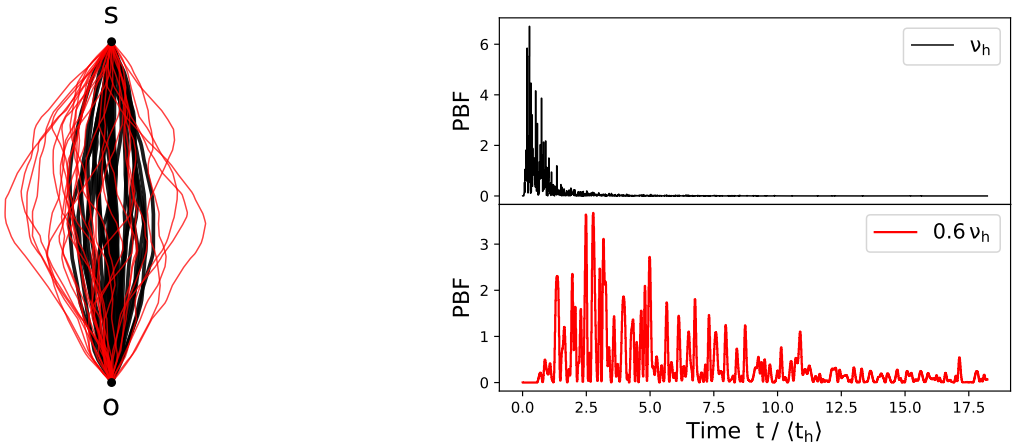


Figure 35. Left: Simulated ray paths for an extended medium with density variations conforming to a Kolmogorov wavenumber spectrum (similar to Cordes et al. 2016), with high frequency ray paths in black and low frequency ray paths in red. Right: Pulse broadening functions (PBFs) corresponding to the ray paths shown in the left panel. **The horizontal axis is time in units of the mean width of the PBF in the top panel, illustrating the much wider PBF at the lower frequency.**

10.4. *Pulse broadening*

Scattered pulses from pulsars are the convolution of a pulse broadening function (PBF) with the "intrinsic" pulse shape emitted by the pulsar. This follows from the linearity of propagation through the ISM. Propagation effects include dispersion and angular deflections from refraction and diffraction. In the ISM context, the PBF is usually defined in terms of the geometrical path length differences between the multiple propagation paths in a ray bundle that contribute to the measured wave field in the observation plane. It therefore does not include any differential dispersion across the bundle of ray paths because it is a small effect that can be considered separately (see section on frequency dependence of DM).

The PBF quantifies the differences in arrival times for pulses propagating along different ray paths. For most pulsar observations (as well as those for fast radio bursts), the LoS geometry may be considered invariant over minute to several hour time spans, depending on the path length through the ISM and on the observation frequency. If scattering occurs primarily in a thin screen, the received angles of arrival are directly related to time delays; however distributed scattering that leads to random walk ray paths does not have this simple property.

When scattering is strong, the PBF comprises a large number of individual propagation paths, so the net wavefield becomes a complex Gaussian process modulated by an envelope function related to the size of the raypath bundle. The

intensity PBF, calculated as the squared magnitude, then comprises a stochastic process with exponential statistics (χ^2_2) modulated by a function that is the ensemble average intensity PBF.

An impulsive signal incident on a phase changing medium yields an impulse response in the measured wavefield $\varepsilon(t,\bar{t}) = h(t,\bar{t})$ which we call the field PBF to distinguish it from the intensity PBF, $p_{\rm d}(t) \equiv |h(t)|^2$ (for which we drop the $\bar{t}$ dependence, making it implicit). PBFs are calculated most often from the geometrical path length differences along the set of propagation paths that instantaneously reach the observer, which is most easily done for thin screens and for random walks through extended media. The PBFs can also be calculated using the Fresnel-Kirchhoff integral, which includes dispersion delays along with geometrical delays.

The field PBF is stochastic, varying rapidly in time t (e.g. ns to s) but slowly in $\bar{t}$ (s to hr). The field PBF is constant for times shorter than the DISS time scale, $\bar{t} \ll \Delta t_{\rm d}$. The PBF example given earlier for a thin screen in Fig. 17 shows the rapid fluctuations of $p_{\rm d}(t)$ with corresponding frequency structure in the spectrum also shown (lower frame). An ensemble average (corresponding to averaging the PBF over many scintillation time scales) yields a smooth PBF with a shape determined by properties of the medium (e.g. β and inner scale), while the spectrum averages to a constant value. To complement the thin screen case shown in Fig. 17, we show in Fig. 35 ray traces (left panel) for a thick medium and PBFs (right panel) for two frequencies to illustrate their strong frequency dependence along with their temporal stochasticity. envelopes that multiply a noise-process.

The field and intensity PBF are related to frequency-domain quantities according to the flow diagram,

$$\begin{array}{ccc} \boxed{\text{Field PBF}\quad h(t)} & \overset{\text{FT}}{\Longleftrightarrow} & \boxed{\widetilde{h}(\nu)} \\ |\cdots|^2 \ \downarrow & & \downarrow \ \text{ACF} \\ \boxed{\text{PBF}\quad p_{\rm d}(t) = |h(t)|^2} & \overset{\text{FT}}{\Longleftrightarrow} & \boxed{\int d\nu\, \Gamma_{\widetilde{h}}(\delta\nu,\nu)} \end{array} , \tag{10.11}$$

where the frequency-domain correlation function is

$$\Gamma_{\widetilde{h}}(\delta\nu,\nu) = \widetilde{h}(\nu_+)\widetilde{h}^*(\nu_-), \qquad \nu_\pm \equiv \nu \pm \delta\nu/2. \tag{10.12}$$

The quantities in each row of Eq. (10.11) are related by a two-way Fourier transform while vertical operations are irreversible: the squared magnitude in the first column and an autocorrelation function in the second column. Recall these are all bandlimited, baseband quantities corresponding to an RF center frequency ν_0 and an analysis bandwidth $B \ll \nu_0$ (i.e. a wideband system is usually processed in narrower subbands with bandwidths B).

The scintillation spectrum is $H(\nu) \propto |\widetilde{h}(\nu)|^2 = \Gamma_{\widetilde{h}}(0,\nu)$ is the primary quantity of interest for ISM studies and is the essential part of the DS in Eq. (10.8). Characterization of frequency structure in $H(\nu)$ is a key element in ToA corrections for scattering mitigation (discussed in Sect. 18.4).

Neither $h(t)$ nor $p_{\rm d}(t)$ or their Fourier transforms are known *a priori* and they are not directly measurable. The field PBF is manifested through the convolution of $h(t)$ with the emitted pulsar signal and various degrees of time averaging; some of its properties are accessible through model fitting of pulse shapes and through frequency-domain analyses (next section).

The field PBF has the form $h(t) = a_{\rm h}(t)m_{\rm h}(t)$, similar to the amplitude modulated noise form for the emitted signal in Eq. (5.14). The PBF factors $a_{\rm h}$ and $m_{\rm h}$ differ fundamentally from those for emission. The amplitude $a_{\rm h}$ is stable over long periods of time (> days), varying on a refraction time scale, but is strongly frequency dependent. By contrast, amplitude variation for emission varies on pulse-period time scales ($\lesssim$ seconds) but varies slowly with frequency. The PBF noise $m_{\rm h}$ is stable over a DISS time scale (seconds to hours) and is correlated over a DISS bandwidth. By contrast emission noise decorrelates over emission time scales equal to the inverse radio frequency, $\nu^{-1} \sim$ ns.

The PBF noise process and the frequency structure of intensity scintillations are two sides of the same coin. Convolution of the PBF with emitted pulses yields small TOA variations for low-DM pulsars at ∼GHz frequencies. Generally, the

instantaneous PBF is inaccessible to measurement (with rare exceptions involving cyclic spectroscopy discussed in Sect. (18.5.4)) so it is not possible to deconvolve the PBF as a means for reducing ToA errors. However some degree of correction is feasible by characterizing scintillation frequency structure and how it changes with time, as discussed in detail in Sect. 18.5.

Scattered pulse shape and scintillation frequency structure: The measured wavefield $\varepsilon(t)$ is the convolution (using subscript e to denote emitted wavefield),

$$\varepsilon(t) = \varepsilon_{\rm e}(t) * h(t) = [a(t)m(t)] * [a_{\rm h}(t)m_{\rm h}(t)]. \tag{10.13}$$

Time averaging a large number of pulses with $h(t)$ constant (i.e. over a span $\ll$ scintillation time) yields a measured pulse

$$I(t) \simeq I_{\rm e}(t) * |h(t)|^2 \equiv I_{\rm e}(t) * p_{\rm d}(t). \tag{10.14}$$

where $p_{\rm d}(t)$ has a noisy form as in Fig. 17 (top panel) and Fig. 35 (right panel). Further averaging over many scintillation times then yields a scattered pulse profile $I(t) = I_{\rm e}(t) * p_{\rm d}(t)$ like those for pulsar J1644-4559 in Fig. 19. Determining the scattering time τ and timing delays from scattering requires model fitting to $I(t)$.

Accessing scattering information is more straightforward in the frequency domain. Fourier transforming Eq. (10.13) yields

$$\widetilde{\varepsilon}(\nu) = [\widetilde{a}(\nu) * \widetilde{m}(\nu)] \times \widetilde{h}(\nu). \tag{10.15}$$

The factor in square brackets yields frequency structure with a characteristic scale $\sim W_a^{-1}$ equal to the reciprocal of the width W_a of $a(t)$. This structure is fully modulated (unity modulation index) in the strong scintillation regime that usually applies for $\nu \lesssim 5\,$GHz. The average of the squared magnitude $I(\nu) = |\widetilde{\varepsilon}(\nu)|^2$ over $N_{\rm p} \gg 1$ pulses converges to a constant with reduced modulation index $m_I \simeq N_{\rm p}^{-1}$. This yields the scintillation spectrum in isolation, $I(\nu) \propto |\widetilde{h}(\nu)|^2$, which can be analyzed to determine the characteristic frequency of the intensity scintillations, i.e. the scintillation bandwidth $\Delta\nu_{\rm d}$.

The pulse broadening time τ is obtained by either pulse-shape modeling or via a frequency structure analysis. Its importance for ToA correction is discussed later. Here we briefly present its role for modeling the Galactic structure of electron density variations and to forecast pulsar timing precision (and for studies of FRBs). Several methods are used to estimate τ:

1. Model fitting of average profiles as an intrinsic shape $I_{\rm e}(t)$ convolved with a PBF $p_{\rm d}(t)$ (e.g. Geyer et al. 2017);
2. Deconvolving average profiles using a template bank of candidate PBFs and the CLEAN algorithm (e.g. Bhat et al. 2003, 2004; Tsai et al. 2017; Kirsten et al. 2019; Young and Lam 2024-02);
3. Inverting scintillation bandwidth ($\Delta\nu_{\rm d}$) determinations using Eq. (9.11); and
4. Using cyclic spectroscopy to obtain higher resolution dynamic spectra and estimate the PBF and characterize its width (Demorest 2011; Walker et al. 2013; Palliyaguru et al. 2015; Dolch et al. 2021; Turner et al. 2023).

Here we present a brief analysis of a sample of τ values obtained using the first three methods. The intent here is to illustrate the variation of the scattering time with DM and show the range of corresponding scattering measures. Later we discuss how constraints on the PBF and τ can be used to correct ToAs for scattering delays.

It is well known that τ correlates with DM albeit with significant scatter, according to the so-called "hockey-stick" relation. Fig. 36 shows measurements of τ scaled to 1 GHz along with a fit using the function $\widehat{\tau}(\mathrm{DM}) = A \times \mathrm{DM}^a(1 + B \times \mathrm{DM}^b)$ (Ramachandran et al. 1997). Fitting to $\log \tau$ yields

$$\widehat{\tau}(\mathrm{DM}) = 1.9 \times 10^{-7}\,\mathrm{ms} \times \mathrm{DM}^{1.5}(1 + 3.55 \times 10^{-5}\mathrm{DM}^3) \tag{10.16}$$

with scatter $\sigma_{\log_{10}\tau} = 0.76$ (Cordes et al. 2022). The plotted measurements include forty-three PTA pulsars with published scattering measurements. Most of these MSPs have $\tau < 1\ \mu$s because they are chosen to have small DMs,

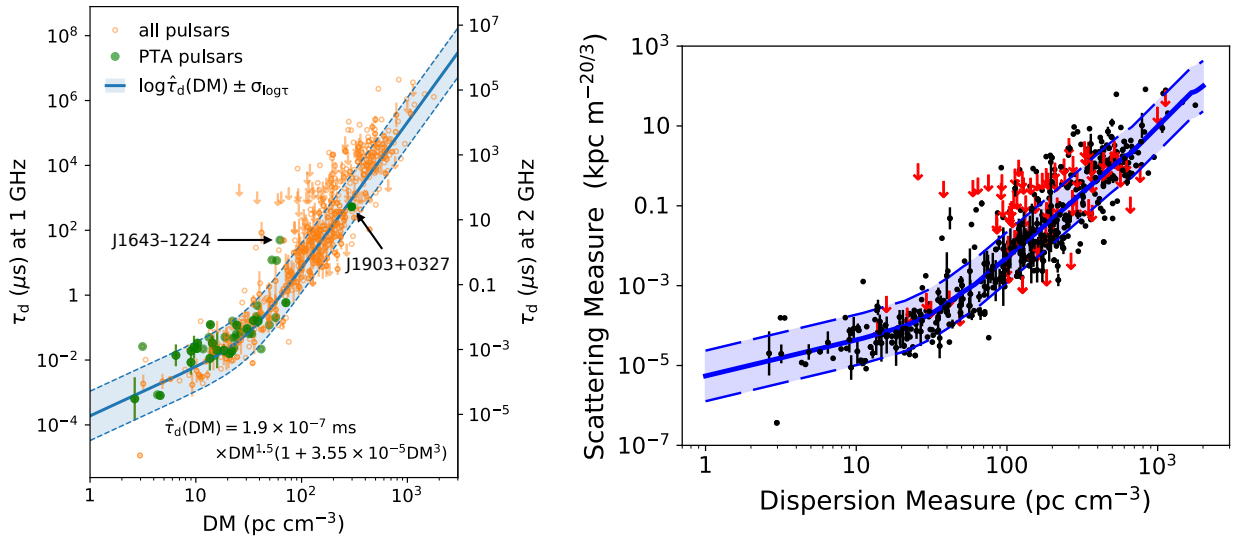


Figure 36. Scattering from known pulsars. Left: scattering time (τ) in μs at 1 GHz vs. DM for Galactic pulsars (including canonical and MSPs) with scattering reported in the literature. Measurements were scaled to 1 GHz assuming $\tau \propto \nu^{-4.4}$. PTA pulsars are highlighted in green. The solid blue line and shaded blue region show the best-fit empirical relation between τ and DM, given by the equation shown. For pulsars with multiple published scattering measurements, the scattering times were averaged and the error bars show the standard deviation of the measurements. Right: Scattering measures vs. dispersion measures. SM values are estimated from pulse broadening times and scintillation bandwidths (see Table 4, assuming $\beta = 11/3$). Downward arrows (red) indicate upper limits, black points represent individual measurements, while those with error bars indicate the *range* of values for a specific pulsar (not the error on the mean of those values). The blue lines and band indicate the mean and $\pm\sigma_{\log\tau}$ range of SM calculated from the τ(DM) relation in Eq. (10.16). The scatter about the mean fit arises from the irregular strength and distribution of scattering regions in the ISM.

which often goes hand in hand with being closer to the observer and brighter. There are a few notable exceptions, such as J1643−1224 with $\tau = 42$ μs, an almost 100% excess from the value expected from the $\tau - \mathrm{DM}$ relation (1 μs). This pulsar lies behind the HII region Sh $2-27$ that contributes 90% of its total DM (Ocker et al. 2020), and which likely also dominates τ (Mall et al. 2022). J1903+0327 has the highest DM and τ of any pulsar timed by current PTAs, but unlike J1643−1224, it is entirely consistent with the $\tau - \mathrm{DM}$ relation. The pulse broadening times and model fit are used to evaluate scattering measures by inverting Expression 9 in Table 4, as shown in the right-hand panel of Fig. 36.

Notable features of the $\tau - \mathrm{DM}$ relation in Fig. 36 include: (1) the approximate factor of ten variation in τ for fixed DM; and (2) the large change in slope of the mean relation from $\tau \propto \mathrm{DM}^{1.5}$ to $\mathrm{DM}^{4.5}$ at DM $\sim 50\,\mathrm{pc\ cm^{-3}}$. The large scatter in τ includes estimation errors from pulse-fitting methodology and from variations in geometrical leveraging: a region midway along the LoS produces the largest scattering time. The increase in slope requires a change in density variations as quantified by a fluctuation parameter that characterizes small cloudlets having a volume filling factor f and internal density fluctuations with wavenumber spectral index β and outer scale l_o,

$$F_\mathrm{c} \equiv \frac{\mathrm{Var}(n_\mathrm{e})/{n_\mathrm{e}}^2}{f l_\mathrm{o}^{\beta-3}} \overset{\beta=11/3}{\simeq} \frac{\zeta\epsilon^2}{f l_o^{2/3}} \tag{10.17}$$

where ζ and ϵ are dimensionless parameters corresponding to cloud-to-cloud and internal density variations, respectively (e.g. Cordes et al. 1991). There is a factor of ~ 20 difference in F_c between the local ISM and the inner Galaxy in the NE2001 electron density model that can account for the slope increase of the $\tau - \mathrm{DM}$ relation. These results underscore the value of pulsars in the solar vicinity that will show much less scattering-induced ToA variations than more distant objects. Though scattering delays can be removed to some extent, methods for doing so are not yet sufficient to make distant pulsars useful for the most demanding timing applications (e.g. nanohertz GW detection).

10.5. *Cyclic spectrum (field correlation function)*

The cyclic spectrum (CS) is a frequency-domain correlation function that exploits the periodic aspect of a signal (Gardner 1991; Antoni 2007). The primary utility of the CS is that it can provide dynamic spectra with resolved scintillations in cases where scintles are narrow in frequency. Second is its potential for estimating the full impulse response $h(t)$ contemporaneously with arrival time data, which, in principle, can aid efforts to correct ToAs for multipath propagation delays (e.g. Demorest 2011; Walker et al. 2013; Palliyaguru et al. 2015; Dolch et al. 2021; Turner et al. 2023). Additionally, the fine frequency resolution used to resolved scintles enables fine-frequency RFI mitigation as a consequence.

The CS of the pulsar signal, $\Gamma_{\widetilde{\varepsilon}}(\delta\nu,\nu)$, is the frequency domain correlation function of the baseband field (analogous to $\Gamma_{\widetilde{h}}(\delta\nu,\nu)$ for the field PBF),

$$\Gamma_{\widetilde{\varepsilon}}(\delta\nu,\nu) \equiv \widetilde{\varepsilon}(\nu_+)\widetilde{\varepsilon}^*(\nu_-) = \Gamma_{\widetilde{h}}(\delta\nu,\nu) \iint dt_1 dt_2\, a(t_1)a(t_2)m(t_1)m^*(t_2)e^{2\pi i(\nu_+ t_1 - \nu_- t_2)}. \tag{10.18}$$

The basis for the CS is a finite FT calculated over a time block T longer than a pulse period but shorter than the DISS time scale, i.e. $P \ll T \ll \Delta t_{\rm d}$. This provides better frequency resolution than PRS for a time block in which the scintillation spectrum $H(\nu)$ is essentially constant. Note also that because the scintillation bandwidth $\Delta\nu_{\rm d}$ is strongly frequency dependent, scaling approximatley as ν^{-4}, the CS analysis needs to be done over bandwidths narrow enough so that $\Delta\nu_{\rm d}$ varies only by a tolerable amount. Including a radiometer noise term, the CS for a single FT is

$$\Gamma_{\widetilde{\varepsilon}}(\delta\nu,\nu) = \widetilde{\varepsilon}(\nu_+)\widetilde{\varepsilon}^*(\nu_-) = \Gamma_{\widetilde{h}}(\delta\nu,\nu)\Gamma_{\widetilde{\varepsilon}_{\rm i}}(\delta\nu,\nu) + \Gamma_{\widetilde{n}}(\delta\nu,\nu) + [\widetilde{h}(\nu_+)\widetilde{\varepsilon}_{\rm i}(\nu_+)\widetilde{n}^*_{\nu_-} + \widetilde{h}(\nu_-)\widetilde{\varepsilon}_{\rm i}(\nu_-)^*\widetilde{n}(\nu_+)], \tag{10.19}$$

where cross terms in square brackets between $\widetilde{n}$ and $\widetilde{\varepsilon}_{\rm i}$ average to zero. However, they contribute significantly to the variance of CS estimates considered later.

To simplify the correlation function we exploit the constancy of $\Gamma_{\widetilde{h}}$ over the time block and average over the rapid decorrelation of the noise process m. We use an ensemble average for the noise while letting $\Gamma_{\widetilde{h}}$ be constant[33]. The noise correlation $\langle m(t_1)m^*(t_2)\rangle = \sigma_m^2\Delta(t_2-t_1)$ vanishes for time differences $|t_1-t_2|$ larger than the inverse bandwidth (e.g. larger than 0.01 to 1 μs) so the amplitude product $a(t_1)a(t_2) \simeq a^2(t_1) \equiv A(t_1)$. Using the FTs $\widetilde{\Delta}$ and $\widetilde{A}$ for Δ and A, respectively, yields

$$\langle\Gamma_{\widetilde{\varepsilon}}(\delta\nu,\nu)\rangle_{P\ll T\ll\Delta t_{\rm d}} \simeq \sigma_m^2\widetilde{A}(\delta\nu)\widetilde{\Delta}(\nu)\Gamma_{\widetilde{h}}(\delta\nu,\nu) + W_n\sigma_n^2{\rm sinc}(\delta\nu T)\widetilde{\Delta}(\nu) \tag{10.20}$$

where ${\rm sinc}(x) \equiv (\sin\pi x)/\pi x$. The second (noise) term has a width $1/T$ vs. $\delta\nu$ but extends over the full frequency band vs. ν.

The cyclic aspect of $\Gamma_{\widetilde{\varepsilon}}$ comes into play when the FT is calculated over a time $T \gg P$ that spans $N_{\rm p}$ periods with the (assumed) same shape $A_0(t)$,

$$A(t) = \sum_{j=0}^{N_{\rm p}-1} a_j A_0(t - jP). \tag{10.21}$$

A strictly periodic train of $N_{\rm p} \gg 1$ identical pulse shapes $A_0(t)$ with $A_0(0) = 1$ and an average amplitude $S_{\nu,{\rm pk}}$ has an FT,

$$\widetilde{A}(\delta\nu) \simeq N_{\rm p}W_{\rm A}S_{\nu,{\rm pk}}\widetilde{A}_{\rm n}(\delta\nu) \times |{\rm sinc}_{\rm d}(\delta\nu P, N_{\rm p})|, \tag{10.22}$$

where $\widetilde{A}_{\rm n}(\delta\nu) = \widetilde{A}_0(\delta\nu)/\widetilde{A}_0(0)$ is normalized to unit maximum and its effective width is $W_{\rm A} \equiv \widetilde{A}_0(0)$. The Dirichlet sinc function, ${\rm sinc}_{\rm d}(x,N) = \sin(N\pi x)/N\sin(\pi x)$, yields peaks at discrete frequencies $\delta\nu_k = k/P$ with k extending to $k_{\rm max} \sim P/W_{\rm A}$, the reciprocal of the pulse duty cycle.

[33] The noise decorrelates on sub-μs time scales for >MHz bandwidths while $h(t)$, if dominated by DISS, decorrelates over minutes to an hour for nearby pulsars used in PTAs. Integration times of > 1 s yield time-bandwidth products $> 10^6$ for the noise, or a fractional error in the correlation function $\lesssim 1\%$.

The number of cyclic frequencies where the amplitude of $\Gamma_{\widetilde{\varepsilon}}$ is significant is of order the reciprocal of the pulse duty cycle, $N_k \sim P/W_{\rm A}$. For millisecond periods $P_{\rm ms}$ the cyclic frequencies $\delta\nu_k = (k/P_{\rm ms})\,{\rm kHz}$ are much smaller than the DISS bandwidths for low-DM pulsars observed at 1.5 GHz. This means that for cyclic frequencies with $k \ll N_k$ the scintillation CS $\Gamma_{\widetilde{h}}(\delta\nu_k, \nu) \simeq \Gamma_{\widetilde{h}}(0, \nu) \equiv |\widetilde{h}(\nu)|^2$, which is the standard scintillation spectrum for the time block in question (c.f. Eq. (10.8)). The frequency resolution is $\delta\nu = 1/T \ll 1/W_{\rm A} \ll 1/P \ll \Delta\nu_{\rm d}$.

We rewrite the CS in Eq. (10.20) (after dropping the subscript on the averaging brackets) as

$$\langle \Gamma_{\widetilde{\varepsilon}}(\delta\nu_k, \nu)\rangle = ({\rm T_{FT}/B})\,\langle {\rm S}_\nu\rangle_\phi\,\widetilde{\rm b}(\nu)\left[\widetilde{\rm A}_{\rm n}(\delta\nu_{\rm k})\Gamma_{\widetilde{\rm h}}(\delta\nu_{\rm k}, \nu) + \frac{{\rm sinc}\,\delta\nu_{\rm k}{\rm T}}{({\rm S/N})_\phi}\right], \tag{10.23}$$

where the bandpass factor is $\widetilde{b}(\nu) = \widetilde{\Delta}(\nu)/\widetilde{\Delta}(0) = B\widetilde{\Delta}(\nu)$. Also, $\langle S_\nu\rangle_\phi \simeq (W_{\rm A}/P)S_{\nu,{\rm pk}}$ is the period averaged flux density (as usually reported for pulsars), $\widetilde{b}(\nu)$ is the receiver bandpass function with width B, and ${\rm sinc}\,x \equiv (\sin\pi x)/\pi x$. The signal to noise ratio is $({\rm S/N})_\phi \equiv \langle S_\nu\rangle_\phi/S_{\rm sys}$ where $S_{\rm sys} = T_{\rm sys}/G$ is the system effective flux density (SEFD) for a telescope with gain G. The first term in square brackets is from the pulsar signal while the second term is from

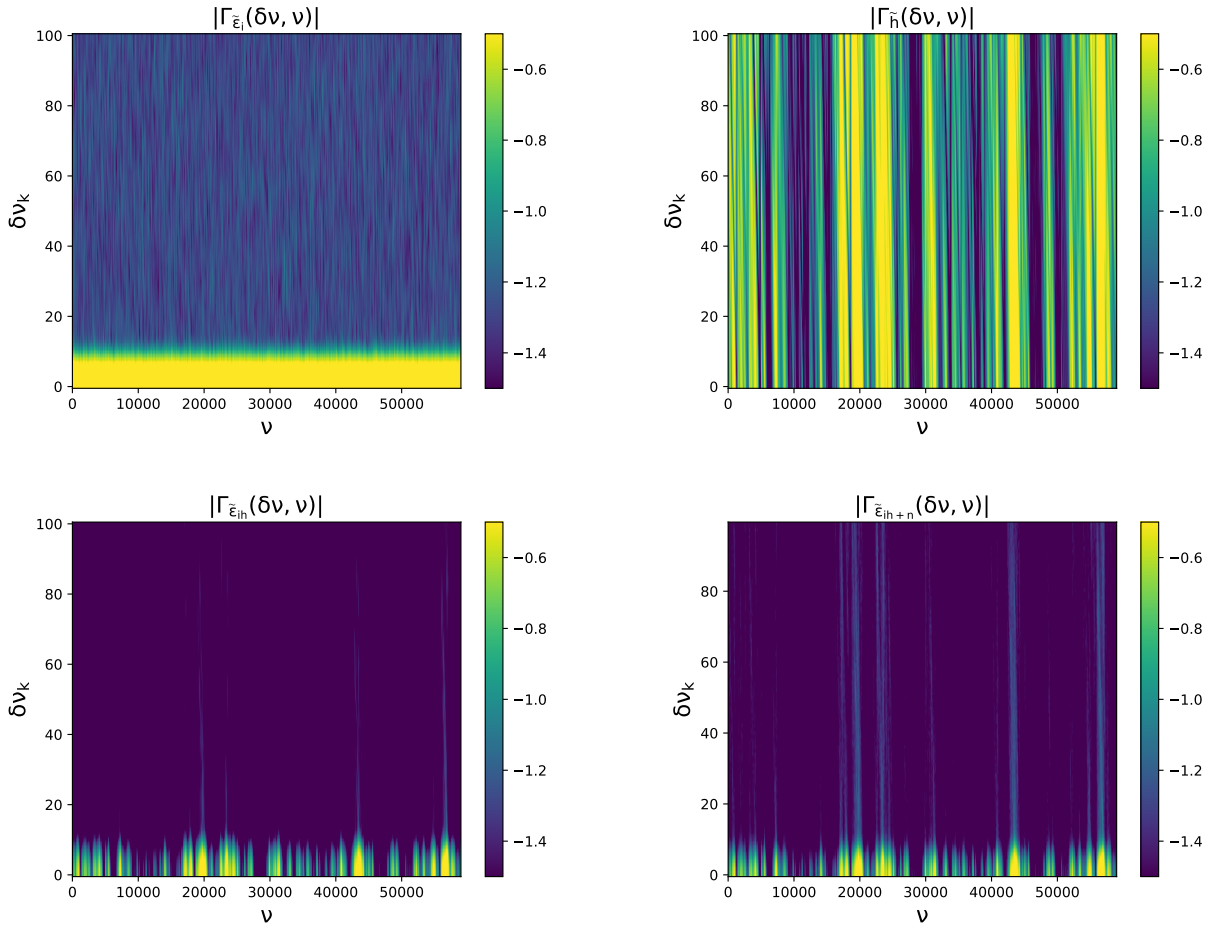


Figure 37. Frequency domain correlation functions (cyclic spectra) of four quantities. They comprise averages over 100 realizations of the pulsar signal while keeping fixed a single realization of the scintillation modulation . The plotted quantities are $\log_{10}$ of the absolute values of the correlation function normalized to unit maximum. The horizontal axis corresponds to radio frequency (in bins) and the vertical axis is the frequency lag $\delta\nu_k = k/P$ corresponding to harmonics in the CS. Each frame is normalized so that the mean across the $\delta\nu_0 = 1$. Top left: CS for the intrinsic pulsar signal $\widetilde{\varepsilon}_{\rm i}$ modeled as amplitude modulated noise. Top right: CS for the scintillation modulation $\widetilde{h}$. Bottom left: CS for the modulated pulsar signal $\widetilde{h} * \widetilde{\varepsilon}_{\rm i}$. Bottom right: CS for the modulated signal + radiometer noise. The case shown here is for ${\rm S/N} \equiv \langle S_\nu\rangle_\phi/S_{\rm sys} = 1$, where $\langle S_\nu\rangle_\phi$ is the period averaged flux density and $S_{\rm sys} = 3\,{\rm Jy}$ is the SEFD for a DSA-2000 class telescope.

additive noise reduced by the $(\mathrm{S/N})_\phi{}^{-1}$ factor. Though $(\mathrm{S/N})_\phi \ll 1$ for most pulsars, the second term is important only for $k = 0$.

Inspection of Eq. (10.23) shows that the scintillation CS $\Gamma_{\widetilde{h}}$ with full phase information can be extracted in cases where the signal-to-noise ratio is large and if the intrinsic pulse shape $\widetilde{A}_0(t)$ (or equivalently $\widetilde{A}_\mathrm{n}$) is known. The latter condition is not usually the case.

When only the scintillation spectrum is wanted (i.e. without phase information) integration over pulse phases where the pulse is strong can be done as follows. The inverse transform of $\Gamma_{\widetilde{\varepsilon}}(\delta\nu_k, \nu)$ with respect to $\delta\nu_k$ yields the phase resolved CS or 'profile spectrum' with a time argument replacing the $\delta\nu$ argument,

$$\langle \Gamma_{\widetilde{\varepsilon}}(t, \nu) \rangle \propto \langle S_\nu \rangle_\phi \, \widetilde{b}(\nu) A_\mathrm{n}(t) * \Gamma_{\widetilde{h}}(t, \nu), \tag{10.24}$$

where a constant term from the sinc function has been excluded. Integration over the time window comprising the pulse then yields the scintillation spectrum.

Fig. 37 shows cyclic spectra $\Gamma_x(\delta\nu, \nu)$ for four quantities: $x =$ (pulsar signal, scintillation modulation, scintillated pulsar signal, and scintillated signal + noise). The signal to noise ratio of the voltage signal is unity, defined as $\langle S_\nu \rangle_\phi / S_\mathrm{sys}$. The plotted quantities are sums over 100 realizations and are evaluated at harmonics $\delta\nu_k = k/P$ of the pulsar period P. Features of the four panels include:

- Top left: The CS of the intrinsic signal is flat across frequency but rolls over vs. $\delta\nu_k$. The number of significant harmonics is approximately the reciprocal of the duty cycle, $P/W \sim 15$.
- Top right: The CS of the scintillation modulation is nearly constant across harmonics but shows the 100% modulations expected vs. frequency.
- Bottom left: the CS of the scintillated pulsar signal shows the frequency structure and rolloff vs. harmonic number.
- Bottom right: additive noise reduces the significance of the frequency structure. This can be compensated for by summing over more realizations. In practice the number of summed individual CS is limited by the scintillation time scale. Most pulsars will have S/N smaller than the unity value used in the simulation.

11. A GALLERY OF PULSE BROADENING FUNCTIONS

Reasons for considering the variety of PBFs are twofold. First, PBFs provide unique information about the ISM, in particular the Galactic distribution of electron density variations and their wavenumber spectrum. Second, optimal timing of pulsars requires removal of chromatic interstellar delays if the primary goal is to obtain achromatic ToAs for the study of pulsar orbits, the neutron star equation of state, and long-wavelength gravitational waves. The second is of course intertwined with the first because proper removal of chromatic delays requires a sufficient understanding of the ISM, viz. how propagation effects on arrival times scale with frequency.

In this section we present a gallery of PBFs for selected media and geometries to illustrate their variety and the complexity of ToA correction for chromatic effects.

Most of the issues related to PBF envelope variations can be illustrated using a thin screen geometry that allows an analytical treatment for many quantities. Quantitative analyses also require consideration of thick media that generally depend on numerical integrations.

11.1. *Thin-screen geometry*

Here we consider scattered images of point sources $I(\boldsymbol{\theta})$ and PBFs $p_\mathrm{d}(t)$ as 'envelope' quantities that exclude stochastic noise (speckles and scintles) already discussed. The PBF is the sum of all *geometric* delays over the scattered image of a point source (Cordes and Lazio 2001),

$$p_\mathrm{d}(t) = \int d\boldsymbol{\theta} \, I(\boldsymbol{\theta}) \delta(t - d' |\boldsymbol{\theta}|^2 / 2c). \tag{11.1}$$

No plasma delays are included because the screens are considered infinitesimally thin and the increments in DM corresponding to the phase change at each position along the screen are small. Simplification of the integral depends on the shape of the image and on any offset from the direct LoS caused by refraction.

Most expressions in the literature consider Gaussian images with no offset from the direct propagation path. For example, a symmetric Gaussian image with RMS angle σ along each axis gives the often used exponential PBF, $p_{\rm d}(t) = \tau^{-1} \exp(-t/\tau)\Theta(t)$, where $\Theta(t)$ is the Heaviside function and $\tau = d'\sigma^2/c$. Figure 38 shows the results from application of Eq. (11.1) and how the e^{-1} points in the image and the PBF are related. A Gaussian image is expected if the phase structure function has a square-law form, $D_\phi(b) \propto b^2$, which is at best only approximated by a screen comprising monoscale density irregularities (e.g. Cronyn 1970; Sutton 1971; Ostashov and Shishov 1978) or a power-law distribution of density scales with $\beta \to 4$.

While the exponential PBF is convenient to use, e.g. for coarse estimation of scattering times τ by model fitting scattered pulse shapes, it is overly simplistic for both ISM and pulsar timing applications. The reasons for this are that (1) Scattering is generally associated with multiple screens and extended media, rather than single thin screens. While scintillation arcs indicate the prominence of thin screens along some lines of sight, they are often multiple rather than single, even for nearby pulsars (McKee et al. 2022; Ocker et al. 2024; Reardon et al. 2025). More distant pulsars encounter even more scattering regions.[34] Thick media (or an ensemble of thin screens) yield PBFs with longer rise times than the sharp rise of a one-sided exponential function (Lambert and Rickett 1999). (2) Direct imaging of scattered pulsars (and other objects, such as active galactic nuclei and interstellar masers) yield elliptical images in some cases, which cause the PBF to differ from a simple exponential (e.g. Desai and Fey 2001; Bower et al. 2014). Image anisotropy is also evident in the detection of inverted "arclets" in pulsar secondary spectra (Brisken et al. 2010; Sprenger et al. 2022; Stinebring et al. 2022). (3) PBFs from the ISM appear to deviate from an exponential form (e.g. Lyne and Thorne 1975; Rickett et al. 2009; Geyer et al. 2017); and (4) refraction-induced offsets of scattering images alter the shapes of all PBFs, as shown below.

Scattering slabs of arbitrary thickness with density variations following a square-law structure function have PBFs that are the n-fold convolution of one-sided exponential functions $\tau_n^{-1} \exp(-t/\tau_n)\Theta(t)$ where $\Theta(t)$ is the Heaviside function (Williamson 1975). The e-folding times τ_n are the eigenvalues of the equation that describes diffusion of rays through a slab. The number of significant eigenvalues depends on the slab's thickness. For a thin screen, only one eigenvalue is significant.

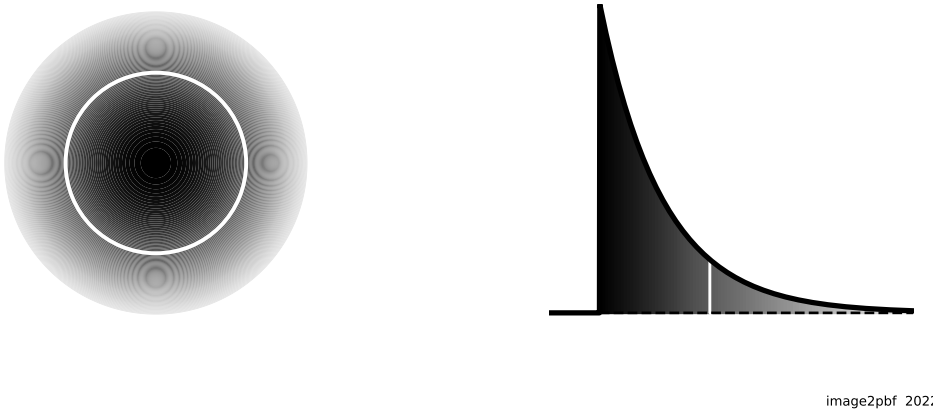


Figure 38. Scattering from a thin screen that produces a circularly symmetric Gaussian image (left) and the corresponding exponential PBF. Darker shading of the image indicates angles with higher probability. The white line indicates the 1/e point in the image and in the PBF.

[34] The relevance of extended media to more distant, high-DM pulsars is corroborated by scintillation arc measurements, which indicate that scintillation arcs become less defined (and detectable) at higher DM, suggesting that arcs are "blurred" by the presence of multiple screens along the LoS (Stinebring et al. 2022; Main et al. 2023).

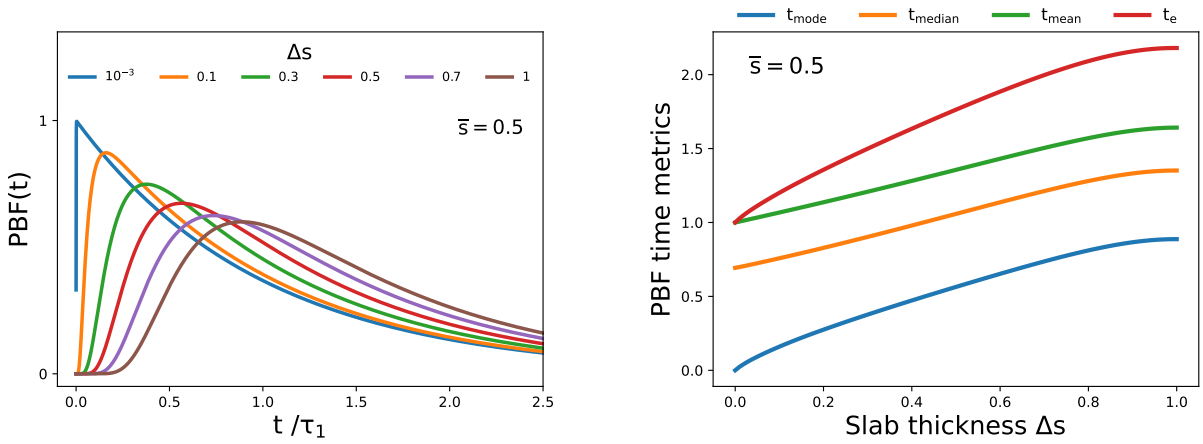


Figure 39. Pulse broadening functions for media with square-law structure functions (Gaussian scattered images). Left: PBFs for slabs midway between source and observer with different fractional thickness Δs for a square-law structure function. Time is normalized by τ_1, the e^{-1} time of the PBF for the thin screen case, which has only one eigenvalue. Finite thickness slabs have multiple eigenvalues that yield PBFs equal to the n-fold convolution of one-sided exponential functions. Right: Time metrics of PBFs for slabs midway between source and observer with different fractional thickness Δs for a square-law structure function.

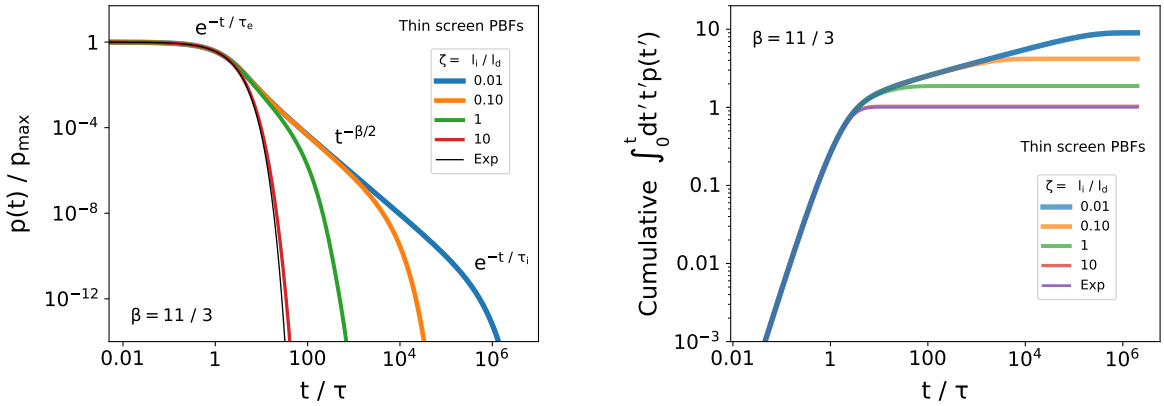


Figure 40. Thin screens with Kolmogorov density fluctuations ($\beta = 11/3$). Left: PBFs for an isotropic Kolmogorov spectrum that illustrate the effects of a small or large inner scale l_i relative to the diffraction scale l_d. The time axis is normalized by the e^{-1} time scale τ_e. Scaling laws for the smallest inner scale ($\zeta = l_\mathrm{i}/l_\mathrm{d} = 0.01$) show three regimes: exponential $\propto e^{-t/\tau_\mathrm{e}}$, power-law $\propto t^{-\beta/2}$, and exponential $\propto e^{-t/\tau_\mathrm{i}}$ at small, intermediate, and large times, respectively. For the largest inner scale, the PBF shows only the exponential scaling that is close to that expected for a Gaussian-shaped scattered image. Right: Cumulative integral showing the contribution to the mean scattering time from the tail of the PBF for different inner scales. The curve for the exponential PBF is nearly indistinguishable from the $\zeta = 10$ (large inner scale) case. (Note that the mean scattering time is only indirectly related to the ToA offset caused by scattering (see Sect. 12.6.2.)

Example PBFs are shown in Fig. 39 for slabs centered midway along the LoS ($\bar{s} = 1/2$) with fractional thicknesses Δs ranging from $\ll 1$ to 1. The rise time and width of the PBFs increase with slab thickness, making it clear that model fitting of pulses with the thin screen PBF will yield biased results for pulsars affected by thick-slab scattering. Indeed Bhat et al. (2004) demonstrated with deconvolution of PBFs from measured pulse shapes that the more rounded rise times of thick-slab PBFs were required for some pulsars.

The mean scattering time $\tau = \sum_n \tau_n \equiv \int dt\, t p_\mathrm{d}(t)$ is equivalent to calculating the mean time for the PBF treated as a probability density function. We compare the mean time with the mode, median and $1/e$ time of the PBFs in Fig. 39.

While the mean and $1/e$ time are equal for a thin screen with a square-law density structure function, they diverge with increasing slab thickness.

11.2. *PBFs from thin and thick media with power-law ('Kolmogorov like') wavenumber spectra*

Media with a power-law wavenumber spectrum spanning a broad range of scales produce non-Gaussian scattering angle distributions and PBF envelopes that depart significantly from an exponential form. In addition, their shapes as well as their $1/e$ scales are frequency dependent: thus *PBFs are not self similar vs. radio frequency.* Ostashov and Shishov (1978) show for $2 < \beta < 4$ and zero inner scale that the image scales asymptotically as $I(\theta) \propto (\theta/\theta_{\rm d})^{-\beta}$ for $\theta/\theta_{\rm d} \gg 1$, where $\theta_{\rm d}$ is the diffraction angle, and the corresponding asymptotic PBF is $p_{\rm d}(t) \propto (t/\tau)^{-\beta/2}$ for $t/\tau \gg 1$ where $\tau = d{\theta_{\rm d}}^2/2c$. As $\beta \to 4$ from below, the PBF is exponential $\propto e^{-t/\tau}$ for small $t \lesssim 2\tau \ln(2/(4-\beta))$ but includes a power-law component $\propto (t/\tau)^{-\beta/2}$ for larger t. A finite inner scale yields a third PBF regime, an exponential decay at very long times $t \gtrsim \tau_{\rm i}$ where $\tau_{\rm i} \propto l_{\rm i}^{-2}$ can be many orders of magnitude larger than the $1/e$ PBF scale.

The three regimes are evident in the PBFs shown in Fig 40 (left panel). For a Kolmogorov spectrum ($\beta = 11/3$) and other cases with $\beta < 4$, the PBF decays more slowly than an exponential (e.g. Lee and Jokipii 1975; Lambert and Rickett 1999) and generally for large $t \gtrsim \tau$, the PBF follows the $t^{-\beta/2}$ scaling until it decays exponentially from an inner scale. For $\beta < 4$, the mean scattering time $\langle t \rangle = \int dt\, t\, p_{\rm d}(t)$ diverges unless the inner scale is finite.

Fig. 40 (right panel) shows the cumulative integral for the mean PBF delay $\langle t \rangle_{p_{\rm d}} = \int dt\, t\, p_{\rm d}(t)$ for $\beta = 11/3$. With the PBFs scaled to the same $1/e$ time scale, t_e, the various curves show that the contribution can be up to ten times larger than for an exponential form. The large delays of long-tailed PBFs are quantified with the ratio $R_t = \langle t \rangle_{p_{\rm d}}\rangle/\tau$ of the average scattering time $\langle t \rangle$ to the $1/e$ time τ_e, as shown in Fig. 41 vs. $\zeta = l_{\rm i}/l_{\rm d}$. This ratio is $R_t \sim 8$ for a small inner scale $\zeta = 0.01$ and declines monotonically to $R_t = 1$, the value for an exponential PBF, as ζ increases. Also shown is the ratio $\sigma_{t_p}/\langle t \rangle_{p_{\rm d}}$, which measures the spread in delays relative to the mean; it too is much larger for small ζ. For shallower density spectra with $2 < \beta < 11/3$, these ratios increase and tend to unity as $\beta \to 4$.

As shown above, if the diffraction scale $l_{\rm d}$ is comparable to or smaller than the inner scale, the PBF tends toward the monoscale case with only an exponential decay. At ~ 1 GHz, typical diffraction scales are $l_{\rm d} \sim 10^4$ km, whereas at $\nu \lesssim 100$ MHz they are $l_{\rm d} \sim 10^3$ km (e.g. Geiger et al. 2025). Empirical determinations of the shape of the PBF or the scaling of the scattering time with frequency yield constraints on the inner scale of order 70 to 800 km (e.g. Bhat et al. 2003; Rickett et al. 2009). PBFs at high radio frequencies therefore will show a long power-law tail while at low frequencies the PBF trend to the exponential. Given that most PTA pulsars are observed near 1 GHz, they largely fall within the $\zeta < 1$ (non-exponential PBF) regime.

As with square-law media, the PBFs for thick Kolmogorov-like media have finite rise times related to the fact that radiation is scattered multiple times along each propagation path. The asymptotic decay of the PBF $\propto t^{-\beta/2}$ is similar to those of thin screen cases. Fig. 42 shows PBFs for different β and for different values of inner scale parametrized by $\zeta = l_{\rm i}/l_{\rm d}$. The PBFs show a finite rise in contrast to the sharp rises seen from thin screen cases. Thick media require numerical integration similar to the approaches in Williamson (1974); Lee and Jokipii (1975); Ostashov and Shishov (1978); Ishimaru (1979) and Lambert and Rickett (1999); our implementation replicates these approaches and will be published elsewhere.

11.3. *Anisotropic scattering and refraction*

Long tailed PBFs arise, as we have shown, from screens or extended media with isotropic density fluctuations and small inner scales that produce circularly symmetric scattered images of point sources. Anisotropic media produce images with elliptical contours and long-tailed PBFs. Refraction that distorts would-be circular images also yield long-tailed PBFs, as we show here. These and previous cases indicate, therefore, that long-tailed PBFs are to be expected generally.

Asymmetric scattered images: For some lines of sight, scattering appears to be caused by anisotropic density irregularities as evidenced in the elliptical shapes of scattered images determined from VLBI and from the properties of pulsar scintillations (Frail et al. 1994; Brisken et al. 2010; Bower et al. 2014; Sprenger et al. 2026). An alternative

cause is refractive distortion of scattered images that would otherwise have circular contours. These two origins for anisotropies result from very different length scales of density variations in the medium, small scales responsible for diffraction and large scales that underly refraction.

Anisotropies are most prominent for nearby pulsars or for distant pulsars that encounter a local region of enhanced scattering, such as a supernova shock or HII region (Brisken et al. 2010; Stinebring et al. 2022; Mall et al. 2022; Ocker et al. 2024; Reardon et al. 2025; Sprenger et al. 2026). It is justified for these cases to consider a thin screen and computing PBFs for anisotropic screens involves a simple transform of the PBFs for isotropic cases.

A screen that causes anisotropic scattering yields a scattered image that is not circularly symmetric. Taking this into account when evaluating the delta function in Eq. (11.1), we obtain the resulting PBF,

$$p_{\rm d}(t) = \frac{c}{d'}\int_0^{2\pi} d\phi\, I(\sqrt{2ct/d'}\cos\phi, \sqrt{2ct/d'}\sin\phi). \tag{11.2}$$

A scattered image with elliptical contours can be written in terms of a symmetric image $I^{\rm iso}$ by replacing (θ_x, θ_y) with $(R^{-1/2}\theta_x, R^{1/2}\theta_y)$ using an axial ratio $R > 1$ to obtain $I(\theta_x, \theta_y) = I^{\rm (iso)}(\theta_x/R^{1/2}, \theta_y R^{1/2})$. This choice aligns the contours with the coordinate axes, with no loss of generality for the resulting PBF. The PBF in turn becomes an integral over azimuthal angle of the PBF from isotropic irregularities,

$$p_{\rm d}(t) = \int_0^{2\pi} d\phi\, p_{\rm d}^{\rm (iso)}\left[\sqrt{2ct/d'}\left(R^{-1}\cos^2\phi + R\sin^2\phi\right)\right]. \tag{11.3}$$

The same transformation applies, in principle, to PBFs from extended media but requires the unphysical assumption that irregularities in the medium have the same axial ratio and orientation along the entire LoS.

Example of elliptical Gaussian scattered images: Applying Eq. (11.3) to the exponential PBF from a circular Gaussian image, we obtain

$$p_{\rm d}(t; R) = \tau_1^{-1} e^{-[(R^2+1)/2R](t/\tau_1)} I_0[((R^2-1)/2R)(t/\tau_1)], \tag{11.4}$$

where $I_0(x)$ is the modified Bessel function and τ_1 is the mean scattering time for $R = 1$ (the exponential PBF case). Note that the PBF is unchanged under a substitution $R \to R^{-1}$. Fig. 43 (left panel) shows examples for five axial ratios and where the image size has been held fixed along one of the axes. In these cases, the solid angle of the image

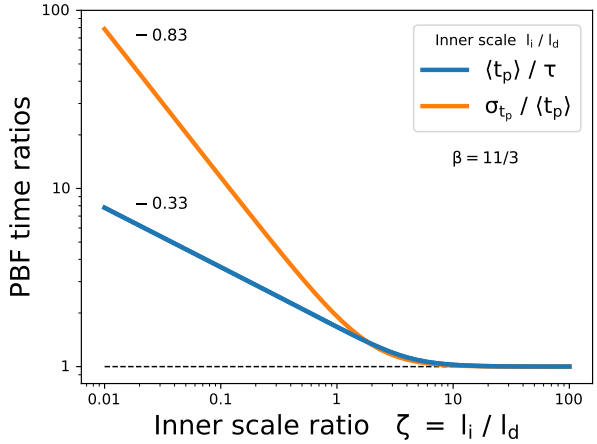


Figure 41. Thin screen scattering time metrics, $\langle t_{\rm p}\rangle/\tau$ and $\sigma_{t_p}/\langle t_{\rm p}\rangle$, vs. the inner scale ratio $\zeta = l_{\rm i}/l_{\rm d}$ for a Kolmogorov medium ($\beta = 11/3$) in the inertial subrange scaling regime. These metrics are, respectively, the mean scattering time and the RMS scattering time in units of the $1/e$ scattering time. They are calculated by treating the PBF as a probability density function. They are much larger than unity for heavy tailed PBFs. For $\zeta \gg 1$, the PBF asymptotes to a one sided exponential and the two ratios asymptote to unity. The two lines are labeled with their logarithmic slopes for small values of ζ.

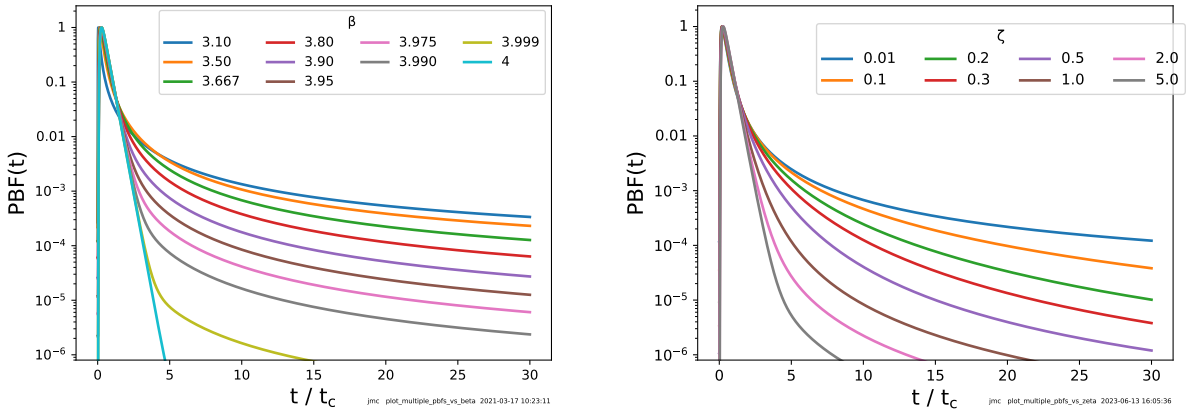


Figure 42. PBFs for thick media with power-law wavenumber spectra as a function of β for negligible inner scale (left) and as a function of dimensionless inner scale $\zeta = l_\mathrm{i}/l_\mathrm{d}$ for $\beta = 11/3$ (right).

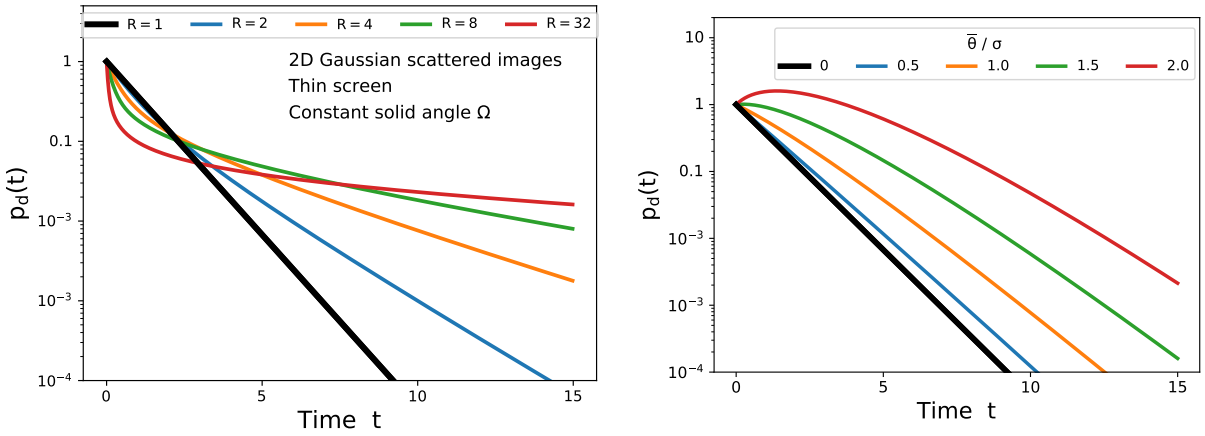


Figure 43. Left: PBFs for scattered images with different axial ratios, R, but calculated from the PBF for a circularly symmetric image, as described in the text. All PBFs are normalized to unit amplitude at $t = 0$. The time axis is defined so that $t = 1$ for the e^{-1} value of the $R = 1$ case. Right: PBFs for a symmetric Gaussian image offset from the direct line of sight by an angle $\overline{\theta}$ in units of σ, the $e^{-1/2}$ width of the Gaussian image. All PBFs are normalized to unit amplitude at $t = 0$. The time axis is defined so that $t = 1$ for the e^{-1} value of the $\overline{\theta} = 0$ case.

scales as R^{-1}, causing the PBF to become more concentrated at the origin. In the limit of $R \gg 1$, the PBF has a characteristic width $\tau = R\tau_1$ and shape, $p_\mathrm{d}(t) = (\pi\tau t)^{-1/2} e^{-t/\tau}$, that differs significantly from the purely exponential form for $R = 1$. For these PBFs, the ratio of the RMS to mean time delay is

$$\frac{\sigma_t}{\langle t \rangle} = \frac{\sqrt{2}(R^2 + R^{-2})^{1/2}}{R + R^{-1}}, \tag{11.5}$$

is unity for a symmetric Gaussian image ($R = 1$) but increases to $\sqrt{2}$ for $R \gg 1$ or $R \ll 1$ (by inspection).

PBFs from anisotropies and image offsets: Generally, scattered images are asymmetric in shape and offset from the direct line of sight due to refraction. Asymmetries can arise from asymmetric diffraction combined with refraction, which causes both convergence and shear of the image (described below) or they can be caused be refraction alone or diffraction alone.

A screen with only a phase gradient shifts the scattered image and increases propagation delays but does not alter the surface brightness. For a shift $\overline{\boldsymbol{\theta}} = (\overline{\theta}_x, \overline{\theta}_y)$, the PBF is given by Eq. (11.2) with the arguments of the image replaced by

$\sqrt{2ct/d'}\cos\phi - \overline{\theta}_x$ and $\sqrt{2ct/d'}\sin\phi - \overline{\theta}_y$). A shifted circularly-symmetric Gaussian image yields, with $\tau \equiv d'\sigma^2/c$,

$$p_{\rm d}(t) = e^{-\overline{\theta}^2/2\sigma^2} I_0(\overline{\theta}\sqrt{t/\tau}/\sigma) \times \left[\tau^{-1} e^{-t/\tau}\Theta(t)\right], \tag{11.6}$$

where $\overline{\theta}^2 = \overline{\theta}_x^2 + \overline{\theta}_y^2$, I_0 is the modified Bessel function of the first kind and the square brackets designate the PBF for a centered image ($\overline{\boldsymbol{\theta}} = 0$). Examples are shown in Fig. 43 (right panel), which demonstrate that offsets make the PBF wider and non-monotonic.

Next we show results where asymmetries and offsets are both caused by refraction from screens with power-law density wavenumber spectra. For these cases we simulate only refraction from the screen and let it modify symmetric Gaussian images. For weak refraction that does not induce any ray crossing, we use a geometric optics approach based on the Fresnel-Kirchhoff diffraction integral. For the geometry shown in Fig. 16, a given observer position $\mathbf{x}_{\rm o}$ yields a stationary phase position $\mathbf{x}_{\rm l} = \overline{\mathbf{x}}$ in the screen. Expanding the screen phase $\phi_r(\mathbf{x})$ to second order about this point gives

$$\phi_{\rm r}(\mathbf{x}) \sim \phi_{\rm r}(\overline{\mathbf{x}}) + \boldsymbol{b}\cdot(\mathbf{x}-\overline{\mathbf{x}}) + \frac{1}{2}(\mathbf{x}-\overline{\mathbf{x}})\cdot\mathbf{C}\cdot(\mathbf{x}-\overline{\mathbf{x}}), \tag{11.7}$$

where $\boldsymbol{b} \equiv \boldsymbol{\nabla}_{\mathbf{x}}\phi_{\rm r}(\overline{\mathbf{x}})$ yields the refraction angle (as viewed by the observer), $\overline{\boldsymbol{\theta}} = -k^{-1}(d_{\rm sl}/d_{\rm so})\boldsymbol{b}$. The 2×2 matrix $\mathbf{C}$ has diagonal elements $C_x = \partial_x^2\phi_{\rm r}(\overline{\mathbf{x}})$ and $C_y = \partial_y^2\phi_{\rm r}(\overline{\mathbf{x}})$ and off-diagonal elements $C_{xy} = C_{yx} = \partial_{xy}^2\phi_{\rm r}(\overline{\mathbf{x}})$, where derivatives are in screen-plane coordinates. A unitary matrix $\boldsymbol{U}$ transforms $\mathbf{C}$ into the diagonal form $\mathbf{C}' = \boldsymbol{U}\mathbf{C}\boldsymbol{U}^\dagger$ (where † indicates matrix transpose) with elements C'_x, C'_y. The rows of $\boldsymbol{U}$ are $(\cos\chi, \sin\chi)$ and $(-\sin\chi, \cos\chi)$ where $\tan 2\chi = 2C_{xy}/(C_x - C_y)$ and the angle χ is the position angle of the distortion. As with polarization position angles, the domain of χ is over π radians. We define the diagonal matrix $\boldsymbol{\gamma}$ with elements G_x and G_y given by $G_{x,y} = (1 + k^{-1}d'C'_{x,y})^{-1}$ where $d' = d_{\rm sl}d_{\rm lo}/d_{\rm so}$.

The magnification of the image is $\mu = |\det \boldsymbol{A}|^{-1} = [(1-\kappa)^2 - \gamma^2]^{-1}$, where

$$\boldsymbol{A} = \begin{pmatrix} 1-\kappa-\gamma_1 & -\gamma_2 \\ -\gamma_2 & 1-\kappa+\gamma_1 \end{pmatrix} \tag{11.8}$$

is written in terms of the 'convergence' κ and 'shear' $\gamma_{1,2}$ of the refraction. Defining $\gamma = \sqrt{\gamma_1^2 + \gamma_2^2}$ in terms of $\gamma_1 = \gamma\cos 2\chi$ and $\gamma_2 = \gamma\sin 2\chi$, these are

$$\kappa = {r_{\rm F}}^2(C_x + C_y)/2 \tag{11.9}$$

$$\gamma = {r_{\rm F}}^2\left[\frac{1}{4}(C_x - C_y)^2 + C_{xy}^2\right]^{1/2} \tag{11.10}$$

$$\tag{11.11}$$

If $I_{\rm d}(\boldsymbol{\theta})$ is the scattered (diffracted) image in the absence of refraction, the refracted image is

$$I_{\rm dr}(\boldsymbol{\theta}) = I_{\rm d}[\boldsymbol{U}^\dagger\boldsymbol{\gamma}^{-1}\boldsymbol{U}(\boldsymbol{\theta} - \overline{\boldsymbol{\theta}})], \tag{11.12}$$

where $\overline{\boldsymbol{\theta}} = -k^{-1}(d_{\rm sl}/d_{\rm so})\boldsymbol{b}$. Refraction renders the scattered image asymmetric and off center regardless of the shape of the unrefracted (but still scattered) image. Finally, the PBF follows by substitution of $I_{\rm dr}(\boldsymbol{\theta})$ into Eq. (11.2).

Fig. 44 shows the $\sim 30\%$ variability of the scattering time for the MSP J1903+0327, with DM = 297 pc cm^{-3} (Geiger et al. 2025). The variability time scale ~ 150 d is consistent with the DM variability and with the estimated refraction time scale of ~ 150 d. The similar $\sim 25\%$ variability of τ for the MSP J1643-1224 with DM= 62.4 pc cm^{-3} (Singha et al. 2024) with ~ 200 d time scale at 0.4 GHz is also consistent with the estimated RISS time scale and that for DM variations. Measuring scattering time variability for more PTA pulsars will require inclusion of higher time and frequency resolutions in PTA observing configurations, which will become routinely possible with instruments like the cyclic spectroscopy backend on the GBT.

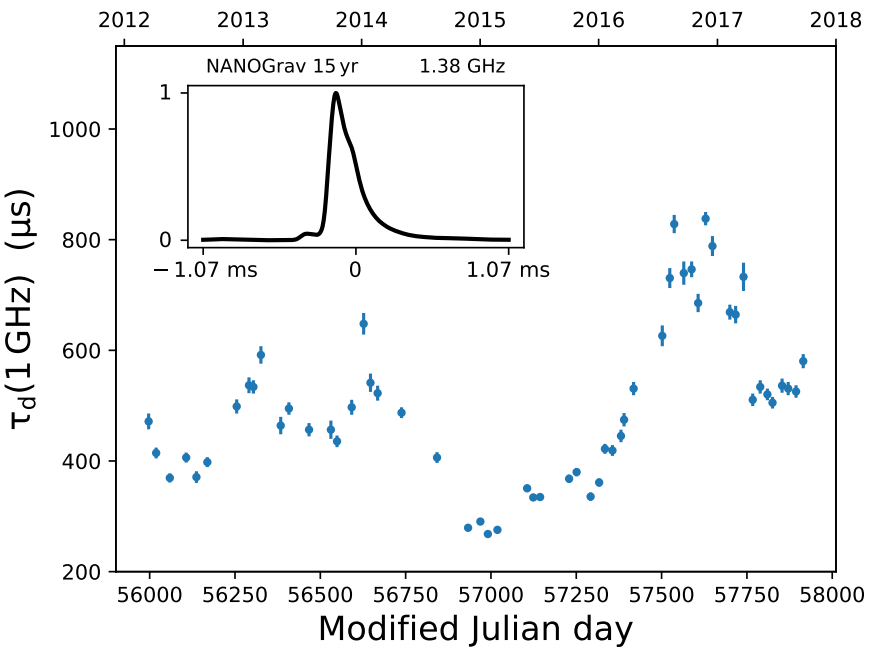


Figure 44. Scattered pulse shape and variations of the scattering time vs. epoch for the MSP J1903+0327. Scattering times were calculated from pulses in the NANOGrav 12.5-yr data set like that shown in the inset (Geiger et al. 2025).

Figures 45–46 show the effects of refracting screens on δDM, intensities, images, and pulse broadening for DM = 10, and 300 pc cm^{-3} where the strength of the refraction is consistent with the pulse broadening specified for each DM and assuming Kolmogorov density fluctuations with negligible inner scale. [Details of the simulations are available on request.] The four panels in each of these figures are:

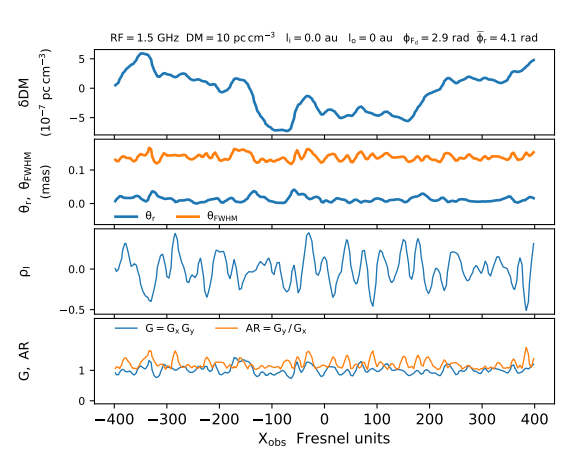
(a) Slices through the screen for δDM(t), the scattering diameter and refraction angle (the centroid of the scattered image), a parameter ρ_I that is related to the orientation of the refracted image, and the refractive gain modulation G of the flux density and the axial ratio of the refracted image. The abscissa is in units of the Fresnel scale.
(b) Wandering of the image centroid in the image plane showing the size of the scattering disk combined with the ensemble average image wandering (gray circle).
(c) Delays vs. position along the observation plane from diffraction $t_{\rm d}$ (red) and refraction $t_{\rm r}$ (blue) and their sum (black).
(d) Images and pulse broadening functions at eight positions along the screen separated by multiple refraction length scales $l_{\rm r}$. The pulse broadening time is indicated in each of the PBF frames.

Trends that can be seen with increasing DM are:

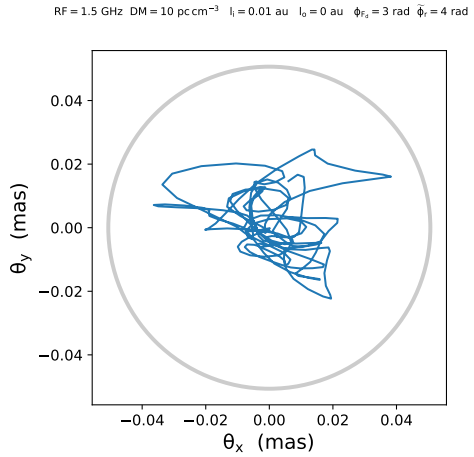
1. Scattering observables (the scattering disk size $\theta_{\rm FWHM}$ and the width of the PBF; c.f. Fig. 36) increase with DM, as expected.
2. Refraction quantities, including angular wandering and refractive ToA delays, *decrease* with increasing DM if refraction is from a wavenumber spectrum consistent with that producing the diffraction. However this trend can be reversed if there is enhanced power on refraction scales $\gtrsim 1$ au.
3. Intensity variations diminish with increasing DM, with $G = G_x G_y$ more closely clustered around unity.
4. Images become more circularly symmetric (axial ratio $\rightarrow 1$).

These trends are consistent with the large body of scattering measurements cited in Sect. 9. In particular, refractive scintillation from a Kolmogorov spectrum is consistent with some of the monitoring observations reported in e.g.

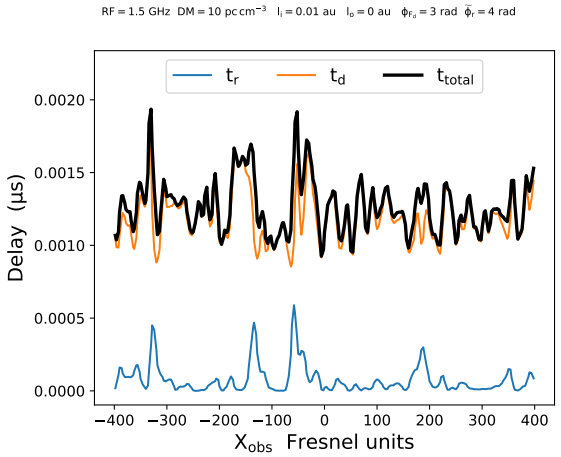
Stinebring and Condon (1990); Kaspi and Stinebring (1992) for slow pulsars and for MSPS (Gitika et al. 2023). These studies also demonstrate that the mean *emitted* flux densities of pulsars appear to be nearly constant. Other cases indicate that discrete structures exist in the ISM that cause enhanced refractive scintillations (e.g. Wang et al. 2023).



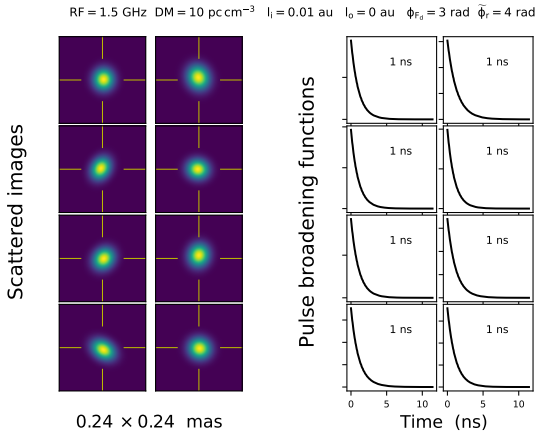
(a) 1D slices across the phase screen.



(b) Image wandering relative to the direct propagation path.



(c) Arrival time delays (diffractive and refractive).



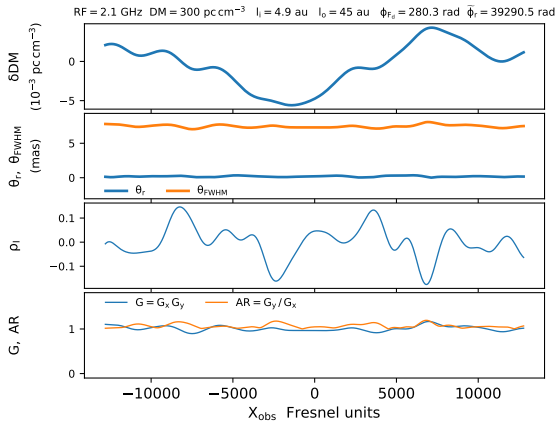
(d) Sample images and PBFs at eight positions along the phase screen.

Figure 45. The effects of refraction on the scattered image, pulse broadening function, and ToA delays at 1.5 GHz for a LoS with dispersion measure DM = 10 pc cm^{-3}. Details are discussed in the text.

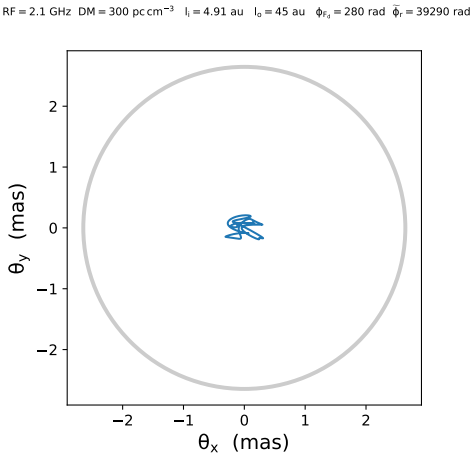
11.4. *Inhomogenous and truncated screens*

The 'textbook' PBFs often considered in pulsar scattering are based on the (usually) tacit assumption that the strength of scattering (e.g. C_n^2) is independent of position in the screen, leading to 'standard' scaling laws vs. frequency for scattering and scintillation parameters. Departures from homogeneity cause the PBF and scaling laws to differ substantially (Cordes and Lazio 2001). In particular, if angles of arrival are bounded by the spatial extent of a scattering region, in contrast to the unbounded AoAs for an infinite screen, the angular size and pulse broadening time can be only weakly dependent on frequency in some frequency ranges, as demonstrated in Cordes and Lazio (2001) (see also Wu et al. 2023).

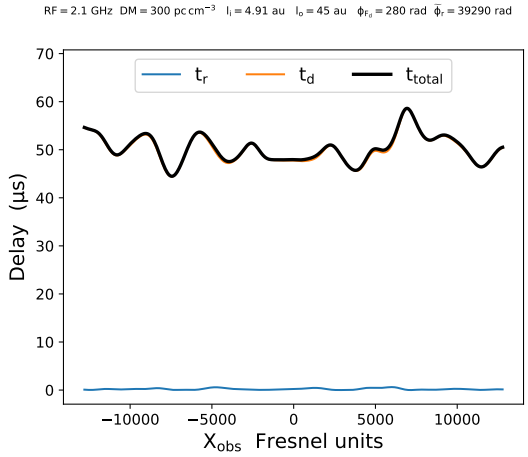
The net frequency dependences depend on the details of the scattering region and will not be discussed further here. The implication for arrival time analyses is that correction of ToAs for scattering delays will likely be imperfect unless



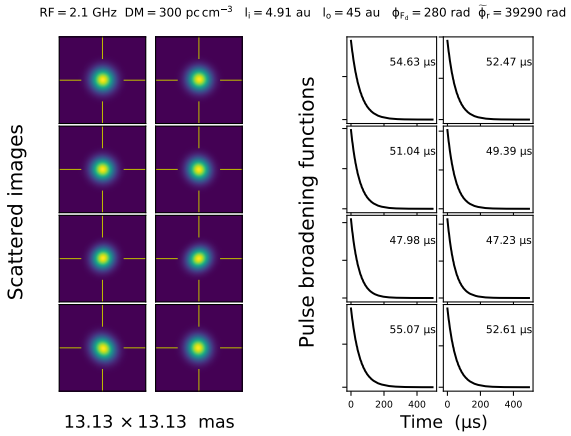
(a) 1D slices across the phase screen.



(b) Image wandering relative to the direct propagation path.



(c) Arrival time delays (diffractive and refractive).



(d) Sample images and PBFs at eight positions along the phase screen.

Figure 46. The effects of refraction on the scattered image, pulse broadening function, and ToA delays at 2.1 GHz for a LoS with dispersion measure DM = 300 pc cm^{-3}. Details are discussed in the text.

it can be demonstrated that scattering regions are well characterized with respect to their spatial distribution as well as for the underlying wavenumber spectrum.

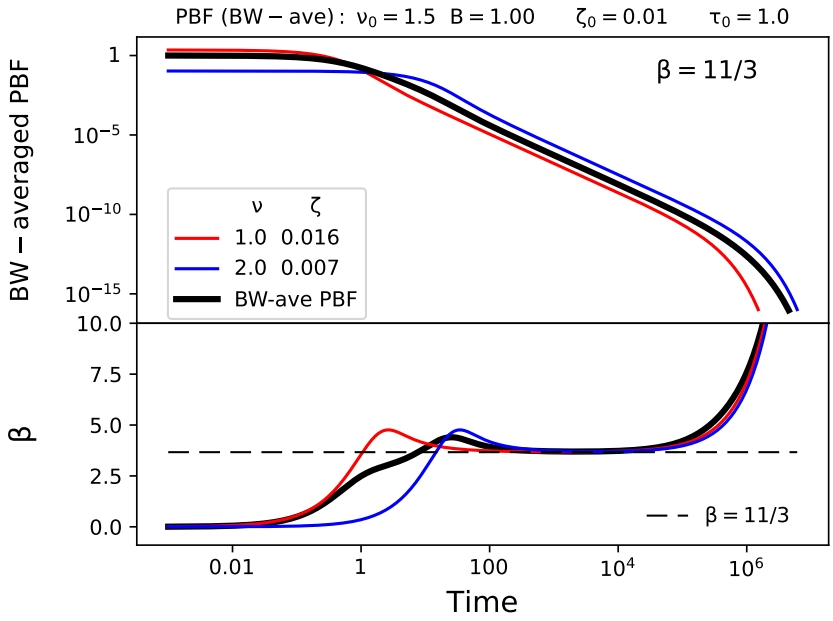


Figure 47. Bandwidth averaging of a power-law PBF for $\beta = 11/3$ for $\zeta_0 = 0.01$ and $\tau_0 = 1$ at the center frequency $\nu_0 = 1.5$. The top panel shows the PBFs and the bottom panel shows values of β inferred from the bandwidth averaged and individual PBFs at the band edges using $\beta = -2d(\ln p_{\rm d})/d\ln\nu$.

11.5. *Bandwidth averaging and phase wrapping*

The PBFs applicable to isolated giant pulses from pulsars or one-off FRBs are as described so far. For periodic sources, however, the effective PBF is 'phase wrapped,' meaning that the PBF acting on previous pulses affects the shape of any given pulse; in averages of N pulses, the net pulse shape is the wrapped, intrinsic pulse shape convolved with a phase-wrapped PBF. Inferences from pulsars about the ISM based on the shape of the pulse need to take wrapping into account. All cases may furthermore be affected by bandwidth averaging. The strong frequency dependence of the scattering time, $\tau \propto \nu^{-x_\tau}$ with $x_\tau = 2\beta/(\beta-2) \simeq 4.4$ implies that averaging of pulses over frequency after dedispersion (e.g. to increase the S/N) also alters the net PBF shape.

Bandwidth averaging of a PL PBF combines PBFs with different $1/e$ scattering times τ and different power-law spans $\propto t^{-\beta/2}$ before rolling off exponentially at a frequency-dependent time related to the inner scale. The net shape differs from that applicable to any single frequency and depends on the pulsar's radiation spectrum. Fig. 47 shows the effects of bandwidth averaging over an octave frequency range. The top panel shows the PBFs at the lowest and highest frequencies along with the average PBF, where a pulsar spectrum $\propto \nu^{-1.5}$ was assumed. The bottom panel shows $\widehat{\beta} = (-1/2)d(\ln p_{\rm d})/d\ln\nu$, which equals the true value, $\beta = 11/3$, over time ranges far beyond the $1/e$ scattering times. The dependence of the PBF shape on the extent of bandwidth averaging certainly factors into any determinations of β from pulse-shape fitting and into arrival time estimation.

Generally, phase wrapping makes heavy-tailed PL PBFs even heavier (shallower). The long PBF tails for media with small inner scales (small ζ) can extend over a large number of pulse periods, adding shallower segments to the initial exponential falloff in an average profile comprising many pulses. Figure 48 shows an example of phase wrapping for $\tau = 1$ and a period $P = 5.1$ (arbitrary units, but could be considered ms). The top panel shows the original and wrapped PBF plotted against pulse phase, while contributions from individual segments from pulse numbers 0 through 100 are shown in the middle panel with inferred β values given to the right of each trace. The bottom panel shows the inferred β from the apparent power-law portion of the wrapped pulse.

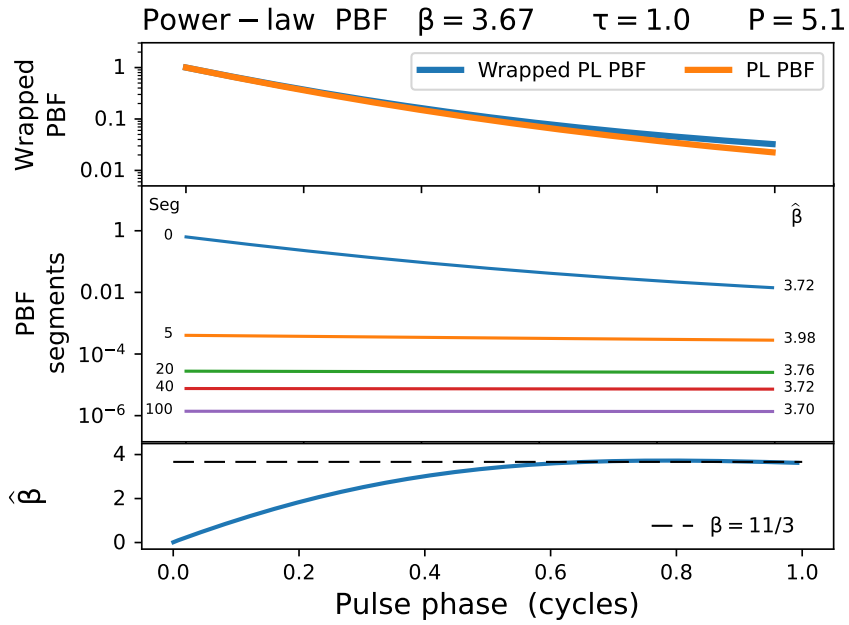


Figure 48. Phase wrapping of a power-law PBF for $\beta = 11/3$, $\tau = 1$, and $P = 5.1$ (in arbitrary time units). (Top panel) initial and wrapped PBFs. (Middle panel) segments of length P that are wrapped into one cycle of pulse phase. The segment number is given to the left of each line and the inferred $\widehat{\beta} = -2d\ln p_{\rm d}/d\ln t$ at the midpoint of each segment. (Bottom panel) values of β inferred from the wrapped PBF.

12. TIMING VARIATIONS FROM CHROMATIC PLASMA EFFECTS

A plethora of systematic and random delays caused by dispersion and scattering contribute to arrival times. While dispersion and scattering are are distinct processes, their mitigation is intertwined in several ways, as we discuss in this section.

A primary chromatic effect on ToAs is simply the change in S/N from intensity scintillations, which can cause large excursions from the mean flux density of a pulsar and affect the matched filtering ToA error discussed earlier.

The modulation index (fractional intensity variation) for DISS is approximately $m_I \simeq N_{\rm scint}^{-1/2}$ where $N_{\rm scint}$ is the number of scintles within the time span and bandwidth of an observation. Low-DM pulsars observed at $\gtrsim 1\,$GHz will yield $N_{\rm scint} \sim 1$ to 10, so changes in flux density and $\Delta t_{\rm S/N}$ are large. Low frequency observations of higher-DM pulsars will show a much smaller range of flux densities.

Dispersion measure variations result from the changing direction and distance to the pulsar combined with density fluctuations in the ISM. The solar corona and Earth's ionosphere contribute less but still need to be considered in the highest precision timing. (e.g. Tiburzi et al. 2021, and references therein). Fortunately, most of the resulting arrival time fluctuations can be removed by careful estimation of DM at each timing epoch. However, such removal is based on imperfect arrival times used to estimate DM, which are themselves imperfect due to a variety of effects. These include the achromatic errors already discussed along with pulse shape distortions from the stochasticity of the PBF, from RFI and instrumental effects (polarization calibration and aliasing), and from the interplay of scintillations and the chromatic aspect of the true pulse shape. It is therefore useful to quantify the full extent of DM variations and then assess to what degree they can be removed.

12.1. *Temporal DM variations* [DM(t)]

In this section we concentrate on the effects of DM variations on timing and defer to Section 10 a discussion of ISM diagnostics and their utility in improving arrival times. Of all the interstellar effects on timing, the DM term $\delta t \propto \nu^{-2}$DM is the largest. The largely (but not completely, c.f. §12.2) deterministic variation of this term with frequency ν allows DM to be estimated with multifrequency timing measurements. One might be tempted to think that this term can be removed completely (to within random ToA measurement errors). However, other chromatic effects yield systematic ToA offsets, so there is always consequential leakage of DM fluctuations into timing residuals (see Sect. **??**).

Fig. 31 shows the DM time series for PSR J1909-3744. It appears to be the superposition of a downward secular trend, a stochastic ISM component with a red power spectrum, and a yearly oscillation due to the cyclical intersection of the LoS with the solar corona. This and similar time series have been analyzed by a number of authors (e.g. Keith et al. 2012; Lam et al. 2015, 2016b; Jones et al. 2017; Madison et al. 2019; Hazboun et al. 2022) using structure function analyses of data from PTA programs on millisecond pulsars. The motivation of those studies has been to characterize electron density fluctuations of the ISM and the solar corona, of interest in their own right, but they also contribute to an understanding of the overall noise budget for pulsar timing and to ongoing efforts to improve timing precision.

We focus on stochastic DM variations from the ISM that have red, power-law spectra. While early timing analyses did not remove these variations (e.g. Downs and Reichley 1983), current practice aims to do so. The temporal spectrum of DM is power-law in form for the inertial range of wavenumbers in the stochastic density spectrum of Eq. (9.1),

$$S_{\rm DM}(f) = \left[\frac{\pi^{1/2}}{(2\pi)^{\beta-3}}\frac{\Gamma((\beta-1)/2)}{\Gamma(\beta/2)}\right] {\rm SM}_{\rm eff} v_x^{\beta-2} f^{-(\beta-1)}. \tag{12.1}$$

For Kolmogorov fluctuations ($\beta = 11/3$), the DM spectrum is

$$\begin{aligned} S_{\rm DM}(f) &= \frac{1}{2^{2/3}\pi^{1/6}}\frac{\Gamma(4/3)}{\Gamma(11/6)}\frac{{\rm SM}_{\rm eff}}{v_x}\left(\frac{f}{v_x}\right)^{-8/3} \\ &\simeq \frac{(5.86\times10^{-5}\,{\rm pc\ cm^{-3}})^2}{\rm cy\ yr^{-1}}\left(\frac{\rm SM}{10^{-3.5}\,{\rm kpc\ m^{-20/3}}}\right) v_{100}^{5/3} f^{-8/3} \\ &\simeq \frac{(7.70\times10^{-5}\,{\rm pc\ cm^{-3}})^2}{\rm cy\ yr^{-1}}\left(\frac{\tau_1/1\,\mu{\rm s}}{d'/1\,{\rm kpc}}\right)^{5/6} v_{100}^{5/3} f^{-8/3} \end{aligned} \tag{12.2}$$

where frequencies are in cy yr^{-1}, v_x is in units of 100 km s^{-1}; the first evaluation is in terms of a scattering measure SM $= 10^{-3.5}$ kpc m$^{-20/3}$ and the second evaluation is expressed using a scattering time $\tau_1 = 1\,\mu s$ at 1 GHz and a 1 kpc effective distance. The corresponding arrival time fluctuations have the same spectral form,

$$S_{t_{\rm DM}}(f) = (K_{\rm DM}/\nu^2)^2 S_{\rm DM}(f) \simeq \frac{(0.319\,\mu{\rm s})^2}{\rm cy\ yr^{-1}}\left(\frac{\tau_1/1\,\mu{\rm s}}{d'/1\,{\rm kpc}}\right)^{5/6} v_{100}^{5/3}\,\nu^{-4} f^{-8/3} \tag{12.3}$$

where $K_{\rm DM} = cr_{\rm e}/2\pi \simeq 4149\,\mu s$ for standard DM units. Note that these expressions do not include a rolloff at high fluctuation frequencies due to scattering-cone averaging. Rolloff is discussed in §15.3.

12.1.1. *Pulse frequency variations*

Though pulse phase and arrival times are the usual focus of timing analyses, the effects of DM(t) on pulse frequency can also be considered (Armstrong 1984; Jenet et al. 2011). The variation in pulse phase, $\delta\phi_{\rm pulse} = \delta t/P$, corresponds to a change in pulse frequency $\delta f_{\rm pulse} = d\delta\phi_{\rm pulse}/dt$ and a fractional change in pulse frequency $y \equiv \delta f_{\rm pulse}/f_{\rm pulse} = (cr_{\rm e}/2\pi\nu^2)(d{\rm DM}/dt)$. The power spectrum of y is related to the DM spectrum by use of the Fourier derivative theorem,

$$S_y(y) = (cr_{\rm e})^2\nu^{-4} f^2 S_{\rm DM}(f). \tag{12.4}$$

For the inertial subrange of a Kolmogorov spectrum this gives

$$S_y(y) = \frac{\pi^{1/2}\Gamma(4/3)}{(2\pi)^{2/3}\Gamma(11/6)}\frac{(cr_{\rm e})^2}{\nu^4}{\rm SM}_{\rm eff}\, v_x^{5/3}\, f^{-2/3} \simeq \frac{(3.30\times10^{-10})^2}{\rm cy\ yr^{-1}} \times {\rm SM}_{\rm eff}\, v_x^{5/3}\, f^{-2/3}. \tag{12.5}$$

Jenet et al. (2011) discuss the effects of pulse-frequency variations on the detection of lightyear-wavelength gravitational waves. To a large extent these variations are removed when ToAs are referenced to infinite frequency using DM estimates at each epoch. However, this procedure is not perfect, yielding residual dispersive delays and thus pulse-frequency fluctuations. Jenet et al. (2011) compare the residual spectrum with other cases where all but 0.1% or 1% of the fluctuations in y are removed.

12.1.2. *ToA error from asynchronous frequency sampling of DM delays*

One cause for imperfect removal of dispersion delays is the estimation of DM(t) from multifrequency ToAs obtained at slightly different epochs (Lam et al. 2015).

First consider arrival times made at a single frequency (strictly, using a narrowband system at some center frequency ν) that is corrected for the dispersion delay using a DM value from an unspecified procedure. If a timing precision of σ_t μs is needed at frequency ν, the required precision for DM is $\delta\mathrm{DM} \lesssim \sigma_t\,\nu^2/K_{\mathrm{DM}} \simeq 2.41\times10^{-4}\,\mathrm{pc\ cm^{-3}} \times \nu^2\sigma_t(\mu\mathrm{s})$ **with ν in GHz here and elsewhere in this section.** The requirement is more stringent at lower frequencies. Inspection of Fig. 31 for J1909-3744 and of the DM time series for another 66 pulsars in Agazie et al. (2023a) and in papers for other PTA groups cited earlier indicates that DM estimation errors for the best pulsars satisfy this requirement but high DM pulsars at low frequencies may not, such as MSPs observed with LOFAR (Donner et al. 2020). More widely spaced frequencies yield higher DM precision, all else being equal, but the measurements need to be made at closely spaced epochs. That has been problematic for some observing programs because telescope logistics can require changes in instrumentation that span several days. Widely spaced receiver bands used for instantaneous wide frequency coverage at some observatories and wideband receiver systems now being deployed with continuous coverage over $\gtrsim 3:1$ frequency ranges **(i.e. highest to lowest frequencies in the receiver band)** provide the needed simultaneous measurements and obviate the problem.

Legacy data, however, retain the issues associated with non-simultaneous dual-frequency measurements. The consequences are easily estimated from the DM structure function. Lam et al. (2015) analyzed the effects of dual frequency measurements $(\nu_{\mathrm{l}}, \nu_{\mathrm{h}})$ made asynchronously at epochs $t_{1,2}$ spread by a day or more. The ToA at each frequency and epoch is modeled as $t_\nu = t_\infty + \nu^{-2}K_{\mathrm{DM}}\mathrm{DM}(t)$ where (for now) we ignore other contributions. Estimating DM as if it were constant yields

$$\widehat{\mathrm{DM}} = \frac{\nu_{\mathrm{l}}^{-2}\mathrm{DM}(t_1) - \nu_{\mathrm{h}}^{-2}\mathrm{DM}(t_2)}{\nu_{\mathrm{l}}^{-2} - \nu_{\mathrm{h}}^{-2}} = \frac{R^2\mathrm{DM}(t_1) - \mathrm{DM}(t_2)}{R^2-1}, \tag{12.6}$$

where $\widehat{\mathrm{DM}}$ is the estimated DM and $R \equiv \nu_{\mathrm{h}}/\nu_{\mathrm{l}}$ is the frequency ratio. When used to estimate the DM-corrected ToA, $\widehat{t}_\infty = t_{\nu_{\mathrm{h}}} - K_{\mathrm{DM}}\nu_{\mathrm{h}}^{-2}\widehat{\mathrm{DM}}$, the DM difference $\Delta\mathrm{DM}(t_1,t_2) = \mathrm{DM}(t_2) - \mathrm{DM}(t_1)$ yields a ToA error,

$$\delta t_\infty = \frac{K_{\mathrm{DM}}}{\nu_{\mathrm{h}}^2}\left(\frac{R^2}{R^2-1}\right)\Delta\mathrm{DM}(t_1,t_2). \tag{12.7}$$

The RMS δt_∞ is then written in terms of the DM structure function,

$$\sigma_{\delta t_\infty}(\Delta t) = \frac{K_{\mathrm{DM}}}{\nu_{\mathrm{h}}^2}\left(\frac{R^2}{R^2-1}\right)D_{\mathrm{DM}}^{1/2}(\Delta t). \tag{12.8}$$

We ignore the contribution from a linear variation in DM associated with the change in distance from a pulsar's motion. This is easier to identify and remove than the stochastic variations. Using previous expressions, we write the RMS ToA error for a Kolmogorov medium (inertial subrange scaling) as

$$\sigma_{\delta t_\infty}(\Delta t) = \left(\frac{R^2}{R^2-1}\right) \times \begin{cases} \dfrac{23.7\,\mathrm{ns}}{\nu_{\mathrm{h}}^2}\left(\dfrac{\mathrm{SM_{eff}}}{10^{-3.5}\ \mathrm{kpc\ m^{-20/3}}}\right)^{1/2}\left(\dfrac{\mathbf{v}_{p_\perp}}{100\ \mathrm{km\ s^{-1}}}\right)^{5/6}\Delta t_{\mathrm{days}}^{5/6} \\ \qquad \text{or} \\ \dfrac{6.54\,\mathrm{ns}}{\nu_{\mathrm{h}}}\left[\dfrac{\Delta t_{\mathrm{days}}}{\Delta t_{\mathrm{DISS}}(\nu_{\mathrm{h}})/10^3\,\mathrm{s}}\right]^{5/6}, \end{cases} \tag{12.9}$$

where units are shown explicitly (except for frequency, which is in GHz. The second form uses the relation of $D_{\rm DM}$ to the phase SF, $D_{\rm DM}(\tau) = (\lambda r_{\rm e})^{-2} D_\phi(\mathrm{v}_\perp \tau)$, and the connection of the scintillation time scale $\Delta t_{\rm DISS}$ to the spatial scale $\mathrm{v}_{\rm eff}\Delta t_{\rm ISS}$ where $D_\phi(\mathrm{v}_{\rm eff}\Delta t_{\rm DISS}) = 1\,\mathrm{rad}^2$. We have used $\Delta t_{\rm DISS}$ measured at the higher frequency $\nu_{\rm h}$ and expressed it in units of 10^3 s, a representative value for a low-DM pulsar. If an ancillary measurement of $\Delta t_{\rm DISS}$ at a frequency $\nu_{\rm ISS}$ is used instead, then $\Delta t_{\rm DISS}(\nu_{\rm h})$ in Eq. (12.9) is replaced by $\nu_{\rm h}\nu_{\rm ISS}^{-2/(\beta-2)}\Delta t_{\rm DISS}(\nu_{\rm ISS}) = \nu_{\rm h}\nu_{\rm ISS}^{-6/5}\Delta t_{\rm DISS}(\nu_{\rm ISS})$ for $\beta = 11/3$.

12.2. *Chromatic DM variations* [DM(ν)]

Dispersion measures are usually defined as simple LoS integrals of the electron density along a single propagation path, which yields the deterministic ν^{-2} dependence for the resulting timing delay. Measured DM values are actually chromatic because multipath propagation like that illustrated in Fig. 35 is strongly frequency dependent. The DM differs between ray paths and as the geometry changes with epoch, the collective DM varies. The time scale for such variations is the time needed for the bundle of ray paths to move by an amount equal to its width, which is the same as the RISS time scale. As a consequence, the frequency dependence of the ray bundle's transverse extent causes the DM at any epoch to also vary with frequency.

The DM(ν) effect is intermixed with chromatic variations of the average emitted pulse shape, making it difficult to isolate. However evidence for it has been reported (e.g. Cordes et al. 1990; Ramachandran et al. 2006; Donner et al. 2019; Kaur et al. 2022).

The differential DM between propagation paths results from variations in electron densities and *not* from the different physical path lengths. The latter dominate the scattering time (pulse broadening time) τ described earlier, which is typically much less than a second for most pulsars at radio frequencies ~ 1 to 2 GHz used for precision timing. The associated DM increment from $\lesssim 1$ light second of extra path length is $\overline{n}_{\rm e}c \sim 10^9$ cm^{-2} for $\overline{n}_{\rm e} = 0.03$ cm^{-3}, or a negligible $\delta\mathrm{DM} \sim 3\times10^{-10}$ pc cm^{-3}.

The frequency dependence of the DM (Cordes et al. 2016, hereafter CSS16) results from spatial averaging of ray paths caused by scattering. At observation frequency ν and location $\mathbf{x}$, the DM is the LoS integral of the convolution of a smoothing function $A_\nu(\mathbf{x}, z)$ with the electron density,

$$\overline{\mathrm{DM}}(\nu, \mathbf{x}) = \langle \mathrm{DM}(\mathbf{x})\rangle + \int_0^D dz' \int_{-\infty}^{\infty} d\mathbf{x}'\, A_\nu(\mathbf{x}', z')\delta n_{\rm e}(\mathbf{x}', z'), \tag{12.10}$$

where the frequency-independent term $\langle \mathrm{DM}(\mathbf{x})\rangle$ is the ensemble average (denoted by angular brackets) of the integrated electron density $\overline{n}_{\rm e}$. The appropriate smoothing function has a z-dependent, 2D area corresponding to the transverse cross section of the ray bundle. The scattered image seen by an observer can be used as a starting point but defining $A_\nu(\mathbf{x})$ requires knowledge of the strength of scattering vs. z. The image shape is also a function of the type of medium. In the following we drop the $\mathbf{x}$ dependence on $\overline{\mathrm{DM}}$ and consider integrals centered on only a single position for calculating $\overline{\mathrm{DM}}$ at a particular epoch.

12.2.1. *Two-frequency DM difference*

Cordes et al. (2016) analyzed the consequences for timing errors based on dual-frequency measurements for estimating DM and considered wideband cases using a numerical approach. After summarizing those results we present a new analysis for measurements over arbitrarily wide bands, which are more in concert with modern timing programs.

The calculation for the two-frequency case proceeds similarly to the treatment of asynchronous sampling in Sect. 12.1.2. When the DM is estimated from ToAs obtained at two widely separated frequencies, the measured ToA includes an error ϵ_ν (from radiometer noise, intrinsic pulse jitter, and DISS),

$$t_\nu = t_\infty + K_{\rm DM}\nu^{-2}\overline{\mathrm{DM}}(\nu) + \epsilon_\nu. \tag{12.11}$$

If DM is assumed to be frequency independent, the ToAs at two spot frequencies $\nu_\mathrm{l} < \nu_\mathrm{h}$ measured simultaneously (or nearly so, i.e. within a few hours to a day) yield,

$$\widehat{\mathrm{DM}} = \frac{t_{\nu_\mathrm{l}} - t_{\nu_\mathrm{h}}}{K_\mathrm{DM}({\nu_\mathrm{l}}^{-2} - {\nu_\mathrm{h}}^{-2})}, \tag{12.12}$$

and an estimate for t_∞ and its error,

$$\widehat{t}_\infty = t_{\nu_\mathrm{h}} - \frac{K_\mathrm{DM}\widehat{\mathrm{DM}}}{{\nu_\mathrm{h}}^2} = \frac{R^2 t_{\nu_\mathrm{h}} - t_{\nu_\mathrm{l}}}{R^2 - 1}, \qquad \delta\hat{t}_\infty \equiv \widehat{t}_\infty - t_\infty = \frac{R^2 \epsilon_{\nu_\mathrm{h}} - \epsilon_{\nu_\mathrm{l}}}{R^2 - 1}, \tag{12.13}$$

where $R \equiv \nu_\mathrm{h}/\nu_\mathrm{l}$ (as before). The error diverges as $R \to 1$ and the error in the high-frequency ToA dominates the overall error for a large frequency ratio.

An illustration of the mis-estimation of arrival times is shown schematically in Fig. 49 for ToA measurements at the two spot frequencies ν_l and ν_h on two separate dispersion curves (black points on the two solid lines). For this figure we ignore the effects from additive noise ϵ_ν to focus on the systematic error. The estimated dispersion measure $\widehat{\mathrm{DM}}$ yields a dispersion curve that connects the two black points and extrapolates to an incorrect $\widehat{t}_\infty \neq t_\infty$ as shown.

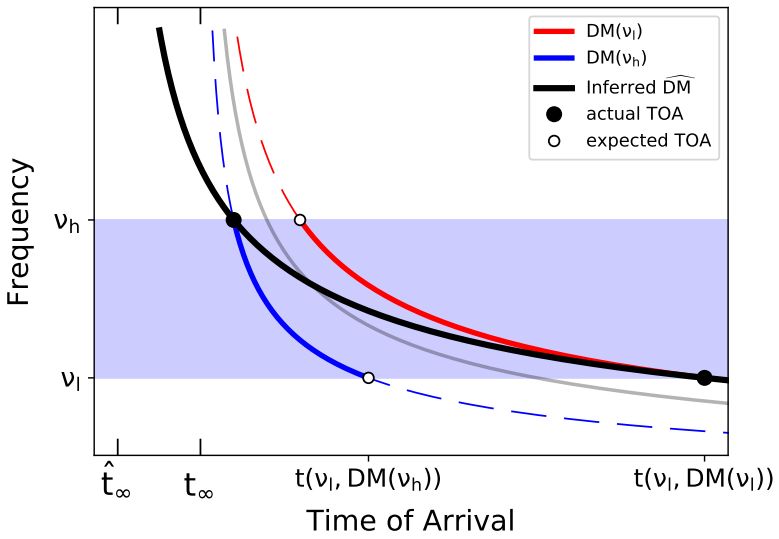


Figure 49. Illustration of the error in the dedispersed arrival time. Arrival times at two spot frequencies $\nu_\mathrm{l}, \nu_\mathrm{h}$ (filled black circles) are delayed by different dispersion measures, $\mathrm{DM}(\nu_\mathrm{l})$ and $\mathrm{DM}(\nu_\mathrm{h})$ (blue and red, respectively). Estimation of an assumed frequency-independent $\widehat{\mathrm{DM}}$ (black curve) then leads to an incorrect infinite frequency arrival time, $\widehat{t}_\infty$, that is earlier than the true value, t_∞.

The frequency dependence of DM of course only alters the error to

$$\delta\hat{t}_\infty = \frac{K_\mathrm{DM}}{\nu^2}\left(\frac{R^2}{R^2-1}\right)\Delta\overline{\mathrm{DM}}(\nu_\mathrm{h}, \nu_\mathrm{l}) + \left(\frac{R^2\epsilon_{\nu_\mathrm{h}} - \epsilon_{\nu_\mathrm{l}}}{R^2-1}\right), \tag{12.14}$$

where $\Delta\overline{\mathrm{DM}}(\nu_\mathrm{h}, \nu_\mathrm{l}) = \overline{\mathrm{DM}}(\nu_\mathrm{h}) - \overline{\mathrm{DM}}(\nu_\mathrm{l})$.

12.2.2. *Wideband timing errors from chromatic DM variations*

The effects of chromatic DMs for wideband systems are obtained by averaging Eq. (12.10) over frequency and calculating the ensemble mean and variance of the result. This averaging takes into account that the ray bundle's cross

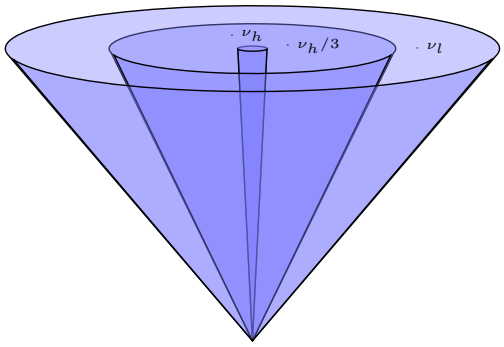


Figure 50. Scattering cones that illustrate spatial averaging of electron density variations at the highest and lowest frequencies, $\nu_{\rm h}$ and $\nu_{\rm l}$, and an intermediate frequency $\nu_{\rm h}/3$. The observer is at the apex and the tops of the cones represent cross-sectional areas in either the plane of a thin screen that scatters incident radiation or midway along the LoS in an extended medium. The diameters of the conal cross sections are shown to scale $\propto \nu^{-\beta/(\beta-2)} \propto \nu^{-11/5}$ for measurements that sample the inertial range of a Kolmogorov spectrum ($\beta = 11/3$).

section is a strong function of location along the line of sight, as illustrated in Fig. 50. It can also include the S/N vs. frequency through appropriate weighting. Here we summarize results derived in Appendix E.

The analysis yields the error in the *estimated* DM for measurements made over a frequency range $\nu_{\rm l}, \nu_{\rm h}$. Two cases are given: one with uniform coverage over the entire frequency range and another in the limit where two spot frequencies are used to estimate DM (as in the previous section). The results also can be applied to arbitrary variations of $\rm C_n^2$ along the LoS, including thin screens, finite-width slabs, or a uniform medium with $\rm C_n^2 =$ constant. We obtain

$$\sigma_{\overline{\rm DM}}(R,\nu_{\rm h}) = \left[{\rm Var}(\delta\widehat{\rm DM})\right]^{1/2} = G_\beta Q_\beta r_{\rm e} c^{\beta/2} d_{\rm so}^{(\beta-2)/2} \nu_{\rm h}^{-\beta/2}\, I_{\rm DM}^{1/2}(R,\beta)\,{\rm SM}, \tag{12.15}$$

$$\sigma_{t_\infty}(R,\nu_{\rm h}) = [{\rm Var}(t_\infty)]^{1/2} = \left(\frac{K_{\rm DM}}{\nu_{\rm h}^2}\right)\left[\frac{I_{t_\infty}(R,\beta)}{I_{\rm DM}(R,\beta)}\right]^{1/2} \sigma_{\overline{\rm DM}}(R,\nu_{\rm h}) \tag{12.16}$$

where we note that the values of these RMS quantities are referenced to the upper frequency, $\nu_{\rm h}$. The dependence on the frequency range used to estimate DM and t_∞ is contained in the quantities $I_{\rm DM}(R,\beta)$ and $I_{t_\infty}(R,\beta)$ using the frequency ratio $R = \nu_{\rm h}/\nu_{\rm l}$.

The dimensionless quantities I_{t_∞} and $I_{\rm DM}$ are integrals over dimensionless variables $r_{1,2} = \nu_{\rm h}/\nu_{1,2}$ are given by

$$I_{t_\infty}(R,\beta) = \left[\frac{R(R^3-1)}{(R-1)^4}\right]^2 \int_1^R\!\!\int_1^R dr_1 dr_2 \left[1 - \frac{3(R-1)r_1^2}{(R^3-1)}\right]\left[1 - \frac{3(R-1)r_2^2}{(R^3-1)}\right] \Phi_\beta^2(r_1,r_2), \tag{12.17}$$

and

$$I_{\rm DM}(R,\beta) = \left[\frac{3R}{(R-1)^3}\right]^2 \int_1^R\!\!\int_1^R dr_1 dr_2 \left(r_1^2/R - 1\right)\left(r_2^2/R - 1\right) \Phi_\beta^2(r_1,r_2), \tag{12.18}$$

where equal weighting over frequency has been used and

$$\Phi_\beta^2(r_1,r_2) = 2^{-(\beta-2)/2}[V_\beta(r_1) + V_\beta(r_2) - r_2^\beta V_\beta(r_1/r_2)] - 1 \tag{12.19}$$

with

$$V_\beta(x) \equiv [1 + x^{2\beta/(\beta-2)}]^{(\beta-2)/2}. \tag{12.20}$$

For two equally weighted spot frequencies these become

$$I_{t_\infty}(R,\beta) = I_{\rm DM}(R,\beta) = \left[\left(\frac{R^2}{R^2-1}\right) F_\beta(R)\right]^2, \tag{12.21}$$

which is obtained by using the identity $\Phi(x,x) = F_\beta(x)$, where F_β (first defined in CSS16) is

$$F_\beta(r) = \left\{ 2^{(4-\beta)/2} \left[1 + r^{2\beta/(\beta-2)} \right]^{(\beta-2)/2} - r^\beta - 1 \right\}^{1/2}. \tag{12.22}$$

The I_{t_∞} and $I_{\rm DM}$ integrals are shown in Fig. 51 for three values of β and for the wideband case (solid black lines) and the two-frequency case (dashed red lines). While the RMS quantities depend strongly on R, the ratio $I_{t_\infty}(R,\beta)/I_{\rm DM}(R,\beta)$ is less variable.

The factor Q_β depends on the index of the wavenumber spectrum, β,

$$Q_\beta = \frac{(\sqrt{2}\pi)^{4-\beta}\Gamma(2-\beta/2) f_\beta}{\beta - 2}, \tag{12.23}$$

where f_β is defined in Eq. (9.7). All of the line of sight dependence across the source-observer distance $d_{\rm so}$ is contained in G_β,

$$G_\beta^2 = H_\beta {\rm SM}_{\rm eff}/{\rm SM} \tag{12.24}$$

where ${\rm SM}_{\rm eff}$ and H_β involve LoS integrals of $C_{\rm n}^2$,

$$\frac{{\rm SM}_{\rm eff}}{\rm SM} = \frac{\int ds\, C_{\rm n}^2(s)(s/d_{\rm so})^{\beta-2}}{\int ds\, C_{\rm n}^2(s)}, \qquad H_\beta = \frac{\int ds\, C_{\rm n}^2(s)[h(s)]^{\beta-2}}{\int ds\, C_{\rm n}^2(s)}, \tag{12.25}$$

and $h(s)$ defines the width of the ray-path bundle along the LoS. Determination of $h(s)$ generally requires a numerical solution, but for a thin screen it is

$$h(s) = \begin{cases} \dfrac{s}{d_{\rm sl}}\left(1 - \dfrac{s}{d_{\rm so}}\right) & s \le d_{\rm sl}, \\ 1 - \dfrac{s}{d_{\rm so}} & s \ge d_{\rm sl}, \end{cases} \tag{12.26}$$

which has a value $h(d_{\rm sl}) = d_{\rm lo}/d_{\rm so}$ at the screen itself. For a uniform medium it is

$$h(s) = \frac{d_{\rm sl}}{d_{\rm so}}\left(1 - \frac{d_{\rm sl}}{d_{\rm so}}\right). \tag{12.27}$$

Evaluating for a Kolmogorov index $\beta = 11/3$ with a nominal scattering measure ${\rm SM} = 10^{-3.5}\,{\rm kpc\ m^{-20/3}} = 4.53 \times 10^4\,{\rm cm^{-17/3}}$, we obtain $Q_\beta \sim 22$ and

$$\sigma_{\delta t_\infty} = [{\rm Var}(\delta t_\infty)]^{1/2} = 156\,{\rm ns} \times G_\beta\, \nu_{\rm h}^{-23/6} d_{\rm so}^{5/6}\, {\rm SM}_{-3.5} I_{t_\infty}(R,\beta) \tag{12.28}$$

$$\sigma_{\widehat{\delta {\rm DM}}} = [{\rm Var}(\widehat{\delta {\rm DM}})]^{1/2} = 3.76 \times 10^{-5}\,{\rm pc\ cm^{-3}} \times G_\beta \nu_{\rm h}^{-11/6} d_{\rm so}^{5/6}\, {\rm SM}_{-3.5} I_{\rm DM}(R,\beta). \tag{12.29}$$

We note that the dependence on the upper frequency $\nu_{\rm h}$ for the excess DM variation is $\sigma_{\widehat{\delta {\rm DM}}} \propto \nu_{\rm h}^{-11/6}$ for a Kolmogorov spectrum (inertial subrange) while the ToA variation has a much stronger dependence, $\sigma_{\delta t_\infty} \propto \nu_{\rm h}^{-23/6}$. The actual ToA error also depends on the frequency ratio R and can be much smaller than the nominal values for a narrowband system, particularly if the upper frequency $\nu_{\rm h}$ is well above 1 GHz.

12.3. *Angle-of-arrival variations*

Structures in the ISM larger than the Fresnel scale $\sqrt{\lambda d'/2\pi} \approx 10^{11}$ cm refract radiation, causing the angle of arrival (AOA) to deviate from an assumed fiducial direction, which itself may differ from the true direction as defined by

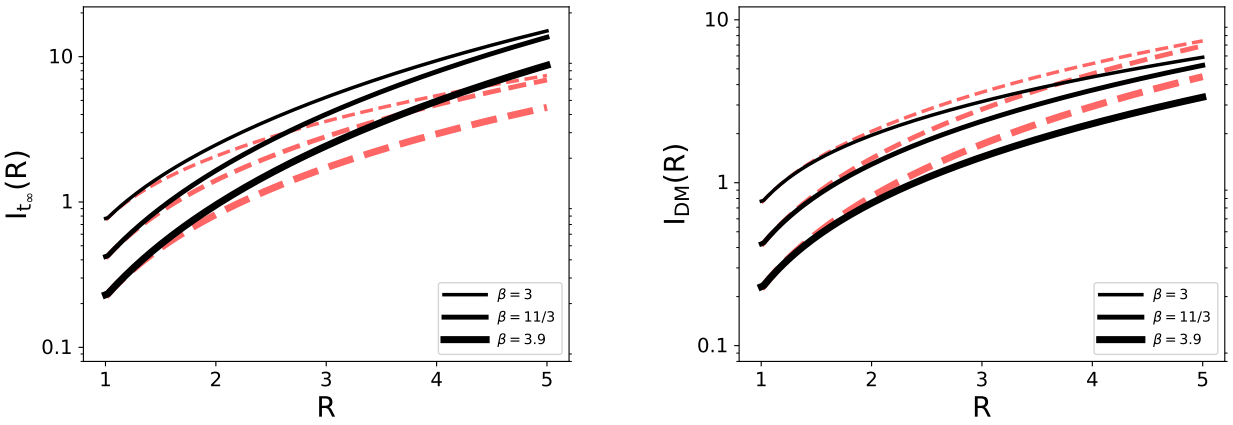


Figure 51. Plot of $I_{t_\infty}(R,\beta)$ and $I_{\rm DM}(R,\beta)$ vs. frequency ratio $R = \nu_{\rm h}/\nu_{\rm l}$ for three values of β. Solid lines: wideband case with equal weights using Eq. (12.17) - (12.18). Dashed lines: two-frequency cases using Eq. (12.21).

the vacuum geodesic. Assuming the topocentric and barycentric AoAs are the same (after accounting for aberration and Doppler shift from Earth's motion), pulses will arrive earlier or later than expected for the fiducial direction. Translation of topocentric ToAs to the solar system's barycenter (SSBC) involves accounting for the Römer delay (as well as other delays), $\Delta t_{\rm \ Römer} = \widehat{\mathbf{n}} \cdot \mathbf{r}_{\oplus}(t)$, where $\widehat{\mathbf{n}}$ is the pulsar direction and $\mathbf{r}_{\oplus}$ is the Earth-SSBC vector.

If the actual arrival direction differs from $\widehat{\mathbf{n}}$ by a refraction angle $\theta_{\rm r}$, the associated error in the ToA at the SSBC is

$$\Delta t_{\rm AOA} \approx \frac{1}{2c} d' {\theta_{\rm r}}^2 \approx 1.21\ \mu s\ d' {\theta_{\rm r}}^2 \tag{12.30}$$

for d' in kpc and $\theta_{\rm r}$ in mas. Values for $\theta_{\rm r}$ can be much smaller or much larger than a mas depending on the particular pulsar LoS and on frequency. The delay increases at lower frequencies as ν^{-4} if refraction is produced by a discrete cloud but scales as $\nu^{-49/15}$ for a Kolmogorov medium where ray averaging from diffraction alters the scaling. The first case scales similarly to the pulse broadening time and would be partially removed by a ToA fitting function designed to account for scattering. Less removal would occur for the second case.

The second effect associated with transformation of ToAs to the SSBC (Foster and Cordes 1990) is proportional to $\theta_{\rm r}$. Assuming a circular orbital frequency $\Omega_{\oplus}$, and defining the SSBC to Earth vector as $\mathbf{r}_{\oplus}$, and source direction $\widehat{\mathbf{n}}$, the offset is

$$\Delta t_{\rm AOA,SSBC} = c^{-1} \widehat{\mathbf{n}} \cdot \mathbf{r}_{\oplus}(t) \approx c^{-1} r_{\oplus} \theta_{\rm r}(t) \cos b_{\rm e} \cos \Omega_{\oplus}(t - t_p) \approx 2.4\ \mu s\, \theta_{\rm r}({\rm mas}) \cos {\rm b_e} \cos \Omega_{\oplus}({\rm t - t_p}), \tag{12.31}$$

where $r_{\oplus}/c \approx 500$ s. The eccentricity of the Earth's orbit ~ 0.017 implies additional harmonics in the ToA perturbation but these are smaller by powers of the eccentricity. This offset scales with frequency as ν^{-2} if a discrete cloud dominates refraction but refraction from a Kolmogorov medium yields an RMS variation $\theta_{\rm r}({\rm RMS}) \propto \nu^{-49/30}$.

12.4. *PBF stochasticity from nanoseconds to years*

PBFs vary on time scales of nanoseconds to years, depending on the integration time relative to various scattering and scintillation time scales. Fig. 52 shows three averaging regimes for PBFs defined analogously to scattered images (Narayan and Goodman 1989).

An averaging time shorter than the DISS time scale $\Delta t_{\rm d} \sim$minutes to hours yields a noisy PBF like those shown in Figs. 17 and 35. The noise pattern remains constant for averaging times $\ll \Delta t_{\rm d}$. Radio timing programs generally integrate over multiple DISS times, yielding a less noisy PBF that better reveals the envelope portion of the PBF. Even so, an epoch average is still subject to refractive distortion of the PBF by electron density variations much larger than diffraction scales. Only by averaging over many epochs should a PBF shape approximating an ensemble average

be expected. In principle, this would imply averaging times greater than the crossing time of the outer scale, which could be Myr for an outer scale $l_o \sim 100\,\mathrm{pc}$ (c.f. Fig. 33).

This long a time scale is of low relevance, however. First, for density fluctuations dominated by a Kolmogorov spectrum, refractive distortion is dominated by scales $\sim l_\mathrm{r} \ll l_o$, the 'refraction' scale applicable to RISS, which is of order the typical diameter $\sim$ au of the ray path bundle along which pulses propagate. Second, other structures exist in the ISM that superpose with Kolmogorov fluctuations and dominate refraction episodically with time scales of days to months (e.g. Rickett et al. 1984; Coles et al. 1987).

The range of random and systematic errors from scattering discussed in the next sections originate from the effects identified for the three regimes shown in the figure.

12.5. *Rapid stochasticity of PBFs and ToA noise*

Multipath effects on ToAs are dominated by changes in the PBF shape, which are both systematic and stochastic, and cause net changes in measured pulse profiles. These in turn cause mis-estimation of DM that further perturb estimates of DM-corrected ToAs.

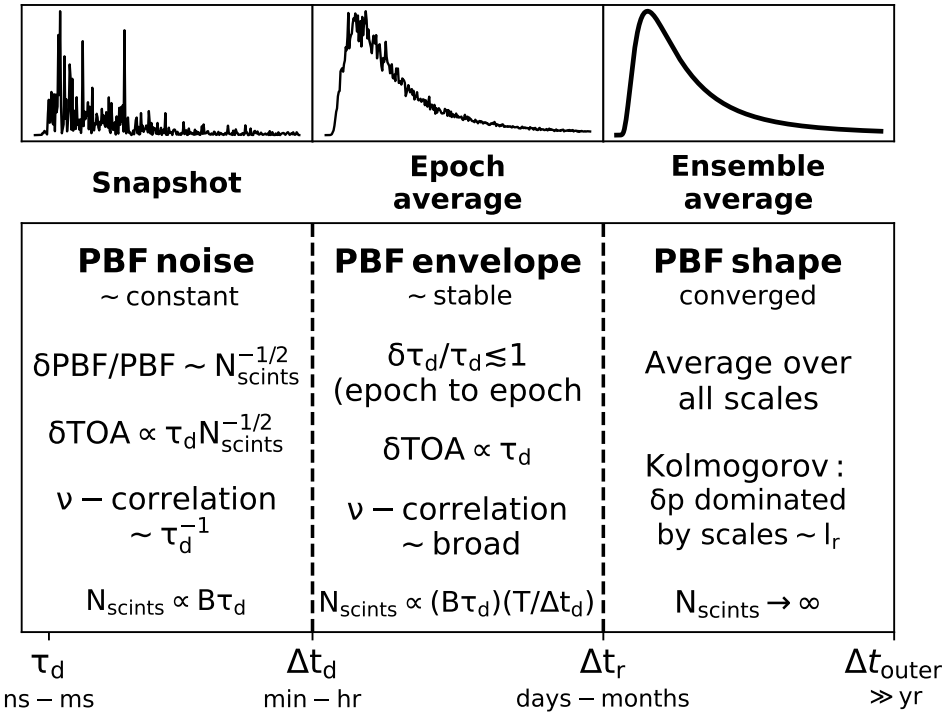


Figure 52. Averaging regimes for PBFs analogous to the description of snapshot and averaging regimes presented by Narayan and Goodman (1989) for scattered images. The snapshot case (left) corresponds to averages over less than a DISS time scale, Δt_d that include some number of scintles across frequency. An epoch average spans many scintillation times and includes many more scintles, producing a more stable PBF shape than for a snapshot. However, such averages are subject to distortions caused by refraction from larger density fluctuations than those that cause diffraction. Only by averaging over all refraction-induced PBF variations is the ensemble average PBF obtained. For a Kolmogorov spectrum, however, refraction is dominated by scales of order the refraction scale l_r defined earlier.

Scattered profiles are the convolution (denoted by an asterisk) of a scaled and time-shifted intrinsic pulse shape $I_{\rm i}(t) = aU(t - t_0)$ with the PBF,

$$I(t) = a\,U(t - t_0) * p(t, \tau) = a \int dt'\, U(t - t_0 - t')p(t', \tau), \tag{12.32}$$

where a is a linear scale factor and t_0 is the arrival time in the absence of scattering; we include an explicit argument τ as the characteristic $1/e$ time scale of the PBF.

The pulse broadening function is defined as the set of delays associated with multipath propagation through ionized gas. As such, it comprises geometrical path length differences caused by both diffraction and refraction. Stochasticity of the PBF, both short and long term, causes statistical perturbations of ToAs. On pulse-to-pulse time scales, the PBF follows the 'envelope × noise' form that yields a systematic delay from the envelope combined with a random error from PBF noise. For long integrations at a given epoch ($T \gg \Delta t_{\rm d}$) and a wide bandwidth ($B \gg \Delta\nu_{\rm d}$), many scintles are averaged over in the ToA estimate, diminishing but not eliminating the random error.

We discuss two consequences of PBF noise on arrival times. The first concerns induced variations in the effective center frequency of a measurement if dedispersion is not employed or if it is executed with an inaccurate DM value. The second TOA perturbation arises from the short-term variability of the PBF itself. Together, they illustrate the utility of using both the time and frequency domains in characterizing these propagation effects as well as mitigating them.

Both effects arise from the finite number of scintles in the time-frequency plane used to form a pulse profile and calculate an arrival time. For a total time T and bandwidth B, the number of scintles is approximately

$$N_{\rm scint} \equiv N_\nu N_{\rm t} \simeq (1 + \eta_\nu B/\Delta\nu_{\rm d})(1 + \eta_t T/\Delta t_{\rm d}), \tag{12.33}$$

where η_ν and η_t are filling factors for scintles with values ~ 0.2 to 0.4 that depend slightly on the medium and on radio frequency.

12.5.1. *Scintillation induced changes in effective center frequency*

Dedispersion removes delays $\propto {\rm DM}(\nu^{-2} - \nu_{\rm ref}^{-2})$ with respect to a specified reference frequency. No error in arrival time results if the correct value of DM is used. In some early timing analyses of long period pulsars (pre-1990s, e.g. Downs and Reichley 1983) differential dispersion delays across narrow receiver bands were considered small and no dedispersion was done. However, without dedispersion, diffractive intensity scintillations across the band shift the effective center frequency stochastically on a time scale equal to the scintillation time $\Delta t_{\rm d} \sim$ (minutes to hours), causing a variable dispersion delay. If a rectangular bandpass of bandwidth B contains a large number of scintles but is small enough so that the pulsar's intrinsic flux density and scintillation parameters are roughly constant, the effective center frequency shifts by $\Delta\nu_{\rm DISS}$ with an RMS value $\sigma_\nu = B/\sqrt{12 N_{\rm scint}}$. This yields an ensemble mean dispersion delay (for DM in pc cm^{-3} and ν in GHz) $t_\nu = (cr_e/2\pi\nu^2){\rm DM} \simeq 4.15\,{\rm ms}\,\nu^{-2}\,{\rm DM}$ and RMS fluctuations about the mean delay,

$$\sigma_{t_\nu} \approx \frac{dt_\nu}{d\nu}\sigma_\nu = \left(\frac{2\sigma_\nu}{\nu}\right) t_\nu \simeq 2.4\,{\rm ms}\left(\frac{B}{\nu}\right)\frac{\rm DM}{\sqrt{\nu^2 N_{\rm scint}}}. \tag{12.34}$$

Early timing measurements with fractional bandwidths $B/\nu \sim 10^{-3}$ on low-DM pulsars yielded small errors relative to other ToA errors. A counterexample where this scintillation effect dominated other errors is the bright Vela pulsar (e.g. Downs and Krause-Polstorff 1986).

Modern dedispersion methods (post-detection dedispersion with channelized intensities or coherent dedispersion), if done with an incorrect value of DM, will also yield (small) ToA errors from this effect. Post detection methods divide B into narrow channels with DM delays removed between channels. Intrachannel dispersion produces a TOA error given by replacing B in Eq. (12.34) with the channel width $\Delta\nu_{\rm c}$. If the DM used for dedispersion is in error, the TOA error is calculated by replacing DM with the DM error δDM. Such errors may arise due to interstellar variance in DM and usage of a non-contemporaneous value of DM in the dedispersion. DM errors are typically $< 10^{-3}$ pc cm^{-3}, so this will yield a small error $\lesssim 1\,\mu$s that adds to the larger error, $\delta t_\nu \propto \nu^{-2}\delta{\rm DM}$.

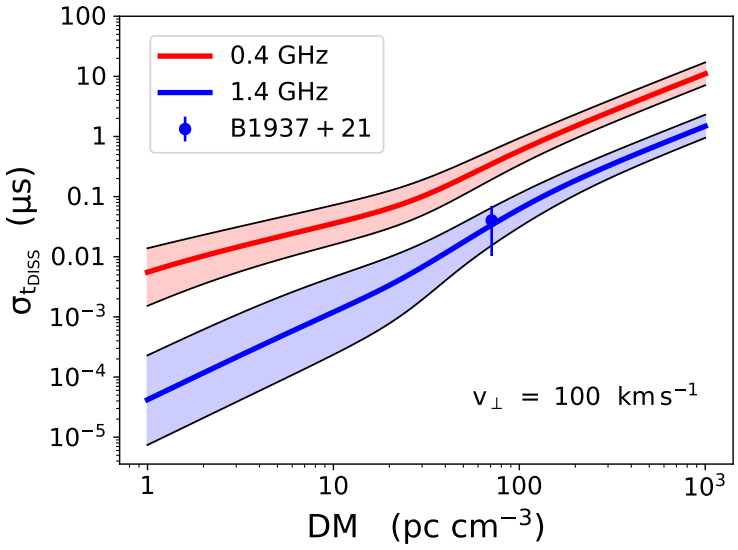


Figure 53. The RMS FSE error $\sigma_{t_{\rm DISS}}$ plotted vs. DM evaluated using the 'hockey stick' relation (Eq. (10.16)) to evaluate τ from DM and Eq. (12.38). with $B = 0.1\,$GHz. The black point (with 10× actual error) is from a timing analysis of the MSP B1937+21 that determined the DISS timing error by subtracting (in quadrature) the S/N and jitter timing errors (JMC, unpublished analysis).

12.5.2. *Rapid changes in PBF shape (the "finite scintle error" (FSE))*

The noise process in the PBF (c.f. Fig. 35) is due to the specific set of random path delays contributing to the measured wavefield, which also yield constructive and destructive interference across frequency.

For an integration time much less than the diffractive scintillation time, $T \ll \Delta t_{\rm d}$ the realization of PBF noise is approximately constant, so $N_{\rm t} = 1$; $\Delta t_{\rm d}$ can range from seconds (for heavily scattered pulsars with large transverse velocities) to hours and it introduces an arrival time error that varies on the same time scale. This regime corresponds to the set of inequalities,

$$\tau \ll T \ll \Delta t_{\rm d} \ll \Delta t_{\rm r}, \tag{12.35}$$

where $\Delta t_{\rm r}$ is the refraction time scale. A noisy PBF then typically corresponds to the presence of multiple scintles across the receiver bandwidth, often with $N_\nu \gg 1$.

The character of the noise process depends on the number of scintles N_ν in the bandwidth B. Heuristically, if the band is narrower than a scintle, $B \lesssim \Delta\nu_{\rm d}$ (e.g. for low-DM pulsars measured at high frequencies), the imposed phase variation across the band $\Delta\phi \lesssim 1\,$rad, yielding a group delay $\tau \sim \Delta\phi/2\pi B \lesssim 0.16\nu^{-1}\,$ns for B in GHz. When $N_\nu \gg 1$, the $\sim 1\,$rad phase gradient across each scintle gives a larger delay $\tau \sim 1/2\pi\Delta\nu_{\rm d} \sim 0.16 \times (1\,{\rm MHz}/\Delta\nu_{\rm d}), \mu$s. These delays are statistical with an average τ consistent with the uncertainty relation in Eq. (9.11).

For a scattered impulse, the ToA variance[35] from the finite number of scintles is formally given by (Appendix I) the integral over the (squared) PBF envelope (i.e. the ensemble average of the PBF, $\langle p(t)\rangle$) is,

$$\sigma^2_{t_{\rm DISS}}(\nu_0) \simeq B_{\rm eff}^{-1} \int dt\, t^2 \langle p(t;\nu_0)\rangle^2 \tag{12.36}$$

where the effective bandwidth is the integral $B_{\rm eff}^{-1} = \int d\nu\, |b(\nu)|^2$ over the squared field (voltage) bandpass function, $b(\nu)$, defined to have bandwidth B and unit area. For a rectangular bandpass, $B_{\rm eff} = B$.

[35] Note that the RMS FSE effect is denoted $\sigma_{t_{\rm DISS}}$ here but in other contexts we will use alternative notation, $\Delta t_{\rm DISS}$, $\Delta t_{\rm FSE}$, and $\Delta t_{\delta p}$, for convenience. This is indicated in Table 11.

For long integration times $T \gg \Delta t_{\rm d}$ (e.g. over an observing session $\sim 1\,$hr) over which the scintillation frequency structure changes and thus p varies, the net RMS delay involves an integral over the 2D intensity correlation function $\Gamma_I(\delta\nu, \tau)$. This correlation function can be calculated in closed form only for a square-law structure function but not for realistic media. The details are not of interest and so we use a heuristic approach in the following.

Each scintle contributes an RMS delay $\sim \tau$, corresponding to a phase change ~ 1 rad across $\Delta\nu_{\rm d}$; the integrated effect over $N_{\rm scint}$ scintles in the $B - T_{\rm int}$ plane yields an RMS time shift,

$$\sigma_{t_{\rm DISS}} \sim \tau/\sqrt{N_{\rm scint}}, \tag{12.37}$$

with $N_{\rm scint}$ given approximately by Eq. (12.33). For observations with moderate scattering that is determined by electron density fluctuations in the inertial subrange, we derive a simple scaling law by calculating $\Delta\nu_{\rm d}$ and $\Delta t_{\rm d}$ in terms of τ (c.f. Table 4). From $\tau \sim d'{\theta_{\rm d}}^2/2c$ we obtain $\Delta t_{\rm d} = l_{\rm d}/{\rm v}_{\rm eff} = \lambda/2\pi\theta_{\rm d}{\rm v}_{\rm eff}$ and $\Delta\nu_{\rm d} = C_1/2\pi\tau$. This gives

$$\sigma_{t_{\rm DISS}} \simeq \frac{[cd'\tau(\nu)]^{1/4}}{2\pi\sqrt{\eta_\nu \eta_t B T \nu v_{\rm eff}}} \simeq 0.052\,\mu s \times \frac{(d'\tau)^{1/4}}{\sqrt{(B_{0.1} T_3\, v_{100}\, \nu}} \propto \nu^{-8/5}, \tag{12.38}$$

where τ in μs is evaluated at ν in GHz, the bandwidth B is in units of 0.1 GHz, d' is in kpc, and the effective velocity $v_{\rm eff}$ is in units of $100\,{\rm km}^{-1}$.

Fig. 53 shows $\sigma_{t_{\rm DISS}}$ for two radio frequencies using the expression for τ(DM) in Eq. (10.16). We have approximated distances as $d' = ({\rm DM}/n_{\rm e})/(1 + {\rm DM}/1000\,{\rm pc\,cm^{-3}})$ with $n_{\rm e} = 0.03\,{\rm cm^{-3}}$. This empirical approach implies an asymptotic scaling for the ToA error, $\sigma_{t_{\rm DISS}} \propto \nu^{-4.9}{\rm DM}^{11/8}$.

We now present scaling laws for the RMS FSE timing variation $\sigma_{t_{\rm DISS}}$ for more general conditions. The scaling of $\sigma_{t_{\rm DISS}}$ with frequency depends on the scattering time τ along with the number of scintles included in the time-bandwidth product $(T \times B)$ of a timing measurement. The scaling law is different for the four cases where T and/or B are larger or smaller than the characteristic scintle size, i.e. whether $N_{\rm t}$ and/or N_ν are unity or much larger than unity. The scaling laws also depend on whether the scattering is strong or superstrong, which are defined, respectively, as whether scintillations are dominated by scattering from electron density length scales in the inertial subrange $l_i \ll l \ll l_o$, or by the inner scale. We obtain the scaling laws by using the relations between $\Delta\nu_{\rm d}$, $\theta_{\rm d}$, $\Delta t_{\rm d}$ and τ given just before Eq. (12.38) to calculate N_ν and $N_{\rm t}$ in terms of the scattering time τ. The frequency scaling of the scattering time is $\tau \propto \nu^{-X_\tau}$ with $X_\tau = 2\beta/(\beta - 2)$ in the inertial-subrange regime (as in Table 4) and $X_\tau = 4$ (independent of β) for hyperstrong scattering where the inertial scale of density fluctuations is the dominant scattering scale.

Table 5 gives frequency scaling laws for the different regimes for the frequency scaling law for $\Delta t_{\rm PBF} \propto \nu^{-X}$, which shows the dependence on the type of medium (β), whether the scattering is strong or superstrong, and on the bandwidth and integration time relative to the DISS bandwidth and time scale. We do not give a scaling law for the weak scattering regime where $N_{\rm t} = N_\nu = 1$ and $\tau \sim 1/2\pi\nu$ is negligible, typically less than a nanosecond.

In current PTA programs, the scattering strength is typically strong but not superstrong at the ~ 1 to 2 GHz frequencies used for observing low to moderate DM pulsars. Future work that makes more extensive use of sub-GHz frequencies and extends the pulsar sample to higher-DM fluctuations will encounter the superstrong regime. That will also be true for non-PTA timing studies of high-interest pulsars, such as those in the Galactic center.

12.6. *Slow stochasticity of PBF envelopes and ToA bias*

ToAs are often obtained using integration times and bandwidths encompassing a large number of scintles, which make the finite-scintle error subsidiary to other errors. Epoch to epoch, however, the PBF envelope could change through any inhomogeneity of the scattering strength, e.g. variations in scattering measure SM; this is unlikely on time scales of years given that SM is plausibly determined by ISM structures on large scales that might take centuries or more for lines of sight to cross. More likely is variable refraction from more rapidly crossed scales that alter the ray bundle as the LoS traverses the medium. Refraction associated with the density spectrum will cause changes on time scales similar to intensity variations from RISS, which varies on time scales of hours to days for pulsars that are weakly scattered (low DM and high ν measurements) and weeks to years for larger scattering (high DM , low ν). These time

Table 5. Scaling Laws for Finite Scintle ToA Error ($\sigma_{t_{\rm DISS}}$)

Regime	Scattering[a] strength	$\frac{T}{\Delta t_{\rm d}}$	$\frac{B}{\Delta\nu_{\rm d}}$	Frequency index X in ν^{-X}				
				X_τ	X_{N_t}	X_{N_ν}	$X_{\sigma_{t_{\rm DISS}}}$	$X^{\rm (Kol)}_{\sigma_{t_{\rm DISS}}}$
Low DM, high ν	strong	$\ll 1$	$\ll 1$	$\frac{2\beta}{\beta-2}$	0	0	$\frac{2\beta}{\beta-2}$	$\frac{22}{5}$
Low DM, high ν, high velocity v	strong	$\gg 1$	$\ll 1$	$\frac{2\beta}{\beta-2}$	$\frac{2}{\beta-2}$	0	$\frac{2\beta-1}{\beta-2}$	$\frac{19}{5}$
Moderate DM, low velocity v,	strong	$\ll 1$	$\gg 1$	$\frac{2\beta}{\beta-2}$	0	$\frac{2\beta}{\beta-2}$	$\frac{\beta}{\beta-2}$	$\frac{11}{5}$
Moderate-high DM, typical velocity v	strong	$\gg 1$	$\gg 1$	$\frac{2\beta}{\beta-2}$	$\frac{2}{\beta-2}$	$\frac{2\beta}{\beta-2}$	$\frac{\beta-1}{\beta-2}$	$\frac{8}{5}$
High DM, low ν, typical velocity v	superstrong	$\gg 1$	$\gg 1$	4	1	4	$\frac{3}{2}$	$\frac{3}{2}$

[a] *Strong scattering* corresponds to scaling laws applicable for the inertial subrange of the electron density spectrum. *Superstrong scattering* corresponds to scintillations dominated by the inner scale of the density spectrum.

scales differ substantially between different pulsars for the same ν-DM combinations due to differing effective velocities. Also, refraction from larger-scale structures ($\gtrsim$ AU) that superpose with stochastic density variations can yield much larger changes in PBFs.

Temporal variations in the PBF shape are also frequency dependent. Coupled with the chromaticity of intrinsic pulse shapes, the cumulative, non-dispersive arrival time variations have dependences on frequency that require a careful mitigation approach unique to each pulsar.

12.6.1. *Inapplicability of the 'mean-shift' scattering regime*

The stark difference between exponential and PL PBFs is demonstrated by considering the *mean-shift regime*. If the PBF is much narrower than the intrinsic pulse (width $W_{\rm u}$) for *all* times where the PBF contributes significantly to the convolution in Eq. (12.32), a first-order Taylor expansion of the intrinsic shape, $U(t-t'-t_0) \simeq U(t-t_0) + (dU(t-t_0)/dt)t'$ yields a scattered profile that is simply a shift of the intrinsic shape, $I_{\rm d}(t) \simeq aU(t-t_0-\langle t\rangle_p)$, where $\langle t\rangle_p = \int dt\, t\, p(t)$. For an exponential PBF with $\tau \ll W_{\rm u}$, the mean-shift regime applies. However, this deceptively simple result masks two issues. First, the mean shift $\langle t\rangle_p$ is not the same as the characteristic scattering time τ, as demonstrated in §12.6.2. Second, the linear expansion underlying the mean-shift breaks down for heavy-tailed PBFs[36] that extend well beyond the intrinsic pulse width.

Fig. 54 exhibits the biases that result from fitting with an exponential PBF when a power-law PDF actually applies. We simulated measured average profiles by numerically scattering an assumed Gaussian pulse as the emitted pulse using a heavy-tailed PBF like those shown in Sect. 11 for a Kolmogorov spectrum ($\beta = 11/3$) and a small inner scale (small ζ). Template fitting was then done using incorrect templates comprising a Gaussian pulse convolved with an

[36] 'Heavy tailed' means that the PBF is not exponentially bounded for a significant time range, though we emphasize that PBFs are exponentially bounded at very large times due to the inner scale of the medium.

exponential PBF. We show results for three different widths for the 'emitted' pulse to illustrate that the degree of bias depends on the widths of both the emitted pulse and the PBF.

The left panel shows the scattering time estimate $\widehat{\tau}_{\rm GE}$ for a Gaussian pulse scattered by a PBF with $\beta = 11/3$ and $\zeta = 0.01$. The arrival-time bias (right panel) depends on the kind of template used for estimating arrival times:

1. If scattering is ignored by usage of a Gaussian template (wide solid lines), the ratio of ToA to τ exceeds unity for small τ and declines to < 1 for larger τ. The ToA bias is larger for wider pulses.
2. If a G*E template (i.e. a Gaussian convolved with an exponential PBF) is used with scattering time fixed to the true value of τ (thin solid lines), the bias is smaller but shows the same trends as with a G-only template;
3. If τ is optimized with a G*E template, the ToA bias is *negative* (dashed lines).

The excess of the scattering time estimate over the true scattering time declines with larger τ and wider Gaussian pulses. While the ratio of ToA to τ asymptotes to zero for large τ, the ToA bias is still significant for values of τ encountered in many pulsar timing contexts. Lastly, the bias is expected to decrease for PBFs from media with $\beta \to 4$ or those for which scattering is dominated by a 'large' inner scale. We note that PTA measurements in the 1 to 2 GHz range on typically low to moderate DMs will involve heavy tailed PBFs like that used in the simulations.

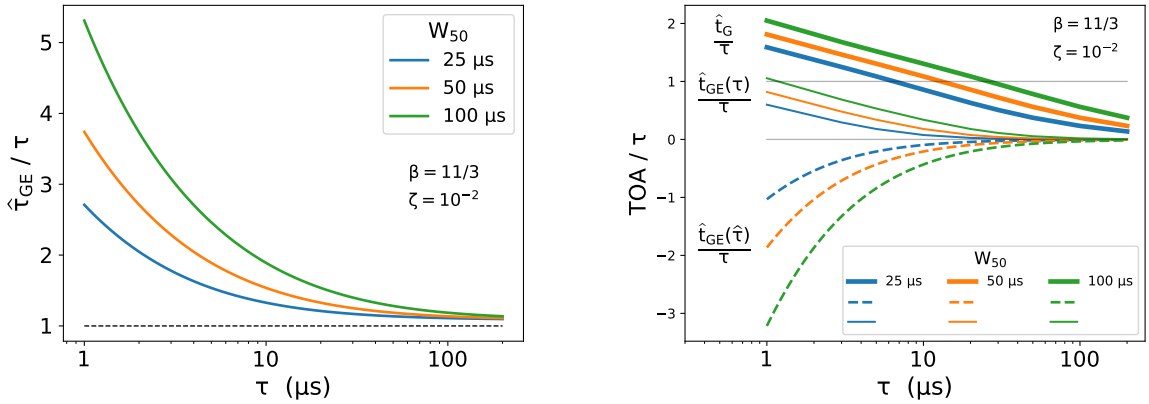


Figure 54. Bias of scattering time and arrival time estimates when exponential PBFs are used to fit Gaussian pulses scattered by a Kolmogorov medium ($\beta = 11/3$) with a small inner scale, $\zeta = 0.01$. The three Gaussian widths used are designated in the legend. Left: The ratio of estimated $\widehat{\tau}_{\rm G*E}$ to true scattering time τ for a G*E template applied to a G*PL pulse. The ratio decreases as the scattering time becomes a larger fraction of the Gaussian width W_{50}. Right: The ratio of ToA estimate to scattering time τ for three different pulse-fitting approaches and three different Gaussian widths; $\widehat{t}_{\rm G}$ is the ToA obtained with a Gaussian-only (G) template. $\widehat{t}_{\rm G*E}(\tau)$ is the ToA obtained with a G*E template with a scattering time fixed to the true scattering time; and $\widehat{t}_{\rm G*E}(\widehat{\tau})$ is the ToA obtained with a G*E template with an estimated scattering time $\widehat{\tau}$ that optimizes the pulse fitting (minimum mean-squared difference).

We conducted additional simulations to quantify how the mean-shift regime applies to (pseudo) data profiles that involve an exponential PBF but fails for those with PL PBFs. For one set of cases, we generated Gaussian emitted pulses scattered with an exponential PBF (G*E) but template fitted using only a Gaussian template (G). Other cases involve data profiles comprising Gaussian pulses convolved with a power-law PBF (G*PL) that are template fitted with either a G or a G*E template. We do not show results for a G*PL template because they would show zero bias.

Fig. 55 (left panel) shows the ratio $\widehat{t}/\tau$ plotted against $\tau/W_{\rm u}$ to indicate the degree of ToA bias associated with a particular template-fitting procedure. For the exponential PBF, the mean-shift regime can be seen to apply for $\tau/W_{\rm u} \ll 1$ where $\widehat{t}/\tau = 1$ (red curve in the left-hand panel). However, the mean-shift result is violated by the Kolmogorov cases (blue and green curves) which show $\widehat{t} > \tau$ for small $\tau/W_{\rm u}$. This discordance follows from the long tail of the Kolmogorov PBF when the inner scale is small (Sect. 11). For both kinds of PBF, $\widehat{t} < \tau$ by increasing

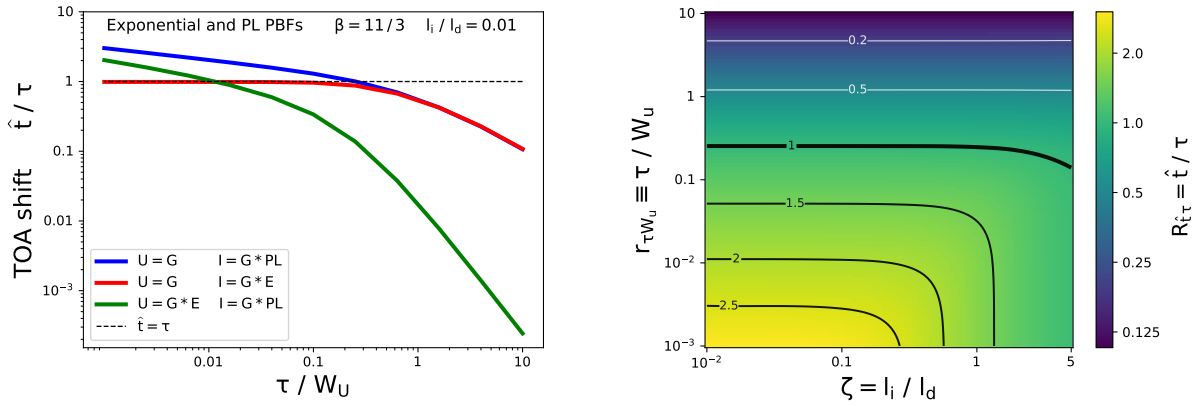


Figure 55. Simulated arrival time shifts resulting from template fitting of Gaussian pulses scattered by thin phase screens. Left: The normalized shift $\widehat{t}/\tau$ is plotted vs. $\tau/W_{\rm u}$, where $W_{\rm u}$ is the width (FWHM) of the assumed Gaussian pulse scattered by either an exponential PBF or a PBF from a power-law medium with $\beta = 11/3$ and a small inner scale, $\zeta = l_i/l_{\rm d} = 0.01$. The scattering time τ is the $1/e$ width for both kinds of PBF. The red curve is for a Gaussian-exponential pulse with a Gaussian template. The blue curve is for a power-law PBF convolved with a Gaussian that is also template fitted with the same Gaussian. The green curve results from the same pulse shape as for the blue curve but with a template comprising the Gaussian convolved with an exponential PBF having the same τ as the power-law PBF. For larger values of $l_i/l_{\rm d}$, the blue lowers to values asymptotically closer to unity for $\tau/W_{\rm u} \lesssim 0.1$. Right: Shift ratio $R_{\widehat{t}/\tau} = \widehat{t}/\tau$ vs. $\zeta = l_i/l_{\rm d}$ and $r_{\tau W_{\rm u}} = \widehat{\tau}/W_{\rm u}$, shown as pseudo color and contours with levels of $R_{\widehat{t}/\tau}$ marked.

amounts for $\tau/W_{\rm u} > 1$. This indicates that in most cases, the ToA shift differs from τ. The ISM yields epoch-dependent τ values, so any correction for variable PBF envelopes must take into account the ratio of τ to the intrinsic width. The trends shown here for a Gaussian pulse extend to arbitrary pulse shapes with finite widths. The right panel of Fig. 55 shows the bias in $\widehat{t}/\tau$ as a function of the normalized inner scale ζ along with $\tau/W_{\rm u}$.

In practice, ToAs are obtained over a wide frequency range for estimation and removal of chromatic propagation delays. These estimates are affected by the well known chromaticity of the scattering time, $\tau \propto \nu^{-x_\tau}$ with $x_\tau \sim 4$ but they are also affected by the non self-similar PBF shapes from the strong variation of the diffraction scale $l_{\rm d}$ with frequency, which alters $\zeta = l_i/l_{\rm d}$ and thus the PBF shape.

For a thin screen and strong scattering and using $l_{{\rm d}_\theta}$ (c.f. Table 4, item 6),

$$l_{{\rm d}_\theta} = \frac{1}{2\pi\nu}\left[\frac{cd'}{\tau(\nu)}\right]^{1/2} \simeq 1.53\times10^4\,{\rm km}\ \times\frac{1}{\nu}\left[\frac{{\rm d}'}{\tau(\nu)}\right]^{1/2} \tag{12.39}$$

for ν in GHz, d' in kpc, and τ in microseconds. Using Eq. (12.39) and $l_i = 10^3\,{\rm km}\,l_{i3}$,

$$\zeta \equiv \frac{l_i}{l_{{\rm d}_\theta}} \simeq 0.0653\times(\nu l_{i3})\left(\frac{\tau}{d'}\right)^{1/2}, \tag{12.40}$$

so $\zeta \ll 1$ and a heavy tailed PBF is expected for nominal values, which are relevant to most MSPs observed in PTA programs. For heavily scattered pulsars, $\zeta \gtrsim 1$ and the PBF can satisfy the requirements for the mean-shift regime because it tends toward an exponential form.

Table 6 shows the phase space for scattering corrections in terms of ζ and the ratio $\tau/W_{\rm u}$. For the mean-shift regime to apply (upper left quadrant in the table), the PBF must be exponentially bounded with the ratio $r_{\tau W_{\rm u}} = \tau/W_{\rm u} \ll 1$. A power-law medium with an asymptotically exponential PBF also requires $\zeta \gg 1$. Together, these two conditions constrain the scattering time to the range,

$$234\,\mu{\rm s}\times(\nu l_{i3})^{-2}d' \ \ll\tau\ll\ 10^3\,\mu{\rm s}\ \times W_{\rm u}. \tag{12.41}$$

The mean-shift regime applies to heavy scattering of pulsars with wide pulses. The other three quadrants require full pulse-shape modeling[37] or deconvolution of the PBF from measured pulses in timing analyses. One of these is the lower left quadrant applicable to the precision timing of MSPs for PTAs.

Table 6. Scattering Correction Phase Space

Inner scale regime	$r_{\tau W} = \tau/W_{\rm u}$	
$\zeta = l_i/l_{\rm d}$	$\ll 1$	$\gg 1$
$\zeta \gg 1$ ($l_{\rm d}$ small $\rightarrow$ τ large)	**Mean shift regime** $I(t) = aU(t - \langle t \rangle_p$ PBF $\rightarrow$ Exp Large DM, low ν Large $W_{\rm u}$ Large P pulsars, magnetars	**Modeling required** $I(t) = aU * p$ PBF $\longrightarrow$ Exp Large DM, low ν Small $W_{\rm u}$ Many pulsars
$\zeta \ll 1$ ($l_{\rm d}$ large $\rightarrow$ τ small)	**Modeling required** $I(t) = aU * p$ Heavy-tailed PL PBF Small DM, high ν Small to large $W_{\rm u}$ MSPs to magnetars Most PTA pulsar data	**Modeling required** $I(t) = aU * p$ Heavy-tailed PBF Small DM, high ν Very small $W_{\rm u}$ Microstructure, nanoshots

12.6.2. *Time delays from heavy tailed PBF envelopes*

The variety of PBF envelopes has implications for diagnosing and correcting arrival times for scattering delays. Here we make the important distinction between the *PBF delay*, the mean delay calculated by treating the PBF as a probability density function, and the *excess ToA* induced by the PBF through convolution with the intrinsic pulse shape. Generally they are not the same. We first discuss PBF delays and then analyze measureable ToA delays that are of greater importance to pulsar timing applications.

Arrival time delays caused by PBFs are generally smaller than the mean PBF.

Template fitting to obtain an arrival time estimate is equivalent to maximizing the cross correlation $C_{IU}(t)$ between the profile and template U,

$$\partial_t C_{IU}(\widehat{t}) = 0 \qquad \text{where} \qquad C_{IU}(t) = \int dt' U(t') I(t' + t - t_0), \tag{12.42}$$

Inspection of C_{IU} indicates that a template identical to the profile shape, $U \propto I$, yields an unbiased estimate $\widehat{t} = t_0$. However, the variability of interstellar effects and the also chromatic and sometimes variable intrinsic pulse shapes guarantee that this will rarely apply[38]. Whether departures of profile shapes from template shapes are important depends on the emitted pulse profile, on the ISM along the line of sight, and on the radio frequency. Low DM pulsars observed at high frequencies are less likely to manifest the consequences of pulse shape discrepancies. Given that timing programs cover increasingly wider frequency spans (especially to lower frequencies) and are likely to extend to higher-DM pulsars with more sensitive telescopes, shape mismatches are highly likely to be important in order to obtain the best timing precision.

[37] Note that a template that includes scattering, albeit with a fixed amount, will yield ToA errors due to epoch dependence of the scattering.

[38] X-and γ-ray timing are not affected by interstellar plasma propagation but profiles are energy dependent. Low energy X-ray pulses can be affected by scattering from interstellar grains as well as being absorbed. These effects are not expected to be epoch dependent, at least on time scales of years.

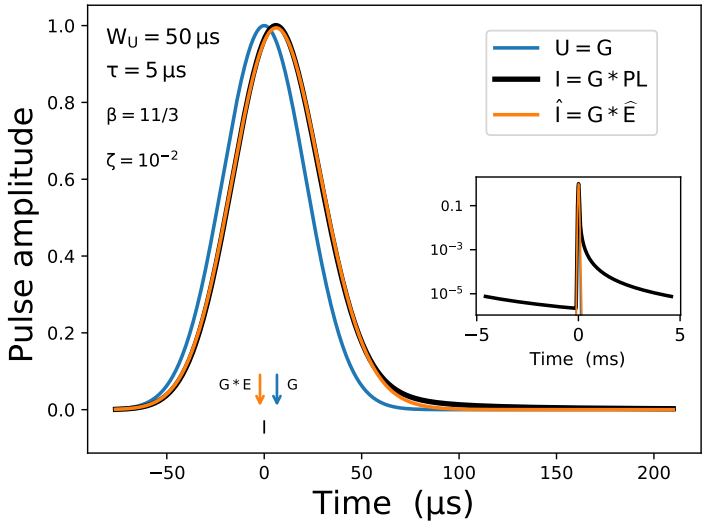


Figure 56. Fitting of scattered pulses and the resulting ToA offsets. The Gaussian intrinsic profile (blue) is scattered with a Kolmogorov PBF with $\zeta = 0.01$ (corresponding to an inner scale that is 1% of the diffraction scale, $l_{\rm d}$). The scattered profile (black) is fitted with a Gaussian (G) template that has the same width W_U as the intrinsic profile and it is also fitted with a template comprising a Gaussian convolved with an exponential PBF (G*E, orange); the exponential PBF has an e^{-1} scale that yields a best fit to the scattered profile. The true ToA in this case is zero but both templates lead to an error, as shown with the downward arrows. The G template yields a positive ToA error while the G*E template yields a negative ToA error. Inset: a zoom-in of the pulse on a log vertical scale that shows the long tail of the actual PBF, which would extend further than the 10 ms period of the simulated pulse but is truncated at one period.

Power-law media yield heavy-tailed PBFs and resulting delays that can be substantially larger than those expected from an exponential PBF, as shown in §11.2.

Fig. 56 shows an example Gaussian pulse scattered with a Kolmogorov PBF with a finite inner scale ($\zeta = 0.01$). The Gaussian width (FWHM) is 50 μs and the scattering time is $\tau = 5\,\mu s$. A perfect template (equal to the Gaussian convolved with the true PL PBF) would yield zero ToA for this example (black tick mark shown at the bottom of the figure). A Gaussian-only (G) template yields a positive ToA error of $6.53\,\mu s$ while a best fit using an exponential PBF convolved with a Gaussian (G*E) yields a negative ToA error of $-2.16\,\mu s$. The inset shows the wraparound of the long tail of the PBF. The scattered profile can be evaluated as the convolution of the intrinsic pulse over a single pulse period P with a synchronously averaged ('folded') PBF envelope given by

$$p_{\rm wrap}(t) = \sum_{m=0}^{M} p(t + mP). \tag{12.43}$$

Heavy tailed PBFs can extend beyond the $1/e$ time scale τ by many orders of magnitude. The multiplicative factor is $(2\pi/\zeta)^2 = (2\pi l_{\rm d}/l_i)^2 \gg 1$ for $\zeta \ll 1$. Even for low-DM pulsars with small $\tau = 10$ ns, the tail contributes significantly across the entire period of most MSPs, as demonstrated in the inset of Fig. 56.

Results for power-law PBFs are shown in Fig. 57 (left panel) for a Gaussian intrinsic pulse shape and a variable (e.g. with epoch) $\tau(\bar{t})$, giving $I = {\rm G} * {\rm PL}(\tau)$. A template comprising a Gaussian pulse and PBF with a fixed τ_0 $U = {\rm G} * {\rm PL}(\tau_0)$ yields systematic ToA offsets when scattering differs from that of the template (right panel). The different cases show that the ToA error depends on both the scattering time and the widths of the unscattered pulses and is positive or negative depending on the difference $\Delta\tau = \tau(\bar{t}) - \tau_0$.

12.6.3. *ToA shifts from scattering islands*

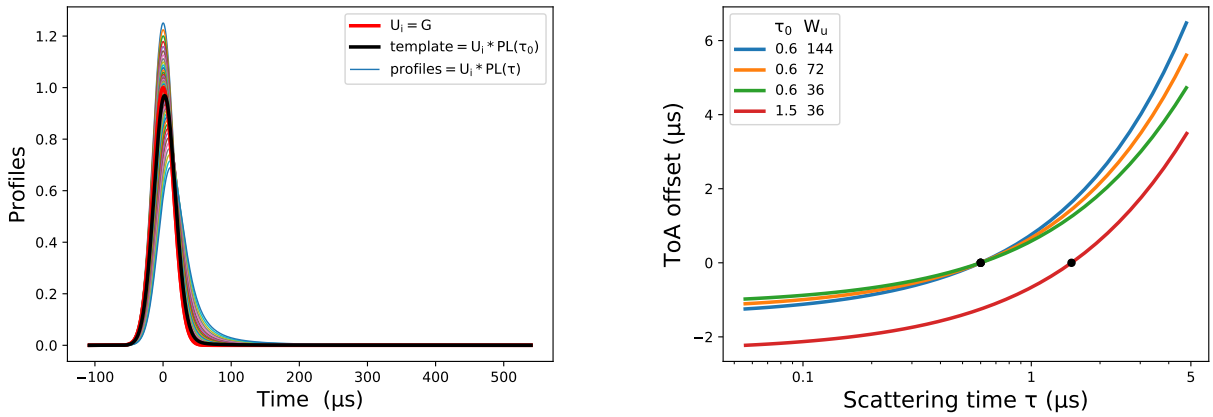


Figure 57. Arrival time analysis of scattered pulses using a fixed template. Left: Simulated scattered pulse profiles. The intrinsic shape is a Gaussian function with width (FWHM) $W_{\rm U} = 36\,\mu$s. The template equals the intrinsic shape convolved with a PBF with fixed $\tau_0 = 1.5\,\mu$s. The heavy-tailed PBF shape is for a thin screen having Kolmogorov fluctuations and small inner scale. Individual profiles are calculated with scattering times ranging from 0.1 to $10\times\tau_0$. Right: ToA offset vs scattering time when a template with fixed scattering time τ_0 is applied to profiles having a range of scattering times τ. The curves apply to different combinations of template width $W_{\rm U}$ and template scattering times, as indicated in the legend in μs. Black circles show the expected zero ToA offsets that result from identical profile and template scattering times.

The PBF envelopes utilized in the analysis of the previous section and that commonly appear in the literature (e.g. Lee and Jokipii 1975; Ostashov and Shishov 1978; Lambert and Rickett 1999) are highly idealized because they are based on simple scattering geometries and media. Refraction, truncated screens, and inhomogeneous scattering across screens (§11.4) present numerous types of departures from the simplest geometries, too many to make generalized conclusions. Instead we consider an alternate setup where multipath takes the form of multiple ($N_{\rm i}$) distinct images, each yielding a pulse that is a copy of the template.

The relevance of multiple image islands comes from studies of scintillation secondary spectra, which sometimes indicate the presence of two or more separate image patches (e.g. Hemberger and Stinebring 2008; Brisken et al. 2010). These typically comprise a dominant image combined with subimages with substantially less flux density. However, the corresponding pulses can arrive significantly later than the primary pulse. Here we assess how the strength of a subimage and its delay combine to influence the net arrival time.

The measured pulse is the superposition of a strong, primary pulse with unit amplitude and $N_{\rm i}$ weaker pulses with amplitudes $\epsilon_j \ll 1$ and delays Δ_j,

$$I(t) = U(t - t_0) + \sum_{j=0}^{N_{\rm i}-1} \epsilon_j U(t - t_0 - \Delta_j). \tag{12.44}$$

Template fitting with $U(t)$ gives a ToA offset from t_0 written in terms of the template's ACF, $R_U(\tau) \propto \int dt\, U(t)U(t+\tau)$,

$$\delta t_{\rm mult} \simeq \frac{\sum_j \epsilon_j R'_U(\Delta_j)}{R''_U(0) + \sum_j \epsilon_j R''_U(\Delta_j)} \quad \xrightarrow[W_{\rm a}=\text{width@ } 1/e]{\text{Gaussian}} \quad \sum_j \epsilon_j \Delta_j e^{-(\Delta_j/W_{\rm a})^2}, \tag{12.45}$$

where the final expression assumes a Gaussian pulse with width $W = W_{\rm a}/\sqrt{2}$ and that $\sum_j \epsilon_j R_U(\Delta_j) \ll 1$.

For a single extra image, the maximum offset is $\delta t_{\rm dual} \simeq \epsilon\Delta/e$ for $\Delta = W$ and the offset is zero if the two pulses coincide ($\Delta = 0$) or are far apart ($\Delta \gg W$). An example indicates the sensitivity to the presence of a weak secondary image. For $\Delta = W = 100\,\mu$s, $\delta t_{\rm dual} < 100\,$ns requires $\epsilon < 2.7\times10^{-3}$. On the other hand, a smaller separation $\Delta = 1\,\mu$s yields the same limit on $\delta t_{\rm dual}$ for a brighter secondary pulse with $\epsilon < 0.27$.

Extra subimages render additional stochasticity to PBF shapes that certainly require empirical characterization rather than textbook modeling. However, the stability of the PBF envelope over multiple epochs can help. Monitoring of pulsars indicates that scattering patches can persist for months or years (Hill et al. 2005) with smooth evolution of their structure.

12.6.4. *Implications for the frequency scaling of timing offsets from scattering*

Of interest here is the frequency scaling of systematic timing offsets for low-DM MSPs used in PTAs. Recall that if the actual scattering were from an exponential PBF and $\tau \ll W_{\rm u}$, the offset would be $\widehat{t} = \tau$. The left hand panel of Fig. 55 shows that the ToA offset $\widehat{t}/\tau > 1$ if scattering is from a heavy-tailed PBF and template fitting is done with an unscattered pulse shape[39]. The deviation from unity increases for smaller values of $r_{\tau W}$. For a specific pulsar, this corresponds to higher frequency measurements.

The ToA shifts shown in Fig. 55 (right panel) for different ζ values indicate that smaller values of $\tau/W_{\rm u}$ yield larger fractional ToA shifts $\widehat{t}/\tau$ and the largest ToA shifts are for $\zeta \lesssim 0.1$. This regime applies to nearly all of the MSPs used in PTAs. We also see for $\zeta \ll 1$ that $R_{\widehat{t}\tau} = \widehat{t}/\tau$ is nearly independent of ζ but depends systematically on $r_{\tau W}$ (e.g. blue line in the left panel of Fig. 55).

Frequency scaling: The net scaling law with frequency combines the scaling $\tau \propto \nu^{-x_\tau}$ with the scaling of $\widehat{t}/\tau$ with $\tau/W_{\rm u}$ when a Gaussian template is used. Numerically we find for $\tau/W_{\rm u} \ll 1$ that $\widehat{t}/\tau \propto (\tau/W_{\rm u})^{-x_{\widehat{t}\tau}}$ with $x_{\widehat{t}\tau} \simeq 0.168$ (blue curve in left panel of Fig. 55). Then $\widehat{t} \propto \nu^{-x_{\widehat{t}}}$ with $x_{\widehat{t}} = x_\tau(1 - x_{\widehat{t}\tau}) \simeq 3.66$ for $x_\tau = 2\beta/(\beta - 2) = 4.4$ for $\beta = 11/3$. For larger ratios $\tau/W_{\rm u} \gtrsim 1$, $x_{\widehat{t}\tau}$ increases as the blue curve steepens, yielding smaller $x_{\widehat{t}}$ and a shallower variation of $\widehat{t}$ with frequency. *The essential point is that the dependence of the ToA delay on frequency is weaker than that of the scattering time τ and it gets progressively weaker at lower frequencies.*

Scattering corrections: Improvement of arrival times can be implemented in two alternate ways. First is pulse-shape modeling (template fitting) that includes PBF effects in the templates used to obtain ToAs. The second approach obtains ToAs using a template that incorporates scattering incorrectly (via an incorrect τ or incorrect shape) but makes post-facto scattering corrections by using using appropriate terms in a ToA model. The latter approach is made problematic by chromatic PBFs that lead to non-trivial scalings of scattering-induced delays with frequency.

An example case is for an MSP with DM $= 10\,{\rm pc\ cm^{-3}}$ and scattering time $\tau \simeq 6.2\,{\rm ns}$ at 1 GHz estimated from the hockey-stick relation (Eq. (10.16)). This gives $\zeta \simeq 0.018\, l_{i3} \nu^{-6/5}$ for $\beta = 11/3$. Applying this scaling law to multifrequency observations spanning 0.4 to 2 GHz, we obtain ranges of 7:1 and 1200:1 for ζ and τ, respectively, which imply that profiles and ToAs would span two or more of the quadrants identified in Table 6. The degree to which dispersion and scattering delays are mitigated depends on how carefully systematic PBF envelope effects are dealt with (along with finite-scintle effects as well).

Singha et al. (2024) explored scattering corrections on simulated data using an exponential PBF and two alternative frequency scalings for the scattering time, $\tau \propto \nu^{-22/5}$ (the Kolmogorov inertial subrange value) and $\tau \propto \nu^{-4}$, which applies to a Kolmogorov medium with a large inner scale or to a monoscale medium with scales $a \gg l_{\rm d}$. In their study, scattered profiles generated over a wide frequency band yielded biased DM estimates when a template devoid of scattering was applied, as expected, given the positive time shifts imposed by the asymmetric PBF. Bias was eliminated when the template included scattering, also as expected. We note two issues with the approach used. First, it is inconsistent to use an exponential PBF and any frequency scaling other than $\tau \propto \nu^{-4}$. Second, while simulations showed that scattering imposed with an exponential PBF could be recovered by model fitting with an exponential PBF, application to actual pulses that include scattering by a heavy-tailed PBF would not recover the scattering, as we have shown in Sect. 12.6.2. The bias and enhanced random errors due to mismatch between model and actual PBFs is discussed further in the next section.

[39] There is also an offset if the template includes scattering with an exponential PBF.

12.7. *Systematic timing errors from mismatched templates and PBFs*

Removal of PBF-shape effects in ToA estimates raises several thorny issues. First, the epoch dependence of PBFs requires a template that has the PBF for each epoch 'baked in' if scattering delays are to be removed perfectly. Second, both the width and the shape of the PBF are chromatic. The PBF's characteristic width scales as the pulse broadening time $\tau \propto \nu^{-x_\tau}$ with $x_\tau \sim 4$. More importantly, its actual shape depends on frequency if the inner scale is finite and comparable to the diffraction scale $l_{\rm d}$ at any of the observation frequencies. This is more likely at lower frequencies given the scaling $l_{\rm d} \propto \nu^{2\beta/(\beta-2)} \propto \nu^{22/5}$ for the Kolmogorov inertial subrange. An optimal template therefore needs to be frequency dependent for this reason as well as to account for the chromaticity of the intrinsic pulse shape (Sect. 6.3). Third, while significant prior information is known about scaling laws of pulse broadening from the ISM, uncertainties in those scaling laws and the effects of variable refraction yield systematic errors in ToA estimates. The last conundrum is the desireability of using a template that is constant vs. epoch, which guarantees that mismatches with the true pulse shape at any epoch require post-fitting mitigation.

To assess systematic timing errors, we consider application of Eqs. (12.32)-(12.42) using model shapes $U_{\rm m}$ and $p_{\rm m}$ to form a profile model,

$$I_{\rm m}(t) = a_{\rm m} U_{\rm m}(t - t_{\rm m}) * p_{\rm m}(t, \tau_{\rm m}), \tag{12.46}$$

that is fitted to a measured data profile, where frequency dependences of all quantities are implicit.

Optimal TOA estimation requires fitting with $U_{\rm m} = U$ and $p_{\rm m} = p$, to obtain the correct ToA t_0, pulse broadening time τ, and pulse amplitude a to within uncertainties determined by additive noise[40]. However, both $U_{\rm m}$ and $p_{\rm m}$ will differ from the true shapes. In practice, this optimal situation is never realized due to imprecision in the knowledge of either U or p, largely caused by the chromaticity of intrinsic pulse shapes and the epoch dependence of PBFs.

Fitting with $U_{\rm m} \neq U$ or $p_{\rm m} \neq p$ yields systematic errors in arrival time and also in the scattering time $\tau_{\rm m}$. These errors propagate into the ToA estimate for t_∞ (c.f. Eqs. (3.3) and (12.11)) because multifrequency ToAs are used to estimate DM for extrapolation to infinite frequency and, ideally, there should be a similar extrapolation for scattering delays. As for characterization of the ISM using the scattering time, its scaling with frequency, $\tau_{\rm m} \propto \nu^{-\widehat{x}_\tau}$ is also highly affected by mismatches.

Various methods have been used to model intrinsic profile shapes on a pulsar-by-pulsar basis; they reduce but do not eliminate the difference between the true and modeled profile shapes at a specific frequency. One method adopts a model profile equal to a measured high frequency profile (minimally affected by scattering) convolved with a fixed-shape PBF (such as the one-sided exponential) with a scale parameter $\tau(\nu) \propto \nu^{-x_\tau}$ where x_τ is either fixed at some value or also included as a fitting parameter. This approach originated shortly after the discovery of pulsars and is summarized briefly in (Williamson 1972, and references therein) and analyzed in (Geyer and Karastergiou 2016). Given that the exponential PBF is unlikely to be an accurate representation of the true PBF in most cases, systematic errors should be expected not only in ToAs but also in τ and x_τ, as also discussed by (Geyer and Karastergiou 2016).

Fig. 58 shows the effects of mismatches on the scaling of scattering times with frequency. Simulated Gaussian pulses with different widths $W_{\rm u}$ are scattered with a heavy tailed PBF for a value $\zeta = 0.1$ at a reference frequency ν_0 and a scaling $\zeta(\nu) \propto \zeta \propto (\nu/\nu_0)^{-2/(\beta-2)}$. Fitting scattered pulses using an exponential PBF yields values of τ that deviate from true values by amounts that are frequency dependent. High frequency values for τ are biased high because the exponential PBF needs to be broader to accommodate the heavy tail of the 'true' PBF (left panel). The effect is exacerbated for larger $W_{\rm u}$. The implied scaling laws $\tau \propto \nu^{-x_\tau}$ have exponents (right panel) that are always smaller than the index of 4.4 if the correct PBF had been used.

Examples of shallow frequency scalings for τ (i.e. $x_\tau < 4$) include an average index $x_\tau \simeq 3.44 \pm 0.13$ (Löhmer et al. 2001) from an analysis of nine strongly scattered pulsars and $x_\tau \simeq 3.4 \pm 0.2$ for B1933+16 (Löhmer et al. 2004). A wide range of index values above, below, and consistent with $x_\tau = 4.4$ were reported by Lewandowski et al. (2013) while low-frequency observations at 118-180 MHz (Wu et al. 2023; Filothodoros et al. 2024) show shallow scalings.

[40] Actual uncertainties also include pulse jitter and the finite scintle effect, but for the sake of discussion in this section we ignore those distinct contributions.

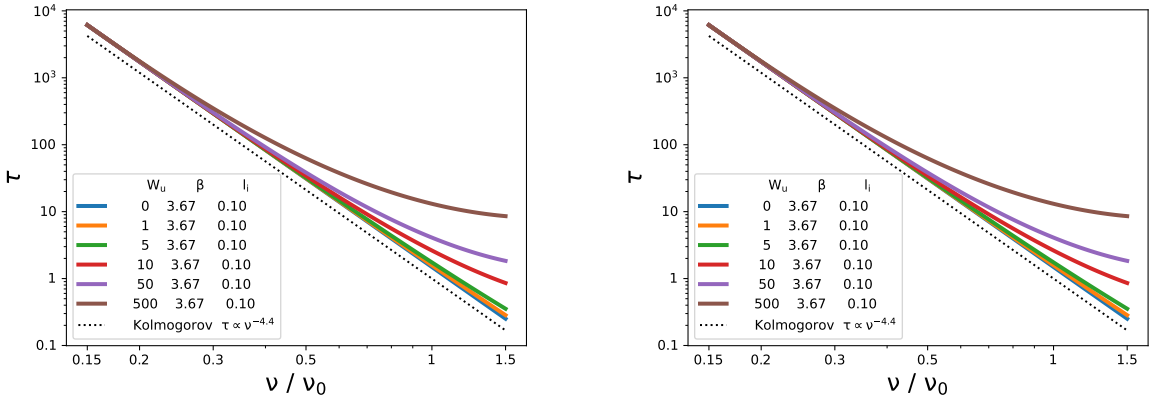


Figure 58. Effects of an incorrect PBF: Scaling of the estimated scattering time τ vs. frequency for power-law scattering with $\beta = 11/3$ and a small inner scale $l_i = 0.1$ in units where the diffraction scale $l_{\rm d_0} = 1$ at a reference frequency ν_0. The quantity $\zeta(\nu) = (l_i/l_{\rm d_0})(\nu/\nu_0)^{-2/(\beta-2)} \rightarrow \zeta_0(\nu/\nu_0)^{-6/5}$ increases with decreasing frequency, shortening the tail of the PBF. Left: $\tau(\nu)$ vs. ν showing curves for different intrinsic (unscattered) pulse widths $W_{\rm u}$ where τ (arbitrary units) is determined by model fitting the intrinsic shape scattered with an exponential PBF instead of the true power-law PBF. The dotted line shows the Kolmogorov scaling $\propto \nu^{-4.4}$ for the inertial subrange. Right: Exponent of the apparent scaling law $\tau(\nu) \propto \nu^{-x_\tau}$.

The overall tendency is for shallow scalings to be more prevalent for distant, high-DM pulsars observed at higher frequencies and for somewhat lower DMs observed at lower frequncies. This might suggest greater departures from a Kolmogorov spectrum for high-DM pulsars in the inner Galaxy but that cannot account for the shallow scalings for low-frequency observations. We are inclined to interpret many of these results as due to fitting bias ensuing from mismatches of adopted and actual PBFs and intrinsic profile shapes. Exponential PBFs used in all of these studies combined with chromaticity of intrinsic shapes will tend to yield underestimates of the true x_τ. In some cases, however, the underestimates may be real and caused by confinement of the dominant scattering region transverse to the LoS (Cordes and Lazio 2001) rather than being due to a genuine non-Kolmogorov scaling. This latter interpretation was applied to the scattering seen from J0826+2637 (Filothodoros et al. 2024; Wu et al. 2023). These authors also found that measurements of scintillation structure at higher frequencies yielded $x_\tau = 4.58 \pm 0.16$ (consistent with the Kolmogorov index $x_\tau = 4.4$) while pulse shape modeling for lower-frequency data using an exponential PBF and a Gasussian pulse shape yielded $x_\tau = 2.7 \pm 0.1$. This discordance could be due to transverse scattering confinement, as the authors concluded or it instead may simply be the result of fitting bias. A thorough discussion of scaling laws, fitting bias, and conclusions about the scattering properties of the ISM is deferred to another paper (in preparation).

13. CHROMATIC LEAKAGE INTO ACHROMATIC ARRIVAL TIMES AND RESIDUALS

The goals of most, though not all, timing analysis concern achromatic terms in arrival times, such as those due to gravitational waves or post-Newtonian terms in orbital motions of pulsars in binaries. For these applications chromatic plasma effects are a nuisance; however, for studies of Galactic structure of ionized gas and for probing very compact, discrete structures that underlie ESEs, they are a unique source of information.

Chromatic leakage into hoped-for achromatic timing residuals is inevitable. The overriding question is what is its amplitude relative to achromatic terms and whether they are mitigable. In this section, the removal of chromatic terms from arrival times is discussed with special attention paid to particular procedures that cause chromatic leakage.

To emphasize leakage effects, we re-visit some of the previous results. The barycentric ToA at frequency ν (where the delay and Doppler corrections to the topocentric TOA have been made) is expressed similarly to Eq. (12.11), but with the scattering-averaged DM delay combined with a lump chromatic term and excluding the error term ϵ_ν:

$$t_\nu = t_\infty + K_{\rm DM}\overline{\rm DM}(\bar{t},\nu)/\nu^2 + t_{\rm C}(\bar{t},\nu), \tag{13.1}$$

where the dependence on epoch $\bar{t}$ is shown explicitly.

We again consider ToAs obtained at two frequencies $\nu_{\rm l,h}$, with ratio $R \equiv \nu_{\rm h}/\nu_{\rm l} > 1$, and at two epochs $\bar{t}_{\rm l,h}$, respectively. These are the center frequencies of two well separated (non-overlapping) bands. Then $\widehat{\rm DM}$ is calculated under the false assumption that DM is constant and that the $t_{\rm C}$ terms are absent. The achromatic ToA is estimated as $\widehat{t}_\infty = t_{\nu_{\rm h}} - {\nu_{\rm h}}^{-2} K_{\rm DM} \widehat{\rm DM}$, which is in error by an amount,

$$\delta\hat{t}_\infty = t_\infty - \widehat{t}_\infty = + \frac{K_{\rm DM}}{{\nu_{\rm h}}^2} \left(\frac{R^2}{R^2 - 1} \right) \Delta\overline{\rm DM}_{1,2} + \frac{t_{\rm C1} - R^2 t_{\rm C2}}{R^2 - 1}, \tag{13.2}$$

where the simplified notation uses $\overline{\rm DM}_1 \equiv \overline{\rm DM}(\bar{t}_{\rm l}, \nu_{\rm l})$, $t_{\rm C1} = t_{\rm C}(\bar{t}_{\rm l}, \nu_{\rm l})$ etc. and defines $\Delta\overline{\rm DM}_{1,2} = \overline{\rm DM}_1 - \overline{\rm DM}_2$. Ideally $\delta\hat{t}_\infty = 0$ but the assumptions underlying Eq. (13.2) lead to non-zero residuals with superposed terms having different fluctuation statistics, including several lumped together into $t_{\rm C}$.

Contributions from DM stochasticity: Variations vs. both epoch and frequency (c.f. Sect. 12.1-12.2) yield chromatic errors in $\widehat{t}_\infty$:

1. *Asynchronous arrival times:* The epoch dependence of DM alone (without frequency dependence or contributions from $t_{\rm C}$) yields a chromatic error when two epochs are used to calculate DM. Using the DM structure function $D_{\rm DM}(\Delta t) \propto (\Delta t)^{\beta-2}$ (in the inertial subrange for the ISM),

$$\sigma_{t_\infty,{\rm DM}(t)} = \frac{K_{\rm DM}}{\nu_{\rm h}} \left(\frac{R^2}{R^2 - 1} \right) D_{\rm DM}^{1/2}(\bar{t}_{\rm h} - \bar{t}_{\rm l}). \tag{13.3}$$

   This contribution vanishes of course when observations are at the same epoch[41].

2. *Frequency dependent DM:* Now including DM chromaticity, same epoch observations ($\bar{t}_{\rm l} = \bar{t}_{\rm h} = \bar{t}$) give a contribution

$$\sigma_{t_\infty,{\rm DM}(\nu)} = \frac{K_{\rm DM}}{\nu_{\rm h}} \left(\frac{R^2}{R^2 - 1} \right) D_{\rm DM}^{1/2}(0, \nu_{\rm l}, \nu_{\rm h}). \tag{13.4}$$

Contributions from interstellar refraction and diffraction: The summed contributions to $t_{\rm C}(\bar{t}, \nu) = \sum_j t_{{\rm C}j}(\bar{t}, \nu)$ include random, zero-mean and systematic biases that arise from interstellar refraction and diffraction. The chromaticity of emitted pulses ('profile evolution') also contributes but is not explicitly quantified here. The different terms have a variety of dependences on RF ν and fluctuation frequency f that make their removal problematic. Attempts to do so have mostly relied on subtracting a single term in the ToA expression with an assumed RF dependence (e.g. Hemberger and Stinebring 2008) or have made use of Gaussian process modeling (e.g. Kulkarni et al. 2024), like that used for DM fluctuations (e.g. Kulkarni et al. 2024) with an assumed or fitted RF dependence. Chromatic fluctuations inevitably remain in timing residuals with these approaches and that may remain true regardless of the approach. The contributions of these undesired terms are pulsar and LoS dependent, so they must be managed on a case by case basis.

1. *Diffractive pulse broadening ($t_{{\rm C}\tau}$):* As demonstrated in Sect. 12.6.2, the time delay $t_{{\rm C}\tau}$ from pulse broadening is typically less than the $1/e$ broadening time τ. There is a complicated dependence of the ensuing error $t_{\infty,\tau}$ on the particular forms of the emitted pulse shape and PBF as well as on the template used for ToA estimation. While the amplitude and RMS value of $t_{\infty,\tau}$ cannot be expressed generally, the fluctuations of $\tau(\bar{t}, \nu)$ with epoch will be 'low-pass' in form with a characteristic time scale comparable to the RISS time scale $\Delta t_{\rm r}$ of order days or more.

2. *Refractive delays ($t_{{\rm C}\tau_{\rm r}}$):* The refractive delay $\tau_{\rm r} \simeq d' {\theta_{\rm r}}^2/2c$ is a consequence of image or ray-path wandering, differing from the effects of multipath propagation that underly the diffractive delay. The refraction angle $\theta_{\rm r} < \theta_{\rm d}$ for Kolmogorov like media with $\beta < 4$ and small inner scales (c.f. Fig. 45-46) and varies on RISS time scales. The delay $\tau_{\rm r} \propto {\theta_{\rm r}}^2$ will vary more rapidly by about a factor of $\sqrt{2}$ but both will have a low-pass spectrum.

[41] Interstellar Kolmogorov-like DM variations of significance are not expected for time separations less than about one day. Small ionospheric contributions vary diurnally and stochastically. Interplanetary contributions will vary with solar elongation and the solar cycle. Only for lines of sight near the Sun might there be significant variations on sub-day variations.

3. *Refractive error in barycentric ToAs (t_{Cssbc}):* The SSBC transformation error discussed previously scales linearly with θ_r and varies on RISS time scales.

This summary of prominent chromatic effects illustrates that the net chromatic ToA error involves a variety of RF dependences that are accompanied by a mixture of fluctuation spectra, discussed further in the next section. Mitigating the effects is unlikely to be optimal in operations on flawed ToAs, at least not with just one or two model terms. The alternative or complementary approach is to minimize chromatic effects on ToAs to begin with.

14. GAUSSIAN AND NON-GAUSSIAN TIMING FLUCTUATIONS

Timing fluctuations generally comprise Gaussian-like processes (via the central limit theorem) intermixed with those with non-Gaussian statistics. Contributions to these categories come from effects intrinsic to the pulsar and from extrinsic propagation effects. *Gaussian elements:* Spin stochasticity takes on several forms. Large-amplitude glitches occur sparsely and with preferred signs, i.e. spinups with $\Delta f_s > 0$. Spin noise (aka 'timing noise') is a sustained process that tends to be random-walk like (c.f. §4.1) and, for some cases, is made up of identifiable, discrete jumps in spin frequency or its derivative. Unlike glitches, these events are much smaller and show both signs. In other objects, individual events cannot be identified due to lack of statistical sensitivity and possibly due to a high event rate (e.g. many events per month). Generally, spin noise does not appear to be a Gaussian process for cases with a low event rate while high-rate objects can be modeled as such. The prominent red noise in J1939+2134 is consistent with a dense random walk process that is consistent with a Gaussian process.

Rapidly changing ToA errors from pulse jitter, finite scintle numbers from DISS, and radiometer noise are consistent with Gaussian, white-noise processes. Jitter is largely statistically independent between pulses[42], leading to a Gaussian error distribution when a large number of pulses is averaged, as is usually the case. The same holds for additive noise and for errors from template fitting. A ToA is usually estimated over a time-frequency block spanning many scintles, so the CLT applies for the finite scintle effect as well.

Propagation through the ISM will produce some fluctuations that are Gaussian. Those that do will be associated with Kolmogorov density variations and those that do not arise from discrete structures that superpose with Kolmogorov variations. Gaussianity likely holds for DM variations produced by Kolmogorov density fluctuations because DM is contributed to along most of the path length and there is also averaging over the bundle of ray paths reaching an observer (§12.2). Variations in the scattering time τ on long time scales will also be Gaussian if refraction is induced by Kolmogorov-like density fluctuations.

Non-Gaussian elements: Spin variations are non-Gaussian for pulsars that manifest discrete events as glitches or as the elements of the red noise process. Most MSPs do not show such events except for a few that show glitches. However, a sizable fraction of MSPs does show red noise consistent with spin noise as discussed below in Sect. 16.

Emission in pulsar magnetospheres can produce pulse variations other than single-pulse phase jitter. Changes between pulse-shape modes are consistent with stationary Markov processes in some cases (Cordes 2013), involving a small number of discrete states that persist for several to a large number of spin periods[43]. Arrival time variations will be clustered in multiple peaks in histograms of ToA residuals if only a small number of state changes (e.g. profile mode changes with a small set of preferred shapes) occur during an integration time (typically $\lesssim 1$ hr). If many occur, ToA variations will tend toward a Gaussian process. Fortunately, MSPs show very little such state changes though there are a few examples in the literature.

Refractive caustics from propagation through discrete plasma structures produce several timing effects that are event-like in nature. These include (1) strong intensity variations that influence template fitting errors; (2) discrete DM events accompanied by refraction angle variations; and (3) refractive distortion of pulse broadening functions with

[42] Correlations between single pulses are seen in CPs in the form of drifting subpulses and mode changes, but these typically decorrelate after ∼ten or so spin periods (Basu et al. 2019, and references therein).

[43] State changes discussed here are changes in pulse shape or in pulse fluctuations. They do not refer to objects that show transitions between radio and X-ray emitting phases (e.g. Stappers et al. 2014; Baglio et al. 2023).

attendant timing offsets, as discussed earlier. Collectively, these effects are associated with the 'extreme scattering event' (ESE) phenomenon[44].

ESEs involve plasma lensing effects that have been seen in radio light curves of AGNs, including the original discovery by Fiedler et al. (1987) and other notable cases (e.g. Bannister et al. 2016) and in pulsar timing data (Coles et al. 2015; Kerr et al. 2018), including the MSP J1939+2134 (B1937+21) (Cognard et al. 1993) and the MSP J1643-1224 that is behind the HII region Sh 2-27 (Maitia et al. 2003; Ocker et al. 2020; Ding et al. 2023). As with the simulations shown in Figs. 59 and 60, plasma lensing can be more prominent in timing signatures than in flux densities. This is particularly the case for low-DM MSPs monitored in PTA programs because DISS variations can easily mask the lensing's effect on the intensity. The main point, however is that the episodic nature of plasma events represent departures from Gaussian statistics that might otherwise prevail.

ESE events seen in intensity time series are accompanied by changes in DM and angle of arrival, as discussed in §12.3, and by alterations of PBFs discussed in §11.3. Refraction angles $\theta_{\rm r}$ from a discrete plasma structure scale natively as ν^{-2} and the related timing delays scale as ν^{-2} and ν^{-4}, respectively, and thus match or nearly match those from DM delays and scattering. However, time delays along propagation paths where diffraction and refraction both occur will depart from these scalings.

The effects of a plasma lens are demonstrated in a simulation that also includes Kolmogorov fluctuations. Fig. 59 shows simulated intensity slices and histograms. In the top row the intensity trough is easily seen amid the scattering from a screen with $\phi_{\rm Fd} = 1\,$rad but is not obvious in the bottom panels where lensing is combined with a stronger screen having $\phi_{\rm Fd} = 5\,$rad. The intensity histogram for the first case shows a strong departure from the exponential form expected without the lens. For the stronger diffraction screen, the histogram is consistent with an exponential except for depletion at intensities about 13 times the mean.

Fig. 60 shows the resulting images, PBFs, and arrival times obtaind by ray tracing. The simulation parameters are approximately match a pulsar with DM $= 20\,$pc cm^{-3} combined with a plasma lens with a small DM depth of $5 \times 10^{-5}\,$pc cm^{-3}. The first panel shows $\delta{\rm DM}(t)$ and the other three panels show the resulting changes in (1) angular size and location of the scattered image (second panel from top); (2) the intensity modulation 'gain' and image axial ratio in the third panel; and (3) the timing perturbations (bottom panel). Note that the timing perturbations as shown exclude DM delays and thus represent extra variations that are a consequence of angular broadening and angular wandering of the image.

Fig. 61 shows how the image shape and location and the corresponding PBF varies between 16 locations across the observation plane. Images are well centered on the direct line of sight except at locations near the plasma lens. PBFs maximize at $t = 0$ for most cases but dramatically shift to larger times when the lens is intersected.

[44] These events are more refractive than scattering (diffractive) in nature, so the term is a misnomer.

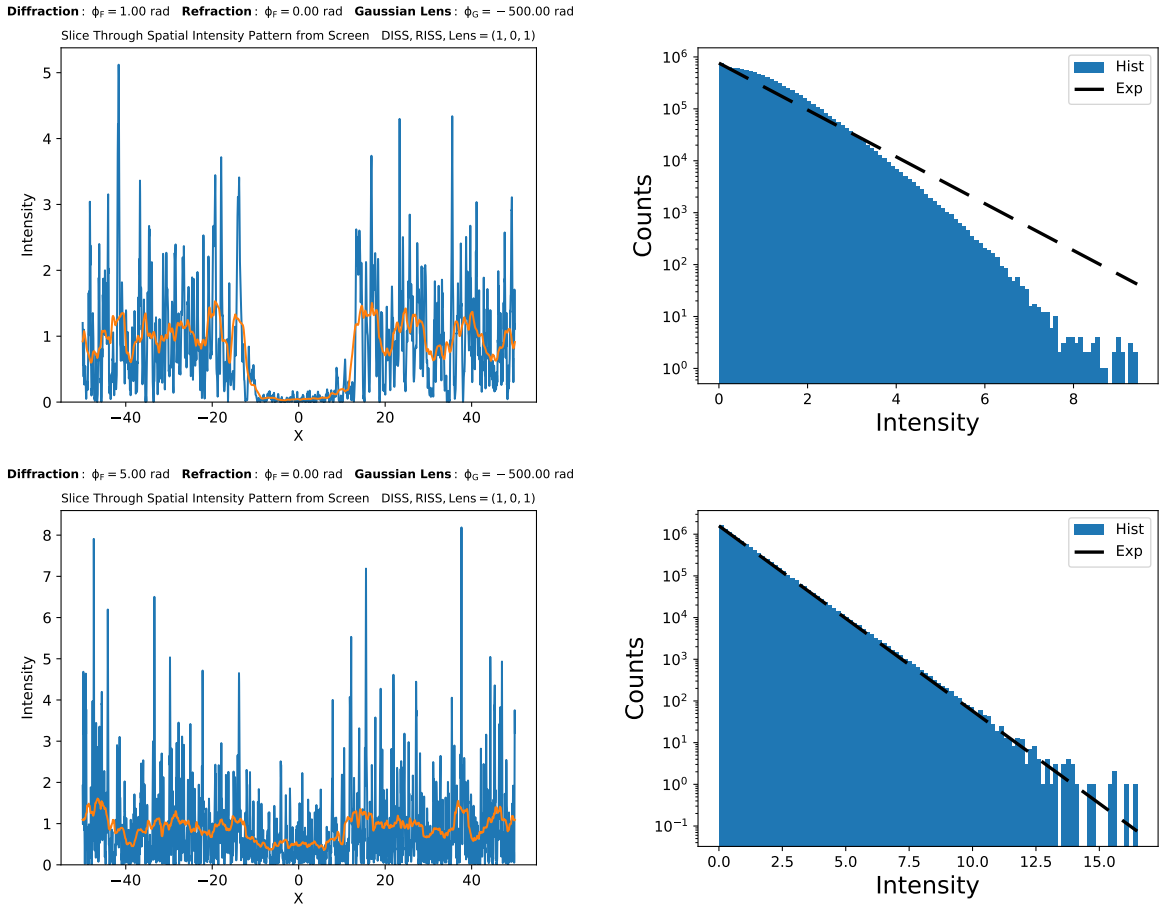


Figure 59. Simulated effects of combined scattering and plasma lensing on a pulsar's intensity. Left panels: the apparent intensity plotted against a slice across the observation plane. Right panels; histograms of intensities across the entire 2D observation plane. Top row: for a weak scattering screen with $\phi_{\mathrm{F_d}} = 1$ rad. Bottom row: for a stronger screen with $\phi_{\mathrm{F_d}} = 5$ rad. Intensities are normalized to a mean of unity. The simulated data were produced by evaluating the Fresnel-Kirchhoff diffraction integral for a phase screen that includes diffraction and a Gaussian plasma lens. The simulation method is described in Sect. F.

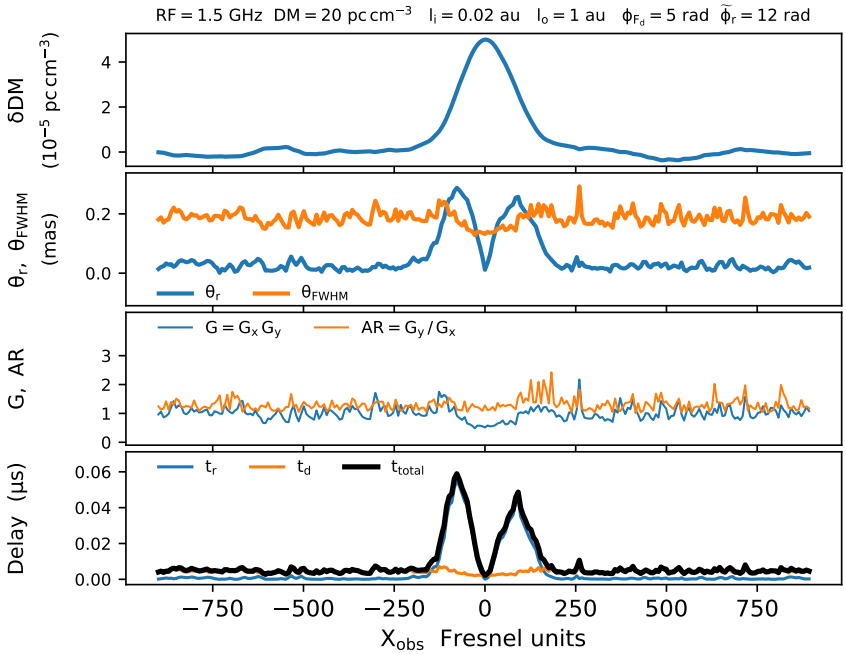


Figure 60. Results for a screen with Kolmogorov refractive variations combined with a plasma lens. Quantities are plotted vs. position along the screen plane that passes through the plasma lens at $X = 0$. Top frame: DM plotted vs. position in the observation plane. Second from top: angular size $\theta_{\rm FWHM}$ and centroid refraction angle $\theta_{\rm r}$. Third from top: Geometrical optics gain G and image axial ratio G_y/G_x. Bottom: Time delays: the scattering time $t_{\rm d}$ is determined by the width of the image while the refraction time $t_{\rm r}$ includes the offset of the image from the direct path, which is substantial for positions on either side of the direct path ($X = 0$). Lengths are measured in Fresnel scale units, $r_{\rm F} = (\lambda D/2\pi)^{1/2} \sim 10^{11}$ cm.

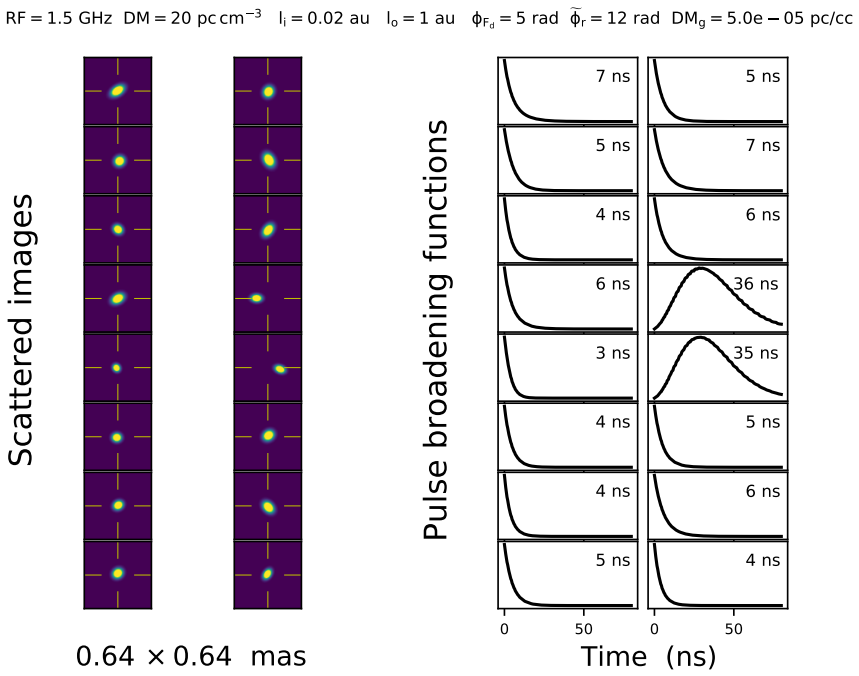


Figure 61. Simulation results for a refracting screen with Kolmogorov fluctuations combined with a plasma lens. Left: images at 16 locations along the observation plane, showing their variable shapes and offsets. Right: the corresponding PBFs and mean delays.

15. FLUCTUATION SPECTRA OF TIMING DELAYS AND RESIDUALS

The numerous processes already discussed contribute to the net fluctuation spectrum of timing residuals. Some have white noise signatures while others have red spectra with power concentrated at lower frequencies. We distinguish between a red power-law spectrum $\propto f^{-X}$ that extends to frequencies less than T^{-1} (where T is the length of a time series) and a 'low-pass' spectral form that is flat and then declines for f greater than a bandwidth B. Red power-law processes, such as pulsar spin noise and the GW stochastic background, yield increasing timing residual variance as T increases given the rise in spectral amplitude at lower frequencies. By contrast, processes with low-pass spectra have constant variance for $T \times B > 1$, examples of which are the 'white' noise processes[45] discussed earlier: template fitting errors, jitter, and the DISS finite scintle effect. Other interstellar effects also approximately show the low-pass form. Here we summarize the spectral models for the salient noise processes discussed in previous sections.

Nomenclature: We remind the reader that in the following subsections, ν refers to radio frequency, f_s refers to spin frequency, and f refers to fluctuation frequency.

15.1. *White noise processes*

Radiometer noise and jitter: Signal-to-noise dependent timing errors from radiometer noise ($\Delta t_{\rm S/N}$) are uncorrelated for ToAs obtained from profiles computed from independent sets of pulses. The same is true for jitter errors ($\Delta t_{\rm J}$). Across radio frequency, they differ because radiometer-noise errors are uncorrelated between non-overlapping frequency channels while jitter is highly correlated. In the time and RF domains, the cross correlations are then $\langle \Delta t_{\rm S/N}(t_i,\nu_k)\Delta t_{\rm S/N}(t_j,\nu_l)\rangle = \sigma_{t_{\rm S/N}}^2\delta_{ij}\delta_{kl}$ and $\langle \Delta t_{\rm J}(t_i,\nu_k)\Delta t_{\rm J}(t_j,\nu_l)\rangle = \sigma_{t_{\rm J}}^2\delta_{ij}$. The ensemble average fluctuation spectra are thus constant in fluctuation frequency but chromatic in radio frequency ν via the noise temperature, receiver characteristics, and pulse chromaticity,

$$S_{\rm S/N}(f,\nu) = S_{\rm S/N_0}(\nu) \quad \text{and} \quad {\rm S_J(f,\nu) = S_{J,0}}(\nu). \tag{15.1}$$

The spectral coefficients equal the time-domain variance divided by the Nyquist frequency, $f_{\rm Ny} = f_{\rm cadence}/2$, where $f_{\rm cadence}$ is the rate of TOA sampling, e.g. $\sim 10\,{\rm cy\,yr^{-1}}$. The S/N contribution is uncorrelated in both epoch and frequency[46] so the RMS error for thet two-frequency measurement is of the form $\sigma_{t_{\infty,\rm W}} = \sqrt{R^4\sigma_2^2+\sigma_1^2}/(R^2-1)$, where $\sigma_{1,2}$ are the RMS errors at the two frequencies, which generally differ. The spectral level for $\Delta t_{\rm S/N}$ is affected by the variable signal strength of the pulsar caused by DISS, RISS, and caustics from plasma lensing. Jitter is highly correlated across frequency, giving a different form, $\sigma_{t_\infty} = R^2\sigma_J/(R^2-1)$ where σ_J is the error in an individual measured ToA.

Finite scintle effect: The rapid shape changes of PBFs from finite numbers of scintles yield a ToA spectrum that is technically of low-pass form,

$$S_{\rm DISS}(f,\nu) = S_{\rm LP}(f, B_{\rm fse}, \nu), \tag{15.2}$$

where the bandwidth $B_{\rm fse} \simeq \Delta t_{\rm d}^{-1}$ is roughly the inverse of the DISS time scale, i.e. $B_{\rm fse} \simeq 1\,{\rm mHz}\,(10^3\,{\rm s}/\Delta t_{\rm d})$. On a practical basis, however, ToAs are usually obtained from profiles with integrations $T \gtrsim \Delta t_{\rm d}$ so the ToA error from this effect is effectively independent between ToAs. Consequently, the spectrum for the residual time series from this effect is essentially white,

$$S_{\rm DISS}(f,\nu) = S_{\rm fse,0}(\nu), \tag{15.3}$$

but it is strongly dependent on RF and T (Sect. 12.5.2). The spectral coefficient is $S_{\rm fse,0}(\nu) = \sigma_{t_{\rm DISS}}^2/f_{\rm Ny}$.

[45] Like all real-world processes, these do not have spectra that are strictly white but are simply flat over a wide bandwidth. In sampled data, values of these processes are assumed to be statistically independent.

[46] Radiometer noise is uncorrelated between different time samples and frequency channels of a multichannel system, for example.

15.2. *Achromatic red noise with power-law spectral components*

Spin noise: Stochastic spin variations (as opposed to glitches, which are large discontinuous events; Sect. 4), display red spectra with a range of spectral indices among pulsars (see Sect. 4.4)

$$S_{\rm spin}(f) = S_{\rm spin,0} f^{-X_{\rm spin}}, \quad 4 \lesssim X_{\rm spin} \lesssim 6. \tag{15.4}$$

Referring back to Sect. 4.4, some pulsars reveal that the spin noise comprises the superposition of individual events in the spin frequency $f_{\rm s}$ or its derivative $\dot{f}_{\rm s}$. Step functions in either of these yield corresponding spectra scaling as f^{-4} or f^{-6}, respectively.

GW stochastic background (GWSBG): The GWSBG that is apparently manifested in PTA data (Sect. 1) may originate from the superposition of GWs from a population of supermassive black-hole binaries, that appears as a power-law like spectrum for arrival-time perturbations with the possibility of flattening at the lowest frequencies sampled by the $T \simeq$ 15-20 yr data sets. The angular correlation of timing residuals between pulsars results from GWs affecting spacetime near the Earth (Hellings and Downs 1983). However, GWs passing through each pulsar's location contribute timing variance equal to that of the Earth-term GWs that is uncorrelated between pulsars. The pulsar-term GWs therefore contribute power-law noise to timing residuals that we represent with the same form as spin noise,

$$S_{\rm GW}(f) = S_{\rm GW,0} f^{-X_{\rm gw}}, \quad X_{\rm gw} \simeq 4 \text{ to } 4.3. \tag{15.5}$$

Asteroid noise: The spectrum of timing noise produced by an asteroid belt around a pulsar (Sect. 4.6) is typically shallower than that produced by GWs or spin noise, but steeper than that produced by interstellar processes (Sect. 4.6):

$$S_{\rm ast}(f) = S_{\rm ast,0} f^{-X_{\rm ast}}, \quad X_{\rm ast} \simeq 3 \text{ to } 3.67. \tag{15.6}$$

The spectral index $X_{\rm ast} = (2\beta_{\rm a}+7)/3$, where $\beta_{\rm a}$ is the index in the radial distribution of asteroids, $f_a(a) \propto a^{\beta_{\rm a}-1}$. Example values of $\beta_{\rm a}$ include $\beta_{\rm a} = 1$, corresponding to a uniform distribution in orbital radius, and $\beta_{\rm a} = 2$, corresponding to a disk with a uniform surface density of asteroids. These correspond to $X_{\rm ast} = 3$ and $X_{\rm ast} = 11/3$, respectively.

15.3. *Chromatic red noise with low-pass cutoffs*

Most of the interstellar effects comprise time-correlated noise with stationary statistics, yielding a variance contribution with little or no dependence on the length of time series T if T is greater than the correlation time. The exception is DM variations, which are sensitive to the full range of scales in electron density and for which an outer scale $\sim 1\,$pc would require $T \gtrsim 10^4\,$yr. In all cases, however, the spatial averaging from multipath propagation, which underlies the chromaticity of DM, yields smoothed variations in DM and other quantities with a time scale of order the refractive scintillation (RISS) time scale $\Delta t_{\rm r}$ (§9.3). This truncates fluctuation spectra for frequencies $f \gtrsim \Delta t_{\rm r}^{-1}$. We account for this low-pass filtering with a factor $S_{\rm LP}(f, B)$. It has an unspecified form but is approximately flat and rolls off for frequencies $f \gtrsim B$ with $B \propto \Delta t_{\rm r}^{-1}$.

Dispersion measures: A single propagation path through the ISM yields DM(t) with structure function $D_{\rm DM}(\Delta t) \propto (\Delta t)^{\beta-2}$ (in the inertial subrange) for a medium with a power-law wavenumber spectrum. This corresponds to a red fluctuation spectrum $S_{\rm DM}(f) \propto f^{-(\beta-1)} \overset{\beta=11/3}{\rightarrow} f^{-8/3}$. Ideally, DM($t$) is estimated at each epoch and dispersion delays are removed from arrival times. However, the multifrequency methodology used for DM estimation combined with multipath propagation introduces the low-pass factor into the spectrum,

$$S_{\overline{\rm DM}}(f, \nu) \propto f^{-X_{\rm dM}} S_{\rm LP}(f, B_{\overline{\rm DM}}, \nu_{\rm l}, \nu_{\rm h}), \qquad X_{\rm dM} = \beta - 1 \tag{15.7}$$

with a fluctuation bandwidth dependent on the frequency range $[\nu_{\rm l}, \nu_{\rm h}]$ used, over which $\Delta t_{\rm r}$ varies as $\nu^{-\beta/(\beta-2)} \overset{\beta=11/3}{\rightarrow} f^{-11/5}$. The highest frequency $\nu_{\rm h}$ yields the fastest RISS so the spectrum will extend to $B_{\overline{\rm DM}} \sim \Delta t_{\rm r}^{-1}(\nu_{\rm h})$. An example (simulated) spectrum is shown in Cordes et al. (2016, Fig. 5).

DMs from asynchronous arrival times: The TOA error from asynchronous dual-frequency measurements scales as $\Delta{\rm DM} = \overline{\rm DM}(\bar{t}_1, \nu_{\rm l}) - \overline{\rm DM}(\bar{t}_2, \nu_{\rm h})$ and its variance is calculated from the DM structure function (Sect. 12.1.2; see also

Lam et al. (2015)). For small $|\bar{t}_2 - \bar{t}_1|$ this difference acts as a derivative. From the Fourier derivative theorem this yields a factor of f^2 that multiplies the spectrum of DM. Including the low-pass factor, the spectrum is

$$S_{\Delta\mathrm{DM,async}}(f, \bar{t}_1, \bar{t}_2) \propto f^{-(\beta-3)} S_{\mathrm{LP}}(f, B_{\Delta\mathrm{DM}}). \tag{15.8}$$

For $\beta = 11/3$ the spectrum is shallow, $S_{\Delta\mathrm{DM,async}} \propto f^{-2/3}$ for $f \ll B_{\Delta\mathrm{DM}} \simeq 1/\Delta t_{\mathrm{r}}(\nu_{\mathrm{h}})$.

Frequency dependent DMs: Scattering cone averaging is responsible for the radio frequency dependence of $\overline{\mathrm{DM}}(\bar{t}, \nu)$, so the DM increment $\Delta\overline{\mathrm{DM}}$ has a low-pass fluctuation spectrum,

$$S_{\overline{\mathrm{DM}}}(f, \nu_{\mathrm{l}}, \nu_{\mathrm{h}}) \propto S_{\mathrm{LP}}(f, B_{\overline{\mathrm{DM}}}, \nu_{\mathrm{l}}, \nu_{\mathrm{h}}), \tag{15.9}$$

with $B_{\overline{\mathrm{DM}}} \simeq \Delta t_{\mathrm{r}}(\nu_{\mathrm{h}})^{-1}$, as can be seen by inspection of the simulated spectrum shown in Cordes et al. (2016, Fig. 5), which demonstrates that the spectral amplitude decreases as $\nu_{\mathrm{l}} \to \nu_{\mathrm{h}}$ and the bandwidth increases with larger ν_{h} because Δt_{r} is smaller at higher radio frequencies.

Variations in scattering and refraction parameters: Relevant quantities here are the scattering time τ, the scintillation bandwidth $\Delta\nu_{\mathrm{d}} \propto \tau^{-1}$, the DISS time scale Δt_{d}, and the RISS time scale Δt_{r}. The refraction angle $\boldsymbol{\theta}_r = k^{-1}\boldsymbol{\nabla}_\perp\phi(\mathbf{x})$ has a wavenumber spectrum $P_{\boldsymbol{\theta}_\mathbf{r}}(\mathbf{q}_\perp) = {q_\perp}^2 P_\phi(\mathbf{q}_\perp, 0)$ related to but less steep (by virtue of the gradient) than either the phase spectrum P_ϕ or the spectrum for the electron density $P_{\delta n_e}$. Sampling the refraction angle θ_r across the observation plane gives a temporal spectrum $S_{\theta_{\mathrm{r}}}(f) \propto f^{-(\beta-3)}$ multiplied by the low-pass factor. AoA variations thus have a shallow spectrum for a Kolmogorov medium, $S_{\theta_{\mathrm{r}}}(f) \propto f^{-2/3}$.

Refraction from power-law media varies on the refraction time scale Δt_{r}; refraction alters the shape of the ray-path bundle and thus affects all multipath effects (Sect. 11.3). Stationary fluctuations with a characteristic bandwidth $B_{\mathrm{r}} \sim 1/\Delta t_{\mathrm{r}}$ (i.e. lowpass in form) are expected where B_{r} is RF dependent because $\Delta t_{\mathrm{r}} \propto \nu^{-11/5}$ so $B_r \propto \nu^{11/5}$.

For a Kolmogorov-type medium, refraction delays are smaller than τ, so we discuss the latter first. As indicated in Sect. 12.6.2, ToA delays (and thus timing residuals) are related to but not equal to the scattering time τ and the RF dependence of ToA delays is nontrivially related to that of τ because it depends on the methodology used to estimate ToAs while addressing the scattering delay. We consequently write the spectrum for timing perturbations caused by epoch dependence of τ in the low-pass form,

$$S_\tau(f) = S_{\tau,0} S_{\mathrm{LP}}(f, B_\tau, \nu). \tag{15.10}$$

Angle of arrival (AoA) variations: Refraction of the ray-path bundle causes a refraction delay $\Delta t_{\mathrm{AOA}} \simeq d'{\theta_{\mathrm{r}}}^2/2c$ that has a shallow spectrum. A detailed treatment for a thin screen and Kolmogorov spectrum ($\beta = 11/3$) yields a refraction-angle spectrum (Appendix H), extending to $B_{\mathrm{AoA}} \simeq \Delta t_{\mathrm{r}}^{-1}$,

$$S_{\theta_{\mathrm{r}}}(f) = \frac{1}{\sqrt{2}(2\pi)^{1/6}} \frac{\Gamma(1/3)}{\Gamma(5/6)} \frac{(\lambda^2 r_{\mathrm{e}})^2\,\mathrm{SM}}{v_x} \left(\frac{f}{v_x}\right)^{-2/3}, \quad f \lesssim B_{\mathrm{AoA}} \sim \Delta t_{\mathrm{r}}^{-1}. \tag{15.11}$$

Note that low-DM pulsars observed at high frequencies have small refraction times, $\Delta t_{\mathrm{r}} \lesssim$ few days, so the spectrum extends to $\gtrsim$cy yr^{-1}. With a typical observing cadence $\Delta t_{\mathrm{obs}} \sim 1$ month, the spectrum is aliased to form essentially a flat spectrum. In that situation, a low-pass spectral form with bandwidth $\sim \Delta t_{\mathrm{obs}}^{-1}$ would be appropriate,

$$S_{\delta\mathrm{t,AOA}}(f) = S_{\delta\mathrm{t,AOA},0} S_{\mathrm{LP}}(f, \Delta t_{\mathrm{obs}}^{-1}, \nu). \tag{15.12}$$

The spectrum of ${\theta_{\mathrm{r}}}^2$ is the convolution of $S_{\theta_{\mathrm{r}}}(f)$ with itself and scales as $f^{-1/3}$ for a Kolmogorov spectrum and generally as $f^{-(2\beta-7)}$ for $3 < \beta < 4$ with a maximum at a small wavenumber determined by a combination of the inner and outer scales. Thus we expect this contribution to ToA fluctuations to scale as

$$S_{\delta\mathrm{t,AOA}}(f) \propto f^{-1/3} \quad \text{for } f \lesssim B_{\mathrm{AoA}}. \tag{15.13}$$

AoA variations introduce another timing error related to the translation of topocentric ToAs to the solar system's barcyenter. If the assumed pulsar direction $\hat{\mathbf{n}}$ differs from the actual, refracted direction (Foster and Cordes 1990), the ToA error has the form (assuming for simplicity a circular orbit), $\Delta t_{\rm AOA,SSBC} \simeq \theta_{\rm r}(r_E/c)\cos[\Omega_{\rm E}(t-t_p)]$, where $r_{\rm E}$ and $\Omega_{\rm E}$ are the Earth's orbital radius and orbital frequency and t_p is an offset related to the pulsar's direction.

The ensemble average spectrum is a low-pass form (for $\theta_{\rm r}$) convolved with a delta function from the sinusoidal variation, yielding a shift of the low-pass spectrum

$$S_{\delta{\rm t,SSBC}}(f) = S_{\rm AOA,SSBC,0} S_{\rm LP}(f - \Omega_{\rm E}/2\pi, B_{\rm r}, \nu). \tag{15.14}$$

The bandwidth of the low-pass factor is determined by the refraction time scale, $B_{\rm r} \simeq (\Delta t_{\rm r})^{-1}$. For low-DM pulsars $\Delta t_{\rm r} \ll 1\,$yr so $B_{\rm r} \gg 1\,{\rm cy\,yr^{-1}}$ and the orbital shift is barely discernible. Stronger scattering from high-DM pulsars or even low-DM pulsars observed at low frequencies $< 1\;$ GHz will have longer RISS time scales; the resulting narrower bandwidths make the orbital shift more manifest and thus the spectrum departs even more from a power-law form.

The sampling cadence $T_{\rm cadence}$ of a PTA program combined with the refraction time scale $\Delta t_{\rm r}$ and total time span T determine whether $\Delta t_{\rm AOA,SSBC}$ is manifested as white noise in a specific radio band (and which will differ between bands; we refer to this as 'chromatic white noise'), a low-pass spectrum, or a bandpass spectrum. The refraction time $\Delta t_{\rm r}$ is strongly frequency and LoS dependent but can range from hours for high-frequency observations of low-DM pulsars to months or years for high-DM pulsars at low frequencies:

1. *White noise:* $\Delta t_{\rm r} < T_{\rm cadence} \ll T$: When refraction angle variations are undersampled, they are statistically independent, corresponding to data with a white-noise representation. This regime applies to low-DM pulsars or high frequency observations.
2. *Correlated noise:* $T_{\rm cadence} < \Delta t_{\rm r} < 1\,{\rm yr} \ll T$: A longer refraction time that is still small compared to one year yields $\Delta t_{\rm AOA,SSBC}$ that appears as red noise with a low-pass form. (Moderate DM pulsars observed at $\sim 1\,{\rm to}\,2\,$GHz frequencies.)
3. *Bandpass noise:* $T_{\rm cadence} < 1\,{\rm yr} < \Delta t_{\rm r} \ll T$: Refraction times longer than about one year allow the coherence of the cosine term in $\Delta t_{\rm AOA,SSBC}$ to manifest. (Large DM pulsars or low frequencies.)

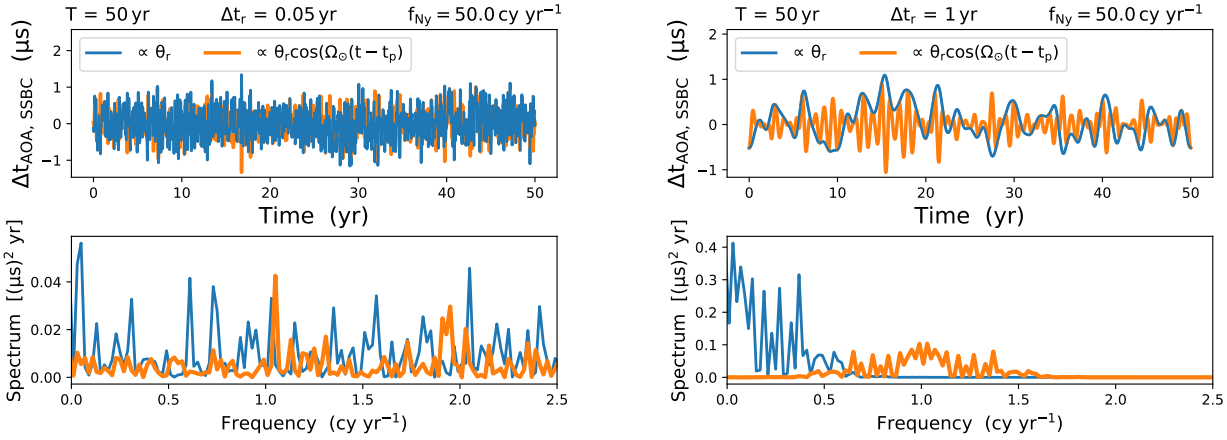


Figure 62. Time series and spectra for the refraction angle $\theta_{\rm r}(t)$ and the barycentric delay $\Delta t_{\rm AOA,SSBC}$. Simulated refraction angles with 1 mas RMS comprise 5000 samples over 50 years that yield RMS($\Delta t_{\rm AOA,SSBC}$) $\sim 0.27\,\mu s$ for a direction in the ecliptic plane. Refraction angles were simulated as a process with a Gaussian correlation function that captures the essential features but is only a coarse approximation to a Kolmogorov medium. Left: undersampled variations in refraction angle with $\Delta t_{\rm r} = 0.05\,{\rm yr} \ll T_{\rm cadence}$ yield uncorrelated samples in $\Delta t_{\rm AOA,SSBC}$ and a white noise spectrum. Right: a longer refraction time $\Delta t_{\rm r} = 1\,{\rm yr}$ allows the coherence of the cosine term in $\Delta t_{\rm AOA,SSBC}$ to be manifested in the bandpass spectrum.

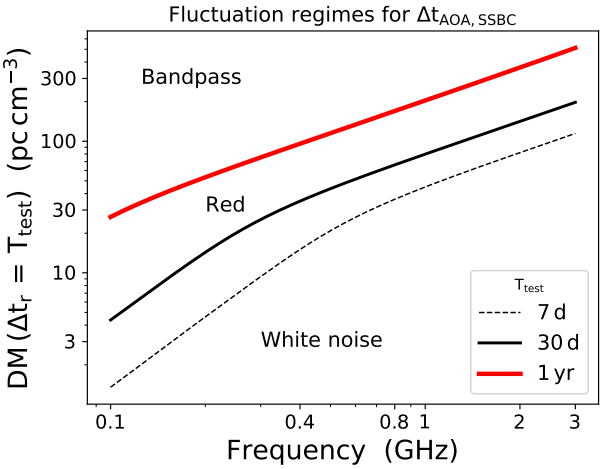


Figure 63. Plot showing regimes for the noise character of the stochastic barycentric correction delay. As a function of observation frequency, the DM corresponding to equality of the refraction time scale $\Delta t_{\rm r}$ with a specified test time $T_{\rm test}$ is shown. Two test values correspond to observation cadence (7 d and 30 d) and another corresponds to the yearly period of the cosine in the delay expression.

Figure 62 shows results from a toy model for refraction angles that illustrate the white noise and bandpass noise regimes. Refraction angles were generated by convolving white noise with a Gaussian kernel with width equal to $\Delta t_{\rm r}$. Time series for $\Delta t_{\rm AOA,SSBC}$ are shown in the top panels with and without the cosine factor to demonstrate its effect. Spectra are shown in the bottom panels.

Timing programs require measurements over wide frequency ranges to enable estimation of plasma propagation delays. These ranges can cut across the regime boundaries shown in the figure. The lowest-DM pulsars are largely immune to crossover because the barycentric delay will appear as 'chromatic white noise' at all relevant frequencies. Moderate-DM pulsars up to DM = 100 pc cm^{-3} will show temporal correlation at low frequencies and white noise at high frequencies.

Figure 63 shows the noise regimes in the DM-ν plane where the lines correspond to values of DM where $\Delta t_{\rm r} = T_{\rm test}$ with values for $T_{\rm test}$ equal to representative observing cadences of 7 and 30 d and the yearly oscillation period of the barycentric delay.

Figures 62 and 63 illustrate temporal aspects of the barycentric delay and their dependence on DM and radio frequency. The RMS refraction angle scales as $\nu^{-49/30}\tau_1$ (where τ_1 is the scattering time at 1 GHz, c.f. Table 4). For a specific pulsar and epoch, the barycentric delay (and refraction angle) will vary differently from the ν^{-2} frequency dependence of the DM delay and thus will not be removed without an additional chromatic term in the fitting function at each epoch.

15.5. *Intrinsic pulse shape variations*

The simplest summary of intrinsic pulse profiles is that large-N pulse averages are epoch independent but chromatic. Pulsars that show state changes between profile shapes ('mode changes') require N to be large enough to average over mode changes. The average profiles of pulse sequences for an individual mode are consistent with having epoch independent shapes. A notable exception to epoch independence is the MSP J1713+0747 that showed a sudden change in shape that was both chromatic and time dependent as it relaxed back to its original shape after about two years (Xu et al. 2021; Singha et al. 2021; Jennings et al. 2024b). These changes lend themselves to a description in the time domain rather than in Fourier-space. Timing residuals nonetheless show variations on time scales comparable to those of GW perturbations in the nanohertz band that must be carefully mitigated. It is possible that smaller events like those in J1713+0747 data are also present. Collectively, if frequent enough, they could produce variations not unlike those associated with spin noise. Indeed, profile changes associated with changes in orientation or structure of the magnetosphere might reflect torque events that would produce spin noise.

15.6. *Instrumental discontinuities*

It is inevitable that changes in instrumentation occur during multiyear timing programs. These can involve any elements along the signal path from the feed antennas to the analog to digital converters. Discontinuities or jumps also occur in the synchronization of observatory clocks to UTC. Pulsar timing analyses take these (mostly) known jumps into account but there are certain to be residual effects. Discontinuities in arrival times occurring at random epochs correspond to random walks in the residuals that have an f^{-2} spectral signature (Sect. 4.2). If these are due to clock offsets, the spectrum is achromatic. But jumps in imperfect polarization calibration are chromatic (e.g. Rogers et al. 2024b) and would have an f^{-2} fluctuation spectrum.

15.7. *Aliasing of fluctuation spectra*

Figure 64 (left panel) shows schematically the integration time and cadence for typical PTA data sets where an integration time $T_{\rm int}$ is used to obtain a TOA at epochs separated by an interval $T_{\rm cadence}$. The Nyquist frequency is $f_{\rm Ny} = 1/2T_{\rm cadence}$. Matching this to the bandwidth of the integrated signal $\sim 1/T_{\rm int}$ corresponds to $T_{\rm cadence} = T_{\rm int}/2$.

PTA data are grossly undersampled because $T_{\rm cadence} \gg T_{\rm int}$ due to telescope time constraints combined with choices about how target signals (e.g. GW perturbations) can be sampled. The corresponding schematic spectrum (right panel) shows the unaliased and aliased frequencies for this situation and indicates which frequencies are aliased into the Nyquist band. The integration time for typical PTA data sets $T_{\rm int} \sim 0.5$ hr corresponds to a bandwidth for TOA variations $f_{\rm rolloff} = 1/T_{\rm int} \sim 0.24$ mHz (HWHM), which happens to be much larger than the frequency range of GW signals thought to be strong enough to detect with PTAs.

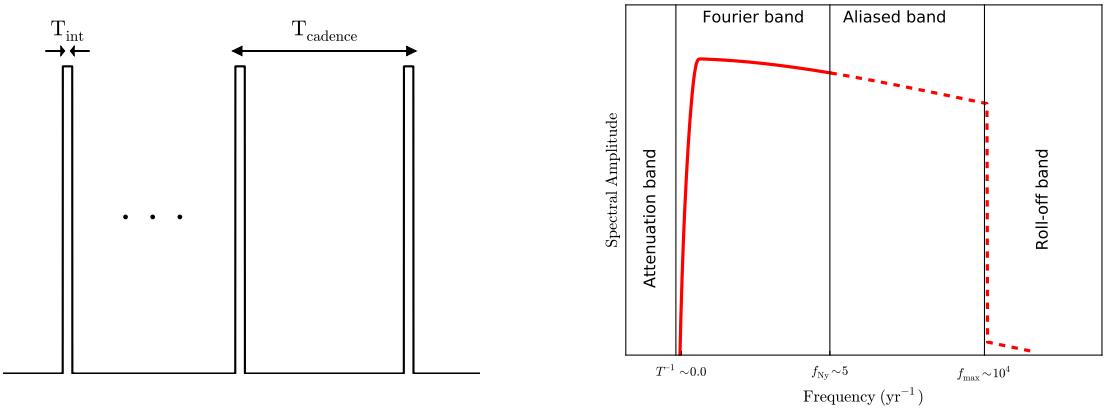


Figure 64. Left: Sampling of pulsar timing data showing the integration-time interval $T_{\rm int}$ at each epoch and the separation $T_{\rm cadence}$ between epochs ('cadence') . Right: Schematic spectrum showing the attenuation band where low frequencies are attenuated by the finite data span T, the Fourier band of unaliased frequencies below the Nyquist frequency, the aliased band, and the rolloff band related to the bandwidth of each sampled TOA for frequencies $f \gtrsim f_{\rm max} \sim T_{\rm int}^{-1}$.

For typical PTA data, the aliasing is severe. We show that it is inconsequential for steep power laws (steeper than f^{-3}) but can be important for chromatic leakage into timing residuals by interstellar delays. Let $[0, f_{\rm Ny}]$ be the range of frequencies into which all spectral amplitudes are mapped. True frequencies in this interval are unaliased but the estimated spectrum $S(f)$ for $f \in [0, f_{\rm Ny}]$ receives contributions from

$$f_{\rm true} = \begin{cases} f \\ 2jf_{\rm Ny} - f \; j = 1, 2, \ldots, j_{\rm max} \\ 2jf_{\rm Ny} + f \; j = 1, 2, \ldots, j_{\rm max} \end{cases} \tag{15.15}$$

with $j_{\rm max} \sim (f_{\rm max} - f_{\rm Ny})/2f_{\rm Ny}$. The aliased spectrum is (e.g. Kirchner 2005)

$$S_a(f) = S(f) + \sum_{j=1}^{j_{\rm max}} \left[S(2jf_{\rm Ny} - f) + S(2jf_{\rm Ny} + f)\right]. \tag{15.16}$$

Figure 65 shows examples of power-law spectra $S(f) \propto f^{-X}$ with spectral indices X relevant to timing fluctuations from interstellar processes, spin noise, and GWs. For most of these cases, distortion by aliasing is minimal, becoming significant only for shallow spectra with $X < 2$. The apparent spectral index $X_{\rm a}$ (also shown in the legend) departs significantly from X for $X = 5/3$ and especially for $X = 2/3$ where the aliased spectrum is nearly flat with $X_{\rm a} = 0.04$. This last case applies to chromatic leakage of DMs obtained from asynchronous arrival times, which are relevant to much of the PTA used to report discovery of the stochastic GW background. The $X = 2/3$ case also applies to refraction and the transfer of ToAs to the SSBC. Note that when white noise is aliased, its spectrum remains flat.

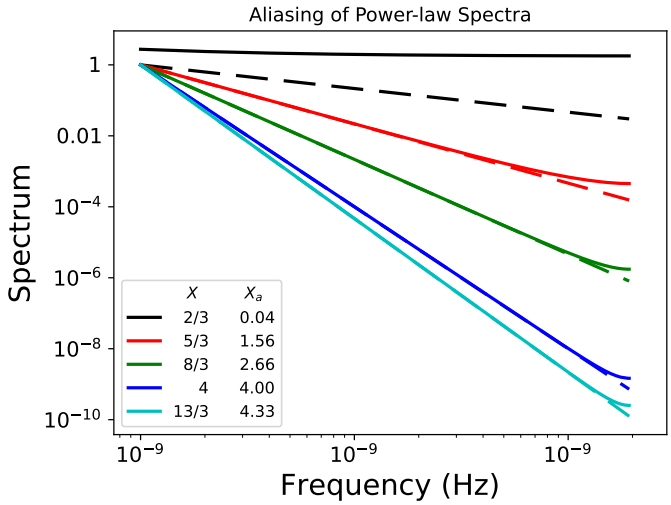


Figure 65. Examples of power law spectra $S(f) \propto f^{-X}$ that extend to 1.7×10^{-3} Hz (dashed lines) but are aliased into the Nyquist band, $f \leq f_{\rm Ny} = 2 \times 10^{-7}$ Hz and distorted (solid lines). The aliased spectra have apparent spectral indices $X_{\rm a}$ evaluated at $f = 1\,{\rm cy\,yr^{-1}}$, as indicated in the legend.

15.8. *Example spectra for four MSPs*

To illustrate fluctuation spectral shapes and the differences between pulsars, we show schematic spectra for four exemplar MSPs. They are chosen to represent the span of conditions encountered across the MSP population, including those with predicted low and high noise variance from the neutron star spin or the ISM along the LoS.

Spectra display a subset of the effects described in the paper in order to highlight the more prominent effects in comparison to the red noise from the stochastic GW background. The included effects are red spin noise, residual DM variations, the arrival time variation resulting from the $\Delta t_{\rm AOA,SSBC}$ term, and from the stochastic GW background. Spectra are shown for 30-yr data sets, about 50% longer than typical data sets for MSPs that dominate PTA sensitivity to GWs.

J0509+1856 ($P = 4.06\,$ms, DM $= 38.3\,$pc cm^{-3}): This pulsar shows large white noise due to its relatively wide pulse and pulse jitter. However, it is predicted to have low spin noise and will contribute significantly to GW detection sensitivity in multi-decade long data sets.

J1903+0327 ($P = 2.15\,$ms, DM $= 297.5\,$pc cm^{-3}): This relatively weak, large-DM pulsar shows large scattering broadening of its pulse. Consequently it will never contribute to GW sensitivity but it is an important object for demonstrating ISM effects on timing precision (e.g. Geiger et al. 2025). The oscillations at frequencies near $10^{-7}\,$Hz are due to the $\Delta t_{\rm AOA,SSBC}$ term, which are prominent for this object and not the lower-DM cases because of the large scattering.

J1909−3944 ($P = 2.95\,$ms, DM $= 10.4\,$pc cm^{-3}): This is one of the best MSPs used in PTAs owing to its narrow pulse. It contributes significantly to the evidence for detection of the GWSBG reported in 2023.

J1939+2134 (B1937+21) ($P = 1.56\,$ms, DM $= 71.02\,$pc cm^{-3}): This bright MSP has a narrow width, like J1909−3944, and would be the best MSP for PTA work were it not for its very strong, achromatic red noise from spin fluctuations (or possibly from asteroid noise). The oscillations at frequencies near $10^{-7}\,$Hz are due to the $\Delta t_{\rm AOA,SSBC}$ term, as with J1903+0327.

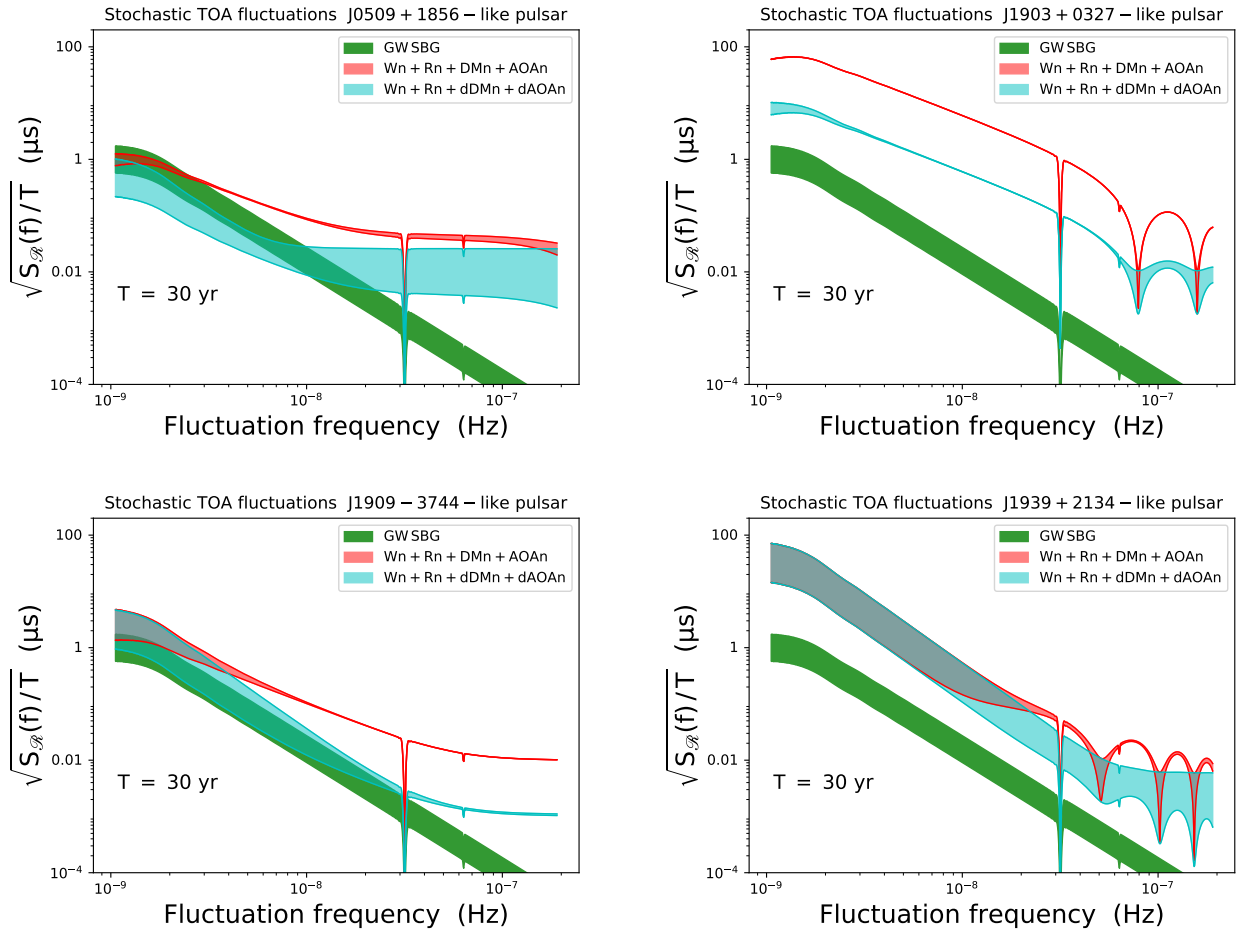


Figure 66. Example noise spectra based on *predicted* contributions from white noise, spin noise, and ISM fluctuations for four pulsars. The spectra are based on time series spanning $T = 30\,\mathrm{yr}$ and are shown as $\sqrt{S_{\mathcal{R}}(f)/T}$, where $S_{\mathcal{R}}(f)$ is the spectrum of timing residuals, obtained by multiplying the prefit spectrum by the transmission function. The GW stochastic background (green) is compared with the total noise spectrum both before (red) and after (cyan) mitigation of interstellar effects. It is assumed that mitigation reduces the spectral contribution by 10%. Top left: J0509+1856 has a wider pulse than the other three MSPs, so its template fitting error is the largest by a factor ~ 15; Top right: J1903+0327 is a high DM pulsar with a discernible scattering tail on its pulse shape, so its noise spectrum even after 10% mitigation is dominated by interstellar noise. Bottom left: J1909-3744 is a low-DM pulsar with a narrow pulse; it has a relative high $\dot{f}_{\mathrm{s}}$ so its predicted spin noise contributes significantly to its overall noise spectrum. Bottom right: J1939+2134 (B1937+21) is dominated by achromatic red noise from spin variations (or possibly orbital noise from an asteroid belt around the pulsar.) Here and in the top right panel, oscillations at frequencies near $10^{-7}\,\mathrm{Hz}$ are due to the $\Delta t_{\mathrm{AOA,SSBC}}$ term.

16. RED NOISE ASSESSMENT OF MSPS IN PTAS

Among the set of papers announcing the identification of the nanohertz GW background is a description of the properties of the NANOGrav PTA as a GW detector (Agazie et al. 2023c). Similar detector properties were presented for the Australian PPTA (Reardon et al. 2023a), the Chinese PTA (Xu et al. 2023), the European PTA (EPTA Collaboration et al. 2023), the Indian PTA (Srivastava et al. 2023), and subsequently for the MeerKAT PTA (Miles et al. 2025).

Table 2 of Agazie et al. (2023c) presents characterizations of red noise in the timing residuals of the 25 MSPs for which it could be identified out of the 67 MSPs comprising the NANOGrav PTA. Each MSP has an attributed power spectrum of the form $A_{\rm rn}(f/f_{\rm ref})^{-\gamma_{\rm rn}}$ with $A_{\rm rn}$ in dimensionless units and $f_{\rm ref} = 1\,{\rm cy\,yr^{-1}}$ (Appendix B). Mean values for $A_{\rm rn}$ range from $\sim 1.3\times10^{-15}$ to 1.3×10^{-12}. In the same dimensionless quantity, the strength of the background is $A_{\rm gw} = 2.4^{+0.7}_{-0.6}\times10^{-15}$ if the frequency index is held fixed at $\gamma_{\rm gw} = 13/3$ or $A_{\rm gw} = 6.4^{+4.2}_{-2.7}\times10^{-15}$ for a best-fit index $\gamma_{\rm gw} = 3.2\pm0.6$. We list the results from Agazie et al. (2023c) in Table 7.

Similar analyses by other PTA groups also separate timing residuals into chromatic (ISM) and achromatic (spin and GW) terms. The ranges of $A_{\rm rn}$ and $\gamma_{\rm rn}$ for the 31 MSPs in the PPTA program (Reardon et al. 2023a, Table 1), six in the EPTA program (Chalumeau et al. 2022, Table 5), and eight in the InPTA program (Srivastava et al. 2023, Table IV) are similar to those in Table 7, and characterization of the high-quality MSP J1909−3744 is in good agreement, except for the InPTA analysis, which gives a much higher amplitude and shallower index than the other PTAs. The predicted red-noise amplitude $A_{\rm rn}$ for J1909−3744 also agrees with the NANOGrav, PPTA, and EPTA measurements. However, other MSPs show measurements from these three PTAs that are only in modest agreement, generally, that likely reflect the different time spans, data quality, and analysis methods. A detailed comparison of all PTA data sets is clearly needed but is beyond the scope of this article.

Fig. 67 shows the amplitudes and indices for the 25 pulsars plotted against their dispersion measures. In the top panel, the range of values for $A_{\rm gw}$ quoted in Agazie et al. (2023c) are shown as blue bands. Also shown as a red band is the wide range estimated for red noise from interstellar propagation effects and spin noise. Red lines show the estimated range for several combined interstellar effects that produce red noise with a low-pass spectral form as discussed in Sect. 15. The three lines are based on the τ(DM) relation of Eq. (10.16) including the uncertainty $\sigma_{\log_{10}\tau} = 0.76$ for τ.

To calculate the range of interstellar contributions, we include the variability with epoch of ToA variations associated with: (1) the scattering time τ; (2) the frequency dependence of DM; and (3) the effects of refraction on the translation of ToAs to the SSBC. All three quantities vary roughly on the same time scale $\Delta t_{\rm r}$ as RISS. The first two effects dominate at large DMs but are subdominant at low DMs where refraction produces a bigger effect on ToAs.

Variations in the scattering time τ are represented as $\delta\tau \sim \epsilon_\tau\tau$ with $\epsilon_\tau = 0.1$, in accordance with the fluctuations seen in the high-DM MSP J1903+0327 (e.g. time series in Fig. 44 and labeled in Fig. 67). We also assume that only a fraction $m_\tau = 0.2$ of $\delta\tau$ is manifested in arrival times (c.f. discusssion in Sect. 12.6.2), yielding $\sigma_{t_\tau} = m_\tau\epsilon_\tau = 0.02\tau$. Variations in τ at the lower frequency(ies) used in the timing analysis dominate the net error in the DM-corrected ToA. We conservatively evaluate τ at $\nu_0 = 1.5$ GHz because we emphasize the range at larger values of DM, such as ${\rm DM} = 297\,{\rm pc\,cm^{-3}}$ for J1903+0327, for which this frequency would be appropriate. Lower frequencies are used for most MSPs monitored in PTAs, so we underestimate the role of this effect at low DMs, but it is subdominant to the refraction effect anyway.

For the contribution from frequency dependent DMs, we use Eq. (12.29) with the scattering measure calculated form τ (c.f. Table 4, item 1). We assume a uniform medium and $\beta = 11/3$ that gives $G_\beta = 1/\sqrt{\beta-1} \to \sqrt{3/8}$ and use $\nu_{\rm h} = 2\,{\rm GHz}$ with $R = 1$ (a 2:1 frequency range), giving $I_{t_\infty}(R,\beta) \simeq 1.5$.

Finally, the RMS refraction angle $\theta_{\rm r}$ is given in terms of τ by item 8 of Table 4, which is the refraction angle produced by length scales equal to the width of the ray-path bundle (i.e. scattering cone) of multiple propagation paths. Geometrical optics for a fixed plasma cloud would yield $\theta_{\rm r} \propto \nu^{-2}$ but the scattering cone gets larger at lower frequencies, yielding a net Kolmogorov scaling $\theta_{\rm r} \propto \nu^{-49/30}$. This differs from the native refraction scaling and also from the dispersion scaling $\propto \nu^{-2}{\rm DM}$. The ToA variation is given by Eq. (12.31). We ignore the sinusoidal dependence (see discussion in

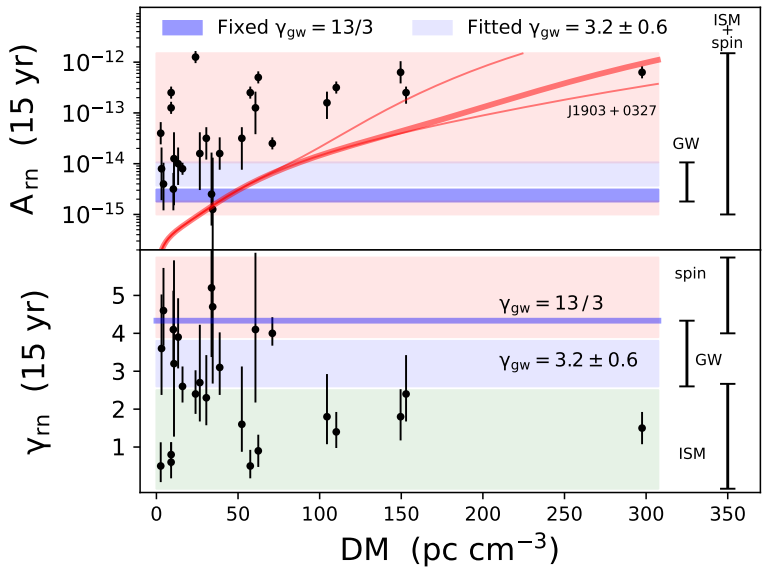


Figure 67. Red noise analysis of 25 pulsars presented in Table 2 of Agazie et al. (2023c) for NANOGrav's 15 yr dataset. Top panel: the dimensionless spectral amplitude $A_{\rm rn}$. Amplitude ranges for the GW stochastic background are indicated for two cases: (dark blue) the GW frequency index was held fixed at $\gamma_{\rm gw} = 13/3$ and (light blue) the index was fitted for along with the amplitude. The wide range of amplitudes for ISM and spin noise is indicated in red shading. The red lines indicate a preliminary analysis of the ISM fluctuations from frequency-dependent DMs, errors in the translation of ToAs to the SSBC, and variations in scattering time τ. The heavy red line is based on the mean τ(DM) relation and the thin lines are the $\pm\sigma_{\log_{10}\tau}$ departures from the mean. The high DM MSP J1903+0327 is indicated (rightmost black circle with error bar on the top and bottom frames) as an example where ISM fluctuations clearly dominate its red noise, consistent with the small $\gamma_{\rm rn} < 4$ spectral index. Bottom panel: frequency index $\gamma_{\rm rn}$ with ranges for spin noise, ISM effects, and GWs indicated.

Sect. 12.3) but assume that DM fitting removes 50% of the ToA variation and we use a nominal 1.5 GHz frequency for this term.

Calculation of the net dimensionless parameter for ISM effects, $A_{\rm ism}$, uses Eq. (B.10) after combining the three effects in quadrature to yield $\sigma_{t,\rm ism}$. The RISS time scale (Item 13 in Table 4) is used to calculate the bandwidth of the combined low-pass process as $B_{\rm L} = 1/\Delta t_{\rm r}$, which is a function of radio frequency ν and epoch. For the shape of the low-pass spectrum we use a Gaussian function, $S_{\rm L}(f) = \exp\left[-(f/2B_{\rm L})^2\right]$. The ISM A parameter is necessarily a function of fluctuation frequency and for slow RISS with $\Delta t_{\rm r} \gg 1\,$yr, the low-pass factor $S_{\rm L}(f = f_{\rm ref} = 1\,{\rm cy\,yr^{-1}}) \ll 1$. This becomes important for large-DM pulsars but is not a large effect for the DM range shown in Fig.67.

Armed with the analysis of the red noise properties of the general pulsar population in Sect. 4 and the fluctuation spectra of chromatic processes in Sect. 12, we assess the dominant cause for red noise in each of the 25 objects.

Table 7 presents assessments for the 25 MSPs analyzed in Agazie et al. (2023c). Columns 2-4 give the DM and spin parameters, which pertain to interstellar and spin noise effects, respectively. The NANOGrav 15 yr values for $A_{\rm rn}$ and $\gamma_{\rm rn}$ are repeated here in columns 5-6 from Table 2 of (Agazie et al. 2023c) and the spin noise analysis of Sect. 4 is presented as $A_{\rm rsn}$ in column 7 and its ratio to A from the NANOGrav analysis in column 8. The red-noise classification based on both analyses is in column 9. The overall assessment in column 10 combines factors based on interstellar processes combined with the red noise and spin analyses. This also involves inspection of time series for DM and timing residuals given in Agazie et al. (2023c). The assessments in the final column Table 7, though based in part on these quantitative criteria, are ultimately subjective in nature.

We use the following criteria to assign a pulsar to one of three classes:

1. **GW background:** Dominance by the stochastic background is indicated if the timing residuals yield $A_{\rm rn} \sim A_{\rm gw}$ and a steep power is identified with $\gamma_{\rm rn} \sim 4$. We use estimates for $A_{\rm gw}$ based on the common red noise process identified by multiple PTA groups. ISM effects can be ruled out on this basis and also if the pulsar's DM is small (e.g. $\lesssim 20\,{\rm pc\ cm^{-3}}$), which implies chromatic leakage is small. Further corroboration follows if the predicted red spin noise is smaller than observed.

2. **Red spin noise:** If a steep spectrum $\gamma_{\rm rn} \gtrsim 4$ is indicated and the measured red noise amplitude is significantly larger than $A_{\rm gw}$, dominance by spin noise is likely (or possibly orbital noise from asteroids, though there is little precedence for conclusive evidence for asteroid belts, only plausibility). Low-DM lines of sight will produce only weak or negligible contributions and they will not yield steep spectra.

3. **Interstellar noise leakage:** Interstellar red noise from refraction is indicated for large-DM pulsars if the frequency index $\gamma_{\rm rn} \lesssim 2$ and if $A_{\rm rn} > A_{\rm gw}$. ISM effects give native frequency indices $\gamma_{\rm ism}$ ranging from 2/3 to 5/3 for a Kolmogorov spectrum, the smallest of these for non-contemporaneous frequency observations for DM estimation or for the effect of angular wandering on barycentric ToAs. Aliasing flattens the noise process for $\gamma_{\rm ism} < 1$ (c.f. Fig. 65).

Table 7. Individual RN model parameter values and 68% credible intervals for pulsars with significant detections of RN. Note that $A_{\rm rn}$ is expressed in strain amplitude to match $A_{\rm gw}$ from the GW analysis; both are unitless.

				NANOGrav 15yr[a]		Spin noise analysis			
Pulsar	DM	P	$\dot{\rm P}$	$\log_{10} A_{\rm rn}^{15\,\rm yr}$	$\gamma_{\rm rn}^{15\,\rm yr}$	$\log_{10} A_{\rm rsn}$	$\frac{A_{\rm rsn}}{A_{\rm gw}}$	$\frac{\rm RN}{\rm type}$	Overall assessment
	(pc cm^{-3})	(s)	(10^{-20} s s^{-1})						
(1)	(2)	(3)	(4)	(5)	(6)	(7)	(8)	(9)	(10)
B1855+09	13.3	0.0054	1.78	$-14.0^{+0.3}_{-0.4}$	$3.9^{+1.0}_{-0.8}$	-14.9	0.56	gw	gw
B1937+21	71.0	0.0016	10.50	$-13.6^{+0.1}_{-0.1}$	$4.0^{+0.4}_{-0.3}$	-13.6	10.65	rsn	rsn
B1953+29	104.5	0.0061	2.97	$-12.8^{+0.2}_{-0.3}$	$1.8^{+1.1}_{-0.7}$	-14.7	0.89	gw	ism
J0030+0451	4.3	0.0049	1.02	$-14.4^{+0.4}_{-0.5}$	$4.6^{+1.1}_{-0.9}$	-15.1	0.33	gw	gw
J0437−4715	2.6	0.0058	5.73	$-13.4^{+0.2}_{-0.2}$	$0.5^{+0.6}_{-0.4}$	-14.3	1.92	rsn	ism?
J0610−2100	60.7	0.0039	1.23	$-12.9^{+0.3}_{-0.5}$	$4.1^{+2.0}_{-1.9}$	-14.9	0.49	gw	rsn
J0613−0200	38.8	0.0031	0.96	$-13.8^{+0.3}_{-0.3}$	$3.1^{+0.9}_{-0.7}$	-15.0	0.45	gw	gw?
J1012+5307	9.0	0.0053	1.71	$-12.6^{+0.1}_{-0.1}$	$0.8^{+0.3}_{-0.3}$	-14.9	0.55	gw	ism
J1600−3053	52.3	0.0036	0.95	$-13.5^{+0.2}_{-0.6}$	$1.6^{+1.5}_{-0.7}$	-15.0	0.39	gw	ism?
J1614−2230	34.5	0.0032	0.96	$-14.9^{+1.0}_{-0.8}$	$4.7^{+1.6}_{-2.0}$	-15.0	0.44	gw	gw
J1643−1224	62.4	0.0046	1.85	$-12.3^{+0.1}_{-0.1}$	$0.9^{+0.4}_{-0.4}$	-14.8	0.66	gw	ism
J1705−1903	57.5	0.0025	2.15	$-12.6^{+0.1}_{-0.1}$	$0.5^{+0.4}_{-0.3}$	-14.5	1.28	rsn	ism
J1713+0747	16.0	0.0046	0.85	$-14.1^{+0.1}_{-0.1}$	$2.6^{+0.5}_{-0.4}$	-15.2	0.28	gw	gw
J1738+0333	33.8	0.0059	2.41	$-14.6^{+0.8}_{-0.6}$	$5.2^{+1.3}_{-1.8}$	-14.8	0.73	gw	gw?
J1744−1134	3.1	0.0041	0.89	$-14.1^{+0.4}_{-0.6}$	$3.6^{+1.4}_{-1.2}$	-15.1	0.33	gw	gw
J1745+1017	24.0	0.0027	0.27	$-11.9^{+0.1}_{-0.1}$	$2.4^{+0.6}_{-0.5}$	-15.5	0.13	gw	?
J1747−4036	152.9	0.0016	1.31	$-12.6^{+0.1}_{-0.2}$	$2.4^{+1.0}_{-0.7}$	-14.6	1.03	rsn	ism
J1802−2124	149.6	0.0126	7.26	$-12.2^{+0.2}_{-0.2}$	$1.8^{+0.7}_{-0.6}$	-14.5	1.33	rsn	ism
J1853+1303	30.6	0.0041	0.87	$-13.5^{+0.2}_{-0.4}$	$2.3^{+1.1}_{-0.7}$	-15.1	0.32	gw	gw?
J1903+0327	297.5	0.0022	1.88	$-12.2^{+0.1}_{-0.1}$	$1.5^{+0.4}_{-0.4}$	-14.5	1.24	rsn	ism
J1909−3744	10.4	0.0029	1.40	$-14.5^{+0.3}_{-0.4}$	$4.1^{+1.0}_{-0.9}$	-14.8	0.70	gw	gw
J1918−0642	26.6	0.0076	2.57	$-13.8^{+0.4}_{-0.7}$	$2.7^{+1.5}_{-1.0}$	-14.8	0.63	gw	ism?
J1946+3417	110.2	0.0032	0.32	$-12.5^{+0.1}_{-0.1}$	$1.4^{+0.5}_{-0.4}$	-15.5	0.13	gw	ism
J2145−0750	9.0	0.0161	2.98	$-12.9^{+0.1}_{-0.1}$	$0.6^{+0.5}_{-0.4}$	-15.0	0.41	gw	ism
J2234+0611	10.8	0.0036	1.20	$-13.9^{+0.5}_{-0.9}$	$3.2^{+2.7}_{-1.9}$	-14.9	0.50	gw	gw?

[a] From Agazie et al. (2023c).

17. PROFILE MODELING SUMMARY AND ARRIVAL TIME MODELS

We assert the point of view that optimal estimation of *achromatic* ToAs (i.e. after mitigation of chromatic effects) should be done epoch-by-epoch. This requires contemporaneous estimation of DM and scattering delays (through *profile modeling*) rather than analyzing chromatic ToAs in long, multiepoch time series to remove offsets peculiar to any given epoch. This echoes the conclusion in Iraci et al. (2024) that an "epoch-wise"' approach yields greater accuracy for removing DM variations than methods that utilize piecewise linear fitting, the DMX method, (e.g. NANOGrav Collaboration et al. 2015; Shapiro-Albert et al. 2021)), or Gaussian process (GP) modeling (e.g. van Haasteren and Vallisneri 2014)[47]. Moreover, our statement applies to *all* chromatic terms that vary with epoch[48], which require more intricate fitting of ToAs than usage of only a ν^{-2} dispersion term, as is well known (Cordes et al. 1990; Ramachandran et al. 2006; Cordes and Shannon 2010; Cordes et al. 2016; Lam et al. 2018b; Kaur et al. 2022; Singha et al. 2024; Donner et al. 2019; Lam et al. 2020). Inclusion of non-dispersive chromatic terms has been explored with GP noise modeling (e.g. EPTA Collaboration et al. 2023; Larsen et al. 2024), but with scattering expressed in timing equations with explicit ν^{-4} frequency scalings. We have shown that timing delays differ from scattering times and that delays originate from multiple processes that are epoch dependent with differing frequency dependences. This leads to mismatch between templates and profiles resulting in systematic ToA offset errors. Moreover, these errors generally do not scale as ν^{-4}.

The recourse, at the very least, is to weight contemporaneous measurements more strongly than those from adjacent epochs. This might entail a more sophisticated GP modeling approach. For example, GP modeling of *profiles* rather than of individual terms in measured ToAs could better account for slowly varying chromatic effects. However, it would not capture the more rapidly varying effects (e.g. finite scintle effect, refraction).

Solely using single-epoch data for achromatic ToA estimation is therefore the optimal approach. This is much more feasible now that wideband (3:1 or larger) receivers are available to provide simultaneous frequency coverage and more sensitive telescopes are available. Previously, DM estimation required separate dual or multiple band observations spread over multiple days or longer, necessitating multiepoch fitting. With determinations from single-epoch measurements, the quality of the results will be less dependent on the cadence of timing observations.

Myriad effects contribute to arrival times, many of which are distractions from the goals of some applications but are nonetheless diagnostic of instrumental parameters important for establishing the veracity of an analysis and may be of interest for ancillary astrophysics. This section consolidates the dominant effects into empirical timing model(s) suitable for quantitative analysis, taking into account that ToA estimates are methodology dependent. Addressing biases requires consideration of how the effects of interstellar plasma processes are intertwined with the chromaticity of emitted pulse shapes. A detailed analysis in Appendix G is summarized here.

17.1. *Profile modeling*

Profiles are formed by synchronously averaging $M \gg 1$ single pulses (equivalent to an integration time $M \times P$, where P = pulse period) in a bandwidth B at center frequency $\overline{\nu}$ and epoch $\overline{t}$. In the following, M and B are implicit and we ignore any distortions from instrumentation (including polarization miscalibration) and RFI. These distortions are of course unavoidable in actual measurements and could dominate if astrophysical delays are mitigated to a large degree.

Define $U_{\rm i}$ as the intrinsic average profile (i.e. upon emission) that is scattered by the PBF p to produce $U_{\rm s} = U_{\rm i} * p$. The three quantities U, p, and $U_{\rm s}$ are all stochastic. We make use of two kinds of averages: an ensemble average denoted by angular brackets $\langle \cdots \rangle$ and an average over epochs $\langle \cdots \rangle_{\overline{t}}$ indicated with a subscript $\overline{t}$. We assume ergodicity so that in the limit $\overline{t} \to \infty$ the epoch average converges to the ensemble average.

[47] We note that alternate criteria discussed by Iraci et al. (2024) imply that GP modeling and DMX fitting can be superior to epoch-wise fitting in some cases. However, epoch-wise fitting is more heavily influenced by pulse signal-to-noise ratios so improved telescope sensitivity can alter this comparison.

[48] By and large this implies interstellar refraction, scattering, and dispersion but also applies to any systematic shape changes in emitted pulse profiles, which in some cases are also chromatic.

The intrinsic and scattered profiles and scattering function are written in terms of their ensemble averages and deviations,

$$U_{\rm i} = \langle U_{\rm i}\rangle + \delta U_{\rm i}, \qquad U_{\rm s} = \langle U_{\rm s}\rangle + \delta U_{\rm s}, \quad \text{and} \quad p = \langle {\rm p}\rangle + \delta p. \tag{17.1}$$

The scattered profile is then

$$\langle U_{\rm s}\rangle = \langle U_{\rm i}\rangle * \langle {\rm p}\rangle \tag{17.2}$$

$$\delta U_{\rm s} = \delta U_{\rm i} * \langle {\rm p}\rangle + \langle U_{\rm i}\rangle * \delta p + \delta U_{\rm i} * \delta p. \tag{17.3}$$

With complete generality, all terms in these expressions are functions of $t, \overline{\nu}$, and $\bar{t}$ but the mean intrinsic pulse shape $\langle U_{\rm i}\rangle$ is now assumed to be epoch independent (with exceptions, as previously mentioned). The deviation $\delta U_{\rm s}$ includes intrinsic pulse jitter in $\delta U_{\rm i}$ and fast and slow variations of the PBF in δp, all of which are epoch dependent and chromatic.

The measured profile in Stokes I is

$$I(t, \overline{\nu}, \bar{t}) = A(\overline{\nu}, \bar{t}) \times U_{\rm s}(t - t_0(\overline{\nu}, \bar{t}), \overline{\nu}, \bar{t}) + N(t, \overline{\nu}, \bar{t}). \tag{17.4}$$

The pulse amplitude $A(\overline{\nu}, \bar{t})$ includes scintillation modulations (DISS and RISS) of the emitted flux density that are epoch dependent and chromatic. DISS modulations are attenuated by bandwidth and temporal averaging for high-DM pulsars or low-frequency observations. Modulations can be large for low-DM pulsars at 1 to 2 GHz, thus affecting the S/N-related ToA error (c.f. Equations (6.3), (6.8), and (6.9)).

The arrival time $t_0(\nu, \bar{t})$ includes contributions to the net propagation time from pulsar to observatory but *not* those effects that alter the pulse shape. It therefore includes interstellar dispersion and its temporal variability along with single-path refraction but it excludes shape-changing effects from multipath propagation. As such, this ToA term is intended to correspond to propagation from a specific location in a pulsar's magnetosphere that corotates with the neutron star. The additive noise term $N(t, \overline{\nu}, \bar{t})$ is from radiometer noise, which is uncorrelated between different $\overline{\nu}$ and $\bar{t}$.

Without any shape changes ($\delta U_{\rm s} = 0$), the pulse model in Eq. (17.4) would strictly satisfy the conditions for matched filtering (§6) and the only ToA error would be from additive noise, $N(t, \overline{\nu}, \bar{t})$. That shape changes do occur implies that ToA errors will always be larger than those predicted for matched filtering.

17.2. *Template modeling* and matching

Errors in ToAs depend on the methodology for implementing template matching and in particular the choice of template. A matched filter by definition maximizes the S/N of the filter output. However, even if a template nearly yields the maximum theoretical S/N, it does not eliminate ToA *bias*. The chromaticity and epoch dependence of measured pulse profiles essentially guarantees that this bias will always be present. Existing practices make use of different kinds of templates in the matched filtering process described in §6.

Briefly, several alternatives have been employed, as summarized in Table 8 and elaborated on here:

Analytic template model: A template comprising one or more analytic components (e.g. Gaussian functions) typically does not explicitly include scattering; however, scattering in data used to form synthetic templates may have affected the fitting of these components, albeit at low levels for low-DM pulsars. It will therefore yield both systematic and random ToA errors. To match actual profile chromaticity, particularly with multicomponent profiles, synthetic templates need to include frequency dependent amplitudes, widths, and pulse phases.

A common approach models the intrinsic pulse shape $\langle U_{\rm i}\rangle$ as a superposition of Gaussian components,

$$U_{\rm m}(t, \nu, \bar{t}) = \sum_j g_j(\nu, \bar{t}) \exp\left[-(2\sqrt{\ln 2}(t - t_j(\nu, \bar{t}))/W_j(\nu, \bar{t}))^2\right], \tag{17.5}$$

with individual amplitudes g_j, locations t_j and widths W_j (FWHM). Generally, all three quantities vary with frequency and also, in principle, with epoch. However, pulsars providing the best timing results evidently have

Table 8. Templates and timing errors induced by scattering

Template type	Intrinsic Pulse Shape (U)	PBF (p)	Chromatic ToA cause	TOA correction
True (hypothetical)	(for center frequency $\overline{\nu}$ and epoch $\overline{t}$)			
	$U_{\rm i}(t,\overline{\nu},\overline{t})$	$p(t,\overline{\nu},\overline{t})$	None [a]	0
	$U_{\rm i}(t,\nu_{\rm ref},\overline{t})$	$p(t,\nu_{\rm ref},\overline{t})$	Chromatic $U_{\rm i}$	$t_{\delta U_{\rm s}}(\nu,\nu_{\rm ref},\overline{t})$
Empirical (where $\langle\cdots\rangle_{\overline{t}}$ indicates average over available epochs, $\overline{t}$)				
1. 2D (U_2)	$\langle {\rm U}(t,\nu,\overline{\rm t})\rangle_{\overline{t}}$	$\langle {\rm p}(t,\nu,\overline{\rm t})\rangle_{\overline{t}}$	Epoch dependences [b]	Customized
2. 1D (U_1) (fixed at $\nu_{\rm ref}$)	$\langle {\rm U}(t,\nu_{\rm ref},\overline{\rm t})\rangle_{\overline{t}}$	$\langle {\rm p}(t,\nu_{\rm ref},\overline{\rm t})\rangle_{\overline{t}}$	Epoch dependences and chromaticity [b]	
Synthetic model	Multi-Gaussian: [c] $U_{\rm g}(t,\overline{\nu},\overline{t})$	Exponential: [d] $e^{-t/\tau(\overline{\nu},\overline{t})}\Theta(t)$	U, p mismatches	$\Delta t_{G*E}(\overline{\nu},\overline{t})$
		Power law: [e] ${\rm PL}(t,\overline{\nu},\tau(\overline{t}),\boldsymbol{\Theta}_{\rm PL})$	U mismatch	$\Delta t_{G*PL}(\overline{\nu},\widehat{\tau}_{\rm d}(\overline{t}),\delta\widehat{\boldsymbol{\Theta}}_{\rm PL})$
		$\boldsymbol{\Theta}_{\rm PL}=(\beta,l_i,\boldsymbol{\theta}_{\mathbf{x}})$	Parameter errors	
Coherent deconvolution	Estimated $\widehat{U}$	Estimated $\widehat{p}$	Estimation errors	$\Delta t_{CS}(\overline{\nu},\widehat{t})$
Estimates for scattering times, $\widehat{\tau}_d(\overline{t})$				
1. Dynamic spectrum analysis (ACF, secondary spectrum)			Estimation error	$\Delta t_\tau(\widehat{\tau}_d(\overline{\nu},\overline{t}\vert U,p)$
2. Cyclic spectrum analysis			Estimation error	$\Delta t_\tau(\widehat{\tau}_d(\overline{\nu},\overline{t}\vert U,p)$

[a] No ToA offset from template-profile mismatch. ToA errors from white noise effects are implicit.

[b] Epoch dependence of p due to $\tau(\nu,\overline{t})$ and (rarely) epoch dependence of U. Chromaticity of intrinsic pulse and PBF shapes.

[c] Multicomponent Gaussian model: $U_{\rm g}(t,\nu,\overline{t})=\sum_j a_j\exp\left[-(2\sqrt{\ln 2}(t-t_j(\nu,\overline{t}))/W_j(\nu,\overline{t}))^2\right]$

[d] $\Theta(t)$ = Heaviside function

[e] $\boldsymbol{\Theta}_{\rm PL}$ = parameter vector for power-law PBF that includes $\boldsymbol{\theta}_{\mathbf{x}}$, a vector of parameters for the spatial distribution of scattering regions (e.g. thin screen, thick slab, transversely bounded clouds, etc; $\delta\boldsymbol{\Theta}_{\rm PL}$ denotes errors in these parameters.

very little intrinsic variability with epoch. The Crab pulsar is a counterexample: its spindown time $\sim 10^3$ yr is short enough that secular changes in pulse shape have been discerned since its discovery more than half a century ago (Lyne et al. 2013). Another is the MSP J1713+0747 that shows changes in profile in the form of episodic events (c.f. §6.4. **Recent work (Bhat et al. 2026a) suggests that a significant fraction of MSPs displays subtle epoch-to-epoch profile changes that are achromatic while others show chromatic changes mostly due to scattering.**

Empirical template at each frequency: Multifrequency templates built from measured pulses necessarily include scattering, albeit from an epoch or range of epochs that differ from those of profile data used to obtain

ToAs. This removes intrinsic profile chromaticity (to the extent that it is epoch independent) but will only partially remove systematic ToA errors from scattering.

Empirical template at a single frequency and epoch ($\nu_{\rm template}$ and $\bar{t}_{\rm template}$): Application of a single-frequency template to multifrequency profiles yields chromatic ToA errors if, as is common, profiles evolve with frequency. Correction for profile chromaticity requires a lookup table of timing offsets ('FD' parameters). Scattering baked into the template generally differs from that in the profile even after scaling a representative scattering time to each frequency (epoch dependence!). Template fitting thus removes some but not all scattering contributions.

Template matching can be applied in two ways: simultaneously over a wide band using a 2D template or on a narrow-band, channel-by-channel basis covering the same total band. **In the literature, the phrase 'wideband timing' is often applied to the first of these (template matching in two dimensions, time and frequency) while 'narrowband timing' applies to the channel-by-channel approach. There are two ways to accomplish the channel-by-channel approach: one is to use a single one-dimensional template that typically yields systematic frequency-dependent biases requiring subsequent correction; the other is to use multichannel templates, one for each frequency channel, that ideally removes frequency dependent biases. We consider the 'wideband' vs. 'narrowband' nomenclature to be misleading given that the same data are used in both methods. Our main purpose in the following is to describe the ensuing errors due to departures from the underlying assumptions of these methods.**

Application of two-dimensional empirical templates : The 2D template is the profile shape averaged over many epochs for each frequency $\overline{\nu}$ in a multichannel system spanning a total bandwidth B and denoised to minimize ToA estimation errors. Ignoring the multiplier A in Eq. (17.4), the 2D template,

$$\widehat{U}_2(t,\overline{\nu},\bar{t}) = \langle I(t,\overline{\nu},\bar{t})\rangle_{\bar{t}}, \tag{17.6}$$

is the basis for 'pulse portrait' fitting pioneered by Liu et al. (2014) and Pennucci et al. (2014, 2016). It is related to the ensemble average shape as $\widehat{U}_2 = \langle U_{\rm s}\rangle + \langle \delta U_{\rm s}\rangle_{\bar{t}}$. Averaged over a large number of epochs, the difference $\langle \delta U_{\rm s}\rangle_{\bar{t}}$ reduces to a small value that we ignore in the following.

Construction of 2D templates is done empirically by integrating a large number of pulses from multiple epochs. In Pennucci et al. (e.g. 2014), measured pulses are further modeled as multiple Gaussian components as is also done for **1D templates** discussed above. With 2D timing (the so-called 'wideband timing' method) the 2D template can be applied as a 2D cross correlation (or by least squares fitting in the 2D Fourier domain) with 2D profiles to yield DM($\bar{t}$) and a ToA at a specified reference frequency (e.g. Nobleson et al. 2022).

At each frequency $\overline{\nu}$, the cross correlation of the template and profile, $\widehat{U}_2(t,\overline{\nu},\bar{t}) * I(t,\overline{\nu},\bar{t})$ includes two terms. The leading term is the delayed autocorrelation of $\langle U_{\rm s}\rangle$, yielding a ToA estimate equal to the true value, $t_0(\overline{\nu},\bar{t})$. The second term is the cross correlation $\langle U_{\rm s}\rangle * \delta U_{\rm s}$, which adds a perturbation $\Delta t_{\delta U_{\rm s},\delta p}(\overline{\nu},\bar{t})$ from pulse jitter and PBF fluctuations, both fast (finite number of scintles) and slow (e.g. refractive modulation of the PBF).

Application of one-dimensional templates: Alternative to 2D template fitting, individual ToAs can be obtained for each subband frequency $\overline{\nu}$ across the total bandwidth B, which are then fitted to give DM($\bar{t}$) and a ToA at a reference frequency. **One version of this method employs a single 1D template at a reference frequency** $\nu_{\rm ref}$,

$$\widehat{U}_1(t,\nu_{\rm ref},\bar{t}) = \langle I(t,\nu_{\rm ref},\bar{t})\rangle_{\bar{t}} \equiv \widehat{U}_2(t,\nu_{\rm ref},\bar{t}), \tag{17.7}$$

that is applied to individual profiles at each frequency $\overline{\nu}$. In this case, the first term of the CCF of $\widehat{U}_1$ with a profile adds a bias to the true ToA due to profile chromaticity, $\Delta t_{U_{\rm ref},U}(\overline{\nu})$. Profile chromaticity manifests as changes of widths and pulse phases of profile components with frequency. The second term yields a stochastic delay from pulse jitter and PBF variations like that for the 2D template, $\Delta t_{\delta U_{\rm s},\delta p}(\overline{\nu},\bar{t})$, but it will differ quantitatively due to the different template. The net ToA is written as

$$\widehat{t}(\overline{\nu},\bar{t}) = t_0(\overline{\nu},\bar{t}) + \Delta t_{U_{\rm 1ref},U}(\overline{\nu}) + \Delta t_{\delta U_{\rm s},\delta p}(\overline{\nu},\bar{t}). \tag{17.8}$$

The first perturbation, $\Delta t_{U_{1\rm ref},U}(\overline{\nu})$, is the systematic error from profile chromaticity ('profile evolution'). It is addressed in NANOGrav timing analyses by modeling it as a power series in $(\ln \overline{\nu})$,

$$\widehat{\Delta t}_{U_{1\rm ref},U_1}(\overline{\nu}) = \sum_{l=1}^{N_l} \Delta t_l^{(\rm pe)} (\ln \overline{\nu})^l. \tag{17.9}$$

The coefficients $\Delta t_l^{(\rm pe)}$ and their optimal number N_l are determined from a fit to profiles over many epochs for each pulsar. Random errors in the coefficients are small if profiles have large-enough S/N but systematic errors arise if profiles show secular evolution. Note that the coefficients include contributions from scattering as well as intrinsic profile chromaticity.

A second version of channel-by-channel template fitting uses different templates for each frequency channel that are essentially 1D cuts through the 2D template described above. This approach avoids the bias that drives the need for FD parameters and is very similar to a full 2D fitting approach (indeed covering the same overall frequency band). However, it may yield slightly different responses to frequency-dependent scattering and RFI that affect profiles chromatically.

17.3. *PBF models*

A model for the pulse broadening function $p_{\rm m}$ enters into ToA estimation either directly through inclusion in template modeling as in Eq. (17.5) or indirectly with empirical templates. For any model, the $1/e$ time τ is strongly frequency dependent and also epoch dependent from refraction (and possibly other causes).

Exponential PBF: A common choice is the single-parameter exponential form, $p_{\rm E}(t,\tau) = \tau^{-1} \exp(-t/\tau)\Theta(t)$ (Θ = Heaviside function) described earlier (Sect. 11.1). The exponential PBF is almost always a poor choice because it can apply only under special conditions that are not applicable to precision timing of low-DM MSPs. First, it requires a thin screen scattering geometry but more importantly it applies to either a monoscale medium or one with a large inner scale, l_i, compared to the diffraction scale, $l_{\rm d}$ (e.g. Lambert and Rickett 2000). Such a medium is inconsistent with observations of low-DM pulsars. Nonetheless it has seen extensive, but problematic, use in pulse modeling.

Power-law PBFs: A better choice is $p_{\rm PL}$, a 'power-law' PBF from a medium with a power-law electron density spectrum, such as the Kolmogorov spectrum with a small inner scale (Sect. 11.2). The parameters of PL models are the $1/e$ scattering time τ and $\mathbf{\Theta}_{\rm PL} = (\beta, l_i, \Theta_{\mathbf{x}})$, where β is the spectral index of the density spectrum, l_i is the inner scale, and $\Theta_{\mathbf{x}}$ is a vector of parameters for the spatial distribution of scattering regions along and transverse to the LoS.

Consequences of mismatched profile elements: A template model inevitably differs from a measured profile shape due to mismatches between the modeled and actual intrinsic shapes or PBF shapes. Template fitting accordingly yields systematic ToA offsets that accompany random errors.

As with empirical templates, we express the model intrinsic profile and model PBF in terms of their average forms or shapes and departures from them,

$$U_{\rm m} = \langle U_{\rm i} \rangle + (U_{\rm m} - \langle U_{\rm i} \rangle) \equiv \langle U_{\rm i} \rangle + \delta U_{\rm m} \tag{17.10}$$

$$p_{\rm m} = \langle {\rm p} \rangle + (p_{\rm m} - \langle {\rm p} \rangle) \equiv \langle {\rm p} \rangle + \delta p_{\rm m}. \tag{17.11}$$

Together these give a model scattered profile,

$$U_{\rm ms} = U_{\rm m} * p_{\rm m} = \langle U_{\rm s} \rangle + \delta U_{\rm ms}, \tag{17.12}$$

that deviates from the actual scattered pulse $\langle U_{\rm s} \rangle$ by

$$\delta U_{\rm ms} = \delta U_{\rm m} * \langle {\rm p} \rangle + \langle U_{\rm i} \rangle * \delta p_{\rm m} + \delta U_{\rm m} * \delta p_{\rm m}. \tag{17.13}$$

17.4. *Arrival time equations*

There is no unique choice of equation for modeling long sequences of multiepoch ToAs. The adequacy of a ToA expression is illustrated by considering a sequence of models ranging from simplistic to comprehensive.

17.4.1. *No ISM terms*

First, suppose ISM effects are completely absent but pulse profiles are chromatic and epoch independent. This is hypothetical in the radio context but would apply to very high frequency ($\gg 10\,\mathrm{GHz}$) measurements, including non-radio observations from the millimeter band to gamma-rays. Though propagation effects are largely achromatic in these bands[49] emitted pulses are frequency or energy dependent, typically.

The ToA model is written compactly (with the center frequency $\overline{\nu}$ and epoch $\overline{t}$ implicit) as,

$$\widehat{t}_\nu = t_\infty + t_{\mathrm{mismatch}} + \Delta t_{\mathrm{S/N}} + \Delta t_{\mathrm{J}}, \tag{17.14}$$

where t_∞ is the target ToA that would include all achromatic effects related to the spin and orbit of the neutron star combined with astrometric terms and gravitational wave perturbations[50]. The t_{mismatch} term is nonzero if a reference-frequency template is applied to profiles at all frequencies (or energies in the high-energy context). Errors from radiometer noise and pulse jitter have temporal white-noise statistics. We keep them separate here because they differ statistically across frequency, as discussed previously. If epoch independent, t_{mismatch} is determinable from measurements built up over many epochs on each pulsar. This is the basis for the FD ('frequency dependent') parameters used in NANOGrav's chromatic mismatch model,

$$\widehat{t}_{\mathrm{mismatch}}(\nu) = \sum_{k=1}^{n} c_k (\ln \nu)^k, \tag{17.15}$$

where the number of terms and coefficients c_k are determined on a pulsar-by-pulsar basis. This appears adequate for many pulsar timing applications (Dolch et al. 2014; NANOGrav Collaboration et al. 2015; Zhu et al. 2015).

Fig. 68 shows chromatic template profiles, difference profiles, and timing offsets across ~ 1 to 2 GHz. These are based on the 2D profile modeling by Pennucci (2019). Though the profiles differ very little by eye, ToA differences of a sizable fraction of a microsecond occur for MSP J1713+0747 though they are only $\sim 10\,\mathrm{ns}$ for J1909-3744 owing to its narrow pulse. The offset curve for J1713+0747 is consistent with that based on measured profiles shown by Dolch et al. (2014, Figure 4).

The shape of t_{mismatch} vs. ν is methodology dependent, contingent on the template used to determine ToAs. As such it generally crosses zero with an arbitrary zero point. This implies that a power-law model such as $t_{\mathrm{mismatch}}(\nu) \propto \nu^{-X_{\mathrm{mismatch}}}$ cannot account for this term. On the other hand, the chromatic mismatch model (Eq. (17.15)) can handle zero crossings of t_{mismatch}.

Similarly the two dimensional template method for ToA estimation over wide frequency bands (Pennucci et al. 2014) also accounts for profile chromaticity. With strict epoch independence, the t_{mismatch} term can be removed to essentially arbitrary precision under the conditions outlined here. In the radio band chromatic, epoch dependent ISM effects (and RFI) may obviate this possibility because they require attention to epoch dependent scattering and the chromaticity of PBF shapes for power-law media.

[49] Note however that scattering off interstellar grains can induce multipath propagation even in X-rays (e.g. Mauche and Gorenstein 1986).

[50] We associate t_∞ with the rotational phase of a fiducial point on the neutron star's surface or, equivalently, the average location in the magnetosphere for emission at a particular frequency, which is achromatic and epoch independent (at least over time spans much less than the spindown time). Differential emission times vs. frequency in the pulsar's magnetosphere (c.f. Fig. 10) are then included in the chromaticity of the pulse profile.

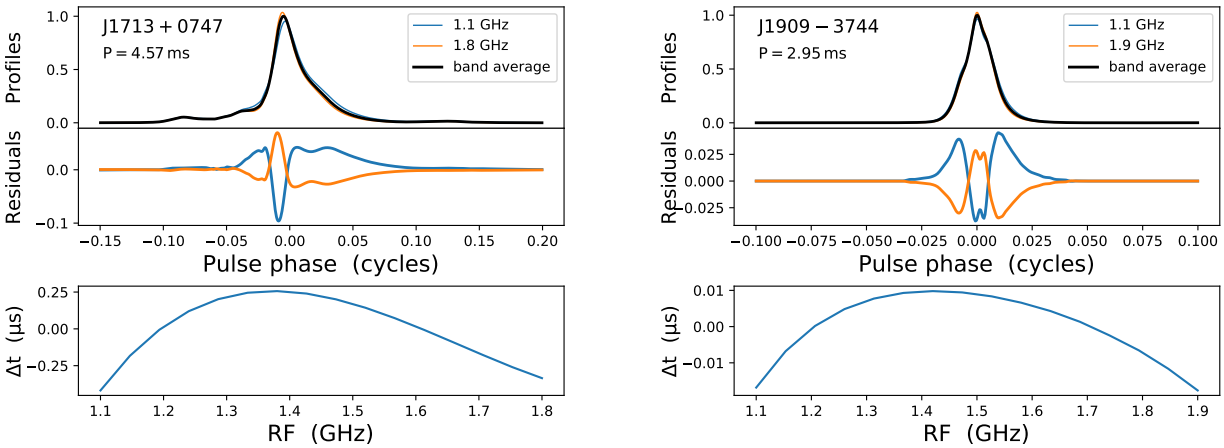


Figure 68. Timing offsets caused by profile chromaticity for two MSPs. Top panels: profiles at band edges and a full-band average profile. Middle panels: profile differences from the band average. Bottom panels: relative timing offset by using the band average as a template and removing a fit for a ν^{-2} DM term. Profiles are generated using the interpolation method developed by Pennucci (2019) as applied in the 15-yr NANOGrav data set (https://zenodo.org/records/16051178) and using software obtained at https://github.com/pennucci/PulsePortraiture and implemented by M. Lam.

17.4.2. *Inclusion of an epoch independent dispersion term*

Inclusion of a dispersion term with DM that varies with epoch but is achromatic (no scattering) yields the next simplest case,

$$\widehat{t}_\nu = t_\infty + \frac{K_{\rm DM}\mathrm{DM}(\bar{t})}{\nu^2} + t_{\rm mismatch} + \Delta t_{\rm S/N} + \Delta t_{\rm J}, \tag{17.16}$$

In principle, multifrequency observations and prior determination of $t_{\rm mismatch}$ can remove the DM term to a precision limited only by the white noise terms. If applied to radio pulsars, this model would lead to chromatic leakage into estimates of t_∞ caused by scattering, which causes DM to be chromatic.

17.4.3. *Full expression for ToAs at the SSBC*

Motions of the pulsar, ISM, and observer introduce epoch dependence in all propagation effects, including refraction and multipath propagation from scattering that also require differing chromatic terms in the timing equation. Pulse distortion from the convolution with the PBF induces short term and long term timing offsets. Refraction, which varies on day to several month time scales, causes image wander and distortion of the PBF (Sect. 11.3).

We account for the epoch and frequency dependent DM term $\overline{\mathrm{DM}}(\nu,\bar{t})$ by expanding $\overline{\mathrm{DM}}(\nu,\bar{t}) = \langle\overline{\mathrm{DM}}(\overline{\nu},\bar{t})\rangle_B + \delta\overline{\mathrm{DM}}(\nu,\bar{t})$ as an average over the receiver bandwidth and a fluctuating part. Translation of ToAs to the SSBC requires clock corrections and accounting for Doppler shifts and astrometric errors. Details of these and other corrections are well discussed in (e.g.) Stairs (2003), Edwards et al. (2006), and Taylor (2021). Here we include an additional error term in the translation to the barycenter related to the Römer term for the difference in propagation times to a terrestrial observatory and to the SSBC; it is nominally achromatic, involving the geometric path length difference with parallax and proper motion of the pulsar included. Inclusion of the refraction (AOA) term $\Delta t_{\rm AOA,SSBC}(\bar{t},\overline{\nu})$ renders the Römer term chromatic (Foster and Cordes 1990) in expressions for the arrival time and radio frequencies

referenced to the SSBC[51],

$$\begin{aligned}\widehat{t}_\nu = t_\infty + t_{\rm mismatch}(\overline{\nu},\nu_{\rm ref}) + \frac{K_{\rm DM}\langle\overline{\rm DM}(\overline{\nu},\bar{t})\rangle_B}{\nu^2} \\ + \Delta t_{\rm S/N} + \Delta t_{\rm J} + \Delta t^{\rm (all)}_{\delta p} \\ + \Delta t^{\rm (all)}_{\delta\overline{p}} + \frac{K_{\rm DM}\delta\overline{\rm DM}(\nu,\bar{t})}{\nu^2} + \Delta t_{\rm AOA,SSBC}(\bar{t},\overline{\nu}).\end{aligned} \tag{17.17}$$

The terms are ordered so that the first line of Eq. (17.17) includes the usual target of interest, the achromatic t_∞ term, the epoch-independent mismatch term from chromatic pulse shapes, and the $\overline{\rm DM}$ term with an achromatic DM at epoch $\bar{t}$. The second line includes the well-recognized white-noise terms from the finite S/N, jitter, and DISS/FSE that change rapidly (i.e. statistically independent between non-overlapping data sets), while the third line includes three ToA offsets that vary slowly from changes in PBF shape, the chromatic DM term, and the AOA/SSBC term.

The physical origin of the terms and their fluctuation properties with respect to epoch $\bar{t}$ and fluctuation frequency f are summarized in more detail:

1. t_∞ includes all achromatic contributions from a deterministic spin model, including spin noise, emission location and direction, and orbital terms (all added to the mean propagation time related to the secularly changing pulsar distance,) and GW perturbations. Spin noise and GW perturbations have red, power-law like spectra and any continuouse-wave GW signals add spectral lines.

2. $t_{\rm mismatch}(\overline{\nu},\nu_{\rm ref})$ is the timing offset due to profile changes with frequency when the template at $\nu_{\rm ref}$ is used for template fitting at other frequencies. It is defined to be epoch independent; pulsars that show epoch dependent profiles do so on a variety of time scales; those with discontinuous 'mode' changes would show f^{-4} spectra while variations like that of J1713+0747 would have amorphous spectra (note however that this kind of profile change would be mitigated through modeling in the time domain, not the spectral domain).

3. $K_{\rm DM}\nu^{-2}\overline{\rm DM}(\bar{t},\overline{\nu})_B$ is the dispersion term associated with the average DM across the bandwidth B for center frequency $\overline{\nu}$ and scales strictly as ν^{-2}. Its variations with epoch conform to a power law spectrum determined by the wavenumber spectrum of the electron density with enhancements by discrete interstellar structures. Additional contributions from the solar wind and Earth's ionosphere are typically much smaller but are variable over a wide range of time scales.

4. $\Delta t_{\rm S/N} + \Delta t_{\rm J} + \Delta t^{\rm (all)}_{\delta p}$ from radiometer noise, pulse jitter, and the DISS/FSE effect have different radio frequency dependences but combine as white temporal noise for ToAs obtained from data that do not overlap in epoch or, for $\Delta t^{\rm (all)}_{\delta p}$, epochs separated by more than a DISS time scale (minutes to hours). Across frequency, $\Delta t_{\rm S/N}$ is uncorrelated between frequency channels (subbands) while $\Delta t_{\rm J}$ is highly correlated over (at least) an octave in frequency. The $\Delta t^{\rm (all)}_{\delta p}$ term is intermediate with a correlation bandwidth $\Delta\nu_{\rm d}$ much smaller than an octave but often spanning multiple frequency channels.

5. $\Delta t^{\rm (all)}_{\delta\overline{p}}(\bar{t},\overline{\nu})$ is the timing offset from long term temporal changes in PBF shape; it has a flat spectrum that rolls off at approximately the inverse of the RISS time scale, $f \sim \Delta t^{-1}_{\rm RISS}$.

6. $K_{\rm DM}\delta\overline{\rm DM}(\nu,\bar{t})/\nu^2$ is the chromatic error from the scattering-induced frequency dependence of DM. It also has a flat spectrum that rolls off at $f \sim \Delta t^{-1}_{\rm RISS}$ (Cordes et al. (2016, Figure 5) and Sect. 12.2).

7. $\Delta t_{\rm AOA,SSBC}(\bar{t},\overline{\nu})$ from the barycentric translation of ToAs caused by interstellar refraction that varies both stochastically and cyclically with a yearly period. The spectrum is a shallow power law with rolloff at $f \sim \Delta t^{-1}_{\rm RISS}$ shifted to a centroid of $1\,{\rm cy\,yr^{-1}}$.

[51] Both the solar wind and the ISM contribute to refraction but our focus is on the interstellar contribution. For impact parameters of a line of sight greater than $20\,{\rm deg} \ll 1\,{\rm au}$, refraction in the solar wind (Fomalont et al. 2009) is smaller than from the ISM. Some pulsars are observed close to the Sun, so refraction from the Sun should be investigated in more detail for those cases.

18. ToA ERROR CORRECTIONS

Raw arrival times from template fitting include all delays and pulse distortions imposed at the pulsar and during propagation (and instrumental effects peculiar to each observing system.).

Any departure of a measured pulse profile's shape from that of the template yields an arrival time offset. Shape differences can be imposed by propagation, instrumentation, or RFI. They also occur statistically from the finite number of pulses used to form a profile. Systematic changes in shape occur as 'mode changes' (predominantly in CPs) where single pulses are drawn from two or more pulse populations whose averages converge to different template shapes.

18.1. *Mitigation of intrinsic (emitted) pulse shape variations (jitter etc.)*

Correlations between profile shape and timing offset can be exploited as the basis for ToA error correction. These methods have been explored using a variety of techniques, including principal component analysis (PCA), as we will discuss here.

Suppose a pulse shape parameter $S_{\rm p}$ is determined for a sequence of average profiles, each comprising the sum of N pulses. Profiles differ for the reasons cited above (along with additive noise) and the shape parameter could be as simple as the amplitude ratio of two components or it could be the projection of a profile onto one or more of the basis functions from PCA. Departures $\delta S = S_{\rm p} - \langle S_{\rm p}\rangle$ from the shape parameter $\langle S_{\rm p}\rangle$ of the template may correlate with corresponding timing offsets $\delta t = t_{\rm p} - \langle t_{\rm p}\rangle$. A linear ToA corrector that minimizes the mean-square difference between the corrected ToA $t_{\rm c}$ and the true ToA is

$$t_{\rm c} = t + (\sigma_{t_{\rm p}}/\sigma_{S_{\rm p}})\rho_{\rm S,t}\delta S, \tag{18.1}$$

where $\rho_{\rm S,t}$ is the correlation coefficient, t is the nominal ToA and the correction involves the RMS values of $t_{\rm p}$ and $S_{\rm p}$. If the shape parameter, $S_{\rm p}$, depends on the absolute phase alignment of the profile, this procedure can lead to overcorrection, reducing ToA differences from all sources rather than only those caused by differences in profile shape. For this reason, only shape parameters which are independent of profile alignment (such as the amplitude ratio of two components, or the overall skewness of the profile, but not, e.g., the central phase of a component) should be used for correction. The efficacy of the error correction, as measured by the RMS corrected ToA, $\sigma_{t_{\rm c}} = \sigma_{t_{\rm p}}(1-\rho^2_{\rm S,t})^{1/2}$ requires a large correlation coefficient to make significant improvements. To reduce the RMS error by 50% requires $|\rho_{\rm S,t}| = \sqrt{3}/2 \simeq 0.87$.

The earliest attempt of this type of ToA correction was by Downs and Krause-Polstorff (1986, Appendix) in their analysis of timing variations based on a profile shape analysis method. Trying several types of shape parameters, they found no significant correlation for the Vela pulsar and only $\sim 30\%$ correlation for two pulsars (B1818−04 and B1911−04) out of the other 21 pulsars in the JPL timing program (Downs and Reichley 1983). A retrospective analysis using results in Sect. 12.5.1 implies that the lack of correlation for the JPL sample is due to the absence of dedispersion of the S-band data[52]. As shown in Sect. 12.5.1, interstellar scintillation causes the effective center frequency to vary on a diffractive scintillation time scale, producing timing variations (c.f. Eq. (12.34)) without significant changes in pulse shape. For the bright Vela pulsar, this effect dominates the jitter error, which in turn is larger than the radiometer noise contribution. In this situation, no correlation is expected, because changes in effective center frequency do not modify the pulse shape.

Usage of PCA for pulse shape and related studies was done by Blaskiewicz (1991), Demorest (2007), and Osłowski et al. (2011). Correction of ToAs from the very bright MSP J0437−4715 using PCA yielded a 20% reduction in ToA error (Osłowski et al. 2011) and a similar reduction on a long-period pulsar by Lin et al. (2018). Recent work further developed PCA-based tools for characterizing pulse shape variations of simulated data and pulses from the Vela pulsar (Jennings et al. 2024a) and transitory shape variations from the MSP J1713+0747 (Jennings et al. 2024b). Application to ToA correction to the Vela pulsar yielded a 30% reduction in ToA error (Jennings 2021). Shape

[52] The JPL program used a narrow bandwidth at S-band that yielded small dispersion smearing of pulses, so no dedispersion was deemed necessary.

parameters derived from principal components are not necessarily independent of profile alignment, and so, in general, ToA estimators based on them can overcorrect. For small ToA differences, this overcorrection can be largely eliminated by ensuring the principal components used are orthogonal to the derivative of the average profile shape (Osłowski et al. 2011). Alternatively, the ToA can be estimated directly using a maximum likelihood or maximum *a posteriori* method (Jennnings et al., in prep.), which eliminates overcorrection even when ToA differences are large.

Simulations of average profiles indicate that intrinsic phase jitter for pulsars with single-component profiles yields negligible correlation between pulse shapes and arrival times. However, there are significant correlations (and thus ToA improvements) for multicomponent profiles with strong amplitude variability of individual pulses with some degree of overlap in pulse phase (Jennings 2021). More dramatic changes from shape shifter pulsars, like those that display profile 'mode changes' (mostly seen in canonical pulsars) produce large correlations and thus significant corrections to ToAs (e.g. Nathan et al. 2023).

18.2. *Removing DM variations*

While DM delays dominate all other chromatic perturbations, completely removing them is confounded by refraction, scattering, and intrinsic pulse profile chromaticity. In §17 we briefly summarized two main approaches, one that operates on single-epoch pulse profiles and ToAs and an alternative that separates chromatic terms in long sequences of many-epoch ToAs (e.g. using DMX and Gaussian process models). Comparisons of methods have been presented by Iraci et al. (2024). Contributions to DM from the solar wind (SW) are absorbed in DM estimates so, to within the precision of those estimates, no special modeling of the SW is required. However, close approaches of lines of sight to the Sun yield rapidly changing DM(t) that requires special attention, including the possibility of excision of those epochs from timing analyses.

In the following we first consider pulsar-frequency combinations where scattering can be ignored even if $\ll 100\,$ns precision timing is striven for. Then we consider alternative approaches for making single-epoch corrections for dispersion and scattering.

18.3. *Conditions where ToA scattering bias is negligible*

To motivate the selection of pulsars based on allowable tolerance levels for scattering, we use a simplified ToA expression, $t_\nu = t_\infty + \nu^{-2} K_{\rm DM}{\rm DM} + \epsilon_\nu$, where the ToA at frequency ν is the sum of the true ToA t_∞, a dispersion term, and an error term ϵ_ν. Though timing measurements are now made with broadband receivers, the essential issues are illustrated using ToAs at two frequencies $\nu_{\rm l} < \nu_{\rm h}$ with ratio $R = \nu_{\rm h}/\nu_{\rm l} > 1$. These are used to estimate and remove the DM term, yielding an error for t_∞,

$$\delta\hat{t}_\infty = t_\infty - \widehat{t}_\infty = \frac{\epsilon_{\nu_{\rm l}} - R^2\epsilon_{\nu_{\rm h}}}{R^2-1} = \epsilon_{\nu_{\rm h}} \times \frac{(R^{X_\epsilon} - R^2)}{R^2-1}, \tag{18.2}$$

The high frequency error is enhanced by the R^2 factor but if ToA errors scale as $\epsilon_\nu \propto \nu^{-X_\epsilon}$ with $X_\epsilon > 2$, the low frequency error dominates the net error, as in the second equality. We showed earlier that the chromatic error is generally smaller than the scattering time and the scaling index X_ϵ is itself chromatic and satisfies $X_\epsilon \lesssim X_\tau$ where $X_\tau = 22/5$ for the Kolmogorov inertial subrange. It is therefore conservative to require the scattering time $\tau_{\nu_{\rm l}}$ to be less than some specified amount. Assuming $X_\epsilon > 2$ for ToA errors, Eq. (18.2) implies that the lowest frequency used by a PTA is the primary determinant of the DM-corrected ToA. Scattering delays can be ignored if they are below a chosen maximum and we invert the empirical expression for scattering times in Eq. (10.16) to derive the corresponding maximum DM.

No correction is needed if $\tau(\nu) < \tau_{\rm max}$ for a fixed value of $\tau_{\rm max}$, [53], which we choose to be $\tau_{\rm max} = 10\,$ns as a best-case value, yielding a constraint on frequency,

$$\nu \geq (\tau_1/\tau_{\rm max})^{1/X_\tau} \simeq 2.8\,{\rm GHz} \times [(10\,{\rm ns}/\tau_{\rm max})\tau_1]^{5/22}. \tag{18.3}$$

[53] An alternative is to require that only one scintle fills the bandwidth B, equivalent to having no frequency-dependent scintillation modulation, but since bandwidths differ between receivers, we prefer a constant maximum value.

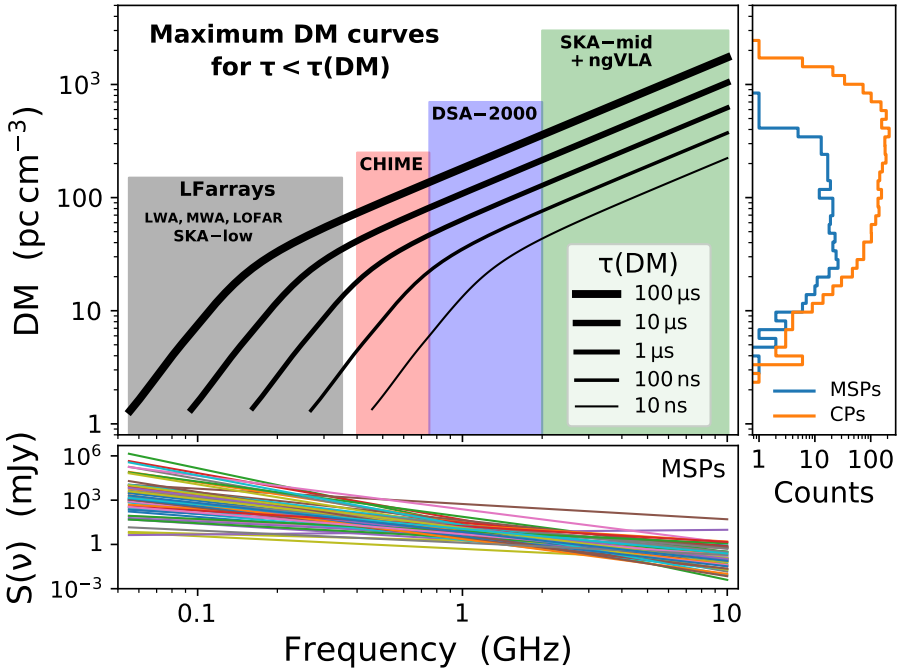


Figure 69. Scattering times vs. DM and radio frequency along with flux density spectra for MSPs and DM number counts for MSPs and CPs. Frequency bands of particular telescopes are indicated. Largest frame: lines of constant τ vs DM and frequency (black curves) calculated using the mean of the τ(DM) relation (Eq. (10.16)) shown in Fig. 36. There is substantial variation about these curves. Bottom frame: flux density vs. frequency for MSPs that have catalogued flux densities at 0.4 and 1.4 GHz (Manchester et al. 2005). Extrapolations to $\lesssim 0.1$ GHz are uncertain given that some pulsars show turnovers in their spectra. Right panel: DM histograms for MSPs and CPs in the Milky Way disk; globular cluster pulsars are excluded.

Fig. 69 shows lines of constant τ as a function of DM and frequency for scattering times from 10 ns to 100 μs along with frequency ranges for several low-frequency arrays and CHIME along with bands covered by forthcoming arrays (DSA-2000, SKA-mid, and the ngVLA). Current PTA programs by worldwide collaborations (CPTA, EPTA, InPTA, MPTA, NANOGrav, and PPTA) use a large number of telescopes approximately coincident with the band indicated for DSA-2000.

For a telescope covering a specific frequency range, like those indicated in the figure, the lowest frequency determines whether the timing analysis can avoid mitigation of scattering. For example, pulsars with DM $\lesssim 4$ pc cm^{-3} satisfy the condition $\tau(\mathrm{DM}, \nu) \leq 100$ ns for the CHIME frequency band (0.4 to 0.8 GHz), DM $\lesssim 20$ pc cm^{-3} for the 0.7 to 2 GHz band for DSA-2000, and DM $\lesssim 75$ pc cm^{-3} for timing programs with 2 GHz as the lowest frequency. Low-frequency arrays will require scattering mitigation to achieve 100 ns precision. Conducting observations at high frequencies is limited by the generally steep decline in flux densities, as shown in the bottom panel of Fig. 69. Given the typically steep spectra of radio pulsars, observations from ~ 1 to 2 GHz generally offer a good compromise between minimizing interstellar delays and maximizing signal-to-noise ratios. Magnetars have flat radio spectra, allowing observations at much higher frequencies where scattering is minimal, but even at low frequencies, interstellar scattering delays are completely dominated by intrinsic spin noise in those objects.

While restricting PTA programs to low-DM pulsars is one strategy, the DM histograms in the right-hand panel of Fig. 69 show that scattering mitigation for MSPs with DM > 20 pc cm^{-3} could increase the sensitivity to GWs, perhaps significantly, by virtue of the sheer increase in pulsar numbers.

Timing programs with other goals, such as orbit monitoring of relativistic double neutron star binaries, need not have such demanding requirements on scattering times because other factors can determine the achievable precision in those cases, such as the longer periods with their correspondingly wider pulses and their larger attendant pulse jitter.

18.4. *Mitigation of rapid PBF variations related to scintillation fluctuations*

ToA errors from scattering include rapid variations from the finite scintle effect (FSE, Sect. 12.5.2) combined with an epoch-dependent bias related to the scattering time τ. We consider the FSE here and ToA bias in the next sections. The FSE error is a zero mean error resulting from the variable number of scintles contributing to a TOA or, equivalently, from the stochasticity of the intensity PBF.

Fig. 70 shows simulated ToA variations and scintillation bandwidth estimates for 1000 realizations of a PBF for a thick medium (the results do not depend strongly on the type of medium). The left panels show δToA plotted against the $1/e$ scattering time estimated directly from PBF realizations and plotted against the scintillation bandwidth estimated from ACFs of the scintillation spectrum. The right hand panel shows a scatter plot of δToA and $\Delta\nu_{\rm d}$ along with a regression line. The ToA and $\Delta\nu_{\rm d}$ are typically (in these simulations) anticorrelated at $r_{\delta t,\Delta\nu_{\rm d}} = -39$ to -25%.

Anticorrelation of δToA with $\Delta\nu_{\rm d}$ implies a positive correlation with the scattering time, $r_{\delta t,\tau} = -r_{\delta t,\Delta\nu_{\rm d}}$. This correlation allows correction of the TOAs using an expression analogous to Eq. (18.1) $t_c = t - r_{\delta t,\tau}(\sigma_{ToA}/\sigma_\tau)(\tau - \langle\tau\rangle)$, yielding a reduction in ToA error by a factor $R_{\rm c} = (1 - r^2_{\delta t,\tau})^{1/2}$. For $r_{\delta t,\tau} \simeq 0.35$, the reduction factor is $R_{\rm c} \simeq 0.94$, i.e. only a 6% reduction.

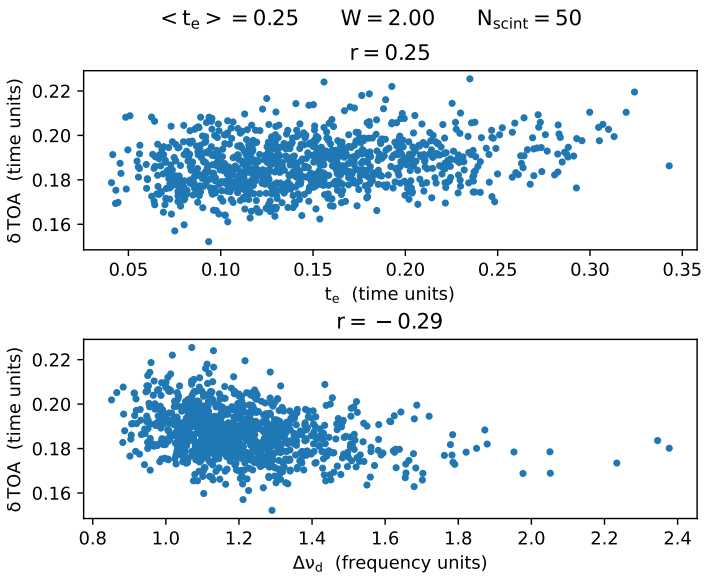


Figure 70. Simulations for a thick medium with a square-law structure function (1000 realizations). Top: δToA vs $1/e$ scattering time estimated directly from the noisy PBF. Bottom: δToA vs. scintillation bandwidth estimated from an ACF analysis of the scintillation spectrum $H(\nu)$.

18.5. *Mitigation of slow epoch-to-epoch scattering time (τ) variations*

To tackle the epoch-dependent variability of scattering, mitigation of scattering for timing purposes is best done using at-least contemporaneous and preferably simultaneous data for DM and scattering timing determinations. These quantities vary on a refractive time scale ($\Delta t_{\rm r}$, Table 4; see also Geiger et al. (2025)) which can range from hours to months or longer, depending on radio frequency and the particular line of sight. The alternative use of scattering/scintillation data from separated epochs can only partially mitigate scattering at a particular epoch. We focus here on the simultaneous case.

Use cases for scattering mitigation divide into two categories defined by the degree of scattering:

1. *Incoherent deconvolution of scattering:* This applies to strongly scattered pulsars with unresolvable scintillation structure. Distant pulsars observed at low frequencies will manifest scattering solely as pulse broadening because the scintillation bandwidth $\Delta\nu_{\rm d}$ is too small to resolve due to a combination of FT resolution limits and low S/N.

   A notable use case for incoherent deconvolution is its application to any special pulsar of interest at a large distance in the Galactic plane owing to its rarity. Large scattering times $\gtrsim 1$ ms, for example, would correspond to scintles with widths $\Delta\nu_{\rm d} \lesssim 160$ Hz and rapid DISS time scales too small to be isolated in most data sets. This implies contributions to pulse broadening in a typical data set from a large number of scintles (c.f. Eq. (12.33)) and an uncorrectable ToA error from the finite scintle effect (Sect. 12.5.2). However, the much larger systematic ToA offset can be mitigated through deconvolution.

   Arrival times can be a byproduct of deconvolution of an intensity PBF or pulse-shape modeling, with accuracy dependent on the fidelity of the modeled to actual shapes of the intrinsic pulse and PBF.

   Incoherent deconvolution of an intensity pulse broadening function from measured pulse shapes would be followed by template fitting at each frequency to obtain ToAs; these would be fitted for DM and dispersion delays then removed, as usual.

   Alternatively, the measured pulse can be forward modeled by convolving a model intrinsic pulse shape with candidate PBFs to identify the best PBF (e.g. Bhat et al. 2003; Geiger et al. 2025). As discussed previously, a mis-modeled intrinsic shape will introduce biased values for the scattering time and ToA as will a mis-matched PBF. This procedure can be repeated for all frequency channels and then a DM-corrected ToA can be estimated.

   The general flow of these methods is

$$\begin{array}{ll} \text{profile} & I(\phi,\nu;\bar{t}) \\ & + \\ \text{PBF} & p(t,\nu;\bar{t}) \end{array} \longrightarrow \text{model pulse and ToA } \widehat{t}_\nu \tag{18.4}$$

2. *Coherent deconvolution of scattering and high-resolution spectroscopy:.* Pulsars with resolvable scintillation structure allow alternative procedures. MSPs observed in current PTAs and other low-DM pulsars fall into this category. Timing error corrections can be based on detailed analysis of scintillation structure using several approaches, including phase-resolved spectroscopy (PRS) and cyclic spectroscopy (CS).

   To correct biased arrival times, first estimate the pulse broadening time τ or the DISS bandwidth $\Delta\nu_{\rm d} = C_1/2\pi\tau$ and then use the known pulse template to determine the ToA offset caused by τ. Recall that the ToA offset is generally not a simple function of τ (c.f. § 12.6.2). Calculate biased multifrequency arrival times using a fixed template followed by fitting and removal of multiple chromatic terms from the ToAs, one of which is for scattering, which is epoch dependent, and another for intrinsic profile chromaticity, which is largely epoch independent[54].

   The flow of this method involves two parallel steps

   (a) ToAs at frequency ν are obtained through template fitting of a profile at frequency ν and epoch $\bar{t}$:

$$\text{profile } I(\phi,\nu,\bar{t}) \longrightarrow \text{template fit} \longrightarrow \widehat{t}_\nu. \tag{18.5}$$

   (b) In parallel, the dynamic spectrum (DS) is produced by phase resolved spectroscopy (PRS) or by cyclic spectroscopy (CS) and an estimate for the ToA correction $\Delta t_\nu^{(c)}(\widehat{\tau}_{\rm d})$ is derived from the scintillation bandwidth $\widehat{\Delta\nu}_{\rm d}$,

$$\text{PRS or CS} \longrightarrow \text{dynamic spectrum (DS) } I(\nu,t,\bar{t}) \longrightarrow \widehat{\Delta\nu}_{\rm d} \longrightarrow \widehat{\tau}_{\rm d} \longrightarrow \delta\widehat{t}_\nu(\widehat{\tau}_{\rm d}). \tag{18.6}$$

   For high signal to noise cases, *coherent* deconvolution is a possibility. It makes use of the phase information in the CS to obtain the field PBF $\widetilde{h}$ and the intrinsic pulse shape. This effectively deconvolves the field PBF from the measured voltage signal:

$$\text{CS} \longrightarrow \text{unscattered pulse shape and PBF} \longrightarrow \text{corrected ToA}. \tag{18.7}$$

[54] The transitory pulse shape changes for J1713+0747 represent a counterexample (Lam et al. 2018a; Xu et al. 2021; Lam 2021; Lin et al. 2021; Singha et al. 2021; Jennings et al. 2024b)

18.5.1. *Intensity (incoherent) deconvolution of pulse broadening*

Inversion of scattering through deconvolution with noisy data is almost always problematic. With high enough S/N, an intensity PBF, if known, can be deconvolved from profiles. Two methods for doing so make use of Fourier transform division or application of the CLEAN algorithm. The first is based on the convolution theorem applied to the measured profile and an assumed PBF shape. With no additive noise, the FT of the intrinsic shape is simply the ratio of FTs, $\widetilde{U}(\nu) \propto \widetilde{I}(\nu)/\widetilde{p}(\nu)$ (Kuz'min and Izvekova 1993). However, additive noise makes this approach essentially infeasible because noise causes large excursions of the ratio.

The CLEAN algorithm, developed for deconvolution of the point spread function (PSF) from radio images obtained with aperture synthesis, has been used for a broader range of applications than interferometic imaging. It operates by iteratively subtracting a scaled and angle-shifted PSF from an image. For pulse profiles, an assumed PBF plays the role of the PSF and the pulse profile for the image. Without *a priori* knowledge of the PBF shape, iteration over a bank of PBF shapes can be applied to both identify the best PBF and determine the accompanying intrinsic pulse shape (Bhat et al. 2003, 2004; Tsai et al. 2017; Young and Lam 2024-02). A boundary condition that aids identification of the optimal PBF is that the resulting intrinsic intensity profile must be non-negative[55]. Application to heavily scattered pulsars (Bhat et al. 2004) shows that some LoS favor a thin screen PBF having a rapid rise time while others favor a thick medium with a slower rise.

Intensity deconvolution has the advantage that it can be applied to pulse profiles with long integration times $\gg \Delta t_{\rm ISS}$ and potentially high signal-to-noise ratios. However, to be useful, the pulse broadening must be "discernible," which we define as $\tau \gtrsim \epsilon W = \epsilon \mathrm{f_{DC}} P$ (W = unscattered pulse width, $\mathrm{f_{DC}}$ = pulse duty cycle) with $\epsilon \sim 0.1$.

Figure 71 shows regions in DM-period space where incoherent deconvolution is feasible for frequencies from 0.1 to 5 GHz assuming a constant duty cycle $\mathrm{f_{DC}} = 0.05$. If a period-dependent duty cycle is used, e.g. $\mathrm{f_{DC}} \propto P^{-1/2}$, the curves are not dramatically different except for small periods where the duty cycle is large, requiring a larger broadening time to satisfy the condition. Since the MSPs used in precision timing have pulse widths much narrower than predicted by the $P^{-1/2}$ scaling that applies to long-period pulsars (Rankin 1990; Maciesiak et al. 2012), the fixed duty-cycle curves are appropriate.

[55] Deconvolution with CLEAN has not been applied to other Stokes profiles, e.g. Q, U, V or $L = \sqrt{Q^2 + U^2}$. Particular objects may provide an advantage for discerning the PBF if the Stokes profile is narrower than the total intensity. However, Q, U and V are not constrained to be non-negative while L, though non-negative, is biased by off-pulse noise that needs subtraction.

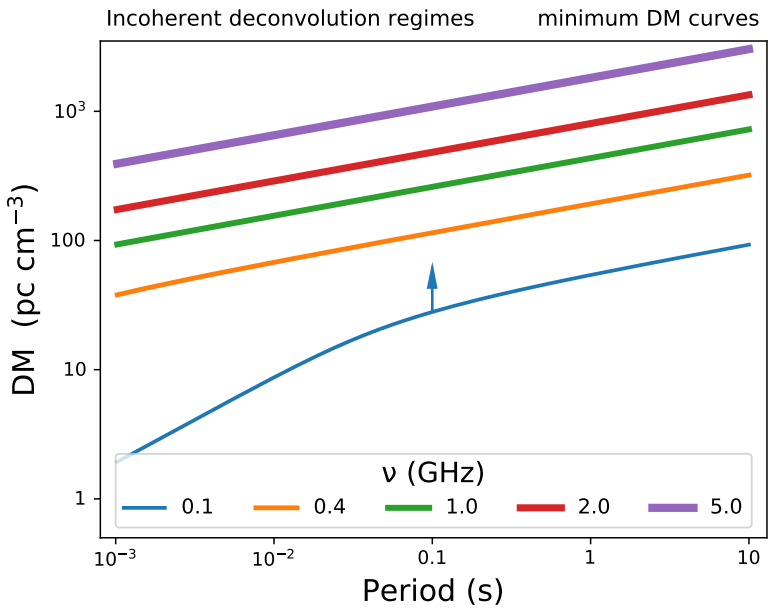


Figure 71. Regions in the DM-Period plane where it is efficacious to incoherently deconvolve the pulse-broadening function. The area above each line indicates the appropriate DM and pulse-period range for each frequency as indicated by the arrow.

18.5.2. *Forward modeling of pulse shapes*

Forward modeling involves convolution of an intrinsic profile model with candidate PBFs to identify the best PBF among a family of PBFs. As discussed in §17.3 , the best model PBFs are those drawn from electron densities with power-law wavenumber spectra, which can account for the variety of shapes encountered across all degrees of scattering. However, these (and any other analytical shapes) do not account for PBF distortions from refraction (§11.3), leading to mismatches between the model and actual PBF. As discussed previously, mis-modelling of the intrinsic shape and/or the PBF cause bias in the estimated scattering time and ToA (e.g., see also Lentati et al. 2017).

This procedure can be repeated for each frequency channel, making use of the expected frequency dependence of both τ and the PBF shape to aid estimation of the PBF parameter vector $\mathbf{\Theta}_{\rm PL}$. The resulting ToAs can then be analyzed to estimate DM and t_∞.

Customized profile modeling: As argued in Sect. 12.6.4, profile modeling with the correct shapes for the intrinsic pulse and PBF can completely remove the ToA error associated with the PBF envelope applicable at a given frequency and epoch.

A potential modeling scheme can proceed as follows. The PBF envelope $p(t, \nu; \bar{t})$ depends on the inner scale of the electron density wavenumber spectrum and is not generally self-similar vs. frequency. In contrast, an exponential PBF scales only by the single parameter, $\tau(\nu)$. It is most likely that the inner scale l_i is epoch independent for most pulsars, at least over the decades long time spans of PTA data. The key determinants of the PBF shape are β, the spectral index of the wavenumber spectrum, and the ratio $\zeta = l_i/l_{\rm d}(\nu)$, where the diffraction scale $l_{\rm d}(\nu)$ depends on the strength of scattering as well as on β. The method would be applied to each pulsar, requiring a preliminary analysis to determine basic parameters, and then an epoch-by-epoch analysis to obtain ToAs:

1. Use multiepoch, multi-frequency observations to determine β and l_i for the line of sight. At each epoch, simultaneous fitting over a bank of functions for both the intrinsic pulse and the PBF ideally will yield a determination of l_i and β. An analysis similar to this has been done by Geiger et al. (2025). In the few cases where l_i has been determined, values range from ~ 35 to ~ 1000 km (e.g. Moran et al. 1990; Spangler and Gwinn 1990; Molnar et al. 1995; Bhat et al. 2004; Rickett et al. 2009). The inner scale may be associated with the thermal proton

gyroradius or the proton inertial length, which involve the electron temperature, magnetic field, and electron density. Since all of these vary across the ISM, the inner scale almost certainly varies along an LoS as well as between different LoS.

2. The applicable value of β from pulse shape fitting may show much more regularity than exists in the literature (e.g. Lewandowski et al. 2013; Lewandowski et al. 2015; Geyer et al. 2017) owing to the bias effects discussed in Sect. 12.7. A working conjecture is that use of a fixed value for $\beta = 11/3$ in pulse modeling will suffice for the estimation of the inner scale in step 1.

3. For a sustained timing program, the intrinsic shape model $U_{\rm m}(t, \nu)$ and values for β and l_i from preliminary stages are used to model the pulse shape at each epoch and subband, yielding both the e^{-1} scattering time and the ToA(ν) as well as additional corroboration for the input values for β and l_i based on subband to subband results from the modeling.

Complications in pulse modeling result from interstellar refraction, which causes distortion of the applicable PBF that varies on refraction times of days for low-DM pulsars and weeks, months, or longer for high-DM pulsars. The severity of refractive distortion needs to be assessed on a case by case basis. At worst, corrections of ToAs for scattering will be limited by un-modeled refraction effects so that mere subtraction of a delay estimate based on the e^{-1} broadening time of method 1 is the best approach.

18.5.3. *Correction of ToAs using extant or contemporaneous estimates of the pulse broadening time τ.*

This approach uses a bulk, value for τ based on multiepoch measurements, which cannot correct for rapid FSE errors that are statistically independent between epochs. It can partially correct for slow, epochal changes in the shape of the PBF envelope (e.g. from refraction) if multi-epoch measurements are employed. The method involves estimation in subbands narrow enough so that $\tau(\nu)$ is close to constant over the subband and then use $\tau(\nu)$ from all subbands to correct ToAs for the scattering-induced error $\Delta t_{\delta p}$. This error is a function of the shapes of the intrinsic pulse and the PBF with frequency dependence unique to each pulsar. Simulations show that the systematic error is generally negative for some frequencies and positive for others. This cannot be captured as a Gaussian process but is better dealt with (for wideband systems) by model fitting ToAs obtained at each individual epoch.

18.5.4. *Scattering corrections using template fitting + dynamic spectrum analysis*

When scintillation structure is resolved in frequency, scattering corrections to ToAs can be derived from the scintillation bandwidth obtained from the DS. The DS itself is obtained from phase-resolved spectroscopy (PRS) or cyclic spectroscopy (CS), the choice depending on the ratio of scattering time to pulse width. Using a DS based on the same data (same time span and frequency band) as the ToA estimate, an autocorrelation analysis of the DS vs. frequency lag yields the scintillation bandwidth. The scattering time then follows from the uncertainty relation (Eq. (9.11)), $\widehat{\tau}_{\rm d} = C_1/2\pi\widehat{\Delta\nu}_{\rm d}$. The ToA correction $\Delta t_\nu^{(c)}(\tau)$ is generally a nonlinear function of τ dependent on the intrinsic pulse shape and PBF (§12.7). It therefore needs to be customized for each pulsar as a predetermined lookup table. One type of error associated with this procedure derives from not knowing the exact value of C_1 for real-world PBFs.

Fig. 72 identifies areas in the DM-frequency plane where a DS analysis is useful vs. those where scattering is too large for precision timing or too small to require mitigation. CS is required for large DMs and/or lower frequencies because $\Delta\nu_{\rm d}$ cannot be resolved with PRS, as indicated. Also shown are the relevant frequency ranges for the same telescopes indicated in Fig. 69.

The potential for coherent deconvolution is if the field PBF can be determined contemporaneously from the same data used to calculate ToAs. Doing so makes use of the phase information in the CS to obtain the field PBF $\widetilde{h}$ and the intrinsic pulse shape. This effectively deconvolves the field PBF from the measured voltage signal (e.g. Demorest 2011; Walker et al. 2013; Palliyaguru et al. 2015; Dolch et al. 2021; Turner et al. 2023, 2024). Coherent deconvolution strives to use CS to obtain the complex $h(t)$, which is essentially a task of *phase retrieval* of its Fourier transform, $\phi_{\rm CS}(\nu) = \arg\{\widetilde{h}(\nu)\}$. This has been demonstrated for the MSP J1939+2134 (B1937+21) in the afore cited papers but

it has not yet been used to obtain arrival times with greater precision than standard methods. Further work is needed in technique development and real-time access and processing of voltage data.

One approach uses the phase of $\left\langle \Gamma_{\widetilde{h}}(\delta\nu,\nu)\right\rangle_{P\ll T\ll\Delta t_{\rm d}}$,

$$\Phi_\Gamma(\delta\nu,\nu) = \phi_{\widetilde{h}}(\nu+\delta\nu/2) - \phi_{\widetilde{h}}(\nu-\delta\nu/2), \tag{18.8}$$

(where additive noise is ignored) to estimate the derivative for small $\delta\nu$,

$$\frac{d\phi_{\widetilde{h}}(\nu)}{d\nu} \simeq \frac{\Phi_\Gamma(\delta\nu,\nu)}{\delta\nu}. \tag{18.9}$$

Upon integration, this yields an estimated phase $\widehat{\phi}_{\widetilde{h}} \equiv \phi_{\rm CS}$ to within a constant. Unfortunately, unless statistical errors in $\Phi_\Gamma(\delta\nu,\nu)$ are very small, the derived phase will random walk away from the true solution. Also, numerical evaluation of the phase will inevitably introduce multiple 2π phase wraps that need to be dealt with.

An alternative approach avoids direct use of the phase by seeking an iterative solution for $\widetilde{h}$ that yields convergence to the measured $\left\langle \Gamma_{\widetilde{h}}(\delta\nu,\nu)\right\rangle_{P\ll T\ll\Delta t_{\rm d}}$. Simulations demonstrate the viability of this approach on idealized data and for the bright MSP J1939+2134 (e.g. Walker et al. 2013; Palliyaguru et al. 2015; Dolch et al. 2021). As of yet, the method has not yielded improvements in ToA estimates.

It is possible that coherent deconvolution will be fruitful in future, high S/N data. Though determination of $h(t)$ from the cyclic spectrum is not unique, it may be sufficient to at least partially correct TOAs and deconvolve the pulse shape. The regime in which this approach may work is expressed with the inequalities,

$$W_{\rm A} \sim 2\pi\tau_d \ll P \le T \ll \frac{\Delta t_{\rm d}}{N_{\rm b}}, \tag{18.10}$$

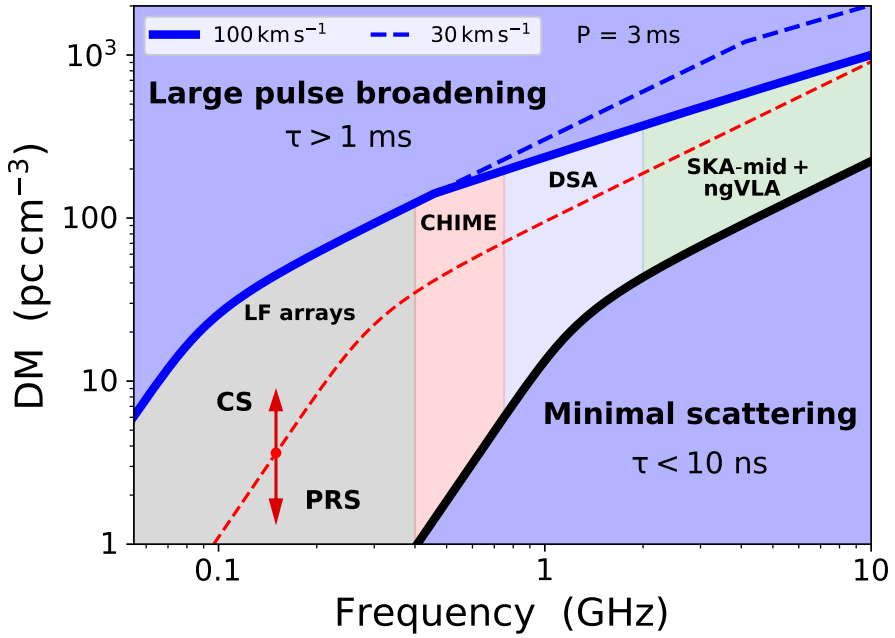


Figure 72. The DM-frequency plane for scattering mitigation using DS analyses. The region between the heavy blue and black lines is amenable to estimation of scattering corrections with DS obtained either using cyclic spectroscopy (CS) or phase-resolved spectroscopy (PRS) with the boundary indicated by the red dashed line. DMs below the black line correspond to negligible scattering in no need of mitigation while above the heavy blue line scintles are too small to allow a DS analysis, The blue dashed line shows the case where the effective speed is 30 km s^{-1} rather than 100 km s^{-1}.

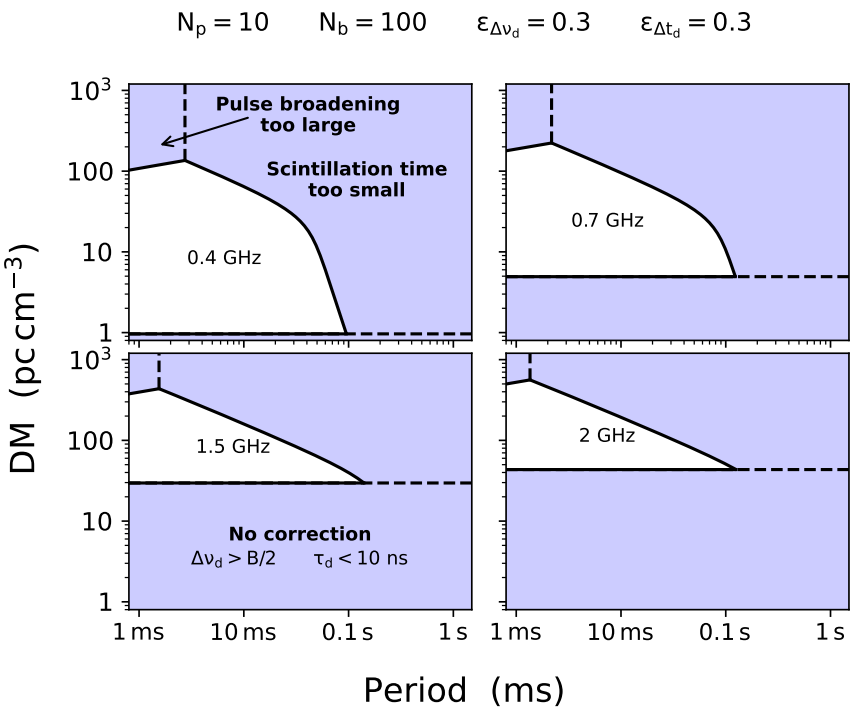


Figure 73. Regions in the DM vs. period plane where CS is potentially viable at four different frequencies (white). Excluded regions are based on Eq. (J.37), (J.39), and (J.41) and described in the text.

based on requiring the intrinsic pulse width W_A and scattering time to be much less than the pulse period, which in turn is much less than the time T used to calculate an individual FT. A large number of separate FT blocks need to be averaged to reduce errors. The aggregate time of $N_b \times T$ data blocks must be much less than scintle durations (Δt_d). The pulsar signal must have high S/N, which is a separate requirement from Eq. (18.10). Using the hockey-stick expression for τ in Eq. (10.16) and Δt_d expressed in terms of τ, we produce the allowed ranges in DM and P shown in Fig. 73 that satisfy the inequalities of Eq. (18.10). It is clear that coherent deconvolution is viable only for pulsars with short periods and small DMs for frequencies $\sim$0.4 to 1.4 GHz. The cases shown are for $N_b = 100$.

In principle, the phase space for coherent deconvolution can potentially be applied to MSPs with DM $\gtrsim 100$ pc cm^{-3} for timing programs covering 0.4 to 2 GHz (or higher). However, signal to noise considerations imply that only a few MSPs may satisfy the conditions using 100-m class telescopes. However $\sim$ 300-m class telescopes (Arecibo, FAST, DSA-2000, and SKA) can enlargen this number. At present, coherent deconvolution requires further experimentation. Nonetheless, even when a full coherent deconvolution is not possible, the cyclic spectrum a remains a useful tool for RFI mitigation given the fine frequency resolution it enables. Whether this should be done routinely is a resource-specific question, but should become increasingly feasible with growing compute power.

18.5.5. *Phase retrieval with the Hilbert Transform (HT)*

The scintillation spectrum $H(\nu, \bar{t}) \equiv |\widetilde{h}(\nu, \bar{t})|^2$, though possessing no phase information, can be used as the basis for deriving a *minimum delay field PBF*. As with CS, implementation of an Hilber transform (HT)-based method requires high S/N data. Though not yet used in scattering mitigation, it may find application in niche circumstances. Here we summarize the utility of the HT. A more detailed, exploratory analysis is given in NANOGrav Memorandum 9 (2012-2025)[56].

[56] J.M. Cordes, *Correction Methods for Interstellar Pulse Broadening*, https://nanograv.org/science/memos-white-papers

Generally a function cannot be determined uniquely from the magnitude of its FT or from its autocorrelation function (e.g. Scargle 1981). Additional conditions may yield a unique result, modulo S/N uncertainties as with the CS approach. A thorough discussion of conditions required for phase retrieval is given in Klibanov et al. (1995). For a causal function, the real and imaginary parts of its FT are related by an HT, as with the Kramers-Kronig relations for dispersion relations in dielectrics. The Hilbert transform yields a phase $\phi_{\rm HT}(\nu)$ corresponding to the *minimum delay* solution for the time-domain function,

$$\phi_{\rm HT}(\nu) = \frac{1}{\pi}\,\mathcal{P}\int_{-\infty}^{\infty} d\nu'\,\frac{\ln|\tilde{h}(\nu)|}{(\nu-\nu')}, \tag{18.11}$$

where $\mathcal{P}$ denotes Cauchy principal component and $|\widetilde{h}(\nu)| = \sqrt{H(\nu,\bar{t})}$ is the FT magnitude at epoch $\bar{t}$ for a snapshot shorter than the scintillation time $\Delta t_{\rm d}$. That is, $H(\nu,\bar{t})$ is well approximated by the DS at a fixed time if the DS has sufficiently averaged out fluctuations from pulsar self noise. The implied signal flow going from the DS to an HT-based field PBF is

$$\left\langle|\widetilde{\varepsilon}(\nu)|^2\right\rangle_{P\ll T\ll\Delta t_{\rm d}} \;\longrightarrow\; |\widetilde{h}(\nu)|^2 \;\longrightarrow\; \phi_{\rm HT}(\nu) \;\longrightarrow\; \widetilde{h}_{\rm HT}(\nu) \;\longrightarrow\; h_{\rm HT}(t). \tag{18.12}$$

If the field PBF decreases monotonically, such as the one-sided exponential function, it can be determined uniquely using the HT. Empirical studies based on secondary spectra show (Brisken et al. 2010; Stinebring et al. 2022), however, that PBFs are not monotonic and can be multimodal, albeit with peaks that generally are substantially smaller than the PBF's maximum. In this case the width of the HT solution is biased low. For quasi-monotonic PBFs[57], there is a systematic relationship between the width of the HT and actual PBFs. An example is given in Fig. 15 of Memo 9 cited above, showing that the mean delay of the HT-PBF is on average ∼70% of the mean of the true PBF. This delay is, of course, not the same as the ToA correction, so further analysis like that described earlier is needed to relate the PBF width to the correction.

Cyclic spectroscopy may play a role in providing high-resolution intensity dynamic spectra for cases where scintles are too small in frequency extent to be resolved with standard setups for pulsar timing (i.e. where frequency resolution is determined by dedispersion contraints). However, data from low-DM pulsars with resolved scintles can be treated without recourse to CS.

18.6. *Assessment of MSPs for scattering mitigation*

ToA correctability for a specific MSP depends on its pulse properties, the DM (and scattering) depth along its line of sight, and especially on observation frequency. Here we evaluate individual MSPs at four frequencies (0.4, 0.7, 1.5, and 2 GHz) for 20% fractional bandwidths using conditions derived in Appendix J. The primary constraint is that the net arrival time have an error below a specified ceiling of 1 μs, which we choose as a useful fiducial value. Some MSPs require no correction at the higher frequencies while others cannot be plausibly corrected to this precision.

In the following we use the following units: Frequency ν and bandwidth B are in GHz; period P and pulse width $W_{\rm A}$ are in ms. The system equivalent flux density (SEFD) $S_{\rm sys}$ is in Jy and the period-average flux density S_ϕ is in mJy. Scattering times τ_1 at 1 GHz are in μs and $\Delta\nu_{\rm d}$ is the scintillation bandwidth in MHz. The effective scattering screen distance d' is in kpc and the effective velocity $\rm v_{eff}$ is referenced to 100 km s^{-1}.

Expressions used to assess each MSP are as follows:

1. *Scattering times:* We evaluate scattering times using the empirical τ(DM) relation (Eq. (10.16) and a frequency scaling $\tau \propto \nu^{X_\tau}$ with index $X_\tau = 22/5$, appropriate for scattering dominated by scales in the inertial subrange of a Kolmogorov spectrum. High DM pulsars observed at low frequencies will manifest the effects of the inner scale and reduce the index to $X_\tau = 4$. We invert Eq. (10.16) to obtain a DM value or frequency corresponding to a specified scattering time.

[57] I.e. those for which there is a prevailing decay superposed with small bumps.

2. *No scattering correction needed:* Requiring $\tau \leq \tau_{\rm max}$ for a fixed maximum $\tau_{\rm max}$ implies a lower bound on frequency. For $\tau_{\rm max} = 10\,{\rm ns}$ (but using τ_1 in μs, as above),

$$\nu > (\tau_1/\tau_{\rm max})^{1/X_\tau} \simeq 2.8\,{\rm GHz} \times [(10\,{\rm ns}/\tau_{\rm max})\tau_1]^{5/22}. \tag{18.13}$$

Fig. 69 shows curves of constant τ in the DM -ν plane. These can be used to identify where the scattering time is too small to warrant correction.

3. *Scattering too large:* Scattering is deemed too large to correct if a $100\epsilon_\tau$% accuracy determination of τ exceeds $\delta\tau_{\rm max}$. Using τ_1 and $\delta\tau_{\rm max}$ with the same units,

$$\nu < (\epsilon_\tau\tau_1/\delta\tau_{\rm max})^{1/X_\tau} = 0.35\,{\rm GHz} \times [(\epsilon_\tau/0.01)(\tau_1/\delta\tau_{\rm max})]^{5/22}. \tag{18.14}$$

The nominal 1% accuracy in determining τ is generous in the sense that it is difficult to achieve, causing fewer pulsars to be ruled out than might be more realistic.

4. *Cyclic spectroscopy required:* This condition occurs when resolving scintles in frequency requires FFTs longer than the pulse width. If $\tau(\nu)$ is small enough, standard phase-resolved spectroscopy (PRS) is sufficient to provide a dynamic spectrum (DS) from which the scintillation bandwidth $\Delta\nu_{\rm d}$ and τ can be estimated. For PRS, the maximum FT length is restricted to the pulse width $W_{\rm A}$, yielding frequency resolution $\Delta\nu \gtrsim W_{\rm A}^{-1}$. We require that it be a fraction $\epsilon_{\Delta\nu_{\rm d}} = 0.1$ of the scintillation bandwidth, $W_{\rm A}^{-1} < \epsilon_{\Delta\nu_{\rm d}}\Delta\nu_{\rm d}$. With $W_{\rm A}$ in ms units,

$$\nu < (2\pi\tau_1/\epsilon_{\Delta\nu_{\rm d}}C_1W_{\rm A})^{1/X_\tau} \simeq 0.53\,{\rm GHz} \times (\tau_1/C_1W_{\rm A})^{5/22}. \tag{18.15}$$

5. *Errors on estimates of scintillation bandwidth from a dynamic spectrum:* An ACF analysis of the DS yields $\Delta\nu_{\rm d}$ with errors from radiometer noise (N) and from the finite number of scintles (FSE) spanned by the DS. The fractional errors are derived in Appendix J: (a) Fractional error in $\Delta\nu_{\rm d}$ from radiometer noise (based on PRS with frequency resolution $\delta\nu = W_{\rm A}^{-1}$):

$$\begin{aligned}\varepsilon^{\rm (N)}_{\Delta\nu_{\rm d}} &\simeq \frac{2K_{\Delta\nu_{\rm d}}S_{\rm sys}}{\langle S_\nu\rangle_\phi}\left(\frac{W_{\rm A}/P}{BT_{\rm total}W_{\rm A}\Delta\nu_{\rm d}}\right)^{1/2}\\ &\simeq 10^{-4} \times \left(\frac{S_{\rm sys}/3\,{\rm Jy}}{\langle S_\nu\rangle_\phi/1\,{\rm mJy}}\right)\left(\frac{W_{\rm A}}{P}\right)^{1/2}\frac{1}{\sqrt{(B(T_{\rm total}/1\,{\rm h})W_{\rm A}\Delta\nu_{\rm d}]}}.\end{aligned} \tag{18.16}$$

(b) Fractional error in $\Delta\nu_{\rm d}$ from the finite number of scintles:

$$\varepsilon^{\rm (FSE)}_{\Delta\nu_{\rm d}} \simeq N_{\rm scint}^{-1/2} \simeq 8.4\times10^{-3}\times\nu^{14/5}\left(\frac{d'}{\tau_1^3}\right)^{1/4}\frac{1}{\sqrt{B(T_{\rm total}/1\,{\rm h})(v/100\,{\rm km\,s^{-1}})}} \tag{18.17}$$

where the number of scintles contributing to the DS is assumed large,

$$N_{\rm scint} \simeq \eta_t\eta_\nu(B/\Delta\nu_{\rm d})(T/\Delta t_{\rm d}) \simeq 3960\nu^{-28/5}\,B_{\rm GHz}T_{1000}v_{100}\,\left(\tau_1^3/d'\right)^{1/2} \gg 1. \tag{18.18}$$

Fig. 74 shows the number of MSPs that fall into the different correctability categories for four frequency bands. Assessments are made only if flux density measurements are available in the ATNF pulsar catalog (Manchester et al. 2005). Results for the NANOGrav sample (69 objects) are shown in the left panel and for a larger, non-overlapping sample of 159 MSPs in the right panel. We emphasize that the NANOGrav sample overlaps significantly with those of other Northern-hemisphere PTA programs (those by the CPTA and EPTA), so we consider it to be representative of the MSPs included in PTA programs. The non-NANOGrav sample includes some of the MSPs observed in other PTA programs but the key feature of the non-NANOGrav sample for the discussion here is that it extends to significantly higher DMs, for which interstellar effects are much larger.

A summary of trends that can be inferred from the figure include:

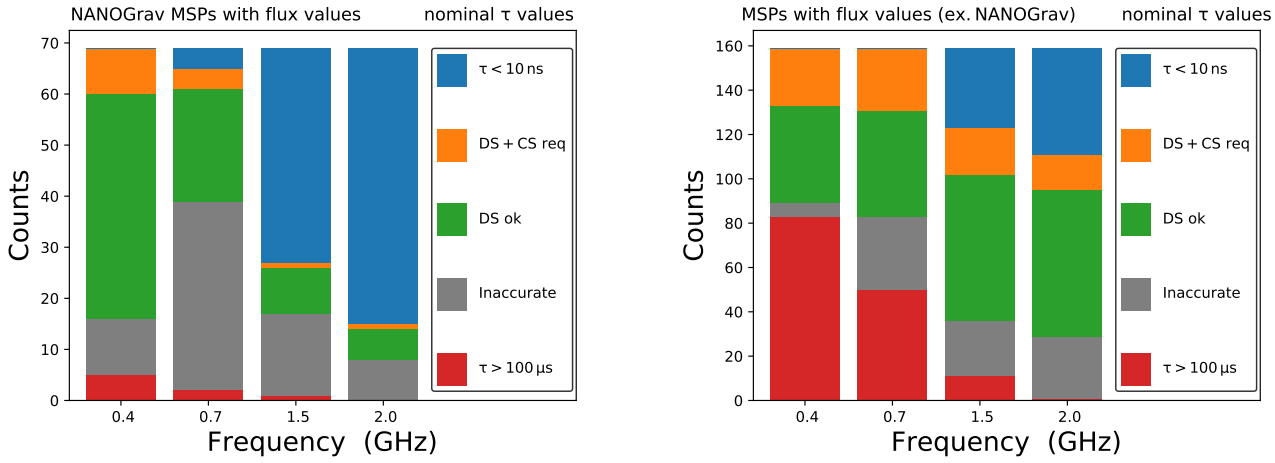


Figure 74. Bar charts showing counts in the scattering categories. Left: NANOGrav pulsars (only those with flux density values included) Right: Other MSPs with flux density values.

1. The fraction of scattering influenced ToAs (those with scattering times $> 10\,\mathrm{ns}$ shown in colors other than blue) is sizable at 0.4 GHz in the NANOGrav sample (left panel) but declines rapidly with increasing frequency (DISS = diffractive interstellar scintillations).
2. The fraction of scattering influenced ToAs is significantly larger for the 159 MSP sample that excludes NANOGrav MSPs (right panel) than for the 69 NANOGrav-only MSPs. This reflects the smaller mean DM for the NANOGrav sample, $\langle \mathrm{DM}_{\mathrm{NANOGrav}} \rangle = 29\,\mathrm{pc\ cm^{-3}}$ compared to $\langle \mathrm{DM}_{\mathrm{ex-NANOGrav}} \rangle = 105\,\mathrm{pc\ cm^{-3}}$.
3. The corresponding mean scattering times are a factor of ten larger for the 159 MSP sample compared to the NANOGrav sample, based on the mean $\tau-$DM relation (Eq. (10.16)).
4. The fraction of pulsars that can benefit from scattering determinations from DS analysis depends on whether rapid or slow distortions of profiles are considered:
   (a) Rapid variations from the finite number of scintles in a DS: about 17% at 0.4 GHz, dropping to 5% at 0.7 GHz and zero at 1.5 GHz and above.
   (b) Slow variations from changes in the scattering time and PBF shape (from refraction): about 34% at 0.4 GHz and 10% at 1.5 GHz.
5. For MSP-frequency combinations that can benefit from an analysis of dynamic spectra, phase-resoloved spectroscopy (PRS) suffices for the majority of the cases (green) while CS is needed for ∼10 to 30% (red), depending on frequency and whether the NANOGrav or non-NANOGrav sample is considered.

19. SPIN NOISE TRIAGE

MSPs are used in PTAs because they are much more spin stable than canonical pulsars and, per unit telescope time, they provide a much larger number of pulses for averaging down emission self white noise (e.g. pulse jitter). However, red spin noise (or possibly orbital asteroid noise that mimics spin noise) is manifested in some MSPs at levels that can mask the red GW background signal. Since, by definition, red spin noise is correlated over long time spans, its effects in a PTA can be averaged down only by summing over a large number of MSPs. This mandates that MSPs should be culled for PTA science on the basis of displaying minimal spin noise.

To select MSPs for PTAs, red spin noise for a newly discovered pulsar initially can use measurements of the spin period and its time derivative to evaluate the empirical spin noise scaling law from SC10 (Eq. (4.10),(4.11)). Actual measurements of spin noise require a year or more of timing data to distinguish systematic astrometric errors from red stochastic spin noise. Auxiliary VLBI-based astrometry can aid this process (Madison et al. 2013; Wang et al. 2017), but it too requires at least a year of data to measure proper motion and parallax. In addition, linking the extragalactic and solar-system reference frames poses additional uncertainties at the early stages of a VLBI program (Liu et al. 2023; Evgenievich Rodin 2024).

The current pulsar sample comprises ~ 3750 pulsars, including ~ 545 MSPs with periods $P \leq 10$ ms, of which 356 are not in globular clusters (Manchester et al. 2005). These numbers are expected to grow dramatically from ongoing pulsar surveys given that the total number of active pulsars in the Galaxy may be as large as $100k$ (e.g. Swiggum et al. 2014). A model dependent estimate is that only about 20% of MSPs are sufficiently spin stable over a ten-year span to be useful for inclusion in a PTA (Shannon and Cordes 2010). Other factors of course also limit inclusion, including all of the effects discussed previously.

A reasonable approach is to place a cap on the predicted RMS spin-noise over a specified time block for an MSP to warrant inclusion in a PTA. We estimate the data span $T_{\rm r} \propto \sigma^{1/2}_{\rm spin\,noise}$ needed to reach a nominal maximum level of red spin noise $\sigma_{\rm spin\,noise} = 0.1\,\mu$s; it utilizes the SC10 scaling law (Eq. (4.10)) along with the assumption that spindown rates $\dot f_{\rm s}$ follow that for magnetic dipole radiation. This yields the time needed for the RMS spin noise to reach $\sigma_{\rm spin\,noise}$,

$$T_{\rm r} = \left(\frac{\sigma_{\rm spin\,noise}}{C_2 {f_{\rm s}}^{\alpha_{\rm r}} |\dot f_{\rm s}|^{\beta_{\rm r}}}\right)^{1/\gamma_{\rm r}} \simeq 0.4\,{\rm yr}\left(\frac{P^{0.95}_{\rm ms}}{B^{1.1}_9}\right)\left(\frac{\sigma_{\rm spin\,noise}}{0.1\,\mu s}\right)^{1/2}, \tag{19.1}$$

for spin periods in ms and surface fields $B = 10^9 B_9$ G. We have expressed $\dot f_{\rm s}$ in terms of the surface magnetic field assuming magnetic dipole radiation dominates spindown of the neutron star. The surface magnetic field is related to $\dot P$ by $B_{\rm surface} = 10^9 B_9\,G$ where $B_9 \sim 3.2(P\dot P_{-20})^{1/2}$ with $\dot P_{-20} = \dot P/(10^{-20}\,s\,s^{-1})$.

Fig. 75 shows $T_{\rm r}$ vs. spin period for surface magnetic field strengths that span MSPs to magnetars, with recycled pulsars in double NS binaries and canonical pulsars in between. Most MSPs have estimated surface fields between 10^8 and 10^9 G. The figure indicates that the lowest field objects will take several years for spin noise to be manifested in timing residuals whereas those with the shortest periods and larger fields $\gtrsim 10^9$ G will show red spin noise in less than a year. A similar approach can be used to prioritize MSPs with negligible spin noise on time scales of interest for GW detection (tens of years) and those with spin noise too large to be useful.

Timing stability better than $0.1\,\mu s$ over a span $T = 10\,$yr, say, requires short period MSPs with the smallest magnetic fields. Objects with larger spin noise can be included in PTAs if their number $N_{\rm pulsar}$ is large enough to average spin variance down as $N^{-1/2}_{\rm pulsar}$ detection statistics for correlated Earth-term GW effects.

20. EVALUATING TIMING QUALITY OF INDIVIDUAL PULSARS

As pulsar timing methodology has developed over the last few decades, several factors that influence the utility of a pulsar for precision timing applications have been identified. So far the achievable S/N of an average pulse profile has been the dominant factor for many objects, though pulse distortions from interstellar propagation are also prominent. However, arrival time precision is only part of the story because other physical effects influence the true arrival

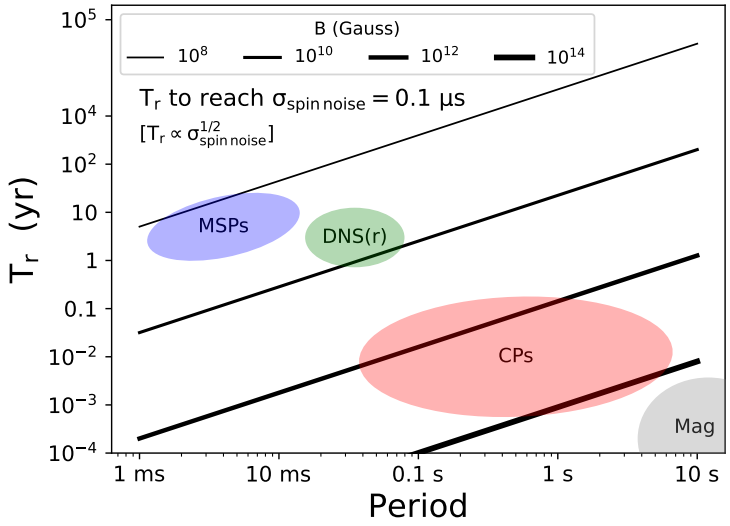


Figure 75. Time $T_{\rm r}$ needed for a timing data set to yield red spin noise at an RMS level $\sigma_{\rm spin\,noise} = 0.1\,\mu$s vs spin period. It scales as $T_{\rm r} \propto \sigma^{1/2}_{\rm spin\,noise}$. Lines are shown for surface magnetic field strengths from 10^8 to 10^{14} G. Ellipses indicate the approximate locations of distinct pulsar populations: MSPs, double neutron star binaries (recycled component), canonical pulsars, and magnetars. The curves are only indicative of approximate times because there is substantial variance in the red spin noise scaling law and they are based on a simplistic relation between field strength and spin frequency derivative based on the magnetic dipole scaling (i.e. a braking index $n = 3$).

times. The regularity of pulse periodicities is affected by stochastic effects occurring in or near the NS such as spin fluctuations, emission fluctuations, and orbital noise that alter arrival times. Interstellar delays, if imperfectly removed, also contribute to the overall timing noise budget for a pulsar.

Here we define quality measures that enable a thorough comparison of MSPs with regard to *achievable ToA precision* and *timing stability*. In aggregate the measures can be used for assessing whether a given MSP would be competitive among other MSPs in its contribution to the overall sensitivity of a pulsar timing array (PTA). For other applications where a pulsar is monitored for purposes unique to it, such as orbit and mass determinations, the quality measures provide the basis for ToA optimization, such as using longer integration times or alternative radio bands.

We define quality measures (QMs) $Q_{\rm a}$ such that larger values mean better ToA precision or better timing stability, where a = SNR,J, DISS, spin, PBF, DM(t), DM(ν). The first three of these correspond, respectively, to ToA errors from the finite SNR of a pulse profile, from pulse jitter, and diffractive scintillations that perturb ToAs on short time scales (seconds to hours). The others produce slowly changing perturbations from spin variations and changes in DM and scattering as the line of sight traverses different ISM electron density fluctuations. These effects are major subjects of this paper, with reference to Sect. 4 (spin and orbital noise), Sect. 6 (template fitting), and Sect. 12 (chromatic effects, primarily the ISM).

Table 9 summarizes the QMs with partial scaling laws and pointers to equations developed later in this section. Mitigation possibilities are also listed.

Several phenomena are not included in this brief inventory of quality measures. First are those that represent *departures from the assumed average pulse shape stability vs. epoch*. By and large, average profiles and their chromaticity appear to be epoch-independent once instrumental factors are accounted for (e.g. Brook et al. 2018). A few notable exceptions are discussed in Sect. 6.4.

Second are *telescope site dependent factors*, especially the level of radio frequency interference (RFI) that differs greatly between sites and is episodic (e.g. diurnal variations) and worsening secularly. Another is calibration methodology

Table 9. Pulsar Timing Quality Measures [a]

Measure	Expression [b, c]	Eq. Number	Mitigation/Comments [d]
Rapid TOA Variations ($\lesssim$ hours)			
$Q_{\rm S/N}$	$6.8(P/n_c W^3)^{1/2} S_\phi$	(20.1)	SEFD, B, $T_{\rm int}$
$Q_{\rm J}$	$30/(3W_{\rm c}\sqrt{P})$	(20.3)	$T_{\rm int}$
$Q_{\rm DISS}$	$21.2(\nu v_{100})^{1/2}/(D\tau)^{1/4}$	(20.5)	DM, ν, B, $T_{\rm int}$
Slow TOA Variations ($\gtrsim$ days)			
$Q_{\rm spin}$	$252\, P^{0.8}\dot{P}_{-20}^{-1.1} T_{\rm yr}^{-2}$	(20.6)	None except pulsar choice
Q_τ	τ^{-1}	(20.9)	Fitting vs. ν, DM, ν
$Q_{\rm DM(t)}$	$32\,\nu^{1/6}(1-R^{-2})[(v_{100}\Delta t_{\rm days})^2\tau/D]^{-5/12}$	(20.11)	DM, Simultaneous ν coverage
$Q_{\rm DM(\nu)}$	$1.9\,\nu^{1/6}\tau^{-5/6} I_{t_\infty}^{-1}(R, \beta = 11/3)$	(20.13)	DM, Fitting function vs. ν. Coefficient is for $R \sim 2$.
Total QM	$\sum_j w_j Q_j$		

[a] **Units:**
All quality measures have units of μs^{-1}.
Telescope/observation parameters: $S_{\rm sys} = 3\,$Jy, $n_{\rm pol} = 2$, $B = 0.1\,$GHz, $T_{\rm int} = 10^3\,$s, $\nu = 1\,$GHz, $R = \nu/(\nu - B)$.
Pulsar parameters: S_ϕ in mJy, D in kpc, P in ms; $\dot{P}_{-20} = \dot{P}/(10^{-20}\,{\rm s\,s^{-1}})$;
$W, W_{\rm c}, \tau$ in μs; n_c dimensionless, DM in pc cm^{-3}, $v_{100} = {\rm v}_\perp/(100\,{\rm km\,s^{-1}})$.

[b] Scaling laws show pulsar-dependent parameters but telescope/observation parameters are implicit; see indicated equation numbers for dependences.

[c] τ can be measured directly or from the scintillation bandwidth, $\tau \simeq (2\pi\Delta\nu_{\rm d})^{-1}$. It can also be estimated from the τ(DM) 'hockey stick' relation, $\tau(\mu s) \simeq \nu^{-4.4}({\rm DM}/303)^{3/2}[1 + ({\rm DM}/30.4)^3]$.

[d] Mitigations: choosing pulsars (and telescope parameters) with large QMs optimizes a PTA.
DM: smaller DM, $S_{\rm sys}$: smaller $S_{\rm sys}$ = system equivalent flux density, ν: higher frequency, B: larger bandwidth, $T_{\rm int}$: longer integration time.

that mitigates instrumental polarization. The generally large linear (and sometimes significant circular) polarization fraction among pulsars requires accurate calibration to avoid pulse shape changes that affect ToA estimates. The efficacy of polarization calibration is intertwined with contamination from RFI and is therefore equally difficult to quantify.

Third is *orbital noise* from asteroids or from spin-orbit interactions in "black widow" binaries where white dwarf companions undergo ablation from the pulsar wind, producing variable amounts of orbital debris (Bochenek et al. 2015) Black widow pulsars are generally excluded from PTAs for this reason, but the presence of an asteroid belt is plausible, though it has not been firmly established for any MSP.

After defining quality measures, we apply them to MSPs in the current NANOGrav PTA as a representative sample of MSPs to exemplify their utility. Other PTA groups in the northern hemisphere monitor many of the same pulsars and future studies can compare the results and incorporate MSPs from the southern hemisphere in the PPTA and MPTA programs. After showing results that put high weight on template fitting errors, we then recalculate the quality measures for anticipated improvements in telescope sensitivity and greater flexibility in frequency band usage and time allocations on a pulsar by-pulsar basis. The Python code used to calculate these quality measures is described in Appendix L and is available on GitHub (https://github.com/jmcordes/PTQ).

20.1. *Quality measures for fast ToA fluctuations*

Additive noise in template fitting, pulse jitter, and diffractive scintillations perturb arrival times that change during intraday observing sessions (e.g. Lam et al. 2016a). The template fitting error depends on properties of both the pulsar and the telescope. Jitter is intrinsic to the pulsar while diffractive scintillations are caused by the ISM along the line of sight. The template fitting error is a white noise process vs. both time and frequency. Jitter is also a white noise

process vs. time but is highly correlated across frequency. DISS differs by being correlated over finite ranges of time and frequency: seconds to hours and kHz to 100s of MHz, respectively.

We assess these three processes separately and later combine them as a weighted sum.

20.1.1. *Template fitting*

The quality measure is the reciprocal of the ToA error $\sigma_{t_{\rm S/N}}^{-1}$ from Eq. (6.6) - (6.10),

$$Q_{\rm S/N} = \sigma_{t_{\rm S/N}}^{-1} \propto S_\phi \left(\frac{n_{\rm c_2} P}{n_{\rm c_1}^2 W_{\rm c}^3} \right)^{1/2} . \tag{20.1}$$

An expression for S/N is given in Eq. (6.5). Pulsars rank higher if they are brighter, have longer periods, and have profiles with narrower (and more) components[58].

A more sensitive telescope or longer net integration time can improve a weaker pulsar to the same timing precision as a stronger pulsar with identical period and pulse-shape factors. A quality measure that excludes the flux density is

$$Q_{\rm S/N,no\,flux} = \frac{Q_{\rm S/N}}{\langle S_\nu \rangle} \propto \left(\frac{n_{\rm c_2} P}{n_{\rm c_1}^2 W_{\rm c}^3} \right)^{1/2} . \tag{20.2}$$

This measure is useful, for example, when considering a pulsar that is too weak for current telecopes but becomes viable with a larger telescope. We use this measure in Sect. 20.3.1. Among MSPs in the NANOGrav 15-yr data set, the largest $Q_{\rm S/N}$ are for J1939+2134 (B1937+21), J0437−4715, and J1909−3744 in rank order while for $Q_{\rm S/N,no\,flux}$, which excludes flux densities, J1909−3744 has the top rank owing to its narrow pulse followed by B1937+21. Dropping to 54-th is J0437−4715 due to its wide pulse and in spite of its longer period.

20.1.2. *Pulse jitter*

The rms ToA error from pulse jitter is given by Eq. (7.3) - (7.5). If we account for n_c separate components with the same width $W_{\rm c}$ and same jitter parameter, the ToA error is smaller by a factor $\sqrt{n_{\rm c_4}}/n_{\rm c_2}$ where $n_{\rm c_4} = \sum_j (a_j/a_{\rm max})^4 \leq n_{\rm c_2}$. The jitter quality measure is then

$$Q_{\rm J} = \sigma_{t_{\rm J}}^{-1} = \frac{1}{F_{\rm J} W_{\rm c}} \left(\frac{n_{\rm c_2}}{n_{\rm c_4}^{1/2}} \right) \left(\frac{T_{\rm int}}{P} \right)^{1/2} . \tag{20.3}$$

The jitter measure favors pulsars with more narrow components and shorter periods.

20.1.3. *Diffractive ISS PBF variations ('finite scintle effect')*

For pulsars that show strong scintillations, RMS ToA errors associated with stochastic variations in the PBF are $\sim \tau/N_{\rm scint}^{1/2}$, where the number of scintles $N_{\rm scint}$ is given by Eq. (12.33). For nearby pulsars and high-frequency observations, the number of scintles is small, but no less than unity as long as strong scintillation applies. Above a transition frequency of about 2 GHz for the nearest pulsars, scintillations become weak and PBF variations become unimportant. However, PTA programs use widely spread frequencies that invariably include those where scintillations are strong even if higher frequencies are not.

Using $\tau \simeq d_{\rm so}{\theta_{\rm d}}^2/c$ along with $\Delta\nu_{\rm d} = C_1(2\pi\tau)^{-1}$ and $\Delta t_{\rm d} \sim l_{\rm d}/v_{\rm eff}$ where $l_{\rm d} \sim \lambda/2\pi\theta_{\rm d}$, we obtain

$$\sigma_{t_{\rm DISS}} = \frac{\tau}{N_{\rm scint}^{1/2}} \simeq \frac{[cd'\tau(\nu)]^{1/4}}{2\pi\sqrt{\eta_\nu \eta_t B T \nu v_{\rm eff}}} \tag{20.4}$$

[58] Note $n_{\rm c_1} \leq n_{\rm c_2}^{1/2}$ by the Cauchy-Schwarz inequality. If all n_c components have the same amplitude, then $Q_{\rm S/N} \propto \sqrt{n_c}$.

where the broadening time τ is measured at frequency ν.

The DISS quality measure is the inverse of $\sigma_{t_{\rm DISS}}$ (Eq. (12.37) - (12.38)),

$$Q_{\rm DISS} = \sigma_{t_{\rm DISS}}^{-1} = \frac{2\pi\sqrt{\eta_\nu \eta_t B T \nu v_{\rm eff}}}{[cd'\tau(\nu)]^{1/4}} \tag{20.5}$$

This measure favors pulsars that are less scattered, closer, and have higher effective velocities.

20.2. *Quality measures for slow timing variations*

20.2.1. *Spin fluctuations*

We use the results given in §4.4 and express $\sigma_{t_{\rm spin}}$ in terms of period $P = \nu^{-1}$ and period derivative $\dot{P} = -\dot{\nu}P^2$ to obtain a quality measure

$$Q_{\rm spin} = \sigma_{t_{\rm spin}}^{-1} = C_2 P^{\alpha+2\beta} \dot{P}^{-\beta} T^{-2} \simeq 252\,\mu{\rm s}^{-1} P_{\rm ms}^{0.8\pm0.22} \dot{P}_{-20}^{-1.1\pm0.1}, \tag{20.6}$$

where $\dot{P}_{-20}$ is $\dot{P}$ in units of $10^{-20}\,{\rm s\,s^{-1}}$ and the spin period is in ms.

This measure appears to favor longer periods and smaller period derivatives. However, P and $\dot{P}$ are related using the relation for the surface magnetic field $B \propto \sqrt{P\dot{P}}$, yielding $Q_{\rm spin} \propto B^{-2\beta} P^{\alpha+3\beta}$. The net effect is that MSPs with low magnetic fields have larger $Q_{\rm spin}$ than canonical pulsars in spite of the period dependence that favors longer-period pulsars.

20.2.2. *Long term variations of the pulse broadening time*

To develop this quality measure, we employ a simplified timing model for two-frequency observations. A more detailed account would address the use of broadband receivers covering 2:1 or larger frequency ranges. Denoting arrival times as $t_\nu \equiv t(\nu)$ and $t_{1,2} = t_{\nu_{1,2}}$ at two spot frequencies with $\nu_2 > \nu_1$, we naively model them with $t_\nu = t_\infty + t_{\rm DM} + \varepsilon(t)$ using a dispersion delay $t_{\rm DM} = \nu^{-2} K_{\rm DM}\,{\rm DM}$ and a (for now unspecified) chromatic error term $\varepsilon(t)$ adding to the desired 'infinite frequency' ToA, t_∞. The errors in the estimated DM and t_∞ are similar to the analysis yielding Eq. (12.13) - (12.14) in Sect. 12.2.1,

$$\delta\widehat{\rm DM} \equiv \widehat{\rm DM} - {\rm DM} = \frac{\nu_2^2(\varepsilon_1 - \varepsilon_2)}{K_{\rm DM}(R^2-1)}, \qquad \text{and} \qquad \delta\hat{t}_\infty \equiv \widehat{t}_\infty - t_\infty = \frac{R^2\varepsilon_2 - \varepsilon_1}{R^2-1}, \tag{20.7}$$

where, as before, the frequency ratio $R = \nu_2/\nu_1 > 1$.

If exact templates are used at the two frequencies, the systematic errors $\varepsilon_{1,2} = 0$. (Recall we are analyzing the no radiometer-noise case here and we furthermore ignore any intrinsic chromaticity of the pulse shapes). This applies if the PBFs and intrinsic pulse shapes are known exactly. This is never the case, as we have demonstrated, so systematic ToA errors arise from epochal variability in the pulse shape whether intrinsic or, more likely, from changes in the PBF.

As seen in Sect. 12.6.1 - 12.6.4, ToA errors due to mismatched templates from scattering can exceed the scattering time τ, especially for small τ values, and are a different proportion of the scattering time at different frequencies. Also, depending on template choice, the ToA error can be of either sign. Given the variety of conditions and choices, we take a simplified approach to develop a metric.

We proceed by associating the systematic error with a multiple of the scattering time, $\epsilon_{1,2} = m_{1,2}\tau_{1,2}$ and we adopt a frequency scaling $\tau \propto \nu^{-x_\tau}$ with $x_\tau = 22/5$ and $\zeta = l_i/l_{{\rm d}_\theta} \propto \nu^{-6/5}$ for the Kolmogorov inertial subrange regime.

For low-DM MSPs, $\tau/W_{\rm u} \ll 1$ and ζ is also small at L-band frequencies. For example, scaling $\tau = 0.1\,\mu s$ at 1 GHz implies $\tau/W_{\rm u} \sim 10^{-3}$ for a 100 μs pulse width and using Eq. (12.40), $\zeta \lesssim 0.1$ even at 0.4 GHz. Inspection of Fig. 55 then shows that $\delta\hat{t}_\infty/\tau \simeq m_1 \sim m_2 \sim 2.5$ for the entire frequency range $\gtrsim 0.4$ GHz. For $R^2 \gg 1$ (wide frequency separation), the error is approximated as

$$\delta\hat{t}_\infty \simeq -m_2\sqrt{\tau_1\tau_2} = -m_2\tau_0(\nu_1\nu_2/\nu_0^2)^{-x_\tau/2}. \tag{20.8}$$

If τ_ν were constant vs. epoch this error would simply be an unimportant bias in ToAs that would be absorbed in the timing analysis if observing frequencies were the same at all epochs. However, as shown in §11.3, refraction from large-scale electron density fluctuations in the ISM will cause τ_ν to vary on time scales from days to years for weakly scattered and strongly scattered pulsars, respectively. In principle, these variations can be partially mitigated by measuring the scintillation bandwidth $\Delta\nu_{\rm d} \propto \tau^{-1}$ at each epoch vs. frequency and correcting ToAs accordingly. Actual RMS variations in τ on month to year time scales can be as large as 100% (§ 12; Hemberger and Stinebring 2008) and correction of ToAs will not be perfect.

We define a quality measure from Eq. (20.8) by simply using the reciprocal of $\tau(\nu)$, the scattering time at a fiducial frequency ν and using the τ(DM) expression of Eq. (10.16),

$$Q_\tau = \tau(\nu)^{-1} \simeq 1\,\mu s^{-1} \times \nu^{4.4}({\rm DM}/303)^{-3/2}[1 + ({\rm DM}/30.4)^3]^{-1}. \tag{20.9}$$

This measure favors less scattered pulsars and/or ToAs obtained at higher frequencies. While the ToA error is dominated by the lower (or lowest) frequency used in a multi-frequency timing program, a comparison of pulsars can use a single representative frequency for evaluating Q_τ. However, any detailed comparison needs to consider specific radio frequencies used for observations of different MSPs.

20.2.3. *Temporal DM variations and asynchronous multifrequency observations*

Most extant timing data have relied on multiple frequency measurements obtained at different epochs. Lam et al. (2015) evaluated the timing error incurred from measurements made at slightly different epochs in terms of the DM structure function. For epoch separations of Δt (a few days or less), the ToA error is given by Eq. (12.7) - (12.9) and the quality measure is evaluated for $\beta = 11/3$ as the reciprocal,

$$Q_{{\rm DM}(t)} = \sigma_{t_\infty}^{-1} = 2\pi\nu_{\rm h}(1 - R^{-2}) \left[\frac{\Delta t}{\Delta t_{\rm ISS}(\nu_{\rm h})}\right]^{-5/6} \tag{20.10}$$

An alternative form follows by expressing $\Delta t_{\rm ISS}$ in terms of the pulse-broadening time and effective velocity,

$$\begin{aligned} Q_{{\rm DM}(t)} &= (2\pi\nu_{\rm h})^{(4-\beta)/2}(1 - R^{-2})(v_{\rm eff}T_{\rm int})^{-(\beta-2)/2} \left[\frac{\tau(\nu_{\rm h})}{cd'}\right]^{-(\beta-2)/4} \\ &\simeq (2\pi\nu_{\rm h})^{1/6}(1 - R^{-2})(v_{\rm eff}T_{\rm int})^{-5/6} \left[\frac{\tau(\nu_{\rm h})}{cd'}\right]^{-5/12}. \end{aligned} \tag{20.11}$$

20.2.4. *Frequency-dependent DMs*

RMS timing errors from the frequency dependence of DM are given by Eq. (12.29). We evaluate it using a constant geometric factor $G_\beta = 1$. The resulting QM is

$$Q_{{\rm DM}(\nu)} = \sigma_{t_{{\rm DM}(\nu)}}^{-1} = \frac{6.41\,\mu s^{-1}\,\nu^{23/6}}{{d_{\rm so}}^{5/6}{\rm SM}_{-3.5}I_{t_\infty}(R, \beta = 11/3)}. \tag{20.12}$$

Casting SM in terms of the pulse broadening time, we have an alternate form

$$Q_{{\rm DM}(\nu)} = \frac{1.88\mu s^{-1}\,\nu^{1/6}}{\tau^{5/6}I_{t_\infty}(R, \beta = 11/3)}. \tag{20.13}$$

This measure also favors less-scattered pulsars but is agnostic to effective velocity.

For our analysis below, we use a nominal 2:1 ratio that gives $I_{t_\infty}(R = 2, \beta = 11/3) \sim 1$. A PTA comprising pulsars with a wide range of DMs and different frequency ranges would likely be used for different objects; in that case I_{t_∞} would be included in the evaluation of $\sigma_{\delta t_\infty}$ and the quality measure.

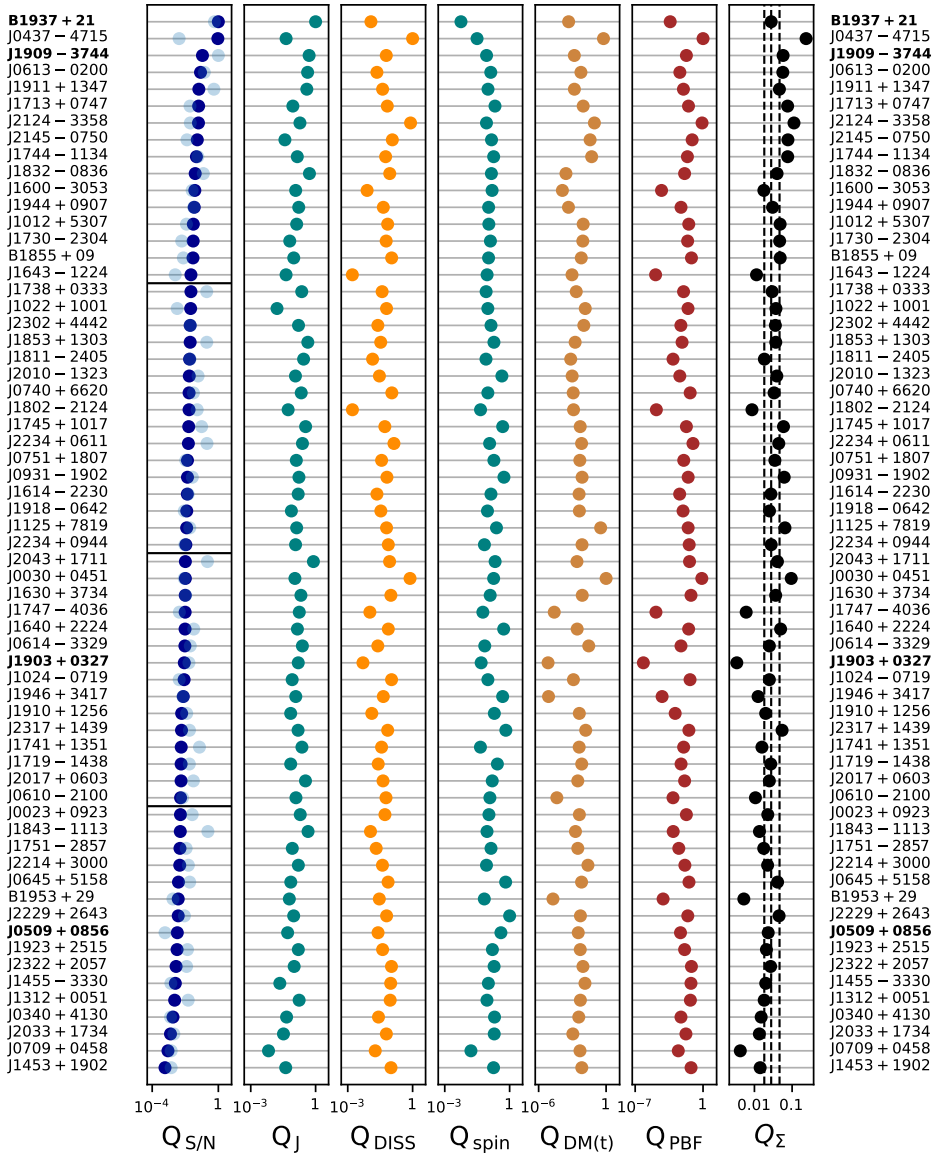


Figure 76. Quality measures for 63 MSPs ordered using $Q_{\rm S/N}$ in the first column. Darker horizontal lines indicate quartile boundaries in $Q_{\rm S/N}$. Also shown in the first column with fainter symbols is $Q_{\rm S/N,no\,flux}$, which measures the relative potential for improved ToAs using more sensitive telescopes; it has been rescaled to cover the same range as $Q_{\rm S/N}$. The next five columns are for $Q_{\rm J}$, $Q_{\rm DISS}$, $Q_{\rm spin}$, $Q_{\rm DM(t)}$, and $Q_{\rm PBF}$ as defined in the text. The last column gives the weighted sum Q_Σ of the logarithms of the other Q values. Vertical dashed lines indicate quartile boundary values for Q_Σ. Pulsars in bold font are discussed as exemplars of timing quality in NANOGrav's detector characterization paper (Agazie et al. 2023c).

20.3. *Meta-analysis of quality measures*

Fig. 76 shows Q values for 63 pulsars in NANOGrav's timing program. Pulsars are ranked according to $Q_{\rm S/N}$ in the first column, which also shows $Q_{\rm S/N,no\,flux}$ values as fainter symbols. The Q values for each of the first five columns are normalized to unit maximum and the last column gives the weighted sum

$$Q_\Sigma = \sum_j w_j \log Q_j, \quad j = (\text{S/N, J, DISS, spin, DM(t), PBF}). \tag{20.14}$$

Weights sum to unity, $\sum_j w_j = 1$. We use logarithms (base 10) to mitigate the dominance of any one quality measure given the several to many orders of magnitude that they span.

In the following we choose weights to illustrate trends in the ranking of MSPs; they are not to be taken as optimal in any sense. However, we expect that individual and aggregated quality measures like the ones we suggest will be helpful for incorporating additional MSPs into PTAs. Eventually, it is conceivable that weights can be based on quantitative measures of a pulsar's contribution to the overall PTA sensitivity to GWs. However, the type of GW (i.e. stochastic background vs. GWs produced by individual sources of CW signals or memory bursts) influences sensitivity calculations and thus will affect the choice of weights.

20.3.1. *Initial MSP comparisons*

For the initial comparison shown in Fig. 76, we use weights $w_j = (0.35, 0.05, 0.05, 0.35, 0.1, 0.1)$ that reflect current PTA observations where most MSPs have ToA estimates limited by template fitting errors with some contribution from jitter and DISS and where overall timing residuals receive contributions from red spin noise, unmodeled epoch-dependent DM variations, and changes in the pulse broadening from scattering. Our subjective choice of weights Vertical dashed lines in the last column indicate divisions between quartiles of Q_Σ. Four 'exemplar' pulsars indicated in bold font, J0509+0856, J1903+0327, J1909−3744, and J1939+2134 (B1937+21), are discussed in detail in NANOGrav's 15-yr detector characterization paper (Agazie et al. 2023c) and we therefore refer to them here.

Inspection of the first column shows that B1937+21 has the best quality with respect to ToA precision obtained from template fitting but it is in only the second to best quartile of Q_Σ because it manifests significant red spin noise (or possibly stochastic asteroid noise (Shannon et al. 2013) and scintillations also contribute to short-time scale TOA perturbations (Lam et al. 2016a).

Comparison of the values shown in the first two columns indicate that ToAs can be improved for a significant number of pulsars. If all pulsars are timed with the same telescope, receiver, and integration time, $Q_{\rm S/N}$ is the relevant quantity for comparing MSPs. However, a significant number of pulsars show values for $Q_{\rm S/N,no\,flux}$ (faint symbols) that substantially exceed $Q_{\rm S/N}$. This indicates that they possess intrinsic properties (period, pulse width, and number of pulse components) that can be exploited to optimize ToAs by using longer integrations or a larger telescope (for example). By contrast, J0437−4715 ranks second in $Q_{\rm S/N}$ because it is bright but is intrinsically worse than many MSPs because it has a wide pulse. Nonetheless with weights that favor $Q_{\rm S/N}$ and the proximity of the pulsar to the solar system (hence small interstellar effects), this pulsar has a large Q_Σ. In the next section we use an alternate scheme that weights spin noise more strongly and puts J0437−3744 at much lower rank. The third ranked pulsar in $Q_{\rm S/N}$, J1909−3744 (another exemplar) ranks in the first quartile of Q_Σ because it has a narrow pulse and has small interstellar contributions.

The two remaining exemplars, J0509+0856 and J1903+0327, rank in the second lowest and lowest quartiles of Q_Σ, respectively. The first of these has poor values of $Q_{\rm S/N}$ and $Q_{\rm S/N,no\,flux}$. The large interstellar contributions to the timing of the large-DM object J1903+0327 make it the lowest ranked object of the entire set of pulsars in $Q_{\rm DM(t)}$, $Q_{\rm PBF}$, and subsequently Q_Σ. In principle, the timing of this pulsar could be improved significantly using observations at higher frequencies, as discussed in Lam et al. (2018b), especially with a future large collecting area telescope such as the Next Generation Very Large Array (ngVLA).

Table 10. Top two pulsar quartiles ranked by Λ_Σ.

MSP	Quartile	Λ_Σ	Q_Σ	$\log_{10} Q_{\rm S/N}$
J1745+1017	1	0.68	0.57	0.66
J0931-1902	1	0.66	0.54	0.66
J1640+2224	1	0.64	0.48	0.62
J2317+1439	1	0.63	0.39	0.62
J2043+1711	1	0.63	0.49	0.58
J2124-3358	1	0.63	0.79	0.64
J1713+0747	1	0.63	0.79	0.67
J1832-0836	1	0.63	0.72	0.58
J1744-1134	1	0.62	0.75	0.66
J0030+0451	1	0.61	0.49	0.62
J1909-3744	1	0.61	0.85	0.59
J2229+2643	1	0.60	0.31	0.59
J2010-1323	1	0.60	0.59	0.60
J0613-0200	1	0.60	0.82	0.62
J1853+1303	1	0.59	0.61	0.57
J1125+7819	1	0.59	0.52	0.62
J0645+5158	2	0.59	0.32	0.58
J1911+1347	2	0.58	0.79	0.57
J2234+0611	2	0.58	0.57	0.56
J2145-0750	2	0.58	0.77	0.64
J1012+5307	2	0.55	0.68	0.57
B1855+09	2	0.55	0.68	0.57
J1630+3734	2	0.55	0.48	0.53
J0740+6620	2	0.55	0.58	0.51
J0437-4715	2	0.54	0.96	0.62
J0751+1807	2	0.54	0.54	0.55
J1730-2304	2	0.53	0.68	0.57
J1944+0907	2	0.53	0.70	0.52
J2017+0603	2	0.53	0.38	0.49
J2302+4442	2	0.52	0.61	0.54
J1946+3417	2	0.51	0.43	0.49

20.3.2. *Forward looking MSP comparison*

Future timing observations generally will be made with more sensitive telescopes having greater collecting areas and improved receivers. For these, errors associated with S/N become secondary for many objects. Wideband systems deployed on current and future telescopes will likely decrease timing errors associated with temporal DM fluctuations, though frequency-dependent DMs would be important for low frequency observations of higher DM objects (Cordes et al. 2016). For these reasons we compute a second sum that weights jitter, spin, and DISS more strongly, $w_j = (0.25, 0.15, 0.15, 0.35, 0, 0.1)$.

We also employ a sigmoid transformation that normalizes all of the (log) quality measures into the same range, $[0, 1]$, and further limits the domination of an aggregate quality measure by any single measure. Using a logistic function $\mathcal{S}(x) = (1 + e^{-x})^{-1}$ and letting $l_j \equiv \log Q_j$ we transform the measures using the median $l_{\rm m}$ and RMS σ_l to calculate a weighted sum Λ_Σ of $\Lambda_j \in [-1, 1]$, where

$$\Lambda_j = \mathcal{S}\left(\frac{l_j - l_{\rm m}}{\sigma_l}\right), \qquad \Lambda_\Sigma = \sum_j w_j \Lambda_j. \tag{20.15}$$

Results are shown in Fig. 77, which demonstrates how the new weights affect the placement of pulsars and especially the exemplar MSPS. Table 10 lists the MSPs in the top two quartiles.

To enable MSP comparisons more visually, Fig. 78 shows Λ_j for each pulsar plotted as a closed curve calculated from a spline fit to the individual values. Objects are divided into four quartiles in Λ_Σ. The enclosed area of each curve is normalized by the area (π) of the unit circle and the average normalized area is given for each quartile. An ideal pulsar would appear as the circle shown with unit radius and would have unit normalized area.

The heavy black lines in the figure correspond to the four exemplar objects discussed above. One of the best pulsars in PTA observations is J1909−3744 and it correspondingly falls in quartile 1. The large DM (297 pc cm^{-3}) MSP J1903+0327 is in the fourth quartile because its large scattering is not compensated by other factors. The other two objects are in the third quartile for differing reasons: B1937+21 shows large achromatic spin noise and large interstellar contributions that outweigh its high quality in terms of its jitter and S/N, while J0509+0856 has a large template fitting error given its wide pulse, which is about 15 times wider than those from J1909−3744 and B1937+21 and three times that of J1713+0747.

21. SUMMARY AND RECOMMENDATIONS

This review presented an end-to-end study, from the neutron star to the radio telescope, of effects and processes that influence the utility of radio pulsars in timing metrology.

We emphasize again that the best timing precision is obtained from millisecond pulsars due to their much lower spin noise compared to other pulsars and because, in a fixed measurement time, they provide a much larger number of pulses for averaging down pulse jitter. However, not all MSPs are suitable for the most demanding application: as detectors of long wavelength (light year) gravitational waves. A combination of spin noise, diverse pulse widths and jitter, gravitational potential noise (in globular clusters), and measurement noise combine with stochastic interstellar propagation to render only a fraction of MSPs suitable for PTA work. Shannon and Cordes (2010), for example, estimate 20% of MSPs are suitable based on spin noise considerations alone. Some, but not all, of these factors can be mitigated. We summarize key findings below, placing emphasis on considerations for inclusion of MSPs in PTAs and on the opportunities and limits for TOA error mitigation.

21.1. *Building a Pulsar Timing Array*

A useful way to summarize our results is to consider building a PTA from scratch. This first involves selecting MSPs based on criteria like those already used for existing PTAs and using elements from our study. Next is to optimize ToA estimation and identify constituents of the covariance matrix used for ToA modeling.

We describe the main steps as follows, where we take a forward looking approach that assumes broad frequency coverage during observations at a single epoch. Simultaneous measurements over a 3:1 frequency range, for example, allow ToAs to be optimized for each epoch at the 'front end' of an overall pipeline rather than through covaiance matrix modeling that is applied to multiepoch ToAs. We also eschew usage of dimensionless fudge factors (e.g. EFAC and ECORR) to alter error contributions from template matching and pulse jitter, which actually can be calculated using known information about observations for each pulsar.

1. **Select/cull pulsars for the array:** Some pulsars are simply unsuitable for high-precision timing, due to effects that are both intrinsic (primarily, red spin noise) and extrinsic (e.g., ISM-induced timing offsets). To aid the selection of MSPs for PTAs and identify methods for optimizing timing programs, we developed a set of metrics for assessing pulsar quality. These metrics take into account timing errors related to spin noise, pulse jitter, the signal-to-noise ratio of pulse measurements, and interstellar scattering, each with its own quality factor that are combined into a composite quality factor. These were applied to and calibrated against the current MSP sample in NANOGrav's PTA. Appendix L describes Python code that calculates quality factors for any MSP either in absolute terms or in comparison with the current best MSP observed in multiple PTA programs, MSP J1909-3744[59].

   Spin noise, in particular, cannot be mitigated when it is too large; it can only be avoided by excluding pulsars from a PTA. Spin noise is achromatic (not dependent on radio frequency) and is to some extent degenerate with power-law noise in the stochastic GW background. Fortunately they can be distinguished by the fact that GW perturbations are partially correlated between pulsars, while spin noise is of course not. In principle, GW

[59] The code is available on GitHub (https://github.com/jmcordes/PTQ))

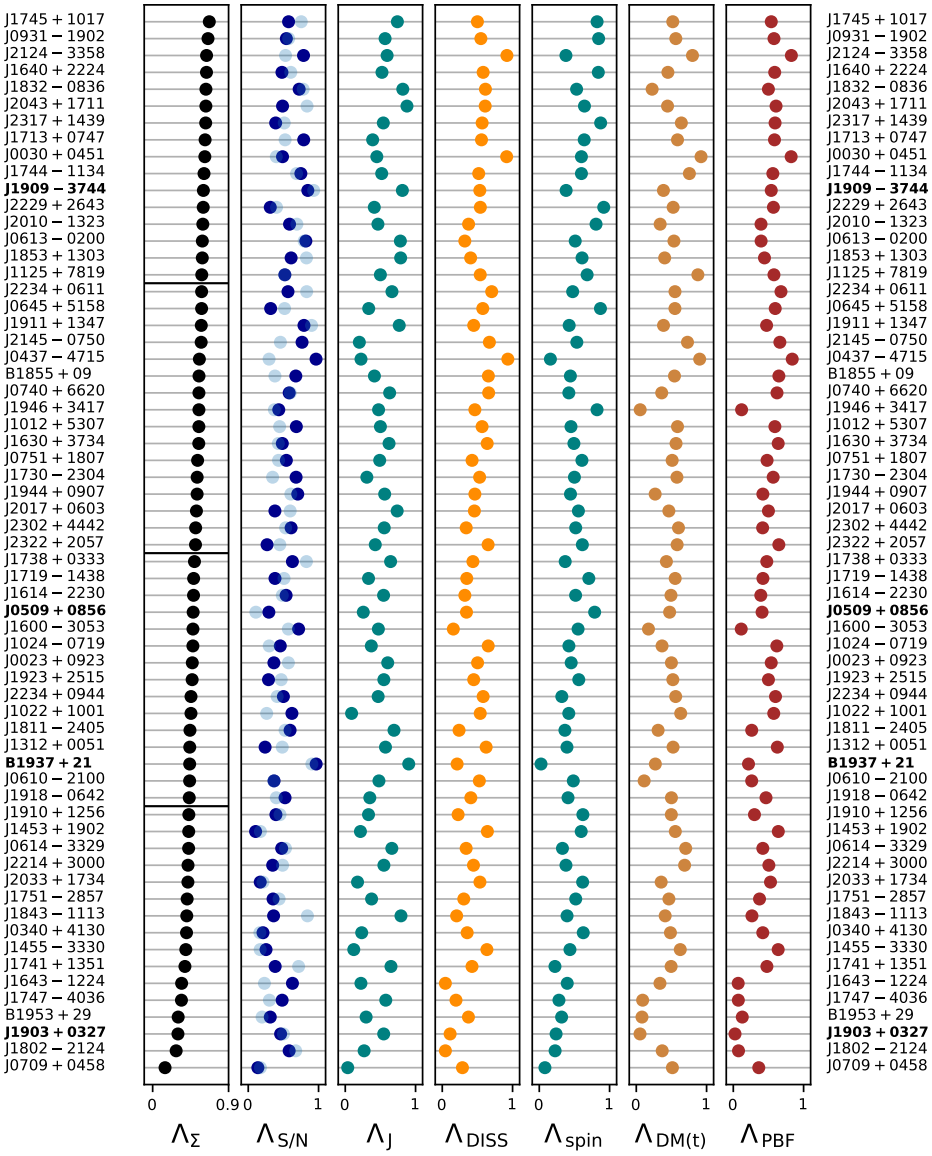


Figure 77. Quality measures for 63 MSPs ordered using Q'_Σ in the first column. Darker horizontal lines indicate quartile boundaries. Other columns show individual transformed Q values, including both $Q'_{S/N}$ and $Q'_{S/N,\text{no flux}}$ in the second column. Pulsars in bold font are discussed as exemplars of timing quality in NANOGrav's detector characterization paper (Agazie et al. 2023c).

detection involves combining signals from all pulsars in the PTA to build up the GW signal relative to other red noise contributions, which are statistically independent between MSPs. However, there are insufficient numbers of MSPs in current PTAs to allow inclusion of those with large spin noise because they will inhibit GW detection and characterization. In special cases, such as a CP orbiting a black hole, the scientific value of the target pulsar may override concerns about red noise.

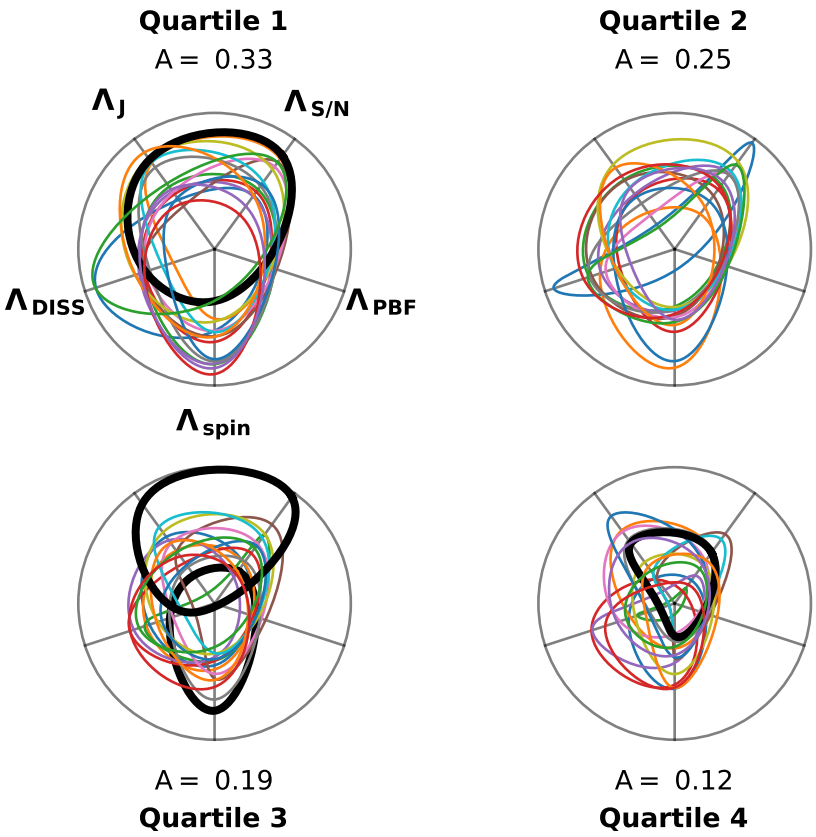


Figure 78. Logistic quality measures for 63 MSPs split into four quartiles in Λ_Σ. For each pulsar a closed curve is plotted that connects Λ values on axes corresponding to each of the individual measures. The average enclosed area of the curves is given for each quartile, normalized to unit maximum for the ideal pulsar. The four thick black curves correspond to the four exemplar objects discussed in the text. The high quality MSP J1909−3744 is in quartile 1 while J1939+2134 (B1937+21) and J0509+0856 are in quartile 3 as the upper and lower black curves, respectively, and the large-DM MSP J1903+0347 is in the fourth quartile due to its large consequential scattering.

2. **Design an optimized observing program:** Once pulsars have been selected for a PTA, an optimal combination of observing frequency, dwell time, and cadence must be determined. These considerations should take into account the following factors:

   Large observing bandwidths are critical for precise estimation of all chromatic noise effects, most of which are induced by propagation through the ISM. Wideband systems provide greater bandwidth and thus larger pulse signal-to-noise ratios, and they can provide better determination of plasma propagation terms in the arrival time equation. However, wideband systems are also subject to departures of the simplest dispersion law ($\Delta t \propto \mathrm{DM}/\nu^2$) caused by multipath propagation. The choice of observing frequency thus involves a trade-off between pulsars' steep intrinsic spectra, which yield higher flux densities at lower frequencies, and ISM-induced timing offsets, which also increase inversely with frequency.

   The optimal dwell time should beat down pulse jitter, but will also depend on the ISM characteristics along the LoS. In general, the scaling of jitter-induced timing errors with integration time means that shorter integrations can be accommodated for pulsars with shorter periods and narrower pulse components. However, when the scintillation timescale is long compared to the dwell time, one must consider TOA variance due to diffractive scintillation (the finite scintle effect). Large observing bandwidths mitigate the finite scintle effect, and thus provide another means of optimizing the dwell time per pulsar.

The cadence of observing epochs is most relevant when combining datasets that cover disparate frequency bands in order to determine DM (as well as scattering). The TOA error induced by asynchronous DM estimation scales almost linearly with the temporal separation between observing epochs (e.g. Eq. (12.9)). Here again, wideband systems reduce the need for observations at different frequencies made at slightly different epochs, because the DM can be determined more precisely from a single observing epoch with a single receiver.

3. **Estimate ToAs at each epoch, including corrections:** Individual TOAs should be optimized empirically at each epoch. Even with suitable choices of template, ToA errors in excess of those expected from idealized matched filtering are expected. Equation (17.17) illustrates the full arrival time equation, including timing delays from all relevant effects. Terms that are most amenable to correction are $t_{\rm mismatch}$ and the average $\overline{\rm DM}$ term (epoch dependent, achromatic); this latter term is addressed by all current ToAs but may not have been optimized with respect to the influence of scattering. Terms that may be partially correctible include $\Delta t_{\rm J}$ and $\Delta t_{\delta p}^{\rm (all)}$. A jitter correction may emerge from PCA applied to pulse profile sequences; attempts to date have given only modest improvements. Short term PBF variations (finite number of scintles) may be correctible if scintillations are carefully monitored through DS with sufficient time and frequency resolutions. Uncorrectable terms or residual errors include $\Delta t_{\rm S/N}$, $\Delta t_{\rm J}$, and $\Delta t_{\delta p}^{\rm (all)}$. Optimized observations and processing can minimize these but they are mostly irreducible. We now discuss possible corrections.

   Rapid profile variations and resulting ToA errors: Systematic template mismatch, pulse jitter, and rapid PBF variability (finite scintle effect) are potentially correctible, to varying degrees. Template mismatch produces a systematic error while jitter and the FSE effect yield random errors. Jitter is potentially correctible if the net profile change in an N-pulse average is systemtically related to the TOA offset. The FSE effect is correctible if CS can be used to determine the instantaneous PBF on time scales $\lesssim \Delta t_{\rm d}$, the DISS time scale $\sim$ minutes.

   Slow changes correlated over multiple epochs: Intrinsic profile changes, like the transitory events seen in MSP J1713+0747, which eventually decay to the pre-event profile shape, can be mitigated through epoch-dependent profile modeling. This can be done using PCA, for example, but whether it is better than simple excision of ToAs from epochs during an event needs to be evaluated on a case-by-case basis. The same statement holds for other pulsars that show episodes of profile shape changes (e.g. Shannon et al. 2016).

   Several ISM perturbations have time scales on the order of $\Delta t_{\rm r}$, the characteristic time scale for RISS (refractive scintillations). In general, this is determined by the transverse extent of the bundle of scattered rays and the speed with which the LoS changes. For a single, thin screen along the LoS the width of the ray bundle $\sim l_{\rm r}$ and net time scale are simply related and the characteristic refraction timeis $\Delta t_{\rm r} \sim l_{\rm r}/{\rm v}_{\rm eff}$ (c.f. Table 4).

   ISM perturbations include slow departures of PBFs from the ensemble shape due to variable refraction, which shifts the ray bundle, slow AOA variations that alter the translation of ToAs to the SSBC, and the frequency dependence of DM. Analysis of dynamic spectra using PRS or CS can provide 'at epoch' estimates of the scattering time or possibly the PBF shape, which can track refractive distortions of the PBF. We emphasize that determination of the PBF shape and its effect on ToAs need to be based on the same data employed for initial ToA estimates (e.g. using template matching with a fixed template). We also underscore that usage of an exponential PBF is unsuitable in PTA contexts because it introduces biases in ToA corrections.

   Once scattering time estimates are available, ToA corrections for slow scattering variability can be based on a look-up table for ToA offsets based on the actual intrinsic profile shape and relevant PBF. This is described in more detail below. AOA variations are harder to track but might be quantified using drift rates in dynamic spectra, $d\nu/dt$ of scintles.

   Scattering-corrected ToAs will lead to better (unbiased) estimates for DM. Whether the chromaticity of DM can be corrected is unclear. The sustained form for DM(ν) over a refraction time may provide the basis for its determination. Further exploration of this is rqeuired. On the other hand, the consequences of DM chromaticity are very small for low-DM (e.g. $\lesssim 50\,{\rm pc\ cm^{-3}}$) pulsars observed at $\gtrsim 0.8\,$GHz frequencies. Utlizing higher-DM pulsars and lower frequencies may require special attention.

   Discrete interstellar refraction and delay events, seen as 'extreme scattering events' are sustained over periods of weeks to months. Delays from ESEs are generally expected, through modeling, to include a mixture of dispersion delays, AOA delays, the combined effects from multiple images that may be produced. These are not easily modelable and, as discussed earlier, will produce non-Gaussian timing residuals.

These considerations will be increasingly important as PTAs expand the number of included MSPs, which will likely require adding higher-DM pulsars than those in current PTAs. As shown in Sect. 18.6, scattering corrections for higher-DM pulsars (or observations at lower frequencies than typically used in PTAs even for the current sample) require resolution of scintillation frequency structure. This is more challenging for high-DM/low-frequency combinations and in some cases requires incorporation of cyclic spectroscopy methods.

4. **Model remaining errors and variances:** Not all terms in the arrival time equation can be fully corrected and some are simply uncorrectable. The remaining ToA errors require inclusion in the covariance matrix used to optimize parameter estimation of a comprehensive timing model and for GW detection.

   Three terms are well known to always require inclusion in the covariance matrix: (1) Template fitting errors from radiometer noise, which are dependent on epoch, telescope, receiver, and the degree of refractive and diffractive scintillations; (2) Uncorrectable jitter, whose variance is largely epoch-dependent and is broadband, decorrelating only over frequency ranges larger than about an octave; and (3) Red noise, including spin and orbital noise, as well as residual ISM noise that is only partially corrected.

   Additional terms arise from uncorrected PBF variations on both rapid and slow time scales. Quantifying their contributions to the covariance matrix requires consideration of the specific methodology used for template matching. The same holds for intrinsic profile variations and whether TOAs are corrected or excised.

   Attention is also required for the stationarity and gaussianity of residual errors and fluctuations. The simplest form of nonstationarity is the variation in radiometer noise with epoch due to changes in receivers (and telescopes). Also, RISS alters the effective flux density of a pulsar, causing modulations of the template-fitting variance. Terms that are well approximated as Gaussian processes include ToA errors from radiometer noise, jitter, and rapid PBF changes. Spin variations (c.f. discussion in Sect. 4.4), yields mixtures of (likely) Gaussian variations and discrete events. DM and multipath effects are also Gaussian processed intermixed with strong modulations of observables due to caustic events.

21.2. *Customized scattering mitigation for individual MSPs*

We have demonstrated with simulations how ToA offsets depend on astrophysical aspects of scattering as well as methodological details of template matching. The most general conclusion is that ToA offsets are smaller than than the scattering time τ at a given frequency and also scale with frequency differently than the scattering time. Furthermore, the ToA offset is function of both the intrinsic pulse shape as well as the PBF shape.

Scattering corrections of ToAs thus require a customized analysis for each pulsar. These would comprise simulations that convolve the adopted template profile (assumed to be devoid of any scattering[60]) with a family of assumed PBFs. These PBFs would be parameterized with the underlying density spectrum index β and inner scale l_i. Measured scattering times τ provide an estimate for the diffraction scale $l_{\rm d}(\nu_{\rm ref})$ at a reference frequency $\nu_{\rm ref}$ which yields the parameter $\zeta(\nu) = l_i/l_{\rm d}(\nu)$ for power-law PBFs. Recall that an exponential PBF with an achromatic shape is generally a poor choice for constructing templates for precision timing. Asymptotically, however, very strong scattering yields a small $l_{\rm d}$ and a large value fir ζ for which the PBF tends toward an exponential if scattering is confined to a small fraction of the line of sight.

The steps of a multifrequency analysis would be:

1. Choose a template to use as a starting point. Ideally this would be a 'de-scattered' profile or one obtained at a frequency where scattering has a minimal effect on the shape. Intrinsic profile chromaticity is also an issue that can be addressed by multifrequency profile modeling that excludes scattering but includes frequency dependent amplitudes, widths, and positions of Gaussian components (e.g. Kramer et al. 1994; Geiger et al. 2025).
2. Choose a PBF shape according to β and inner scale l_i.
3. Use a measurement of scattering time at a reference frequency $\nu_{\rm ref}$ to evaluate $\zeta(\nu) = l_i/l_{\rm d}(\nu)$ where $l_{\rm d}(\nu)$ is related to $\tau(\nu)$.

[60] Of course templates based on measured pulses will likely include some level of scattering but this is small for low-DM pulsars. In practice, some templates are based on Gaussian component modeling of measured profiles, which excludes scattering to a large degree.

4. Generate frequency dependent PBFs using β, $\zeta(\nu)$, and $\tau(\nu)$.
5. Convolve the intrinsic shape $U(t, \nu)$ with each PBF $p(t, \nu, \tau)$ using a grid of τ values.
6. Using a so-generated template (which may differ from that used in step 1), determine the ToA offset as a function of τ and frequency.
7. Use the results as a lookup table for a ToA correction that is a function of $\nu, \tau(\nu)$ and implicitly depends on the intrinsic profile shape and on ISM turbulence parameters (β and l_i). The correction is most robust for a contemporaneous measurement of $\tau(\nu)$ based on a large number of scintles (c.f. Sect. 18.5.5).

Acknowledgements: We thank numerous colleagues, including those in the NANOGrav, the EPTA, the PPTA, the MPTA, the InPTA, and the CPTA collaborations along with others for discussions about pulsar timing over the last several decades. We thank the NANOGrav collaboration for providing data from its 15-yr data release (Agazie et al. 2023a) used to make Figs. 1, 4, 6, 12, 18, 20, 31, 32, and 33. We thank M. Vivekanand for providing data from his paper (Vivekanand 2020, Fig 5) also used in Fig. 33. We thank Ryan Shannon for unpublished data used for Fig. 11. We thank Matthew Kerr for providing data on the Vela pulsar used in Fig. 24. This research has made use of the EPN Database of Pulsar Profiles maintained by the University of Manchester, available at: http://www.jodrellbank.manchester.ac.uk/research/pulsar/Resources/epn/. It also made extensive use of the ATNF Pulsar Caralogue (Manchester et al. 2005) http://www.atnf.csiro.au/research/pulsar/psrcat. This work was supported by NSF Physics Frontiers Center award numbers 1430284 and 2020265, which support the NANOGrav project.

STATEMENTS AND DECLARATIONS

Competing interests: There are no competing interests for any of the authors.

Funding: All authors are members of the NANOGrav Physics Frontiers Center, which has been supported by the U.S. National Science Foundation Physics Frontiers Center under award numbers 1430284 and 2020265.

Appendices

Appendix A. Nomenclature

Table 11. Acronyms, terms, and symbols

Item	Definition	Typical Units
Acronyms and terms:		
Astrophysical		
AGN	Active galactic nucleus	
CP	Canonical pulsar	
DGR	Differential galactic rotation	—
DNS	Double neutron star	
ESE	Extreme scattering event	
GC	Galactic center	
IDV	Intraday varaible (AGN)	
IHV	Intrahour variable (AGN)	
MSP	Millisecond pulsar	—
MW	Milky Way	—
Methods and statistical quantities		
ACF, ACV, CCF	Autocorrelation, autocovariance, and crosscorrelation functions	
AD, AV	Allan deviation $\sigma_{\overline{y}}$ and Allan variance $\sigma^2_{\overline{y}}$ of dimensionless frequency y	—
AMN	Amplitude modulated noise	—
AMPSN	Amplitude modulated shot noise (SAMPSN = Scintillated AMPSN)	—
CS	Cyclic spectrum or spectroscopy	—
DS	Dynamic spectrum (intensity vs. time and frequency)	
FWHM	Full width at half maximum	
HWHM	Half width at half maximum	
MF	Matched filter	
PCA	Principal component analysis	
PRS	Phase resolved spectrum or phase resolved spectroscopy	—
SEFD $\equiv S_{\rm sys}$	System equivalent flux density $= T_{\rm sys}/G$	Jy
SS	Secondary spectrum (power spectrum of dynamic spectrum)	
SWIMS	Stochastic wideband impulse modulated self-noise	—
VLBI	Very long baseline interferometry	
Propagation		
AOA	Angle of arrival	various
DISS	Diffractive interstellar scintillation	—
Line of sight Measures:		
DM	Dispersion Measure	pc cm^{-3}

Table 11 *continued on next page*

Table 11 *(continued)*

Item	Definition	Typical Units
DM(ν)	Chromatic DM due to multipath averaging	pc cm^{-3}
EM	Emission measure	pc cm^{-6}
SM	Scattering measure	kpc m$^{-20/3}$
RM	Faraday rotation measure	rad m^{-2}
PBF	Pulse broadening function	—
RISS	Refractive interstellar scintillation	
Scintles	Intensity features in the time-frequency plane caused by diffractive scattering	intensity like
TOA	Time of arrival	various
Units		
au	Astronomical unit	
Jy	Jansky (unit of flux density)	
mas	milliarc second	
Symbols:		
$\langle X \rangle$	Ensemble average of a quantity X	
$\langle X \rangle_x$	Average of X over another quantity x (e.g. time, frequency, or phase)	
α	Exponent in phase structure function	
β	Exponent in wavenumber spectrum for n_e (11/3 for Kolmogorov)	
B	Receiver bandwidth	MHz, GHz
C_n^2	Coefficient in electron-density wavenumber spectrum	m$^{-20/3}$
C_1	Constant in uncertainty relation, $2\pi\Delta\nu_d\tau_d = C_1$	—
c	Speed of light	cm s^{-1}
D_{DM}	Structure function for dispersion measures	pc cm$^{-3}{}^2$
D_{n_e}	Structure function for electron density	cm^{-6}
D_{N_e}	Structure function for electron column density	cm^{-4}
D_ϕ	Phase structure function	radians^2
d_p	Total degree of polarization	—
$\Delta(\tau)$	Normalized ACF of noise	
$\Delta\nu_d$	Decorrelation bandwidth for diffractive scintillation (DISS); (also scintillation or diffraction bandwidth)	kHz or MHz
$\Delta\nu_r$	Decorrelation bandwidth for refractive scintillation (RISS);	MHz or GHz
$\Delta\nu_{sb}$	Spectral broadening bandwidth	Hz
δt	Time Lag	
δI	Intensity fluctuation	
δn_e	Fluctuation in free electron density	cm^{-3}
$\delta\mathbf{x}$	Spatial offset in observation plane	
$\Delta\omega$	Difference in galactic rotation rate	
Δt_d	Diffractive scintillation (DISS) time scale	various
Δt_r	Refractive scintillation (RISS) time scale	various
d_{lo}	Distance from Lens (or layer or screen) to observer	kpc
d_{sl}	Source-lens (or layer or screen) distance	kpc
d_{so}	Source-observer distance	kpc
E and ε	Electric field and baseband electric field	
ϵ	fractional electron density variation = RMS(δn_e)/n_e	
ζ	Dimensionless inner scale or fractional density variance	
η	Mean-square scattering angle per unit distance	mas kpc^{-1}

Table 11 *continued on next page*

Table 11 *(continued)*

Item	Definition	Typical Units
$\eta_{\rm t}, \eta_\nu$	Dimensionless coefficients for calculating numbers of scintles	—
$F_{\rm c} = \zeta\epsilon^2/f_{\rm f} l_o^{\beta-3}$	Cloudlet model parameter for relating SM to DM	$\rm pc^{-2/3}$ (Kolmogorov)
$\widetilde{F} = F_{\rm c}/l_i^{4-\beta}$	Cloudlet model parameter for calculating scattering time	$(\rm pc^2\,km)^{-1/3}$ (Kolmogorov)
$F_{\rm J}$	Jitter parameter	—
$f_{\rm f}$	Volume filling factor in cloudlet model	
$f_{\rm Nyq}$	Nyquist frequency	
$f_{\rm s}, \dot{f}_{\rm s}, \ddot{f}_{\rm s}$	Pulsar spin frequency and its first two time derivatives	Hz, $\rm Hz\,s^{-1}$, $\rm Hz\,s^{-2}$
$f_{\rm yr}$	Frequency of 1 $\rm yr^{-1}$	$\rm yr^{-1}$
f_α	Numerical factor in structure function	
$f_{\rm J}$	Dimensionless jitter factor for calculating TOA jitter	
Γ_I	Intensity correlation function	
$\Gamma_{\delta I}$	Intensity covariance function	
Γ_ε	Spatial correlation function of wavefield	
G	Telescope gain	$\rm K\,Jy^{-1}$
$I, Q, U, V, L = Q + iU$	Stokes parameters	Jy or mJy
I_{t_∞}	Factor in the calculation of TOA error from frequency-dependent DMs	—
$I_{\rm DM}$	Factor in calculation of frequency-dependent DMs	—
$K_{\rm DM} = cr_{\rm e}/2\pi \times \rm pc/GHz^2$	Constant in the expression for dispersion time delay $t = K_{\rm DM}\nu^{-2}{\rm DM}$	s
λ, ν	Electromagnetic wavelength and frequency	cm, Hz
$l_{\rm d}, l_{{\rm d}_\theta}, l_{{\rm d}_I}$	Spatial scale in diffraction pattern (alternative definitions)	various
ℓ, b	Galactic coordinates	deg
l_i, l_o	Inner and outer scales of electron-density variations ($\equiv 2\pi/q_i, 2\pi/q_o$)	various
$m_{\rm DISS}$	Scintillation modulation index (= rms / mean)	—
m_M	Modulation index of M	—
ν	Radio frequency	GHz
$N_{\rm dof}$	Number of degrees of freedom in scintillations	—
$N_{\rm scint} = N_\nu N_{\rm t}$	Number of independent scintillation features (scintles) averaged	—
N_ν	Number of independent scintillation features averaged over frequency	—
$N_{\rm t}$	Number of independent scintillation feasures averaged over time	—
$n_{\rm pol}$	Number of polarization channels	—
n_e	Free electron density	$\rm cm^{-3}$
$P_{\delta n_e}(\mathbf{q})$	Wavenumber spectrum for the electron density	$(\rm length)^{-3}$
P	Pulse period	s
$\dot{P}$	Period derivative = dP/dt	$\rm s\,s^{-1}$
$\mathbf{q}$	Wavenumber (3D vector)	$(\rm length)^{-1}$
q_o, q_i	Lower and upper wavenumber cutoffs of $P_{\delta n_e}$	various
$Q_{\rm S/N}$, $Q_{\rm J}$, $Q_{\rm DISS}$, Q_τ, $Q_{\rm spin}$,, $Q_{\rm DM(t)}$, $Q_{\rm DM(\nu)}$, $Q_{\rm PBF}$, Q_Σ, $Q_{\Sigma LS}$	Quality measures for TOA effects	μs^{-1}
r_e	Classical electron radius	cm
R	Ratio of a pair of frequencies (≥ 1)	—
$\sigma_I, \sigma_Q, \sigma_U, \sigma_V, \sigma_L$	RMS values of Stokes parameters	
$\sigma_{t_{\rm S/N}}$	RMS TOA error from radiometer noise (S/N dependent)	ns or μs
$\sigma_{t_{\rm J}}$	RMS TOA error from pulse jitter	ns or μs
$\sigma_{t_{\rm DISS}} \equiv \Delta t_{\rm DISS} \equiv \Delta t_{\delta p}$	RMS TOA error from diffractive scintillations (finite scintle effect)	ns or μs
$\sigma_{t_{\rm spin}}$	RMS residual from spin or torque noise of a neutron star	ns or μs

Table 11 *continued on next page*

Table 11 *(continued)*

Item	Definition	Typical Units
$\sigma_{t_{\mathrm{DM(t)}}}$	RMS residual due to asynchronous multifrequency observations	ns or μs
$\sigma_{t_{\mathrm{DM}(\nu)}}$	RMS residual due to chromaticity of DM from multipath propagation	ns or μs
σ_θ	RMS angle of arrival	
S_{sys}	SEFD = T_{sys}/G	Jy
S_{psr}	Pulsar period averaged flux density	mJy, Jy
S/N	Signal-to-noise ratio	—
$\mathrm{sinc}(x)$	sinc function = $(\sin \pi x)/\pi x$	—
s	Location along line of sight, $s = 0$ at source	
τ	lag time in correlation function or characteristic pulse scattering time	various
τ_{d}	Characteristic pulse scattering time	various
t	Time	various
t_{s}	Slow time (e.g. $\gg$ s)	various
t, TOA	Time of arrival	various
t_∞	TOA with chromatic delays removed ('infinite frequency')	ns or μs
t_{e}	Emission time at source	various
t_C	Non-dispersive chromatic delays	μs
τ or τ	Scattering time constant (1/e)	various
t_{sep}	Separation time between multi-frequency observations	
T_{int}	Integration time or data span at a single epoch	various
T_{data}	Total time span data set for an individual pulsar	yrs
T_{sys}	System (radiometer) temperature	K
U	Template shape normalized to unit peak amplitude	
ϕ	Phase perturbation from refractive index perturbations	rad
$\mathbf{v}_{\mathrm{eff}}$	Vector effective velocity	km s^{-1}
$\mathbf{v}_{\mathrm{obs}}$	Observer's velocity	
$\mathbf{v}'$	Pulsar velocity	
W or W_{U}	Pulse width (FWHM)	various
x_τ	Exponent in scaling law for pulse broadening time $\tau(\nu) \propto \nu^{-x_\tau}$	

NOTE—Wherever a symbol appears in the text with a caret (^) it refers to an estimate of that quantity.

Appendix B. Spectral representations

Spectra are defined as one-sided (positive frequencies only) so that the variance σ_X^2 of a quantity X is related to its spectrum $S_X(f)$ by

$$\sigma_X^2 = \int_0^\infty df\, S_X(f). \tag{B.1}$$

A variety of spectral representations are used in the pulsar, PTA, and GW literature, which are summarized here, though not all are utilized in the paper:

Power spectrum of TOA perturbations $\Delta t(t)$:	$S_{\Delta t}(f)$
Power spectrum of timing residuals $\mathcal{R}(t)$:	$S_{\mathcal{R}}(f)$
Power spectrum of dimensionless strain $h(t)$:	$S_h(f)$
Amplitude spectrum for dimensionless strain:	$h_c(f)$
Energy spectrum of GWs:	$S_E(f)$
Energy density of GWs per unit log frequency:	$\rho_{\rm gw}(f)$
Power spectrum as fraction of closure density:	$\Omega_{gw}(f) = \rho_{\rm gw}(f)/\rho_c$

These are related according to the following relations (e.g. Moore et al. 2015):

$$h_c^2(f) = f S_h(f) = \left(\frac{3H_0^2}{2\pi^2}\right)\frac{\Omega_{\rm gw}(f)}{f^2} = \frac{4G}{\pi c^2}\frac{S_E(f)}{f} = 12\pi^2 f^3 S_{\Delta t}(f), \tag{B.2}$$

where H_0 is the Hubble constant and G is the gravitational constant. The coefficient $12\pi^2 = 3(2\pi)^2$ in the last equality involving $S_{\Delta t}(f)$ includes $(2\pi)^2$ from the Fourier derivative theorem and a factor of 3 from all-sky averaging of the TOA perturbation.

The residuals spectrum $S_{\mathcal{R}}(f)$ is the power spectrum of the timing residual $\mathcal{R}(t)$, the difference between the timing perturbation $\Delta t(t)$ and a model fit $\widehat{\Delta t}(t)$,

$$\mathcal{R}(t) = \Delta t(t) - \widehat{\Delta t}(t). \tag{B.3}$$

Empirical spectral models often use a power law form with an implicit frequency range,

$$S(f) = S_0 \left(\frac{f}{f_{\rm ref}}\right)^{-X}, \tag{B.4}$$

where $f_{\rm ref}$ is a reference frequency (often specified as $1\,{\rm cy\,yr^{-1}}$ in PTA contexts). Motivated by representations for the GW amplitude spectrum,

$$h_{\rm c}(f) = A\left(\frac{f}{f_{\rm ref}}\right)^{\alpha} \tag{B.5}$$

using a dimensonless amplitude, A, the spectrum for ToA perturbations from GWs (before any model fitting that removes fluctuation power), is

$$S_{\Delta t}(f) = \frac{A_{\rm gw}^2}{12\pi^2}\left(\frac{f}{f_{\rm ref}}\right)^{-X_{\rm gw}}, \qquad X_{\rm gw} = 3 + 2\alpha. \tag{B.6}$$

The residuals spectrum $S_{\mathcal{R}}(f)$ has the same form as $S_{\Delta t}(r)$ but with an implied lower frequency cutoff related to the data span length T, $f_{\rm min} \propto 1/T$. More generally, the residuals spectrum is the ToA perturbation spectrum scaled by a *transmission function* that accounts for variance removed by the multi-parameter fit to the arrival times.

For example, the simplest model for the nanohertz stochastic background gives $\alpha = -2/3$ and $X_{\rm gw} = 13/3$ (Phinney 2001; Jaffe and Backer 2003).

Generalizing the relation between Eq. (B.4) and Eq. (B.6), we have

$$A = 2\pi\sqrt{3}\left[f_{\rm ref}^3 (f/f_{\rm ref})^X S(f)\right]^{1/2}. \tag{B.7}$$

Application to several classes of stochastic noise includes the following:

1. *Power-law noise:* The dimensionless amplitude, $A_{\rm PL} = 2\pi\sqrt{3}\left[f_{\rm ref}^3 S_0\right]^{1/2}$ is independent of fluctuation frequency,

2. *White noise:* With spectral index $X = 0$, noise with time-domain RMS $\sigma_{\rm w}$ in a bandwidth $B_{\rm w}$ has amplitudes $S_0 = \sigma_{\rm w}^2/B_{\rm w}$ and $A_{\rm w} = 2\pi\sqrt{3}(f_{\rm ref}/B_{\rm w})^{1/2} f_{\rm ref}\sigma_{\rm w}$. A time series of sampled data with uniform spacing δt has a bandwidth $B_{\rm w}$ equal to the Nyquist frequency, $f_{\rm Ny} = 1/2\delta t$. For instance, white noise ToA errors with $\sigma_{\rm w} = 0.1\,\mu$s in data obtained roughly monthly with $\delta t = 0.1\,$yr has Nyquist frequency $f_{\rm Ny} = 5\,{\rm cy\,yr^{-1}}$ and amplitudes yields a spectral amplitude

$$S_0 = 2\times 10^{-3}\,\mu{\rm s}^2\,{\rm yr}\left(\frac{\delta t}{0.1\,{\rm yr}}\right)\left(\frac{\sigma_{\rm w}}{0.1\,\mu{\rm s}}\right)^2, \tag{B.8}$$

   and a dimensionless strain spectrum with $\alpha = 3/2$ and

$$A_{\rm w} = 1.54\times 10^{-14}\left(\frac{\delta t}{0.1\,{\rm yr}}\right)^{1/2}\left(\frac{\sigma_{\rm w}}{0.1\,\mu{\rm s}}\right). \tag{B.9}$$

3. *Low-pass spectra:* A spectral form $S(f) = S_0 L(f)$ with low-pass shape normalized to $L(0) = 1$ has bandwidth $B_L \sim 1/W_L$ and W_L is the correlation time for the process. If the variance is σ_L^2, then $S_0 = \sigma_L^2/B_L = \sigma_L^2 W_L$. This relation is largely unaffected by the removal of a second-order polynomial, as is done in pulsar timing analysis to fit for a pulsar's spin rate and its derivative, if the length of the time series $T \gg W_L$, which we assume.

   While a power-law form is not a good model for a low-pass spectrum, PTA studies characterize the GW background with a power law that is then compared with contributions from other processes, whether or not they have power-law spectra. Non power-law spectra have equivalent A values that are frequency dependent, as seen by inspection of Eq. (B.7). Estimated values for the corresponding X values are also frequency and data dependent in other ways. For a low-pass spectrum the dimensionless amplitude is

$$A_L(f) = 2\pi\sqrt{3}\left[f_{\rm ref}^3 (f/f_{\rm ref})^X S_L(f)\right]^{1/2}. \tag{B.10}$$

   Evaluating at $f = f_{\rm ref}$ and assuming $B_L > f_{\rm ref}$ (or $W_L < 1\,$yr) we have $S_L(f_{\rm ref}) = S_0$ and $A_L(f_{\rm ref}) = 2\pi\sqrt{3}\left(f_{\rm ref}^3\sigma_L^2 W_L\right)^{1/2}$. For $\sigma_L = 0.1\,\mu$s, W_L in yr, and $f_{\rm ref} = 1\,{\rm cy\,yr^{-1}}$ the spectral amplitudes are

$$S_0 = 10^{-2}\,\mu{\rm s}^2\,{\rm yr}\left(\frac{W_L}{1\ {\rm yr}}\right)\left(\frac{\sigma_L}{0.1\,\mu{\rm s}}\right)^2, \tag{B.11}$$

$$A_L(f_{\rm ref}) = 2\pi\sqrt{3}\left(f_{\rm ref}^3\sigma_L^2 W_L\right)^{1/2} = 3.45\times 10^{-14}\left(\frac{W_L}{1\ {\rm yr}}\right)^{1/2}\left(\frac{\sigma_L}{0.1\,\mu{\rm s}}\right)^2, \tag{B.12}$$

   Processes with low-pass spectra will yield data-dependent values for A and X for a power-law model. Using simulations, we find that frequency indices X for low-pass processes are smaller than those for the GW background and pulsar spin noise, i.e. $X_L \lesssim 3$. Simulated time series comprising low-pass noise with RMS σ_L added to white noise with RMS $\sigma_{\rm w}$ were analyzed by first subtracting a second-order polynomial to mimic the removal of a spin-down polynomial from arrival time data. The resulting spectra $S(f)$ were fitted with a model of the form $a + X\log(S) + c$ for $f \le f_{\rm c}$ where $f_{\rm c}$ is a cutoff frequency and a constant amplitude c for $f > f_{\rm c}$. Least squares fitting for all four parameters yields frequency indices X that depend on the bandwidth of the low-pass noise and the 'signal'-to-noise ratio, S/N $= \sigma_L/\sigma_{\rm w}$. Indices averaged over 1000 realizations and over S/N from 0.5 to 5 were $\langle X\rangle \simeq -1.8 \pm 0.8$. For different S/N values, $\langle X\rangle$ and σ_X were -1.2 and 0.9 for S/N $= 0.5$ and -2.3 and 0.6 for S/N $= 5$.

Appendix C. Structure functions

Structure functions are a useful tool for parameterizing red spin noise that complement frequency-domain methods. Following Rutman (1978), CD85, D'Alessandro et al. (1995), and Lam et al. (2015), the $m^{\rm th}$ order structure function of the spin phase[61] is the mean-square expectation,

$$D_\phi^{(m)}(t,\tau) \equiv \langle [\Delta_\phi^{(m)}(t,\tau)]^2 \rangle, \tag{C.1}$$

where the $m^{\rm th}$ phase increment is

$$\Delta_\phi^{(m)}(t,\tau) \equiv \sum_{\ell=0}^{m} (-1)^\ell \binom{m}{\ell} \, \phi\,[t + (m-\ell)\tau]. \tag{C.2}$$

Phase increments are useful for removing trends in time series. A polynomial of order $m-1$ is removed by the $m^{\rm th}$ order increment, so the mean value of a time series is removed by the first order increment $\Delta_\phi^{(1)} = \phi(t+\tau) - \phi(t)$ while a linear trend is removed by the second order increment. Removal of a quadratic by the third order increment implies that the structure function for timing residuals formed by fitting and removing a quadratic spin phase, $\widehat{\phi}_2(t)$, is identical to the third order structure function of the original phase. I.e. if $\mathcal{R}(t) = \phi(t) - \widehat{\phi}_2(t)$, then $D_{\mathcal{R}}^{(3)}(\tau) = D_\phi^{(3)}(\tau)$. In practice, fitting functions include more terms than just the spindown polynomial, but these remove much less variance of the red noise.

Phase increments vs. t are useful for event detection in the phase or one of its derivatives. A step function in the $k^{\rm th}$ derivative appears as a pulse in the $(k+1)^{\rm th}$ increment and the corresponding structure function is the variance for a comparison Gaussian process that serves as a null hypothesis for the presence of individual events, as discussed in CD85 (§ IVa).

Structure functions are good probes of non-stationary, red noise processes because they are less vulnerable to spectral 'leakage,' by virtue of the fact that they act similarly to derivatives, whose spectra are less steep than the original process[62]. The power spectrum $S_\phi(f)$ is defined so that the phase variance is the integral over non-negative frequencies $\langle \phi^2(t) \rangle \equiv \int_0^\infty df\, S(f)$. To keep notation simple, the spectrum can correspond to any or all of the stochastic phase terms discussed earlier and it can stand for either the pre-fit phase or post-fit residuals.

The phase autocorrelation function (ACF) $R_\phi(\tau)$ is the Fourier transform of the spectrum (the Wiener-Khinchin theorem) using a Fourier kernel $e^{2\pi i f \tau}$. Any time (or long term epoch) dependence of the ACF is implicit but we recognize that phase fluctuations may have nonstationary statistics. Red noise combined with a finite data span T has this property and the phase variance $\sigma^2_{\rm red}(T) = R_\phi(0)$ generally depends on T raised to some positive power.

Structure functions of any order can be written in terms of the ACF and thus related to the spectrum (Rutman 1978) by

$$D_\phi^{(m)}(\tau) = \int df\, S_\phi(f) \sin^{2m}(\pi f \tau). \tag{C.3}$$

Depending on the process, one or more of the SFs can be independent of time and depend only on τ. This is more likely for higher order SFs. The relevant frequency range for the ensemble average implied in Eq. (C.3) is determined by the spectrum itself, but for finite data sets of length T, the lower frequency limit for the spectrum of *phase residuals* is $f_{\rm l} \equiv \eta/T$ where $\eta \simeq 1$ depends on the fitting function used to form the residuals. The upper frequency limit $f_{\rm h}$ becomes the Nyquist frequency $f_{\rm Ny} = 1/2\Delta t$ for data sampled at time intervals Δt.

[61] We freely refer to the phase in either units of cycles or temporal units (usually microseconds), depending on the context.
[62] The Fourier derivative theorem states that $dx(t)/dt$ of a process with spectrum $S_x(f)$ has a spectrum $(2\pi f)^2 S_x(f)$.

Appendix D. Modulated complex noise

Time-domain processes comprising modulations of a complex noise process appear in two contexts: the emitted pulsar signal and the impulse response from multipath propagation through the interstellar medium. The statistical properties of each of these processes are similar, so we present here a generic description that applies to both cases.

Define $z(t) = x(t)m(t)$ as the product of a real pulse-like amplitude $x(t)$ and complex, Gaussian noise $m(t)$ with bandwidth B. The noise has stationary statistics with zero mean $\langle m \rangle = 0$, variance $\langle |m|^2 \rangle = \sigma_m^2$ and autocorrelation function

$$\langle m(t)m^*(t') \rangle = \sigma_m^2 \Delta(t - t'). \tag{D.1}$$

The quantity $\Delta(t)$ has a width equal to the reciprocal of the signal bandwidth $\sim B^{-1}$ and is assumed to be much narrower than $x(t)$. The noise m is therefore flat (i.e. 'white') over the bandwidth. The 'intensity' is the squared magnitude $Z(t) = |z|^2 = x^2(t)|m(t)|^2$. In the following we consider $x(t)$ to be deterministic (not stochastic).

Properties of the squared modulated noise $M = |m|^2$ are

1. Modulation index, m_M: $1 + m_M^2 \equiv \langle M^2 \rangle / \langle M \rangle^2 = 2$. This value is a property of complex Gaussian noise. If m were real, the value would be three.
2. Spectrum: the spectrum of $z(t)$, $S_z(\nu) \equiv |\widetilde{z}(\nu)|^2$, has mean $\langle S_z(\nu) \rangle = \sigma_m^2 \widetilde{\Delta}(\nu) R_x(0)$ where $R_x(0) = \int dt\, x^2(t)$. The mean square of the spectrum is $\langle S_z^2(\nu) \rangle = 2 \langle S_z(\nu) \rangle$.
3. Spectral autocorrelation function:

$$R_{S_z}(\delta\nu) = \sigma_n^4 \left\{ R_x^2(0) \widetilde{\Delta}(\nu) \widetilde{\Delta}(\nu + \delta\nu) + [\widetilde{\Delta}(\nu + \delta\nu)]^2 S_X(\delta\nu) \right\}, \tag{D.2}$$

   where $X \equiv x^2$ and

$$S_X(\nu) = \left| \widetilde{X}(\nu) \right|^2 = \left| \int dt\, X(t) e^{2\pi i \nu t} \right|^2. \tag{D.3}$$

The two equal-amplitude terms of the frequency correlation function in Eq. (D.2) comprise a broad component determined by the receiver bandpass function $\widetilde{\Delta}$ and a narrow spike associated with the modulation x.

Product of two complex Gaussian noise processes: Let $z = xy$ be the product of two complex noise processes x and y like that described in Appendix D. Defining $X = |x|^2$, $Y = |y|^2$, and $Z = |z|^2$, the squared modulation indices $m_X^2 \equiv \langle X^2 \rangle / \langle X \rangle^2 - 1$ etc. are related as

$$1 + m_Z^2 = (1 + m_X^2)(1 + m_Y^2). \tag{D.4}$$

If x and y have (complex) Gaussian statistics, then $m_X = m_Y = 1$ and $m_Z = \sqrt{3}$.

If x and y are Fourier transforms of time-domain processes, they will generally have complex Gaussian statistics by the central limit theorem. The resulting spectrum Z will manifest two characteristic frequency scales determined by those of X and Y individually.

Appendix E. ToA variations from frequency-dependent dispersion deasures

The chromaticity of dispersion measures $\overline{\mathrm{DM}}(\nu)$ caused by multipath propagation was initially identified by Cordes et al. (1990); Ramachandran et al. (2006) and also by Donner et al. (2019); Kaur et al. (2022); Kumar et al. (2025) subsequent to the theory developed by Cordes et al. (2016, hereafter CSS16). CSS16 presented the consequences for pulsar timing for both dual-frequency estimates of DM and wideband measurements using analytical and simulation methods, respectively.

Here we present a more general analytical treatment for arbitrary frequency coverage that extends the analytical approach in CSS16 for two spot frequencies. A multifrequency data set $\mathcal{D} = \{t_\nu, \nu_\mathrm{l} \le \nu \le \nu_\mathrm{h}\}$ comprising $N_\nu \gg 1$ frequency channels is analyzed here in the continuum approximation. The total frequency ratio $R \equiv \nu_\mathrm{h}/\nu_\mathrm{l}$ can be much larger than unity for recently developed wideband receivers.

To calculate the effects of $\overline{\mathrm{DM}}(\nu)$ in isolation of other chromatic propagation effects, we adopt a minimal model for ToAs that includes the infinite frequency ('true') ToA , a dispersion term, and measurement error,

$$t_\nu = t_\infty + K_\mathrm{DM}\,\nu^{-2}\overline{\mathrm{DM}}(\nu) + \epsilon_\nu, \tag{E.1}$$

where the overbar denotes that DM is averaged over scattered propagation paths, $K_\mathrm{DM} = cr_\mathrm{e}/2\pi$, and additive noise from measurement errors is statistically independent between frequencies and has variance σ_ν^2.

We estimate t_∞ and DM as parameters of a fitting function,

$$t_\nu = \widehat{t}_\infty + K_\mathrm{DM}\,\nu^{-2}\widehat{\mathrm{DM}}, \tag{E.2}$$

using a cost function $C = \int d\nu\, w_\nu (t_\nu - \widehat{t}_\nu)^2$ with weights[63] $w_\nu \propto \sigma_\nu^{-2}$. Unless stated otherwise, integrals are over the entire frequency interval $[\nu_\mathrm{l}, \nu_\mathrm{h}]$. The resulting least squares solutions are

$$\begin{aligned}\widehat{t}_\infty &= t_\infty + \frac{K_\mathrm{DM}}{\Delta}(j_4 l_2 - j_2 l_4)\\ \widehat{\mathrm{DM}} &= \Delta^{-1}(j_0 l_4 - j_2 l_2),\end{aligned} \tag{E.3}$$

where we have defined

$$j_n = \int d\nu\, w_\nu\, \nu^{-n}, \tag{E.4}$$

$$l_n = \int d\nu\, w_\nu\, \nu^{-n}\overline{\mathrm{DM}}(\nu), \tag{E.5}$$

$$\Delta = j_0 j_4 - j_2^2. \tag{E.6}$$

To assess the extra variance that results from DM chromaticity we reference $\overline{\mathrm{DM}}(\nu)$ to the highest frequency, ν_h,

$$\overline{\mathrm{DM}}(\nu) = \overline{\mathrm{DM}}(\nu_\mathrm{h}) + \left[\overline{\mathrm{DM}}(\nu) - \overline{\mathrm{DM}}(\nu_\mathrm{h})\right] \equiv \overline{\mathrm{DM}}(\nu_\mathrm{h}) + \Delta\overline{\mathrm{DM}}(\nu, \nu_\mathrm{h}). \tag{E.7}$$

Parameter estimates are then

$$\widehat{t}_\infty = t_\infty + \frac{K_\mathrm{DM}}{\Delta}\int d\nu\, w_\nu\, \nu^{-2}\left[j_4 - j_2\nu^{-2}\right]\Delta\mathrm{DM}(\nu, \nu_\mathrm{h}), \tag{E.8}$$

$$\widehat{\mathrm{DM}} = \mathrm{DM}(\nu_\mathrm{h}) + \Delta^{-1}\int d\nu\, w_\nu\, \nu^{-2}\left[j_0\nu^{-2} - j_2\right]\Delta\mathrm{DM}(\nu, \nu_\mathrm{h}). \tag{E.9}$$

[63] For simplicity we assume a diagonal covariance matrix for the errors ϵ_ν. It is trivial, but less useful analytically, to extend the analysis to an arbitrary covariance matrix.

E.1. *Errors in ToA and DM Estimates*

To express results in terms of frequency ratios, we make a change of variable to $r = \nu_{\rm h}/\nu$ to obtain errors in t_∞ and $\widehat{\rm DM}$ due solely to the frequency dependence of $\overline{\rm DM}$,

$$\delta\widehat{t}_\infty = \frac{K_{\rm DM}}{\nu_{\rm h}\Delta}\int_1^R dr\, W_r\left[j_4 - j_2(r/\nu_{\rm h})^2\right]\Delta{\rm DM}(\nu_{\rm h}/r,\nu_{\rm h}) \tag{E.10}$$

$$\delta\widehat{\rm DM} = (\nu_{\rm h}\Delta)^{-1}\int_1^R dr\, W_r\left[j_0(r/\nu_{\rm h})^2 - j_2\right]\Delta{\rm DM}(\nu_{\rm h}/r,\nu_{\rm h}). \tag{E.11}$$

We apply these results to two cases, one with constant weights $w_\nu = 1$ over the frequency range $[\nu_{\rm l},\nu_{\rm h}]$ with ratio $R = \nu_{\rm h}/\nu_{\rm l}$ and another where $\nu_{\rm l}$ and $\nu_{\rm h}$ are two spot frequencies. The weights for the two-frequency case are

$$w_\nu = (1/2)[\delta(\nu-\nu_{\rm l}) + \delta(\nu-\nu_{\rm h})], \tag{E.12}$$

which, for dimensionless frequencies, corresponds to

$$w_r = (r/2)[\nu_{\rm h}^{-1}\delta(r-1) + \nu_{\rm l}^{-1}\delta(r-R)] = \frac{r}{2\nu_{\rm h}}[R\delta(r-R) + \delta(r-1)]. \tag{E.13}$$

The errors in $\widehat{t}_\infty$ from the frequency dependence of $\overline{\rm DM}$ for the two cases are

$$\delta\widehat{t}_\infty = \frac{K_{\rm DM}}{\nu_{\rm h}^2}\times\begin{cases}\dfrac{R(R^3-1)}{(R-1)^4}\displaystyle\int_1^R dr\,\left[1-\frac{3(R-1)r^2}{(R^3-1)}\right]\Delta{\rm DM}(\nu_{\rm h}/r,\nu_{\rm h}), & w_\nu = \text{constant}\\[2ex] -\left(\dfrac{R^2}{R^2-1}\right)\Delta{\rm DM}(\nu_{\rm l},\nu_{\rm h}), & \text{two frequencies.}\end{cases} \tag{E.14}$$

The corresponding errors in the estimated DM are

$$\delta\widehat{\rm DM} = \begin{cases}\dfrac{3R}{(R-1)^3}\displaystyle\int_1^R dr\,\left(\frac{r^2}{R}-1\right)\Delta{\rm DM}(\nu_{\rm h}/r,\nu_{\rm h}), & w_\nu = \text{constant}\\[2ex] \left(\dfrac{R^2}{R^2-1}\right)\Delta{\rm DM}(\nu_{\rm l},\nu_{\rm h}), & \text{two frequencies.}\end{cases} \tag{E.15}$$

E.2. *Variances*

The variances of $\delta\hat{t}_\infty$ and $\delta\widehat{\rm DM}$ are given by the ensemble averages of $(\delta\widehat{t}_\infty)^2$ and $(\delta\widehat{\rm DM})^2$. These involve the cross correlation function

$$\Gamma_{\Delta\overline{\rm DM}}(\nu_1,\nu_2,\nu_3;\beta) \equiv \langle\Delta{\rm DM}(\nu_1,\nu_3)\Delta{\rm DM}(\nu_2,\nu_3)\rangle\,, \tag{E.16}$$

which is evaluated in §E.3 along with the quantity $\Phi_\beta(r_1,r_2)$,

$$\Gamma_{\Delta\overline{\rm DM}}(\nu_1,\nu_2,\nu_3;\beta) = \Phi_\beta^2(r_1,r_2)J_{\rm DM}(\nu_{\rm h},\beta) \tag{E.17}$$

where $J_{\rm DM}$, evaluated later in this section, integrates the scattering medium over the bundle of ray paths,

$$J_{\rm DM}(\nu_{\rm h},\beta) = \frac{(2\pi)^2\Gamma(2-\beta/2)}{\beta-2}\int d\overline{z}\,{\rm C}_{\rm n}^2(\overline{z})\,\sigma_X^{\beta-2}\overline{z},\nu_{\rm h}). \tag{E.18}$$

The variances of the estimates for arrival time and DM are then

$${\rm Var}(\delta\hat{t}_\infty) = \left(\frac{K_{\rm DM}}{\nu_{\rm h}^2}\right)^2 J_{\rm DM}(\nu_{\rm h},\beta)\,I_{t_\infty}(R,\beta) \tag{E.19}$$

$${\rm Var}(\delta\widehat{\rm DM}) = J_{\rm DM}(\nu_{\rm h},\beta)\,I_{\rm DM}(R,\beta). \tag{E.20}$$

The dimensionless integrals I_{t_∞} and $I_{\rm DM}$ over dimensionless frequency ratios $r_{1,2} = \nu_{\rm h}/\nu_{1,2}$ for the wideband case with w_ν = constant are given by

$$I_{t_\infty}(R,\beta) = \left[\frac{R(R^3-1)}{(R-1)^4}\right]^2 \int_1^R\!\!\int_1^R dr_1 dr_2 \left[1 - \frac{3(R-1)r_1^2}{(R^3-1)}\right]\left[1 - \frac{3(R-1)r_2^2}{(R^3-1)}\right] \Phi_\beta^2(r_1,r_2), \tag{E.21}$$

and

$$I_{\rm DM}(R,\beta) = \left[\frac{3R}{(R-1)^3}\right]^2 \int_1^R\!\!\int_1^R dr_1 dr_2 \left(r_1^2/R - 1\right)\left(r_2^2/R - 1\right) \Phi_\beta^2(r_1,r_2), \tag{E.22}$$

For two equally weighted spot frequencies, these are

$$I_{t_\infty}(R,\beta) = I_{\rm DM}(R,\beta) = \left[\left(\frac{R^2}{R^2-1}\right) F_\beta(R)\right]^2, \tag{E.23}$$

which is obtained by using the identify $\Phi(x,x) = F_\beta(x)$, where F_β, first defined in CSS16, is given in Eq. E.52. These integrals are shown in Fig. 51 for three values of β and for both the wideband and two-frequency cases.

The quantity $J_{\rm DM} \propto \int d\overline{z}\, {\rm C}_{\rm n}^2(\overline{z})\, \sigma_X^{\beta-2}(\overline{z},\nu_{\rm h})$ integrates ${\rm C}_{\rm n}^2$ over the bundle of ray paths that reach the observer. Because σ_X also depends on ${\rm C}_{\rm n}^2$, the integral generally depends on the square of the scattering measure, $J_{\rm DM} \propto {\rm SM}^2$, but it also depends on the detailed distribution of ${\rm C}_{\rm n}^2(\overline{z})$ in both factors comprising the integrand.

We simplify the expression for $J_{\rm DM}$ by first expressing σ_X in a form that isolates quantities that depend on the distribution of ${\rm C}_{\rm n}^2$ along the LoS

$$\sigma_X(s,\nu_{\rm h}) = d_{\rm so}\sigma_{\theta_{\rm d}} \left(\frac{{\rm SM}_{\rm eff}}{\rm SM}\right)^{1/(\beta-2)} h(s), \tag{E.24}$$

where $d_{\rm so}$ is the source-observer distance (as used elsewhere), $\sigma_{\theta_{\rm d}}$ is the RMS scattering angle produced by a medium with plane wave incidence, ${\rm SM}_{\rm eff}$ is the effective scattering measure that takes into account the geometry of the scattering medium (thin screen, thick slab, uniform, etc.), and $h(s)$ is a dimensionless quantity that defines the extent of the raypath bundle and is also geometry dependent.

The RMS scattering angle is

$$\sigma_{\theta_{\rm d}} = \frac{\lambda}{\sqrt{2}\pi}\left[\frac{f_\beta(\lambda r_{\rm e})^2{\rm SM}}{2}\right]^{1/(\beta-2)} = \frac{1}{\pi}\left[\frac{c^\beta r_{\rm e}^2 f_\beta {\rm SM}}{2^{\beta/2}\nu^\beta}\right]^{1/(\beta-2)} \tag{E.25}$$

where f_β is given in Eq. (9.7). The effective scattering measure is given by

$$\frac{{\rm SM}_{\rm eff}}{\rm SM} = \frac{\displaystyle\int ds\, {\rm C}_{\rm n}^2(s)(s/d_{\rm so})^{\beta-2}}{\displaystyle\int ds\, {\rm C}_{\rm n}^2(s)} \tag{E.26}$$

and has representative values,

$$\frac{{\rm SM}_{\rm eff}}{\rm SM} = \begin{cases} 1 & \text{Plane wave incidence} \\ (d_{\rm sl}/d_{\rm so})^{\beta-2} & \text{Thin screen} \\ (\beta-1)^{-1} & \text{Uniform medium,} \end{cases} \tag{E.27}$$

where we have used ${\rm C}_{\rm n}^2(s) = {\rm SM}\delta(s - d_{\rm sl})$ for a thin screen at a source-screen distance $d_{\rm sl}$.

The ray bundle shape $h(s)$ generally requires a numerical solution. For a thin screen it is

$$h(s) = \begin{cases} \dfrac{s}{d_{\rm sl}}\left(1 - \dfrac{s}{d_{\rm so}}\right) & s \le d_{\rm sl}, \\ 1 - \dfrac{s}{d_{\rm so}} & s \ge d_{\rm sl}, \end{cases} \tag{E.28}$$

which has a value $h(d_{\rm sl}) = d_{\rm lo}/d_{\rm so}$ at the screen itself. For a uniform medium it is

$$h(s) = \frac{d_{\rm sl}}{d_{\rm so}}\left(1 - \frac{d_{\rm sl}}{d_{\rm so}}\right). \tag{E.29}$$

The ray bundle shape is integrated along the line of sight to yield another dimensionless quantity,

$$H_\beta = \frac{\int ds\, \mathrm{C}_{\rm n}^2(s)[h(s)]^{\beta-2}}{\int ds\, \mathrm{C}_{\rm n}^2(s)}, \tag{E.30}$$

which has values of $(d_{\rm lo}/d_{\rm so})^{\beta-2}$ for a thin screen and $H_\beta = \int_0^1 ds\,[s(1-s)]^{\beta-2} = 0.0564$ for a uniform medium with $\beta = 11/3$.

Defining, as in CSS16,

$$G_\beta^2 = H_\beta \mathrm{SM_{eff}}/\mathrm{SM} \tag{E.31}$$

$$Q_\beta^2 = \frac{(\sqrt{2}\pi)^{4-\beta}\Gamma(2-\beta/2) f_\beta}{\beta - 2}, \tag{E.32}$$

where Q_β and G_β depend on the spectral index of the density spectrum while G_β also depends on the specific distribution of $\mathrm{C}_{\rm n}^2$ along the LoS. We then have

$$J_{\rm DM}(\nu_{\rm h}, \beta) = (G_\beta Q_\beta)^2 c^\beta r_{\rm e}^2 \nu_{\rm h}^{-\beta} d_{\rm so}^{\beta-2}\, \mathrm{SM}^2 \tag{E.33}$$

The final expressions for the variances are given by Eq. E.19-E.20 using the above defined quantities. Evaluating for a Kolmogorov index $\beta = 11/3$ with a nominal scattering measure $\mathrm{SM} = 10^{-3.5}\,\mathrm{kpc\ m^{-20/3}} = 4.53 \times 10^4\,\mathrm{cm^{-17/3}}$, we obtain $Q_\beta^2 = 485$ and

$$\sigma_{\delta t_\infty} = [\mathrm{Var}(\delta t_\infty)]^{1/2} = 156\,\mathrm{ns} \times G_\beta\, \nu_{\rm h}^{-23/6} d_{\rm so}^{5/6}\, \mathrm{SM}_{-3.5} I_{t_\infty}(R, \beta) \tag{E.34}$$

$$\sigma_{\delta\widehat{\rm DM}} = [\mathrm{Var}(\delta\widehat{\rm DM})]^{1/2} = 3.76 \times 10^{-5}\,\mathrm{pc\ cm^{-3}} \times G_\beta \nu_{\rm h}^{-11/6} d_{\rm so}^{5/6}\, \mathrm{SM}_{-3.5} I_{\rm DM}(R, \beta), \tag{E.35}$$

where $\mathrm{SM}_{-3.5} = \mathrm{SM}/(10^{-3.5}\,\mathrm{kpc\ m^{-20/3}})$. We note that the dependence on the upper frequency $\nu_{\rm h}$ for the excess DM variation is $\sigma_{\delta\widehat{\rm DM}} =\propto \nu_{\rm h}^{-11/6}$ for a Kolmogorov spectrum (inertial subrange) while the ToA variation has a much stronger dependence, $\sigma_{\delta t_\infty} =\propto \nu_{\rm h}^{-23/6}$. The actual ToA error also depends on the frequency ratio R and can be much smaller than the nominal values for a narrowband system, particularly if the upper frequency $\nu_{\rm h}$ is well above 1 GHz.

E.3. *Derivation of the cross correlation* $\Gamma_{\Delta\overline{\rm DM}}(\nu_1, \nu_2, \nu_3)$

The cross correlation is expanded into the sum of four autocorrelation functions,

$$\Gamma_{\Delta\overline{\rm DM}}(\nu_1, \nu_2, \nu_3) = C_{\delta\overline{\rm DM}}(\nu_1, \nu_2) + C_{\delta\overline{\rm DM}}(\nu_3, \nu_3) - C_{\delta\overline{\rm DM}}(\nu_2, \nu_3) - C_{\delta\overline{\rm DM}}(\nu_1, \nu_3), \tag{E.36}$$

where the cross correlation of $\delta\overline{\rm DM} = \overline{\rm DM} - \langle \mathrm{DM}\rangle$ between frequency pairs is

$$\begin{aligned} C_{\delta\overline{\rm DM}}(\nu_1, \nu_2) &= \left\langle \delta\overline{\rm DM}(\nu_1, \mathbf{x}) \delta\overline{\rm DM}(\nu_2, \mathbf{x})\right\rangle \\ &= \iint d\mathbf{x}' d\mathbf{x}'' \iint dz' dz''\, A_{\nu_{\rm h}}(\mathbf{x}', z') A_{\nu_{\rm l}}(\mathbf{x}'', z'') A_{\nu_1}(\mathbf{x}') A_{\nu_2}(\mathbf{x}'') \langle \delta n_e(\mathbf{x}', z') \delta n_e(\mathbf{x}'', z'')\rangle. \end{aligned} \tag{E.37}$$

The z integrals are from 0 to d and the $\mathbf{x}$ integrals are over an infinite plane[64]. To proceed, a change of variables is made from $\mathbf{x}', \mathbf{x}''$ to $\overline{\mathbf{x}} = (\mathbf{x}' + \mathbf{x}'')/2$ and $\delta\mathbf{x} = \mathbf{x}' - \mathbf{x}''$ and from z', z'' to $\overline{z} = (z' + z'')/2$ and $\delta z = z' - z''$. The

[64] Extension over an infinite plane will not apply to bounded media, as discussed by Cordes and Lazio (2001). A bounded medium will alter the frequency dependence of any multipath propagation.

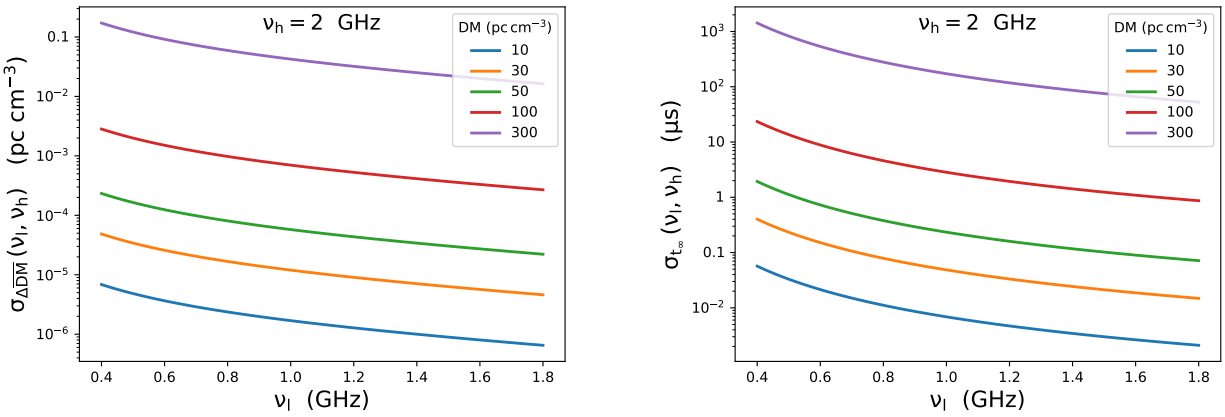


Figure 79. Left: Plot of the RMS excess DM variation due to chromatic multipath propagation for different values of the total DM that are used to calculate the total DM. Right: Plot of the RMS variation in t_∞ due to chromatic multipath propagation for different values of the total DM that are used to calculate the total DM.

resulting integral over $\overline{x}$ yields the cross-correlation function for the averaging function,

$$C_A(\delta\mathbf{x}, \delta z, \overline{z}, \nu_1, \nu_2) = \int d\overline{\mathbf{x}}\, A_{\nu_1}(\overline{x} + \delta\mathbf{x}/2, \overline{z} + \delta z) A_{\nu_2}(\overline{x} - \delta\mathbf{x}/2, \overline{z} - \delta z), \tag{E.38}$$

which we assume changes slowly in $\overline{z}$ compared to density variations, and thus set $\delta z = 0$ in the argument and rewrite simply as $C_A(\delta\mathbf{x}, \overline{z}, \nu_1, \nu_2)$.

The density correlation function is written in terms of the wavenumber spectrum,

$$\langle \delta n_e(\overline{\mathbf{x}} + \delta\mathbf{x}, \overline{z} + \delta z) \delta n_e(\overline{\mathbf{x}} - \delta\mathbf{x}, \overline{z} - \delta z) \rangle = \int d\mathbf{q}\, e^{i\mathbf{q}_\perp \cdot \delta\mathbf{x} + q_z \delta z} P_{\delta n_e}(\mathbf{q}, \overline{z}). \tag{E.39}$$

The integration over δz gives $2\pi\delta(q_z)$ and the integration over $d\mathbf{q}_\perp$ yields the Fourier transform[65] of $C_A(\delta\mathbf{x}, \overline{z}, \nu_1, \nu_2)$,

We adopt a Gaussian smoothing function with RMS spatial scale σ_X for the bundle of rays comprising the scattering cone,

$$A_\nu(\mathbf{x}, z) = \left[2\pi\sigma_X^2(\nu, z)\right]^{-1} e^{-x^2/2\sigma_X^2(\nu,z)}, \tag{E.40}$$

that yields a Fourier transform for the cross-correlation function also Gaussian in form,

$$\widetilde{C}_A(\mathbf{q}_\perp, \nu_1, \nu_2, \overline{z}) = (2\pi)^{-2} e^{({q_\perp}^2/2)[\sigma_X^2(\nu_1,\overline{z}) + \sigma_X^2(\nu_2,\overline{z}]}. \tag{E.41}$$

The two-frequency cross correlation becomes

$$C_{\delta\overline{\mathrm{DM}}}(\nu_1, \nu_2) = 2\pi \int d\overline{z} \int d\mathbf{q}_\perp\, P_{\delta n_e}(\mathbf{q}_\perp, 0, \overline{z}) e^{-({q_\perp}^2/2)[\sigma_X^2(\nu_1,\overline{z}) + \sigma_X^2(\nu_2,\overline{z})]}. \tag{E.42}$$

Using the power-law form for $P_{\delta n_e}(\mathbf{q})$ for $2 < \beta < 4$ with an exponential rolloff from the inner scale and using $d\mathbf{q}_\perp = 2\pi q_\perp dq_\perp$, we require an integral of the form

$$\int_{y_0}^{\infty} dy\, y^{1-\beta} e^{-ay^2} = \int_0^{\infty} dy\, y^{1-\beta} e^{-ay^2} - \int_0^{y_0} dy\, y^{1-\beta} e^{-ay^2}. \tag{E.43}$$

We make use of the integral (GR 3.478.1),

$$\int_0^{\infty} dy\, x^{v-1} e^{-ux^p} = p^{-1} u^{-v/p} \Gamma(v/p), \tag{E.44}$$

[65] Note that the convention used for Fourier transforms is $\widetilde{g}(q) = (2\pi)^{-1} \int dx\, e^{-iqx} g(x)$. Thus a factor $(2\pi)^{-1}$ is introduced for each dimension of a Fourier transform.

which holds for $u, v, p > 0$. Thus to apply it for $2 < \beta < 4$ we integrate by parts to obtain

$$I = \int_{q_o}^{\infty} dq_\perp \, {q_\perp}^{1-\beta} e^{-(q_\perp/q_i)^2} = \frac{1}{(\beta-2)} \left[q_o^{2-\beta} e^{-a q_o^2} + \frac{2a q_o^{4-\beta}}{4-\beta} - a^{(\beta-2)/2} \Gamma(2-\beta/2) \right], \tag{E.45}$$

with $a = [\sigma_X^2(\nu_1, \overline{z}) + \sigma_X^2(\nu_2, \overline{z})]/2 + 1/q_i^2$. This is further simplified by taking into account that the outer scale is much larger than the width of the scattering cone $\sim \sigma_X$ at relevant radio frequencies which, in turn, is much larger than the inner scale. This impies $a q_o^2 \lll 1 \lll (q_o/q_i)^2$ and

$$I \approx \frac{1}{(\beta-2)} \left[q_o^{2-\beta} + \frac{2a q_o^{4-\beta}}{4-\beta} - a^{(\beta-2)/2} \Gamma(2-\beta/2)) \right]. \tag{E.46}$$

We then have

$$C_{\delta\overline{\mathrm{DM}}}(\nu_\mathrm{l}, \nu_\mathrm{h}) \approx \frac{(2\pi)^2}{\beta-2} \int d\overline{z} \, \mathrm{C}_\mathrm{n}^2(\overline{z}) \left[q_o^{2-\beta} + \frac{2a q_o^{4-\beta}}{4-\beta} - a^{(\beta-2)/2} \Gamma(2-\beta/2) \right]. \tag{E.47}$$

The first term in square brackets is independent of frequency so its contribution vanishes when substituted into Eq. (E.36). The second term is linear in the σ_X^2 terms at the two frequencies and also cancels. Using the third term and substituting for the relevant values of a we obtain

$$\Gamma_{\Delta\overline{\mathrm{DM}}}(\nu_1, \nu_2, \nu_3) = \frac{(2\pi)^2 \Gamma(2-\beta/2)}{\beta-2} \Phi_\beta^2(r_1, r_2) \int d\overline{z} \, \mathrm{C}_\mathrm{n}^2(\overline{z}) \, \sigma_X^{\beta-2}(\overline{z}, \nu_3) \tag{E.48}$$

where the frequency ratios $r_1 = \nu_3/\nu_1$ and $r_2 = \nu_3/\nu_2$ are used in the dimensionless function,

$$\Phi_\beta^2(r_1, r_2) = 2^{-(\beta-2)/2} [V_\beta(r_1) + V_\beta(r_2) - r_2^\beta V_\beta(r_1/r_2)] - 1 \tag{E.49}$$

with

$$V_\beta(x) \equiv [1 + x^{2\beta/(\beta-2)}]^{(\beta-2)/2}. \tag{E.50}$$

We note that for equal values of the arguments,

$$\Phi_\beta(r, r) = F_\beta(r), \tag{E.51}$$

where $F_\beta(r)$ is the function defined in CSS16 for the case where a pair of frequencies is used to calculate $\widehat{\mathrm{DM}}$ and $\widehat{t}_\infty$ rather than the wideband continuum range of frequencies considered here,

$$F_\beta(r) = \left\{ 2^{(4-\beta)/2} \left[1 + r^{2\beta/(\beta-2)} \right]^{(\beta-2)/2} - r^\beta - 1 \right\}^{1/2}. \tag{E.52}$$

This quantity is shown in Fig. 80 for three values of β.

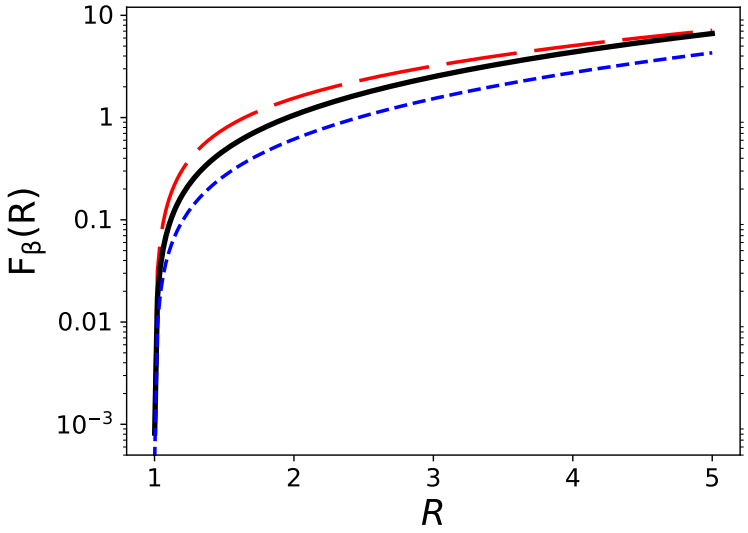


Figure 80. Plot of $F_\beta(R)$ vs. frequency ratio $R = \nu_\mathrm{h}/\nu_\mathrm{l}$ for several values of β. This function is applicable to the two-frequency case as presented in CSS16.

Appendix F. Simulation of propagation through thin plasma screens

F.1. *Diffraction and lensing from a thin screen*

To create Fig. 59, we evaluated the wavefield at an observer location $(\mathbf{x}, d)$ using a two dimensional Fresnel-Kirchhoff diffraction integral for a thin screen that imposes a phase $\phi_{\rm s}(x)$ on an incident plane wave,

$$E(\mathbf{x}) = \int d\mathbf{x}'\, K(\mathbf{x}-\mathbf{x}')e^{i\phi_{\rm s}(\mathbf{x}')}, \tag{F.1}$$

where $K(\mathbf{x}) = (2\pi i {r_{\rm F}}^2)^{-1} e^{i|\mathbf{x}-\mathbf{x}'|^2/2{r_{\rm F}}^2}$ is the propagation kernel and the Fresnel scale is $r_{\rm F} = \sqrt{\lambda d/2\pi}$. The screen phase includes a Gaussian lens $\phi_g(\mathbf{x}) \propto \exp\bigl(-|\mathbf{x}|^2/a^2\bigr)$ combined with a stochastic phase $\phi_{\rm K}(\mathbf{x})$. The latter is drawn from a Kolmogorov medium with spectrum of the form of Eq. (9.1) with an inner scale $l_i = 2\pi/q_i$ imposed as an exponential factor $\exp\bigl[-(q/q_i)^2\bigr]$ and outer scale determined by the size of the spatial grid used to evaluate $E(\mathbf{x})$. A realization of $\phi_{\rm K}$ is calculated by using the average phase spectrum $S_\phi(\mathbf{q}_\perp) = 2\pi(\lambda r_{\rm e})^2 {\rm SM}\, \exp\bigl[-(q/q_i)^2\bigr] {q_\perp}^{-\beta}$ to shape complex white noise $\mathcal{N}(\mathbf{q}_\perp)$,

$$\phi_{\rm K}(\mathbf{q}_\perp) \sim S_\phi^{1/2}(\mathbf{q}_\perp)\mathcal{N}(\mathbf{q}_\perp). \tag{F.2}$$

The convolution in Eq. (F.1) is executed by taking the inverse FT of the product of FTs of the kernel and the screen phase factor.

F.2. *Refractive distortions of scattered Images and PBFs*

We outline simulations described in the main text that demonstrate the effects of stochastic refraction screens on observable quantities. For simplicity, we employ a circularly symmetric scattered image shape in the absence of refraction. Non-Gaussian images like those from a Kolmogorov medium and images caused by asymmetric scattering could be used instead, though the essential features of the examples shown here would not be altered significantly. We thus use an unrefracted scattered image seen by an observer with RMS angles $\sigma_x = \sigma_y = \sigma$. The corresponding RMS diffraction angle is $\sigma_{\rm d} = (d_{\rm so}/d_{\rm sl})\sigma$. For a source much further from the observer than the screen, $d_{\rm so}/d_{\rm sl} \to 1$ and $\sigma_{\rm d} \to \sigma$.

We calculate the scattering parameters of a thin screen by specifying the DM for the LoS and inferring the scattering strength from the τ(DM) relation for Galactic pulsars (the 'hockey stick' relation in Eq. (10.16)). After scaling from 1 GHz to the frequency of interest, the diffraction and refraction scales $l_{\rm d}$ and $l_{\rm r}$ are calculated along with the value of the phase structure function across a Fresnel scale. Using the electromagnetic wavenumber $k = 2\pi/\lambda$ and Fresnel scale $r_{\rm F} = \sqrt{d'/k} = \sqrt{\lambda d'/2\pi}$,

$$l_{\rm d} = \frac{1}{k\sigma_{\rm d}} = \frac{1}{k}\left(\frac{d'}{c\tau}\right)^{1/2} = \frac{1}{2\pi\nu}\left(\frac{cd'}{\tau}\right)^{1/2} = \frac{r_{\rm F}}{(2\pi\nu\tau)^{1/2}} \equiv \frac{r_{\rm F}}{u} \tag{F.3}$$

$$l_{\rm r} = d_{\rm lo}\sigma = d'\sigma_{\rm d} = \frac{{r_{\rm F}}^2}{l_{\rm d}} \equiv u r_{\rm F}, \tag{F.4}$$

where another quantity u is also used to relate the Fresnel scale to the diffraction and refraction scales. For a Gaussian image, the scattering time and scintillation bandwidth $\Delta\nu_{\rm d}$ are related as

$$2\pi\tau\Delta\nu_{\rm d} = 1, \tag{F.5}$$

implying that

$$u = \sqrt{2\pi\tau} = \left(\frac{\nu}{\Delta\nu_{\rm d}}\right)^{1/2}. \tag{F.6}$$

By definition, $D_\phi(l_\mathrm{d}) = 1\,\mathrm{rad}^2$ and we use a scaling of the phase structure function with baseline $\boldsymbol{b}$ for a medium with an isotropic power-law wavenumber spectrum with index β and assume that b is intermediate between the inner and outer scales (the intertial subrange),

$$D_\phi(\boldsymbol{b}) = (b/l_\mathrm{d})^{\beta-2} \equiv \phi_\mathrm{F}^2 (b/r_\mathrm{F})^{\beta-2}, \quad l_i \ll b \ll l_o, \tag{F.7}$$

where the second equality defines the RMS phase between a pair of points in the screen separated by one Fresnel scale,

$$\phi_\mathrm{F} = (r_\mathrm{F}/l_\mathrm{d})^{(\beta-2)/2} = u^{(\beta-2)/2}. \tag{F.8}$$

Since we specify the unrefracted scattered image using the parameters given above, we do not need to simulate the fine spatial scales in the screen that would cause scattering. Instead, we simulate only those scales $l \gtrsim l_\mathrm{r}$ that cause refraction by drawing realizations that conform to the wavenumber spectrum with wavenumbers $q \lesssim 2\pi/l_\mathrm{r}$.

A refraction screen is generated by shaping complex Gaussian noise in the frequency domain with a shape function related to the target wavenumber spectrum as $[P_{\delta n_e}(q)]^{1/2}$ with the required wavenumber cutoffs (c.f. Eq. (9.1)). To exclude any scales that would diffract rather then refract, the upper wavenumber cutoff is set to $q_\mathrm{max} = 2\pi/l_\mathrm{r}$. The largest scale corresponds to half the screen size. The shaped complex noise is inverse Fourier transformed to give $\phi_\mathrm{r}(\mathbf{x})$ which is then normalized to give a phase structure function equal to ϕ_F^2 across a length of one Fresnel scale. Enhanced refraction can be implemented by increasing ϕ_F from the value needed to account for the diffraction. This approach can be generalized to anisotropic scattering by using a different wavenumber spectrum.

Appendix G. Inventory of timing effects from dispersion, scattering, and refraction

This section itemizes and aggregates contributions to arrival time estimates when a model template is applied to a measured profile. The error from additive noise is excluded here except in our final expressions. We assume that the profile and template both include an intrinsic pulse shape convolved with a pulse broadening function. The time argument t extends across one pulse period (one cycle of phase), $\overline{\nu}$ is the center frequency of a channelized signal with narrow bandwidth $\Delta\nu_{\rm ch}$, and $\bar{t}$ is the epoch of observation. The epoch corresponds to the mean time of an observation block of duration T used to construct an average profile and estimate a ToA. Multiple profiles obtained in the same observing session (e.g. subaverages obtained over $\sim 1\,$hr) have different epochs in this framework. However, profiles from different frequency channels spanning a total bandwidth B obtained during the same time block are considered to have identical epochs[66]. In the following, it is assumed that sufficient averaging has been done over time and frequency (i.e. time-frequency product $\gg 1$) that we can ignore self-noise (as defined in §§5.4, 7.1) and ignore cross terms between radiometer noise and the pulsar signal.

The intrinsic (emitted) pulse $U_{\rm i}$, pulse broadening function p, and scattered pulse $U_{\rm s}$ are defined according to:

Actual pulse:

Quantity		Terms	Arguments	Description
$U_{\rm i}$	=	$\langle U_{\rm i}\rangle + \delta U_{\rm i}$	$(t,\overline{\nu},\bar{t})$	Intrinsic pulse
p	=	$\langle {\rm p}\rangle + \delta p$	$(t,\overline{\nu},\bar{t})$	Pulse broadening function
$U_{\rm s}:$	=	$U_{\rm i} * p = \langle U_{\rm s}\rangle + \delta U_{\rm s}$	$(t,\overline{\nu},\bar{t})$	Scattered pulse
$\langle U_{\rm s}\rangle$	=	$\langle U_{\rm i}\rangle * \langle {\rm p}\rangle$	$(t,\overline{\nu},\bar{t})$	Ensemble average scattered pulse
$\delta U_{\rm s}$	=	$\delta U_{\rm i} * \langle {\rm p}\rangle + \langle U_{\rm i}\rangle * \delta p + \delta U_{\rm i} * \delta p$	$(t,\overline{\nu},\bar{t})$	Deviation from ensemble average scattered pulse
$\langle U_{\rm s}\rangle_{\bar{t}}$	=	$\langle U_{\rm s}\rangle + \langle \delta U_{\rm s}\rangle_{\bar{t}}$	$(t,\overline{\nu})$	Scattered pulse averaged over epochs,

where we use the notation here, as elsewhere, $\langle\cdots\rangle_x$ to denote an average of a quantity over x.

The model pulse includes analogous elements,

Model pulse:

Quantity		Terms	Arguments	Description
$U_{\rm m}:$	=	$\langle U_{\rm i}\rangle + \delta U_{\rm m},$	$(t,\overline{\nu})$	Model intrinsic pulse
$\delta U_{\rm m}$	=	$U_{\rm m} - \langle U_{\rm i}\rangle$		Model - actual
$p_{\rm m}:$	=	$\langle {\rm p}\rangle + \delta p_{\rm m}$	$(t,\overline{\nu})$	model Pulse broadening function
$\delta p_{\rm m}$	=	$p_{\rm m} - \langle {\rm p}\rangle$		Model - actual
$U_{\rm ms}:$	=	$U_{\rm m} * p_{\rm m} = \langle U_{\rm s}\rangle + \delta U_{\rm ms}$	$(t,\overline{\nu})$	Model scattered pulse
$\delta U_{\rm ms}$	=	$U_{\rm ms} - \langle U_{\rm s}\rangle$	$(t,\overline{\nu})$	Model - actual average scattered pulse
	=	$\delta U_{\rm m} * \langle {\rm p}\rangle + \langle U_{\rm i}\rangle * \delta p_{\rm m} + \delta U_{\rm m} * \delta p_{\rm m}$		Deviation of model scattered pulse from ensemble average scattered pulse

The scattered pulse $U_{\rm s}$ is fitted with the model by cross correlating it with the model scattered pulse, $U_{\rm ms}$, and finding the time lag of maximum correlation. This is equivalent to least-squares fitting in the Fourier domain, as described in the main text. The cross correlation function (CCF) includes four terms (where we use the same asterisk notation for both cross-correlation and convolution; context should help avoid any confusion between the two operations),

Template fit: $U_{\rm ms} = {\rm template}\quad U_{\rm s} = {\rm profile}\quad {\rm CCF} = \langle U_{\rm ms}(t+\tau)U_{\rm s}(t-t_0)\rangle_t \rightarrow U_{\rm ms} * U_{\rm s}$

$$U_{\rm ms} * U_{\rm s} = \langle U_{\rm s}\rangle * \langle U_{\rm s}\rangle + \langle U_{\rm s}\rangle * \delta U_{\rm s} + \delta U_{\rm ms} * \langle U_{\rm s}\rangle + \delta U_{\rm ms} * \delta U_{\rm s}$$

The scattered profile includes terms that are stochastic due to pulse jitter and from PBF variations (rapid variations from the finite scintle effect and slow variations due to refraction). The template includes a term from mismatch between its shape and that of the measured profile, which leads to a systematic ToA error.

[66] Typically the difference in arrival times due to dispersion delays across a wide band B are much smaller than the integration time T. The main utility of the epoch variable here is to provide a time argument for slowly changing processes from the ISM and, less prevalent, intrinsic changes in profile shape.

The properties of fluctuating terms are:

Quantity	**Cause**	**Change rate**	**Correlation scales**
$\delta U_{\rm i}$	Jitter	F = Fast	High correlation across $\overline{\nu}$
δp :	Finite scintle number	F	DISS
	Refraction	S = Slow	RISS
$\delta U_{\rm s}$	Jitter + finite scintles + refraction	F + S	Jitter + DISS + RISS
$\delta U_{\rm m}$	$U_{\rm m} - \langle U_{\rm i}\rangle$: shape mismatch	None (S)	Systematic error
$\delta p_{\rm m}$	$p_{\rm m} - \langle {\rm p}\rangle$: shape mismatch	None (S)	Systematic error
$\delta U_{\rm ms}$	Combined $\delta U_{\rm m}, \delta p_{\rm m}$: shape mismatches	None (S)	Systematic error

Terms in the CCF, fluctuation properties, ToA contribution

The CCF of template and profile is an average over time t,

$$\widehat{C}(\tau) = \langle U_{\rm ms}(t+\tau) * U_{\rm s}(t-t_0)\rangle_t = (\langle U_{\rm s}\rangle + \delta U_{\rm ms})) * (\langle U_{\rm s}\rangle + \delta U_{\rm s})\,, \tag{G.1}$$

where we drop the arguments in the rightmost equality. Note that $\delta U_{\rm ms}$ and $\delta U_{\rm s}$ each comprise three terms. The CCF expands into 16 terms that yield a total of 21 terms in the ToA, one equal to the true ToA (in the absence of additive noise) from the cross correlation of $\langle U_{\rm s}\rangle$ in the template model with $\langle U_{\rm s}\rangle$ in the profile, and the remaining 20 from pulse stochasticity (jitter and scattering) and shape mismatches between the template and profile. These 21 terms are itemized as,

Term	**Cause**	**Term in ToA**	**Comment**
$\langle U_{\rm s}\rangle * \langle U_{\rm s}\rangle$	ACF of $\langle U_{\rm s}\rangle$ with argument $\tau - t_0$	$t_0(\overline{\nu}, \bar{t})$	True ToA
$\delta U_{\rm ms} * \langle U_{\rm s}\rangle$	Mismatch of intrinsic profile ($\delta U_{\rm m}$)	$t_{\delta U_{\rm m}}$	Systematic error
	Mismatch of PBFs ($\delta p_{\rm m}$)	$t_{\delta p_{\rm m}}$	Systematic error
	Combined mismatches ($\delta U_{\rm m}, \delta p_{\rm m}$)	$t_{\delta U_{\rm m}\delta p_{\rm m}}$	Systematic error
$\langle U_{\rm s}\rangle * \delta U_{\rm s}$	Jitter	$\Delta t_{\rm J}$	F
	DISS finite scintles	$\Delta t_{\delta p} \equiv \Delta t_{\delta p,{\rm FSE}}$	F
	Refraction	$\Delta t_{\delta\overline{p}} \equiv \Delta t_{\delta p,{\rm Refraction}}$	S
$\delta U_{\rm ms} * \delta U_{\rm s} =$	Combined model and actual terms		
$(\delta U_{\rm m} * \langle {\rm p}\rangle) * (\delta U_{\rm i} * \langle {\rm p}\rangle)$	U mismatch + jitter	$\Delta t_{\delta U_{\rm m}\delta U_{\rm i}}$	F
$(\delta U_{\rm m} * \langle {\rm p}\rangle) * (\langle U_{\rm i}\rangle * \delta p)$	U mismatch, δp, $\delta\overline{p}$	$\Delta t_{\delta U_{\rm m}\delta p}$	F
		$\Delta t_{\delta U_{\rm m}\delta\overline{p}}$	S
$(\delta U_{\rm m} * \langle {\rm p}\rangle) * (\delta U_{\rm i} * \delta p)$	U mismatch, jitter, δp, $\delta\overline{p}$	$\Delta t_{\delta U_{\rm m}\delta U_{\rm i}\delta p}$,	F
		$\Delta t_{\delta U_{\rm m}\delta U_{\rm i}\delta\overline{p}}$	F
$(\langle U_{\rm i}\rangle * \delta p_{\rm m}) * (\delta U_{\rm i} * \langle {\rm p}\rangle)$	p mismatch, jitter	$\Delta t_{\delta p_{\rm m}\delta U_{\rm i}}$	F
$(\langle U_{\rm i}\rangle * \delta p_{\rm m}) * (\langle U_{\rm i}\rangle * \delta p)$	p mismatch, δp, $\delta\overline{p}$	$\Delta t_{\delta p_{\rm m}\delta p}$	F
		$\Delta t_{\delta p_{\rm m}\delta\overline{p}}$	S
$(\langle U_{\rm i}\rangle * \delta p_{\rm m}) * (\delta U_{\rm i} * \delta p)$	p mismatch + jitter, δp, $\delta\overline{p}$	$\Delta t_{\delta p_{\rm m}\delta U_{\rm i}\delta p}$	F
$(\delta U_{\rm m} * \delta p_{\rm m} * (\delta U_{\rm i} * \langle {\rm p}\rangle)$	U, p mismatches, jitter	$\Delta t_{\delta U_{\rm m}\delta U_{\rm i}}$	F
$(\delta U_{\rm m} * \delta p_{\rm m} * (\langle U_{\rm i}\rangle * \delta p)$	U, p mismatches, δp, $\delta\overline{p}$	$\Delta t_{\delta U_{\rm m}\delta p_{\rm m}\delta p}$	F
		$\Delta t_{\delta U_{\rm m}\delta p_{\rm m}\delta\overline{p}}$	S
$(\delta U_{\rm m} * \delta p_{\rm m} * (\delta U_{\rm i} * \delta p)$	U, p mismatches, jitter, δp, $\delta\overline{p}$	$\Delta t_{\delta U_{\rm m}\delta p_{\rm m}\delta U_{\rm i}\delta p}$	F
		$\Delta t_{\delta U_{\rm m}\delta p_{\rm m}\delta U_{\rm i}\delta\overline{p}}$	F

Comments:

We have separated those effects that simply delay the emitted pulse from those that introduce ToA variations by distortion of the pulse. Dispersion delays are included in the former along with several achromatic contributions while scattering and multiple imaging from lensing are included in the latter.

In the first column δp refers to all temporal changes in the PBF (fast and slow) while in the middle two columns δp refers to rapid changes from the finite scintle effect and $\delta\overline{p}$ corresponds to slow changes in the envelope shape caused by refraction.

Systematic ToA terms are denoted as t_X while random errors are denoted as Δt_X.

Comments in the last column include designation of a term as varying with epoch fast (F) or slow (S).

The 21 terms in the third column are described as follows:

I. The true ToA $t_0(\overline{\nu},\overline{t})$ comprises:
   (a) t_∞, which includes all achromatic contributions (spin, orbit, astrometric, gravitational)
   (b) $t_{\rm DM}(\overline{\nu},\overline{t})$ = dispersion delays, including frequency dependent DMs
   (c) $\Delta t_{\rm AOA,SSBC}$, the observatory to solar system barycentric time offset due to refraction (Sect. 12.3).

II. The next three terms are time offsets, $t_{\delta U_{\rm m}}, t_{\delta p_{\rm m}}$, and $t_{\delta U_{\rm m}\delta p_{\rm m}}$, caused by differences between model shapes $U_{\rm m}$ and $p_{\rm m}$ and the true ensemble average shapes, $\langle U_{\rm i}\rangle$ and $\langle {\rm p}\rangle$.

III. Terms 5 through 7 are random errors from jitter and the finite scintle effect, which vary rapidly, and a slowly varying term resulting from changes in the PBF vs. epoch. We denote rapid PBF changes as δp and slow changes as $\delta\overline{p}$, where the overline connotes the envelope of the PBF discussed earlier.

IV. The remaining 14 ToA contributions result from the nine terms in the cross correlation contribution $\delta U_{\rm ms} * \delta U_{\rm s}$; we group into fast (F) or slow(S) terms as labeled in the last column. We obtain a consolidated fast term $\Delta t^{\rm (F)}_{\delta U_{\rm ms}\delta U_{\rm s}}$ that varies rapidly due to jitter and the finite scintle effect (DISS time scales $\sim$ minutes),

$$\begin{aligned}\Delta t^{\rm (F)}_{\delta U_{\rm ms}\delta U_{\rm s}} = {}& \Delta t_{\delta U_{\rm m}\delta U_{\rm i}} + \Delta t_{\delta U_{\rm m}\delta p} + \Delta t_{\delta U_{\rm m}\delta U_{\rm i}\delta p} + \Delta t_{\delta p_{\rm m}\delta U_{\rm i}} + \Delta t_{\delta p_{\rm m}\delta p} \\ & + \Delta t_{\delta p_{\rm m}\delta U_{\rm i}\delta p} + \Delta t_{\delta U_{\rm m}\delta U_{\rm i}} + \Delta t_{\delta U_{\rm m}\delta p_{\rm m}\delta p} + \Delta t_{\delta U_{\rm m}\delta p_{\rm m}\delta U_{\rm i}\delta p},\end{aligned} \tag{G.2}$$

   and $\Delta t^{\rm (S)}_{\delta U_{\rm ms}\delta U_{\rm s}}$ varies slowly due to refraction (RISS time scales) and rarely from secular or episodic changes in intrinsic pulse shape (c.f. J1713+0747),

$$\Delta t^{\rm (S)}_{\delta U_{\rm ms}\delta U_{\rm s}} = \Delta t_{\delta U_{\rm m}\delta\overline{p}} + \Delta t_{\delta p_{\rm m}\delta\overline{p}} + \Delta t_{\delta U_{\rm m}\delta p_{\rm m}\delta\overline{p}}. \tag{G.3}$$

Fortunately many of these terms are similar in statistical character and can be merged for modeling and statistical inference. We write the net ToA from model fitting now also including the matched filtering error from additive noise $\Delta t_{\rm S/N}$ (recall up to now in this appendix we have assumed noiseless signals),

$$\begin{aligned}\widehat{t}_\nu = {}& t_0 + t_{\delta U_{\rm m}} + t_{\delta p_{\rm m}} + t_{\delta U_{\rm m}\delta p_{\rm m}} \\ & + \left[\Delta t_{\rm S/N} + \Delta t_{\rm J} + \Delta t_{\delta p} + \Delta t_{\delta U_{\rm ms}\delta p}\right]_F \\ & + \left[\Delta t_{\delta\overline{p}} + \Delta t_{\delta U_{\rm ms}\delta\overline{p}}\right]_S .\end{aligned} \tag{G.4}$$

This can be consolidated further by combining the two terms involving δp and the two terms involving $\delta\overline{p}$:

$$\widehat{t}_\nu = t_0 + t_{\rm mismatch} + \left[\Delta t_{\rm S/N} + \Delta t_{\rm J} + \Delta t^{\rm (all)}_{\delta p}\right]_F + \left[\Delta t^{\rm (all)}_{\delta\overline{p}}\right]_S . \tag{G.5}$$

The systematic offsets from template-profile mismatch are combined into the term $t_{\rm mismatch} = t_{\delta U_{\rm m}} + t_{\delta p_{\rm m}} + t_{\delta U_{\rm m}\delta p_{\rm m}}$. If a single template at a reference frequency $\nu_{\rm ref}$ is used, the 'FD' correction used by NANOGrav is associated with this term. Since 'FD' (meaning frequency dependent) applies to all terms, we refer to this particular term as the 'chromatic mismatch' term for this choice of template.

The rapidly varying random errors are the usual S/N, jitter, and FSE errors with the latter affected by template mismatch.

The slowly varying error is from changes in the PBF with epoch, manifested as a change in apparent scattering time τ, which is most likely caused by refraction that alters the PBF shape. Note again that refraction also alters the centroid of the scattered image and thus also the width and shape of the PBF (Sect. 11.3). The centroid shift yields a purely refractive time delay $\Delta t_{\rm AOA}$ given by Eq. (12.30) that could be itemized separately in Eq. (G.5), but we subsume it here into the $\Delta t^{\rm (all)}_{\delta\overline{p}}$ term. This term is not equal to τ for the case where a PBF is excluded from the template and it is not equal to $\delta\tau = \tau - \tau_{\rm template}$ when a fixed value $\tau_{\rm template}$ for the scattering time is included in the template but the τ for the profile differs.

Mismatch is from the quantities $\delta U_{\rm m} = U_{\rm m} - \langle U_{\rm i}\rangle$ and $\delta p_{\rm m} = p_{\rm m} - \langle {\rm p}\rangle$ that appear in

$$\delta U_{\rm ms} * \langle U_{\rm s}\rangle = \delta U_{\rm m} * \langle {\rm p}\rangle + \langle U_{\rm i}\rangle * \delta p_{\rm m} + \delta U_{\rm m} * p_{\rm m}.$$

The PBFs are normalized to unit area so the area of the difference $\delta p_{\rm m}$ is zero, Suppose the actual, mean PBF is a heavy-tailed PL form while the model PBF is an exponential. Their difference is positive at small lags $t \lesssim \tau$, negative for $t \gtrsim \tau$, and asymptotes to zero at $t \gg \tau$.

G.1. *With epoch-dependent dispersion and multipath propagation*

Motion of the pulsar and observer introduce epoch dependence in all propagation effects, including refraction and multipath propagation from scattering that also require complex chromatic terms in the timing equation. Pulse distortion from the convolution with the PBF induces short term and long term timing offsets. Refraction, which varies on day to several month time scales, causes image wander and distortion of the PBF. Overall we obtain the full expression in Eq. (G.5) with $t_0(\nu)$ expanded,

$$\widehat{t}_\nu = t_\infty + \frac{K_{\rm DM}\overline{\rm DM}(\nu,\bar{t})}{\nu^2} + \left[\Delta t_{\rm S/N} + \Delta t_{\rm J} + \Delta t^{\rm (all)}_{\delta p}\right]_F + t_{\rm mismatch}(\overline{\nu},\nu_{\rm ref},\bar{t}) + \left[\Delta t^{\rm (all)}_{\delta\overline{p}}\right]_S . \tag{G.6}$$

where $\overline{\rm DM}(\nu,\bar{t})$ is the DM applicable to frequency ν at epoch $\bar{t}$. Expanding $\overline{\rm DM}(\nu,\bar{t}) = \langle\overline{\rm DM}(\nu,\bar{t})\rangle_\nu + \delta\overline{\rm DM}(\nu,\bar{t})$ as an average over the receiver's frequency range with a fluctuating part, the ToA equation becomes

$$\begin{aligned}\widehat{t}_\nu = t_\infty &+ \frac{K_{\rm DM}\langle\overline{\rm DM}(\nu,\bar{t})\rangle_\nu}{\nu^2} + \left[\Delta t_{\rm S/N} + \Delta t_{\rm J} + \Delta t^{\rm (all)}_{\delta p}\right]_F \\ &+ t_{\rm mismatch}(\overline{\nu},\nu_{\rm ref},\bar{t}) + \left[\Delta t^{\rm (all)}_{\delta\overline{p}}\right]_S + \frac{K_{\rm DM}\delta\overline{\rm DM}(\nu,\bar{t})}{\nu^2}.\end{aligned} \tag{G.7}$$

In this last equation, the first line includes the targeted t_∞ term along with the simplest DM term that scales strictly as ν^{-2} accompanied by the rapid white noise terms. The second line includes the $t_{\rm mismatch}$ term conventionally handled through the 'FD' formulation for chromatic mismatch along with the slow term from PBF envelope variations and the frequency-dependent DM terms. These terms vary with frequency differently from each other and from the ν^{-2} scaling of the simplest DM term.

Appendix H. Temporal spectra for screen phase and refraction angle

Here we calculate temporal spectra in terms of the electron-density wavenumber spectrum $P_{\delta n_e}(\mathbf{q}, q_z)$, where the arguments are the two-dimensional wavenumber $\mathbf{q}$ in the screen plane and an orthogonal wavenumber q_z in the mean direction of propagation. We use $S_a(f)$ to denote a temporal spectrum for a quantity a and $P_a(\mathbf{q})$ for its spatial spectrum, Our analysis applies to a screen with time-frozen fluctuations (the Taylor hypothesis) as it is swept across the line of sight in the x direction with velocity v_x.

A general relation between temporal and wavenumber spectra is then

$$S_a(f) = \frac{2\pi}{v_x} \int dq_y \, P_a(2\pi f/v_x, q_y), \tag{H.1}$$

with spectra related to the temporal and spatial Fourier transforms (FTs) $\widetilde{a}(f)$ and $\widetilde{a}(\mathbf{q})$ as

$$S_a(f) = \frac{\langle |\widetilde{a}(f)|^2 \rangle}{\int dt} \quad \text{and} \quad P_a(\mathbf{q}) = \frac{(2\pi)^2 \langle |\widetilde{a}(\mathbf{q})|^2 \rangle}{\int d\mathbf{x}}, \tag{H.2}$$

where integrals in the denominators are over the same domains used to calculate the FTs. Strictly speaking, the expressions are in the limit where these domains become infinite.

The phase is the integral $\phi(\mathbf{x}) = -\lambda r_\mathrm{e} \int ds \, n_\mathrm{e}(\mathbf{x}, s)$ through a screen with thickness much smaller than the source's distance but much larger than the outer scale of density fluctuations. The phase spectra are

$$\Phi(\mathbf{q}) = 2\pi(\lambda r_\mathrm{e})^2 \int ds \, P_{\delta n_e}(\mathbf{q}, 0) \tag{H.3}$$

$$S_\phi(f) = \frac{(2\pi\lambda r_\mathrm{e})^2}{v_x} \int ds \int dq_y \, P_{\delta n_e}(2\pi f/v_x, q_y, 0). \tag{H.4}$$

The spectrum of the refraction angle $\boldsymbol{\theta}_\mathbf{r}(\mathbf{x}) = k^{-1} \boldsymbol{\nabla}_\mathbf{x} \phi(\mathbf{x})$ (with $k = 2\pi/\lambda$) is related to the phase spectrum using the Fourier derivative theorem, giving

$$P_{\boldsymbol{\theta}_\mathbf{r}}(\mathbf{q}_\perp) = k^{-2} |\mathbf{q}|^2 P_\phi(\mathbf{q}) = \frac{(\lambda^2 r_\mathrm{e})^2}{2\pi} q^2 \int ds \, P_{\delta n_e}(\mathbf{q}, 0) \tag{H.5}$$

and a temporal spectrum

$$S_{\theta_\mathrm{r}}(f) = \frac{(\lambda^2 r_\mathrm{e})^2}{v_x} \int ds \int dq_y \, \left[(2\pi f/v_x)^2 + q_y^2 \right] P_{\delta n_e}(2\pi f/v_x, q_y). \tag{H.6}$$

The fluctuation spectrum of ${\theta_\mathrm{r}}^2$ results from the self convolution of S_{θ_r} under the assumption that $\theta_\mathrm{r}(t)$ is a Gaussian process,

$$S_{\theta_r^2}(f) = 2 S_{\theta_\mathrm{r}}(f) * S_{\theta_\mathrm{r}}(f). \tag{H.7}$$

A useful expression follows by relating the fourth and second moments of θ_r, again for a Gaussian process, $\mathrm{Var}({\theta_\mathrm{r}}^2) = 2\mathrm{Var}(\theta_\mathrm{r})^2$. Letting $S_{\theta_r^2}(f) \equiv A_2 g(f)$ where $g(f)$ is the spectral shape, this implies

$$S_{\theta_r^2}(f) = \frac{2[\int df \, S_{\theta_\mathrm{r}}(f)]^2}{\int df \, g(f)} g(f). \tag{H.8}$$

Evaluation for electron densities having a power-law spectrum that is isotropic in wavenumber, $P_{\delta n_e}(\mathbf{q}) = \mathrm{C}_\mathrm{n}^2 q^{-\beta} \exp\left(-(q/q_i)^2\right)$ for $q \geq q_o$ and $3 < \beta < 4$, yields temporal spectra in terms of the scattering measure $\mathrm{SM} = \int ds \, \mathrm{C}_\mathrm{n}^2(s)$,

$$S_\phi(f) = \frac{\sqrt{\pi}}{(2\pi)^{\beta-3}} \frac{\Gamma(\frac{\beta-1}{2})}{\Gamma(\frac{\beta}{2})} \frac{(\lambda r_\mathrm{e})^2}{v_x} \mathrm{SM} \left(\frac{f}{v_x} \right)^{-(\beta-1)}. \tag{H.9}$$

and

$$S_{\theta_{\rm r}}(f) = \frac{\sqrt{\pi}}{(2\pi)^{\beta-3}} \frac{\Gamma(\frac{\beta-3}{2})}{\Gamma(\frac{\beta-2}{2})} \frac{(\lambda^2 r_{\rm e})^2}{v_x} {\rm SM} \left(\frac{f}{v_x}\right)^{-(\beta-3)}. \tag{H.10}$$

These forms assume that the exponential factor $\exp\bigl(-(q/q_i)^2\bigr) \simeq 1$ for wavenumbers that dominate the integral in Eq. (H.6) at relevant frequencies f. The spectrum for ${\theta_{\rm r}}^2$ follows from Eq. (H.8) and (H.6),

$$S_{\theta_r^2}(f) \simeq \frac{2}{(4-\beta)(2\pi)^{2\beta-7}} \left[\frac{\Gamma(\frac{\beta-3}{2})}{\Gamma(\frac{\beta-2}{2})} \frac{(\lambda^2 r_{\rm e})^2}{v_x^{4-\beta}} {\rm SM}\right]^2 f^{-(2\beta-7)}. \tag{H.11}$$

This expression holds for $7/2 < \beta < 4$, including the Kolmogorov spectrum.

For a Kolmogorov spectrum ($\beta = 11/3$), these become

$$S_\phi(f) = \frac{1}{\sqrt{2}(2\pi)^{1/6}} \frac{\Gamma(4/3)}{\Gamma(11/6)} \frac{(\lambda r_{\rm e})^2}{v_x} {\rm SM} \left(\frac{f}{v_x}\right)^{-8/3} \simeq (4.65\times 10^3\,{\rm rad})^2\,{\rm yr} \times \nu^{-2} v_{100}^{5/3}\,{\rm SM}_{-3.5} f^{-8/3}, \tag{H.12}$$

$$S_{\theta_{\rm r}}(f) = \frac{1}{\sqrt{2}(2\pi)^{1/6}} \frac{\Gamma(1/3)}{\Gamma(5/6)} \frac{(\lambda^2 r_{\rm e})^2}{v_x} {\rm SM} \left(\frac{f}{v_x}\right)^{-2/3} \simeq (0.0423\,{\rm mas})^2 {\rm yr} \times \nu^{-4} v_{100}^{-1/3}\,{\rm SM}_{-3.5} f^{-2/3}, \tag{H.13}$$

and

$$S_{\theta_r^2}(f) = \frac{6}{(2\pi)^{1/3}} \left[\frac{\Gamma(1/3)}{\Gamma(5/6)} \frac{(\lambda^2 r_{\rm e})^2}{v_x^{1/2}} {\rm SM}\right]^2 \left(\frac{f}{v_x}\right)^{-1/3} \simeq (0.0787\,{\rm mas})^4\,{\rm yr} \times \nu^{-8} v_{100}^{-2/3}\,{\rm SM}_{-3.5}^2 f^{-1/3}, \tag{H.14}$$

where the approximate equalities are for ν in GHz, v_x in units of $100\,{\rm km\,s^{-1}}$, a fiducial scattering measure ${\rm SM} = 10^{-3.5}\,{\rm kpc\ m^{-20/3}}$, and frequencies in ${\rm cycles\,yr^{-1}}$. For a source at finite distance the AOA is $\theta_{\rm AOA} = (d_{\rm sl}/d_{\rm so})\theta_{\rm r}$ and the spectra for $\theta_{\rm r}$ and θ_r^2 should be multiplied by $(d_{\rm sl}/d_{\rm so})^2$ and $(d_{\rm sl}/d_{\rm so})^4$, respectively, where $d_{\rm sl}$ is the distance of the screen layer from the source and $d_{\rm so}$ is the source-observer distance.

The temporal spectrum for DM is related to the phase spectrum as $S_{\rm DM}(f) = (\lambda r_{\rm e})^{-2} S_\phi(f)$ or

$$S_{\rm DM}(f) \simeq (1.783\times 10^{-4}\,{\rm pc\ cm^{-3}})^2\,{\rm yr} \times v_{100}^{5/3}\,{\rm SM}_{-3.5} f^{-8/3}. \tag{H.15}$$

Appendix I. Derivation of TOA errors from rapid changes in pulse broadening functions

We analyze measured signals for a heterodyned system with a bandpass of bandwidth B centered on frequency ν_0 and shifted to baseband (zero frequency). After propagation through the ISM, the signal is

$$\varepsilon_{\rm h}(t) = h(t) * \varepsilon_{\rm i}(t), \tag{I.1}$$

where the asterisk denotes convolution and $h(t)$ is the impulse response of the ISM over the band sampled by the receiver system. Generally h would include dispersion delays, refraction, and multipath effects but here we restrict it to include only the delays associated with diffraction.

A receiver system with a bandpass function $\tilde{b}(\nu)$ yields

$$\varepsilon(t) = b(t) * \varepsilon_{\rm h}(t) = b(t) * h(t) * \varepsilon_{\rm i}(t), \tag{I.2}$$

where $b(t)$ is the temporal response equal to the inverse Fourier transform of $\tilde{b}$. In the following let $\varepsilon_{\rm i}(t) = \delta(t)$ to get $\varepsilon(t) = b(t) * h(t)$ as the impulse response from scattering combined with the receiver response. The bandpass function $\tilde{b}$ is a 'low pass' function centered on zero frequency with total bandwidth B (across both negative and positive frequencies). For convenience, we define $|\tilde{b}|^2$ to have unit area. Its autocorrelation function (ACF) is then

$$r_{\tilde{b}}(\delta\nu) = \int d\nu\, \tilde{b}(\nu)\tilde{b}^*(\nu + \delta\nu). \tag{I.3}$$

with normalization $r_{\tilde{b}}(0) = 1$ and where the superscript asterisk denotes a complex conjugate. The area of $|\tilde{b}(\nu)|^4$ is the reciprocal of the effective bandwidth, $B_{\rm eff}$. A rectangular bandpass function with bandwidth B has $B_{\rm eff} = B$ and $r_{\tilde{b}}(\delta\nu) = 1 - |\delta\nu|/B$.

We call h the 'field' pulse broadening function (PBF) to distinguish it from the squared magnitude $p(t) = |h|^2$, which is the standard intensity PBF in the limit where the receiver response is much narrower than $h(t)$.

I.1. *Pulse Broadening Function*

Define $\Gamma_{\tilde{\varepsilon}}(\delta\nu)$ as the spectral correlation function of scintillation variations. When averaged over an ensemble, its half-width at half maximum is the scintillation bandwidth, $\Delta\nu_{\rm d}$.

The field PDF $h(t)$ has the form of an envelope function that multiplies a noise-like process. The envelope has duration $\sim \tau_d$, the pulse broadening time, while the noise process varies on inverse-bandwidth time scales. The noise process is a consequence of the particular paths taken by the radiation due to diffraction, which persist over time scales up to about the scintillation time scale, $\Delta t_{\rm ISS}$. It is therefore useful to define two time scales: one for variations on time scales of order the inverse bandwidth (ns) and the other 'epochal' time over an observation of order minutes to hours. The time "t" in $h(t)$ refers to the fast time scale and the epochal time dependence is implicit for now. Here we consider TOA variations due to the finite number of scintles within the receiver bandpass at a fixed epochal time. Later we consider how integrations over epochal time reduce TOA variations.

The total impulse response, including the finite receiver bandwidth, $\epsilon(t) = h(t) * b(t)$, has a frequency-domain ACF

$$\Gamma_{\tilde{\varepsilon}}(\delta\nu) = \int d\nu\, \tilde{b}(\nu)\, \tilde{b}^*(\nu + \delta\nu)\, \tilde{h}(\nu)\tilde{h}^*(\nu + \delta\nu) = \int d\nu\, \tilde{b}(\nu)\, \tilde{b}^*(\nu + \delta\nu)\, \Gamma_{\tilde{h}}(\nu, \delta\nu). \tag{I.4}$$

The corresponding PBF is

$$p(t) = \int dx\, \Gamma_{\tilde{\varepsilon}}(x) e^{2\pi i x t} \tag{I.5}$$

The ensemble averages of these quantities are

$$\langle \Gamma_{\tilde{\varepsilon}}(\delta\nu)\rangle = r_{\tilde{b}}(\delta\nu)\left\langle \Gamma_{\tilde{h}}(\delta\nu)\right\rangle \tag{I.6}$$

$$\langle p(t)\rangle = \int dx\ \langle \Gamma_{\tilde{\varepsilon}}(x)\rangle\, e^{2\pi i x t}, \tag{I.7}$$

where we have dropped the ν-dependence of $\left\langle \Gamma_{\tilde{h}}(\delta\nu)\right\rangle$ by assuming that $\tilde{h}(\nu)$ has stationary statistics over the bandwidth (i.e. the frequency range is small enough that the scintillation bandwidth does not change significantly). Both $|h(t)|^2$ and $p(t)$ have unit area and $\Gamma_{\tilde{h}}(0) = r_{\tilde{b}}(0) = \Gamma_{\tilde{\varepsilon}}(0) = 1$. For wide bandwidths, similar quantities can be defined for subbands.

I.2. *Mean Delay*

The sum of a large number of pulses converges to the pulse shape intrinsic to the pulsar convolved with the ensemble average PBF. Because the PBF is causal, the measured pulsar signal is always delayed by scattering. The TOA shift (of an impulse) is the mean of the PBF,

$$t_p = \int dt\, t\, p(t), \tag{I.8}$$

which has an ensemble average

$$\langle t_p\rangle = \int dt\, t\, \langle p(t)\rangle\,. \tag{I.9}$$

Substituting for $p(t)$ using Eq. (I.5) and using the derivative theorem for Fourier transforms yields

$$\langle t_p\rangle = \int dt\, t \int dx\ \langle \Gamma_{\tilde{\varepsilon}}(x)\rangle\, e^{2\pi x t} = \frac{1}{2\pi i}\int dx\ \langle \Gamma_{\tilde{\varepsilon}}(x)\rangle\, \delta'(x) = -\frac{1}{2\pi i}\left\langle \Gamma'_{\tilde{\varepsilon}}(0)\right\rangle, \tag{I.10}$$

where $\Gamma'_{\tilde{\varepsilon}}(x) \equiv d\Gamma_{\tilde{\varepsilon}}(x)/dx$ and we used the derivative property of the delta function.

The time delay comprises two terms,

$$\langle t_p\rangle = \langle t_b\rangle + \langle t_h\rangle = -\frac{1}{2\pi i}\left[r'_{\tilde{b}}(0) + \Gamma'_{\tilde{h}}(0)\right], \tag{I.11}$$

where the delay due to the causal bandpass filter is $\langle t_b\rangle$ while $\langle t_h\rangle$ is from scattering in the ISM; both are calculated analogously to Eq. (I.8) using $|b(t)|^2$ and $|h(t)|^2$ in place of $p(t)$, respectively. The range of cases encountered includes $\langle t_h\rangle \ll \langle t_b\rangle$ for low-DM pulsars observed at high frequencies while $\langle t_h\rangle \gg \langle t_b\rangle$ for high-DMs and low frequencies.

A commonly-assumed PBF is a one-sided exponential with time constant τ,

$$p(t) = \tau^{-1}\exp(-t/\tau)\Theta(t), \tag{I.12}$$

where $\Theta(t)$ is the Heaviside function. For this case, $\langle t_p\rangle = \tau$ is obtained from either Eq. (I.9) or (I.10). For more realistic PBFs, such as the heavy-tailed PBFs associated with a Kolmogorov or other power-law media, $\langle t_p\rangle$ is generally larger than τ.

I.3. *Delay Variance*

First we consider the case where the integration time is much less than the scintillation time, corresponding to the case of static geometry. Later we consider the opposite case where the scintillation time is much larger than the scintillation time.

The stochasticity of $p(t)$ causes mean square TOA fluctuations

$$\langle t_p^2 \rangle = \langle t_p \rangle^2 + \sigma_{t_p}^2 = \iint dt dt' \, tt' \, \langle p(t) p(t') \rangle = -\frac{1}{(2\pi)^2} \frac{d^2}{dx dx'} \left[\langle \Gamma_{\widetilde{\varepsilon}}(x) \Gamma_{\widetilde{\varepsilon}}(x') \rangle \right]_{x=x'=0}. \tag{I.13}$$

The expectation in Eq. (I.13) is

$$\begin{aligned} \langle \Gamma_{\widetilde{\varepsilon}}(x) \Gamma_{\widetilde{\varepsilon}}(x') \rangle = \iint & d\nu d\nu_+ \, \tilde{b}(\nu) \tilde{b}^*(\nu + x) \tilde{b}(\nu_+) \tilde{b}^*(\nu_+ + x') \\ & \times \left\langle \tilde{h}(\nu) \tilde{h}^*(\nu + x) \tilde{h}(\nu_+) \tilde{h}^*(\nu_+ + x') \right\rangle. \end{aligned} \tag{I.14}$$

To an excellent approximation, $\tilde{h}(\nu)$ is a complex Gaussian process when scintillations are strong, so the fourth moment can be expanded into products of second moments[67],

$$\left\langle \tilde{h}(\nu) \tilde{h}^*(\nu + x) \tilde{h}(\nu_+) \tilde{h}^*(\nu_+ + x') \right\rangle = \left\langle \Gamma_{\tilde{h}}(x) \right\rangle \left\langle \Gamma_{\tilde{h}}(x') \right\rangle + \left\langle \Gamma_{\tilde{h}}(\nu_+ - \nu + x') \right\rangle \left\langle \Gamma_{\tilde{h}}(\nu - \nu_+ + x) \right\rangle. \tag{I.15}$$

The first term in the expansion yields the square of the mean delay, $\langle t_p \rangle^2$, while the second term yields the variance of t_p,

$$\sigma_{t_p}^2 = -\frac{1}{(2\pi)^2} \iint d\nu d\nu_+ \, \frac{d^2}{dx dx'} \left[B_{\nu,x} B_{\nu_+,x'} \left\langle \Gamma_{\tilde{h}}(\nu_+ - \nu + x') \right\rangle \left\langle \Gamma_{\tilde{h}}(\nu - \nu_+ + x) \right\rangle \right]_{x=x'=0}. \tag{I.16}$$

where we have defined $B_{\nu,x} \equiv \tilde{b}(\nu) \tilde{b}^*(\nu + x)$.

The double derivative yields four combinations of individual derivatives of the $B_{\nu,x}$ and $\langle \Gamma_{\tilde{h}} \rangle$ factors evaluated at $x = x' = 0$,

$$\begin{aligned} &\text{(I)} \quad B'_{\nu,0} B'_{\nu_+,0} \left\langle \Gamma_{\tilde{h}}(\nu_+ - \nu) \right\rangle \left\langle \Gamma_{\tilde{h}}(\nu - \nu_+) \right\rangle \equiv B'_{\nu,0} B'_{\nu_+,0} \left| \left\langle \Gamma_{\tilde{h}}(\nu - \nu_+) \right\rangle \right|^2 \\ &\text{(II)} \quad B_{\nu,0} B'_{\nu_+,0} \left\langle \Gamma_{\tilde{h}}(\nu_+ - \nu) \right\rangle \left\langle \Gamma'_{\tilde{h}}(\nu - \nu_+) \right\rangle \\ &\text{(III)} \quad B'_{\nu,0} B_{\nu_+,0} \left\langle \Gamma'_{\tilde{h}}(\nu_+ - \nu) \right\rangle \left\langle \Gamma_{\tilde{h}}(\nu - \nu_+) \right\rangle \\ &\text{(IV)} \quad -B_{\nu,0} B_{\nu_+,0} \left\langle \Gamma'_{\tilde{h}}(\nu_+ - \nu) \right\rangle \left\langle \Gamma'_{\tilde{h}}(\nu - \nu_+) \right\rangle \equiv B_{\nu,0} B_{\nu_+,0} \left| \left\langle \Gamma'_{\tilde{h}}(\nu - \nu_+) \right\rangle \right|^2. \end{aligned}$$

Generally, all terms contribute to the delay variance. However terms I - III are important only for the case where the scintillation bandwidth is comparable to or larger than the measurement bandwidth $B_{\rm eff}$. In the regime where $\Delta\nu_{\rm d} \ll B_{\rm eff}$, the four terms contribute to the variance respectively as $B_{\rm eff}^{-2}(\Delta\nu_{\rm d}/B_{\rm eff})$, $B_{\rm eff}^{-2}$, $B_{\rm eff}^{-2}$, and $B_{\rm eff}^{-2}(B_{\rm eff}/\Delta\nu_{\rm d})$. In this regime, therefore, term IV will exceed the next largest terms by a factor proportional to the number of scintles across the band.

I.3.1. *Narrow-scintle Regime*

For $\Delta\nu_{\rm d} \ll B_{\rm eff}$, the delay variance becomes

$$\sigma_{t_p}^2 \approx \frac{1}{(2\pi)^2} \iint d\nu d\nu_+ \, B_{\nu,0} B_{\nu_+,0} \left| \left\langle \Gamma'_{\tilde{h}}(\nu - \nu_+) \right\rangle \right|^2. \tag{I.17}$$

We simplify Eq. (I.17) by changing variables from ν, ν_+ to $\overline{\nu} = (\nu + \overline{\nu})/2$ and $\delta\nu = \nu - \nu_+$ and by defining $B_\nu = |\tilde{b}(\nu)|^2$ (which equals $B_{\nu,0}$ used before but simplifies the notation) and its frequency-domain correlation function,

$$\widetilde{R}_B(\delta\nu) = \int d\nu \, B_\nu B_{\nu+\delta\nu}. \tag{I.18}$$

[67] Note that the fourth moment of a complex Gaussian process expands into two terms while a real process expands into three.

The inverse Fourier transform of $\widetilde{R}_B$ is $R_B(t)$, which has an area identically equal to $B_{\rm eff}$. This yields

$$\sigma_{t_p}^2 \approx -\frac{1}{(2\pi)^2}\int d\delta\nu\, \widetilde{R}_B(\delta\nu)\left|\left\langle\Gamma'_{\tilde{h}}(\delta\nu)\right\rangle\right|^2. \tag{I.19}$$

By using the relation between $p(t)$ and $\left\langle\Gamma_{\tilde{h}}(\delta\nu)\right\rangle$ we obtain

$$\sigma_{t_p}^2 = \iint dtdt'\, tt'\, \langle p(t)\rangle\, \langle p(t')\rangle\, R_B(t-t'). \tag{I.20}$$

In the limit of narrow scintles where $\Delta\nu_{\rm d} \ll B$, the bandpass correlation $R_B(t-t')$ tends to a delta function $\delta(t-t')$ with area $B_{\rm eff}^{-1}$ and the delay variance simplifies to

$$\sigma_{t_p}^2 \approx B_{\rm eff}^{-1}\int dt\, t^2\, \langle p(t)\rangle^2. \tag{I.21}$$

Exponential PBF: For $\langle p(t)\rangle = \tau^{-1}\exp(-t/\tau)\Theta(t)$, the time integral yields $\tau/4$ and $\sigma_{t_p} \approx \sqrt{\tau/B_{\rm eff}}/2$. Using the relation $2\pi\tau\Delta\nu_{\rm d} = 1$ for this PBF[68], we obtain

$$\sigma_{t_p} = \frac{\tau}{\sqrt{2B_{\rm eff}/\pi\Delta\nu_{\rm d}}} \tag{I.22}$$

which can be expressed in terms of the number of scintles within the band[69]

$$N_\nu = \frac{B_{\rm eff}}{\pi\Delta\nu_{\rm d}}, \tag{I.23}$$

to yield

$$\sigma_{t_p} = \frac{\tau}{\sqrt{2N_\nu}}. \tag{I.24}$$

I.3.2. *Integration Times Longer than the Scintillation Time*

For integration times T smaller than the diffractive scintillation time scale ($\Delta t_{\rm ISS}$) the PBF is static because multipath scattering has a steady (but frequency dependent) configuration of propagation paths. Observations of nearby pulsars at high frequencies often involve this situation for the entirety of a 1/2 to one hour observation. However for other cases T can be much longer than the scintillation time scale, causing the pattern of scintles within the receiver bandpass to change. To distinguish between short time scales as used above — which range from the inverse bandwidth to some multiple of the pulse broadening time — from longer times, we introduce the time $t_s \in [0, T]$ that can span many scintillation time scales. The correlation function of $\tilde{h}$ at time t_s becomes

$$\Gamma_{\tilde{h}}(\delta\nu, \delta t_s) = \tilde{h}(\nu, t_s)\tilde{h}^*(\nu, t_s + \delta t_s) \tag{I.25}$$

and the time-integrated PBF is

$$p(t) = T^{-1}\int_0^T dt_s\ \ \tilde{b}(\nu)\,\tilde{b}^*(\nu+\delta\nu)\,\Gamma_{\tilde{h}}(\delta\nu; 0). \tag{I.26}$$

The ensemble average of $p(t)$ is independent of T in this treatment though in reality complications arise from epoch to epoch variations due to refraction in the ISM. The delay variance is calculated as before and the fourth moment of $\tilde{h}$ becomes (c.f. Eq. (I.15)),

$$\left\langle\tilde{h}(\nu,t_s)\tilde{h}^*(\nu+x,t_s)\tilde{h}(\nu_+,t'_s)\tilde{h}^*(\nu_+ + x', t'_s)\right\rangle = \\ \left\langle\Gamma_{\tilde{h}}(x,0)\right\rangle\left\langle\Gamma_{\tilde{h}}(x',0)\right\rangle + \left\langle\Gamma_{\tilde{h}}(\nu_+ - \nu + x, t_s - t'_s)\right\rangle\left\langle\Gamma_{\tilde{h}}(\nu - \nu_+ + x', t_s - t'_s)\right\rangle. \tag{I.27}$$

[68] Generally $2\pi\tau\Delta\nu_{\rm d} = C_1$ with C_1 ranging from 1 to 2, depending on the scattering medium but the constant is unity for a thin screen that produces an exponential PBF.

[69] The number of scintles is defined so that the rms intensity over the band is $\sigma_I/\langle I\rangle = N_\nu^{-1/2}$.

The first term in the expansion corresponds to $\langle t_p \rangle^2$ and the second term yields the variance. For scintles that are narrow compared to the bandwidth, we obtain the extension of Eq. (I.19)

$$\sigma^2_{t_p} \approx \frac{1}{(2\pi)^2 T} \int d\delta t_s \left(1 - \frac{|\delta t_s|}{T}\right) \iint d\nu d\nu_+ \, B_{\nu,0} B_{\nu_+,0} \left| \left\langle \Gamma'_{\tilde{h}}(\nu - \nu_+, \delta t_s) \right\rangle \right|^2, \tag{I.28}$$

where the derivative of the ACF is with respect to the frequency lag, $\nu - \nu_+$. A change of variables gives

$$\sigma^2_{t_p} \approx \frac{1}{(2\pi)^2 T} \int d\delta t_s \left(1 - \frac{|\delta t_s|}{T}\right) \int d\delta\nu \, \widetilde{R}_B(\delta\nu) \left| \left\langle \Gamma'_{\tilde{h}}(\delta\nu, \delta t_s) \right\rangle \right|^2. \tag{I.29}$$

When scintles are also short in duration compared to the integration time T, we obtain

$$\sigma^2_{t_p} \approx \frac{1}{(2\pi)^2 T} \int d\delta t_s \int d\delta\nu \, \widetilde{R}_B(\delta\nu) \left| \left\langle \Gamma'_{\tilde{h}}(\delta\nu, \delta t_s) \right\rangle \right|^2. \tag{I.30}$$

Generally, $\left\langle \Gamma'_{\tilde{h}}(\delta\nu, \delta t_s) \right\rangle$ is not factorable into time-lag and frequency-lag factors so there is no general analog of Eq. (I.20), (I.21). However, the rms t_p will still scale similarly to Eq. (I.24) as $\tau/\sqrt{2N_s}$ where the number of scintles in the large $B_{\rm eff}T$ limit is $N_s \propto B_{\rm eff}T/\Delta\nu_{\rm d}\Delta t_{\rm d}$.

Appendix J. Dynamic spectra computation and estimation errors

The dynamic spectrum (DS) is considered for a wide total bandwidth and time span encompassing many scintillation time scales. It is simply the power spectrum calculated from Fourier transforms, but the lengths of those FTs relative to the pulse period offer alternative specific methods. The spectrum comprises frequency structure from both the emitted signal (amplitude modulated noise) and from multipath propagation through the ISM. The primary utility of the DS for pulsar timing is to provide a good estimate of the scintillation bandwidth. Fortunately, averaging spectra over multiple pulses diminishes emission structure so that scintillation features dominate. This contrasts with the average pulse profile that includes the intrinsic pulse shape along with scattering, regardless of how many pulses are averaged.

Good estimation of DISS parameters requires a DS containing many scintles resolved in frequency and time. Larger scattering yields smaller scintles, so sampling requirements are more stringent for larger DM pulsars observed at lower frequencies. For the largest DMs and lowest frequencies, the scintles are unresolvable and only pulse-shape fitting will yield an estimate for τ.

Denoting the lowest and highest frequencies of the DS as $\nu_{\rm l}$ and $\nu_{\rm h}$, respectively, voltage data are obtained over a total bandwidth $B = \nu_{\rm h} - \nu_{\rm l}$ and time span T with resolutions $\Delta\nu$ and Δt. To satisfy the estimation conditions , we require $\Delta\nu \ll \Delta\nu_{\rm d} \ll B$ and $\Delta t \ll \Delta t_{\rm d} \ll T$, where the DISS bandwidth $\Delta\nu_{\rm d}$ and DISS time scale $\Delta t_{\rm d}$ are defined in the standard way[70]. Two approaches for obtaining dynamic spectra are as follows.

J.1. *Phase-resolved spectroscopy (PRS)*

If the DISS bandwidth is large enough, a running spectrum across pulse phase is obtained with FFT lengths $\mathrm{T_{FT}} \lesssim \mathrm{W_A}$, where $W_{\rm A}$ is the pulse width (i.e. the width of the squared amplitude modulation in the AMN model.). Multiple FFTs done across the pulse width (if $\mathrm{T_{FT}} \ll \mathrm{W_A}$) and over multiple periods are then combined (as squared magnitudes) to form a DS with frequency resolution $\Delta\nu = \mathrm{T_{FT}^{-1}}$ and time resolution $\Delta t = N_{\rm p} \times P$ by averaging spectra in phase bins over $N_{\rm p}$ periods, corresponding to 1 to 10 s, typically.

Nyquist sampling of complex voltage data requires sample intervals $\Delta t_{\rm Ny} = 1/B$. Resolving scintles requires $\Delta\nu \lesssim \Delta\nu_{\rm d}$ and $\Delta t \lesssim \Delta t_{\rm d}$. Using the maximum FFT length with the uncertainty relation Eq. (9.11) gives $1/W_{\rm A} \lesssim 1/\mathrm{T_{FT}} = 1/(\mathrm{N_p P}) \lesssim \mathrm{C_1}/2\pi\tau$, or

$$\frac{2\pi\tau}{C_1} \lesssim \mathrm{T_{FT}} \lesssim \mathrm{W_A} \lesssim \mathrm{P} \ll \Delta\mathrm{t_d}, \tag{J.1}$$

where we consider the DISS time scale $\Delta t_{\rm d}$ to be the largest. For a thin screen, the scintillation time scale is

$$\Delta t_{\rm d}(\nu) = \frac{a_\beta}{2\pi\nu \mathrm{v_{eff}}} \left(\frac{cd'}{\tau}\right)^{1/2} \simeq 143\,\mathrm{s} \times \frac{\nu^{6/5}}{v_{100}} \left(\frac{d'}{\tau_1}\right)^{1/2}, \tag{J.2}$$

where $a_\beta \equiv 1/2^{(4-\beta)/2(\beta-2)} \simeq 0.93$ for $\beta = 11/3$ and where ν is in GHz, $v_{100} = \mathrm{v_{eff}}/(100\,\mathrm{km\,s^{-1}})$, $d' = s(1-s)d$ is the effective distance in kpc for a screen at fractional distance s from the pulsar, and τ_1 is the scattering time in μs at 1 GHz.

The constraint on the scattering time,

$$\tau \lesssim \frac{W_{\rm A}}{2\pi C_1} \simeq 0.16\,\mathrm{ms} \times \frac{W_{\rm A}(\mathrm{ms})}{C_1}, \tag{J.3}$$

is satisfied by many long period pulsars with $W_{\rm A} \sim 10$ to 100 ms except at low frequencies where $\tau(\nu) \propto \nu^{-4.4}$ can exceed the requirement.

PRS clearly fails if scintles are unresolved using the maximum FFT length indicated in Eq. (J.1). The MSP B1937+21 is a textbook example: with $W_{\rm A} \simeq 45\,\mu s$, the requirement $\tau \lesssim 7\,\mu s$ is violated by the measured $\tau \simeq 25\,\mu s$ at 0.43 GHz.

[70] $\Delta\nu_{\rm d}$ Is the HWHM of the intensity correlation function vs. frequency lag and $\Delta t_{\rm d}$ is the HW at $1/e$ time lag.

J.1.1. *Degrees of freedom in the DS*

In a time series comprising N complex samples, there are $N_{\rm dof} = 2N$ degrees of freedom (dof). For a total time $T_{\rm total}$ and Nyquist sampling over a bandwidth B, this is $N_{\rm dof} = 2BT_{\rm total}$.

A FT of length $N_{\rm FT}$ spanning a time $\mathrm{T_{FT}}$ yields a spectrum with frequency resolution $\Delta\nu = \mathrm{T_{FT}^{-1}}$ and 2 dof per frequency bin.

When $N_{\rm b}$ spectra are averaged over a time $T_{\rm step} = N_{\rm b}\mathrm{T_{FT}}$ to give a single time step in the DS, there are $2N_{\rm b}$ dof/bin.

In a fixed total time $T_{\rm total}$ there are $N_{\rm steps} = T_{\rm total}/T_{\rm step}$ total time steps in the DS, yielding $2N_{\rm FT}N_{\rm b}N_{\rm steps}$ dof/bin. With $N_{\rm FT}$ frequency bins, the total number of dof in the DS is

$$\begin{aligned} N_{\rm dof} &= 2N_{\rm b}N_{\rm steps} \times N_{\rm FT} \\ &= \frac{2N_{\rm b}N_{\rm FT}T_{\rm total}}{N_{\rm b}\mathrm{T_{FT}}} = \frac{2N_{\rm FT}T_{\rm total}}{N_{\rm FT}\Delta t_{\rm Ny}} \\ &= 2BT_{\rm total}, \end{aligned} \tag{J.4}$$

in agreement with $N_{\rm dof}$ in the original time series.

For PRS, spectra are calculated only for an on-pulse window with duty cycle $\sim W_{\rm A}/P$. The number of degrees of freedom for PRS is therefore

$$N_{\rm dof}^{\rm (PRS)} = 2BT_{\rm total}\left(\frac{W_{\rm A}}{P}\right). \tag{J.5}$$

J.1.2. *Error budget of DS*

In building a DS from a voltage time series $\varepsilon(t)$, the spectral estimate from a single FT is

$$S(\nu) = N_{\rm FT}^{-1}|\varepsilon(\nu)|^2. \tag{J.6}$$

For a stochastic signal, fluctuations about the spectral mean are 100% because $\sigma_S/\langle S\rangle = \sqrt{2/N_{\rm dof/bin}}$ and $N_{\rm dof/bin} = 2$. We express this as

$$S(\nu) = \langle S\rangle \times [1 + \mathcal{E}(\sigma_S^2)], \tag{J.7}$$

where $\sigma_S = 1$ and the second term denotes random values drawn from an exponential PDF, $\mathcal{E}(\sigma_S^2) = \sigma_S^{-2}\exp\left(-S/\sigma_S^{-2}\right)\Theta(S)$ where $\Theta(S)$ is the Heaviside (unit step) function. The expression implies that the spectrum is given by the mean plus an error of similar amplitude drawn from an exponential distribution. This form leaves unspecified the correlation frequency of the error: for AMN spectral noise this is $\delta\nu_{\rm corr} \sim W_{\rm A}^{-1}$ while for radiometer noise it is $\delta\nu_{\rm corr} \sim \mathrm{T_{FT}^{-1}}$. For diffractive scintillations $\delta\nu_{\rm corr} \equiv \Delta\nu_{\rm d}$, the scintillation bandwidth.

With PRS, there are $\sim W_{\rm A}/\mathrm{T_{FT}}$ spectra averaged across the pulse in each period and $N_{\rm p}$ periods worth of such spectra are averaged to get a single time step in the DS. This gives $N_{\rm b} = N_{\rm p}W_{\rm A}/\mathrm{T_{FT}} = \mathrm{N_p}/\varepsilon_{\rm W}$, where $\mathrm{T_{FT}} \equiv \varepsilon_{\rm W}\mathrm{W_A}$ and $N_{\rm dof/bin} = 2N_{\rm b}$ per bin.

We then write, after invoking the central limit theorem ($N_{\rm dof/bin} \gg 1$) and denoting a zero mean Gaussian distribution with variance σ^2 as $\mathcal{N}(0,\sigma^2)$,

$$\langle S(\nu)\rangle_{N_{\rm b}} = \langle S\rangle \times \left[1 + \mathcal{N}(0, N_{\rm b}^{-1})\right]. \tag{J.8}$$

For the scintillated AMN signal with additive noise, we write $I(\nu) = S(\nu) + N(\nu)$ and express the block-averaged spectrum as

$$\langle I(\nu)\rangle_{N_{\rm b}} = H(\nu)\langle S_\nu\rangle_\phi\left(\frac{P}{W_{\rm A}}\right) \times \left[1 + \mathcal{N}(0, N_{\rm b}^{-1})\right] + \sigma_N \times \mathcal{N}(0, N_{\rm b}^{-1}), \tag{J.9}$$

where the DISS modulation $H(\nu)$ is assumed constant over the block average. It has unit mean and unit variance (in strong scattering with no quenching from time-frequency averaging, as here). The rms noise variance in a single FT is for radiometer noise with unit time-bandwidth product, $\sigma_N = S_{\rm sys}$. Adjusting terms, we rewrite the spectrum as

$$\langle I(\nu)\rangle_{N_{\rm b}} = \langle S_\nu\rangle_\phi \left(\frac{P}{W_{\rm A}}\right)\left\{H(\nu)\times\left[1+\mathcal{N}(0,N_{\rm b}^{-1})\right] + \frac{S_{\rm sys}}{\langle S_\nu\rangle_\phi}\left(\frac{W_{\rm A}}{P}\right)\times\mathcal{N}(0,N_{\rm b}^{-1})\right\} \tag{J.10}$$

The signal to noise factor for a single spectrum (i.e. based on one FT) is

$$(S/N)_1 = \frac{\langle S_\nu\rangle_\phi}{S_{\rm sys}}\frac{P}{W_{\rm A}} \simeq 0.011\times\left(\frac{\langle S_\nu\rangle_\phi/1\,{\rm mJy}}{S_{\rm sys}/3\,{\rm Jy}}\right)\left(\frac{0.03}{W_{\rm A}/P}\right), \tag{J.11}$$

where a nominal 1 mJy period averaged flux density and 3% duty cycle are used. The value of $S_{\rm sys} = 3\,{\rm Jy}$ is appropriate for Arecibo/DSA-2000/FAST/SKA-mid class telescopes. In most cases $(S/N)_1 \ll 1$ applies and the errors are radiometer noise dominated. Exceptions are the Vela pulsar with $(S/N)_1 \simeq 90$ and 20 at 0.4 and 1.4 GHz respectively. Among MSPs, J0437-4715 has $(S/N)_1 \simeq 8$ and 2 while J1939+2134 (B1937+21) has $(S/N)_1 \simeq 3.1$ and 0.2 at these frequencies.

The spectrum at a single time step in the DS comprises a block average of $N_{\rm b}$ individual spectra, which we express as

$$\langle I(\nu)\rangle_{N_{\rm b}} = \langle S_\nu\rangle_\phi\left(\frac{P}{W_{\rm A}}\right)\left[H(\nu)+\mathcal{N}(0,\sigma^2_{\rm DS_N})\right], \tag{J.12}$$

where the dimensionless variance of the Gaussian distribution is

$$\sigma^2_{\rm DS_N} = \left[\frac{1+(S/N)_1^{-2}}{N_{\rm b}}\right]. \tag{J.13}$$

Block averaging is critical to ensuring adequate sensitivity to scintillations.

J.1.3. *Errors in estimating $\Delta\nu_{\rm d}$ from the spectral ACF*

The utility of the DS in the pulsar timing context is for estimating the scintillation bandwidth, then the scattering time, and finally a correction to the raw ToA. An ACF of a single spectrum has a width with an associated error due to ACF fluctuations. For a single instance of $\langle I(\nu)\rangle_{N_{\rm b}}$ we do not include fluctuations in $H(\nu)$ because we wish to know the scattering time *for that particular realization of* $H(\nu)$. In another context, we might want an epoch averaged estimate, which would calculate the average ACF from the entire DS (i.e. the average of individual ACFs).

The ACF $R_{I_{\rm b}}(\delta\nu)$ of the spectrum in Eq. (J.12) has a fractional error from radiometer noise near zero lag $\delta\nu = 0^+$ (see section J.3),

$$\varepsilon^{(N)}_{\rm ACF} \equiv \frac{[{\rm Var}R_{I_b}(0+)]^{1/2}}{\langle R_{I_b}(0+)\rangle} \simeq \frac{\left[\sigma^4_{\rm DS_N} + 4\sigma^2_{\rm DS_N}R_S(0^+)\right]^{1/2}}{\sqrt{N_{\rm FT}}\times R_S(0^+)}. \tag{J.14}$$

Substituting other quantities yields

$$\begin{aligned}
\varepsilon^{(N)}_{\rm ACF} &= \frac{2}{\sqrt{N_{\rm FT}N_{\rm b}}}\left[1+(S/N)_1^{-2}\right]^{1/2}\left\{1+N_{\rm b}^{-1}[1+(S/N)_1^{-2}]\right\}^{1/2} \\
&\overset{(S/N)_1\ll 1}{\simeq} \frac{2}{(S/N)_1\sqrt{N_{\rm FT}N_{\rm b}}}\left\{1+N_{\rm b}^{-1}(S/N)_1^{-2}\right\}^{1/2} \\
&\overset{N_{\rm b}^{1/2}(S/N)_1\gg 1}{\simeq} \frac{2}{(S/N)_1\sqrt{N_{\rm FT}N_{\rm b}}} \\
&\simeq \frac{2}{(S/N)_1}\left(\frac{P}{T_{\rm total}BW_{\rm A}}\right)^{1/2} \\
&\simeq 2\left(\frac{S_{\rm sys}}{\langle S_\nu\rangle_\phi}\right)\left(\frac{W_{\rm A}}{T_{\rm total}BP}\right)^{1/2}
\end{aligned} \tag{J.15}$$

In the second to last step we assume the DS comprises $N_{\rm b} = (W_{\rm A}/P)(T_{\rm total}/{\rm T_{FT}}) = ({\rm W_A/P})({\rm T_{total}B/N_{FT}})$ total blocks where we include a duty cycle factor $W_{\rm A}/P$ and we relate the sampling time to bandwidth, $\delta t = 1/B$, which gives ${\rm T_{FT}} = {\rm N_{FT}/B}$.

Note that the last result can be obtained by considering the number of noise degrees of freedom included in the ACF for PRS (Eq. (J.5))

$$\varepsilon^{(N)}_{\rm ACF} \simeq \frac{2}{(S/N)_1}\left(\frac{2}{N^{\rm (PRS)}_{\rm dof}}\right)^{1/2}. \tag{J.16}$$

The resulting fractional error on the scintillation bandwidth $\Delta\nu_{\rm d}$ (defined as the HWHM of the ACF) due to radiometer noise only is

$$\varepsilon^{(N)}_{\Delta\nu_{\rm d}} = K_{\Delta\nu_{\rm d}}\varepsilon^{(N)}_{\rm ACF}\left(\frac{\Delta\nu}{\Delta\nu_{\rm d}}\right)^{1/2}, \tag{J.17}$$

where $\Delta\nu$ is the spectral frequency resolution and the constant $K_{\Delta\nu_{\rm d}} \sim 1$ is dependent on the shape of the ACF[71], which depends on the shape of the PBF. In practice we know the PBF shape only approximately because it is stochastic on both short and long time scales. Substituting for $\varepsilon^{(N)}_{\rm ACF}$ using the last expression in Eq. (J.15) gives

$$\sigma^{(N)}_{\Delta\nu_{\rm d}} \simeq 2K_{\Delta\nu_{\rm d}}\left(\frac{S_{\rm sys}}{\langle S_\nu\rangle_\phi}\right)\left(\frac{W_{\rm A}\Delta\nu\Delta\nu_{\rm d}}{T_{\rm total}BP}\right)^{1/2}. \tag{J.18}$$

J.2. *Cyclic spectroscopy (CS)*

The primary utility of the cyclic spectrum (CS) is that it can provide high-frequency resolution dynamic spectra, as noted. Second is its potential for estimating the full impulse response $h(t)$ contemporaneously with arrival time data, which could improve efforts to correct ToAs for multipath propagation delays (e.g. Demorest 2011; Walker et al. 2013; Palliyaguru et al. 2015; Dolch et al. 2021; Turner et al. 2023).

The CS is defined as

$$\Gamma_{\widetilde{\varepsilon}}(\delta\nu,\nu) = \widetilde{\varepsilon}(\nu+\delta\nu/2)\widetilde{\varepsilon}^{\,*}(\nu-\delta\nu/2) \tag{J.19}$$

and is based on a single FT; averaging over multiple FTs is done later. Inserting the scattered baseband field defined earlier, the CS is

$$\Gamma_{\widetilde{\varepsilon}}(\delta\nu,\nu) = \Gamma_{\widetilde{h}}(\delta\nu,\nu)\iint dt_1 dt_2\, a(t_1)a(t_2)m(t_1)m^*(t_2)e^{2\pi i[\nu(t_1-t_2)+\delta\nu(t_1+t_2)/2]}, \tag{J.20}$$

where

$$\Gamma_{\widetilde{h}}(\delta\nu,\nu) = \widetilde{h}(\nu+\delta\nu/2)\widetilde{h}^{\,*}(\nu-\delta\nu/2) \tag{J.21}$$

is the CS of the field PBF.

Resolving small scintle bandwidths $\Delta\nu_{\rm d}$ simply requires longer FTs than those used with phase resolved spectroscopy. The CS employs FTs spanning multiple periods, ${\rm T_{FT}} \equiv {\rm N_pP}$, but smaller than the scintillation time $\Delta t_{\rm d}$. In fact they need to be much smaller than $\Delta t_{\rm d}$ in order to reduce errors by summing multiple blocks.

For a single FT the full CS that includes radiometer noise and all cross terms is

$$\Gamma_{\widetilde{\varepsilon}}(\delta\nu,\nu) = \widetilde{\varepsilon}(\nu_+)\widetilde{\varepsilon}^{\,*}(\nu_-) = \Gamma_{\widetilde{h}}(\delta\nu,\nu)\Gamma_{\widetilde{\varepsilon}_{\rm i}}(\delta\nu,\nu) + \Gamma_{\widetilde{n}}(\delta\nu,\nu) + [\widetilde{h}(\nu_+)\widetilde{\varepsilon}_{\rm i}(\nu_+)\widetilde{n}^*_{\nu_-} + \widetilde{h}(\nu_-)\widetilde{\varepsilon}_{\rm i}(\nu_-)^*\widetilde{n}(\nu_+)] \tag{J.22}$$

[71] E.g. $K_{\Delta\nu_{\rm d}} \sim 1.16$ for a Gaussian shape (Lenz and Ayres 1992). For an exponential PBF the ACF is Lorentzian and $K_{\Delta\nu_{\rm d}} \sim 1.58$.

where $\nu_\pm \equiv \nu \pm \delta\nu/2$ and cross terms in square brackets between $\widetilde{n}$ and $\widetilde{\varepsilon}_\mathrm{i}$ average to zero. However, they contribute significantly to the variance of CS estimates, as shown below. For zero lag, $\Gamma_{\widetilde{\varepsilon}}(\delta\nu = 0, \nu) = |\widetilde{\varepsilon}(\nu)|^2 = H(\nu)|\widetilde{\varepsilon}_\mathrm{i}(\nu)|^2 + |\widetilde{n}(\nu)|^2$ is proportional to the standard FT spectral estimate for ε (when the cross terms are averaged out).

At minimum, the scintillation spectrum $H(\nu) \equiv |\widetilde{h}(\nu)|^2$ is the quantity of interest to be extracted from the CS. Fluctuations in $H(\nu)$ and $\Gamma_{\widetilde{\varepsilon}_\mathrm{i}}$ from a single FT are 100% about the mean. The exponential statistics of these quantities originates from the stochasticity of the signal, which yields complex Gaussian statistics for the FT by virtue of the central limit theorem. They are reduced by smoothing the spectrum or by averaging spectra obtained from multiple FTs. Assuming the FT length $\mathrm{T_{FT}} = \mathrm{N_p P}$ is chosen to yield the required frequency resolution, spectral smoothing is not an option, so averaging over multiple blocks is mandatory[72].

Ultimately the CS involves the FT $\widetilde{A}(\delta\nu)$ of the periodic modulation function $A(t) \equiv a^2(t)$, which is defined before propagation and so does not include scattering. A strictly periodic train of $N_\mathrm{p} \gg 1$ identical pulse shapes $A_0(t)$ with $A_0(0) = 1$ multiplied by an average amplitude $S_{\nu,\mathrm{pk}}$ has an FT,

$$\widetilde{A}(\delta\nu) \simeq N_\mathrm{p} W_\mathrm{A} S_{\nu,\mathrm{pk}} \widetilde{A}_\mathrm{n}(\delta\nu) \times |\mathrm{sinc_d}(\delta\nu P, N_\mathrm{p})|, \tag{J.23}$$

where $\widetilde{A}_\mathrm{n}(\delta\nu) = \widetilde{A}_0(\delta\nu)/\widetilde{A}_0(0)$ is normalized to unit maximum and its effective width is $W_\mathrm{A} \equiv \widetilde{A}_0(0)$. The Dirichlet sinc function, $\mathrm{sinc_d}(x, N) = \sin(N\pi x)/N\sin(\pi x)$, yields peaks at discrete frequencies $\delta\nu_k = k/P$ with k extending to $k_\mathrm{max} \sim P/W_\mathrm{A}$, the reciprocal of the pulse duty cycle. CS can also be used to extract the full profile (i.e. across all of pulse phase) by using a larger number of harmonics than k_max, integrating over ν, and inverse transforming $\widetilde{A}_\mathrm{n}$.

The CS for a single FT spanning a time much greater than the inverse bandwidth but much shorter than the scintillation time Δt_d is given by an ensemble average over noise terms while $\Gamma_{\widetilde{h}}$ is fixed. This gives

$$\langle \Gamma_{\widetilde{\varepsilon}}(\delta\nu_k, \nu)\rangle = (\mathrm{T_{FT}/B})\,\langle \mathrm{S}_\nu\rangle_\phi\, \widetilde{\mathrm{b}}(\nu) \left[\widetilde{\mathrm{A}}_\mathrm{n}(\delta\nu_\mathrm{k})\Gamma_{\widetilde{\mathrm{h}}}(\delta\nu_\mathrm{k}, \nu) + \frac{\mathrm{sinc}\,\delta\nu_\mathrm{k}\mathrm{T}}{(\mathrm{S/N})_\phi}\right], \tag{J.24}$$

where the bandpass factor is $\widetilde{b}(\nu) = \widetilde{\Delta}(\nu)/\widetilde{\Delta}(0) = B\widetilde{\Delta}(\nu)$. Also, $\langle S_\nu\rangle_\phi \simeq (W_\mathrm{A}/P)S_{\nu,\mathrm{pk}}$ is the period averaged flux density (as usually reported for pulsars), $\widetilde{b}(\nu)$ is the receiver bandpass function with width B, and $\mathrm{sinc}\,x \equiv (\sin\pi x)/\pi x$. The signal to noise ratio is $(\mathrm{S/N})_\phi \equiv \langle S_\nu\rangle_\phi/S_\mathrm{sys}$ where $S_\mathrm{sys} = T_\mathrm{sys}/G$ is the system effective flux density (SEFD) for a telescope with gain G. The first term in square brackets is from the pulsar signal while the second term is from additive noise reduced by the $(\mathrm{S/N})_\phi{}^{-1}$ factor. Though $(\mathrm{S/N})_\phi \ll 1$ for most pulsars, the second term is important only for $k = 0$.

The inverse transform of $\Gamma_{\widetilde{\varepsilon}}(\delta\nu_k, \nu)$ with respect to $\delta\nu_k$ yields the phase resolved CS or 'profile spectrum' with a time argument replacing the $\delta\nu$ argument,

$$\langle \Gamma_{\widetilde{\varepsilon}}(t, \nu)\rangle \propto \langle S_\nu\rangle_\phi\, \widetilde{b}(\nu) A_\mathrm{n}(t) * \Gamma_{\widetilde{h}}(t, \nu), \tag{J.25}$$

where a constant term from the sinc function has been excluded.

J.2.1. *CS estimation errors*

The 100% errors in the CS from a single FT (even with infinite S/N) are a consequence of the complex Gaussian statistics of the FT. To show this we calculate the variance of $\Gamma_{\widetilde{\varepsilon}}(\delta\nu_k, \nu)$,

$$\mathrm{Var}\left[\Gamma_{\widetilde{\varepsilon}}(\delta\nu_k, \nu)\right] = \left[(\mathrm{T_{FT}/B})\,\langle \mathrm{S}_\nu\rangle_\phi\right]^2 \widetilde{b}(\nu_+)\widetilde{b}(\nu_-) \left\{\left|\Gamma_{\widetilde{h}}(\delta\nu_k, \nu)\right|^2 + (\mathrm{S/N})_\phi{}^{-2} + (\mathrm{S/N})_\phi{}^{-1}[H(\nu_+) + H(\nu_-)]\right\}, \tag{J.26}$$

There is only weak dependence of the variance on $\delta\nu_k$ and no explicit dependence on the shape $\widetilde{A}_\mathrm{n}(\delta\nu_k)$ in the total variance. *However*, the dependence on $\widetilde{A}_\mathrm{n}(\delta\nu_k)$ is hidden in the partition of variance into the real and imaginary parts of $\Gamma_{\widetilde{\varepsilon}}$, which evolves with the variation of $\widetilde{A}(\delta\nu_k)$ vs. $\delta\nu_k$.

[72] In this regard, the example in Demorest (2011) for B1937+21 at 430 MHz is informative. Long FTs with $N_\mathrm{p} = 87$ were used for coherent dedispersion of the 30 ms dispersion time across the 4 MHz band. This yields frequency resolution. $\Delta\nu \sim 1/N_\mathrm{p}P \simeq 7.4$ Hz, far smaller than scintle widths $\Delta\nu_\mathrm{d} \sim 1/2\pi\tau \sim 25$ kHz for $\tau \sim 40\,\mu s$. The CS was then degraded by a factor of 87 to yield a resolution $\Delta\nu \sim 0.642$ kHz which is the resolution corresponding to $1/P$. Paradoxically, if FT lengths of $N_\mathrm{p} = 1$ were used for the CS computation (after initial coherent dedispersion), the resolution would be limited by the pulse width to $\Delta\nu \sim (30\,\mu s)^{-1} \simeq 33$ kHz, insufficent for resolving scintles. Thus the CS using $N_\mathrm{p} \gg 1$ exploits the rapid sampling of voltage data, $\Delta t = 0.25\,\mu s$ to provide a large Nyquist frequency and also provides the needed frequency resolution.

Fig. 81 shows the mean and RMS variation of $\Gamma_{\widetilde{\varepsilon}}(\delta\nu_k, \nu)$ vs ν for fixed $\delta\nu_k$.

Partition of variance in the real and imaginary parts is shown in Fig. 82, which shows the RMS $\Gamma_{\widetilde{\varepsilon}}$ for the total (scattered + noise) signal (top panel), scintillated intrinsic signal (middle), and intrinsic signal (bottom). The variance is entirely in the real part at $\delta\nu_k = 0$, but equipartitions into the real and imaginary parts for $\delta\nu_k \gtrsim W_{\rm A}^{-1}$. The asymptotic variances for $\Gamma_{\widetilde{\varepsilon}}$ are constant in $\delta\nu_k$ while the other correlations, $\Gamma_{\widetilde{\epsilon}+\widetilde{n}}$ and $\Gamma_{\widetilde{\varepsilon}_{\rm s}}$ decline slowly due to the scintillation modulation.

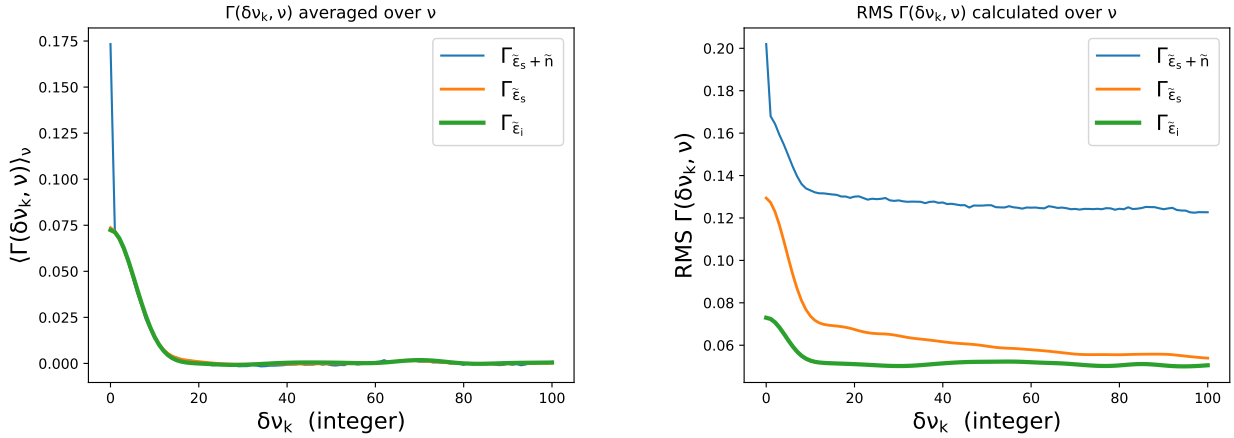


Figure 81. Average and RMS cyclic spectra vs. frequency lag, Left: Averages over frequency ν for the cyclic spectra of the intrinsic field $\widetilde{\varepsilon}_{\rm i}$, the scattered field $\widetilde{\varepsilon}_{\rm s}$ that includes scintillations, and the total field that includes radiometer noise. Radiometer noise decorrelates in one sample, producing the spike in the CS. Right: RMS values of the cyclic spectra which combine contributions from the real and imaginary parts.

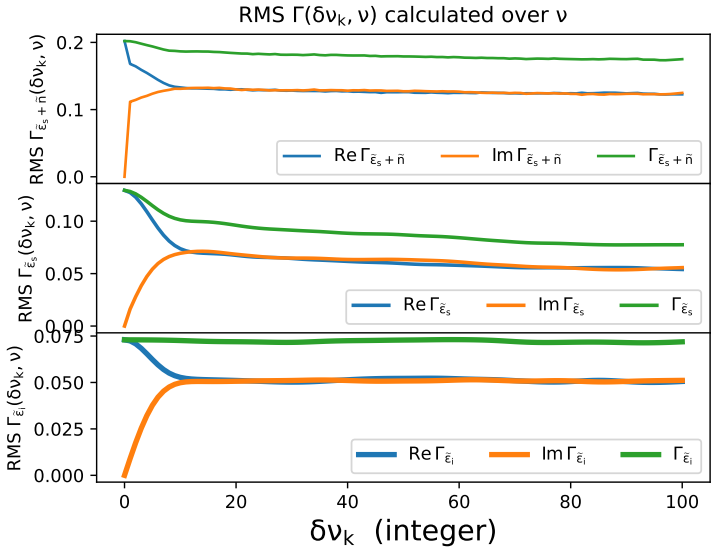


Figure 82. RMS of cyclic spectra vs $\delta\nu_k$ showing how fluctuations are distributed between the real and imaginary parts. In each case, the fluctuations are all in the real part for $\delta\nu_k = 0$.

Fluctuations near the origin:

For small $0 < \delta\nu_k \ll W_{\rm A}^{-1} \ll \Delta\nu_{\rm d} \ll B$ most of the variance is in the real part of $\Gamma_{\widetilde{\varepsilon}}$ and we have $\Gamma_{\widetilde{h}}(\delta\nu_k, \nu) \sim H(\nu_+) \sim H(\nu_-) \simeq H(\nu)$,

Single block: The variance is

$$\begin{aligned} {\rm Var}\left[\Gamma_{\widetilde{\varepsilon}}(\delta\nu_k,\nu)\right] &\simeq \left[({\rm T_{FT}/B})\,\langle {\rm S}_\nu\rangle_\phi \widetilde{\rm b}(\nu)\right]^2 ({\rm S/N})_\phi{}^{-2}\left[1 + H(\nu)({\rm S/N})_\phi\right]^2 \\ &\simeq \langle\Gamma_{\widetilde{\varepsilon}}(0,\nu)\rangle^2 \left\{1 + [H(\nu)({\rm S/N})_\phi]^{-1}\right\}^2 \end{aligned} \tag{J.27}$$

where the variance is written in terms of the mean CS in the last step. For large $({\rm S/N})_\phi$, we see that the CS has 100% errors.

We write the unaveraged CS in terms of the average CS and a statistical part,

$$\Gamma_{\widetilde{\varepsilon}}(\delta\nu_k,\nu) \equiv \langle\Gamma_{\widetilde{\varepsilon}}(\delta\nu_k,\nu)\rangle + \delta\Gamma_{\widetilde{\varepsilon}}(\delta\nu_k,\nu), \tag{J.28}$$

where for $({\rm S/N})_\phi \gg 1$, $\delta\Gamma_{\widetilde{\varepsilon}}(\delta\nu_k,\nu)$ is drawn from a one-sided exponential PDF (see Table)

$$\delta\Gamma_{\widetilde{\varepsilon}}(\delta\nu_k,\nu) \sim \mathcal{E}_1(\mu_{\Gamma_{\widetilde{\varepsilon}}}), \qquad \text{where} \;\; \mu_{\Gamma_{\widetilde{\varepsilon}}} = \sqrt{{\rm Var}([\Gamma_{\widetilde{\varepsilon}}(\delta\nu_k,\nu)])}. \tag{J.29}$$

For smaller $({\rm S/N})_\phi$, the distribution is a combination of exponential PDFs from the signal and from radiometer noise.

Block averaging: The only way to reduce CS estimation errors is by averaging over multiple data blocks (assuming the frequency resolution is fixed). This reduces the variance by a factor $N_{\rm b}^{-1}$ for a PDF that converges to a Gaussian form. In this case,

$$\delta\Gamma_{\widetilde{\varepsilon}}(\delta\nu_k,\nu) \sim \mathcal{N}(0,\sigma^2_{\Gamma_{\widetilde{\varepsilon}}}), \qquad \text{where} \;\; \sigma^2_{\Gamma_{\widetilde{\varepsilon}}} = {\rm Var}([\Gamma_{\widetilde{\varepsilon}}(\delta\nu_k,\nu)]) \simeq N_{\rm b}^{-1}\left\langle\Gamma_{\widetilde{\varepsilon}}(\delta\nu_k,\nu)\right\rangle^2. \tag{J.30}$$

Fluctuations away from the origin: For $\delta\nu_k \gtrsim W_{\rm A}^{-1}$ where $\widetilde{A}(\delta\nu_k)$ is negligible, the real and imaginary parts of $\Gamma_{\widetilde{\varepsilon}}$ have equal variance.

Single block: The real and imaginary parts are each drawn independently from a two-sided exponential distribution, which we write as a a complex, two sided exponential distribution (see Table),

$$\delta\Gamma_{\widetilde{\varepsilon}}(\delta\nu_k \gg W_{\rm A}^{-1},\nu) \sim \mathcal{E}_2^{(\rm c)}(0,\sigma^2_{\Gamma_{\widetilde{\varepsilon}}}). \tag{J.31}$$

Block averaging: The CLT implies convergence to a complex Gaussian PDF such that

$$\delta\Gamma_{\widetilde{\varepsilon}}(\delta\nu_k,\nu) \sim \mathcal{N}^{(\rm c)}(0,\sigma^2_{\Gamma_{\widetilde{\varepsilon}}}), \qquad \text{where} \;\; \sigma^2_{\Gamma_{\widetilde{\varepsilon}}} \simeq N_{\rm b}^{-1}\left\langle\Gamma_{\widetilde{\varepsilon}}(\delta\nu_k,\nu)\right\rangle^2. \tag{J.32}$$

Implications for CS utility: If the CS is used solely to produce a dynamic spectrum, the sensitivity analysis for estimation of $\Delta\nu_{\rm d}$ using PRS also applies here. The signal to noise ratio of the scintillated pulsar signal in the CS need not be large in that case because determination of $\Delta\nu_{\rm d}$ is often dependent only on the total number of scintles in the DS.

However, if the CS is used to determine the field PBF $\widetilde{h}(\nu)$ itself using methods like those discussed in Walker et al. (2013); Dolch et al. (2021), the requirements are much more stringent. In this case, the statistical errors must be small enough to allow solution for $\widetilde{h}(\nu)$ from data spanning less than $\Delta t_{\rm d}$ rather than utilizing the full DS extending over a large multiple of $\Delta t_{\rm d}$. If the CS errors are scintle (not noise) dominated, the single block errors are 100% and the $N_{\rm b}$-block errors are $\simeq N_{\rm b}^{-1/2}$. If we require that $H(\nu)$ be determined to a precision better than $\epsilon_H \ll 1$, then we require $N_{\rm b} > \epsilon_H^{-2}$ while also requiring that the blocks extend over no more than a fraction $\epsilon_{\Delta t_{\rm d}}$ of the scintillation time, $N_{\rm b} N_{\rm p} P = \epsilon_{\Delta t_{\rm d}} \Delta t_{\rm d}$. The combined constraints on $N_{\rm b}$ are

$$\epsilon_H^{-2} \lesssim N_{\rm b} \lesssim \epsilon_{\Delta t_{\rm d}} \Delta t_{\rm d}/N_{\rm p} P. \tag{J.33}$$

For 10% error on H and ten samples per scintle ($\epsilon_{\Delta\nu_{\rm d}} = 0.1$), we have

$$100 \times (0.1/\epsilon_H)^2 \lesssim N_{\rm b} \lesssim 10^4 \times (\epsilon_{\Delta t_{\rm d}}/0.3)(\Delta t_{\rm d}/100\,{\rm s})(3\,{\rm ms}/P) N_{\rm p}^{-1}. \tag{J.34}$$

To resolve scintles, we must have $N_{\rm p} \gtrsim (P\epsilon_{\Delta\nu_{\rm d}}\Delta\nu_{\rm d})^{-1} = 2\pi\tau/\epsilon_{\Delta\nu_{\rm d}} P$. If $N_{\rm p} \gg 1$, the number of blocks is more constrained and may be insufficent for heavily scattered millisecond pulsars.

J.2.2. *Role of Pulse Jitter*

Departure from strict periodicity results from time jitter of pulse centroids. Gaussian distributed jitter $\Delta t_{\rm J}$ of each pulse with RMS $\sigma_{\rm J}$ reduces $\widetilde{A}$ by a form factor,

$$\eta_{\rm J}(\delta\nu) = e^{-2(\pi\delta\nu\sigma_{\rm J})^2}. \tag{J.35}$$

If we restrict the reduction in all $k_{\rm max} = P/W_{\rm A}$ harmonics to no more than $1/x$ the RMS jitter is bounded by

$$\sigma_{\rm J} < \frac{W_{\rm A}}{\pi}\left(\frac{\ln x}{2}\right)^{1/2}. \tag{J.36}$$

For $x = 2$ ($< 50\%$ reduction), $\sigma_{\rm J} < 0.19 W_{\rm A}$, roughly the amount of single-pulse jitter seen in most pulsars (e.g. Shannon and Cordes 2012; Lam et al. 2016a). Larger RMS jitter reduces the number of harmonics that otherwise could have been detectable. This reduction is unavoidable because measured average pulses include jitter. In effect, the pulse shape $A(t)$ used above should be viewed as including phase jitter.

J.2.3. *Constraints on CS parameters*

The viability of CS for obtaining dynamic spectra depends on sampling constraints and on estimation errors. The conditions needed are therefore pulsar and frequency dependent:

1. CS is unnecessary if the scintillation bandwidth exceeds half the receiver bandwidth, $\Delta\nu_{\rm d} \geq B/2$. Using $B = f_B\nu$ and $\Delta\nu_{\rm d} = C_1/2\pi\tau$ along with $\tau = \tau_1\nu^{-X_\tau}$ with $X_\tau = 22/5$. CS cannot be applied for frequencies above

$$\nu_{\rm no\,CS} = \left(\frac{1000\pi f_B\tau_1}{C_1}\right)^{1/(X_\tau-1)} \simeq 10.7\,{\rm GHz}\times\left(\frac{f_B\tau_1}{C_1}\right)^{5/17}. \tag{J.37}$$

2. Resolving scintles requires $\mathrm{T}_{\rm FT}^{-1} = (\mathrm{N_p P})^{-1} \ll \Delta\nu_{\rm d} = \mathrm{C}_1/2\pi\tau$ which we write as $\mathrm{T}_{\rm FT}^{-1} \equiv \epsilon_{\Delta\nu_{\rm d}}\Delta\nu_{\rm d} \ll \Delta\nu_{\rm d}$ with $\epsilon_{\Delta\nu_{\rm d}} \ll 1$. For ten samples per $\Delta\nu_{\rm d}$ (i.e. $\epsilon_{\Delta\nu_{\rm d}} = 0.1$)

$$N_{\rm p} \gg \frac{2\pi\tau}{C_1 P} \quad \text{or} \quad N_{\rm p} = \frac{2\pi\tau}{\epsilon_{\Delta\nu_{\rm d}} C_1 P} \simeq \frac{0.063\,\nu^{-22/5}\tau_1}{(\epsilon_{\Delta\nu_{\rm d}}/0.1) C_1 P({\rm ms})} \tag{J.38}$$

   where τ_1 is the scattering time at 1 GHz in μs units. This expression suggests that CS is indicated only for large scattering times τ and low frequencies. However, even for moderate scattering times, CS is needed because phase resolved spectroscopy is limited to a resolution $\Delta\nu \simeq W_{\rm A}^{-1}$ that is sufficient only for $W_{\rm A} \gtrsim 63\,\mu s\,\tau(\mu s)/C_1\epsilon_{\Delta\nu_{\rm d}}/0.1)$. MSPs with narrow pulse widths, such as B1937+2214 mentioned above, do not satisfy this condition and require $N_{\rm p} > 1$ at 0.4 GHz.

   This condition can be written as $\nu \geq \nu_{\Delta\nu_{\rm d}}$ with

$$\nu_{\Delta\nu_{\rm d}} = \left(\frac{2\pi\tau_1}{\epsilon_{\Delta\nu_{\rm d}} C_1 N_{\rm p} P}\right)^{1/X_\tau} \simeq 0.53\,{\rm GHz}\times\left[\frac{\tau_1}{(\epsilon_{\Delta\nu_{\rm d}}/0.1) C_1 N_{\rm p}\,P({\rm ms})}\right]^{5/22}. \tag{J.39}$$

3. Reducing CS variance by maximizing the number of blocks $N_{\rm b}$ is in tension with the use of $N_{\rm p} \gg 1$ FTs to resolve scintles (condition 2). Their product $N_{\rm p}N_{\rm b}$ is constrained by $N_{\rm b}\mathrm{T_{FT}} = \mathrm{N_p N_b P} \lesssim \Delta\mathrm{t_d}$, where $\Delta t_{\rm d}(\nu) \propto \nu^{6/5}$ is the scintillation time (Eq. (J.2)). If an error $\epsilon_{\rm tol} = 1/\sqrt{N_{\rm b}}$ is specified, the FT length is limited by

$$N_{\rm p} \lesssim \frac{\epsilon_{\rm tol}^2\Delta t_{\rm d}}{P} \simeq 1.43\times10^3\left(\frac{\epsilon_{\rm tol}}{0.1}\right)^2\left(\frac{\nu^{6/5}}{v_{100}P({\rm ms})}\right)\left(\frac{d'}{\tau_1}\right)^{1/2}, \tag{J.40}$$

   where, as before, ν is in GHz, v_{100} is the effective transverse velocity in units of 100 km s^{-1}, and the effective distance d' is in kpc. This limit on $N_{\rm p}$ becomes small for longer periods, lower frequencies, and larger scattering times.

Expressed as a frequency limit $\nu \gtrsim \nu_{\Delta t_{\rm d}}$ and using the scintillation time expressed in terms of its value at 1 GHz, $\Delta t_{\rm d}(\nu) = \Delta t_{\rm d1}\nu^{2/(\beta-2} \rightarrow \Delta t_{\rm d1}\nu^{6/5}$,

$$\nu_{\Delta t_{\rm d}} = \left(\frac{N_{\rm p}N_{\rm b}P}{\Delta t_{\rm d1}}\right)^{(\beta-2)/2} \simeq 0.016\,{\rm GHz}\left(\frac{N_{\rm p}N_{\rm b}v_{100}P({\rm ms})}{1000}\right)^{5/6}\left(\frac{\tau_1}{d'}\right)^{5/12}. \tag{J.41}$$

4. The last constraint derives from the net fractional errors on $\widetilde{\Gamma}_\varepsilon$ and $\widehat{H}(\nu)$ from S/N considerations. Large values of $({\rm S/N})_\phi$ are uncommon. The ~ 5 Jy flux density of the Vela pulsar at 0.4 GHz exceeds $S_{\rm sys}$ only for the largest telescopes with effective diameters $\gtrsim 300$ m. For most other cases, $({\rm S/N})_\phi \ll 1$. Restricting the fractional error to $\epsilon_H \ll 1$ implies $\epsilon_H\sqrt{N_{\rm b}k_{\rm max}}({\rm S/N})_\phi \geq 1$ or

$$({\rm S/N})_\phi \geq \left(\epsilon_H\sqrt{N_{\rm b}k_{\rm max}}\right)^{-1} \simeq 0.058 \times \left(\frac{0.1}{\epsilon_H}\right)\left(\frac{10^3}{N_{\rm b}}\frac{30}{k_{\rm max}}\right)^{1/2}. \tag{J.42}$$

The MSP J1939+2134 (B1937+21) satisfies this condition in Arecibo data with $S_{\rm sys} \simeq 4$ Jy and $S_\phi(0.43\,{\rm GHz}) = 240$ mJy while using $N_{\rm b} = 7.7 \times 10^4$ blocks across 120 s and $k_{\rm max} \simeq 20$ (Demorest 2011). This yields $({\rm S/N})_\phi \simeq 0.06 \gg 0.008$.

Conditions 1 to 3 can be rewritten as constraints on the period P, dispersion measure DM, and frequency ν evaluating τ_1 and the effective distance d' in terms of DM. We evaluate the constraints by calculating τ_1 from the empirical τ(DM) relation. That relation shows substantial scatter ($\sigma_{\log_{10}\tau} \simeq 0.76$) but these amount to only a factor of 1/2 to 2 spread in the constraints given the indices of τ_1 in Eq. (J.37), (J.39), and (J.41).

J.3. *ACF Statistics*

From a given spectrum we want to determine the autocorrelation width of frequency structure. Here we wish to know the error on the signal part of the ACF caused by additive white noise. Let $I = S + N$ where S corresponds to the DISS spectrum and N is additive noise. Assume N has Gaussian statistics (via the CLT applied to a spectrum produced with a sufficient degree of averaging) and let it have zero mean and correlation function $\langle N_j N_k\rangle = \sigma_N^2\delta_{jk}$ using the Kronecker delta δ_{jk}. Assume that S is correlated over a relatively large number of samples.

The ACF of a spectrum with N samples is

$$R_I(\delta\nu) = N^{-1}\sum_{j=0}^{N-\delta\nu} I_j I_{j+\delta\nu} \tag{J.43}$$

where $I_j I_{j+\delta\nu} = S_j S_{j+\delta\nu} + N_j N_{j+\delta\nu} + S_j N_{j+\delta\nu} + S_{j+\delta\nu}N_j$.

The ensemble mean ACF receives no contributions from the $S \times N$ cross terms,

$$\langle R_I(\delta\nu)\rangle = N^{-1}\sum_{j=0}^{N-\delta\nu} S_j S_{j+\delta\nu} + \sigma_N^2\delta_{\delta\nu,0} \equiv R_S(\delta\nu) + \sigma_N^2\delta_{\delta\nu 0}. \tag{J.44}$$

The mean-square ACF at a lag $\delta\tau = 0+$ avoids the noise spike at zero lag but is contributed to by cross terms between S and N,

$$\left\langle R_I^2(0+)\right\rangle \simeq \langle R_I(\delta\nu)\rangle^2 + N^{-1}\left[\sigma_N^4 + 4\sigma_N^2 R_S(0)\right]. \tag{J.45}$$

The second term is the variance of the ACF that implies a fractional ACF error,

$$\frac{[{\rm Var}R_I(0+)]^{1/2}}{\langle R_I(0+)\rangle} \simeq \frac{\left[\sigma_N^4 + 4\sigma_N^2 R_S(0)\right]^{1/2}}{\sqrt{N}\times R_S(0)}. \tag{J.46}$$

The first term dominates for low S/N. For large S/N, i.e. $R_S^{1/2}(0)/\sigma_N \gg 1$, the fractional error is

$$\frac{[\mathrm{Var}R_I(0+)]^{1/2}}{\langle R_I(0+)\rangle} \simeq \frac{2\sigma_N}{\sqrt{N \times R_S(0)}}. \tag{J.47}$$

Errors in the ACF translate into an error on the estimate of its characteristic width, $\widehat{W}_S$. Let W_S equal the true width in samples. The fractional error on the estimate is

$$\frac{\sigma_{\widehat{W}_S}}{W_S} \simeq \frac{1}{\sqrt{W_S}} \frac{[\mathrm{Var}R_I(0+)]^{1/2}}{\langle R_I(0+)\rangle}. \tag{J.48}$$

Using these expressions, a specified error on W_S can be back propagated into a requirement on the S/N of the data.

Appendix K. Hilbert transform solutions for non-minimum delay functions

For a function that does not have the minimum-delay property, the minimum-delay phase still has a role. Let $\tilde{h}_{\rm HT}(\nu)$ be the FT obtained using the HT to calculate the minimum-delay solution. The true FT for more general functions can be written as (e.g. Oppenheim et al. 1999, Chapter 5)

$$\tilde{h}(\nu) = \tilde{h}_{\rm HT}(\nu) Z(\nu), \tag{K.1}$$

where $Z(\nu)$ is an "all-pass" filter with unit amplitude that comprises some number of zeros of $\exp(-2\pi i\nu)$ in the complex plane and that changes only the phase. The all-pass filter can be written as the product of Q individual factors involving the zeros s_j^{-1} where $\exp(2\pi i\nu) = 0$,

$$Z(\nu) = \prod_{j=0}^{Q-1} \left(\frac{e^{-2\pi i\nu} - s_j}{1 - s_j^* e^{-2\pi i\nu}} \right), \tag{K.2}$$

and where each factor and thus Z has unity magnitude. The numerical task is to determine the values for s_j ($2Q$ unknowns) and the value of Q itself. Determination is aided by the fact that the zeros s_j^{-1} are outside the unit circle and by the possibility that Q is much smaller than the overall length of a time series.

Appendix L. Quality Measure Evaluation Code

Quality measures can be evaluated for an individual pulsar using `PTQ.py`, available at GitHub (J. M. Cordes, PTQ, (2025), GitHub respository, https://github.com/jmcordes/PTQ), which includes a description and several convenience functions.

```
usage: PTQ.py [-h] [-psr PSR] [-p0 P0] [-p1 P1] [-d D] [-vtrans VTRANS] [-wc WC] [-nc NC]
              [-s S1400] [-tau TAU] [-nu_tau NU_TAU] [-B BW] [-Tint TINT] [-Ssys SSYS]
              [-npol NPOL] [-Tyr TYR] [-bKol BKOL] [-Fj FJ] [-nu_eval NU_EVAL] [-v]

Calculates quality measures using input data for an MSP. Outputs metrics that compare
the pulsar to other MSPs. JMC 2023 Jun - 2024 Nov 5, 2025 May 19-22 Input information needed:
psrname P, Pdot period, period derivative sec and s/s D distance kpc vtrans transverse pulsar
speed km/s tau pulsar broadening time microsec nu_tau RF for pulsar broadening time GHz Wc
Component width microsec nc Number of components dimensionless Alternative to Wc, nc
(not yet implemented): template file from which Weff is determined (equivalent to Wc, nc)
Metrics file: 'QMcalcs_metrics_20241105.npz'

optional arguments:
  -h, --help            show this help message and exit
  -psr PSR, --psr PSR   Pulsar name (for labeling) (default: J1909-3744)
  -p0 P0, --p0 P0       pulse period (sec) (default: 0.002947108069160717)
  -p1 P1, --p1 P1       period derivative (s/s) (default: 1.402541e-20)
  -d D, --d D           pulsar distance (kpc) (default: 1.14)
  -vtrans VTRANS, --vtrans VTRANS
                        Transverse pulsar speed (km/s) (default: 200.19)
  -wc WC, --wc WC       Profile component width (microsec)) (default: 45.6489)
  -nc NC, --nc NC       Number of profile components (default: 1)
  -s S1400, --s1400 S1400
                        Period averaged flux density (mJy)) (default: 1.8)
  -tau TAU, --tau TAU   Pulse broadening time (microsec) (default: 0.033263530451980036)
  -nu_tau NU_TAU, --nu_tau NU_TAU
                        Radio frequency of pulse broadening time (GHz) (default: 1)
  -B BW, --BW BW        Bandwidth (GHz) (default: 0.1)
  -Tint TINT, --Tint TINT
                        Total integration time per epoch (sec) (default: 1000.0)
  -Ssys SSYS, --Ssys SSYS
                        SEFD (Jy (default: 3)
  -npol NPOL, --npol NPOL
                        Number of polarization channels (int (default: 2)
  -Tyr TYR, --Tyr TYR   Time range for calculating spin noise (yr) (default: 1)
  -bKol BKOL, --bKol BKOL
                        Wavenumber spectrum spectral index (dimensionless)
                        (default: 3.6666666666666665)
  -Fj FJ, --FJ FJ       Jitter parameter (dimensionless) (default: 0.3333333333333333)
  -nu_eval NU_EVAL, --nu_eval NU_EVAL
                        RF for evaluating pulsar (GHz) (default: 1.4)
  -v, --V               Verbose to get detailed output (default: False)
```

REFERENCES

Agazie G, Alam MF, Anumarlapudi A, et al (2023a) The NANOGrav 15 yr Data Set: Observations and Timing of 68 Millisecond Pulsars. ApJL951(1):L9. https://doi.org/10.3847/2041-8213/acda9a, arXiv:2306.16217 [astro-ph.HE]

Agazie G, Anumarlapudi A, Archibald AM, et al (2023b) The NANOGrav 15 yr Data Set: Evidence for a Gravitational-wave Background. ApJL951(1):L8. https://doi.org/10.3847/2041-8213/acdac6, arXiv:2306.16213 [astro-ph.HE]

Agazie G, Anumarlapudi A, Archibald AM, et al (2023c) The NANOGrav 15 yr Data Set: Detector Characterization and Noise Budget. ApJL951(1):L10. https://doi.org/10.3847/2041-8213/acda88, arXiv:2306.16218 [astro-ph.HE]

Alam MF, Arzoumanian Z, Baker PT, et al (2020) The nanograv 12.5 yr data set: Observations and narrowband timing of 47 millisecond pulsars. The Astrophysical Journal Supplement Series 252(1):4. https://doi.org/10.3847/1538-4365/abc6a0, URL https://dx.doi.org/10.3847/1538-4365/abc6a0

Allan DW (1966) Statistics of atomic frequency standards. IEEE Proceedings 54:221–230. https://doi.org/10.1109/PROC.1966.4634

Anderson PW, Itoh N (1975) Pulsar glitches and restlessness as a hard superfluidity phenomenon. Nature 256:25–27. https://doi.org/10.1038/256025a0

Antoni J (2007) Cyclic spectral analysis in practice. Mechanical Systems and Signal Processing 21:597–630. https://doi.org/10.1016/j.ymssp.2006.08.007

Antoniadis J, Freire PCC, Wex N, et al (2013) A Massive Pulsar in a Compact Relativistic Binary. Science 340(6131):448. https://doi.org/10.1126/science.1233232, arXiv:1304.6875 [astro-ph.HE]

Armstrong JW (1984) Interstellar scintillation and ultra-low-frequency gravitational wave observations. Nature307(5951):527–528. https://doi.org/10.1038/307527a0

Armstrong JW, Rickett BJ, Spangler SR (1995) Electron density power spectrum in the local interstellar medium. ApJ 443:209–221

Backer DC (1970) Peculiar pulse burst in PSR 1237+25. Nature 228:1297–1298

Backer DC (1973) Pulsar Fluctuation Spectra and the Generalized Drifting-Subpulse Phenomenon. ApJ182:245–276. https://doi.org/10.1086/152134

Backer DC, Hellings RW (1986) Pulsar timing and general relativity. ARA&A 24:537–575

Backer DC, Rankin JM, Campbell DB (1975) Pulsar fluctuation spectra and the generalized drifting-subpulse phenomenon. II. ApJ197:481–487. https://doi.org/10.1086/153533

Backer DC, Kulkarni SR, Heiles C, et al (1982) A millisecond pulsar. Nature 300:615–618

Baglio MC, Coti Zelati F, Campana S, et al (2023) Matter ejections behind the highs and lows of the transitional millisecond pulsar PSR J1023+0038. A&A677:A30. https://doi.org/10.1051/0004-6361/202346418, arXiv:2305.14509 [astro-ph.HE]

Baker D, Brisken W, van Kerkwijk MH, et al (2023) High-resolution VLBI astrometry of pulsar scintillation screens with the θ - θ transform. MNRAS 525(1):211–220. https://doi.org/10.1093/mnras/stad2318, arXiv:2212.01417 [astro-ph.IM]

Bannister KW, Stevens J, Tuntsov AV, et al (2016) Real-time detection of an extreme scattering event: Constraints on galactic plasma lenses. Science 351(6271):354–356. https://doi.org/10.1126/science.aac7673, URL https://www.science.org/doi/abs/10.1126/science.aac7673, https://www.science.org/doi/pdf/10.1126/science.aac7673

Bartel N, Morris D, Sieber W, et al (1982) The mode-switching phenomenon in pulsars. ApJ 258:776–789

Basu A, Shaw B, Antonopoulou D, et al (2022) The Jodrell bank glitch catalogue: 106 new rotational glitches in 70 pulsars. MNRAS510(3):4049–4062. https://doi.org/10.1093/mnras/stab3336, arXiv:2111.06835 [astro-ph.HE]

Basu R, Mitra D, Melikidze GI, et al (2019) Classification of subpulse drifting in pulsars. MNRAS482(3):3757–3788. https://doi.org/10.1093/mnras/sty2846, 1810.08423

Bell JF, Bailes M, Manchester RN, et al (1997) Timing measurements and their implications for four binary millisecond pulsars. MNRAS 286:463–469

Bertotti B, Carr BJ, Rees MJ (1983) Limits from the timing of pulsars on the cosmic gravitational wave background. MNRAS 203:945–954

Bhat B, Keith MJ, Carli E, et al (2026a) Time-correlated profile variability in the MeerKAT Pulsar Timing Array. MNRAS552(2):stag1715. https://doi.org/10.1093/mnras/stag1715, arXiv:2609.09919

Bhat B, Keith MJ, Cognard I, et al (2026b) A glitch in the millisecond pulsar J0900−3144. MNRAS545(1):staf2034. https://doi.org/10.1093/mnras/staf2034, 2511.11336

Bhat NDR, Cordes JM, Chatterjee S (2003) A CLEAN-based Method for Deconvolving Interstellar Pulse Broadening from Radio Pulses. ApJ 584:782–790

Bhat NDR, Cordes JM, Camilo F, et al (2004) Multifrequency Observations of Radio Pulse Broadening and Constraints on Interstellar Electron Density Microstructure. ApJ605(2):759–783. https://doi.org/10.1086/382680, arXiv:astro-ph/0401067 [astro-ph]

Biggs JD (1992) An analysis of radio pulsar nulling statistics. ApJ 394:574–580

Bilitza D, Pezzopane M, Truhlik V, et al (2022) The international reference ionosphere model: A review and description of an ionospheric benchmark. Reviews of Geophysics 60(4):e2022RG000792. https://doi.org/https://doi.org/10.1029/2022RG000792, URL https://agupubs.onlinelibrary.wiley.com/doi/abs/10.1029/2022RG000792, e2022RG000792 2022RG000792, https://agupubs.onlinelibrary.wiley.com/doi/pdf/10.1029/2022RG000792

Blandford R, Teukolsky SA (1976) Arrival-time analysis for a pulsar in a binary system. ApJ 205:580–591

Blandford R, Narayan R, Romani RW (1984) Arrival Time Analysis for a Millisecond Pulsar. Journal of Astrophysics and Astronomy 5(4):369–388. https://doi.org/10.1007/BF02714466

Blaskiewicz MM (1991) Observational Constraints on Pulsars: Location of the Emission Region and Pulse Shape Stability on Decade Time Scales. PhD thesis, Cornell University, New York

Bochenek C, Ransom S, Demorest P (2015) The Feasibility of Using Black Widow Pulsars in Pulsar Timing Arrays for Gravitational Wave Detection. ApJL813(1):L4. https://doi.org/10.1088/2041-8205/813/1/L4, 1509.06662

Bondonneau L, Theureau G, Cognard I (2018) Pulsar observations with NenuFAR. In: Di Matteo P, Billebaud F, Herpin F, et al (eds) SF2A-2018: Proceedings of the Annual meeting of the French Society of Astronomy and Astrophysics, p Di

Bondonneau L, Grießmeier JM, Theureau G, et al (2021) Pulsars with NenuFAR: Backend and pipelines. A&A652:A34. https://doi.org/10.1051/0004-6361/202039339, 2009.02076

Borovsky JE (2020) Plasma and magnetic-field structure of the solar wind at inertial-range scale sizes discerned from statistical examinations of the time-series measurements. Frontiers in Astronomy and Space Sciences 7. https://doi.org/10.3389/fspas.2020.00020, URL https://www.frontiersin.org/articles/10.3389/fspas.2020.00020

Bower GC, Deller A, Demorest P, et al (2014) The Angular Broadening of the Galactic Center Pulsar SGR J1745-29: A New Constraint on the Scattering Medium. ApJL 780(1):L2. https://doi.org/10.1088/2041-8205/780/1/L2, arXiv:1309.4672 [astro-ph.GA]

Bower GC, Deller AT, Demorest PB, et al (2025) Long-term Astrometric Monitoring of the Galactic Center Magnetar PSR J1745−2900. ApJ988(2):168. https://doi.org/10.3847/1538-4357/ade0be, 2506.02348

Boynton PE, Groth EJ, Hutchinson DP, et al (1972) Optical Timing of the Crab Pulsar, NP 0532. ApJ175:217. https://doi.org/10.1086/151550

Brisken WF, Macquart JP, Gao JJ, et al (2010) 100 micro arcsec resolution vlbi imaging of anisotropic interstellar scattering toward pulsar b0834+06. ApJ 708(1):232–243. https://doi.org/10.1088/0004-637X/708/1/232, URL https://doi.org/10.1088/0004-637X/708/1/232, arXiv:0910.5654 [astro-ph.GA]

Britton MC (2000) Radio astronomical polarimetry and the lorentz group. ApJ532(2):1240–1244. https://doi.org/10.1086/308595, arXiv:astro-ph/9911101 [astro-ph]

Brook PR, Karastergiou A, McLaughlin MA, et al (2018) The NANOGrav 11-year Data Set: Pulse Profile Variability. ApJ868(2):122. https://doi.org/10.3847/1538-4357/aae9e3, arXiv:1810.08269 [astro-ph.HE]

Chakrabarti S, Chang P, Profumo S, et al (2026) Constraints on a dark matter subhalo near the sun from pulsar timing. Phys Rev Lett 136:041201. https://doi.org/10.1103/29xz-nt5z, URL https://link.aps.org/doi/10.1103/29xz-nt5z

Chalumeau A, Babak S, Petiteau A, et al (2022) Noise analysis in the European Pulsar Timing Array data release 2 and its implications on the gravitational-wave background search. MNRAS509(4):5538–5558. https://doi.org/10.1093/mnras/stab3283, 2111.05186

Charlot P, Jacobs CS, Gordon D, et al (2020) The third realization of the International Celestial Reference Frame by very long baseline interferometry. A&A644:A159. https://doi.org/10.1051/0004-6361/202038368, arXiv:2010.13625 [astro-ph.GA]

Chepurnov A, Lazarian A (2010) Extending the Big Power Law in the Sky with Turbulence Spectra from Wisconsin Hα Mapper Data. ApJ 710(1):853–858. https://doi.org/10.1088/0004-637X/710/1/853, arXiv:0905.4413 [astro-ph.GA]

Clegg AW, Fey AL, Lazio TJW (1998) The Gaussian Plasma Lens in Astrophysics: Refraction. ApJ496(1):253–266. https://doi.org/10.1086/305344, astro-ph/9709249

Codona JL, Creamer DB, Flatté SM, et al (1986) Two-frequency intensity cross-spectrum. Radio Science 21(5):805–814. https://doi.org/10.1029/RS021i005p00805, URL http:https://doi.org/10.1029/RS021i005p00805

Cognard I, Backer DC (2004) A Microglitch in the Millisecond Pulsar PSR B1821-24 in M28. ApJL612:L125–L127. https://doi.org/10.1086/424692, arXiv:astro-ph/0407546

Cognard I, Bourgois G, Lestrade JF, et al (1993) An extreme scattering event in the direction of the millisecond pulsar 1937 + 21. Nature366(6453):320–322. https://doi.org/10.1038/366320a0

Coles W, Hobbs G, Champion DJ, et al (2011) Pulsar timing analysis in the presence of correlated noise. mnras 418:561–570. https://doi.org/10.1111/j.1365-2966.2011.19505.x, arXiv:1107.5366 [astro-ph.IM]

Coles WA, Frehlich RG, Rickett BJ, et al (1987) Refractive Scintillation in the Interstellar Medium. ApJ315:666. https://doi.org/10.1086/165168

Coles WA, Kerr M, Shannon RM, et al (2015) Pulsar Observations of Extreme Scattering Events. ApJ808:113. https://doi.org/10.1088/0004-637X/808/2/113, arXiv:1506.07948 [astro-ph.SR]

Conway RG, Kronberg PP (1969) Interferometric measurement of polarization distributions in radio sources. MNRAS 142:11–32

Cordes JM (1976) Pulsar radiation as polarized shot noise. ApJ 210:780–791

Cordes JM (1978) Observational limits on the location of pulsar emission regions. ApJ222:1006–1011. https://doi.org/10.1086/156218

Cordes JM (1986) Space velocities of radio pulsars from interstellar scintillations. ApJ 311:183–196

Cordes JM (2013) Pulsar State Switching from Markov Transitions and Stochastic Resonance. ApJ775(1):47. https://doi.org/10.1088/0004-637X/775/1/47, arXiv:1304.5803 [astro-ph.HE]

Cordes JM, Greenstein G (1981) Pulsar Timing IV. Physical models for timing noise processes. ApJ245:1060–1079

Cordes JM, Hankins TH (1977) Pulsar polarization fluctuations at 430 MHz with microsecond time resolution. ApJ218:484–503. https://doi.org/10.1086/155702

Cordes JM, Hankins TH (1979) Frequency structure of micropulses from pulsar PSR 0950+08. ApJ 233:981–986

Cordes JM, Helfand DJ (1980) Pulsar timing III. Timing noise of 50 pulsars. ApJ 239:640–650

Cordes JM, Lazio TJ (1991) Interstellar scattering effects on the detection of narrow band signals. ApJ 376:123–134

Cordes JM, Lazio TJW (2001) Anomalous Radio-Wave Scattering from Interstellar Plasma Structures. ApJ549(2):997–1010. https://doi.org/10.1086/319442, arXiv:astro-ph/0005493 [astro-ph]

Cordes JM, Lazio TJW (2002) NE2001.I. A New Model for the Galactic Distribution of Free Electrons and its Fluctuations. arXiv e-prints astro-ph/0207156. https://doi.org/10.48550/arXiv.astro-ph/0207156, arXiv:astro-ph/0207156 [astro-ph]

Cordes JM, McLaughlin MA (2003) Searches for fast radio transients. ApJ 596:1142–1154

Cordes JM, Rickett BJ (1998) Diffractive Interstellar Scintillation Timescales and Velocities. ApJ 507:846–860

Cordes JM, Shannon RM (2010) A Measurement Model for Precision Pulsar Timing. arXiv:10103785 arXiv:1010.3785

Cordes JM, Stinebring DR (1984) Multifrequency timing measurements on the millisecond pulsar PSR 1937+214. ApJL277:L53–L56. https://doi.org/10.1086/184201

Cordes JM, Wasserman I (2016) Supergiant pulses from extragalactic neutron stars. MNRAS457:232–257. https://doi.org/10.1093/mnras/stv2948, arXiv:1501.00753 [astro-ph.HE]

Cordes JM, Wolszczan A (1986) Multiple imaging of pulsars by refraction in the interstellar medium. ApJL 307:L27–L32

Cordes JM, Weisberg JM, Boriakoff V (1985) Small–scale electron density turbulence in the interstellar medium. ApJ 288:221–247

Cordes JM, Downs GS, Krause-Polstorff J (1988) JPL pulsar timing observations. V - MACRO and microjumps in the VELA pulsar 0833-45. ApJ330:847–869. https://doi.org/10.1086/166518

Cordes JM, Wolszczan A, Dewey RJ, et al (1990) Timing and scintillations of the millisecond pulsar 1937+214. ApJ 349:245

Cordes JM, Weisberg JM, Frail DA, et al (1991) The Galactic distribution of free electrons. Nature 354:121–124

Cordes JM, Bhat NDR, Hankins TH, et al (2004a) The Brightest Pulses in the Universe: Multifrequency Observations of the Crab Pulsar's Giant Pulses. ApJ 612:375–388

Cordes JM, Kramer M, Lazio TJW, et al (2004b) Pulsars as tools for fundamental physics & astrophysics. NewAR48(11-12):1413–1438. https://doi.org/10.1016/j.newar.2004.09.040, arXiv:astro-ph/0505555 [astro-ph]

Cordes JM, Shannon RM, Stinebring DR (2016) Frequency-dependent dispersion measures and implications for pulsar timing. The Astrophysical Journal 817(1):16. URL http://stacks.iop.org/0004-637X/817/i=1/a=16

Cordes JM, Ocker SK, Chatterjee S (2022) Redshift Estimation and Constraints on Intergalactic and Interstellar Media from Dispersion and Scattering of Fast Radio Bursts. ApJ 931(2):88. https://doi.org/10.3847/1538-4357/ac6873, arXiv:2108.01172 [astro-ph.HE]

Cromartie HT, Fonseca E, Ransom SM, et al (2020) Relativistic Shapiro delay measurements of an extremely massive millisecond pulsar. Nature Astronomy 4:72–76. https://doi.org/10.1038/s41550-019-0880-2, arXiv:1904.06759 [astro-ph.HE]

Cronyn WM (1970) Interstellar Scattering of Pulsar Radiation and Its Effect on the Spectrum of NP0532. Science 168:1453–1455. https://doi.org/10.1126/science.168.3938.1453

Dai S, Hobbs G, Manchester RN, et al (2015) A study of multifrequency polarization pulse profiles of millisecond pulsars. MNRAS449(3):3223–3262. https://doi.org/10.1093/mnras/stv508, arXiv:1503.01841 [astro-ph.GA]

D'Alessandro F, McCulloch PM, Hamilton PA, et al (1995) The timing noise of 45 southern pulsars. MNRAS 277:1033–1046

D'Alessandro F, Deshpande AA, McCulloch PM (1997) Power Spectrum Analysis of the Timing Noise in 18 Southern Pulsars. Journal of Astrophysics and Astronomy 18(1):5–14. https://doi.org/10.1007/BF02714849

Damour T, Deruelle N (1986) General relativistic celestial mechanics of binary systems. II. The post-Newtonian timing formula. Ann Inst H Poincaré (Physique Théorique) 44:263–292

Davis MM, Taylor JH, Weisberg JM, et al (1985) High-precision timing observations of the millisecond pulsar PSR1937 + 21. Nature315(6020):547–550. https://doi.org/10.1038/315547a0

de Jager G, Lyne AG, Pointon L, et al (1968) Measurement of the Distance of Pulsar CP 0328. Nature 220(5163):128–129. https://doi.org/10.1038/220128a0

Deeter JE, Boynton PE (1982) Techniques for the estimation of red power spectra. I. Context and methodology. ApJ 261:337–350

Deller AT, Goss WM, Brisken WF, et al (2019) Microarcsecond VLBI Pulsar Astrometry with PSRπ II. Parallax Distances for 57 Pulsars. ApJ875(2):100. https://doi.org/10.3847/1538-4357/ab11c7, arXiv:1808.09046 [astro-ph.IM]

Demorest P, Lazio J, Lommen A, et al (2009) Gravitational Wave Astronomy Using Pulsars: Massive Black Hole Mergers & the Early Universe. In: astro2010: The Astronomy and Astrophysics Decadal Survey, p 64, https://doi.org/10.48550/arXiv.0902.2968, arXiv:0902.2968

Demorest PB (2007) Measuring the gravitational wave background using precision pulsar timing. PhD thesis, University of California, Berkeley

Demorest PB (2011) Cyclic spectral analysis of radio pulsars. MNRAS416(4):2821–2826. https://doi.org/10.1111/j.1365-2966.2011.19230.x, arXiv:1106.3345 [astro-ph.IM]

Demorest PB, Pennucci T, Ransom SM, et al (2010) A two-solar-mass neutron star measured using Shapiro delay. Nature467(7319):1081–1083. https://doi.org/10.1038/nature09466, arXiv:1010.5788 [astro-ph.HE]

Desai KM, Fey AL (2001) Anisotropic Interstellar Scattering toward the Cygnus Region. ApJS 133(2):395–411. https://doi.org/10.1086/320349

Desai S, Kahya E (2018) Galactic Shapiro delay to the Crab pulsar and limit on weak equivalence principle violation. European Physical Journal C 78(2):86. https://doi.org/10.1140/epjc/s10052-018-5571-0, arXiv:1612.02532 [astro-ph.HE]

Desai S, Kahya EO (2016) Galactic one-way Shapiro delay to PSR B1937+21. Modern Physics Letters A 31(13):1650083. https://doi.org/10.1142/S0217732316500838, arXiv:1510.08228 [astro-ph.GA]

Detweiler S (1979) Pulsar timing measurements and the search for gravitational waves. ApJ 234:1100

Dey L, McLaughlin MA, Wahl HM, et al (2024) Exploring Pulsar Timing Precision: A Comparative Study of Polarization Calibration Methods for NANOGrav Data from the Green Bank Telescope. ApJ977(1):114. https://doi.org/10.3847/1538-4357/ad8c24, arXiv:2406.13463 [astro-ph.HE]

Dickey JM, Weisberg JM, Rankin JM, et al (1981) Statistics of neutral hydrogen absorption toward pulsars. A&A 101:332–341

Ding H, Deller AT, Stappers BW, et al (2023) The MSPSRπ catalogue: VLBA astrometry of 18 millisecond pulsars. MNRAS519(4):4982–5007. https://doi.org/10.1093/mnras/stac3725, arXiv:2212.06351 [astro-ph.HE]

Dohnanyi JS (1969) Collisional Model of Asteroids and Their Debris. J. Geophys. Res.74:2531–2554. https://doi.org/10.1029/JB074i010p02531

Dolch T, Lam MT, Cordes J, et al (2014) A 24 Hr Global Campaign to Assess Precision Timing of the Millisecond Pulsar J1713+0747. ApJ794(1):21. https://doi.org/10.1088/0004-637X/794/1/21, arXiv:1408.1694 [astro-ph.HE]

Dolch T, Stinebring DR, Jones G, et al (2021) Deconvolving Pulsar Signals with Cyclic Spectroscopy: A Systematic Evaluation. ApJ913(2):98. https://doi.org/10.3847/1538-4357/abf48b, arXiv:2008.10562 [astro-ph.HE]

Donner JY, Verbiest JPW, Tiburzi C, et al (2019) First detection of frequency-dependent, time-variable dispersion measures. A&A624:A22. https://doi.org/10.1051/0004-6361/201834059, arXiv:1902.03814 [astro-ph.GA]

Donner JY, Verbiest JPW, Tiburzi C, et al (2020) Dispersion measure variability for 36 millisecond pulsars at 150 MHz with LOFAR. A&A644:A153. https://doi.org/10.1051/0004-6361/202039517, 2011.13742

Doroshenko OV, Kopeikin SM (1990) High Precision Pulse Timing for Single Pulsars. Soviet Ast.34:496

Downs GS, Krause-Polstorff J (1986) JPL Pulsar Timing Observations. IV. Excess Phase Noise. ApJS62:81. https://doi.org/10.1086/191134

Downs GS, Reichley PE (1983) JPL pulsar timing observations. II. Geocentric arrival times. ApJS53:169–240. https://doi.org/10.1086/190890

Downs GS, Reichley PE (1983) JPL pulsar timing observations. II. Geocentric arrival times. ApJS 53:169–240

Draine BT (2011) Physics of the Interstellar and Intergalactic Medium. Princeton University Press

Edwards RT, Stappers BW (2003) Pulse-to-pulse intensity modulation and drifting subpulses in recycled pulsars. A&A 407:273–287

Edwards RT, Hobbs GB, Manchester RN (2006) TEMPO2, a new pulsar timing package - II. The timing model and precision estimates. MNRAS 372(4):1549–1574. https://doi.org/10.1111/j.1365-2966.2006.10870.x, astro-ph/0607664

EPTA Collaboration, InPTA Collaboration, Antoniadis J, et al (2023) The second data release from the European Pulsar Timing Array. II. Customised pulsar noise models for spatially correlated gravitational waves. A&A678:A49. https://doi.org/10.1051/0004-6361/202346842, arXiv:2306.16225 [astro-ph.HE]

EPTA Collaboration and InPTA Collaboration, Antoniadis, J., Arumugam, P., et al (2023) The second data release from the european pulsar timing array - iii. search for gravitational wave signals. A&A 678:A50. https://doi.org/10.1051/0004-6361/202346844, URL https://doi.org/10.1051/0004-6361/202346844

Evgenievich Rodin A (2024) Pulsar Astrometry in the Presence of Low Frequency Noise. arXiv e-prints arXiv:2401.13373. https://doi.org/10.48550/arXiv.2401.13373, arXiv:2401.13373 [astro-ph.IM]

Eya IO, Urama JO, Chukwude AE (2017) Angular momentum transfer and fractional moment of inertia in pulsar glitches. The Astrophysical Journal 840(1):56. https://doi.org/10.3847/1538-4357/aa6b55, URL https://doi.org/10.3847/1538-4357/aa6b55

Fiedler RL, Dennison B, Johnston KJ, et al (1987) Extreme scattering events caused by compact structures in the interstellar medium. Nature326(6114):675–678. https://doi.org/10.1038/326675a0

Filothodoros A, Lewandowski W, Kijak J, et al (2024) Observations of interstellar scattering of six pulsars using polish lofar station pl611. Monthly Notices of the Royal Astronomical Society 528(4):5667–5678. https://doi.org/10.1093/mnras/stae399, URL https://doi.org/10.1093/mnras/stae399, https://academic.oup.com/mnras/article-pdf/528/4/5667/56686431/stae399.pdf

Fisher R, Butterworth EM, Rajwade KM, et al (2024) Radio pulse profile evolution of magnetar Swift J1818.0-1607. MNRAS528(2):3833–3843. https://doi.org/10.1093/mnras/stae271, arXiv:2401.12909 [astro-ph.HE]

Fomalont E, Kopeikin S, Lanyi G, et al (2009) Progress in measurements of the gravitational bending of radio waves using the vlba. The Astrophysical Journal 699(2):1395. https://doi.org/10.1088/0004-637X/699/2/1395, URL https://doi.org/10.1088/0004-637X/699/2/1395

Foster RS, Backer DC (1990) Constructing a pulsar timing array. ApJ 361:300

Foster RS, Cordes JM (1990) Interstellar propagation effects and the precision of pulsar timing. ApJ 364:123–135

Frail DA, Cordes JM, Hankins TH, et al (1991) H i Absorption Measurements toward 15 Pulsars and the Radial Distribution of Diffuse Ionized Gas in the Galaxy. ApJ 382:168. https://doi.org/10.1086/170705

Frail DA, Diamond PJ, Cordes JM, et al (1994) Anisotropic Scattering of OH/IR Stars toward the Galactic Center. ApJL 427:L43. https://doi.org/10.1086/187360, arXiv:astro-ph/9402018 [astro-ph]

Gardner WA (1991) Exploitation of spectral redundancy in cyclostationary signals. IEEE Signal Processing Magazine 8:14–36. https://doi.org/10.1109/79.81007

Geiger A, Cordes JM, Lam MT, et al (2025) The NANOGrav 12.5 yr Data Set: Probing Interstellar Turbulence and Precision Pulsar Timing with PSR J1903+0327. ApJ986(2):191. https://doi.org/10.3847/1538-4357/add0b6, arXiv:2411.08191 [astro-ph.HE]

Gentile PA, McLaughlin MA, Demorest PB, et al (2018) The nanograv 11 yr data set: Arecibo observatory polarimetry and pulse microcomponents. The Astrophysical Journal 862(1):47. https://doi.org/10.3847/1538-4357/aac9c9, URL https://dx.doi.org/10.3847/1538-4357/aac9c9

Geyer M, Karastergiou A (2016) The frequency dependence of scattering imprints on pulsar observations. MNRAS462(3):2587–2602. https://doi.org/10.1093/mnras/stw1724, 1607.04994

Geyer M, Karastergiou A, Kondratiev VI, et al (2017) Scattering analysis of LOFAR pulsar observations. MNRAS470(3):2659–2679. https://doi.org/10.1093/mnras/stx1151, arXiv:1706.04205 [astro-ph.HE]

Gitika P, Bailes M, Shannon RM, et al (2023) Flux density monitoring of 89 millisecond pulsars with MeerKAT. MNRAS526(3):3370–3385. https://doi.org/10.1093/mnras/stad2841, 2309.07564

Golat S, Contaldi CR (2021) Geodesic noise and gravitational wave observations by pulsar timing arrays. Physics Letters B 818:136381. https://doi.org/https://doi.org/10.1016/j.physletb.2021.136381, URL https://www.sciencedirect.com/science/article/pii/S037026932100321X

Goldreich P, Sridhar S (1995) Toward a Theory of Interstellar Turbulence. II. Strong Alfvenic Turbulence. ApJ438:763. https://doi.org/10.1086/175121

Goodman JW (1985) Statistical optics. Wiley-Interscience

Goździewski K, Konacki M, Wolszczan A (2005) Long-Term Stability and Dynamical Environment of the PSR 1257+12 Planetary System. ApJ619(2):1084–1097. https://doi.org/10.1086/426775, astro-ph/0310750

Groth EJ (1975) Timing of the Crab pulsar II. Method of analysis. ApJS 29:443–451

Guillemot L, van Straten W, Cognard I, et al (2025) The polarimetric response of the Nançay Radio Telescope and its impact on precision pulsar timing. A&A699:A104. https://doi.org/10.1051/0004-6361/202553929, arXiv:2505.04990 [astro-ph.HE]

Han D, Kim YS, Noz ME (1997) Stokes parameters as a minkowskian four-vector. Phys Rev E 56:6065–6076. https://doi.org/10.1103/PhysRevE.56.6065, URL https://link.aps.org/doi/10.1103/PhysRevE.56.6065

Hankins TH (1971) Microsecond Intensity Variations in the Radio Emissions from CP 0950. ApJ169:487. https://doi.org/10.1086/151164

Hankins TH, Eilek JA (2007) Radio Emission Signatures in the Crab Pulsar. ApJ 670:693–701. https://doi.org/10.1086/522362, arXiv:0708.2505

Hankins TH, Rankin JM (2009) Arecibo multi-frequency time-aligned pulsar average-profile and polarization database. The Astronomical Journal 139(1):168. https://doi.org/10.1088/0004-6256/139/1/168, URL https://dx.doi.org/10.1088/0004-6256/139/1/168

Hankins TH, Rickett BJ (1975) Pulsar signal processing. In: Methods in Computational Physics Volume 14 — Radio Astronomy. Academic Press, New York, pp 55–129

Hankins TH, Rickett BJ (1986) Frequency dependence of pulsar profiles. ApJ 311:684–693

Hankins TH, Kern JS, Weatherall JC, et al (2003) Nanosecond radio bursts from strong plasma turbulence in the Crab pulsar. Nature422(6928):141–143. https://doi.org/10.1038/nature01477

Hartnett JG, Luiten AN (2011) Colloquium: Comparison of astrophysical and terrestrial frequency standards. Reviews of Modern Physics 83(1):1–9. https://doi.org/10.1103/RevModPhys.83.1, 1004.0115

Hassall TE, Stappers BW, Hessels JWT, et al (2012) Wide-band simultaneous observations of pulsars: disentangling dispersion measure and profile variations. A&A543:A66. https://doi.org/10.1051/0004-6361/201218970, URL https://doi.org/10.1051/0004-6361/201218970, arXiv:1204.3864 [astro-ph.HE]

Hazboun JS, Simon J, Madison DR, et al (2022) Bayesian Solar Wind Modeling with Pulsar Timing Arrays. ApJ929(1):39. https://doi.org/10.3847/1538-4357/ac5829, arXiv:2111.09361 [astro-ph.SR]

Heavner T, Jefferts S, Donley E, et al (2005) Recent improvements in nist-f1 and a resulting accuracy of /spl delta/f/f=0.61/spl times/10/sup -15/. IEEE Transactions on Instrumentation and Measurement 54(2):842–845. https://doi.org/10.1109/TIM.2005.843812

Heiles C (2002) A Heuristic Introduction to Radioastronomical Polarization. In: Stanimirovic S, Altschuler D, Goldsmith P, et al (eds) Single-Dish Radio Astronomy: Techniques and Applications, pp 131–152, https://doi.org/10.48550/arXiv.astro-ph/0107327, arXiv:astro-ph/0107327

Heiles C, Perillat P, Nolan M, et al (2001) Mueller Matrix Parameters for Radio Telescopes and Their Observational Determination. PASP113(788):1274–1288. https://doi.org/10.1086/323289, arXiv:astro-ph/0107352 [astro-ph]

Helfand DJ, Manchester RN, Taylor JH (1975) Observations of pulsar radio emission. III. Stability of integrated profiles. ApJ 198:661–670

Hellings RW, Downs GS (1983) Upper limits on the isotropic gravitational radiation background from pulsar timing analysis. ApJL 265:L39

Hemberger DA, Stinebring DR (2008) Time Variability of Interstellar Scattering and Improvements to Pulsar Timing. apj 674:L37–L40

Hewish A, Wolszczan A, Graham DA (1985) Quasi-periodic scintillation patterns of the pulsars PSR 1133+16 and PSR 1642-03. MNRAS213:167–179. https://doi.org/10.1093/mnras/213.2.167

Hill AS, Stinebring DR, Asplund CT, et al (2005) Deflection of Pulsar Signal Reveals Compact Structures in the Galaxy. ApJL 619:L171–L174. https://doi.org/10.1086/428347, arXiv:astro-ph/0411752

Hobbs G, Lyne AG, Kramer M, et al (2004) Long-term timing observations of 374 pulsars. MNRAS353(4):1311–1344. https://doi.org/10.1111/j.1365-2966.2004.08157.x

Hobbs G, Archibald A, Arzoumanian Z, et al (2010) The International Pulsar Timing Array project: using pulsars as a gravitational wave detector. Classical and Quantum Gravity 27(8):084013. https://doi.org/10.1088/0264-9381/27/8/084013, arXiv:0911.5206 [astro-ph.SR]

Hobbs G, Lyne AG, Kramer M (2010) An analysis of the timing irregularities for 366 pulsars. Monthly Notices of the Royal Astronomical Society 402(2):1027–1048. https://doi.org/10.1111/j.1365-2966.2009.15938.x, URL https://doi.org/10.1111/j.1365-2966.2009.15938.x, https://academic.oup.com/mnras/article-pdf/402/2/1027/3854281/mnras0402-1027.pdf

Hobbs GB, Bailes M, Bhat NDR, et al (2009) Gravitational-Wave Detection Using Pulsars: Status of the Parkes Pulsar Timing Array Project. PASA 26:103–109. https://doi.org/10.1071/AS08023, arXiv:0812.2721

Hosokawa M, Ohnishi K, Fukushima T (1999) Uncertainty of pulsar time scale due to the gravitational time delay of intervening stars and MACHOs. A&A351:393–397

Iraci F, Chalumeau A, Tiburzi C, et al (2024) Pulsar timing methods for evaluating dispersion measure time series. A&A692:A170. https://doi.org/10.1051/0004-6361/202450740, arXiv:2410.22170 [astro-ph.HE]

Ishimaru A (1979) Pulse propagation, scattering, and diffusion in scatterers and turbulence. Radio Science 14(2):269–276. https://doi.org/10.1029/RS014i002p00269

Jacobson-Bell B, Cordes JM, Chatterjee S, et al (2026) The NANOGrav 15 yr and 20 yr Datasets: Timing Events and Pulse Shape Changes. arXiv e-prints arXiv:2604.05453. https://doi.org/10.48550/arXiv.2604.05453, 2604.05453

Jaffe AH, Backer DC (2003) Gravitational waves probe the coalescence rate of massive black hole binaries. ApJ 583:616–631

Jenet FA, Anderson SB, Prince TA (2001) Single-Pulse Characteristics of the Millisecond Radio Pulsar PSR B1937+21 at 430 MHZ. ApJ 546:394–400

Jenet FA, Hobbs GB, Lee KJ, et al (2005) Detecting the Stochastic Gravitational Wave Background Using Pulsar Timing. ApJL 625:L123–L126

Jenet FA, Hobbs GB, van Straten W, et al (2006) Upper Bounds on the Low-Frequency Stochastic Gravitational Wave Background from Pulsar Timing Observations: Current Limits and Future Prospects. ApJ 653:1571–1576. https://doi.org/10.1086/508702

Jenet FA, Armstrong JW, Tinto M (2011) Pulsar timing sensitivity to very-low-frequency gravitational waves. PhRvD83(8):081301. https://doi.org/10.1103/PhysRevD.83.081301, arXiv:1101.3759 [gr-qc]

Jennings RJ (2021) Testing the limits of precision pulsar timing for gravitational wave detection. PhD thesis, Cornell University

Jennings RJ, Cordes JM, Chatterjee S (2020) Pulsar Timing Signatures of Circumbinary Asteroid Belts. ApJ 904(2):191. https://doi.org/10.3847/1538-4357/abc178, arXiv:2007.10388 [astro-ph.HE]

Jennings RJ, Cordes JM, Chatterjee S (2024a) Characterizing the effects of pulse shape changes on pulsar timing precision. arXiv e-prints arXiv:2411.00236. https://doi.org/10.48550/arXiv.2411.00236, arXiv:2411.00236 [astro-ph.HE]

Jennings RJ, Cordes JM, Chatterjee S, et al (2024b) An Unusual Pulse Shape Change Event in PSR J1713+0747 Observed with the Green Bank Telescope and CHIME. ApJ964(2):179. https://doi.org/10.3847/1538-4357/ad2930, arXiv:2210.12266 [astro-ph.HE]

Jensen EA, Heiles C, Wexler D, et al (2018) Plasma interactions with the space environment in the acceleration region: Indications of cme-trailing reconnection regions. The Astrophysical Journal 861(2):118. https://doi.org/10.3847/1538-4357/aac5dd, URL https://dx.doi.org/10.3847/1538-4357/aac5dd

Johnston S, Lower ME (2021) A supernova remnant association for the fast-moving pulsar PSR J0908-4913. MNRAS507(1):L41–L45. https://doi.org/10.1093/mnrasl/slab092, arXiv:2108.09827 [astro-ph.HE]

Jokipii JR (1988) Cosmic rays and the physics of interstellar turbulence. In: Cordes JM, Rickett BJ, Backer DC (eds) Radio Wave Scattering in the Interstellar Medium, pp 48–59, https://doi.org/10.1063/1.37599

Jones ML, McLaughlin MA, Lam MT, et al (2017) The NANOGrav Nine-year Data Set: Measurement and Analysis of Variations in Dispersion Measures. ApJ841(2):125. https://doi.org/10.3847/1538-4357/aa73df, arXiv:1612.03187 [astro-ph.HE]

Jones ML, McLaughlin MA, Roy J, et al (2021) Evaluating Low-frequency Pulsar Observations to Monitor Dispersion with the Giant Metrewave Radio Telescope. ApJ915(1):15. https://doi.org/10.3847/1538-4357/abfdc5, arXiv:2009.08409 [astro-ph.HE]

Kachelrieß M, Mikalsen V (2025) Galactic distribution of supernovae and OB associations. Computer Physics Communications 311:109537. https://doi.org/10.1016/j.cpc.2025.109537, 2409.07124

Kaplan DE, Mitridate A, Trickle T (2022) Constraining fundamental constant variations from ultralight dark matter with pulsar timing arrays. Physical Review D 106(3). https://doi.org/10.1103/physrevd.106.035032, URL https://doi.org/10.1103%2Fphysrevd.106.035032

Kaspi VM, Stinebring DR (1992) Long-Term Pulsar Flux Monitoring and Refractive Interstellar Scintillation. ApJ392:530. https://doi.org/10.1086/171454

Kaspi VM, Taylor JH, Ryba M (1994) High-precision timing of millisecond pulsars. III. Long-term monitoring of PSRs B1855+09 and B1937+21. ApJ 428:713–728

Kaur D, Ramesh Bhat ND, Dai S, et al (2022) Detection of Frequency-dependent Dispersion Measure toward the Millisecond Pulsar J2241-5236 from Contemporaneous Wideband Observations. ApJL930(2):L27. https://doi.org/10.3847/2041-8213/ac64ff, arXiv:2204.07973 [astro-ph.HE]

Keith MJ, Niţu IC (2023) Impact of quasi-periodic and steep-spectrum timing noise on the measurement of pulsar timing parameters. MNRAS523(3):4603–4614. https://doi.org/10.1093/mnras/stad1713, arXiv:2306.03529 [astro-ph.HE]

Keith MJ, Coles W, Shannon RS, et al (2012) Measurement and correction of variations in interstellar dispersion in high precision pulsar timing. mnras 429:2161

Keith MJ, Spiewak R, Lyne AG, et al (2025) Measuring pulsar profile variations with 2D Gaussian process regression. MNRAS540(3):2486–2505. https://doi.org/10.1093/mnras/staf886, arXiv:2505.23413 [astro-ph.HE]

Kerr M, Coles WA, Ward CA, et al (2018) Extreme scattering events towards two young pulsars. MNRAS474(4):4637–4647. https://doi.org/10.1093/mnras/stx3101, arXiv:1712.00426 [astro-ph.HE]

Kirchner JW (2005) Aliasing in 1/ f^{α} noise spectra: Origins, consequences, and remedies. PhRvE71(6):066110. https://doi.org/10.1103/PhysRevE.71.066110

Kirsten F, Bhat NDR, Meyers BW, et al (2019) Probing Pulsar Scattering between 120 and 280 MHz with the MWA. ApJ874(2):179. https://doi.org/10.3847/1538-4357/ab0c05, arXiv:1903.02087 [astro-ph.HE]

Klibanov MV, Sacks PE, Tikhonravov AV (1995) The phase retrieval problem. Inverse Problems 11(1):1. https://doi.org/10.1088/0266-5611/11/1/001, URL https://dx.doi.org/10.1088/0266-5611/11/1/001

Kondratiev VI, Verbiest JPW, Hessels JWT, et al (2016) A LOFAR census of millisecond pulsars. A&A585:A128. https://doi.org/10.1051/0004-6361/201527178, arXiv:1508.02948 [astro-ph.HE]

Kooi JE, Wexler DB, Jensen EA, et al (2022) Modern faraday rotation studies to probe the solar wind. Frontiers in Astronomy and Space Sciences 9. https://doi.org/10.3389/fspas.2022.841866, URL https://www.frontiersin.org/articles/10.3389/fspas.2022.841866

Kopeikin SM (1997) Millisecond and binary pulsars as nature's frequency standards - I.A generalized statistical model of low-frequency timing noise. MNRAS288(1):129–137. https://doi.org/10.1093/mnras/288.1.129

Kopeikin SM, Schäfer G (1999) Lorentz covariant theory of light propagation in gravitational fields of arbitrary-moving bodies. Phys Rev D 60:124002. https://doi.org/10.1103/PhysRevD.60.124002, URL https://link.aps.org/doi/10.1103/PhysRevD.60.124002

Koryukova TA, Pushkarev AB, Kiehlmann S, et al (2023) Multiple imaging of the quasar 2005 + 403 formed by anisotropic scattering. MNRAS526(4):5932–5948. https://doi.org/10.1093/mnras/stad3052, arXiv:2308.15274 [astro-ph.GA]

Kramer M, Wielebinski R, Jessner A, et al (1994) Geometrical analysis of average pulsar profiles using multi-component gaussian fits at several frequencies. I. method and analysis. A&AS 107:515–526

Kramer M, Backer DC, Cordes JM, et al (2004) Strong-field tests of gravity using pulsars and black holes. NewAR48(11-12):993–1002. https://doi.org/10.1016/j.newar.2004.09.020, arXiv:astro-ph/0409379 [astro-ph]

Kramer M, Lyne AG, O'Brien JT, et al (2006) A Periodically Active Pulsar Giving Insight into Magnetospheric Physics. Science 312:549–551

Kramer M, Stairs IH, Manchester RN, et al (2021) Strong-Field Gravity Tests with the Double Pulsar. Physical Review X 11(4):041050. https://doi.org/10.1103/PhysRevX.11.041050, 2112.06795

Krzeszowski K, Mitra D, Gupta Y, et al (2009) On the aberration-retardation effects in pulsars. MNRAS393(4):1617–1624. https://doi.org/10.1111/j.1365-2966.2008.14287.x, 0901.4231

Kulkarni AD, Shannon RM, Reardon DJ, et al (2024) An insight into chromatic behaviour of jitter in pulsars and its modelling: a case study of PSR J0437-4715. MNRAS528(2):3658–3667. https://doi.org/10.1093/mnras/stae041, 2401.03660

Kumar P, Taylor GB, Stovall K, et al (2025) A Multifrequency Census of 100 Pulsars below 100 MHz with LWA: A Systematic Study of Flux Density, Spectra, Timing, Dispersion, Polarization, and Its Variation from a Decade of Observations. ApJ982(2):132. https://doi.org/10.3847/1538-4357/adb97a, arXiv:2501.11862 [astro-ph.HE]

Kuz'min AD, Izvekova VA (1993) Compensation of the pulse profiles of pulsars for interstellar scattering. MNRAS260:724–726. https://doi.org/10.1093/mnras/260.4.724

Lam MT (2021) Evidence for Multiple Pulse-shape Changes during the Third Chromatic Timing Event of PSR J1713 + 0747. Research Notes of the American Astronomical Society 5(7):167. https://doi.org/10.3847/2515-5172/ac1670

Lam MT, Cordes JM, Chatterjee S, et al (2015) Pulsar Timing Errors from Asynchronous Multi-frequency Sampling of Dispersion Measure Variations. ApJ801(2):130. https://doi.org/10.1088/0004-637X/801/2/130, arXiv:1411.1764 [astro-ph.HE]

Lam MT, Cordes JM, Chatterjee S, et al (2016a) The NANOGrav Nine-year Data Set: Noise Budget for Pulsar Arrival Times on Intraday Timescales. ApJ 819(2):155. https://doi.org/10.3847/0004-637X/819/2/155, arXiv:1512.08326 [astro-ph.IM]

Lam MT, Cordes JM, Chatterjee S, et al (2016b) Systematic and Stochastic Variations in Pulsar Dispersion Measures. ApJ821(1):66. https://doi.org/10.3847/0004-637X/821/1/66, arXiv:1512.02203 [astro-ph.HE]

Lam MT, Cordes JM, Chatterjee S, et al (2017) The NANOGrav Nine-year Data Set: Excess Noise in Millisecond Pulsar Arrival Times. ApJ834:35. https://doi.org/10.3847/1538-4357/834/1/35, arXiv:1610.01731 [astro-ph.HE]

Lam MT, Ellis JA, Grillo G, et al (2018a) A Second Chromatic Timing Event of Interstellar Origin toward PSR J1713+0747. ApJ861(2):132. https://doi.org/10.3847/1538-4357/aac770, arXiv:1712.03651 [astro-ph.HE]

Lam MT, McLaughlin MA, Cordes JM, et al (2018b) Optimal Frequency Ranges for Submicrosecond Precision Pulsar Timing. ApJ861(1):12. https://doi.org/10.3847/1538-4357/aac48d, arXiv:1710.02272 [astro-ph.HE]

Lam MT, Lazio TJW, Dolch T, et al (2020) On Frequency-dependent Dispersion Measures and Extreme Scattering Events. ApJ892(2):89. https://doi.org/10.3847/1538-4357/ab7b6b, arXiv:1903.00426 [astro-ph.HE]

Lambert HC, Rickett BJ (1999) On the Theory of Pulse Propagation and Two-Frequency Field Statistics in Irregular Interstellar Plasmas. apj 517:299–317

Lambert HC, Rickett BJ (2000) Radio Scintillation due to Discontinuities in the Interstellar Plasma Density. ApJ 531:883–901

Larsen B, Mingarelli CMF, Hazboun JS, et al (2024) The NANOGrav 15 yr Data Set: Chromatic Gaussian Process Noise Models for Six Pulsars. ApJ972(1):49. https://doi.org/10.3847/1538-4357/ad5291, arXiv:2405.14941 [astro-ph.HE]

Lattimer JM (2021) Neutron Stars and the Nuclear Matter Equation of State. Annual Review of Nuclear and Particle Science 71:433–464. https://doi.org/10.1146/annurev-nucl-102419-124827

Lazio TJW (2004) On the Enhanced Interstellar Scattering toward B1849+005. ApJ613(2):1023–1036. https://doi.org/10.1086/423261, arXiv:astro-ph/0406267 [astro-ph]

Lee KH, Lee LC (2019) Interstellar turbulence spectrum from in situ observations of Voyager 1. Nature Astronomy 3:154–159. https://doi.org/10.1038/s41550-018-0650-6

Lee LC, Jokipii JR (1975) Strong scintillations in astrophysics. II - A theory of temporal broadening of pulses. apj 201:532–543. https://doi.org/10.1086/153916

Lee LC, Jokipii JR (1976) The irregularity spectrum in interstellar space. ApJ 206:735–743

Lentati L, Kerr M, Dai S, et al (2017) Robust estimation of scattering in pulsar timing analysis. MNRAS 468(2):1474–1485. https://doi.org/10.1093/mnras/stx580, arXiv:1703.02108 [astro-ph.IM]

Lenz DD, Ayres TR (1992) Errors Associated with Fitting Gaussian Profiles to Noisy Emission-Line Spectra. PASP104:1104. https://doi.org/10.1086/133096

Lestrade J, Rickett BJ, I. C (1998) Interstellar modulation of the flux density and arrival time of pulses from pulsar b 1937+214. A&A 334:1068

Lewandowski W, Dembska M, Kijak J, et al (2013) Pulse broadening analysis for several new pulsars and anomalous scattering. Monthly Notices of the Royal Astronomical Society 434(1):69–83. https://doi.org/10.1093/mnras/stt989, URL https://doi.org/10.1093/mnras/stt989, https://academic.oup.com/mnras/article-pdf/434/1/69/18497796/stt989.pdf

Lewandowski W, Kowalińska M, Kijak J (2015) The analysis of the largest sample of multifrequency pulsar scatter time estimates. MNRAS 449(2):1570–1583. https://doi.org/10.1093/mnras/stv385, arXiv:1502.06330 [astro-ph.SR]

Lin FX, Lin HH, Luo J, et al (2021) Profile changes associated with dispersion measure events in PSR J1713+0747. MNRAS508(1):1115–1127. https://doi.org/10.1093/mnras/stab2529, arXiv:2106.09851 [astro-ph.HE]

Lin HH, Masui K, Pen UL, et al (2018) Improved pulsar timing via principal component mode tracking. MNRAS475(1):1323–1330. https://doi.org/10.1093/mnras/stx3239

Liu K, Keane EF, Lee KJ, et al (2012) Profile-shape stability and phase-jitter analyses of millisecond pulsars. MNRAS420(1):361–368. https://doi.org/10.1111/j.1365-2966.2011.20041.x, arXiv:1110.4759 [astro-ph.HE]

Liu K, Desvignes G, Cognard I, et al (2014) Measuring pulse times of arrival from broad-band pulsar observations. MNRAS443(4):3752–3760. https://doi.org/10.1093/mnras/stu1420, arXiv:1407.3827 [astro-ph.GA]

Liu N, Zhu Z, Antoniadis J, et al (2023) Systematics of planetary ephemeris reference frames inferred from pulsar timing astrometry. A&A674:A187. https://doi.org/10.1051/0004-6361/202245808, arXiv:2304.14677 [astro-ph.EP]

Liu Y, Verbiest JPW, Main RA, et al (2022) Long-term scintillation studies of epta pulsars: I. observations and basic results. Astronomy & Astrophysics 664:A116. https://doi.org/10.1051/0004-6361/202142552, URL http://dx.doi.org/10.1051/0004-6361/202142552

Löhmer O, Kramer M, Mitra D, et al (2001) Anomalous Scattering of Highly Dispersed Pulsars. ApJL562(2):L157–L161. https://doi.org/10.1086/338324, arXiv:astro-ph/0111165 [astro-ph]

Löhmer O, Mitra D, Gupta Y, et al (2004) The frequency evolution of interstellar pulse broadening from radio pulsars. A&A425:569–575. https://doi.org/10.1051/0004-6361:20035881, arXiv:astro-ph/0406601 [astro-ph]

Lommen AN, Backer DC (2001) Using Pulsars to Detect Massive Black Hole Binaries via Gravitational Radiation: Sagittarius A* and Nearby Galaxies. ApJ562(1):297–302. https://doi.org/10.1086/323491, arXiv:astro-ph/0107470 [astro-ph]

Lorimer D, Kramer M (2005) Handbook of Pulsar Astronomy. Cambridge Observing Handbooks for Research Astronomers, Cambridge University Press, URL https://books.google.com/books?id=OZ8tdN6qJcsC

Lower ME, Bailes M, Shannon RM, et al (2020) The UTMOST pulsar timing programme - II. Timing noise across the pulsar population. MNRAS494(1):228–245. https://doi.org/10.1093/mnras/staa615, arXiv:2002.12481 [astro-ph.HE]

Lyne A, Hobbs G, Kramer M, et al (2010) Switched Magnetospheric Regulation of Pulsar Spin-Down. Science 329(5990):408. https://doi.org/10.1126/science.1186683, arXiv:1006.5184 [astro-ph.GA]

Lyne A, Graham-Smith F, Weltevrede P, et al (2013) Evolution of the Magnetic Field Structure of the Crab Pulsar. Science 342(6158):598–601. https://doi.org/10.1126/science.1243254, arXiv:1311.0408 [astro-ph.HE]

Lyne AG (1971) Mode changing in pulsars. MNRAS 153:27P

Lyne AG, Thorne DJ (1975) Anomalous scattering in the Crab nebula. MNRAS 172:97–108. https://doi.org/10.1093/mnras/172.1.97

Lyne AG, Ritchings RT, Smith FG (1975) The period derivatives of pulsars. MNRAS171:579–597. https://doi.org/10.1093/mnras/171.3.579

Lyne AG, Manchester RN, Taylor JH (1985) The galactic population of pulsars. MNRAS213:613–639. https://doi.org/10.1093/mnras/213.3.613

Maciesiak K, Gil J, Melikidze G (2012) On the pulse-width statistics in radio pulsars - III. Importance of the conal profile components. MNRAS424(3):1762–1773. https://doi.org/10.1111/j.1365-2966.2012.21246.x, 1205.1297

Madison DR, Chatterjee S, Cordes JM (2013) The Benefits of VLBI Astrometry to Pulsar Timing Array Searches for Gravitational Radiation. ApJ777(2):104. https://doi.org/10.1088/0004-637X/777/2/104, arXiv:1210.2469 [astro-ph.HE]

Madison DR, Cordes JM, Arzoumanian Z, et al (2019) The NANOGrav 11 yr Data Set: Solar Wind Sounding through Pulsar Timing. ApJ872(2):150. https://doi.org/10.3847/1538-4357/ab01fd, arXiv:1808.07078 [astro-ph.SR]

Mahajan N, van Kerkwijk MH, Main R, et al (2018) Mode changing and giant pulses in the millisecond pulsar psr b1957+20. The Astrophysical Journal Letters 867(1):L2. https://doi.org/10.3847/2041-8213/aae713, URL https://dx.doi.org/10.3847/2041-8213/aae713

Main RA, Parthasarathy A, Johnston S, et al (2023) The Thousand Pulsar Array programme on MeerKAT - X. Scintillation arcs of 107 pulsars. MNRAS 518(1):1086–1097. https://doi.org/10.1093/mnras/stac3149, arXiv:2211.08471 [astro-ph.HE]

Maitia V, Lestrade JF, Cognard I (2003) A 3 Year Long Extreme Scattering Event in the Direction of the Millisecond Pulsar J1643-1224. apj 582:972–977. https://doi.org/10.1086/344816

Malins JB, White SM, Taylor GB, et al (2018) Modeling the Ionosphere with GPS and Rotation Measure Observations. Radio Science 53(6):724–738. https://doi.org/10.1029/2018RS006559, arXiv:1806.02802 [astro-ph.IM]

Mall G, Main RA, Antoniadis J, et al (2022) Modelling annual scintillation arc variations in PSR J1643-1224 using the Large European Array for Pulsars. MNRAS 511(1):1104–1114. https://doi.org/10.1093/mnras/stac096, arXiv:2201.04245 [astro-ph.HE]

Manchester RN, Johnston S (1995) Polarization properties of two pulsars. ApJL 441:L65–L68

Manchester RN, Hobbs GB, Teoh A, et al (2005) The Australia Telescope National Facility Pulsar Catalogue. AJ129(4):1993–2006. https://doi.org/10.1086/428488, arXiv:astro-ph/0412641 [astro-ph]

Matsakis DN, Taylor JH, Eubanks TM (1997) A statistic for describing pulsar and clock stabilities. A&A 326:924–928

Mauche CW, Gorenstein P (1986) Measurements of X-Ray Scattering from Interstellar Grains. ApJ302:371. https://doi.org/10.1086/163996

McKee JW, Janssen GH, Stappers BW, et al (2016) A glitch in the millisecond pulsar J0613-0200. MNRAS461(3):2809–2817. https://doi.org/10.1093/mnras/stw1442, arXiv:1606.04098 [astro-ph.HE]

McKee JW, Zhu H, Stinebring DR, et al (2022) Probing the Local Interstellar Medium with Scintillometry of the Bright Pulsar B1133 + 16. ApJ 927(1):99. https://doi.org/10.3847/1538-4357/ac460b, arXiv:2112.11980 [astro-ph.HE]

Medvedev M (2026) Theory of striped dynamic spectra of the Crab pulsar high-frequency interpulse. Journal of Plasma Physics 92(1):E22. https://doi.org/10.1017/S0022377826101214, 2602.16955

Melatos A (1997) Spin-down of an oblique rotator with a current starved outer magnetosphere. MNRAS 288:1049–1059

Middleton H, Shannon RM, Bailes M, et al (2025) A simple optimization for the MeerKAT pulsar timing array. MNRAS540(1):603–611. https://doi.org/10.1093/mnras/staf748, 2505.02524

Miles MT, Shannon RM, Bailes M, et al (2022) Mode changing in J1909 - 3744: the most precisely timed pulsar. MNRAS510(4):5908–5915. https://doi.org/10.1093/mnras/stab3549, 2112.00897

Miles MT, Shannon RM, Reardon DJ, et al (2025) The MeerKAT Pulsar Timing Array: the first search for gravitational waves with the MeerKAT radio telescope. MNRAS536(2):1489–1500. https://doi.org/10.1093/mnras/stae2571, 2412.01153

Miller MC, Lamb FK, Dittmann AJ, et al (2021) The Radius of PSR J0740+6620 from NICER and XMM-Newton Data. ApJL918(2):L28. https://doi.org/10.3847/2041-8213/ac089b, arXiv:2105.06979 [astro-ph.HE]

Mingarelli CMF, Casey-Clyde JA, Chang YT, et al (2026) Pulsar timing arrays: the emerging gravitational-wave landscape. arXiv e-prints arXiv:2603.13643. https://doi.org/10.48550/arXiv.2603.13643, arXiv:2603.13643 [astro-ph.HE]

Minter AH, Spangler SR (1996) Observation of turbulent fluctuations in the interstellar plasma density and magnetic field on spatial scales of 0.01 to 100 parsecs. ApJ 458:194–214

Misner CW, Thorne KS, Wheeler JA (1973) Gravitation. W.H. Freeman and Co.

Molnar LA, Mutel RL, Reid MJ, et al (1995) Interstellar Scattering toward Cygnus X-3: Measurements of Anisotrophy and of the Inner Scale. ApJ438:708. https://doi.org/10.1086/175115

Moore CJ, Cole RH, Berry CPL (2015) Gravitational-wave sensitivity curves. Classical and Quantum Gravity 32(1):015014. https://doi.org/10.1088/0264-9381/32/1/015014, arXiv:1408.0740 [gr-qc]

Moran JM, Rodriguez LF, Greene B, et al (1990) The Large Scattering Disk of NGC 6334B. ApJ348:147. https://doi.org/10.1086/168222

NANOGrav Collaboration, Arzoumanian Z, Brazier A, et al (2015) The NANOGrav Nine-year Data Set: Observations, Arrival Time Measurements, and Analysis of 37 Millisecond Pulsars. ApJ813(1):65. https://doi.org/10.1088/0004-637X/813/1/65, arXiv:1505.07540 [astro-ph.IM]

Narayan R, Goodman J (1989) The shape of a scatter-broadened image. I - Numerical simulations and physical principles. MNRAS238:963–1028

Nathan RS, Miles MT, Ashton G, et al (2023) Improving pulsar-timing solutions through dynamic pulse fitting. MNRAS523(3):4405–4412. https://doi.org/10.1093/mnras/stad1660, arXiv:2304.02793 [astro-ph.IM]

Ng C, Wu B, Ma M, et al (2020) The discovery of nulling and mode-switching pulsars with chime/pulsar. The Astrophysical Journal 903(2):81. https://doi.org/10.3847/1538-4357/abb94f, URL https://dx.doi.org/10.3847/1538-4357/abb94f

Nimmo K, Hessels JWT, Kirsten F, et al (2022) Burst timescales and luminosities as links between young pulsars and fast radio bursts. Nature Astronomy 6:393–401. https://doi.org/10.1038/s41550-021-01569-9, arXiv:2105.11446 [astro-ph.HE]

Nobleson K, Agarwal N, Girgaonkar R, et al (2022) Low-frequency wideband timing of InPTA pulsars observed with the uGMRT. MNRAS512(1):1234–1243. https://doi.org/10.1093/mnras/stac532, arXiv:2112.06908 [astro-ph.IM]

Ocker SK, Cordes JM (2026) NE2025: An Updated Electron Density Model for the Galactic Interstellar Medium. arXiv e-prints arXiv:2602.11838. https://doi.org/10.48550/arXiv.2602.11838, 2602.11838

Ocker SK, Cordes JM, Chatterjee S (2020) Electron Density Structure of the Local Galactic Disk. ApJ897(2):124. https://doi.org/10.3847/1538-4357/ab98f9

Ocker SK, Cordes JM, Chatterjee S, et al (2021a) An In Situ Study of Turbulence near Stellar Bow Shocks. ApJ922(2):233. https://doi.org/10.3847/1538-4357/ac2b28, 2107.10371

Ocker SK, Cordes JM, Chatterjee S, et al (2021b) Persistent plasma waves in interstellar space detected by Voyager 1. Nature Astronomy 5:761–765. https://doi.org/10.1038/s41550-021-01363-7, 2105.04000

Ocker SK, Cordes JM, Chatterjee S, et al (2024) Pulsar scintillation through thick and thin: bow shocks, bubbles, and the broader interstellar medium. MNRAS 527(3):7568–7587. https://doi.org/10.1093/mnras/stad3683, arXiv:2309.13809 [astro-ph.HE]

O'Neill NJ, Meyers PM, Melatos A (2024) Analysing radio pulsar timing noise with a Kalman filter: a demonstration involving PSR J1359-6038. MNRAS530(4):4648–4664. https://doi.org/10.1093/mnras/stae770, arXiv:2403.16467 [astro-ph.HE]

Oppenheim AV, Schafer RW, Buck JR (1999) Discrete-time signal processing / Alan V. Oppenheim, Ronald W. Schafer, with John R. Buck., second edition. edn. Prentice-Hall signal processing series, Prentice Hall, Upper Saddle River, N.J

Osłowski S, van Straten W, Hobbs GB, et al (2011) High signal-to-noise ratio observations and the ultimate limits of precision pulsar timing. MNRAS418(2):1258–1271. https://doi.org/10.1111/j.1365-2966.2011.19578.x, arXiv:1108.0812 [astro-ph.GA]

Osłowski S, van Straten W, Demorest P, et al (2013) Improving the precision of pulsar timing through polarization statistics. MNRAS430(1):416–424. https://doi.org/10.1093/mnras/sts662, arXiv:1301.2374 [astro-ph.IM]

Ostashov VE, Shishov VI (1978) Pulse shape of a pulsar scattered in the interstellar medium. Radiophysics and Quantum Electronics 20(6):581–585. https://doi.org/10.1007/BF01033759

Özel F, Freire P (2016) Masses, Radii, and the Equation of State of Neutron Stars. ARA&A54:401–440. https://doi.org/10.1146/annurev-astro-081915-023322, 1603.02698

Palliyaguru N, Stinebring D, McLaughlin M, et al (2015) Correcting for interstellar scattering delay in high-precision pulsar timing: Simulation results. The Astrophysical Journal 815(2):89. https://doi.org/10.1088/0004-637X/815/2/89, URL https://dx.doi.org/10.1088/0004-637X/815/2/89

Pandhi A, Hutschenreuter S, West JL, et al (2022) A method for reconstructing the Galactic magnetic field using dispersion of fast radio bursts and Faraday rotation of radio galaxies. MNRAS516(4):4739–4759. https://doi.org/10.1093/mnras/stac2314, arXiv:2208.06417 [astro-ph.GA]

Park RS, Folkner WM, Williams JG, et al (2021) The JPL Planetary and Lunar Ephemerides DE440 and DE441. AJ161(3):105. https://doi.org/10.3847/1538-3881/abd414

Parthasarathy A, Shannon RM, Johnston S, et al (2019) Timing of young radio pulsars – I. Timing noise, periodic modulation, and proper motion. MNRAS489(3):3810–3826. https://doi.org/10.1093/mnras/stz2383, URL https://doi.org/10.1093/mnras/stz2383, https://academic.oup.com/mnras/article-pdf/489/3/3810/30029986/stz2383.pdf

Pearlman AB, Majid WA, Prince TA, et al (2018) Pulse Morphology of the Galactic Center Magnetar PSR J1745-2900. ApJ866(2):160. https://doi.org/10.3847/1538-4357/aade4d, arXiv:1809.02140 [astro-ph.HE]

Pennucci TT (2019) Frequency-dependent template profiles for high-precision pulsar timing. The Astrophysical Journal 871(1):34. https://doi.org/10.3847/1538-4357/aaf6ef, URL https://dx.doi.org/10.3847/1538-4357/aaf6ef

Pennucci TT, Demorest PB, Ransom SM (2014) Elementary Wideband Timing of Radio Pulsars. ApJ790(2):93. https://doi.org/10.1088/0004-637X/790/2/93, arXiv:1402.1672 [astro-ph.IM]

Pennucci TT, Demorest PB, Ransom SM (2016) Pulse Portraiture: Pulsar timing. Astrophysics Source Code Library, record ascl:1606.013, ascl:1606.013

Perera BBP, DeCesar ME, Demorest PB, et al (2019) The International Pulsar Timing Array: second data release. MNRAS490(4):4666–4687. https://doi.org/10.1093/mnras/stz2857, arXiv:1909.04534 [astro-ph.HE]

Phillips JA, Wolszczan A (1991) Time variability of pulsar dispersion measures. ApJL 382:L27–L30

Phinney ES (2001) A Practical Theorem on Gravitational Wave Backgrounds. arXiv e-prints astro-ph/0108028. https://doi.org/10.48550/arXiv.astro-ph/0108028, arXiv:astro-ph/0108028 [astro-ph]

Porayko NK, Noutsos A, Tiburzi C, et al (2019) Testing the accuracy of the ionospheric Faraday rotation corrections through LOFAR observations of bright northern pulsars. MNRAS483(3):4100–4113. https://doi.org/10.1093/mnras/sty3324, arXiv:1812.01463 [astro-ph.IM]

Rajagopal M, Romani RW (1995) Ultra–Low-Frequency Gravitational Radiation from Massive Black Hole Binaries. ApJ 446:543–549

Rajwade K, Gupta Y, Kumar U, et al (2014) Probing nulling in millisecond pulsars. In: Astronomical Society of India Conference Series, pp 73–77

Ramachandran R, Mitra D, Deshpande AA, et al (1997) Measurement of scatter broadening for 27 pulsars at 327 mhz. MNRAS 290:260–264

Ramachandran R, Demorest P, Backer DC, et al (2006) Interstellar plasma weather effects in long-term multifrequency timing of pulsar b1937+21. ApJ 645:303–313. https://doi.org/10.1086/500634, astro-ph/0601242

Ramani H, Trickle T, Zurek KM (2020) Observability of dark matter substructure with pulsar timing correlations. Journal of Cosmology and Astroparticle Physics 2020(12):033. https://doi.org/10.1088/1475-7516/2020/12/033, URL https://doi.org/10.1088/1475-7516/2020/12/033

Rankin JM (1983) Toward an empirical theory of pulsar emission. I. Morphological taxonomy. ApJ 274:333–358

Rankin JM (1986) Toward an empirical theory of pulsar emission. III. Mode changing ,drifting subpulses and pulse nulling. ApJ 301:901–922

Rankin JM (1990) Toward an Empirical Theory of Pulsar Emission. IV. Geometry of the Core Emission Region. ApJ352:247. https://doi.org/10.1086/168530

Ratcliffe JA (1972) An Introduction to the Ionosphere and Magnetosphere. Cambridge University Press, London

Rathnasree N, Rankin JM (1995) On the approach to stability of pulsar average profiles. ApJ 452:814

Reardon DJ, Zic A, Shannon RM, et al (2023a) The Gravitational-wave Background Null Hypothesis: Characterizing Noise in Millisecond Pulsar Arrival Times with the Parkes Pulsar Timing Array. ApJL951(1):L7. https://doi.org/10.3847/2041-8213/acdd03, arXiv:2306.16229 [astro-ph.HE]

Reardon DJ, Zic A, Shannon RM, et al (2023b) Search for an Isotropic Gravitational-wave Background with the Parkes Pulsar Timing Array. ApJL951(1):L6. https://doi.org/10.3847/2041-8213/acdd02, arXiv:2306.16215 [astro-ph.HE]

Reardon DJ, Main R, Ocker SK, et al (2025) Bow shock and Local Bubble plasma unveiled by the scintillating millisecond pulsar J0437−4715. Nature Astronomy 9:1053–1063. https://doi.org/10.1038/s41550-025-02534-6, arXiv:2410.21390 [astro-ph.HE]

Reddy SH, Kudale S, Gokhale U, et al (2017) A Wideband Digital Back-End for the Upgraded GMRT. Journal of Astronomical Instrumentation 6(1):1641011-336. https://doi.org/10.1142/S2251171716410117

Rickett B (2018-08) Intermittency and Anisotropy in the Ionized Interstellar Medium. In: Weltevrede P, Perera BBP, Preston LL, et al (eds) Pulsar Astrophysics the Next Fifty Years, pp 283–286, https://doi.org/10.1017/S1743921317009206

Rickett B, Johnston S, Tomlinson T, et al (2009) The inner scale of the plasma turbulence towards PSR J1644-4559. MNRAS 395(3):1391–1402. https://doi.org/10.1111/j.1365-2966.2009.14471.x

Rickett BJ (1975) Amplitude-modulated noise - an empirical model for the radio radiation received from pulsars. apj 197:185–191. https://doi.org/10.1086/153501

Rickett BJ (1990) Radio propagation through the turbulent interstellar plasma. araa 28:561–605

Rickett BJ, Coles WA, Bourgois G (1984) Slow scintillation in the interstellar medium. A&A 134:390–395

Roberts JA, Ables JG (1982) Dynamic spectra of pulsar scintillations at frequencies near 0.34, 0.41, 0.63, 1.4, 1.7, 3.2 and 5.0 GHz. MNRAS 201:1119–1138

Rogers AF, van Straten W, Gulyaev S, et al (2024a) Reducing Instrumental Errors in Parkes Pulsar Timing Array Data. ApJ973(2):94. https://doi.org/10.3847/1538-4357/ad656e, arXiv:2407.20015 [astro-ph.IM]

Rogers AF, van Straten W, Gulyaev S, et al (2024b) Reducing Instrumental Errors in Parkes Pulsar Timing Array Data. ApJ973(2):94. https://doi.org/10.3847/1538-4357/ad656e, arXiv:2407.20015 [astro-ph.IM]

Romani RW, Taylor JH (1983) An upper limit on the stochastic background of ultralow-frequency gravitational waves. ApJL 265:L35–L37

Romani RW, Blandford RD, Cordes JM (1987) Radio caustics from localized interstellar medium plasma structures. Nature 328:324–326

Russell CT (2001) Solar wind and interplanetary magnetic field: A tutorial. Washington DC American Geophysical Union Geophysical Monograph Series 125:73–89. https://doi.org/10.1029/GM125p0073

Rusul A, Wen ZG, Yuan JP, et al (2025) Revealing the Unseen: The Discovery of Long-Awaited Radiation from the Intermittent Pulsar PSR B1931+24. arXiv e-prints arXiv:2507.04816. https://doi.org/10.48550/arXiv.2507.04816, arXiv:2507.04816 [astro-ph.HE]

Rutherford N, Mendes M, Svensson I, et al (2024) Constraining the Dense Matter Equation of State with New NICER Mass–Radius Measurements and New Chiral Effective Field Theory Inputs. ApJL971(1):L19. https://doi.org/10.3847/2041-8213/ad5f02, arXiv:2407.06790 [astro-ph.HE]

Rutman J (1978) Characterization of phase and frequency instabilities in precision frequency sources: fifteen years of progress. IEEE Proceedings 66:1048–1075

Rutman R, Walls FL (1991) Characterization of frequency stability in precision frequency sources. IEEE 79:952–960

Sazhin MV (1978) Opportunities for detecting ultralong gravitational waves. Soviet Ast.22:36–38

Scargle JD (1981) Studies in astronomical time series analysis, I. Modelling random process in the time domain. ApJS 45:1–71

Schekochihin AA, Cowley SC, Dorland W, et al (2009) Astrophysical Gyrokinetics: Kinetic and Fluid Turbulent Cascades in Magnetized Weakly Collisional Plasmas. ApJS182(1):310–377. https://doi.org/10.1088/0067-0049/182/1/310, arXiv:0704.0044 [astro-ph]

Sesana A, Figueroa DG (2025) Nanohertz Gravitational Waves. arXiv e-prints arXiv:2512.18822. https://doi.org/10.48550/arXiv.2512.18822, 2512.18822

Seto N, Cooray A (2007) Searching for Primordial Black Hole Dark Matter with Pulsar Timing Arrays. ApJL659(1):L33–L36. https://doi.org/10.1086/516570, astro-ph/0702586

Shamohammadi M, Bailes M, Flynn C, et al (2024) MeerKAT Pulsar Timing Array parallaxes and proper motions. MNRAS530(1):287–306. https://doi.org/10.1093/mnras/stae016, 2401.06963

Shannon RM, Cordes JM (2010) Assessing the Role of Spin Noise in the Precision Timing of Millisecond Pulsars. ApJ725:1607–1619. https://doi.org/10.1088/0004-637X/725/2/1607, arXiv:1010.4794 [astro-ph.SR]

Shannon RM, Cordes JM (2012) Pulse Intensity Modulation and the Timing Stability of Millisecond Pulsars: A Case Study of PSR J1713+0747. ApJ761(1):64. https://doi.org/10.1088/0004-637X/761/1/64, arXiv:1210.7021 [astro-ph.SR]

Shannon RM, Cordes JM, Metcalfe TS, et al (2013) An Asteroid Belt Interpretation for the Timing Variations of the Millisecond Pulsar B1937+21. ApJ 766(1):5. https://doi.org/10.1088/0004-637X/766/1/5, arXiv:1301.6429 [astro-ph.SR]

Shannon RM, Osłowski S, Dai S, et al (2014) Limitations in timing precision due to single-pulse shape variability in millisecond pulsars. MNRAS443(2):1463–1481. https://doi.org/10.1093/mnras/stu1213, URL https://doi.org/10.1093/mnras/stu1213, arXiv:https://academic.oup.com/mnras/article-pdf/443/2/1463/3654347/stu1213.pdf [astro-ph.SR]

Shannon RM, Lentati LT, Kerr M, et al (2016) The disturbance of a millisecond pulsar magnetosphere. The Astrophysical Journal Letters 828(1):L1. https://doi.org/10.3847/2041-8205/828/1/L1, URL https://doi.org/10.3847/2041-8205/828/1/L1

Shapiro-Albert BJ, Hazboun JS, McLaughlin MA, et al (2021) A Study in Frequency-dependent Effects on Precision Pulsar Timing Parameters with the Pulsar Signal Simulator. ApJ909(2):219. https://doi.org/10.3847/1538-4357/abdc29, arXiv:2010.07301 [astro-ph.HE]

Sheikh SZ, MacDonald MG (2021) A statistical analysis of the nulling pulsar population. Monthly Notices of the Royal Astronomical Society 502(4):4669–4679. https://doi.org/10.1093/mnras/stab282, URL https://doi.org/10.1093/mnras/stab282, https://academic.oup.com/mnras/article-pdf/502/4/4669/36392370/stab282.pdf

Simard D, Pen UL, Marthi VR, et al (2019) Disentangling interstellar plasma screens with pulsar VLBI: combining auto- and cross-correlations. MNRAS 488(4):4963–4971. https://doi.org/10.1093/mnras/stz2046, arXiv:1810.07231 [astro-ph.IM]

Singha J, Surnis MP, Joshi BC, et al (2021) Evidence for profile changes in PSR J1713+0747 using the uGMRT. MNRAS507(1):L57–L61. https://doi.org/10.1093/mnrasl/slab098, arXiv:2107.04607 [astro-ph.HE]

Singha J, Joshi BC, Krishnakumar MA, et al (2024) Improving DM estimates using low-frequency scatter-broadening estimates. MNRAS535(1):1184–1192. https://doi.org/10.1093/mnras/stae2405, arXiv:2309.16765 [astro-ph.IM]

Smith CW, Vasquez BJ (2021) Driving and Dissipation of Solar-Wind Turbulence: What Is the Evidence? Frontiers in Astronomy and Space Sciences 7:114. https://doi.org/10.3389/fspas.2020.611909

Sobey C, Johnston S, Dai S, et al (2021) A polarization census of bright pulsars using the ultrawideband receiver on the Parkes radio telescope. MNRAS504(1):228–247. https://doi.org/10.1093/mnras/stab861, arXiv:2103.13838 [astro-ph.HE]

Sosa Fiscella SV, Lam MT, Agazie G, et al (2026) The NANOGrav 15 yr Dataset: Improved Timing Precision with Very Long Baseline Interferometry Astrometric Priors. ApJ999(2):156. https://doi.org/10.3847/1538-4357/ae39c9, 2509.21203

Spangler SR (2005) The strength and structure of the coronal magnetic field. Space Science Reviews 121(1):189–200. https://doi.org/10.1007/s11214-006-4719-7, URL https://doi.org/10.1007/s11214-006-4719-7

Spangler SR, Cordes JM (1988) Interstellar Scattering of the Radio Source 2013+370. ApJ332:346. https://doi.org/10.1086/166660

Spangler SR, Gwinn CR (1990) Evidence for an inner scale to the density turbulence in the interstellar medium. ApJ 353:L29–L32

Sprenger T, Main R, Wucknitz O, et al (2022) Double-lens scintillometry: the variable scintillation of pulsar B1508 + 55. MNRAS 515(4):6198–6216. https://doi.org/10.1093/mnras/stac2160, arXiv:2204.13985 [astro-ph.HE]

Sprenger T, Shi X, Wucknitz O, et al (2026) Imaging without visibilities: FAST-Effelsberg scintillometry of PSR B1508+55. A&A 709:A57. https://doi.org/10.1051/0004-6361/202659097

Srivastava A, Desai S, Kolhe N, et al (2023) Noise analysis of the Indian Pulsar Timing Array data release I. PhRvD108(2):023008. https://doi.org/10.1103/PhysRevD.108.023008, arXiv:2303.12105 [astro-ph.HE]

Stairs IH (2002) Pulsar Observations II. – Coherent Dedispersion Polarimetry, and Timing. In: Stanimirovic S, Altschuler D, Goldsmith P, et al (eds) Single-Dish Radio Astronomy: Techniques and Applications, pp 251–269

Stairs IH (2003) Testing general relativity with pulsar timing. Living Reviews in Relativity 6(1):5. https://doi.org/10.12942/lrr-2003-5, URL https://doi.org/10.12942/lrr-2003-5

Stappers BW, Archibald AM, Hessels JWT, et al (2014) A State Change in the Missing Link Binary Pulsar System PSR J1023+0038. ApJ790(1):39. https://doi.org/10.1088/0004-637X/790/1/39, arXiv:1311.7506 [astro-ph.HE]

Stinebring DR, Condon JJ (1990) Pulsar Flux Stability and Refractive Interstellar Scintillation. ApJ352:207. https://doi.org/10.1086/168528

Stinebring DR, Cordes JM, Rankin JM, et al (1984) Pulsar polarization fluctuations. I. 1408 MHz statistical summaries. ApJS 55:247–277

Stinebring DR, Ryba MF, Taylor JH, et al (1990) Cosmic gravitational-wave background: Limits from millisecond pulsar timing. PhRvL65(3):285–288. https://doi.org/10.1103/PhysRevLett.65.285

Stinebring DR, McLaughlin MA, Cordes JM, et al (2001) Faint Scattering Around Pulsars: Probing the Interstellar Medium on Solar System Size Scales. ApJL 549:L97–L100

Stinebring DR, Rickett BJ, Minter AH, et al (2022) A Scintillation Arc Survey of 22 Pulsars with Low to Moderate Dispersion Measures. ApJ941(1):34. https://doi.org/10.3847/1538-4357/ac8ea8, arXiv:2207.08756 [astro-ph.HE]

Suresh A, Cordes JM (2019) Induced Polarization from Birefringent Pulse Splitting in Magneto-ionic Media. ApJ 870(1):29. https://doi.org/10.3847/1538-4357/aaf004, arXiv:1808.09471 [astro-ph.HE]

Suresh A, Cordes JM, Chatterjee S, et al (2021) 4-8 GHz Spectrotemporal Emission from the Galactic Center Magnetar PSR J1745-2900. ApJ921(2):101. https://doi.org/10.3847/1538-4357/ac1d45, arXiv:2108.05404 [astro-ph.HE]

Sutton JM (1971) Scattering of pulsar radiation in the interstellar medium. MNRAS 155:51–64

Swiggum JK, Lorimer DR, McLaughlin MA, et al (2014) Arecibo Pulsar Survey Using ALFA. III. Precursor Survey and Population Synthesis. ApJ787(2):137. https://doi.org/10.1088/0004-637X/787/2/137, arXiv:1405.7953 [astro-ph.SR]

Tauris TM (2012) Spin-Down of Radio Millisecond Pulsars at Genesis. Science 335(6068):561. https://doi.org/10.1126/science.1216355, arXiv:1202.0551 [astro-ph.SR]

Taylor JH (1992) Pulsar Timing and Relativistic Gravity. Philosophical Transactions of the Royal Society of London Series A 341(1660):117–134. https://doi.org/10.1098/rsta.1992.0088

Taylor JH (1994) Binary pulsars and relativistic gravity. Reviews of Modern Physics 66(3):711–719. https://doi.org/10.1103/RevModPhys.66.711

Taylor JH, Weisberg JM (1982) A new test of general relativity - Gravitational radiation and the binary pulsar PSR 1913+16. ApJ253:908–920. https://doi.org/10.1086/159690

Taylor S (2021) Nanohertz Gravitational Wave Astronomy. Taylor & Francis, https://doi.org/10.1201/9781003240648

Thébault E, Finlay CC, Beggan CD, et al (2015) International geomagnetic reference field: the 12th generation. Earth, Planets and Space 67(1):79. https://doi.org/10.1186/s40623-015-0228-9, URL https://doi.org/10.1186/s40623-015-0228-9

Tiburzi C, Hobbs G, Kerr M, et al (2016) A study of spatial correlations in pulsar timing array data. MNRAS455(4):4339–4350. https://doi.org/10.1093/mnras/stv2143, 1510.02363

Tiburzi C, Shaifullah GM, Bassa CG, et al (2021) The impact of solar wind variability on pulsar timing. A&A647:A84. https://doi.org/10.1051/0004-6361/202039846, arXiv:2012.11726 [astro-ph.HE]

Tsai JWei, Simonetti JH, Kavic M (2017) Analysis of Scattering from Archival Pulsar Data using a CLEAN-based Method. PASP129(972):024301. https://doi.org/10.1088/1538-3873/129/972/024301, arXiv:1701.05675 [astro-ph.HE]

Turner JE, Stinebring DR, McLaughlin MA, et al (2023) Scattering Delay Mitigation in High-accuracy Pulsar Timing: Cyclic Spectroscopy Techniques. ApJ944(2):191. https://doi.org/10.3847/1538-4357/acb6fd, arXiv:2301.12089 [astro-ph.HE]

Turner JE, Dolch T, Cordes JM, et al (2024) A Cyclic Spectroscopy Scintillation Study of PSR B1937+21. I. Demonstration of Improved Scintillometry. ApJ972(1):16. https://doi.org/10.3847/1538-4357/ad5af9, arXiv:2404.13796 [astro-ph.HE]

Unger M, Farrar GR (2024) The Coherent Magnetic Field of the Milky Way. ApJ970(1):95. https://doi.org/10.3847/1538-4357/ad4a54, arXiv:2311.12120 [astro-ph.GA]

Vallisneri M, Taylor SR, Simon J, et al (2020) Modeling the Uncertainties of Solar System Ephemerides for Robust Gravitational-wave Searches with Pulsar-timing Arrays. ApJ893(2):112. https://doi.org/10.3847/1538-4357/ab7b67, arXiv:2001.00595 [astro-ph.HE]

van Haasteren R, Vallisneri M (2014) New advances in the Gaussian-process approach to pulsar-timing data analysis. PhRvD90(10):104012. https://doi.org/10.1103/PhysRevD.90.104012, arXiv:1407.1838 [gr-qc]

van Straten W (2002) Radio Astronomical Polarimetry and Phase-coherent Matrix Convolution. ApJ 568:436–442

van Straten W (2006) Radio astronomical polarimetry and high-precision pulsar timing. ApJ 642:1004–1011. https://doi.org/10.1086/501001, arXiv:astro-ph/0510334

van Straten W (2013) High-fidelity Radio Astronomical Polarimetry Using a Millisecond Pulsar as a Polarized Reference Source. ApJS204(1):13. https://doi.org/10.1088/0067-0049/204/1/13, arXiv:1212.3446 [astro-ph.IM]

Vargas AF, Melatos A (2024) Stochastic and secular anomalies in pulsar braking indices. MNRAS534(4):3410–3422. https://doi.org/10.1093/mnras/stae2326, arXiv:2410.04757 [astro-ph.HE]

Vedantham HK, Readhead ACS, Hovatta T, et al (2017) The Peculiar Light Curve of J1415+1320: A Case Study in Extreme Scattering Events. ApJ845(2):90. https://doi.org/10.3847/1538-4357/aa7741, arXiv:1702.05519 [astro-ph.GA]

Vivekanand M (2020) The 31 yr Rotation History of the Millisecond Pulsar J1939+2134 (B1937+21). ApJ890(2):143. https://doi.org/10.3847/1538-4357/ab6f75, arXiv:1908.03026 [astro-ph.HE]

Wahl HM, McLaughlin MA, Gentile PA, et al (2022) The nanograv 12.5 yr data set: Polarimetry and faraday rotation measures from observations of millisecond pulsars with the green bank telescope. The Astrophysical Journal 926(2):168. https://doi.org/10.3847/1538-4357/ac4045, URL https://dx.doi.org/10.3847/1538-4357/ac4045

Walker MA (2007) Extreme Scattering Events: Insights into the Interstellar Medium on AU-Scales. In: Haverkorn M, Goss WM (eds) SINS - Small Ionized and Neutral Structures in the Diffuse Interstellar Medium, p 299, https://doi.org/10.48550/arXiv.astro-ph/0610737, astro-ph/0610737

Walker MA, Demorest PB, van Straten W (2013) Cyclic Spectroscopy of The Millisecond Pulsar, B1937+21. ApJ779(2):99. https://doi.org/10.1088/0004-637X/779/2/99, arXiv:1310.3535 [astro-ph.HE]

Wang JB, Coles WA, Hobbs G, et al (2017) Comparison of pulsar positions from timing and very long baseline astrometry. MNRAS469(1):425–434. https://doi.org/10.1093/mnras/stx837, arXiv:1704.01011 [astro-ph.HE]

Wang N, Manchester RN, Johnston S (2007) Pulsar nulling and mode changing. Monthly Notices of the Royal Astronomical Society 377(3):1383–1392. https://doi.org/10.1111/j.1365-2966.2007.11703.x, URL https://doi.org/10.1111/j.1365-2966.2007.11703.x, https://academic.oup.com/mnras/article-pdf/377/3/1383/5689745/mnras0377-1383.pdf

Wang PF, Han JL, Han L, et al (2018) Jiamusi pulsar observations. II. Scintillations of ten pulsars. A&A618:A186. https://doi.org/10.1051/0004-6361/201833215, arXiv:1808.06406 [astro-ph.HE]

Wang Z, Wang J, Wang N, et al (2023) Study of pulsar flux density and its variability with Parkes data archive. MNRAS520(1):1311–1323. https://doi.org/10.1093/mnras/stad199, 2301.07367

Weisberg JM, Johnston S, Koribalski B, et al (2005) Discovery of Pulsed OH Maser Emission Stimulated by a Pulsar. Science 309(5731):106–110. https://doi.org/10.1126/science.1112494, arXiv:astro-ph/0505231 [astro-ph]

Weisberg JM, Nice DJ, Taylor JH (2010) Timing Measurements of the Relativistic Binary Pulsar PSR B1913+16. ApJ722(2):1030–1034. https://doi.org/10.1088/0004-637X/722/2/1030, arXiv:1011.0718 [astro-ph.GA]

Wharton RS, Chatterjee S, Cordes JM, et al (2019) VLA Observations of Single Pulses from the Galactic Center Magnetar. ApJ875(2):143. https://doi.org/10.3847/1538-4357/ab100a, arXiv:1905.00632 [astro-ph.HE]

Williamson IP (1972) Pulse broadening due to multiple scattering in the interstellar medium. I. MNRAS157:55. https://doi.org/10.1093/mnras/157.1.55

Williamson IP (1974) Pulse broadening due to multiple scattering in the interstellar medium-111. MNRAS166:499–512. https://doi.org/10.1093/mnras/166.3.499

Williamson IP (1975) The Broadening of Pulses Due to Multipath Propagation of Radiation. Proceedings of the Royal Society of London Series A 342(1628):131–147. https://doi.org/10.1098/rspa.1975.0016

Wolszczan A, Frail DA (1992) A planetary system around the millisecond pulsar PSR1257 + 12. Nature355(6356):145–147. https://doi.org/10.1038/355145a0

Wu Z, Coles WA, Verbiest JPW, et al (2023) Pulsar scintillation studies with lofar: Ii. dual-frequency scattering study of psr j0826+2637 with lofar and nenufar. Monthly Notices of the Royal Astronomical Society 520(4):5536–5543. https://doi.org/10.1093/mnras/stad429, URL https://doi.org/10.1093/mnras/stad429, https://academic.oup.com/mnras/article-pdf/520/4/5536/49333521/stad429.pdf

Xi H, Peng B, Staveley-Smith L, et al (2022) The fast ultra-deep survey (fuds): Observational strategy, calibration and data reduction. Publications of the Astronomical Society of Australia 39:e019. https://doi.org/10.1017/pasa.2022.16

Xu H, Huang YX, Burgay M, et al (2021) A sustained pulse shape change in PSR J1713+0747 possibly associated with timing and DM events. The Astronomer's Telegram 14642:1

Xu H, Chen S, Guo Y, et al (2023) Searching for the Nano-Hertz Stochastic Gravitational Wave Background with the Chinese Pulsar Timing Array Data Release I. Research in Astronomy and Astrophysics 23(7):075024. https://doi.org/10.1088/1674-4527/acdfa5, URL https://dx.doi.org/10.1088/1674-4527/acdfa5, arXiv:2306.16216 [astro-ph.HE]

Xu HW, Zhao RS, Gugercinoglu E, et al (2024) Statistical analysis of pulsar flux density distribution. The Astrophysical Journal 970(2):148. https://doi.org/10.3847/1538-4357/ad5001, URL https://doi.org/10.3847/1538-4357/ad5001

Yan WM, Wang N, Manchester RN, et al (2018) Single-pulse observations of the Galactic centre magnetar PSR J1745-2900 at 3.1 GHz. MNRAS476(3):3677–3687. https://doi.org/10.1093/mnras/sty470, arXiv:1802.07884 [astro-ph.HE]

Yao JM, Manchester RN, Wang N (2017) A New Electron-density Model for Estimation of Pulsar and FRB Distances. ApJ 835(1):29. https://doi.org/10.3847/1538-4357/835/1/29, arXiv:1610.09448 [astro-ph.GA]

You XP, Hobbs G, Coles WA, et al (2007) Dispersion measure variations and their effect on precision pulsar timing. MNRAS 378(2):493–506. https://doi.org/10.1111/j.1365-2966.2007.11617.x, astro-ph/0702366

Young O, Lam MT (2024-02) Redeveloping a CLEAN Deconvolution Algorithm for Scatter-broadened Radio Pulsar Signals. ApJ962(2):131. https://doi.org/10.3847/1538-4357/ad1ce7, 2306.06046

Yuan J, Wang N, Dang S, et al (2024) Characterizing Timing Noise in Normal Pulsars with the Nanshan Radio Telescope. Universe 10(3):105. https://doi.org/10.3390/universe10030105

Zhang YZ, Zhang HL, Wang J, et al (2024) UWLPIPE: Ultra-wide Bandwidth Low-frequency Pulsar Data Processing Pipeline. Research in Astronomy and Astrophysics 24(7):075011. https://doi.org/10.1088/1674-4527/ad4fc4

Zhu H, Baker D, Pen UL, et al (2023) Pulsar Double Lensing Sheds Light on the Origin of Extreme Scattering Events. ApJ 950(2):109. https://doi.org/10.3847/1538-4357/accde0, arXiv:2208.06884 [astro-ph.HE]

Zhu WW, Stairs IH, Demorest PB, et al (2015) Testing Theories of Gravitation Using 21-Year Timing of Pulsar Binary J1713+0747. ApJ809(1):41. https://doi.org/10.1088/0004-637X/809/1/41, arXiv:1504.00662 [astro-ph.SR]